PETROLOGY AND GEOCHEMISTRY OF THE LOWER GROUP CHROMITITES AND HOST ROCKS ON THE FARM ZANDSPRUIT 168 JP, WESTERN BUSHVELD COMPLEX

by

M J BOTHA, B.Sc.(Hons.)(Rhodes)

Thesis submitted in fulfilment of the
requirements for the degree of:

MASTER OF SCIENCE

in the Department of Geology, Rhodes University
P O Box 94, Grahamstown, 6140
South Africa.

JANUARY, 1987

D E C L A R A T I O N

1 December 1986

All work in this thesis is the original work of the writer except where specific acknowledgement is made to the work of others.

SIGNED : .....
M J BOTHA

ADDRESS: Oberholzer Geological Centre
Gold Fields of South Africa Limited
P O Box 6171
OBERHOLZER
2502

MB4AAG

A B S T R A C T

The eight Lower Group chromitite layers of the Ruighoek Pyroxenite in the area west of the Pilanesberg (LG1 - LG7), on the farm Zandspruit 168 JP, were sampled in borehole cores drilled through the succession. The stratigraphic succession falls within Cameron's (1980) units B to E of the Critical Zone. The lowermost layer of the Lower Group, the LG 1 chromitite, is located some 440 metres below the MG 2 (Middle Group) chromitite layer, above which the first appearance of cumulus plagioclase in the Complex is seen. By convention, this horizon is designated the top of the Ruighoek Pyroxenite in the Western Bushveld Complex. Homogeneous units of chromite-bearing orthopyroxenite (bronzitite), exhibiting inconspicuous layering defined in terms of variations in orthopyroxene grain-size, host all but one of the Lower Group layers; the LG 4 chromitite layer is exposed within an olivine-rich subunit 23 metres in thickness (C_3 subunit).

The cumulative thickness of chromitite is 2,92 metres or 0,8 per cent of the studied section, which is 381 metres in thickness. Minimum and maximum thicknesses of the LG1 - LG7 layers exposed in drill core are 17 and 81 centimetres, respectively, with minor chromitite layers ranging between 2 and 5 centimetres in thickness. Weighted mean Cr_2O_3 contents of units B to E vary between 1,17 and 3,22 per cent, with the latter estimate representative of the D_2 subunit which hosts the LG 6 chromitite layer. The LG 6 is correlated with the Steelpoort layer of the Eastern Bushveld Complex, and varies between 76 and 81 centimetres in thickness under a large portion of the farm Zandspruit. An undisturbed succession striking N15°E and dipping 12 - 15°E is depicted within the studied area, which is bounded on the eastern side by the north-striking Frank fault. Major folding of the layered succession is evident to the north of the area, where the layering adjacent to the trace of the fault dips 35° to the southwest.

Particular attention is paid in the present study to (a) the nature of chromitite layers and their host rocks, (b) the contrast between the mineral chemistry of weakly disseminated chromite and grains within massive ore layers, (c) concentrations of Cr, V, Ni, Co, Sc and Ti in orthopyroxene in relation to stratigraphic height, and levels of Sr, Ba and Zr associated with hypothetically pure, intercumulus plagioclase feldspar, and (d) possible mechanisms which induce crystallization of chromitite layers containing 50 per cent Cr_2O_3 from magma with a Cr content of less than 1 000 ppm.

Electron microprobe studies of chromite in relation to mineralogical and textural environment clearly reveal that (a) the proportions of Cr and Al cations are linked to paragenesis: higher Al/Cr ratios characterize olivine-bearing domains, whereas grains intergrown with plagioclase feldspar exhibit low Al/Cr ratios, and (b) Al contents rise with a decline in $Mg/(Mg + Fe^{2+})$ from high values to a value of 0,450, then decrease with a further decline in $Mg/(Mg + Fe^{2+})$. The paragenetically later trend is emphasized in a large population of chromite grains which escaped early encapsulation in orthopyroxene crystals and continued to grow in the environment of intercumulus plagioclase. Within- and between-sample compositional variation of grains in silicate-rich domains is modelled in terms of *in situ* growth increments, diffusive homogenization of zonal structures, and residence time within interstitial melt.

Fractionation trends, as measured by $Mg/(Mg + Fe^{2+})$ ratios in whole-rock and/or microprobe studies of orthopyroxene, are reversed in relation to stratigraphic height towards the top of the B unit and in the overlying C unit. These data are supported, for example, by lower vanadium contents and higher Ni/Sc ratios

in hypothetically pure orthopyroxene. Small olivine crystals in chromite-rich domains are enriched in Ni relative to coarse-grained olivine in adjacent dunite: a feature attributed to early isolation of primocrysts from magma in the former case, and in situ equilibration between olivine crystals and Ni-depleted residual melt in the latter case. Similarly, rising Ni contents and $Mg/(Mg + Fe^{2+})$ ratios of orthopyroxene with increasing stratigraphic height in the footwall of the LG 6 chromitite layer, linked to a progressive decline in orthopyroxene grain-size, are effects which may arise out of early separation of interstitial melt from orthopyroxene cumulates. A model is thus proposed which (a) links the thickness of chromitite layers to the vertical separation between successive layers or the thickness of fine-grained orthopyroxenite in the footwall, (b) ascribes copious nucleation of chromite to liquid mixing of this footwall derived, Cr-depleted contaminant with influxes of hot, primitive magma, and (c) tenders the notion that the present modal proportion of mesostasis in the footwall of a chromitite layer serves as a reciprocal measure of the volume of fractionated exudate.

ACKNOWLEDGEMENTS

Grateful acknowledgement is made to Messrs Rand Mines Limited for graciously affording access to drill cores ZS 3 and ZS 7, permission to use the surface geological map of farm Zandspruit, and for making available the assistance of Mr P Best. I would like to express my sincere gratitude to the South African C.S.I.R., National Geoscience Programme, Sub-Programme: Bushveld Complex, for their financial support over a period of twenty six months. I also extend my gratitude to Messrs Gold Fields of South Africa Limited for permission to use their typing and draughting facilities, and for allowing me an extended leave period in 1986.

I am indebted to Prof. H V Eales for his gracious encouragement, assistance and patience, and to whom I respectfully express my sincere thanks and submit my apologies for the delay in completion of the thesis. Grateful acknowledgement is also made for his granting me access to unpublished ideas and data. I wish to thank Dr. J S Marsh for his support, supervision and practical training in XRF procedures.

I would like to thank Prof. Tony Erlank for allowing me to use the microprobe facilities in the Department of Geochemistry, University of Cape Town, and Dick Rickard for his professional assistance. I also thank Dennis Gouws and Rob Skae for their very considerable help on the Cambridge Microscan at Rhodes University.

Grateful thanks are extended to my fellow research students at Rhodes University, specifically Moose Kruger, Roger Scoon, Mike and Teral Bowen and Andrew Mitchell, all of whom participated in this work to varying degrees by bearing the brunt of certain ideas. I would like to thank Andrew and Dr. Ivan Reynolds, in particular, for their assistance with logging and sampling of drill cores, and Prof. G von Gruenewaldt for providing samples of Lower Zone lithologies. Grateful acknowledgement is made to Lesley Cooper for her constant encouragement and support, and the support of Gold Fields senior staff members, viz., Messrs D Campbell, H Meadon and J P van Zyl, and my colleagues Lessley Walker, Etienne Mouton and Hans Drent.

I would like to thank Cecile Mouton for typing the bulk of the manuscript and Ronel Siepker for draughting the figures.

C O N T E N T S

C O N T E N T S (Cont.)

C O N T E N T S (Cont.)

* * * * *

APPENDICES

LIST OF FIGURES

LIST OF FIGURES (Cont.)

LIST OF FIGURES (Cont.)

LIST OF FIGURES (Cont.)

LIST OF FIGURES (Cont.)

LIST OF FIGURES (Cont.)

LIST OF FIGURES (Cont.)

LIST OF TABLES

LIST OF TABLES (Cont.)

Parantheses denote Tables submitted in text at the given page number

1. INTRODUCTION

Chromite is an early-crystallizing member of the multicomponent spinel group which has the general structural formula AB_2O_4, where A represents Fe(II), Mg, Mn, Ni and Zn, and B represents Cr, Al, Fe(III), V and (Fe(II) + Ti(IV)). In mafic layered complexes, the mineral chemistry of chromite is dominated by a solid-solution of the end-members $FeCr_2O_4$ (ferrochromite), $MgCr_2O_4$ (magnesio- or picrochromite), $MgAl_2O_4$ (spinel sensu stricto), $FeAl_2O_4$ (hercynite) and Fe_3O_4 (magnetite). Ti, Mn, Zn and Ni are present at only minor or trace-element levels. Vanadiferous Fe-Ti spinels occur at stratigraphically higher levels in some layered complexes, separated from the last occurrences of chromite by a considerable vertical thickness of spinel-free gabbroic rocks.

Chromite serves as a highly effective scavenger of chromium in magmatic systems. For example, whereas initial levels of Cr in basic magmas are in the range 200 - 1 500 ppm (Hill and Roeder, 1974; Maurel and Maurel, 1982b), Cr_2O_3 may constitute as much as 50 per cent of the equilibrium spinel phase. Thus, the enrichment factor may be in excess of 1 000 for Cr but close to unity for other elements (e.g., Ti and Al). The ability of spinels to incorporate very substantial amounts of the first row transition elements, and their ubiquitous occurrence in mafic and ultramafic rocks of the crust and upper mantle, stimulates particular interest in this group.

The potential importance of the chemistry and phase relationships of the spinel phase as a "petrogenetic indicator" of the original magma composition, its liquidus temperature, paragenetic order of the phases separating from it, the ambient oxygen fugacity, pressure and subsolidus equilibration processes, has been stressed by numerous authors. Hence, spinel mineral chemistry is potentially of considerable value in the fields of:

1. Geobarometry (Green, 1964; Irvine, 1967; Basu and MacGregor, 1975; Sigurdsson and Schilling, 1976; Sigurdsson, 1977; Suzuki and Shiraki, 1980).

2. Geothermometry (Buddington and Lindsley, 1964; Irvine, 1965; Jackson, 1969; Evans and Frost, 1975; Medaris, 1975; Fujii, 1977; Sinton, 1977; Roeder et al., 1979; Sack, 1982; Lehmann, 1983).
3. Metamorphism (Rumble, 1976; Eales and Reynolds, 1983).
4. Ore genesis (Groves et al., 1977; Eales and Reynolds, op. cit.).

This leads to the suggestion that the only requirement necessary for the resolution of many petrological problems is a quantitative study of the spinel phase. Unfortunately, the realization of this rationale is inhibited by severe problems arising out of essentially two factors:

1. An inadequate knowledge of site occupancy within the spinel structure, which is of critical importance in calculating cation activities (Osborne et al., 1981; Sack, 1982).
2. Spinels exhibit a pronounced compositional sensitivity towards their immediate chemical and physical environment (Roeder et al., 1979; Wilson, 1982).

The former leads to uncertainties in the application of thermodynamic principles, and the latter to difficulties in assessing the degree to which observed compositions may have departed from original liquidus compositions during slow cooling. Ostensibly, chromite remains reactive down to blocking temperatures as low as 600°C (Wilson, 1982). Furthermore, cation diffusivities in oxides appear to be considerably more rapid than in associated ferromagnesian silicates (Eales et al., 1980; Wilson op. cit.). Hence partial or complete homogenization of original and inherited chemical characteristics may effectively camouflage the primary, equilibrium relationships.

By virtue of these uncertainties, it is difficult to gauge the relative importance of a number of parameters which are known to affect spinel composition (reviewed by Eales and Marsh, 1983). A brief discussion of the more significant parameters is given below, and a fuller evaluation will be developed in appropriate parts of the subsequent text.

1. FRACTIONATION

In the case of rapidly cooled rocks, typified by fast growth rates and suppressed exsolution processes, compositional changes as fractionation proceeds would be apparent in the textural relationships and preservation of zonal structures (El Goresy, 1976; El Goresy et al., 1976; Haggerty, 1976; Eales, 1979; Eales and Snowden, 1979; Eales et al., 1980).

In such rocks, there is commonly no hiatus in Cr-spinel crystallization, and a correlation of decreasing Mg/Fe^{2+}, Cr_2O_3 content, and Fe^{3+} + Ti enrichment with declining temperatures is often evident. Reversed orders of crystallization of plagioclase and clinopyroxene after olivine may induce diverse Cr - Al - Fe^{3+} substitution trends in individual grains which reflect the silicate paragenetic order. An important distinction between slowly - and rapidly-cooled magmas is that, in the latter, the duration of spinel crystallization commonly spans a major part of the solidification period, resulting in a wider compositional range.

2. CRYSTAL SETTLING

Until fairly recently, fractionation and crystallization mechanisms of stratiform complexes have been discussed almost exclusively on the basis of the crystal settling hypothesis (Wager and Brown, 1968). Settling of primocrysts was considered to be effective over a considerable thickness of magma or restricted to static layers at the base of the liquid column (Jackson, 1961). Currently, the possibility of in situ nucleation and growth at the floor has been gaining favour (Campbell, 1978; McBirney and Noyes, 1979). In either event, the composition of the residual liquid will necessarily change with progressive crystallization, and cryptic variation in spinel composition is common. It is to be anticipated that rhythmic nucleation of olivine, pyroxene or plagioclase may yield opposing compositional results and cryptic changes may therefore not vary as a smooth function of stratigraphic height in larger intrusions. If resorption of settling olivine primocrysts occurs at depth, as has

been suggested by McDonald (1967), pronounced reversals in the composition of spinels may result.

3. SUBSOLIDUS EQUILIBRATION

The importance of subsolidus equilibration between olivine and spinel has been emphasized by the work of Irvine (1965), Jackson (1969) and Roeder et al. (1979). The principles developed by these authors stress that it is not possible to consider the composition of spinels in isolation from the associated silicates, since the empirical distribution coefficient K_D for the following exchange reaction increases as temperatures decline:

$$Fe^{2+} \text{ (olivine)} + Mg \text{ (spinel)} = Mg \text{ (olivine)} + Fe^{2+} \text{ (spinel)}$$

$$K_D = (X_{Mg}/X_{Fe}{}^{2+})^{olivine} \cdot (X_{Fe}{}^{2+}/X_{Mg})^{spinel}$$

(assuming ideal mixing of Fe^{2+} and Mg in both phases)

where,

$X_{Mg} = Mg/(Mg + Fe^{2+})$

$X_{Fe}{}^{2+} = 1 - X_{Mg}$

and Fe and Mg are given as cation proportions.

Jackson (1969) was the first to introduce experimentally determined thermodynamic constants into the relationship in an attempt to calibrate K_D as a primary geothermometer, and derived the following equation:

$$T = \frac{5580Y_{Cr} + 1018Y_{Al} - 1720Y_{Fe}{}^{3+} + 2400}{0{,}90Y_{Cr} + 2{,}56Y_{Al} - 3{,}08Y_{Fe}{}^{3+} - 1{,}47 + 1{,}987 \ln K_D}$$

where,

T = absolute temperature (K)

$Y_{Cr} = Cr/(Cr + Al + Fe^{3+})$

$Y_{Al} = Al/(Cr + Al + Fe^{3+})$

$Y_{Fe}^{3+} = Fe^{3+}/(Cr + Al + Fe^{3+})$ in octahedral spinel sites.

$Cr + Al + Fe^{3+} = 1$ and Cr, Al and Fe^{3+} are given as cation proportions.

Application of this geothermometer to a wide variety of rocks has clearly shown that uncertainties in the thermodynamic data used by Jackson introduce major errors and that calculated temperatures are often unrealistic (Evans and Frost, 1975; Roeder et al., 1979). The inadequacies of the thermodynamic data prompted empirical calibrations (Evans and Frost, op. cit.; Medaris, 1975) and the choice of alternative thermodynamic data which gave a better correspondence between calculated and experimentally determined values (Roeder et al., op. cit.). A review by Wilson (1982) provides a comparison of results afforded by the different methods. Additional difficulties arise from the observation that the value of K_D is also a function of the modal silicate/spinel ratio (Jackson, 1969; Dick, 1977; Roeder et al., op. cit.; Wilson, op. cit.).

Despite the present discrepancies, it remains clear that subsolidus equilibration represents a potent mechanism for inducing chemical variability in spinel composition, and that calculated temperatures are not primary liquidus temperatures in the case of slowly cooled rocks. In support of this claim, Henry and Medaris (1980) have suggested that localised disequilibrium in olivine-pyroxene-spinel assemblages results from the cessation of equilibration between pyroxenes at temperatures higher than those which preclude olivine-spinel exchange reactions.

4. PRESSURE

The possibility that the Al/Cr ratios of spinels are primarily a function of PT conditions has been considered by many authors. Two opposing viewpoints have been adopted with no apparent reconciliation between them:

(a) Aluminous spinels are stabilized at high pressures (Green, 1964; Sigurdsson and Schilling, 1976; Sigurdsson, 1977; Fisk and Bence, 1980; Suzuki and Shiraki, 1980), and

(b) Pressure has a negligible influence on the trivalent cation proportions of spinels (Dickey and Yoder, 1972; Sinton, 1977).

However, Eales and Marsh (1983) have suggested that the Al/Cr ratios of spinels are a function of the preferential partitioning of Al into either garnet, aluminous pyroxenes or plagioclase and are thereby indirectly influenced by pressure. Furthermore, pressure changes will not perturb the Al/Cr ratio unless reactions occur which produce additional phases which have a higher preference for aluminium.

5. OXYGEN FUGACITY

The role of oxygen fugacity in controlling the compositional variation of spinel and associated ferromagnesian silicates, and in stimulating spinel crystallization, has frequently been stressed (e.g., Ulmer, 1969; Hill and Roeder, 1974; Haggerty, 1976; Fisk and Bence, 1980). Experimental observations indicate that at basaltic magmatic temperatures the crystallization of Cr-spinel may be interrupted at oxygen fugacities less than fO_2 = -log 8,6 (Hill and Roeder, op. cit.), and wholly suppressed at oxygen fugacities lower than fO_2 = -log 10 (Fisk and Bence, op. cit.). In addition, the relative amounts of ferrous and ferric iron in Cr-spinels are deemed to be a function of their levels in the magma during crystallization. However, a fundamental question which has been raised is whether the compositions of Cr-spinels adequately reflect magmatic fO_2 conditions.

Irvine (1965) showed that, in theory, it is possible to establish relative levels of fO_2 in equilibrium olivine-orthopyroxene-spinel assemblages by plotting the spinel compositional parameters $Y_{Fe^{3+}}$ versus $Mg/(Mg + Fe^{2+})$, where $Y_{Fe^{3+}} = Fe^{3+}/(Cr + Al + Fe^{3+})$. Other authors have attempted to quantify the relationship between the fO_2 of the magma and the Fe^{2+}/Fe^{3+} (oxidation) ratio of the spinel which has crystallized from it (Maurel and Maurel, 1982c; Roeder, 1982; Wilson, 1982). The following equation is given by Roeder (op. cit.):

$$\log(Fe^{2+}/Fe^{3+})sp = -0,99 - 0,13 \log fO_2$$

at T = 1 200°C and log fO_2 = -0,68 to -9,0, and by Wilson (op. cit.):

$$\log(Fe^{2+}/Fe^{3+})sp = -0,741 - 0,139 \log fO_2$$

for the temperature range 1 175 - 1 270°C. The potential importance of this approach as a means of establishing the fO_2 parameter of magmatic liquids needs no emphasis and it serves as a more convenient adjunct to solid-electrolyte, intrinsic oxygen fugacity determinations. Unfortunately, the broad application of these equations is constrained by several factors. For example, subsolidus processes may severely alter the original Fe^{2+}/Fe^{3+} ratios; it has been shown by Bevan (1982) and Eales et al. (1984), pertaining to the Rhum and Skye and Bushveld complexes, respectively, that deuteric oxidation of olivine to magnetite + Mg-rich olivine releases Fe_3O_4 which may be incorporated within the coexisting Cr-spinel phase. This would obviously lead to a substantial decrease in the original $(Fe^{2+}/Fe^{3+})_{sp}$ ratio. Further discrepancies may stem from analytical errors and data reduction procedures. The electron microprobe is incapable of distinguishing Fe-speciation and mineral formulae are conventionally calculated on an assumption of stoichiometry. This may be unjustified in some cases.

6. LATE-STAGE REACTION WITH INTERCUMULUS LIQUIDS

Reactions between early-crystallized spinels and cooling intercumulus liquid have been cited as one of the major causes of within-sample variability of spinel compositions in layered cumulate rocks (Henderson and Suddaby, 1971; Henderson, 1975; Cameron, 1977; Ridley, 1977; Hamlyn and Keays, 1979; Henderson and Wood, 1981). For example, continuous reaction between spinels and liquid in the Rhum intrusion has led to a trend of Fe^{3+}-enrichment with Y_{Cr} remaining constant (Henderson, op. cit.). On the other hand, Ridley has documented the following peritectic reaction in an alkali olivine basalt from Rhum:

Al-spinel + melt = Cr-spinel + plagioclase
(with Fe^{3+} remaining constant).

Evidence for the mobility of late-stage intercumulus liquids in slowly cooled layered intrusions has been tendered by Eales (1980) and Irvine (1978 and 1980b). It is envisaged that ingress of presumably volatile-enriched, differentiated liquid into a compacting crystal mush, from underlying layers, may lead to crystal-liquid disequilibrium. The resulting equilibration reactions would tend to further exaggerate the existing spectrum of texturally related spinel compositions.

A proper assessment of the influence of the parameters listed above requires an exceptionally thorough programme of sampling and analysis. Whereas, for example, cryptic variations in olivine and pyroxene may be closely linked with stratigraphic height within a complex, or within its constituent cyclic units, it is by no means conclusively established that the same applies to chrome-spinels. For that reason, the present analytical programme has concentrated on comparisons of the nature of disseminated chromite with that of adjacent anchimonomineralic layers, the correlations between grain-size and composition, and the influence of the immediate host silicate phase.

The Bushveld Complex is a major repository of chromiferous spinels. Apart from accessory occurrences in the Lower Zone, chromitite layers occur within the pyroxenitic and anorthositic subzones of the Critical Zone, which extends from approximately 1 700 m to 3 000 m above the floor of the intrusion. A major hiatus in spinel crystallization exists above the Critical Zone, before the Fe-Ti-spinel phase titanomagnetite appears within the Upper Zone, a gap of ca. 4 000 m (South African Committee for Stratigraphy, 1980; hereinafter denoted SACS). Within the Critical Zone the number of well-developed chromitite layers may be in the region of 30 (Irvine, 1967), but generally the average is 13 "seams" (De Waal, 1975). Additional thin or impersistent layers, or zones of disseminated chromite, are a typical feature. The major questions which are raised may therefore be summarized as follows:

(a) What triggers the nucleation of spinels in copious amounts capable of yielding anchimonomineralic layers approaching one metre in thickness?

(b) Do chromitite layers result from a process of *in situ* growth, or are they deposited by gravitative accumulation of crystals, or perhaps by currents bearing crystals in suspension?

(c) Why does the Lower Zone, composed of approximately 1 700 m of harzburgite, pyroxenite and dunite, contain no more than accessory levels of chromite, a phase which commonly is amongst the first phases to appear on the liquidus?

(d) What causes the disappearance of chromite as a nucleating phase at the top of the Critical Zone?

The present contribution focuses on the first and second questions raised above. The study is based on only a portion of the Lower Critical Zone (Ruighoek Pyroxenite) succession, and cannot therefore address all of the questions raised, nor necessarily provide satisfactory solutions to the others. It does, however, provide quantitative data relating to that portion that has been sampled, and makes an attempt to interpret what is seen there.

2. LITERATURE REVIEW

The occurrence of chromiferous spinels within layered complexes (most notably the Bushveld Complex, Muskox, Stillwater, Great Dyke and Cuillin complexes), minor intrusions (e.g., of the Karoo Tholeiitic Province), basaltic and komatiitic lavas, Alpine peridotites, nodules entrained by kimberlites and alkaline basalts, metamorphic- and lunar rocks and meteorites, has lead to a formidable literature. The present review makes no pretence, therefore, to a complete survey of the occurrence of this mineral. Rather, it is confined to the more relevant parts of this literature. Reviews embracing a wide scope are available in Stevens (1944), Deer et al. (1962), Cameron (1964), Irvine (1967), Wager and Brown (1968), Cameron and Desborough (1969), Stanton (1972), Bunch and Olsen (1975), Malpas and Strong (1975), El Goresy (1976), Haggerty (1976), Rumble (1976), Eales et al. (1980), Eales and Reynolds (1983), and Duke (1983). In this spirit, the review will therefore be confined to the relevance of:

(a) The solubility of Cr in mafic magmas.
(b) The occurrence of chromite within cyclic units constituting layered complexes.
(c) Studies of Cr-spinel within smaller intrusions which do not contain significant amounts of chromite.
(d) Experimental studies leading to the interpretation of natural occurrences.

An assessment of the chromium contents of planetary basalt suites by contributors to the Basaltic Volcanism Study Project (1981) has indicated that, in contrast to komatiites and lherzolites (compositions presumed to approximate that of the earths upper mantle) or mare basalts, terrestrial basalts are characterized by negative chromium anomalies. Furthermore, present-day Mid-Ocean Ridge basalts possess lower Cr concentrations than Archean basalts of equivalent $Mg/(Mg + Fe^{2+})$ mole ratio. Similarly, Eales and Reynolds (1983) have reviewed the compositional variation of chromite in some extrusive and shallow-level intrusive rocks (e.g., Bushveld Complex) of Southern Africa and as shown by the Cr^{3+} content of respective spinel populations, the data suggest that there is a progressive

decline in Cr contents of geologically younger magmas. Explanations proposed to account for the above-mentioned features include:

1. A higher Cr content in the Archean mantle.
2. Different depths of melting.
3. Different thermal gradients.
4. Different degrees of partial melting.
5. Sequential melting.
6. Oxidation state of chromium (i.e., the Cr^{2+}/Cr^{3+} ratio) reflecting differences in fO_2 of the source rocks.
7. Terrestrial melts have fractionated Cr-spinel while in transit to the surface.
8. Mantle heterogeneity.

Thermal constraints, in particular, appear to represent a dominant criterion. For example, the Basaltic Volcanism Study Project (op.cit.) has suggested that komatiites are products of high degrees of partial melting or of sequential melting in which Cr-spinel and clinopyroxene are non-residual phases in the source region. In other basalt types, it is believed that the Cr anomaly results from Cr-spinel being retained in the fusion residua and/or intratelluric fractionation of Cr-spinel occurs. With respect to the oxidation state of chromium in the mantle, the bulk Cr content of a partial melt may be strongly dependent upon the fO_2 conditions of the source and the mineralogy of chromium in the mantle (Burns, 1975a, 1975b, and 1976; Burns and Burns, 1975). Studies of Cr partitioning under controlled fO_2 conditions by Akella et al. (1976), Huebner et al. (1976) and Schreiber and Haskin (1976) have indicated that, whereas Cr^{2+} would preferentially partition into the liquid phase during partial melting (D_o^{Cr} less than unity), Cr^{3+} is retained in octahedral sites of residual Cr-spinel, pyroxenes and possibly olivine. The $(Ar)3d^3$ electronic configuration of the Cr^{3+} ion bestows on it the highest crystal field stabilization energy (CFSE) in crystalline octahedral sites of all the valence states of the first series transition elements. Hence, on the basis of the quasi-crystalline model of silicate melts, the following equilibrium would strongly favour the left hand side:

$$(Cr^{3+}_{oct})^{crystal} \underset{\text{crystallization}}{\overset{\text{fusion}}{\rightleftharpoons}} (Cr^{3+}_{oct})^{melt} + (Cr^{3+}_{tet})^{melt}$$

where "crystal" may be spinel, garnet, pyroxene or olivine, "oct" = octahedral and "tet" = tetrahedral coordination with oxygen (Burns, 1975a and 1976). Furthermore, by virtue of a radius ratio ($r_{Cr^{3+}}/r_{O^{2-}}$) of 0,44, Cr^{3+} is expected to remain in six-fold coordination in mantle minerals irrespective of possible phase transformations that may occur in response to pressure changes.

Although evidence for the presence of the Cr^{2+} ion in silicate melts and minerals is circumstantial (reviewed by Schreiber and Haskin, 1976), experimental data reported by Schreiber and Haskin (op. cit.) indicate that the Cr^{2+} oxidation state should represent as much as 90 per cent of the total chromium in melts at oxygen fugacities more reducing than 10^{-9} - 10^{-11} atmospheres. However, under redox conditions envisaged to be characteristic of terrestrial basaltic magmas (estimates are given by the Basaltic Volcanism Study Project, 1981), chromium is thought to be present exclusively as the Cr^{3+} ion, possibly in response to the following redox interaction of Cr and Fe in the melt (Schreiber and Haskin, op. cit.):

$$Cr^{3+} + Fe^{2+} = Cr^{2+} + Fe^{3+} \quad \text{(equation 11, p. 1237)}$$

where oxidation of Cr^{2+} is favoured by a large difference in oxidation potentials and the anticipated excess of Fe^{3+}. In terms of Burns' (1975a and 1976) partitioning scheme for Cr^{2+} and Cr^{3+} ions between spinel, garnet, pyroxene, olivine and derivative high-pressure polymorphs in the mantle, pressure-released oxidation of most Cr^{2+} to Cr^{3+} occurs in the upper mantle. This may lead to the nucleation of chromite crystallites in olivine, as Cr^{2+} is believed to be stabilized and enriched in tetragonally (Jahn-Teller) distorted, olivine M1 octahedral sites under reducing and/or high-pressure conditions. For reviews of the chromium contents of olivines occluded in diamonds, other terrestrial occurrences and in lunar olivines, the reader is referred to Burns (1975b), Schreiber and Haskin (1976), Matzat and Shiraki (1978), Brown (1980), Deer et al. (1982) and Hervig and Smith (1982). An additional site for

Cr^{2+} ions may be in tetrahedral coordination in spinels of the type $(Mg,Cr^{2+})(Cr^{3+})_2O_4$, which have been synthesized under reducing conditions by Stubican and Greskovich (1975). However, Cr^{2+} has not been detected in lunar spinels. Though this observation tends to negate the presence of divalent chromium in primitive melts, it is possible that the low CFSE of Cr^{2+} in tetrahedral and octahedral spinel sites results in ineffectual competition with Cr^{3+} and Fe^{2+} ions (Mao and Bell, 1975).

It would appear that oxidation of Cr^{2+} in Fe-bearing systems may have played a role in establishing the saturation limits of chromium in basic melts but, while the Cr oxidation ratio within source regions of the earths mantle as a function of geological time and P,T - fO_2 conditions remains unknown, it is perhaps quite acceptable to consider the solubility of chromium strictly in terms of the trivalent cation. By implication, the role of intensive variables, such as pressure, on melt structure may be of importance. Irvine (1977a) has shown that liquids with a low Al_2O_3 abundance require a greater amount of Cr_2O_3 in order to saturate the melt with chromite. This is consistent with the observations of Irvine (1975) and Schreiber and Haskin (1976), and considerations regarding the structural role of Al in silicate liquids (Bottinga and Weill, 1972; Kushiro, 1975; Hess, 1980), viz., aluminous liquids have fewer octahedral sites available for Cr^{3+} ions. Furthermore, it has been suggested that experimentally detected decreases in the viscosities of basaltic and aluminosilicate melts are related to pressure-induced Al^{IV} to Al^{VI} transformations which cause depolymerization of (Al,Si)-O-(Al,Si) linkages (Mysen, 1976; Burnham, 1979). The influence of these coordination changes on crystal-liquid partition coefficients is discussed by Mysen (op. cit.) and Kushiro (op. cit.), but it is extremely difficult to gauge the extent to which the stability field of chromite, a phase in which all the aluminium is octahedrally coordinated, is influenced during ascent of a depolymerized mafic magma.

Whereas Cr^{3+} is a major constituent of chrome spinels, it is a trace element within magmatic liquids. The latter is a function of the geochemical behaviour of trivalent chromium during fusion and crystallization processes, as has been mentioned previously, and the

predominance of olivine in the mantle, a phase which does not accommodate substantial amounts of Cr^{3+} in its structure since coupled substitutions of the following type are not permissible:

$$Cr^{3+} + Al^{3+} = (Mg,Fe)^{2+} + Si^{4+}$$ (Burns, 1975b; Brown, 1980)

Hill and Roeder (1974) and Schreiber and Haskin (1976) indicate, respectively, that at levels as low as 100 ppm Cr or where only a small fraction of the chromium may exist as Cr^{3+} in a melt at atmospheric pressure, Cr^{3+} ions may saturate the melt and chromite is capable of nucleation. Ridley (1979) has presented an explanation for this feature on the basis of the high octahedral site preference energy of the Cr^{3+} cation and the quasi-chemical (Toop and Samis) polymerization model (a review of the latter is available in Wood and Fraser (1978)). The upper solubility limit in natural mafic magmas is not known, but estimates are possible:

ppm Cr	Source of information
300	Hill and Roeder (1974); experimental
1 460	Maurel and Maurel (1982b); experimental
970	Davies et al. (1980); parental Bushveld magma
1 000	Cameron (1978); Bushveld magma
1 600	Irvine (1977b); maximum of Muskox magma
1 250	Sharpe and Hulbert (1982); early Bushveld magma
620	Campbell and Murck (1984); experimental (1300°C)

These estimates are significant when mass balance calculations are made to estimate the amount of liquid from which the spinel phase has separated, i.e., the R factor of chromite (Keays and Campbell, 1981; Campbell et al., 1983). For example, the UG 1 cyclic unit at Union Section Mine averages 2,6 per cent Cr_2O_3 (de Klerk, 1981) and Cameron (1980) has estimated that the weighted average Cr_2O_3 content of the entire Lower Critical Zone in the Eastern Bushveld Complex is 2,08 per cent. The discrepancy between these values and the estimated solubility is clearly a critical feature. Resolution of this paradox is, however, possible in terms of the concept of cyclic units within layered complexes (Jackson, 1961 and 1970; Campbell, 1977). This

concept permits the emplacement of large volumes of liquid, from which a limited degree of crystallization may occur, before the liquid is in turn displaced by a further irruption of magma of the same derivation. The new magma may be regarded as being undepleted with respect to chromium. Operation of this concept has been elegantly illustrated by a documentation of cyclic Ni variations through the Muskox Intrusion (Irvine, 1978 and 1980b), and of Ni and $Mg/(Mg + Fe^{2+})$ variations in olivine and orthopyroxene within cyclic units of the Zimbabwean Great Dyke (Wilson, 1982). Similar features have been recognized in ophiolite complexes and with respect to the Bushveld magma chamber, periodic influxes of new magma have been proposed by numerous authors to account for changes in bulk composition (e.g., Reuning, 1937; Lombaard, 1934; Kuschke, 1940; Van der Walt, 1942; Truter, 1955; Schwellnus et al., 1962; Cousins, 1964 and 1969; Cameron, 1970; Coertze, 1974; Vermaak, 1976; Hamilton, 1977).

In the Stillwater Complex, the Hartley complex of the Great Dyke, and a portion of the Lower Zone of the Bushveld Complex south of Potgietersrus (Hulbert and von Gruenewaldt, 1980), identification of cyclic units in ultramafic members is based on systematic repetitions in the appearance of cumulus phases. A typical unit may be composed of the following lithological succession:

Top : orthopyroxenite
olivine - bronzitite (± chromite)
dunite and/or harzburgite (+ chromite)
chromitite and/or olivine - chromitite
Bottom: dunite (+ chromite)

Characteristically, concentrations of chromite occur in olivine-rich assemblages at or near the base of a cycle. This is followed upwards by olivine - orthopyroxene cumulate assemblages which generally occur as the middle part of each unit, marking the transition from dunite (+ chromite) to chromite-free orthopyroxenite. These features are reviewed by Morse (1980). Recognition of cyclic units on the above basis in the Lower Critical Zone of the Bushveld Complex has not been possible. However, a detailed study by McDonald (1967) indicated at least 20 possible cyclic units in borehole sections of the Ruighoek

Pyroxenite (i.e., the Lower Critical Zone in the Western lobe of the complex) on the farm Ruighoek 169 JP, based on reversals in cumulus orthopyroxene grain-sizes and Fe content. Stemming from an evaluation of these data, Jackson (1970) suggested that chromite-rich layers in this particular section occur at the base of some cycles which are depicted in continuous stratigraphic intervals of orthopyroxenite.

A concept that is currently favoured by many, as an alternative to multiple intrusion, is that of double-diffusive convection. The relevance of the process to magma chambers was first mooted by Turner and Gustafson (1978), and developed in some detail by McBirney and Noyes (1979). This hypothesis requires the stratification of a liquid column into a sequence of stacked cells of limited volumes, each cell differing in composition from the one above, and each in a state of vigorous convection. This is in response to the opposing effects of temperature and composition on liquid density and the large disparity in the diffusivities of heat and chemical components. In situ crystallization is envisaged in the model and its variants proposed by Irvine (1980a, 1980b and 1981), Rice (1981) and Kerr and Turner (1982). Compositional changes resulting from incremental crystallization are transmitted in a step-wise fashion through the residual liquid, a process termed double-diffusive fractional crystallization (Irvine, 1980b). In particular, double-diffusive convection offers an explanation for continued crystallization of certain phases without depletion of essential nutrients in the immediate vicinity of the growing crystals. This is achieved by a combination of vigorous convection within the cell and diffusive exchange of heat and components across the horizontal interface between juxtaposed cells.

Studies of chromite within small intrusions of the Karoo Tholeiitic Province have culminated in an empirical model that accounts for the compositional variation of spinels in terms of fractional crystallization processes (Eales et al., 1980). A tenet of the model is that nucleation of chromian spinel is restricted to the first 30 per cent of crystallization of the parent magma. Three distinct stages in the chemical evolution of Cr-spinels are telescoped within this period:

1. An early stage during which coprecipitation with olivine results in a mild Al-enrichment trend with no change in the Fe^{3+} content.

2. A middle stage marked by the appearance of plagioclase as a crystallizing phase. The substitutional trend reflected is one of Al - depletion and enrichment in Fe^{3+} + (Fe^{2+}, Ti), with Cr remaining essentially constant.

3. The late stage which commences at the onset of clinopyroxene nucleation and growth. Residual Cr^{3+} is rapidly scavenged from the system by the pyroxene and, thereby, crystallization of chromian spinel is terminated.

A final stage involving the precipitation of Fe - Ti oxides occurs in more slowly cooled intrusions. Eales et al. (op cit.) suggest that this model may be applicable to the crystallization of spinels from large intrusions such as the Bushveld Complex. However, there is some difficulty in correlating stratigraphic position with "percentage crystallized" of the magma as the shape of the magma chamber is not known.

Experimental studies of Cr-spinel crystallization from silicate melts have served as important indices of parameters governing its stability, compositional variation and abundance. Usual experimental variables include melt composition, temperature, oxygen fugacity and order of appearance of associated silicate phases. Hill and Roeder (1974) investigated the composition of chromite in natural basaltic melts as a function of fO_2 (at constant temperature) and temperature (at constant fO_2). Additional experiments, in which the Cr content of the melts was varied, indicated that the large stability field of chromite was extended to higher temperatures and lower oxygen fugacities at higher concentrations. A crystallization sequence of a natural basaltic melt as a function of fO_2 and temperature was proposed (Fig. 9 of Hill and Roeder, op. cit.). Apart from being of considerable qualitative value, this diagram has also been used to estimate the temperatures of formation of some Critical Zone chromitite layers (Snethlage and von Gruenewaldt, 1977; Snethlage and Klemm, 1978).

Schreiber and Haskin (1976) studied the effect of oxidation state and temperature on the partitioning of Cr between spinel, pyroxene, olivine and melt in two synthetic silicate systems. Their data indicated that although the amount of Cr-spinel decreased with an increase of the Cr^{2+}/Cr^{3+} ratio of the experimental charge, the Cr content of the spinel was independent of the concentration of Cr^{3+} in the melt. Hence, they concluded that the presence of Cr-rich spinel in natural associations did not imply crystallization from a Cr^{3+}-rich liquid. In a similar study, Alkella et al. (1976) found that the Cr/(Cr+Al) ratio of the spinel was more sensitive to the Mg content of the spinel than to the fO_2 of crystallization. Furthermore, Schreiber and Haskin (op. cit.) noted a positive correlation between the Al_2O_3 content of the liquid and that of the equilibrium spinel, but were reluctant to accept that the Al content of the melt controlled the composition of the nucleating spinel. It is timeous to mention here that Cameron (1980, p. 870) has suggested that abundant nucleation of chromite in the Bushveld magma may have been deferred until the Al_2O_3 content had been enriched by fractionation processes to "necessary levels".

Maurel and Maurel (1982a) investigated the distribution of aluminium between chromian spinel and silicate melt, and reported a positive correlation between $(Al_2O_3)_{spinel}$ and $(Al_2O_3)_{liquid}$. The equation fitted to the data is given as:

$$(Al_2O_3)_{sp} = 0{,}035(Al_2O_3)^{2{,}42}_{liq}$$

where (Al_2O_3) is expressed in weight per cent. The above relationship is shown to be consistent with the data of other authors (e.g., Hill and Roeder, 1974; Fisk and Bence, 1980). Maurel and Maurel (1980b) also assessed the solubility of Cr in basic silicate melts under conditions of fO_2 = - log 3 to - log 9 and T = 1 180 - 1 300°C. In agreement with Hill and Roeder (op.cit.), their data indicated that the concentration of chromium in equilibrium with spinel increased with temperature and/or when fO_2 decreased. The experimentally derived D_{Cr} values, expressed as $D = (Cr_2O_3)_{sp} / (Cr_2O_3)_{liq}$, were in the range 257 - 1 424 and proved to be more

sensitive to temperature variations than to fO_2 of crystallization. Accordingly, they suggested that fluctuations in temperature and/or oxygen fugacity may induce chromium supersaturation in the melt. This conclusion is consistent with the experimental observation of Campbell and Murck (1984) that Cr saturation in basaltic melts is strongly temperature dependent above 1 200°C. However, a fundamental and perplexing question is raised, viz., what mechanism spontaneously induces an abrupt change in the temperature of a large body of magma? In order to accommodate this dilemma, Campbell and Murck (op. cit.) proposed a magma-mixing model that invokes efficient hybridization of a new influx of hot, primitive, Cr-saturated magma with a cooler, fractionated residuum in a gravitationally stable, stratified magma chamber. It is envisaged that the temperature and Cr content of the hybrid magma determine the degree or duration of chromite nucleation.

With respect to the influence of plagioclase nucleation on the Cr/(Cr+Al) ratio of crystallizing Cr-spinels, the experimental data reported by Irvine (1977a) and Fisk and Bence (1980) are compatible with the concept promulgated by Eales et al. (1980) that plagioclase may compete effectively for Al in the melt. However, although there appear to be certain consistencies between experimental data and observed features of natural associations, the application of this information to an understanding of the origin of chromitite layers in large intrusions is problematical and somewhat daunting.

Mechanisms for the formation of chromitite layers in large stratiform mafic intrusions remain the subject of considerable debate. This may be attributed to essentially two aspects. Firstly, there are problems relating to the origin of thin anchimonomineralic layers of considerable lateral extent in either the single or multiple intrusion models, and secondly, there is an inadequate understanding of mechanisms that may account for chromite being periodically isolated as the only stable liquidus phase. An exhaustive review of the proposals is not attempted here as a major part of this may prove to be tautological in subsequent sections. However, the different theories on the origin of chromitite layers may be summarized as follows:

1. Crystallization from a chromite-rich residual liquid (Fockema and Mendelsohn, 1954).
2. Magmatic sedimentation of chromite with a later *in situ* crystallized component from a chromite-rich immiscible liquid (Cameron and Emerson, 1959; McDonald, 1967).
3. Contamination of mafic melt with sialic roof-rock (Irvine, 1975).
4. Periodic irruption of new magma with or without hybridization of evolved (i.e., fractionated residua) and primitive liquids. The relative proportions of the melts, the degree of fractionation of the magma in the chamber, and the rate of mixing, may be important here.
5. Periodic fluctuations in oxygen fugacity (Ulmer, 1969).
6. Pressure fluctuations in response to regional tectonism (Cameron, 1980).
7. Growth of discrete chromitite layers inward from the margins of the intrusion, in concert with their cyclic units, within a double-diffusive convection physical model (Irvine, 1981).

Reference to points 4, 5 or 6 as plausible mechanisms may be found in Kuschke (1940), Van der Walt (1942), Ulmer (1969), Cameron and Desborough (1969), Irvine (1977b), Cameron (1970, 1975, 1977 and 1978), Snethlage and von Gruenewaldt (1977), Snethlage and Klemm (1978), von Gruenewaldt and Worst (1986), Wilson (1982) and Campbell *et al*. (1983). Pertinent reviews are available in Cameron (1980), Wilson (*op. cit*.) and Duke (1983).

3. FIELD RELATIONSHIPS IN THE STUDY AREA

3.1 LOCATION AND GENERAL GEOLOGY

The study area is located on the farm Zandspruit 168 JP in the western lobe of the Bushveld Complex (a locality map is presented in Fig. 1). The coordinates of the centre of the farm are 26°55' and 25°10'S, with the north-western perimeter of the prominent Pilanesberg Alkaline Complex cropping out on the south-eastern portion of the farm. The area underlain by the Critical Zone is virtually featureless and is veneered with 1 - 2 metres of black turf, but low hills of Main Zone gabbro rise some 20 metres above the general level in the eastern sector of the farm. The area is covered by grassland with patches of thorn trees and, by virtue of a low outcrop density, geological mapping is dependent on trenching and extrapolation from boreholes.

A geological map of part of the area is given in Fig. 2. This map was redrawn by the writer from a plan of the surface geology compiled by Messrs Rand Mines Limited. The suboutcrop of the LG 2 chromitite layer lies within 100 metres of the northward-trending, western boundary of the farm, and this represents the lowest member of the layered succession within the farm area. An uninterrupted sequence up to the MG 3 chromitite layer is present, terminated on the eastern side by the north-striking Frank fault, to the east of which only Main Zone rocks are depicted. The apparent throw of this strike-slip fault is not precisely known but must surely exceed 450 metres to have juxtaposed the Middle Group chromitite succession with the Main Zone (based on the generalized columnar sections of Cousins and Feringa (1964) and SACS (1980)). The Frank fault also cuts the Groenfontein-Zandspruit fault zone at a point close to the southern boundary of the farm, with this latter fault zone extending to the north-west at a given bearing of 320°. This latter fault causes the succession to the north-east to be downthrown by approximately 200 metres, and sinistrally displaces the suboutcrop of the LG 6 chromitite layer on the northern side of the fault some 2,5 kilometres to the north-west. A relatively minor fault, striking close to due east and throwing the succession down approximately 25

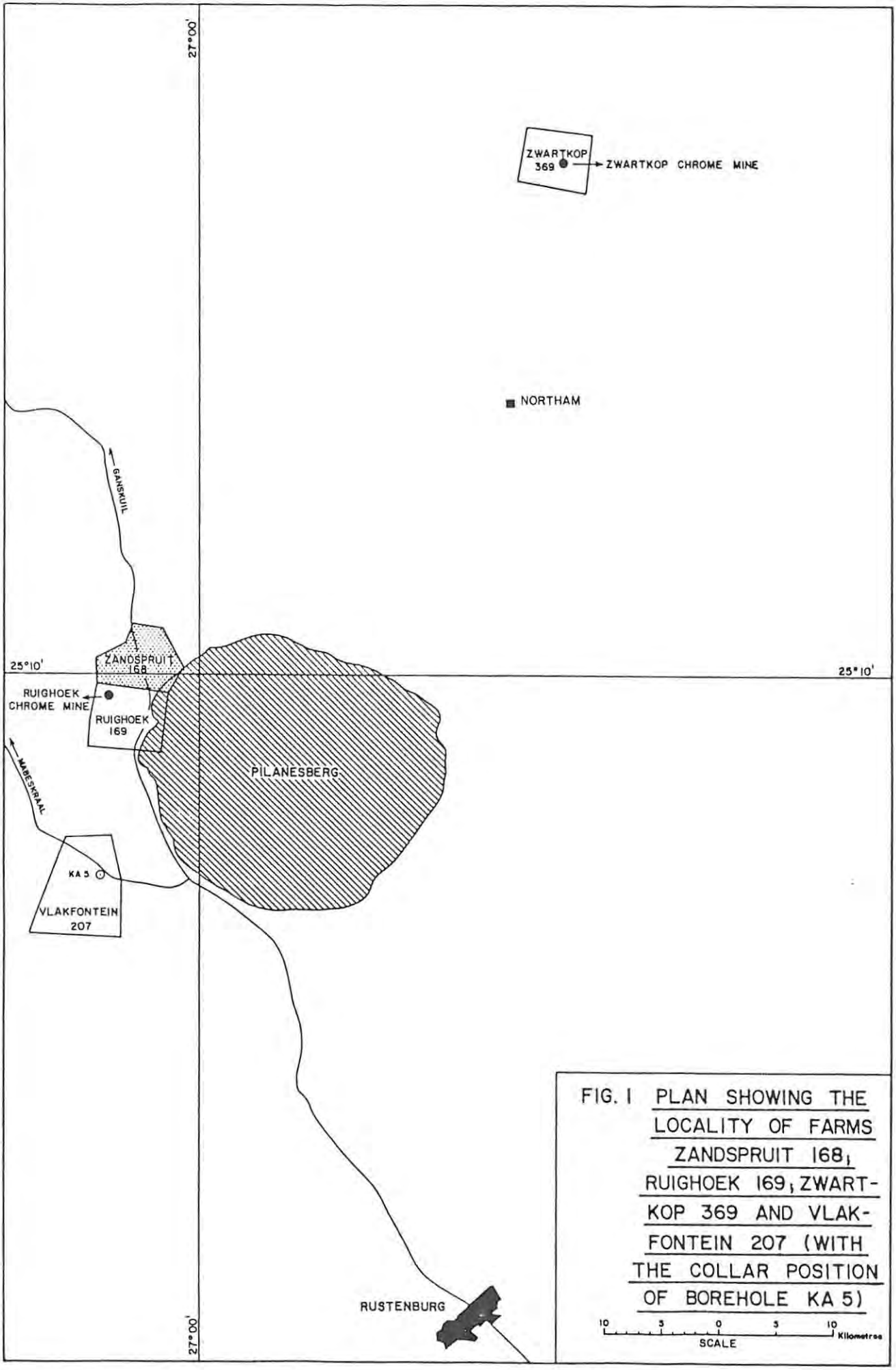

FIG. 1 PLAN SHOWING THE LOCALITY OF FARMS ZANDSPRUIT 168, RUIGHOEK 169, ZWARTKOP 369 AND VLAKFONTEIN 207 (WITH THE COLLAR POSITION OF BOREHOLE KA 5)

metres on its northern side, is located 2,2 kilometres from the southern farm boundary. The study area thus measures 3 kilometres east-west and 2,4 kilometres north-south, and is effectively bounded on the northern, north-eastern and eastern sides by faults. Within this area there occurs an undisturbed succession striking N15°E and dipping 12 - 15° east. Several minor syenitic dykes, presumably part of the Pilanesberg dyke swarm, have been mapped within the area, but are of no significance in the present study.

3.2 THE SUCCESSION OF LAYERED ROCKS

3.2.1 INTRODUCTION

A stratigraphic column is given in Fig. 3, which presents a comparison of the general sequence as determined for the farms Zandspruit 168 JP (this study), Ruighoek 169 JP (McDonald, 1967) and Zwartkop 369 KQ (von Gruenewaldt and Worst, 1986). The localities of these farms in the Western lobe of the complex are indicated in Fig. 1. The sequences shown are correlated in Fig. 3 with Camerons's (1980) type-section and subdivision of the Lower Critical Zone in the north-eastern sector of the Bushveld Complex, referred to as the Mooihoek Pyroxenite (SACS, 1980). The Steelpoort and LG 6 chromitite layers were assumed to be equivalent stratigraphic horizons, in accordance with Hatton and von Gruenewaldt (1982), and served as the datum horizons in the construction of Fig. 3. A broad similarity between the respective sections is apparent and, in particular, the succession at Zandspruit shows a good correspondence with McDonald's northern Ruighoek section. Although there are differences with respect to the number of chromitite layers, their thicknesses and the distance between successive seams, there are two features which are common to both the Mooihoek and Ruighoek Pyroxenites. Firstly, the lower part of the succession contains a greater occurrence of thin chromitite layers, and secondly, olivine-rich rocks occur as two distinct horizons towards the base, with the upper being the thicker subunit.

The following account of the lithological variation in the Zandspruit area is based on a study of drill core sections ZS 7 and ZS 3, which

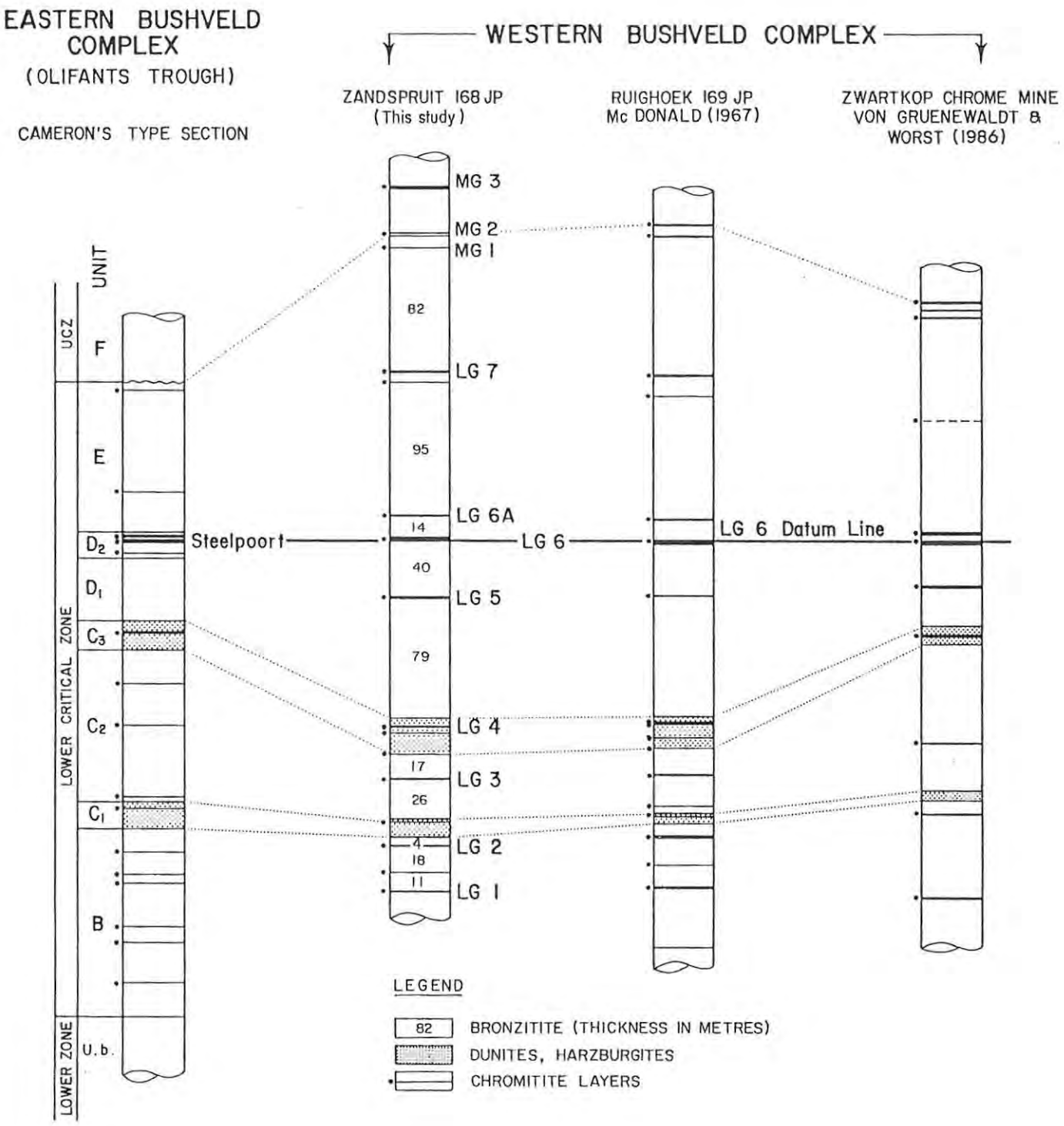

FIG. 3 COMPARATIVE LOG SECTIONS OF THE MOOIHOEK AND RUIGHOEK PYROXENITE STRATIGRAPHIC SUCCESSIONS (UNIT B TO E). THE OLIVINE-RICH C_1 AND C_3 SUBUNITS IN CAMERON'S TYPE SECTION CORRELATE WITH ANALOGOUS LITHOLOGIES IN THE WESTERN BUSHVELD COMPLEX.

ABBREVIATIONS: U.b. = UPPER BRONZITITE;
UCZ = UPPER CRITICAL ZONE

were made available to the writer by Messrs Rand Mines Limited. From an inspection of an additional 38 borehole logs compiled by Messrs Rand Mines Limited, these sections can be regarded as representative of the stratigraphic succession. Borehole section ZS 7, with a collar elevation of 1 101,4 metres above mean sea level, was drilled 300 metres to the south of the Groenfontein-Zandspruit fault zone (see Fig. 2). This vertical borehole intersected the LG 7 chromitite at a depth of 23,4 metres below surface and penetrated to a final depth of 381 metres, some 16 metres below the LG 1 chromitite layer. The cumulative thickness of chromitite, represented by the 8 major Lower Group seams (including the LG 6A layer) and 5 minor layers, is 2,92 metres or 0,8 per cent of the succession. The core was logged in its entirety with the assistance of Mr P Best, a geologist in the employ of Messrs Rand Mines Limited. To compensate for 12,5 metres of core representing the LG 6 chromitite and immediate enclosing rocks which were unavailable, the equivalent stratigraphic succession of borehole ZS 3 was logged due to its proximity to ZS 7. An additional 24 metres of adjacent core from the same section was logged, thereby giving a duplication of 25 metres of the succession. Borehole ZS 3 was collared at an elevation of 1 098,7 metres above mean sea level and intersected the LG 7 chromitite layer at a depth of 76,03 metres below surface. Calculated on the basis of an average dip of 12°E, borehole ZS 3 depicts an intersection of the LG 6 and LG 6A chromitite layers which is 260 metres further down dip and 530 metres to the south of ZS 7 (Fig. 2). The sequence above the LG 7 chromitite to the top of the Ruighoek Pyroxenite (i.e., at the MG 2 chromitite layer according to Cousins and Feringa (1964)) was obtained from a generalized stratigraphic column compiled by Messrs Rand Mines Limited.

3.2.2 THE B UNIT

The B Unit represents the lowermost unit of the Critical Zone and Cameron (1980, p. 847) has placed the Lower Zone - Critical Zone contact in the north-eastern sector of the Bushveld complex at "... the horizon at which there is a distinct increase in postcumulus plagioclase in bronzitite". The first chromitite layer occurs a short distance above this transition. With respect to the study

area, McDonald (1967) reported a 5 centimetre thick chromitite, termed the A or Bottom seam, approximately 38 metres below the LG 1 chromitite layer on the farm Ruighoek. Only one other borehole was drilled deeper than ZS 7 on the farm Zandspruit. Collared near the western boundary of the farm in the hanging-wall of the LG 2 chromitite, this drill core intersected bronzitite with thin chromitite stringers at depths of 46,0, 76,5 and 77,4 metres below the LG 1 chromitite layer. Though it would seem that the distribution of chromitite layers below the LG 1 is impersistent and minor, as is the situation at Zwartkop (von Gruenewaldt and Worst, 1986), the criterion used by Cameron has not been documented in the study area and the base of the Ruighoek Pyroxenite is taken here at some position below these chromitite stringers, probably within 100 metres of the LG 1 chromitite layer. Hence, the final depth of borehole ZS 7 is of the order of 80 metres above the putative base of the B unit.

Two major and one minor chromitite layer occur in the B unit at Zandspruit (Fig. 3). The lowermost intersected, the LG 1 chromitite (locally termed the Lower Groenfontein seam), is 33 centimetres (cm) thick and has sharp foot- and hanging-wall contacts with the enclosing bronzitites. This seam correlates with McDonald's (op. cit.) B chromitite layer on farm Ruighoek. The underlying chromite-poor bronzitites are fairly coarse-grained and sheared, and no grain-size layering or igneous lamination is evident. Extensive shearing parallel to the basal chromitite contact has obscured the finer details of the contact relationships, but a 2 cm wide zone of partially serpentinized, olivine-rich harzburgite is exposed immediately below the chromitite layer. The orthopyroxene within this narrow zone is of the reaction-replacement type and hosts resorbed remnants of olivine. Two textural features are of interest. Firstly, no olivine grains occur in contact with cumulus orthopyroxene crystals or intercumulus plagioclase, and secondly, no intercumulus silicate phases occur within the zone. The lower contact of the latter assemblage is marked by reaction-replacement orthopyroxene in contact with cumulus, medium-grained orthopyroxene crystals depicted in a thin domain characterized by polygonal grain boundaries and no interstitial void volume. This border zone separates the olivine-bearing domain from the underlying,

coarser-grained feldspathic bronzitite. The overlying 11 metres (m) of bronzitite above the chromitite are coarse-grained, chromite-poor and nonlayered (i.e., no igneous lamination is evident), and exhibit a higher modal proportion of intercumulus silicate phases (e.g., plagioclase and phlogopite) than the footwall rocks. A 2 cm thick chromitite (McDonald's C layer) is abruptly developed above this coarse bronzitite, but exhibits a 1 cm wide gradational upper contact with a much finer-grained bronzitite. The 25 cm thick LG 2 chromitite layer (Upper Groenfontein or D seam) occurs ca. 20 m above this minor seam. The intervening bronzitites are chromite-poor and show a well developed igneous lamination. The latter feature is a function of grain shape; an igneous lamination is only developed where the bronzite crystals occur as planar, orientated, elongate laths rather than as a haphazard arrangement of stubby grains. Some 1,5 m below the LG 2 chromitite, a fine-grained bronzitite is depicted which abruptly overlies the medium-grained, laminated bronzitites. A 22 cm thick kimberlite dyke cross-cuts this fine-grained horizon and comprises flow differentiated, euhedral olivine crystals set in a dark brown, opaque mineral-rich matrix. The immediate footwall of the LG 2 chromitite layer is a medium-grained, chromite-poor bronzitite in which a trace modal abundance of small olivine grains sporadically occurs. In this instance, however, these small olivine grains are in mutual contact with cumulus orthopyroxene crystals and, although no reaction-replacement orthopyroxene is present, the olivine-bearing micro-domains are similarly devoid of any intercumulus silicate phases. The hanging-wall contact of the LG 2 is gradational and is composed of a coarse-grained, chromitiferous feldspathic bronzitite. This rapidly grades into non-layered, chromite-poor bronzitites which contain a trace abundance of graphite platelets in addition to the ubiquitous intercumulus plagioclase and hydrous silicate phases.

The top of the B unit is placed here at the first appearance of cumulus olivine crystals above the LG 2 chromitite layer. This olivine-bronzitite layer is exposed 4 m above the LG 2 and the modal olivine content is apparent in hand specimen. The apparent lack of systematic grain-size variations but presence of marked changes in the shape and orientation of orthopyroxene crystals at Zandspruit are features which similarly characterize the B unit of Cameron's (1980)

type-section. One possibly significant discrepancy is the absence of an olivine-chromitite layer which Cameron mapped 33,5 m below the top of the B unit. However, the seemingly restricted occurrence of olivine to the immediate footwall contacts of the LG chromitite layers at Zandspruit is not at variance with the documentation of a similar occurrence at Ruighoek (McDonald, 1967). Base metal sulphide grains are not visible in hand specimen and no pegmatoidal-textured bronzitites are depicted within the succession.

3.2.3 THE C UNIT

A. THE C_1 SUBUNIT

The lowermost olivine-rich interval of the C unit has been denoted the C_1 subunit in Cameron's type-section and is characterized by extremely well developed, fine-scale modal layering. For example, SACS (1980) refer to the work of Cameron and Desborough (1969) who recorded 160 layers in this 16 to 20 m thick subunit. Subsequent detailed studies by Cameron and his students have indicated, however, that no cyclic or rhythmic repetition of the layering is evident. A generalized columnar section of the 12 m thick C_1 subunit at Zandspruit is given in Fig. 4, which includes a detailed log of the single chromite-rich horizon exposed towards the top of the subunit. It is apparent from Fig. 3 that a chromite-rich horizon is similarly located in the upper half of the subunit in other geological areas. Fig. 4 serves to illustrate the pronounced variations in modal abundance of chromite, olivine and orthopyroxene that can be detected in very limited sections and, in particular, shows that the succession of rock-types in relation to stratigraphic height is opposite to that of typical ultramafic cyclic units mentioned previously.

The first 7 m above the base of the subunit (at 330,20 m depth in drill core ZS 7) consist of interlayered chromite-poor bronzitites and olivine-bronzitites. This is followed upward by 5 m of layered dunites, harzburgites and olivine-chromite cumulates. A 2 cm thick massive chromitite layer is developed (McDonalds E layer) within enclosing olivine-chromitites, and both contacts are gradational.

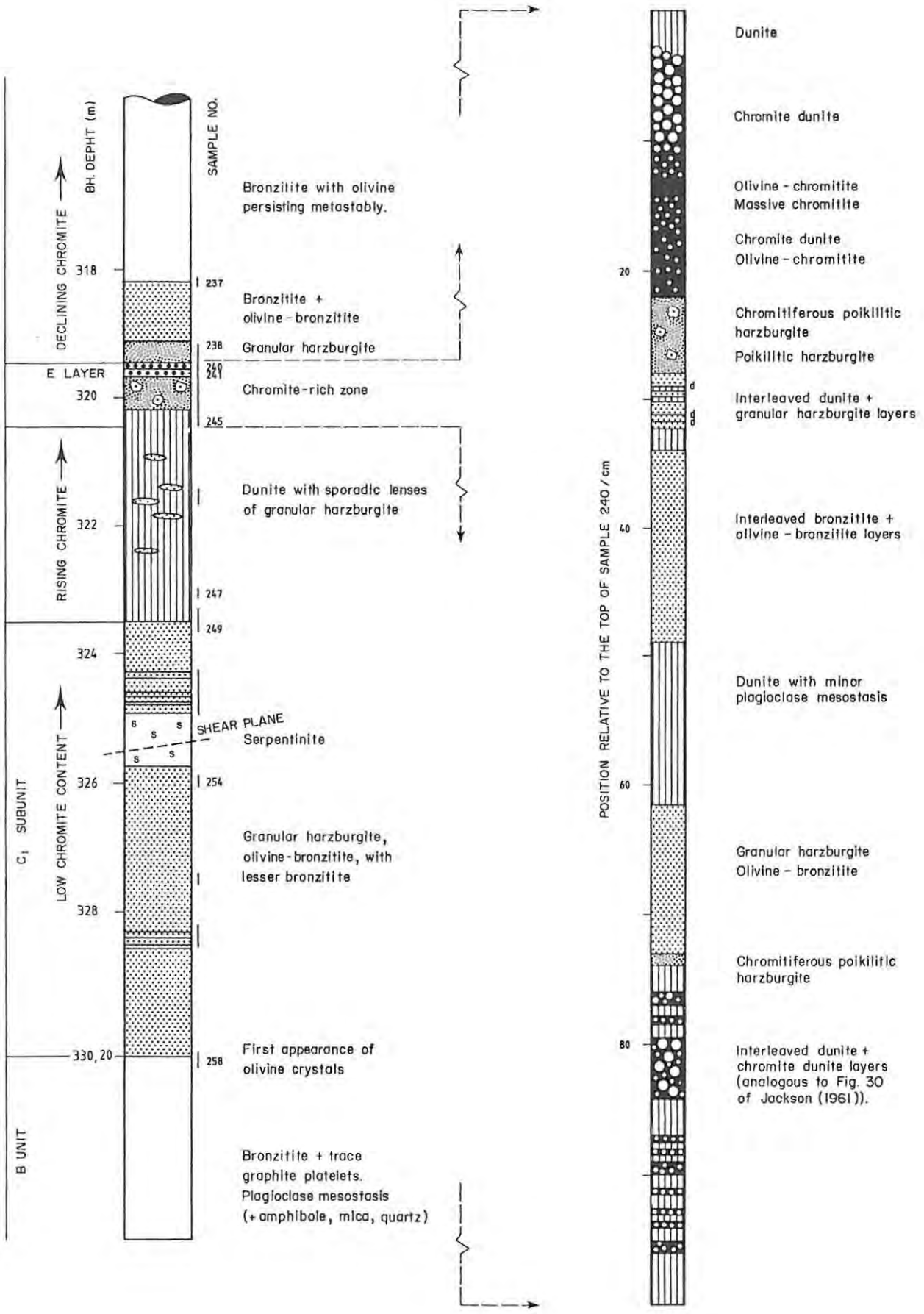

FIG. 4 COLUMNAR LOG SECTION OF THE C_1 SUBUNIT (ZS 7), WITH A DETAILED LOG OF LITHOLOGICAL LAYERING IN JUXTAPOSITION TO THE E CHROMITITE LAYER.

SCALE 1:300

The schematic representation given in Fig. 4 tends to exaggerate the abundance of chromite in the wall-rocks, but an attempt has been made to illustrate the increase in olivine grain-size which occurs across the chromite-rich interval. The latter horizon is overlain by granular harzburgites which grade into olivine-bearing bronzitites. The top of the C_1 subunit (i.e., marked by the disappearance of cumulus olivine) is approximately 1,5 to 4,5 m above the chromitite layer (core loss of 3 m occurred at this level).

Columnar stratigraphic sections of the individual units, showing a wide spectrum of petrographic information, are presented in section 4.2 of the present text (Figs. 8(A) to (E)). Though a discussion of these data is deferred, the reader is referred to these figures if it may assist in the reading of the subsequent text. Logs of boreholes ZS 7 and ZS 3 are presented in Appendix I.

B. THE C_2 SUBUNIT

The C_2 subunit at Zandspruit is composed of 39 m of medium- to coarse-grained, chaotic- and laminated-bronzitites, a 2 m thick interval of layered olivine-rich rocks, and the 17 cm thick LG 3 chromitite layer (also termed the Gossan, G or Intermediate seam). The 5 cm thick F chromitite layer depicted at Ruighoek is not developed in the Zandspruit succession, but an olivine-bearing, chromite-bronzite cumulate layer does occur at approximately this stratigraphic level (see Fig. 3).

The LG 3 chromitite is located ca. 25 m above the base of the subunit in sharp contact with the bronzitite host rocks. A 2 cm thick leader chromitite layer is situated 1 - 2 cm below the LG 3 and, similar to the occurrence at Zwartkop (von Gruenewaldt and Worst, 1986), relict olivine grains occur at the immediate hanging-wall contact of the LG 3 in association with a 2 cm wide zone of reaction-replacement orthopyroxene. Though the textural features are identical to those described by von Gruenewaldt and Worst, and to those seen at the footwall contact of the LG 1 chromitite, this occurrence depicts lobate protrusions of olivine and reaction-replacement orthopyroxene extending 1 - 2 cm into the overlying bronzitite. Olivine

chadacrysts occur in contact with the uppermost chromite grains of the LG 3 layer, but are always separated from the overlying feldspathic bronzitite assemblage by a selvage of structurally continuous, secondary orthopyroxene. The immediate footwall of the thin leader chromitite below the LG 3 layer is also olivine-bearing. However, there is only a very minor development of reaction-replacement orthopyroxene and this fairly chromitiferous bronzitite, composed of polygonal orthopyroxene crystals, exhibits no intercumulus silicate phases.

The upper contact of an anomalous 2 m thick olivine-rich horizon occurs 2 m below the LG 3 chromitite layer in borehole ZS 7. A detailed columnar section of this horizon is presented in Fig. 5 and it is clear that the scale of the layering is similar to that seen in the C_1 subunit. This succession was not intersected in other boreholes on the farm, but no indication of faulting was evident at this level in the ZS 7 drill core. By virtue of the exceptional modal layering and the chromitiferous nature of the basal portion, it would seem that this olivine-bearing horizon represents a lensoid, impersistent structure that is part of the layered succession. Apart from the 25 cm thick olivine-chromite cumulate near the base, layering within this structure is defined by cyclical variations in the modal abundance of cumulus olivine and orthopyroxene. It is noteworthy that the olivine-rich layers are marked by sharp basal contacts and a progressive increase in the modal abundance of orthopyroxene with stratigraphic height. A sympathetic increase in the abundance of intercumulus plagioclase was noted in some of the mineral-graded layers.

The top of the C_2 subunit is marked by two thin chromitite layers separated by a 6 cm bronzitite parting. An appreciable abundance of base metal sulphides occurs in the bronzitite footwall of the lower layer. The upper chromitite layer is 4 cm thick and is bounded on the hanging-wall contact by olivine-chromite cumulates. This chromitite would seem to correlate with McDonald's H layer and is taken here as the base of the overlying C_3 subunit, 14 m above the LG 3 chromitite layer.

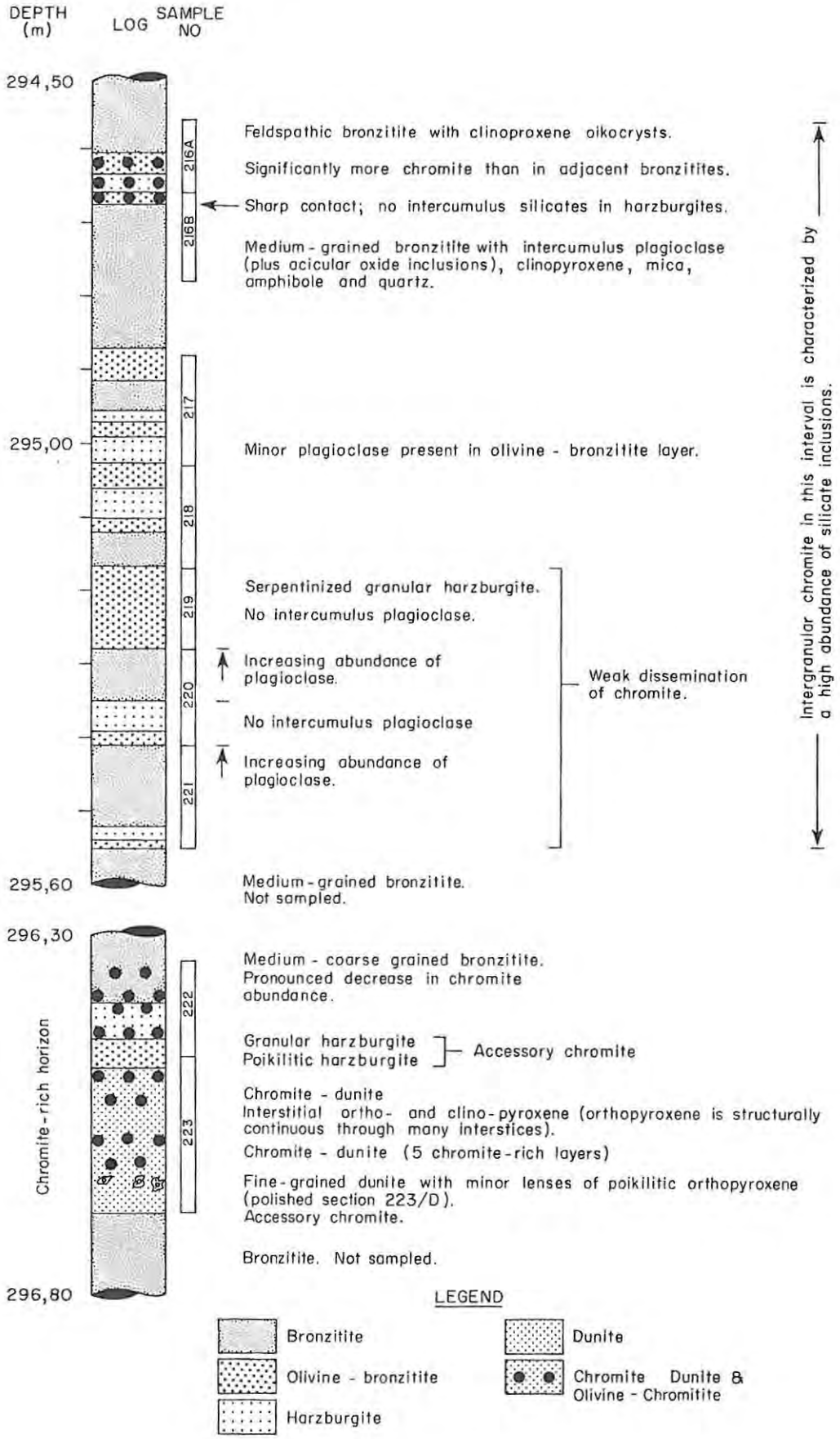

FIG. 5 DETAIL OF MODAL-LAYERING IN AN OLIVINE-BEARING HORIZON WITHIN SUBUNIT C_2, FROM 294,50 TO 296,80 m DEPTH. (LG 3 CHROMITITE AT 292,29 m).

C. THE C_3 SUBUNIT

The C_3 subunit is the upper 23 m thick olivine-rich interval depicted in Fig. 3. Including the basal H chromitite layer, four chromite-rich horizons are developed in this subunit of which the LG 4 chromitite (K, Guinea Fowl or New layer) is of particular interest in that it is the only substantial member of the Lower Group of chromitites developed in an olivine-rich succession.

The first 3 m above the basal H chromitite layer consist of serpentinized dunites. Chromite is an accessory phase and apart from isolated patches of altered intercumulus plagioclase, these olivine cumulates are essentially monomineralic. In contrast, the overlying 11 m of dunite are characterized by lensoid or spheroidal "plates" of harzburgite which can be as much as 20 cm in diameter. The orthopyroxene in these structures is of the reaction-replacement type and individual grains are in structural continuity over large areas. This is followed by the first chromite-rich zone which is 0,5 m in thickness and consists of a lower olivine-chromite cumulate, a 5 cm thick chromitite (with scattered, spherical silicate lenses composed of exceptionally large olivine grains which are partially replaced by secondary orthopyroxene), and an upper chromite-olivine cumulate layer which grades rapidly into chromite-poor dunite. At a distance of 3 m above this chromitite, which is the equivalent of either the I or J layers at Ruighoek, the 17 cm thick LG 4 chromitite is developed within a zone of olivine-chromite cumulates depicting heavy disseminations of chromite. Less than 2 m above the LG 4, chromite reappears in high concentrations and a 0,6 m thick zone of chromite and chromite-olivine cumulates is developed. A further 2,5 m of chromite-poor dunite is present above this layer.

As in the C_1 subunit, the major chromite-rich horizons are located towards the top of the section. Notable by its absence, cumulus bronzite is not present in the C_3 subunit at Zandspruit except for the uppermost 0,5 m, where its weak reappearance presages the considerable thickness of overlying bronzitites of the D_1 subunit. The top of the subunit is exposed at a depth of 252,4 m in the ZS 7 drill core succession.

3.2.4 THE D UNIT

A. THE D_1 SUBUNIT

The D_1 subunit comprises 112 m of bronzitites which vary from coarse-grained assemblages in the basal portion to finer-grained, granular-textured bronzitites through much of the middle and upper intervals. The latter bronzitites are characterized by an exceptionally weak abundance of intercumulus silicate phases and the distinction between these and the bronzitites of the B unit and C_2 subunit is quite marked in hand specimen. Chromite is an accessory to trace constituent at all but two horizons, viz., the 37 cm thick LG 5 chromitite (Roehmer or L layer) which is a laminated succession of chromitite and silicate-rich layers developed 79 m above the base of the subunit, and secondly, a thin chromite-bronzite cumulate layer 25 m above the base. Scattered olivine grains or aggregates of large olivine grains occur sporadically in both coarse and fine-grained bronzitites. Their occurrence is, however, very limited within individual samples and no olivine was seen above the immediate footwall of the LG 5 chromitite layer, where severely altered remnants of olivine occur in a medium- to coarse-grained, granular textured bronzitite. Shearing and alteration are severe at the level of the chromitite layer and most of the interlaminated silicate-rich layers are completely replaced by green serpentine. The uppermost of these layers, however, was seen to be an exceptionally coarse-grained bronzite assemblage hosting base metal sulphides and a trace of olivine remnants and altered pseudomorphs. There is a very abrupt decline in the abundance of chromite to accessory levels above this thin chromitite layer.

Both Cameron (1980) and McDonald (1967) have documented cyclical grain-size variations in the D_1 subunit. Cameron recognized four fining-upward cycles in the Eastern lobe of the complex, of which the upper two culminated in bronzite-chromite cumulates. McDonald, on the other hand, indicated that coarsening upward cycles were depicted at Ruighoek, although the overall trend was one of decreasing grain-size. However, from an inspection of these data, there does not appear to be any obvious correlation between the disposition of the proposed cycles and chromite abundances in the Ruighoek

Pyroxenite succession. Similarly, variations in orthopyroxene grain-size at Zandspruit are well developed (documented in section 4.2 of the present text) and although there may be discrepancies with respect to the number of cycles and their fabric, it is surely of some significance that this particular textural feature is developed at geographically removed localities.

There is some hesitancy as to where the D_1 - D_2 subunit boundary should be drawn in the studied section. In both the ZS 3 and ZS 7 boreholes, however, a thin chromite-bronzite cumulate is developed ca. 7 m below the LG 6 chromitite layer. There is an abrupt increase in orthopyroxene grain-size above this chromitiferous layer, associated with an increase in the modal abundance of intercumulus plagioclase. Furthermore, chromite abundances are significantly higher above this level than in the underlying bronzitites. On this basis, it was decided that the latter chromite-bronzitite layer served as a convenient boundary for the purposes of the study. However, no indication can be given as to the lateral persistence of this particular horizon.

B. THE D_2 SUBUNIT

A continuous section of the D_2 subunit was exposed in borehole ZS 3. Cameron (1980) arbitrarily placed the top of the subunit at 1 m above the Steelpoort Leader chromitite and this division is applicable to the Zandspruit section in that there is a gradation from fine-grained, chromitiferous bronzitites of the LG 6A chromitite hanging-wall to medium-grained, feldspathic bronzitites at this level. The subunit is 21 m thick and hosts the 81 cm thick LG 6 (Magazine, Main or M layer) and 18 cm thick LG 6A (Magazine Leader or N layer) chromitite layers. The upper contacts of the LG 6 and LG 6A are gradational over 0,7 and 0,2 m, respectively, and layering is exceptionally well developed. Heavily disseminated chromite occurs in the immediate footwall of the LG 6 chromitite, but the lower contact of the leader seam is abrupt.

The two chromitites are separated by 12 to 14 m of fine-grained, massive bronzitite in which chromite is an accessory or trace

constituent. The distance between the chromitite layers varies considerably along strike: for example, it is ca. 6 m at Zwartkop (von Gruenewaldt and Worst, 1986) and a mere 1 m in Cameron's type-section. Olivine occurs within the subunit but the textural relationships are complex. Suffice it to say that olivine occurs as sporadic grains in the granular bronzitites below the LG 6 chromitite layers, in the immediate footwall of the LG 6 and in localized microdomains of the hanging-wall. Olivine was not observed in association with the LG 6A chromitite or in bronzitites showing intercumulus plagioclase. However, inspection of drill core ZS 7 did not show an equivalent distribution. For example, no olivine was observed at similar stratigraphic positions below the LG 6 chromitite layer, and coarse-grained, anhedral olivine crystals were observed within silicate partings and in the immediate hanging-wall of the LG 6A chromitite, where a late-stage, replacement-type texture is locally depicted. It is most likely that much if not all of the olivine in this subunit, and in the D_1 subunit, is associated with ultramafic pegmatite bodies similar to those described by Bristow and Wilson (1983).

3.2.5 THE E UNIT

The E unit represents the uppermost section of the Lower Critical Zone. The top of this unit coincides with the first appearance of cumulus plagioclase in the Critical Zone succession, which is generally in the hanging-wall of the MG 2 chromitite layer. The unit at Zandspruit is approximately 183 m thick and consists of a monotonous succession of poorly layered, chromite-poor bronzitites. The LG 7 chromitite layer (Divider or P layer) is developed 93 m above the LG 6A and is composed of a 24 cm thick composite layer of chromitite and chromite-bronzite cumulates (considerable variation in the number and thicknesses of constituent layers is exposed within the study area, with the LG 7 represented as a 5 to 10 cm thick layer in some instances). Olivine is present in both immediate wall rocks, and also occurs sporadically in the underlying bronzitites where it is often associated with weakly disseminated sulphides. Discordant, cross-cutting structures were noted during the logging procedure and it would seem that the coarse-grained , olivine-bearing bronzitites

observed are undoubtedly of the replacement pegmatite-type (e.g., at borehole depths of 27 - 29 m and 39 - 40m). Apart from a 0,5 cm chromitite layer and a thin bronzite-chromite cumulate at depths of 4,3 and 30,1 m below the LG 7, respectively, there are no other significant concentrations of chromite in the E unit up to the level of the Middle Group (MG) of chromitite layers.

The MG 1 chromitite layer is depicted 82 m above the LG 7 layer, and is followed after 8 m of bronzitite by the MG 2^{L} and MG 2^{U} chromitites (L and U denote lower and upper, respectively). The latter are separated by 2,55 m of bronzitite. The MG 3^{L} and MG 3^{U} chromitites, with a parting of 1,6 m of bronzitite, are developed 29 m above the MG 2 chromitite layers. It is not possible to give thicknesses of the individual seams as borehole core of the MG succession was not logged in this study. However, the range is from 26 cm to ca. 70 cm.

3.3 SAMPLING

A total of 330 samples were selected from boreholes ZS 7 and ZS 3, drilled as 4 cm (BX) diameter cores. The sampling interval was 1,5 m and a typical core sample was 10 - 20 cm in length. Where layering was seen to be well developed, a closer sampling interval was used and in some instances up to 1 m of continuous core was removed. The immediate contacts of all the LG chromitite layers were sampled and continuous sections of the minor chromitite layers were obtained. However, only chip samples from the major seams were taken with the exception of the LG 6A chromitite layer (ZS 7), where 19 cm of continuous 1/4-core were made available to this study.

The individual lengths of core were split parallel to the core axis in the laboratory. One half was kept as a reference specimen and thin or polished sections were prepared from the other prior to the preparation of rock powders if required. In order to augment the study, five drill core samples of the harzburgite subzone (Groenfontein Harzburgite) of the Lower Zone were obtained from borehole KA 5 (Kashane), drilled on the farm Vlakfontein 207 JP. The location of the farm to the south-west of the Pilanesberg is shown in

Fig. 1 together with the collar position of KA 5, and an abbreviated columnar section showing the sampled positions is presented in Appendix II. A complete columnar section of borehole KA 5 can be found in Vermaak (1970). Samples KA 410 and KA 729 are representative of chromite-poor Lower Zone orthopyroxenites, and samples KA 552, KA 571 and KA 622 are of harzburgites.

4. PETROGRAPHY

4.1 INTRODUCTION

The assemblage of rocks within the study section is limited to dunites, harzburgites, olivine-orthopyroxenites, orthopyroxenites (bronzitites) and chromitites. A remarkable degree of purity may characterize either the dunites or pyroxenites, in which olivine and orthopyroxene, respectively, may constitute very close to 100 modal per cent of the rock. With increasing modal amounts of chromite in olivine-chromite cumulates, for example, the rock names that have been assigned for classification are: dunite (accessory chromite) - chromite dunite (disseminated chromite) - olivine chromitite (disseminated olivine). The modal limits which characterize these names are not rigorously defined here as modal analyses of the rocks were not performed. An indication of the modal proportion of an intercumulus mineral is given by a qualifying term such as "plagioclase-bearing" if plagioclase is restricted to filling small residual interstices of the cumulus crystal framework, or "feldspathic" if the visually estimated modal proportion of this mineral is in excess of ca. 7 per cent. The purely descriptive usage of the terms adcumulate and mesocumulate, as suggested by Irvine (1982), has been adopted to facilitate discussion; intercumulus minerals may comprise 0 - 7 per cent (by volume) of an adcumulate or adcumulate-textured orthopyroxenite, and 7 - 25 per cent of a mesocumulate. In effect, therefore, a plagioclase-bearing orthopyroxenite may also be termed an orthopyroxene adcumulate. Furthermore, as a means of conveying the distinction between fine-grained and coarse-grained, adcumulate-textured rocks, the term "granular" is reserved for the fine-grained "sugary" end-member displaying polygonal grain boundaries. Hence, the nomenclature that has been adopted in the subsequent text accords with that developed by Wager et al. (1960), Jackson (1961), Cameron and Desborough (1969), and the present tendency to employ cumulus terminology solely on a descriptive basis.

In terms of a gravitative accumulation scenario, Cameron (1969, p. 774) outlined three subsystems that need to be considered in the formation of a cumulate rock:

1. The subsystem of nucleation and initial growth of cumulus phases prior to and during settling.

2. The subsystem consisting of settled crystals and supernatant magma.

3. The subsystem of settled crystals and interstitial liquid.

Subsystem (2) would correlate with the isothermal adcumulus growth mechanism of Wager et al. (1960) if diffusional exchange with the overlying magma is permitted by slow accumulation rates. With the disappearance of the liquid phase, postcumulus crystallization in subsystems (2) and (3) is succeeded by a fourth, subsolidus equilibration system. It is noted that the continuum from (1) to (4) corresponds to progressively lower temperatures. On the assumption that crystallization occurred over a temperature interval of 200°C, Irvine (1970) estimated that the Rustenburg Layered Suite magma(s) cooled at a rate of 1°C per 1 000 years. Cameron's first subsystem mentioned above is most probably geologically instantaneous relative to the protracted period of postcumulus solidification. Thus, it may be anticipated that the rate at which the liquid/crystal ratio tends to small residual values will be influenced by an interplay of the following physical parameters:

1. The mechanism and rate of accumulation (McBirney and Noyes, 1979).
2. Rheological response of the mush with increasing crystal density (Marsh, 1981).
3. Grain-size and shape of the crystals.
4. Efficacy of gravitational compaction, adcumulus growth and sub-liquidus annealing or sintering processes which act to expel interstitial liquid (Coble and Burke, 1963; Vernon, 1970 and 1975; Moore, 1973; Reynolds, 1979).

More from a chemical viewpoint, however, the duration of liquidus and subliquidus crystallization is probably exceeded by the period of subsolidus equilibration due to the very slow cooling rate when in the solid state. Of the four aspects raised above, the grain-size of the associated cumulus silicate minerals may, in particular, impose

the dominant control on the "residence time" of a chromite grain in cooling residual liquid. This is of key concern when addressing the problem of purported chromite reactivity.

The development of textures and growth of crystals from silicate melts have been mimicked in numerous dynamic crystallization studies [for example, those of Gibb (1974), Lofgren (1974 and 1980), Grove and Bence (1977) and Donaldson (1977 and 1979)]. The data reported attest to the interrelated influence of melt composition, structure, viscosity, oxygen fugacity and thermal history on the kinetic growth properties of minerals. In particular, it has been shown that the degree of supercooling (ΔT) of a melt exerts a major control on grain shape, nucleation rate (N) and growth rate (G). Interpolation of this data to slowly cooled, large magmatic systems remains somewhat conjectural, but it is recognized that some degree of supercooling is required before nucleation occurs. Kirkpatrick (1977) has quoted the following theoretical expectations which indicate that N varies more with ΔT than does G:

1. N varies as $\exp(-1/\Delta T^2)$

2. G varies as $\exp(-1/\Delta T)$, if grain growth is controlled by interface attachment kinetics.

In layered complexes it may be more realistic to interpret the influence of ΔT on "bulk crystallization rate" (Kirkpatrick, 1981; Cawthorn, 1982), which is the resultant of N and G for a given degree of supercooling. However, unless accumulation occurs by a process akin to <u>in situ</u> heterogeneous nucleation, there need not be a correlation between ΔT and the crystal flux at the depositional floor. That is to say, the anticipated crystal size decrease in response to a rise in ΔT should not be evident in a layered succession. Semi-quantitive attempts to assess the role of supercooling in the origin of some observed features of layered rocks have been published. For example:

1. Ophitic textures in the Skaergaard chilled margin (Wager, 1961).
2. Rhythmic layering in the Freetown Complex (Hawkes, 1967) and Skaergaard Intrusion (Maaløe, 1978).
3. Anomalous fine-grained granular rocks in the Klokken Gabbro-Syenite Complex, South Greenland (Parsons, 1979), and the Fongen-Hyllingen Complex, Norway (Thy and Esbensen, 1982).

These investigations utilized "crystallinity" (total number of crystals per cm^3 of rock) or "crystal index" (number of crystals per cm^3 of any one mineral) as petrographically derived indices of the crystallization conditions of the magma. This procedure is deemed valid only if N increases with increasing ΔT (Maaløe and Hansen, 1982) and if the measured indices approximate to the instantaneous nucleation density. Though the interpretation of these data is fraught by constraints and uncertainties, it is however significant that Brandeis et al. (1984) have noted large crystal size variations stemming from minor temperature perturbations at low degrees of supercooling.

In this study, close attention has been paid to the possible use of grain-size or, more specifically, to variations in crystallinity of successive samples (crystallinity is defined here as the number of cumulus silicate crystals per cm^3 of rock). The approach used is intended to establish whether gradients in crystallinity are detectable within isomodal vertical sequences of pyroxenite and dunite, and then to interpolate data relating to chromite abundances. Though postcumulus modification of initial grain-size (Cameron, 1969) may have disturbed primary gradients, it is anticipated that long-term cyclic variations may be preserved which could reflect fluctuations in bulk crystallization rate and, thereby, temperature disturbances. It is not possible to assign the observed features unequivocally to either the in situ nucleation mechanism or gravitative accumulation of silicate phases and chromite. In the latter, for example, normal grain-size graded layering (Irvine, 1982) of constituent phases is conventionally regarded as evidence in favour of crystal sorting by cumulus deposition in much the same way as varves or turbidites. A fining-upward succession may equally be depicted in the bottom nucleation model if a progressive increase in nucleation rate occurs (schematically illustrated in Fig. 6), though

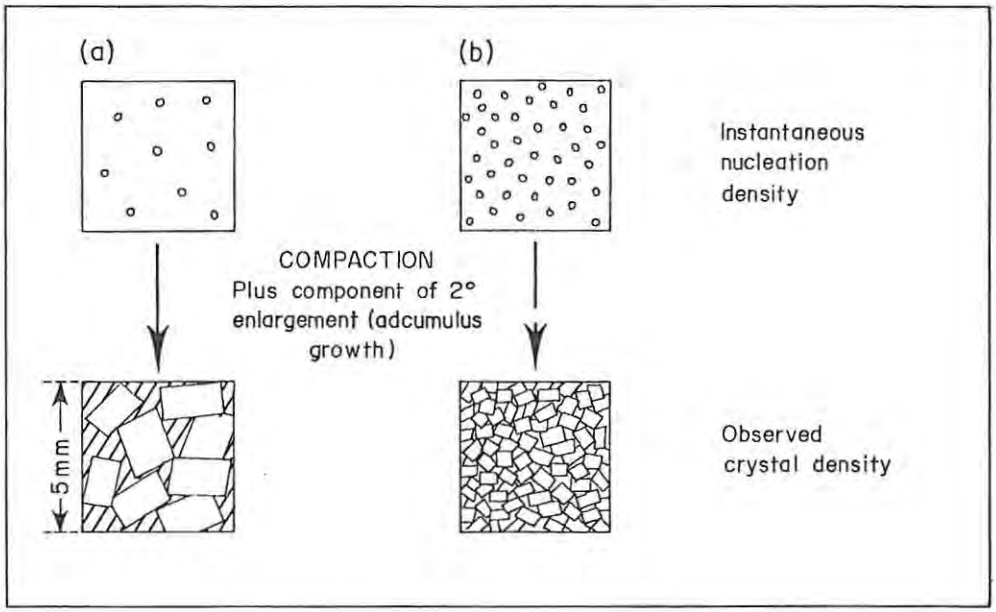

FIG. 6 SCHEMATIC DEPICTION OF THE HYPOTHETICAL INFLUENCE OF NUCLEATION DENSITY ON TEXTURAL FEATURES OBSERVED IN ORTHOPYROXENITES WITHIN THE STUDIED SECTION, ASSUMING IN SITU NUCLEATION OF ORTHOPYROXENE CRYSTALS AT THE BASE OF A LIQUID COLUMN. THE NUMBER OF CRYSTALS SHOWN IN CASES (a) AND (b) CORRESPOND TO MEASURED VALUES FROM THIN SECTIONS, BUT THE RELATIVE PROPORTION OF MESOSTASIS (▨) IS EXAGGERATED FOR ILLUSTRATIVE PURPOSES. IF CASE (b) IS NOT APPLICABLE TO LOWER CRITICAL ZONE CRYSTALLIZATION CONDITIONS (e.g. BY VIRTUE OF ENVISAGED LOW DEGREES OF SUPERCOOLING), RECOURSE MUST BE MADE TO RECRYSTALLIZATION OR MECHANICAL COMPACTION AT AN EARLY STAGE TO ACCOUNT FOR THE PRESENT TEXTURAL FEATURES. THESE CONSIDERATIONS ARE DISCUSSED AT SOME LENGTH IN THE TEXT.

spontaneous high nucleation densities may not exist at very low degrees of supercooling (Cawthorn et al., 1983).

The procedure followed in estimating the crystallinity of individual samples is similar to that adopted by Wager (1961) and Kirkpatrick (1977). A 5 x 5 mm grid of squares was marked in ink on the coverslip of a thin section, cut in an orientation parallel to the drill core axis. While viewed under low magnification with crossed nicols, a count of the number of cumulus silicate crystals in each 25 mm^2 block was made and averaged. This average was multiplied by 4 to give the average number of crystals per cm^2. The number of crystals per cm^3 was obtained from:

$$\text{crystallinity} = (\text{number of crystals per } cm^2)^{3/2}$$

In coarse-grained samples, the estimates of crystallinity were reproducible to within $\pm$ 30 crystals and to $\pm$ 300 crystals in fine-grained granular rocks. In order to limit subjective bias, thin sections were selected at random from a tray and the data plotted on representative columnar sections once all determinations had been completed. The procedure has a number of advantages, of which ease of determination, reproducibility, reduction of sectioning effects and large size of the sampled population are significant considerations. However, it should be appreciated that an exaggerated sensitivity exists at small grain-sizes by virtue of the exponential relationship used in the determination. Fig. 7 graphically illustrates the increase in "crystallinity" of an ideal, close packed array of cubes with incremental reduction of the edge dimension (a). A similar manipulation using a close-packed array of spheres shows no significant departure from this curve.

4.2 THE TEXTURAL FEATURES

The results of measurements yielding estimates of crystallinity are presented in Figs. 8(A) to (E). Fig. 8(A) depicts the estimate of the number of orthopyroxene crystals per cm^3 of pyroxenite as a function of stratigraphic position in the lowermost 105 metres of the

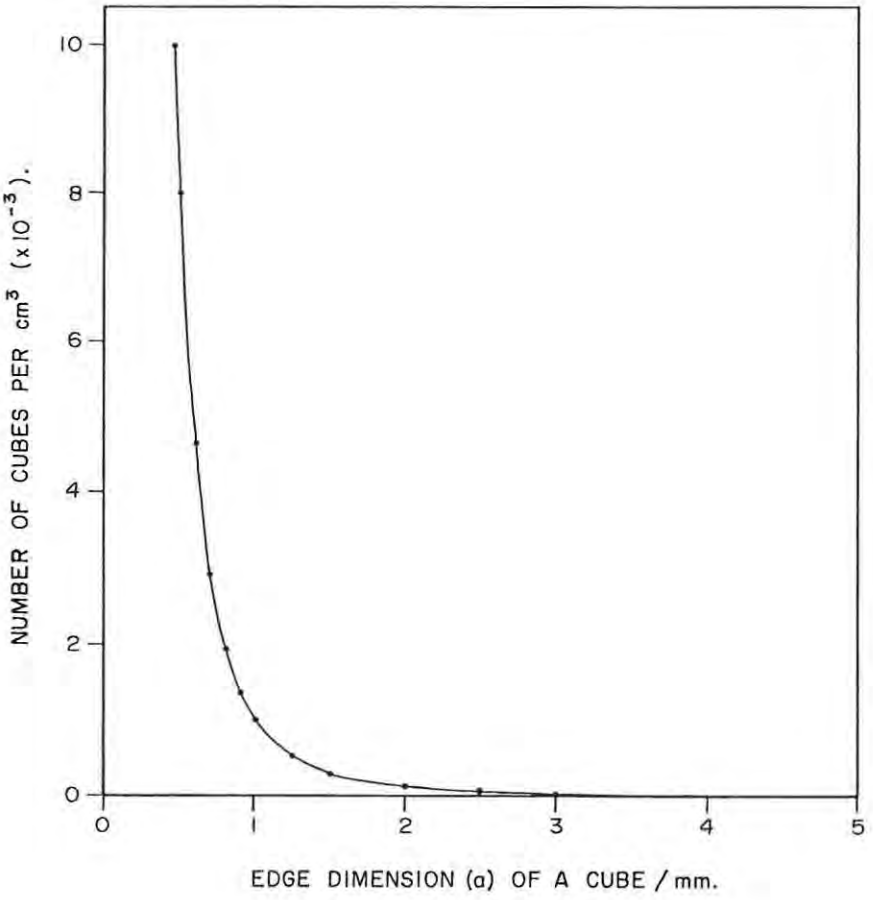

FIG. 7 PLOT OF "CRYSTALLINITY" OF A HYPOTHETICAL CLOSE-PACKED ARRAY OF CUBES VERSUS THE EDGE DIMENSION (a). THERE IS AN EXPONENTAL EXAGGERATION OF THE CRYSTALLINITY AT EDGE DIMENSIONS OF LESS THAN 1 MILLIMETRE.

study section, representing the C_2 subunit and upper 50 metres of the B unit. No crystallinity determinations of samples from the C_1 subunit were obtained by virtue of the extremely fine-scale modal layering in this succession. The number of samples on which Fig. 8(A) is based is 67 and, within each sample, the number of crystals counted in order to make the estimates varied from 100 for coarse-grained rocks to 600 for the finer-grained specimens. The minimum sample spacing is 1,5 metres. Figs. 8(B) to (E) are of similar type but depict successively higher portions of the succession up to the LG 7 chromitite layer. Representative photomicrographs illustrating the textural variations (Figs. 8A(i) to 8C(v)) are provided to augment the petrographic descriptions and the respective figures. A sample for which whole-rock and/or electron microprobe data are available is indicated by an open-square symbol in all the diagrams. No estimates of chromite crystallinity in chromitites were made, nor were they rigorously derived for pyroxenite and dunite samples. However, chromite density may vary from less than one grain per cm^3 in some pyroxenites to very high values in the immediate foot- and hanging-wall rocks of chromitite layers.

4.2.1 BRONZITITES IN THE B UNIT AND C_2 SUBUNIT

Adcumulate- and mesocumulate-textured bronzitites predominate in the B unit and C_2 subunit, varying in crystallinity from 180 to 1 600 crystals/cm^3 of rock (Fig. 8A). Granular-textured varieties, i.e., bronzitites depicting (a) a polygonal mosaic of fine-grained orthopyroxene crystals, (b) higher crystallinity values (e.g., 2 200 crystals/cm^3), and (c) very low modal proportions of intercumulus silicate phases, are only exposed in the footwalls of the LG 2 and LG 3 chromitite layers. Adcumulate-textured bronzitites are composed of a framework of stubby to lath-like orthopyroxene crystals (Figs. 8A(i) and 8A(ii), respectively), with plagioclase as an ubiquitous intercumulus phase. Minor to trace modal proportions of clinopyroxene, amphibole and red mica are common components of the mesostasis, but their modal abundance is always subordinate to plagioclase. Sporadic oikocrysts of clinopyroxene, hosting strongly resorbed chadacrysts of orthopyroxene, are visible in thin section,

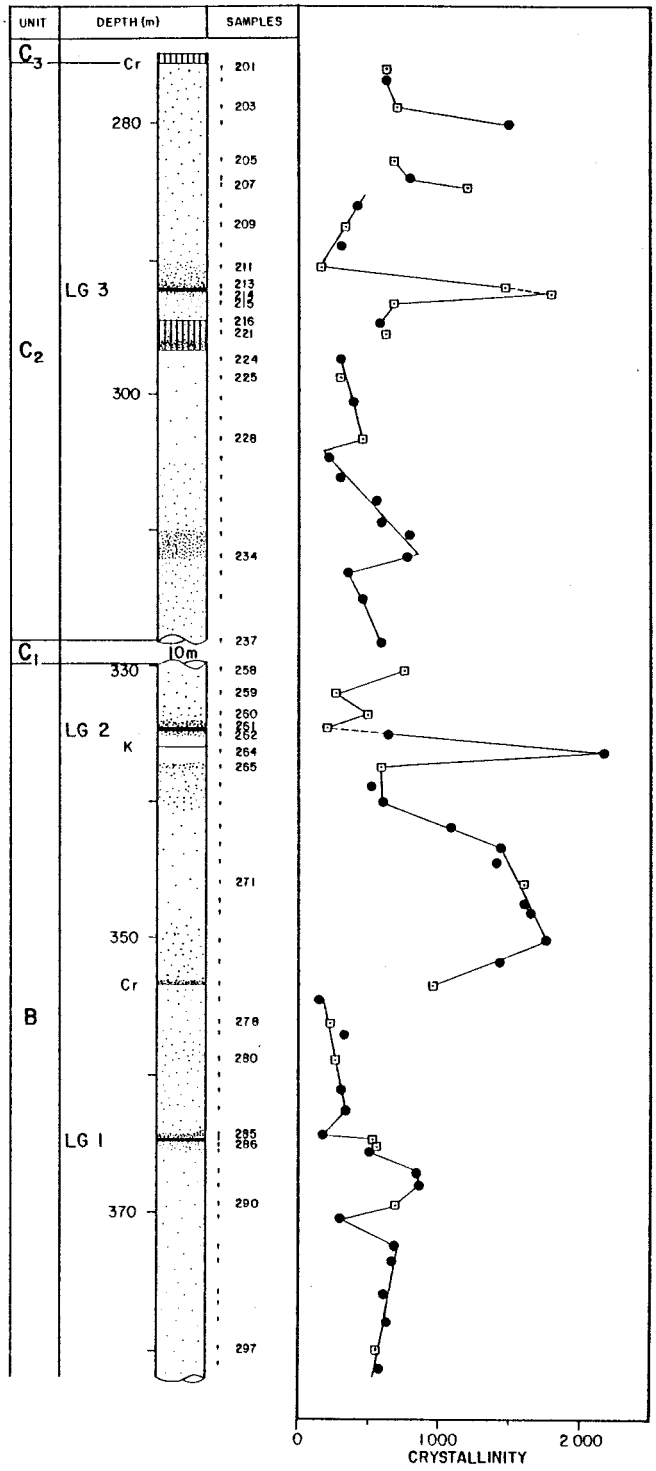

Chromitite

Bronzitite

Olivine - rich rocks

Cr Minor chromitites

K Kimberlite

Microprobe and / or whole - rock data available

FIG. 8(A) VARIATION OF BRONZITE CRYSTALLINITY AS A FUNCTION OF STRATIGRAPHIC POSITION WITHIN THE B UNIT AND C_2 SUBUNIT OF DRILL CORE ZS 7. THE ABUNDANCES OF CHROMITE IN THE SUCCESSION ARE SCHEMATICALLY PORTRAYED BY STIPPLING OF THE BOREHOLE LOG

FIGS. 8A(i) to (v): Photomicrographs of bronzitites within the B unit and C_2 subunit of the studied section. All sections have been photographed with transmitted light under crossed nicols. The scale on Figs. 8A(i) to (iv) is 5cm = 2mm, and 1cm = 100 micrometres (microns) on Fig. 8A(v).

(i): Adcumulate-textured bronzitite exhibiting stubby orthopyroxene crystals and chromite grains intergrown with plagioclase feldspar. Note the anhedral, secondary growth textures of orthopyroxene in juxtaposition to the chromite grains (sample 265; B unit).

(ii): Adcumulate-textured bronzitite exhibiting elongate laths of orthopyroxene (sample 271; B unit).

(iii): Coarse-grained, feldspathic and chromitiferous, mesocumulate-textured bronzitite; hanging-wall of the LG 2 chromitite layer (sample 261). A point of interest is that very few chromite grains are encapsulated or indented within these well-formed orthopyroxene crystals. Secondly, the chromite grains are large ($\pm$ 300 microns) and fairly euhedral. The textural features suggest that both cumulus phases experienced extended growth periods in an unrestricted melt volume, as may be envisaged if they settled through a liquid column. Electron microprobe analysis of these chromite grains indicates Cr_2O_3 contents in excess of 56 wt. %.

i

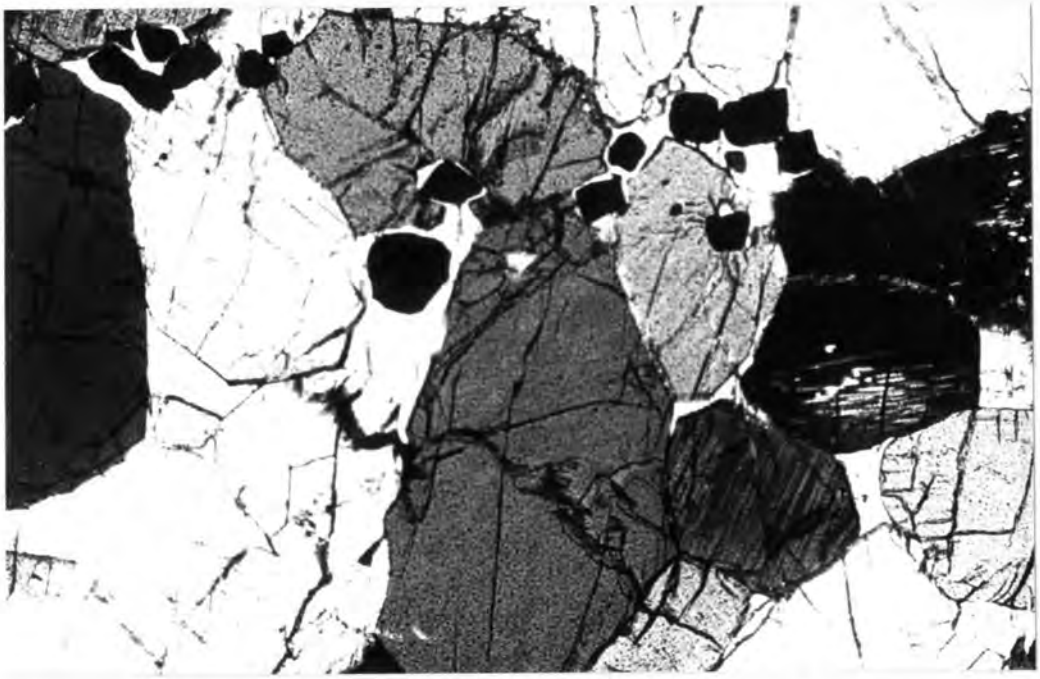

ii

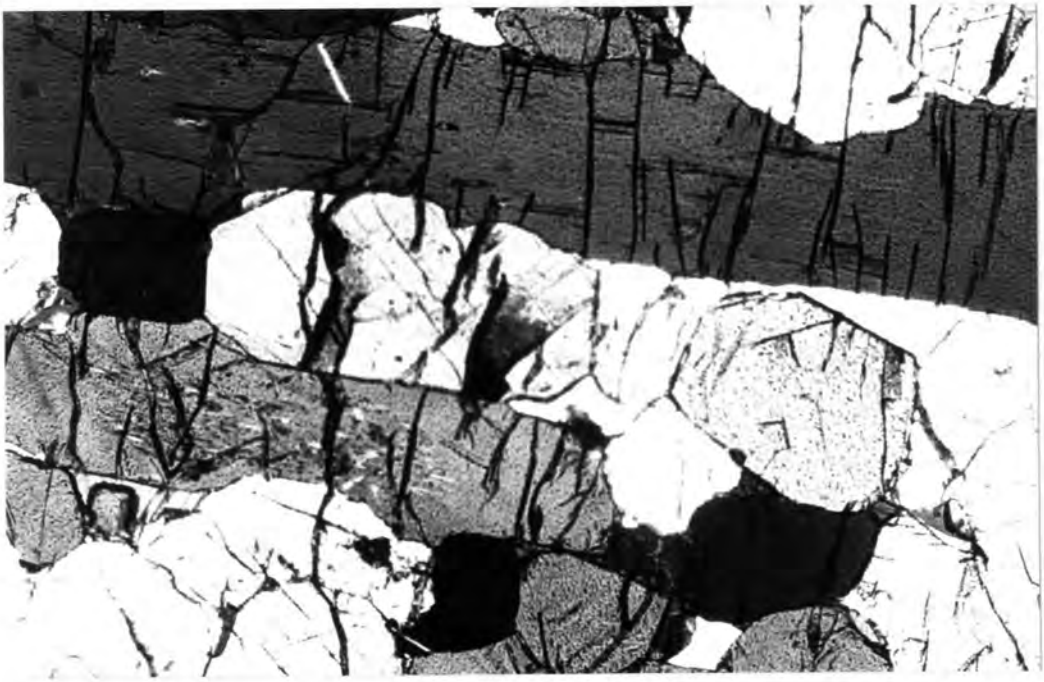

iii

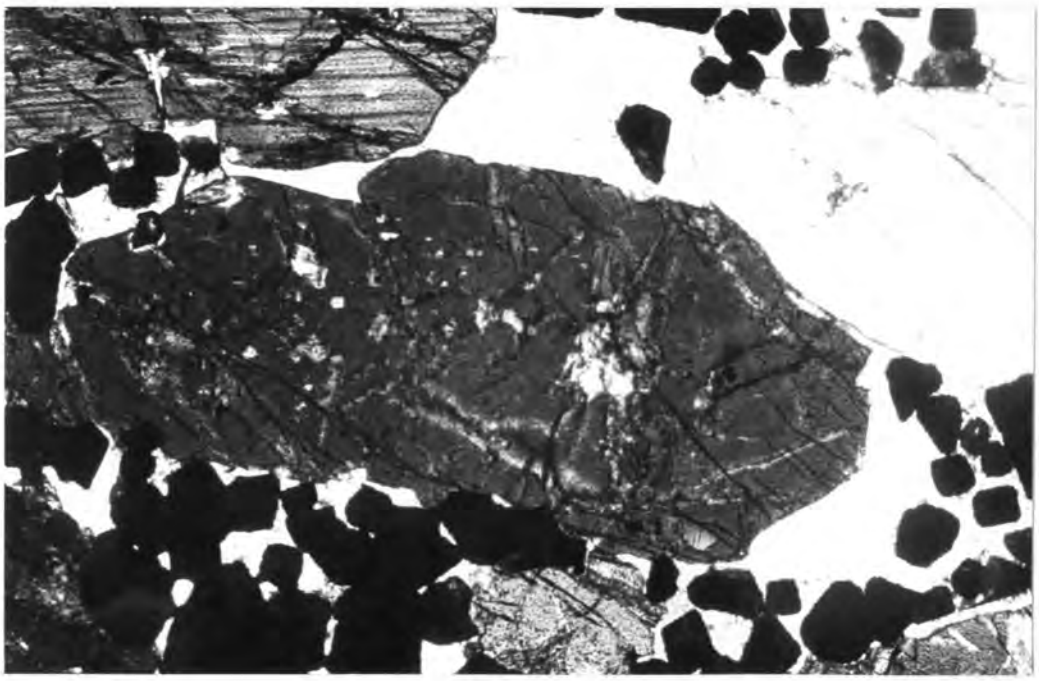

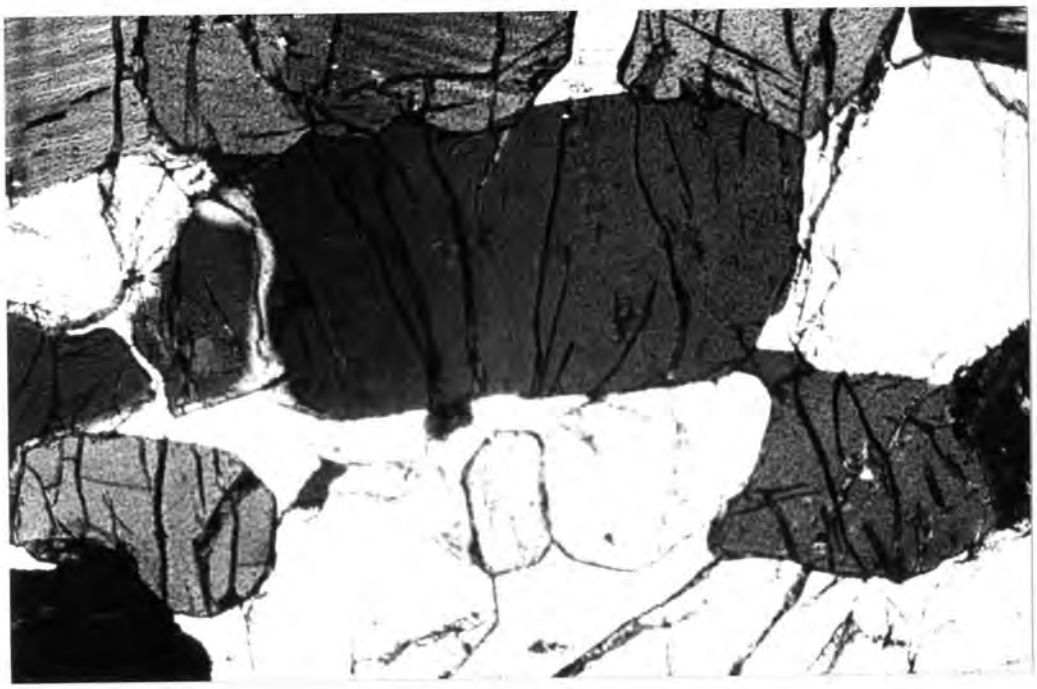

FIGS 8A (iv): Adcumulate-textured bronzitite from the upper portion of the C_2 subunit (sample 203), depicting stubby orthopyroxene crystals and intercumulus plagioclase. Grain-size and shape determines the degree of packing, and thus the proportion of mesostasis.

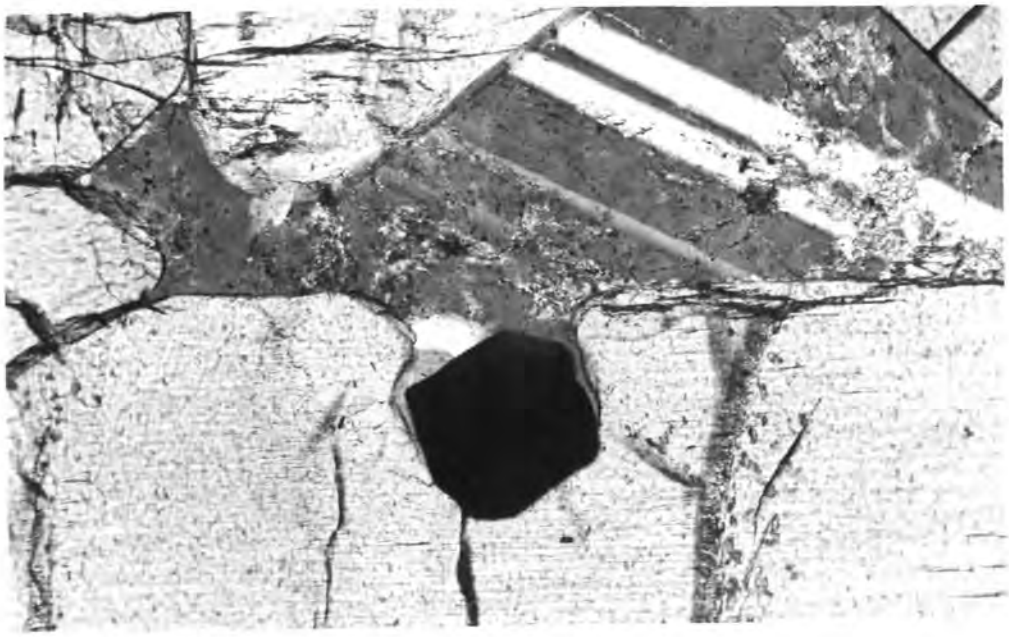

(v): Example of a chromite grain indented to a high degree within an orthopyroxene grain boundary, and intergrown with a selvage of plagioclase feldspar which is in optical continuity with the large intercumulus grain shown (sample 221; bronzitite interleaved with olivine-bronzitite in the footwall of the LG 3 chromitite layer).

but clinopyroxene is normally depicted as an exsolved phase in orthopyroxene crystals and as small, anhedral interstitial grains.

Mesocumulate-textured bronzitites are coarser-grained and this property yields a higher intercumulus silicate fraction. Fig. 8A(iii) presents a photomicrograph of a chromitiferous, feldspathic bronzitite depicted in the immediate hanging-wall of the LG 2 chromitite layer, and serves here as an example of bronzitite with a low crystallinity and high modal proportion of intercumulus plagioclase. Rocks depicting smaller orthopyroxene grain-sizes achieve higher crystallinity and show a proportionate decline in the mesostasis volume (Fig. 8A(iv)). In general terms, there is thus a reciprocal variation between the measured crystallinity of a bronzitite and the interstitial volume. However, this relationship does not hold for a minor suite of medium- to coarse-grained, adcumulate-textured bronzitites which display mutually interfering orthopyroxene grain boundaries and low modal proportions of intercumulus silicate phases. The amphibole, mica, quartz and micropegmatite content of the mesostasis is generally higher in these assemblages (such as samples 225 and 259), but the hydrous mineral content of the mesostasis also rises with increasing stratigraphic height in at least two segments of the succession. These are exposed between the LG 1 and C chromitite layers (samples 285 to 277), and between the LG 2 chromitite layer and the base of the C_1 subunit (samples 261 to 258).

Chromite grains occur as (a) small, euhedral inclusions in orthopyroxene core-domains, (b) larger grains occluded within orthopyroxene rim-domains, and (c) large grains intergrown with the mesostasis or indented to varying degrees in orthopyroxene grain boundaries. The modal content of chromite varies from very low in a high proportion of the bronzitites (e.g., Figs. 8A(ii) and (iv)) to disseminated (e.g., Fig. 8A(iii)) in juxtaposition to chromitite layers. Within any given sample, the number of chromite grains residing in interstices is far in excess of small grains occluded in well-formed orthopyroxene crystals. This feature is evident in Figs. 8A(i) and (iii), and leads to the proposition that all but a few grains nucleated within the interstitial melt volume after some degree of accumulation of orthopyroxene crystals. However, the

inhomogeneous distribution of chromite grains within the bronzitites (Fig. 8A(i)) lends no support to this notion, and it is advocated here that this textural feature stems from surface energy constraints which impose an upper limit on the number and grain-sizes of inclusions. Furthermore, the textures point to primary chromite-orthopyroxene assemblages with high interstitial volumes: subsequent compaction results in the impingement of chromite and orthopyroxene grains, with the residual interstitial volume being governed by orthopyroxene grain-size. It is evident from Figs. 8A(i) and (v), for example, that significant degrees of in situ secondary growth of orthopyroxene in a restricted melt volume must have occurred to yield large chromite grains (> 200 micrometers in diameter) within cupolas in orthopyroxene grain boundaries. These textures are not typical of coarse-grained, mesocumulate-textured assemblages (refer to Fig. 8A(iii)), suggesting therefore that grain-size changes in relation to stratigraphic height are primary features and not wholly a product of secondary processes.

Features which emerge from an inspection of the crystallinity profile depicted in Fig. 8(A) may be summarized as follows:

1. Subtle changes in crystallinity with increasing stratigraphic height are clearly revealed by the data points.
2. Periodic and abrupt reversals in gradients of declining crystallinity with increasing stratigraphic height are depicted.
3. Major changes in crystallinity are evident at the stratigraphic levels of the LG 2 and LG 3 chromitite layers.
4. Minor reversals in crystallinity (i.e., from low to higher) are linked to weak chromite mineralization at some stratigraphic levels (e.g., C chromitite layer and sample 234, which is also olivine-bearing).

4.2.2 DUNITES IN THE C_1 AND C_3 SUBUNITS

Dunites within the studied section are characterized by (a) virtually anchimonomineralic, coarse-grained assemblages of olivine crystals (e.g., with grain diameters of 3 to 5 mm), (b) adcumulate textures, straight grain boundaries and perfect triple junctions, and (c)

variable but typically minor modal proportions of chromite. With increasing chromite abundance in juxtaposition to chromitite layers, yielding chromite dunite and olivine-chromitite lithologies, the diameters of olivine crystals decline but the number of olivine crystals per cm^3 of rock remains constant. This feature is summarized in Fig. 8(B), which shows the variation of olivine crystallinity in relation to stratigraphic height within the C_3 subunit, and in photomicrographs of olivine-chromitite and dunite assemblages presented in Figs. 8B(i) and (ii), respectively. It may thus be inferred that the small olivine crystals depicted in chromite-rich domains (ca. 1 mm in diameter) yield an indication of primocryst grain-sizes, whereas advanced degrees of crystal growth were achieved in chromite-poor domains by virtue of a low initial crystallinity (which may approximate to nucleation density) and unrestricted environment. However, recrystallization in response to subliquidus annealing processes may yield comparable textures (Coble and Burke, 1963).

In principle, annealing of a fine-grained crystalline assemblage to yield coarse particles bounded by straight grain boundaries and triple junctions is achieved at sustained, near-liquidus temperatures by (a) migration of grain boundaries, and (b) growth of larger, six-sided grains at the expense of smaller grains with less than six sides (Stanton, 1972; p. 285). This process is a natural response within the system (of crystalline phases in mutual contact) to reduce the total surface area represented. The efficacy of the process, or rate of grain boundary migration, is dependent on parameters such as initial grain-size, presence of a capillary fluid, number of impurities within the assemblage (e.g., chromite grains in an accumulation of olivine crystals and vice versa) and nature of the crystalline phase. For example, the rate of grain boundary migration is envisaged to be considerably greater for cubic oxide phases (such as chromite and magnetite) than for silicate phases. Within annealed assemblages, an indication of the initial grain-size can be gleaned from microdomains showing a higher, residual porosity (Reynolds, 1979), i.e., domains in which grain annealing was inhibited by one or more impurity. It is thus clear that the uniform crystallinity (or average grain-size) exposed in dunites within the C_3 subunit may represent a limiting condition dictated by the thermodynamic

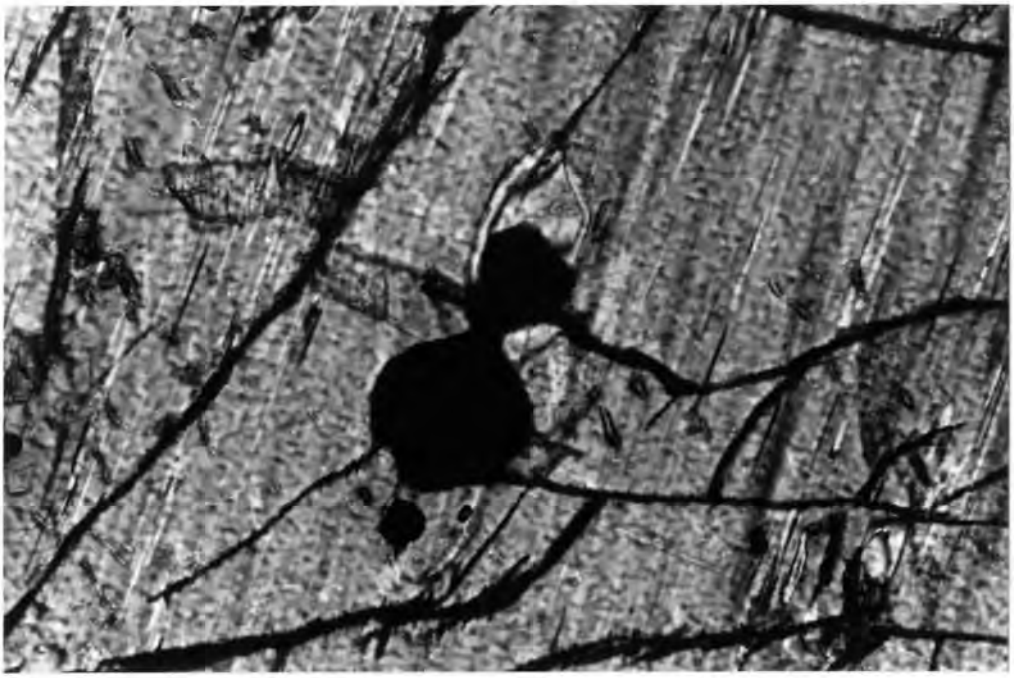

FIG. 45(A): Partial halo of exsolved clinopyroxene nucleated on the grain boundary of a small chromite grain occluded within the core of an orthopyroxene crystal (E unit, sample 70). Section photographed with transmitted light under crossed nicols. The smaller of the chromite grains is 50 microns in diameter. It should be noted that the occurrence of spherical to ellipsoidal blebs of clinopyroxene in juxtaposition to small encapsulated chromite grains is a textural feature common to the entire studied section.

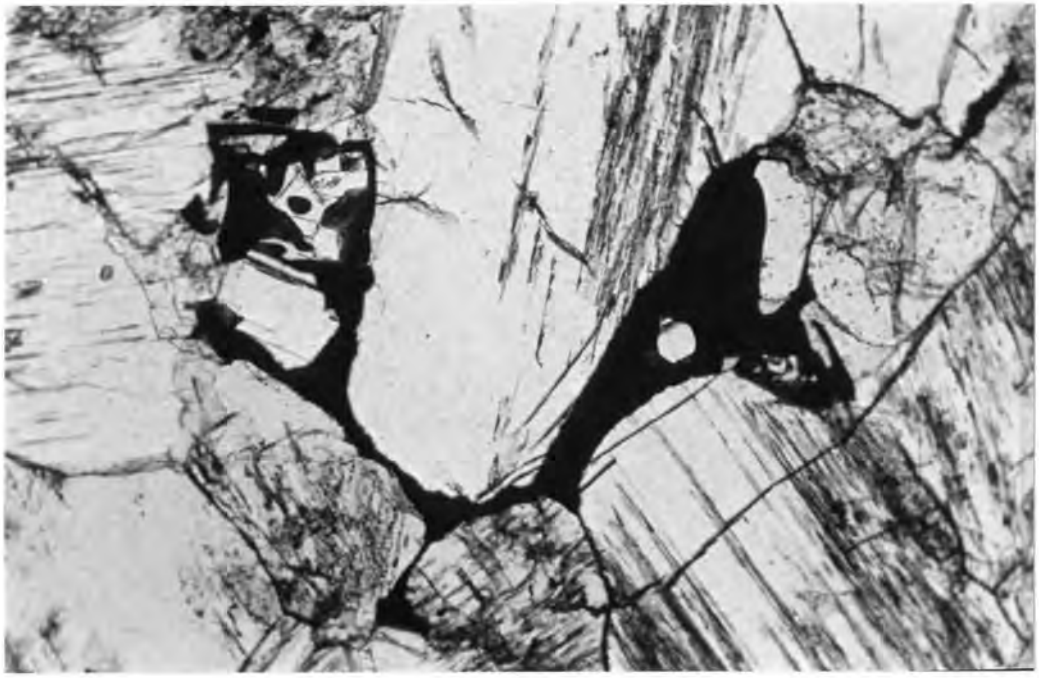

45(B): Interstitial chromite within a medium-grained, granular-textured bronzitite (E unit, sample 50). Note the correspondence between the chromite grain (reflected light microscopy yields no evidence of intracrystalline grain boundaries) and what is described in the present text as a "poorly annealed cavity". Finer-grained bronzitites depicting advanced degrees of annealing or foam texture do not display this feature, thus indicating that it is not a recrystallization phenomenon. Section photographed with transmitted light. Scale 5cm = 1mm.

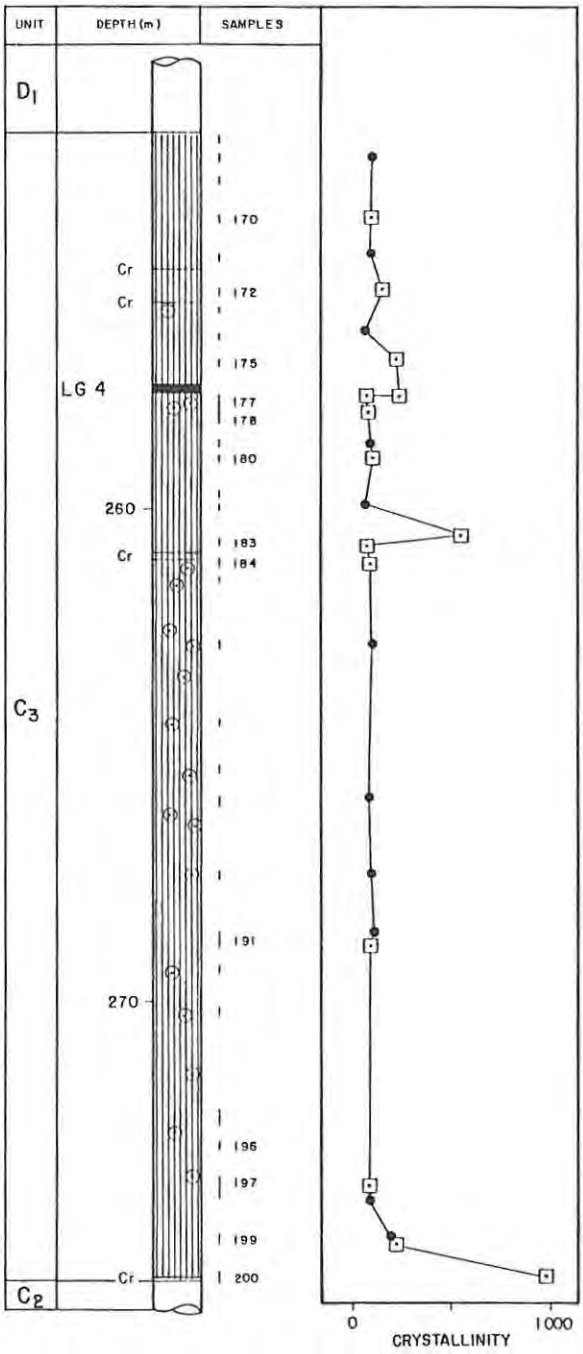

Dunites, chromite dunites, Olivine - Chromitites

Chromitite

Bronzitite

Lenses of poikilitic harzburgite in dunite

FIG. 8(B) VARIATION OF OLIVINE CRYSTALLINITY WITHIN DUNITES, CHROMITE DUNITES AND OLIVINE-CHROMITITES OF THE C_3 SUBUNIT, DRILL CORE ZS 7. NO CUMULUS ORTHOPYROXENE IS DEPICTED IN THIS SUBUNIT (SEE TEXT). CHROMITE - RICH ROCKS OCCUR ADJACENT TO THE CHROMITITE LAYERS

stabilization of olivine grain boundaries, and may stem in part from the absence of co-existing, cumulus orthopyroxene crystals. The latter is consistent with textural features displayed in granular harzburgites and olivine bronzitites of the C_1 subunit, viz., (a) smaller olivine grain-sizes (ca. 2 mm in diameter), (b) curved olivine grain boundaries when abutting against orthopyroxene, concave towards olivine (this feature gives the appearance of olivine being interstitial to orthopyroxene in olivine-poor domains), and (c) a higher incidence of polygonal grain boundaries in granular harzburgites showing higher modal proportions of olivine. However, a fine-grained, polygonal mosaic of olivine crystals, with a crystallinity of 1 000 crystals/cm^3, is exposed at the base of the C_3 subunit (Fig. 8(a); sample 200) and, from microprobe analyses of Ni contents in olivine, the inference is made that annealing effected adjustments in grain-shape but enlargement was achieved by in situ incremental growth. These considerations will be addressed in a subsequent section of the text.

In summation, pervasively serpentinized olivine-bearing lithologies within the studied section depict extremely low modal occurrences of intercumulus silicate minerals. Where present, orthopyroxene, plagioclase, clinopyroxene or mica is seen in poorly annealed cavities. Spheroidal lenses of poikilitic harzburgite, characterized by structurally continuous plates of reaction-replacement orthopyroxene, are common within the lower portion of the C_3 subunit, and quasi-layered structures occur immediately below chromite-rich layers. Varying proportions of olivine chadacrysts, displaying resorption textures, are poikilitically enclosed within these orthopyroxene oikocrysts, with the proportion of residual olivine varying as a reciprocal function of the degree of reaction-replacement. Finally, it is evident from the profile portrayed in Fig. 8(B) that no link between chromite abundance and olivine crystallinity is exposed.

4.2.3. BRONZITITES IN THE D UNIT

The results of orthopyroxene crystallinity measurements at 75 stratigraphic levels within the D unit are summarized in Figs. 8(C)

and (D). Fig. 8(C) depicts the variation in relation to stratigraphic height within drill core ZS 7, whereas Fig. 8(D) contrasts the measured variation within bronzitites of the D_2 subunit exposed in both boreholes. The number of orthopyroxene crystals per cm^3 of rock varies between 100 and 7 000 within the unit: low values are representative of mesocumulate-textured, feldspathic bronzitites (e.g., as shown in Fig. 8C(i)) and coarse-grained, adcumulate-textured bronzitites with a micropegmatitic mesostasis (Fig. 8C(ii)), whereas values in excess of 2 000 crystals/cm^3 are representative of granular-textured varieties (Fig. 8C(iii)). The latter are exposed predominantly in the upper portion of the succession and are characterized by the following textural features:

1. Orthopyroxene grain boundaries are straight and meet in perfect triple junctions.
2. No igneous lamination is displayed.
3. Fine clinopyroxene exsolution lamellae are depicted, and optical zoning within individual crystals is poorly developed to non-existent.
4. The proportion of mesostasis is extremely low, with small interstitial grains of plagioclase or clinopyroxene confined to poorly annealed cavities. Mica, quartz and micropegmatite are not present.
5. Limited degrees of alteration along pyroxene (100) cleavage planes may be observed.
6. Associated chromite grains are small and generally reside within triple junctions (this textural environment is referred to as "intergranular" in the subsequent text).

In contrast, coarse-grained assemblages depict (a) ragged or curved grain boundaries, with occasional well-formed crystal faces, (b) coarse clinopyroxene exsolution lamellae (commonly altered to uralitic amphibole) and optical zoning, (c) plagioclase as an ubiquitous intercumulus phase, with lesser amounts of mica, quartz and micropegmatite, and (d) low proportions of large chromite grains (200 to 400 micrometres in diameter) intergrown with the mesostasis.

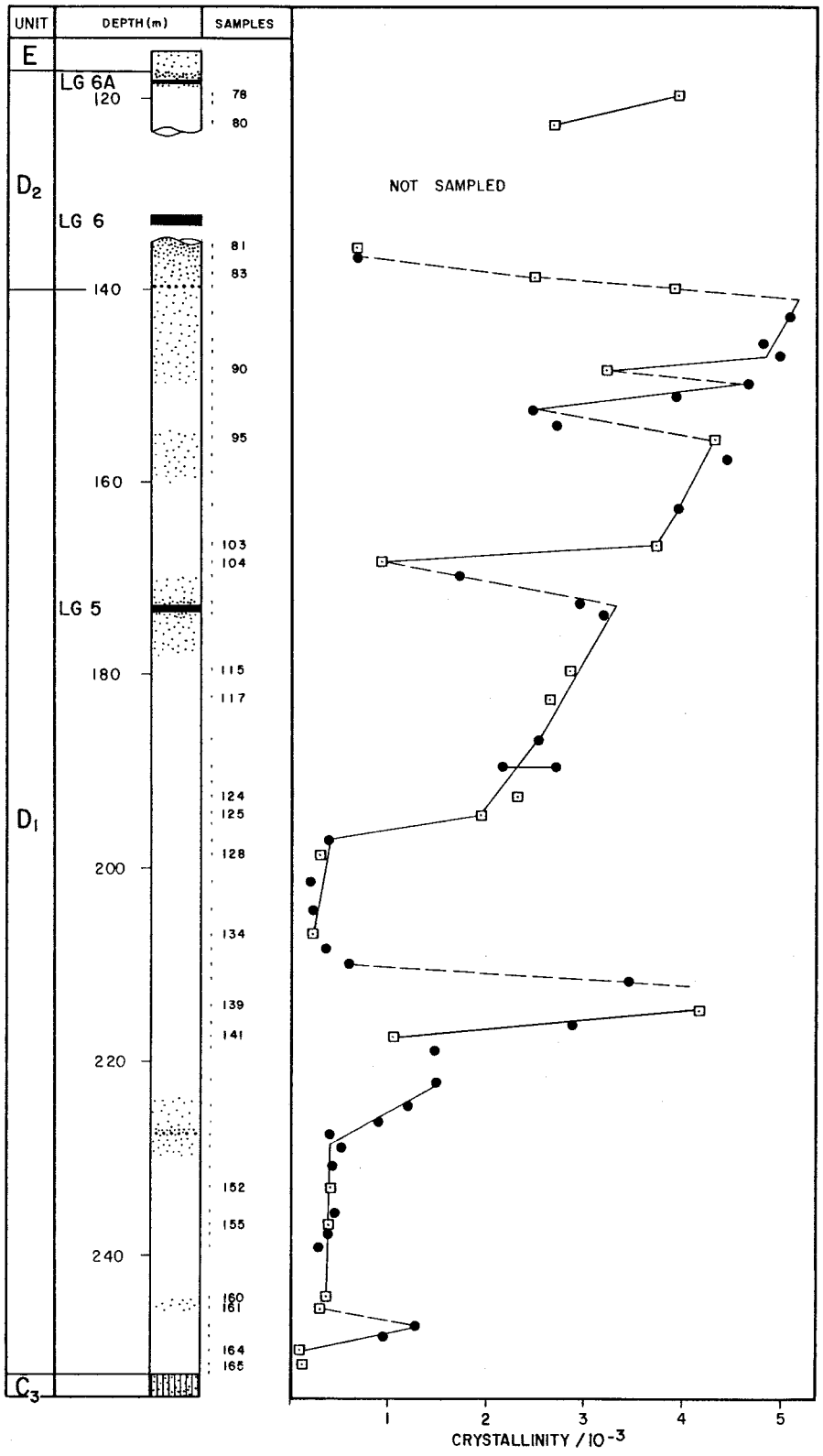

Bronzitite
Chromite Bronzitite
Chromitite
Dunite
Microprobe and / or whole-rock data available
Observed limits of reproducibility (sample 122)

FIG. 8 (C) VARIATION OF BRONZITE CRYSTALLINITY WITHIN THE D UNIT, DRILL CORE ZS 7. STIPPLING OF THE LOG DEPICTS CHROMITE ABUNDANCE

FIGS. 8C(i) TO (v): Examples of bronzitites within the D unit exhibiting a wide range in textural features and orthopyroxene crystallinity. All sections have been photographed with transmitted light under crossed nicols. The scale on Figs. 8C(i) to (v) is the same as on Fig. 8A(i).

(i): Mesocumulate-textured, feldspathic bronzitite depicting well-formed orthopyroxene crystals and irregular to lobate protrusions of orthopyroxene into the plagioclase mesostasis (sample 134). Crystallinity = 180.

(ii): Coarse, adcumulate-textured bronzitite with micropegmatitic mesostasis. Plagioclase is subordinate to the modal proportion of micropegmatite, mica and quartz (sample 155). Crystallinity = 350.

(iii): Granular-textured bronzitite composed of a polygonal mosaic of orthopyroxene crystals (sample 139). Crystallinity = 4120.

4S c

i

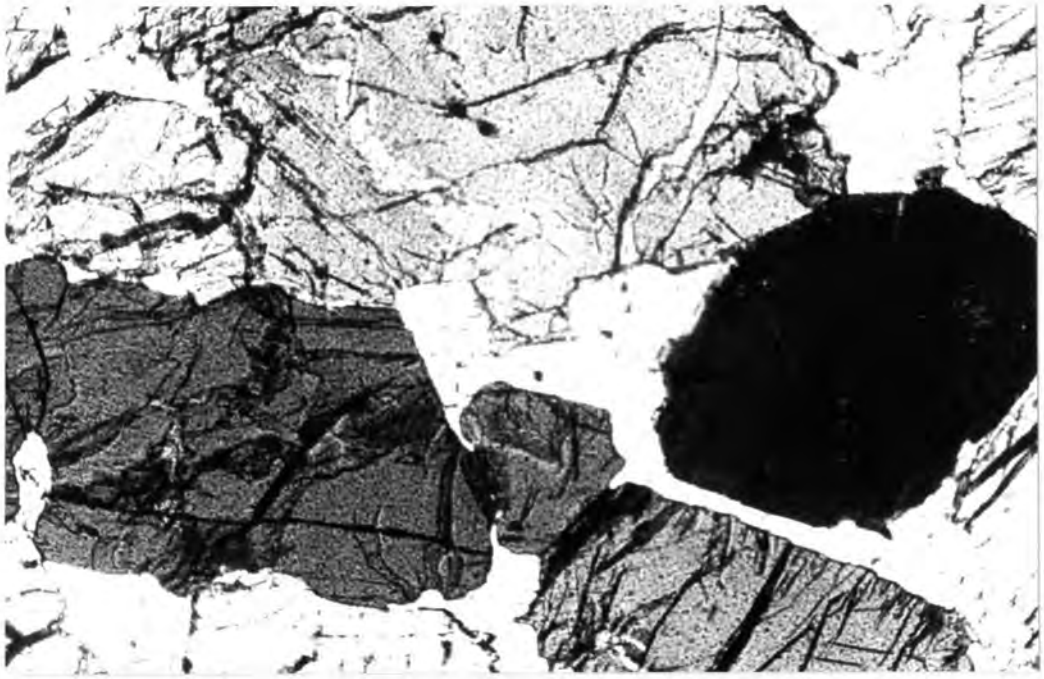

ii

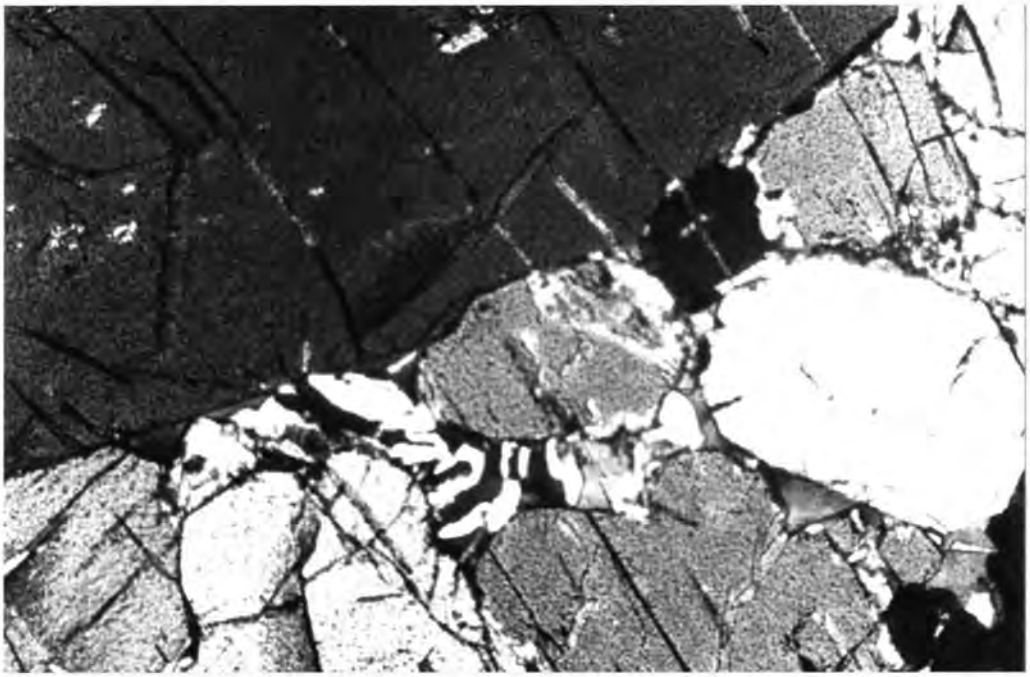

iii

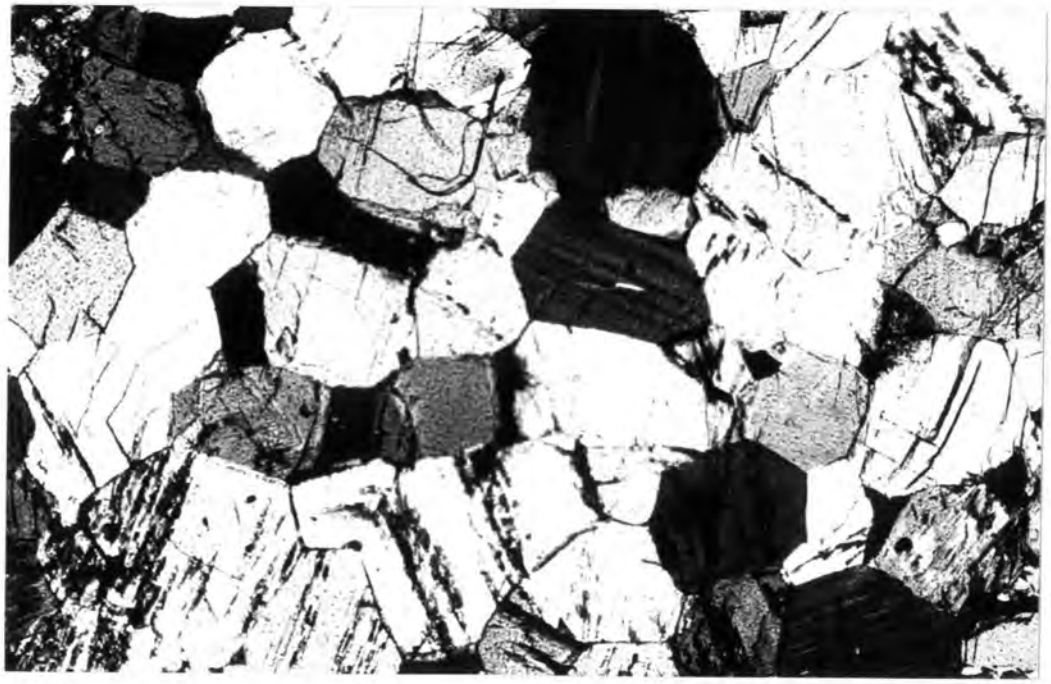

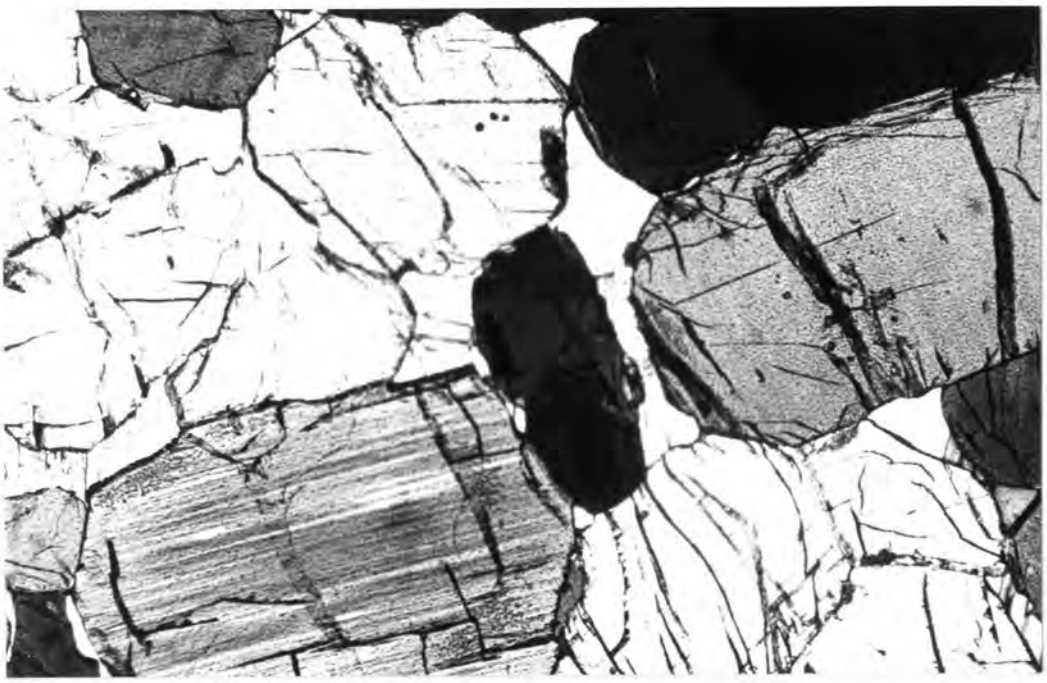

FIG. 8C (iv): Medium-grained, feldspathic bronzitite. Note the well-formed orthopyroxene crystals, conspicuous plagioclase content and absence of chromite (sample 104). Crystallinity = 880.

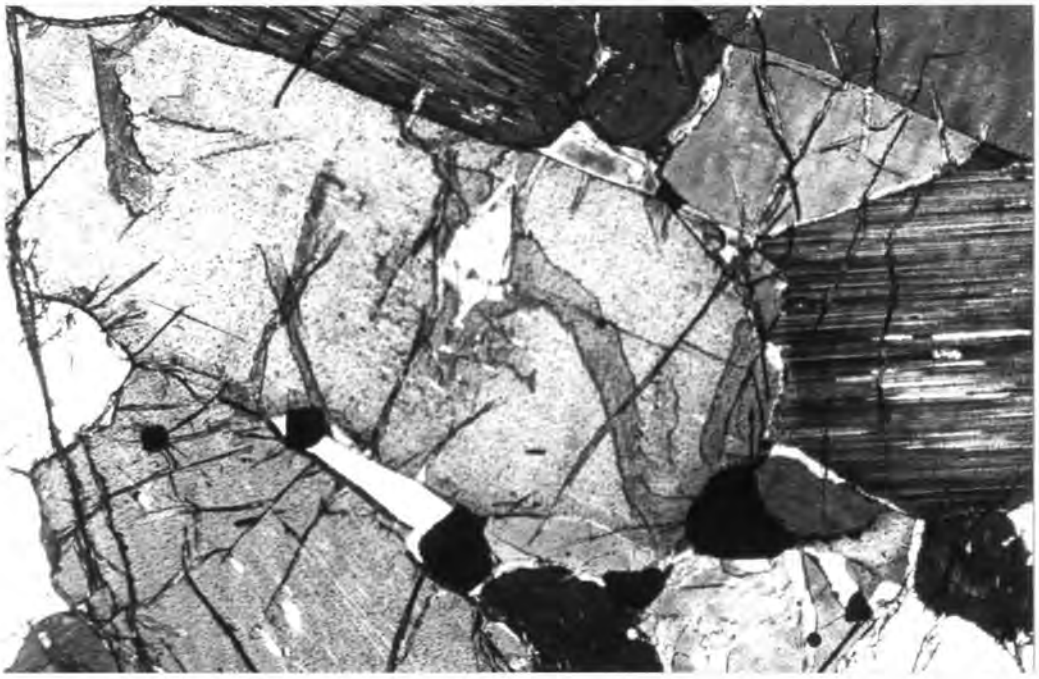

(v): Coarse-grained bronzitite from near the base of the D_2 subunit. Note the large chromite grains between orthopyroxene crystals and smaller grains encapsulated in the rim-domains (sample 81). Crystallinity = 610.

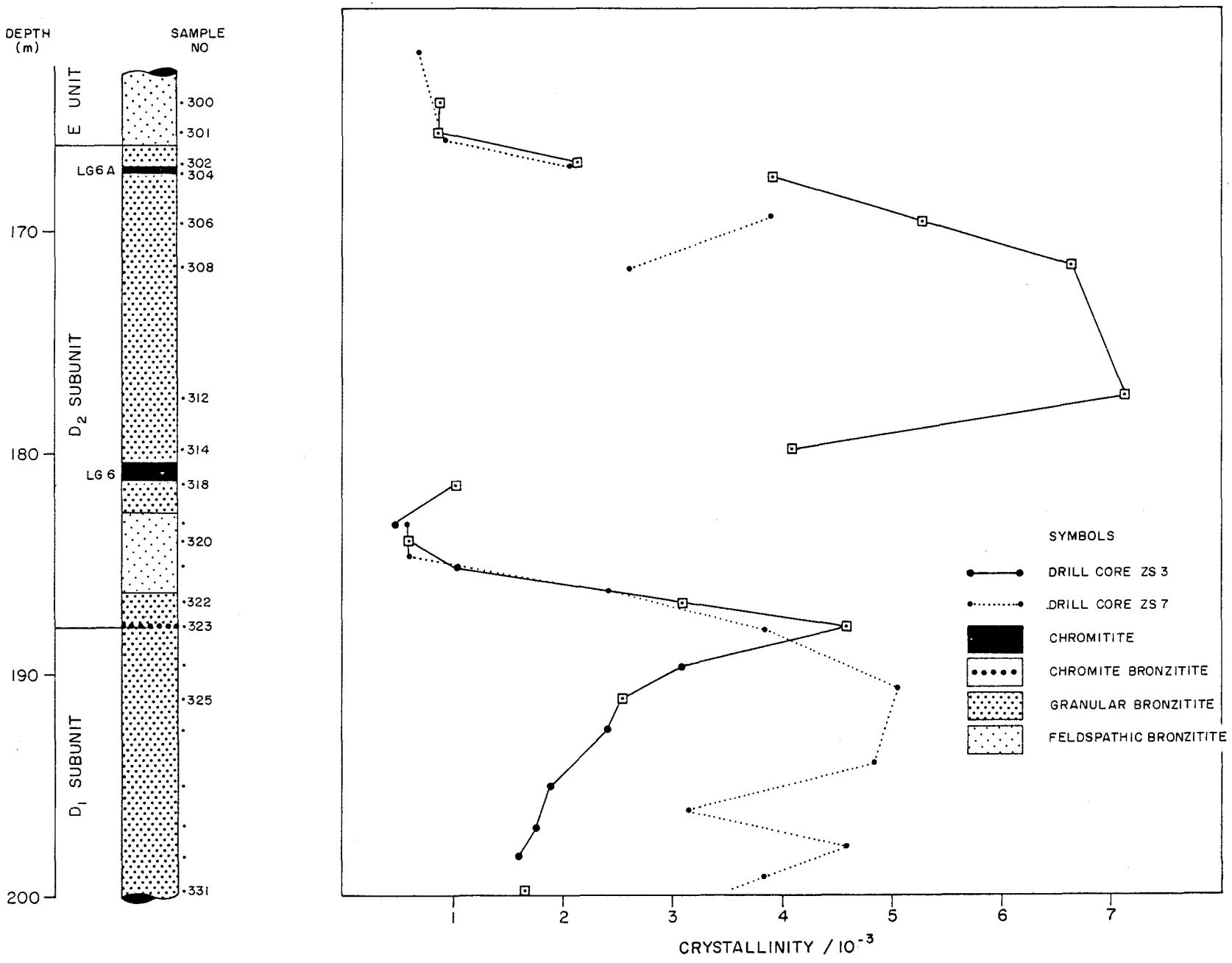

FIG. 8(D) VARIATION OF BRONZITE CRYSTALLINITY WITHIN THE D_2 SUBUNIT, DRILL CORE ZS 3 AND ZS 7.

It is evident from Fig. 8(C) that crystallinity rises irregularly with stratigraphic height in the D_1 subunit. Abrupt changes to lower crystallinity are displayed stratigraphically above the LG 5 chromitite layer (e.g., Fig. 8C(iv)), with a major decline manifested in the basal portion of the D_2 subunit (Figs. 8(C) and (D)). The latter assemblages depict a feldspathic mesostasis and a marked rise in chromite content (Fig. 8C(v)). With respect to the crystallinity profiles presented in the figures, it should be noted that (a) the crystallinity of granular-textured bronzitites varies as a reciprocal function of grain-size, and (b) linear gradients are an artifact of the exponential relationship used in the calculation of crystallinity and the cartesian plot employed. Thus, in real terms, the data points portray a systematic change with increasing stratigraphic height to a limiting, minimum grain-size at the top of the D_1 subunit. This feature is wholly irreconcilable with a process such as recrystallization and it is thus inferred that the marked fluctuation in grain-size within the footwall of the LG 6 chromitite layer, which represents the thickest of the Lower Group of chromitite layers, may reflect a major change in the thermal conditions of the magma. By virtue of the rapid diffusivity of heat, it is improbable that an internally generated temperature gradient could account for the observed features. Thus, textural evidence points to some external influence, such as influx of new hot magma into the chamber, governing fluctuations in nucleation and growth rates.

4.2.4 BRONZITITES IN THE E UNIT

Granular- and adcumulate-textured bronzitites predominate in the E unit of the studied section. The variation of orthopyroxene crystallinity in relation to stratigraphic height is summarized in Fig. 8(E), and it is evident from the disposition of data points that "fining-upward" cycles are depicted within the lower, chromite-poor portion of the unit, whereas "coarsening-upward" cycles characterize the stratigraphic interval bounded by sample 39 and the LG 7 chromitite layer. Notably, however, highest crystallinity values within each putative cycle, arbitrarily denoted 1 to 5 in the figure, rise with increasing stratigraphic height. Furthermore, a point of interest is that the chromitite lens in sample 28, and the LG 7

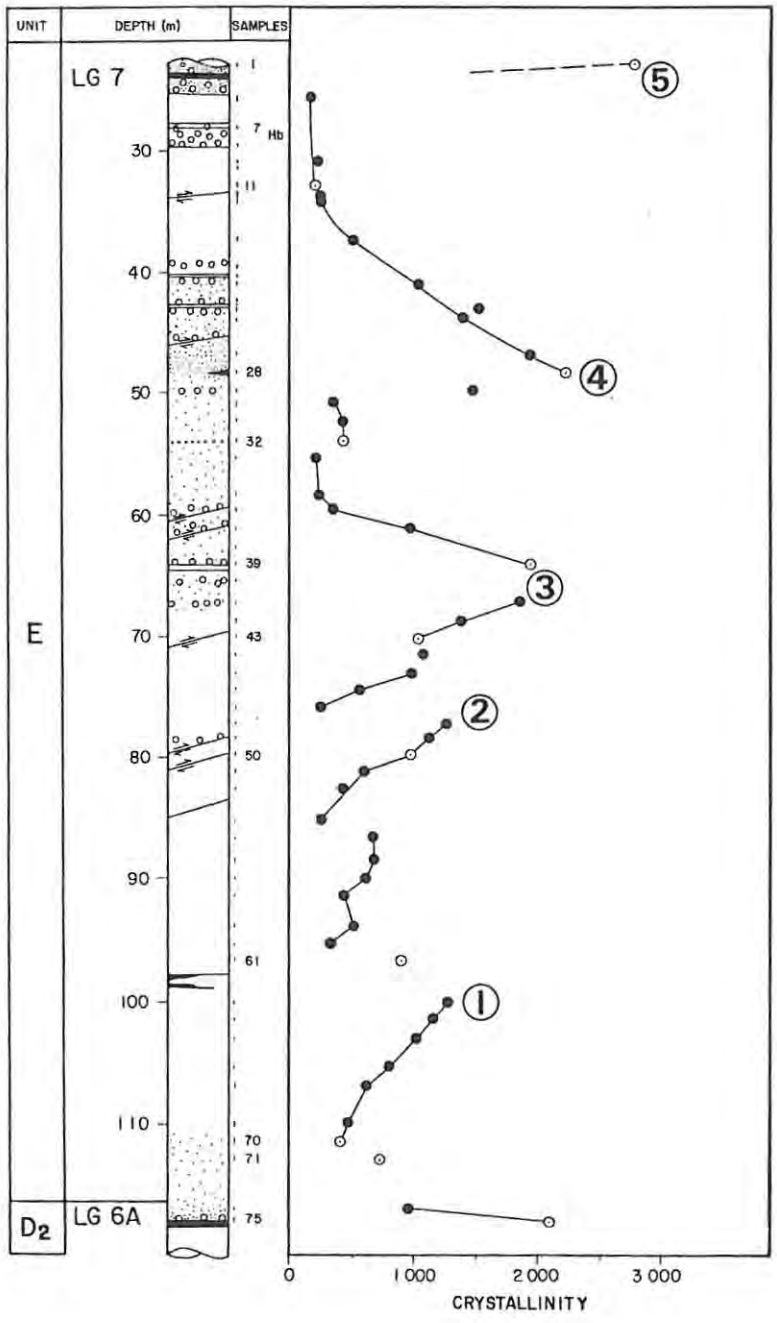

FIG. 8(E) VARIATION OF BRONZITE CRYSTALLINITY WITHIN THE E UNIT, DRILL CORE ZS 7. STIPPLING OF THE BOREHOLE LOG DEPICTS THE RELATIVE ABUNDANCE OF CHROMITE IN THE PYROXENITES

chromitite layer, mark stratigraphic levels at which there is an abrupt change from coarse- to fine-grained assemblages with increasing stratigraphic height (a relationship also noted for the LG 6 and C chromitite layers).

4.2.5 CONCLUSIONS

In summation, no cohesive pattern emerges which links chromite abundance and unique variations in orthopyroxene crystallinity with increasing stratigraphic height. For example, crystallinity declines gradationally then rises abruptly in the footwall successions of the LG 2 and LG 3 layers, whereas a progressive increase followed by an abrupt decrease is evident in the footwall of the LG 6 chromitite layer. However, the study has served to illustrate that (a) repetitive crystallinity gradients are depicted within seemingly homogeneous units of bronzitites, and (b) chromite ores are exposed at stratigraphic levels where significant and abrupt fluctuations in crystallinity are evident. It may be inferred from the contradictions found when trying to generalize changes in crystallinity as precursors to heavy chromite mineralization, that the origin of chromite layers is not linked to rhythmic nucleation and crystal settling, for example, but to some random external influence. This may be either deposition from chromite-charged density currents, or in response to periodic irruptions of hot magma into the chamber. The latter demands that varying degrees of mixing of evolved and primitive melts must ultimately follow, and clearly a diversity of thermal conditions may result. For example, if the liquidus temperature of the hybrid melt is substantially in excess of the pre-existing liquidus temperature, destruction of nucleation sites will ensue; subsequent supercooling to subliquidus temperatures may thus result in abrupt textural lacunae.

4.2.6 CHROMITITE LAYERS

Typical textures exposed in the Lower Group of chromitite layers are illustrated in Fig. 8(F). It is evident that (a) chromite grains exhibit straight to slightly curved crystal faces (as shown in detail

within Fig. 8(G)) which meet at perfect triple junctions, (b) larger grains have six or more sides, and (c) small grains have commonly four sides. These features may thus be regarded as indicative of an annealed assemblage (used here synonymously with the term sintered) which is in thermodynamic equilibrium. A point of interest is that microdomains depicting higher residual pore volumes portray particle sizes which are considerably smaller (Figs. 8(G) and (H)). For example, grain-sizes of 100 microns may occur in juxtaposition to crystals with diameters tending to 1 000 microns. This observation serves to emphasize that present textures within massive ore domains are not representative of primary accumulation textures. Densification by compaction and annealing is thus favoured here as a mechanism by which an accumulation of fine-grained chromite crystals, with a high primary porosity, is converted to a polygonal, anchimonomineralic mosaic displaying foam textures. Supportive evidence is given by the disposition of small grain-sizes at the top and bottom contacts of chromitite layers, grading into a mosaic of coarse, polygonal grains within the central portions (Fig. 8(I)). Arrested welding or suturing of grains and a higher incidence of silicate inclusions (representing incomplete expulsion of capillary fluids) are commonly observed features adjacent to the contacts of layers.

Chromitite layers may have abrupt or gradational contacts with the juxtaposed silicate-rich rocks (Figs. 8(J) and (K)). With the exception of the LG 6 and LG 6A chromitite layers, the major Lower Group layers exhibit very abrupt top and bottom contacts with chromite-poor bronzitites: a feature which is irreconcilable with long-range settling of small chromite grains. In all instances, however, the disparity in grain-size between large grains in massive ore domains and small, dispersed grains occluded within cumulus orthopyroxene crystals is a conspicuous feature (this is evident in Figs. 8(I) and (L)). Notably, the latter grain-sizes (on average 60 to 80 microns in diameter) are also represented within microdomains exhibiting higher proportions of mesostasis in the interiors of chromitite layers (as shown in Fig. 8(H)). In concluding the above, rejection of the classic adcumulus growth theory in favour of grain growth by annealing to account for coarse, polygonal textures within chromitite layers obviously has important implications with respect

to (a) contrasting the compositional variation of chromite in relation to textural and mineralogical environment, and (b) the interpretation of grain-to-grain cryptic changes with stratigraphic height in chromitite layers. In sum, the notion of grain annealing supports the assumption that the compositions of grains within chromitite layers approximate closely to primary liquidus compositions. This assumption follows from the notion that grain annealing induces expulsion of interstitial melt at near-liquidus temperatures, but a point to be recognized is that annealed areas may have "blurred" cryptic variations.

FIGS. 8(F) TO (L) : Photomicrographs of chromite-rich domains within the studied section. All sections have been photographed under plane polarized reflected light.

(F) : Polygonal assemblage of annealed chromite grains within the LG 6A chromitite layer, drill core ZS 7.

(G) : Higher power magnification of a portion of (F), illustrating smaller particle sizes in microdomains with a residual silicate gangue component.

(H) : Microdomain within the LG 3 chromitite layer exhibiting a wide spread in textural features. The domain in the upper right hand side of the photograph portrays small particles intergrown with a silicate mesostasis (serpentine), and is presumed to represent an area within the chromite ore where grain annealing was not effective by virtue of poor compaction. Microprobe analysis of grains in relation to textural environment and grain-size indicates (a) no detectable zoning, and (b) small, isolated particles exhibit higher Cr/Al ratios (2,80) and lower MMF ratios (0,496) than polygonal grains (Cr/Al = 2,70; MMF = 0,512). Section cut normal to drill core axis.

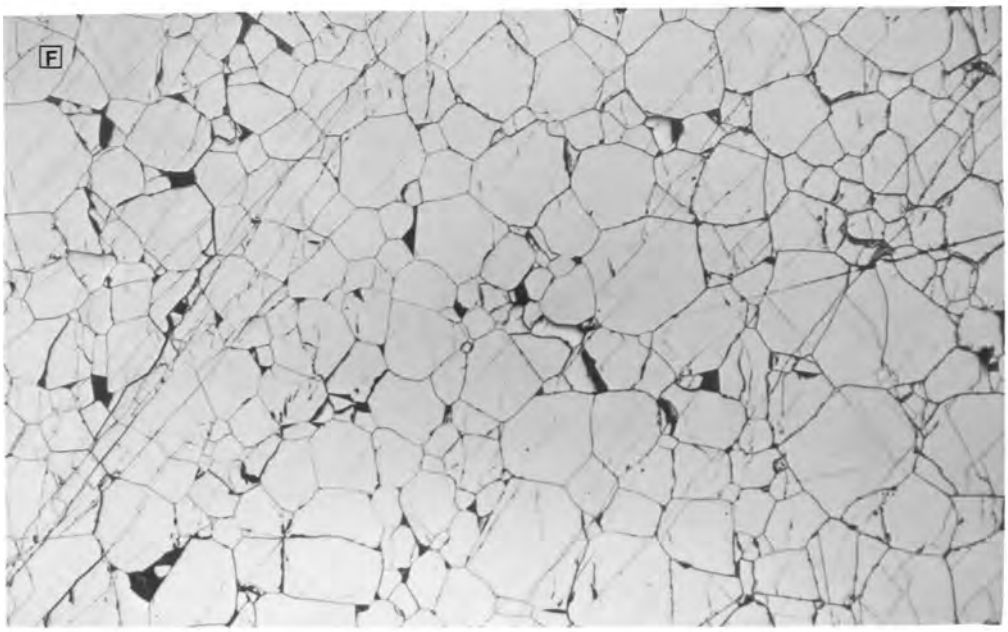
F

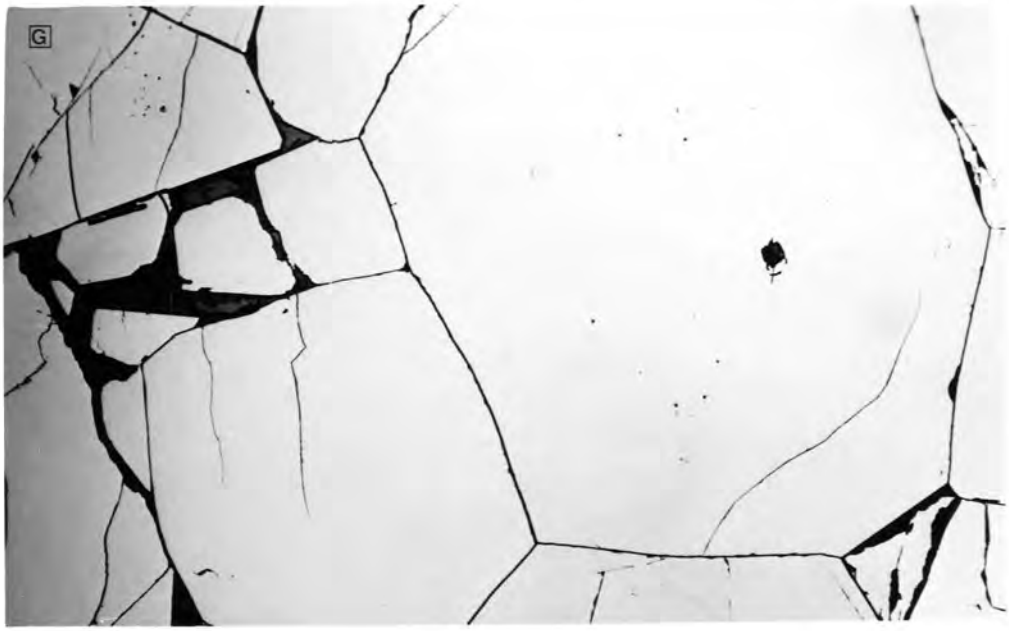
G

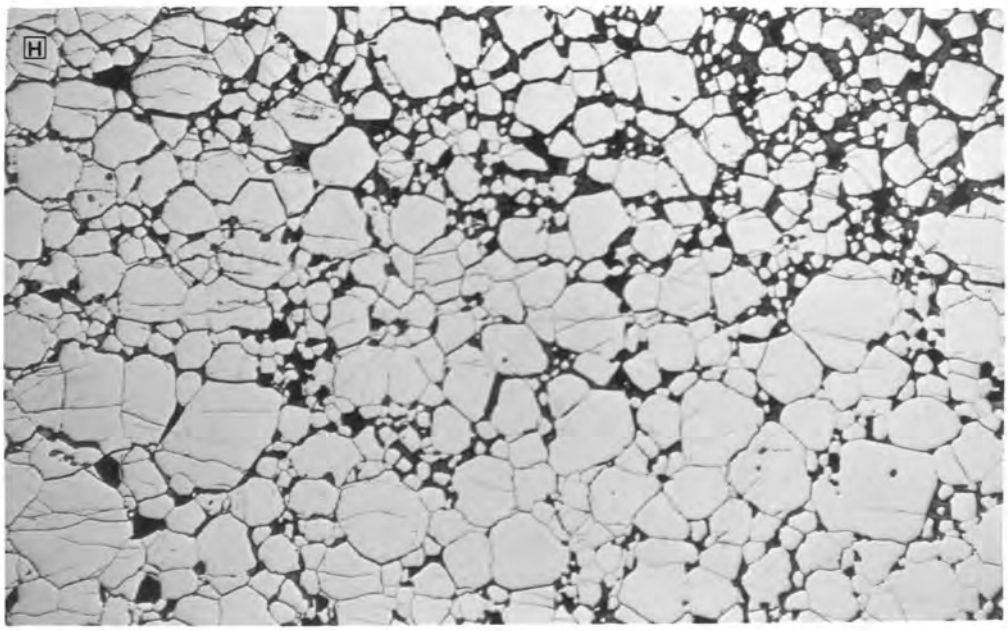
H

FIGS 8 (I) : Chromitite lens depicted within granular-textured bronzitite at the stratigraphic level of sample 28 (E unit). Progressive degrees of grain annealing towards the interior of the chromitite are evident.

(J) : Gradational footwall contact of the LG 3 footwall leader chromitite layer with granular-textured bronzitite. Note the high relief olivine crystals (intergrown with reaction-replacement orthopyroxene) within the chromite-rich domain. Electron microprobe analysis of these olivine crystals indicates magnesian compositions and NiO contents in excess of 0,40% (section 214A).

(K) : Gradational hanging-wall contact of the 2cm thick C chromitite layer within the B unit. Shearing parallel to the base of the layer has obscured the contact relationships (not shown), but these appear to represent an abrupt contact with adcumulate-textured, coarse-grained bronzitite, which grades rapidly downwards into mesocumulate-textured bronzitite. The immediate hanging-wall, however, is a granular-textured and finer-grained bronzitite; a low modal proportion of intercumulus plagioclase appears within 2cm of the upper chromitite contact.

(L) : Textural features portrayed within a layered silicate parting in the LG 6A chromitite layer (drill core ZS 7). The original silicate assemblage within the parting, a medium-grained granular-textured bronzitite depicting impersistent stringers of chromite grains, is replaced to varying degrees by olivine-rich ultramafic pegmatite (not shown in section), but no disturbance of the fine-scale layering is visible: chromite stringers pass through large, structurally continuous olivine crystals, which exhibit undulose extinction stemming from deformation lamellae. Considerable conversion to reaction-replacement orthopyroxene is also shown, suggesting that replacement of the primary bronzite assemblage occurred while pore fluids were still exuding from the juxtaposed chromitite. A point of interest in the photograph is that chromite grains defining the stringers are comparable in size to grains within the massive ore. The possibility exists, therefore, that grain growth is not entirely in response to grain annealing.

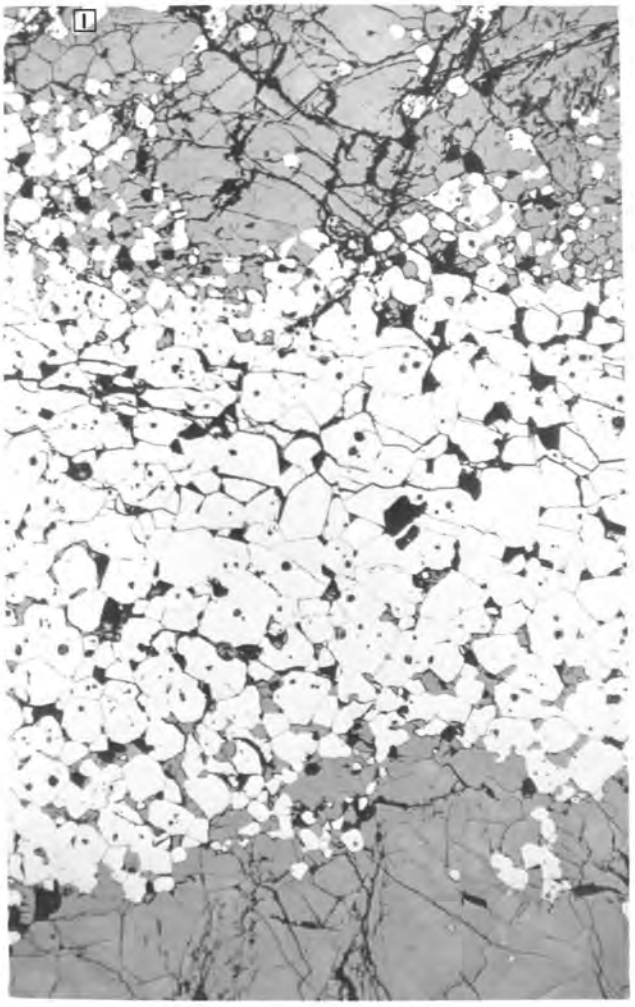
I

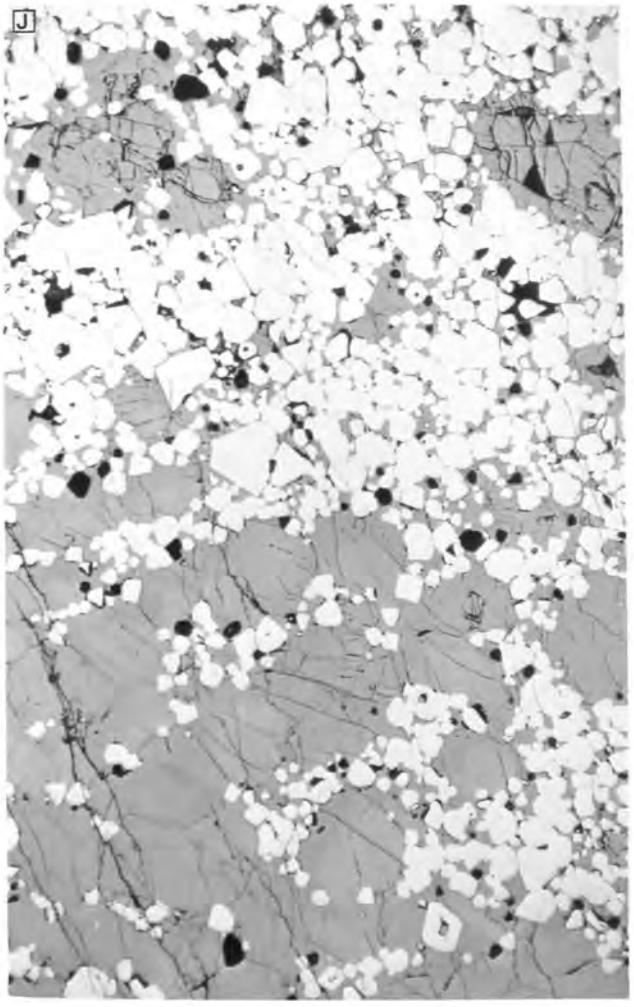
J

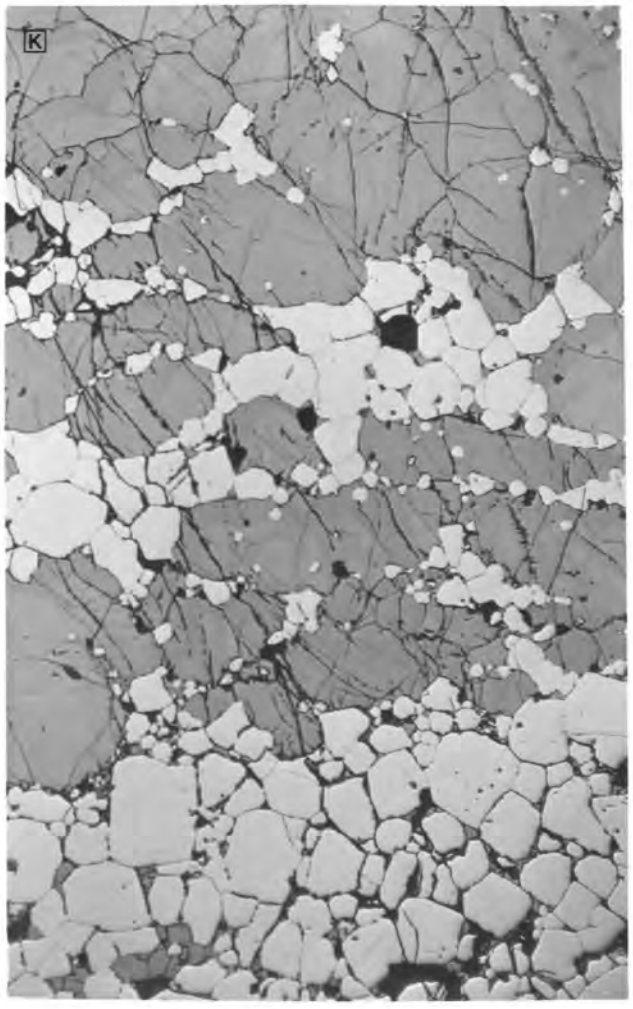
K

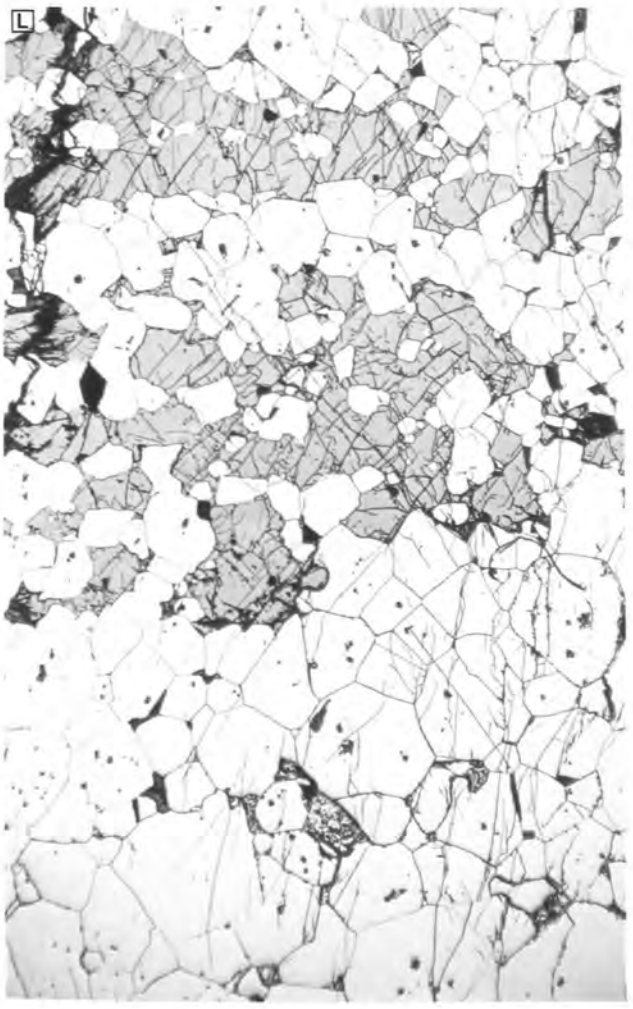
L

5. MINERAL CHEMISTRY OF THE SILICATE PHASES

5.1 INTRODUCTION

As has been discussed in the introductory section, the mineral chemistry of chromite cannot be interpreted in isolation from that of the associated silicate phases. Accordingly, in an attempt to establish the extent of compositional variation within the study section and within individual samples, a detailed analytical programme was undertaken to determine the relative levels of major and minor elements in the coexisting cumulus phases chromite, orthopyroxene and/or olivine as a function of the following parameters:

1. Stratigraphic position.
2. Modal silicate/oxide ratio.
3. Grain size of the individual cumulus species.
4. Proportion and composition of intercumulus silicate phases.

Furthermore, as most of the weakly disseminated and accessory chromite grains occur in the interstices of the cumulus silicate framework, it was considered essential to include analyses of associated intercumulus plagioclase, clinopyroxene, phlogopite and amphibole in the programme.

There is a plethora of reports available in the geological literature dealing with experimental simulation of the distribution of divalent metal cations between olivine and coexisting melt. This information, in conjunction with the simple mineral chemistry of olivine, renders chemical analyses of this phase quite amenable to modelling a number of magmatic parameters (e.g., estimating the degree of fractional crystallization of basaltic magmas or abundances and interelement ratios of Ni, Co, Mn, Sc, Cr^{3+}, Fe^{2} and Mg in the parent magma). However, it is envisaged that significant deviations from primary olivine compositions may also be a typical feature of slowly cooled environments. These might well originate during equilibrium crystallization of trapped liquid in the crystal mush (see Cawthorn, 1982). A further constraint which is imposed is the need to determine the relative modal proportions of the phases present; it is

well established in several studies (Irvine (1965), Jackson (1969), Dick (1977) and Roeder et al. (1979) have demonstrated this very convincingly) that the Mg/Fe^{2+} ratio of chromite and olivine is in part a function of their modal proportions. Equilibria involving orthopyroxene, on the other hand, have not been studied in such detail. The mineral chemistry of orthopyroxene is characterized by complex coupled substitutions involving Al, Cr and Ti (elements common to both pyroxene and chromite) and the distribution of these elements is more rigorously accounted for in terms of reaction constants. An understanding of these substitution mechanisms is of considerable importance in that orthopyroxene is the major repository of Cr in the Lower and Lower Critical Zones by virtue of its modal abundance (Cameron, 1978 and 1980). Given that orthopyroxene is a chain silicate, diffusivities of trivalent cations in the solid state may be insufficiently rapid to obscure zonal structures developed during fractionation. However, there is uncertainty as to whether relict core-rim chemical gradients result from primary growth processes or are a secondary feature resulting from partial or complete equilibration.

A further parameter, the importance of which is extremely difficult to assess quantitatively, is the residence time of a chromite grain within magmatic liquid. A specific example of this is discussed in a subsequent part of the text where it is shown that the level of TiO_2 within chromite grains may be interpreted in relation to the host phases which encapsulate them. It will be shown that occlusion at an early stage of crystallization results in low TiO_2 contents, whereas occlusion at a late stage (by an intercumulus phase such as plagioclase) yields high TiO_2 values.

Compositional profiles have been measured within orthopyroxenes at increasing distances from either occluded chromite or the margins of cumulus orthopyroxene crystals. Particular care was taken to ensure that such data are reliable. The orthopyroxene analyses given in Table 1, for example, were performed on the Cambridge Mark V Electron Microprobe at the University of Cape Town and then repeated with the Rhodes University instrument. In all instances, the analyzing beam was adjusted to a comparable spot-size and positioned immediately adjacent to the previous burn mark. Although a different set of

reference standards was used at the respective Universities (see Appendix III), the agreement between the two sets of data is excellent.

TABLE 1:

TEST ON REPRODUCIBILITY OF MICROPROBE ANALYTICAL DATA

	A	B	C	D
SiO_2	55,32	55,90	55,55	55,48
TiO_2	0,14	0,12	0,11	0,11
Al_2O_3	0,91	0,90	1,14	1,13
FeO	11,36	10,92	11,49	10,85
MnO	0,25	0,23	0,25	0,25
MgO	30,04	30,73	29,92	30,11
CaO	0,92	0,86	1,11	1,34
Cr_2O_3	0,55	0,51	0,55	0,55
TOTAL	99,49	100,14	100,12	99,82
Al/Cr	2,53	2,64	3,13	3,13
MMF	0,825	0,833	0,823	0,832

A - B: Analysis of common spot at (A) University of Cape Town and (B) Rhodes University

C - D: Analysis of common spot at (C) University of Cape Town and (D) Rhodes University

MMF : Cation ratio $Mg/(Mg + Fe^{2+})$

Al/Cr: Atomic ratio

Furthermore, analyses were repeated at Rhodes University on successive days, with the instrument recalibrated on each occasion, and it was found that absolute concentrations of minor elements were reproducible to within the following weight per cent limits (if 70 second integration times were used):

1. TiO_2 : $\pm$ 0,02
2. Al_2O_3: $\pm$ 0,04
3. Cr_2O_3: $\pm$ 0,02

5.2 CUMULUS SILICATE PHASES

5.2.1 OLIVINE

The nesosilicate olivine structure is based on a nearly hexagonal, closest-packed array of oxygens, in which Si^{4+} ions are located in tetrahedral coordination and divalent metal cations (e.g., Mg and Fe) in distorted, non-equivalent M1 and M2 octahedral sites. Chemical analyses of olivines show very low abundances of the following cations which are incompatible with the olivine structure: Ti^{4+}, V^{3+}, Cr^{3+}, Fe^{3+}, Al^{3+} and Na^{+}. Nickel, cobalt, copper and zinc are also present in low concentrations but this is a function of trace abundances of these elements in natural mafic liquids. The reader is referred to Deer et al. (1982) for a comprehensive review of the olivine structure and minor and trace element levels in $(Mg,Fe)_2SiO_4$ olivines, and to Burns (1970) for predictions of site occupancy on the basis of Crystal Field Theory.

The chemical equilibria between olivine and silicate liquids have received considerable attention due to the important role olivine plays in petrogenetic processes. Partition coefficients for the distribution of magnesium and divalent transition elements between olivine and equilibrium melt have been determined as functions of melt composition, temperature, oxygen fugacity and pressure, and have been applied as geothermometers (for example, by Roeder and Emslie (1970), Leeman and Scheidegger (1977), and Longhi et al. (1978)). Compilations of these data are available in Irving (1978) and Deer et al. (op. cit.), and discussions of the influence of intensive and

extensive parameters on these coefficients can be found in, amongst others, Irvine and Kushiro (1976), Arndt (1977), Hart and Davis (1978), Duke and Naldrett (1978), Mysen (1979), Boctor (1982) and Ford et al. (1983).

Roeder and Emslie (op. cit.) were the first to suggest that the distribution of Mg and Fe^{2+} between olivine and melt was insensitive to the temperature or bulk composition of the magmatic system, and proposed the following numerical value for the thermodynamic equilibrium distribution coefficient (K_D) for all mafic rocks:

$K_D = 0,3 \pm 0,03$, where

$K_D = (X_{FeO}/X_{MgO})^{ol} \cdot (X_{MgO}/X_{FeO})^{liq}$

This relationship provides an effective test of whether a given olivine composition is in equilibrium with its whole rock environment (for example, as illustrated by Eales and Marsh (1979), Cawthorn et al. (1979) and Cawthorn (1980)), or as a means of calculating the FeO/MgO ratio of the equilibrium melt. The latter is of considerable value to the study of cumulate rocks. With respect to the nickel content of olivines, Hart and Davis (1978) derived an equation which accommodates the pronounced compositional dependence of $D_{Ni}^{olivine}$:

$$D_{Ni}^{ol} = \frac{124,13}{MgO} - 0,897 \text{ at constant Si/O ratio,}$$

where MgO is given as the weight per cent abundance in the equilibrium liquid. A meaningful manipulation of these equations and measured values of $(X_{Mg})^{ol}$ and NiO in olivine-bearing Bushveld rocks to yield, for example, the height of a liquid column in equilibrium with a given increment of olivine crystals, is unfortunately no simple procedure. However, the diverse mineralogical environments in which olivine occurs in the study section is of considerable interest and the analytical data to be presented here may assist in the understanding of a number of magmatic and subsolidus processes.

The compositions of olivine from the respective units of the Ruighoek Pyroxenite in the study area, and of two Lower Zone samples from borehole KA 5, are presented in Table 2 (see Appendix III for details

of the electron microprobe operating conditions and calibration standards used). The analyses represent the average of two to six microprobe determinations per sample, usually distributed over two crystals. No chemical gradients were detected within olivine crystals in chromite-poor dunites, harzburgites and olivine-bronzitites, except in domains immediately adjacent to occluded or intergranular chromite grains where an exponential rise in the MgO content of the olivine is evident towards olivine-chromite grain boundaries. The radii of these cryptic zonal structures disposed about chromite grains appear to be of the order of 100 - 150 micrometres (microns). Equivalent nickel compositional profiles could not be resolved with the standard operating conditions in use and it is therefore not known whether Ni abundances exhibit a sympathetic cryptic variation. Systematic determinations of the major element compositional profiles were not made (refer to Wilson (1982) for a discussion of the fluorescence effects which have to be corrected for) and the analyses reported in Table 2 are of points well removed from chromite-olivine grain boundaries.

Extremely pronounced compositional profiles were noted in chromite-rich rocks where the boundary conditions of individual olivine grains are strongly enriched in MgO. These compositional gradients are radially disposed within the crystals and the lowest MgO contents occur in the central portion, i.e., the point furthest removed from the circumjacent mantle of chromite grains. A specific example of this is given in the subsequent text. In order to circumvent this problem, a cursory examination of the Mg-count rate was made across the largest visible olivine grain (chosen in order to limit sectioning effects) and the domain corresponding to the lowest count rate was selected for routine analysis. Ideally, however, the major element compositional profiles should be modelled so that the composition at a hypothetically infinite distance from the boundary condition can be ascertained. The analyses cited for samples 172, 177, 178, 183, 184, 200 and 245 are representative of core compositions (unless otherwise specified) and are the best estimates possible given that much of the olivine is pseudomorphed by serpentine minerals in some instances.

TABLE 2:

MICROPROBE ANALYSES OF OLIVINE

SAMPLE	01	07	318.	322	325	331	125	139	152	160	170
SIO2	39.26	38.78	39.12	39.61	39.27	39.53	39.65	39.90	39.32	39.68	39.72
FEO	17.58	20.00	17.30	17.40	16.82	17.48	15.74	15.09	16.44	14.42	13.47
MNO	.24	.25	.22	.25	.23	.24	.20	.19	.20	.18	.21
MGO	42.64	40.59	43.02	43.15	43.09	42.96	44.14	44.84	43.67	44.99	45.42
CAO	.07	.04	.04	.03	.03	.04	.01	.03	.03	.02	.04
NIO	.11	.13	.29	.29	.30	.20	.32	.29	.24	.40	.22
	99.90	99.79	99.99	100.73	99.74	100.45	100.06	100.34	99.90	99.96	99.08
					CATIONS PER 4 OXYGENS						
SI	.9993	.9998	.9948	.9992	.9986	1.0000	.9994	.9995	.9962	.9984	1.0005
Fe^{2+}	.3742	.4312	.3679	.3671	.3577	.3698	.3318	.3161	.3483	.3034	.2837
MN	.0052	.0055	.0047	.0053	.0050	.0051	.0043	.0040	.0043	.0038	.0045
MG	1.6178	1.5598	1.6307	1.6225	1.6332	1.6199	1.6584	1.6742	1.6492	1.6873	1.7053
CA	.0019	.0011	.0011	.0008	.0008	.0011	.0003	.0008	.0008	.0005	.0011
NI	.0023	.0027	.0059	.0059	.0061	.0041	.0065	.0058	.0049	.0081	.0045
	3.0007	3.0002	3.0052	3.0008	3.0014	3.0000	3.0006	3.0005	3.0038	3.0016	2.9995
MMF	0.812	0.783	0.816	0.815	0.820	0.814	0.833	0.841	0.825	0.847	0.857

KEY:

01 Coarse olivine in olivine-bearing granular bronzitite, 1 m above LG 7 chromitite. E unit.

07 Coarse olivine in olivine-rich, sulphide-bearing ultramafic pegmatite assemblage. E unit.

318 Average of 7 analyses of olivine grains in the chromitiferous bronzitite footwall of the LG 6 chromitite. D_2 subunit (BH ZS 3).

322 Anhedral olivine in granular bronzitite, 5 m below top of D_1 subunit (BH ZS 3).

325 Anhedral olivine grain in granular bronzitite, 9 m below top of D_1 subunit (BH ZS 3).

331 Very large olivine grain in ultramafic pegmatite association hosted by granular bronzitite, 18 m below top of D_1 subunit (BH ZS 3).

125 Small anhedral grain in granular bronzitite, 58 m above base of D_1 subunit. Trace abundance of olivine.

139 As in sample 125 (38 m above base of subunit).

152 Large anhedral olivine rimmed by a selvage of secondary orthopyroxene and granular bronzitite. Host rock is a medium- to coarse-grained bronzitite, 19 m above base of D_1 subunit. Textural evidence suggests ultramafic pegmatite association.

160 Minor occurrence of small olivine grains in a bronzitite, 8 m above base of D_1 subunit.

170 Dunite with weak dissemination of chromite, 3 m above LG 4 chromitite (C_3 subunit).

MMF: $Mg/(Mg + Fe^{2+})$ ratio

TABLE 2 (cont.):

SAMPLE	172	177.A	177.B	177.C	178A	180	183B	184A	184B	191B	196D
SIO2	40.06	40.62	40.63	40.49	40.52	39.87	40.27	40.68	39.86	39.93	39.65
FEO	12.45	10.61	11.03	12.29	10.84	14.50	11.53	11.93	12.36	13.72	14.95
MNO	.19	.15	.15	.15	.15	.21	.18	.17	.18	.20	.17
MGO	46.55	48.22	47.62	46.54	48.10	45.52	46.98	47.81	46.91	45.96	45.06
CAO	.05	.03	.03	.03	.04	.04	.04	.05	.03	.03	.03
NIO	.22	.30	.28	.26	.26	.25	.27	.28	0.00	.24	0.00
	99.52	99.93	99.74	99.76	99.91	100.39	99.27	100.92	99.34	100.08	99.86
					CATIONS PER 4 OXYGENS						
SI	.9996	1.0006	1.0042	1.0060	.9994	.9959	1.0029	.9981	.9955	.9968	.9966
Fe^{2+}	.2598	.2186	.2280	.2254	.2236	.3029	.2401	.2448	.2582	.2864	.3143
MN	.0040	.0031	.0031	.0032	.0031	.0044	.0038	.0035	.0038	.0042	.0036
MG	1.7313	1.7704	1.7542	1.7235	1.7683	1.6948	1.7439	1.7485	1.7463	1.7101	1.6881
CA	.0013	.0008	.0008	.0008	.0011	.0011	.0011	.0013	.0008	.0008	.0008
NI	.0044	.0059	.0056	.0052	.0052	.0050	.0054	.0055	0.0000	.0048	0.0000
	3.0004	2.9994	2.9958	2.9940	3.0006	3.0041	2.9971	3.0019	3.0045	3.0032	3.0034
MMF	0.869	0.890	0.884	0.870	0.887	0.848	0.878	0.877	0.871	0.856	0.843

172 Core of coarse olivine grain mantled by continuous chain of chromite grains. Chromite dunite 2 m above LG 4 chromitite.

177A Olivine fragment in serpentine pseudomorph. Base of olivine-chromitite layer near footwall contact of LG 4 chromitite.

177B Olivine remnant in optically continuous, secondary orthopyroxene that also occludes a mantle of chromite grains marking the original olivine grain boundary. Chromitiferous poikilitic harzburgite immediately below 177A.

177C Olivine remnant in reaction-replacement orthopyroxene hosting a weak abundance of euhedral chromite grains, 1 cm below 177 B in poikilitic harzburgite.

178A Core of olivine grain mantled by chromite. Olivine chromitite 1 m below LG 4 chromitite.

180 Coarse-grained olivine in dunite 2 m below LG 4 chromitite.

183B Coarse olivine in chromite dunite 3 m below LG 4 and immediately above a 3 cm thick chromitite layer.

184A Large olivine in spherical silicate inclusion within 4 cm thick chromitite layer, ca. 50 cm below 183 B. This olivine hosts orientated platelets of Cr-spinel.

184B Olivine remnants in chromitiferous poikilitic harzburgite, 4 cm below 184 A.

191B Olivine in chromite-poor dunite, 7 m above base of C_3 subunit. Average of rim and core compositions: CORE X_{Mg} = 0,858, NiO = 0,25%; RIM X_{Mg} = 0,858, NiO = 0,24%.

196D Coarse anhedral olivine in domain showing a high abundance of intercumulus plagioclase and orthopyroxene. Portion of poikilitic harzburgite "plate", 3 m above base of C_3 subunit.

0.00 NiO = NOT DETERMINED

TABLE 2 (cont.):

SAMPLE	197A	197D	199	200A	200B	200C	213B	214.A	214.B	214.C	214.D
SIO2	39.68	39.61	39.87	40.61	40.00	39.94	39.80	39.87	40,39	40.33	40.64
FEO	15.07	14.44	14.77	11.49	13.56	12.75	14.50	12.26	10.98	10.39	9.92
MNO	.19	.21	.22	.16	.16	.16	.21	.15	.14	.15	.13
MGO	45.10	45.17	45.48	48.15	46.43	46.66	45.33	46.99	48.07	48.60	48.97
CAO	.03	.04	.04	.03	.02	.02	.03	.03	.02	.02	.01
NIO	0.00	.26	.23	.36	.34	.36	.32	.42	.39	.41	.40
	100.07	99.73	100.61	100.80	100.51	99.89	100.19	99.72	99.99	99.90	100.06
					CATIONS PER 4 OXYGENS						
SI	.9959	.9961	.9949	.9962	.9939	.9952	.9965	.9935	.9969	.9942	.9973
Fe^{2+}	.3163	.3037	.3082	.2357	.2818	.2657	.3036	.2555	.2266	.2142	.2034
MN	.0040	.0045	.0047	.0033	.0034	.0034	.0045	.0032	.0029	.0031	.0026
MG	1.6871	1.6932	1.6916	1.7606	1.7196	1.7329	1.6917	1.7452	1.7864	1.7857	1.7912
CA	.0008	.0011	.0011	.0008	.0005	.0005	.0008	.0008	.0005	.0005	.0002
NI	0.0000	.0053	.0046	.0071	.0068	.0072	.0064	.0084	.0077	.0081	.0078
	3.0041	3.0039	3.0051	3.0038	3.0061	3.0048	3.0035	3.0065	3.0031	3.0058	3.0025
MMF	0.842	0.847	0.845	0.881	0.859	0.867	0.847	0.872	0.886	0.892	0.898

197A Olivine remnants in large reaction-replacement orthopyroxene oikocryst, 2 m above base of C_3 subunit.

197D Average of rim-core compositions in chromite-bearing dunite with minor intercumulus plagioclase. CORE X_{Mg} = 0,848, NiO = 0,26%; RIM X_{Mg} = 0,847, NiO = 0,26%; 2 m above base of C_3 subunit.

199 Dunite, 70 cm above base of C_3 subunit.

200A First appearance of olivine in C_3 subunit above basal H chromitite layer in olivine-chromitite assemblage. Repeat NiO analyses gave 0,35, 0,36 and 0,36%.

200B Fine-grained olivine in olivine-rich layer, 1 cm above 200 A. Secondary orthopyroxene present. NiO analyses were 0,33 and 0,35%.

200C Olivine rimmed by chromite mantle in chromite dunite, ca. 2 cm above 200 A.

213B Olivine in thin poikilitic harzburgite zone immediately above LG 3 chromitite, C_2 subunit.

214A Olivine in granular-textured bronzitite, 1 cm below leader layer of LG 3 chromitite.

214B Small olivine in bronzitite juxtaposed to lower contact of leader chromitite.

214C Small grain rimmed by secondary orthopyroxene in zone of heavily disseminated chromite at base of leader layer.

214D Core composition of grain within the chromitite.

TABLE 2 (cont.):

SAMPLE	214E	223D	238	245	247	254A	258	286	KA571	KA622
SIO2	41.14	39.63	39.72	39.75	39.83	39.75	39.85	39.90	39.73	39.68
FEO	7.12	14.79	14.66	14.12	13.778	14.80	14.31	14.66	15.26	15.27
MNO	.08	.20	.20	.21	.21	.20	.20	.22	0.20	0.20
MGO	50.91	45.10	45.09	45.48	45.86	44.84	45.31	45.49	44.88	45.00
CAO	.03	.03	.03	.04	.04	.03	.03	.03	0.02	0.02
NIO	.43	.18	.22	.23	.24	.27	.31	.35	0.25	0.14
	99.70	99.93	99.92	99.83	99.95	99.87	100.01	100.65	100.34	100.31
					CATIONS PER 4 OXYGENS					
SI	1.0000	.9957	.9974	.9968	.9961	.9993	.9984	.9952	.9965	.9952
Fe^{2+}	.1447	.3108	.3079	.2961	.2880	.3112	.2998	.3058	.3199	.3201
MN	.0016	.0043	.0043	.0045	.0044	.0043	.0042	.0046	.0042	.0042
MG	1.8845	1.6890	1.6877	1.7000	1.7095	1.6802	1.6921	1.6913	1.6776	1.6820
CA	.0007	.0008	.0008	.0011	.0011	.0008	.0008	.0008	.0004	.0004
NI	.0083	.0036	.0044	.0046	.0048	.0051	.0062	.0070	.0049	.0027
	2.9998	3.0043	3.0026	3.0032	3.0039	3.0007	3.0016	3.0048	3.0035	3.0046
MMF	0.927	0.844	0.845	0.851	0.855	0.843	0.849	0.846	0.839	0.840

214E Rim composition of a small lobate extension between two coarse chromite grains, grain D.

223D Fine-grained granular dunite near base of modally layered succession, C_2 subunit (see Figure 5).

238 Olivine core composition in granular harzburgite near top of C_1 subunit, 40 cm above E chromitite.

245 Large olivine grains from chromite-poor layer in a laminated succession of dunite and chromite dunite layers. C_1 subunit, 1 m below E chromitite.

247 Dunite with a weak dissemination of chromite; C_1 subunit, ca. 2,5 cm below 245. NiO analyses in the range 0,23 - 0,25 wt. %.

254A Granular olivine-bronzitite layer, 4,3 m above base of C_1 subunit. NiO analyses were 0,25, 0,26 and 0,29%.

258 First appearance of cumulus olivine in granular olivine bronzitite at base of C_1 subunit. NiO analyses were 0,29, 0,31 and 0,32%.

286 Large grain in narrow poikilitic harzburgite zone in immediate footwall of LG 1 chromitite, B unit. NiO analyses were 0,34, 0,35 and 0,35%.

KA571 Lower Zone granular harzburgite. KA 5 drill core, borehole depth of 571 feet.

KA622 Lower Zone poikilitic harzburgite with disseminated pentlandite and pyrrhotite. NiO analyses varied between 0,12 and 0,16% (n = 5). KA 5 drill core, borehole depth of 622 feet.

Structural formulae, calculated on the basis of 4 oxygens, are also presented in Table 2. It is noted that the proportions of Si^{4+} cations scatter very closely about the stoichiometric abundance of 1,000 cation, suggesting that Al^{3+} and coupled Cr^{3+}, Ti^{4+} or Na^{+} cations are not present at detectable levels, irrespective of mineralogical environment.

5.2.1.1 OLIVINE IN THE C UNIT

The variation of the olivine compositional parameter $Mg/(Mg+Fe^{2+})$ and the weight (wt.) per cent abundance of NiO in olivine from 20 horizons in the C unit are presented in Fig. 9 as a function of stratigraphic position. The samples are divisible into two subsets:

(a) Chromite-rich samples 172, 177, 178, 183, 184, 200, 214 and 245 which are representative of chromite dunite and olivine-chromitite lithologies in the succession, and

(b) Silicate-rich samples representative of dunites, olivine-bronzitites and harzburgites (respective sample descriptions are given in Table 2).

Samples 213 and 214 in the hanging- and foot-wall of the LG 3 layer, respectively, should be regarded as a separate subset since the genetic origin of olivine at this level is not clear.

The MMF ratio of olivine (MMF = $Mg/(Mg + Fe^{2+})$) in silicate-rich rocks of the C_1 subunit varies between 0,843 and 0,855, with the latter value depicted at the level of sample 247. This adcumulate textured dunite (mean olivine grain-size of 3,3mm) is approximately 40cm above the base of a succession of olivine cumulates which grade upwards into interleaved olivine- and olivine-chromite cumulates (sample 245; typical olivine grain diameters of 1,7 x 2,4mm). The succession underlying this olivine-rich interval comprises bronzitites and olivine-bronzitites, with thin layers of granular harzburgite and dunite. The MMF ratio appears to decline from 0,849 at the base of the subunit to 0,843 at the level of sample 254A (olivine-bronzitite sample), then rises to 0,855 in sample 247. This

is followed upward by a progressive decline to a MMF ratio of 0,845 in sample 238, which marks the re-appearance of orthopyroxene crystals above the olivine-chromite cumulates of the E chromitite layer. The NiO abundance in olivine, however, shows an apparent smooth decline with stratigraphic height from 0,31 wt. per cent at the base of the subunit to 0,22 wt. per cent near the top. Furthermore, a sympathetic variation between NiO and associated MMF ratios in the upper, olivine-rich samples is evident (Fig. 9). Though an equivalent relationship exists between the two orthopyroxene-rich samples in the lower portion of the subunit, the data suggest that a compositional offset or decoupling is manifested in proximity to the sample 247 level. This may correspond to the +7 metre position at which there is an abrupt transition from orthopyroxene-rich to olivine-rich cumulates. Though no significant increase in the modal abundance of chromite occurs at this level, there is however a broad, progressive increase with stratigraphic height, ultimately culminating in the gradational, chromite-rich rocks of the E chromitite layer.

The MMF ratio of olivine within the C_3 subunit appears to vary predominantly as a function of the modal chromite/olivine ratio (Fig. 9). For example, all olivine-rich samples indicate MMF ratios of less than 0,860 with a minimum of 0,842 near the base of the subunit. In contrast, the MMF ratio of olivine in chromite-rich environments is seen to be in excess of 0,860. Furthermore, the highest core composition of 89,0 mol. per cent Fo is representative of an occurrence of small, compositionally zoned olivine grains in an olivine-chromitite layer adjacent to the footwall contact of the LG 4 chromitite (analysis 177 A). Within the same polished thin-section, a chromitiferous poikilitic harzburgite grading into a poikilitic harzburgite is depicted beneath this olivine-chromitite and a pronounced compositional variation is seen. In the chromitiferous microenvironment, remnants of olivine occluded by reaction-replacement (secondary) orthopyroxene have MMF ratios of 0,884 (analysis 177 B), decreasing to 0,870 in the underlying chromite-poor harzburgite (analysis 177 C). An equivalent relationship is depicted in sample 200 at the base of the subunit, where the MMF (olivine) ratio declines from 0,881 in the basal olivine-chromite layer (analysis 200 A) to 0,859 in the immediately overlying, fine-grained

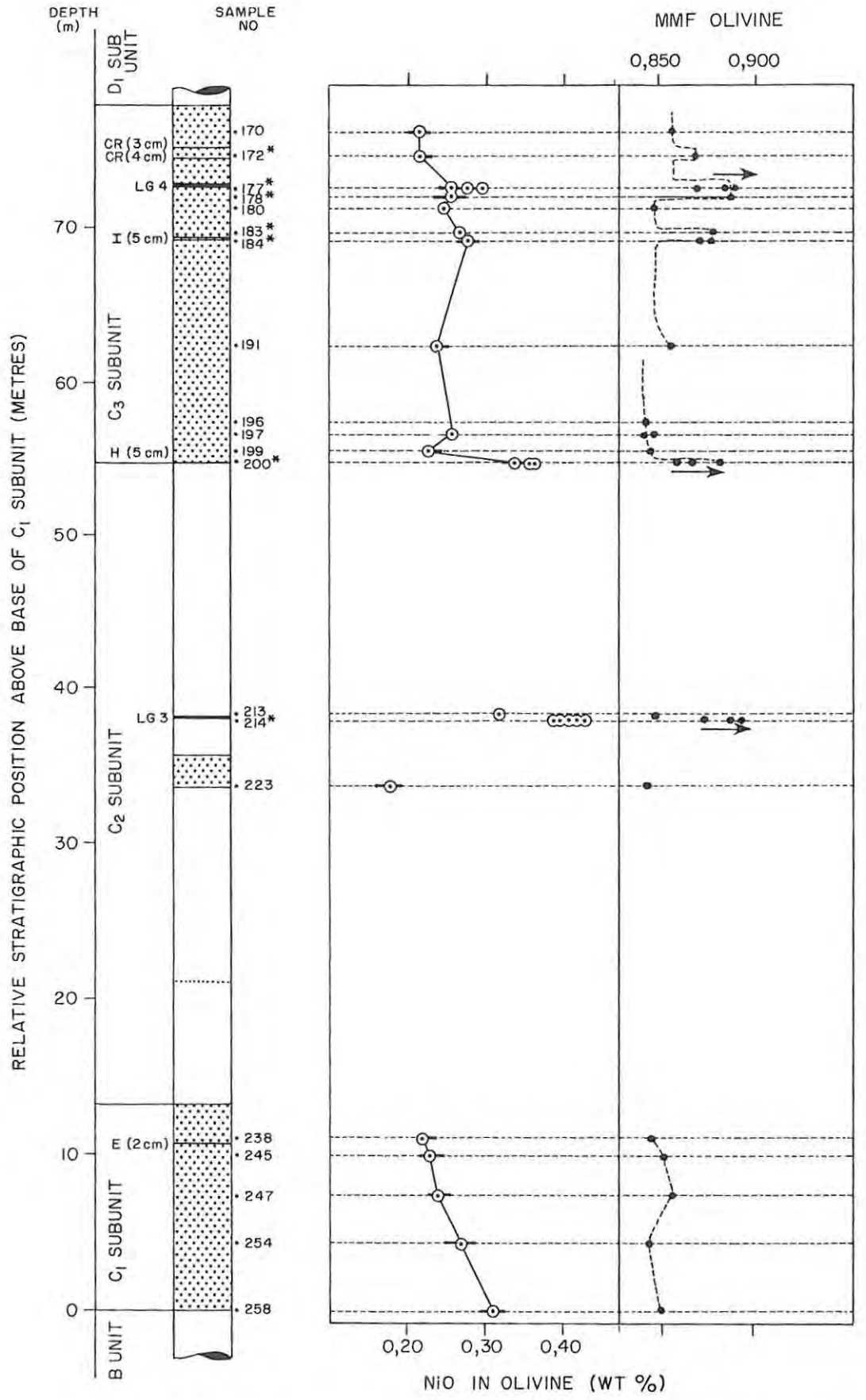

FIG. 9 DIAGRAM ILLUSTRATING THE COMPOSITIONAL VARIATION OF MMF(OLIVINE) AND NiO (OLIVINE) AS A FUNCTION OF STRATIGRAPHIC POSITION IN THE C UNIT. HORIZONTAL BARS DRAWN THROUGH MEAN NiO DATA POINTS DEPICT THE RANGE OBSERVED WITHIN INDIVIDUAL SAMPLES. THE RESPECTIVE MMF (OLIVINE) DATA POINTS ARE MEAN VALUES OF OLIVINE-RICH SAMPLES AND OF INDIVIDUAL GRAINS IN CHROMITE-RICH DOMAINS. SAMPLE NUMBERS BEARING A (*) SYMBOL DENOTE CHROMITE-RICH DOMAINS.

and granular-textured dunite (analysis 200 B). The latter is abruptly overlain by a chromite-olivine layer and the MMF (olivine) ratio within this environment is 0,867 (analysis 200 C). These trends of increasing MMF (olivine) ratio with increasing chromite abundance in individual thin-sections are illustrated via arrowhead symbols in Fig. 9. By virtue of the above observations and constraints imposed by sample distribution, a generalized compositional profile of the cryptic variation in the C_3 subunit is presented in the figure.

NiO in olivine appears to vary as a function of the major element chemistry within the C_3 subunit and, by implication, the modal chromite/olivine ratio (Fig. 9). However, inspection of the data suggests that this may be superimposed on a NiO profile of decreasing concentration with stratigraphic height, from 0,34 - 0,36 wt. per cent NiO at the base of the subunit to 0,22 wt. per cent above the LG 4 chromitite layer. It was mentioned in section 4.2.2 that fine-grained olivine crystals in chromite-rich rocks may be representative of grains that were precluded from in situ secondary enlargement. Hence, the relatively NiO-depleted nature of coarse-grained olivine crystals in dunites may be indicative of diffusional homogenization of zonal growth structures. It is envisaged that successive growth increments of olivine in equilibrium with interstitial magma will have produced a normally zoned structure. Data pertaining to the grain-size relationships are presented in Table 3.

Relative to the small, NiO-rich olivine crystals at the base of the subunit (sample 200), for example, NiO-depleted olivine grains in the overlying dunite (sample 199) have calculated volumes that are ca. 100 times greater. Fig. 10 graphically depicts the trend of declining NiO (olivine) with increasing crystal volume, and the data points appear to portray a limiting condition at coarse grain-sizes. This may suggest that the volume of a growing olivine grain ultimately imposes a compositional buffer; the volume increment required beyond a certain grain-size, in order to significantly alter the final bulk composition of a grain, is excessive for the system crystals + interstitial melt.

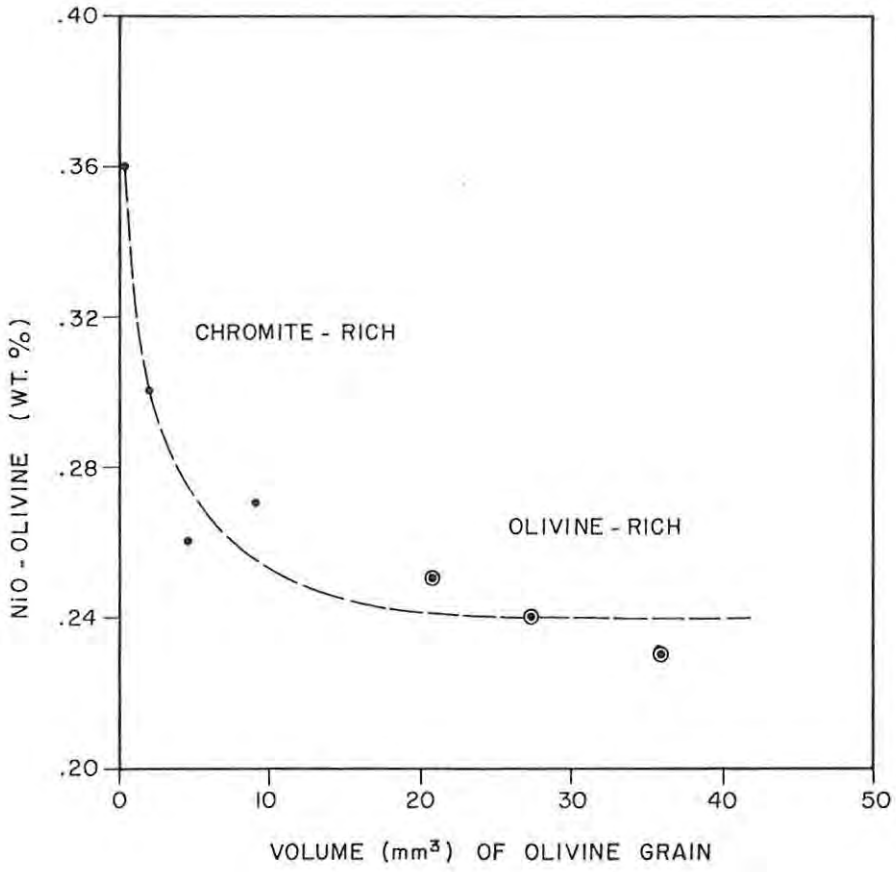

FIG. 10 RELATIONSHIP BETWEEN NiO - OLIVINE AND GRAIN SIZE. REFER TO TABLE 3 FOR A COMPILATION OF THE DATA.

TABLE 3:

OLIVINE GRAIN SIZE - NiO RELATIONSHIPS, C_3 SUBUNIT

SAMPLE	$r_{max}(a)$	$r_{min}(b)$	$V = \frac{4}{3} \pi ab^2 (mm^3)$	NiO (ol)	RELATIVE VOLUME RATIO
200	0,45	0,45	0,38	0,36	1
177 A	0,95	0,70	1,95	0,30	5
178 A	1,20	0,95	4,54	0,26	12
183 B	1,60	1,15	8,86	0,27	23
180	2,20	1,50	20,73	0,25	54
191 B	2,25	1,70	27,23	0,24	72
199	2,50	1,85	35,80	0,23	94

V : volume of olivine grain assuming ellipsoidal shape

r_{max}, r_{min} : radius of maximum and minimum diameters (mm)

Relative volume ratio : V(sample)/0,38 where 0,38 = minimum calculated volume.

NiO(ol): NiO content in wt. %.

Consideration of crystal size may also be of crucial importance in understanding subsolidus re-equilibration of olivine and chromite for the following reason. A small crystal has a high surface area/mass ratio and, thereby, would be more "reactive" to some external chemical influence than a large crystal buffered by a small surface area/mass ratio (sintering in the ceramic industry is a good example). Hence, the relationship depicted in Fig. 10, i.e., increasing NiO (olivine) with decreasing volume or mass, may stem from the enhanced "reactivity" of small olivine grains in chromite-rich environments. In terms of this proposal, a NiO (olivine) abundance of ca. 0,24 wt. per cent represents a primary liquidus concentration prior to diffusional gain from chromite in chromite-rich domains. In terms of the secondary enlargement

concept, however, the primary liquidus composition of olivine in the C_3 subunit may have been 0,36 wt. per cent NiO.

It is notable that the form of the curve in Fig. 10 equates with MMF (olivine) compositional profiles adjacent to chromite-olivine interfaces. An example of this is afforded by analyses of small olivine grains within and adjacent to the leader chromitite of the LG 3 layer (Table 2 sample 214; analyses A - E in order of increasing proximity to chromite-rich domains). A steep MMF (olivine) compositional gradient is observed, rising from 0,872 in the immediate footwall to a boundary condition of 0,927 within the chromitite. Furthermore, analyses D and E serve to indicate that the cryptic zoning within individual grains in chromite-rich domains is very pronounced. The NiO (olivine) concentrations of 0,39 - 0,43 wt. per cent are the highest observed in the C unit and these olivine grains are enriched in NiO relative to other occurrences with comparable MMF ratios (e.g., analyses 177 A - C and 178 A). Similarly, olivine in the thin zone of poikilitic harzburgite immediately above the LG 3 chromitite (analysis 213 B) is enriched in NiO.

Sample 223 is a fine-grained, granular-textured dunite exposed at the base of a modally-layered, 2 m thick zone of olivine-orthopyroxene-chromite cumulates, some 4 metres below the LG 3 chromitite layer. The olivine composition cited in Table 2 is representative of grains which are 3 - 4 cm below a 25 cm thick chromite-rich interval. The MMF (olivine) ratio of 0,844 is comparable with that of olivine in the lowermost dunite in the C_3 subunit (0,845) and the uppermost, olivine-rich harzburgite in the C_1 subunit (0,845). However, the NiO (olivine) concentration at this level is slightly lower (0,16 - 0,19 wt. per cent) than in the above-mentioned layers (0,23 - 0,24 wt. per cent).

The weight per cent abundance of manganese in olivine grains of the C unit shows a position correlation with FeO contents. For example, an olivine rim composition in the leader chromitite of the LG 3 (analysis 214 E) is 0,08 wt. per cent MnO and 7,12 wt. per cent FeO, whereas the core composition of the same grain (analysis 214D) is 0,13 wt. per cent MnO and 9,92 wt. per cent FeO. Similarly, the core

composition of olivine in chromite-rich environments of the C_3 subunit averages 0,16 wt. per cent MnO and 11,65 wt. per cent FeO, whereas the average composition in olivine-rich layers is 0,20 wt. per cent Mno and 14,42 wt. per cent FeO. Data from other occurrences, i.e., in the C_1 subunit, the Lower Zone and dispersed olivine grains in bronzitites of the B, D and E units, are consistent with this relationship (Table 2 and Fig. 11). The abundance of calcium oxide, on the other hand, varies between 0,01 and 0,07 wt. per cent and, by virtue of the lack of experimental reproducibility at this concentration, no correlation with major element composition or mineralogical environment is apparent.

Aluminium and chromium were not detected under the standard operating conditions employed. In order to fix the spectrometer 2Θ offset positions for background readings adjacent to the Al-peak position, the radiation profile of the Al-peak was investigated using a Stillwater olivine reference standard and was found to be flat. With respect to the large olivine crystal showing inclusions of orientated Cr-spinel platelets (within the I chromitite layer of the C_3 subunit, sample 184 A), neither element was detected although extended counting times were employed.

5.2.1.2 OLIVINE IN THE B, D AND E UNITS

The compositional variation of olivine in bronzitites of the B, D and E units is presented in Table 2, and the sample distribution is as follows:

1. E unit : samples 01 and 07
2. D_2 subunit: samples 318 and 322
3. D_1 subunit: samples 325, 331, 125, 139, 152 and 160
4. B unit : sample 286

The textural relationships of these rocks have been mentioned in section 3.2, where it was suggested that some of the occurrences may be related to ultramafic pegmatite bodies of the replacement-type. Sample 07 in the footwall of the LG 7 chromitite is cited here as a typical example. However, the genetic origin of trace abundances of

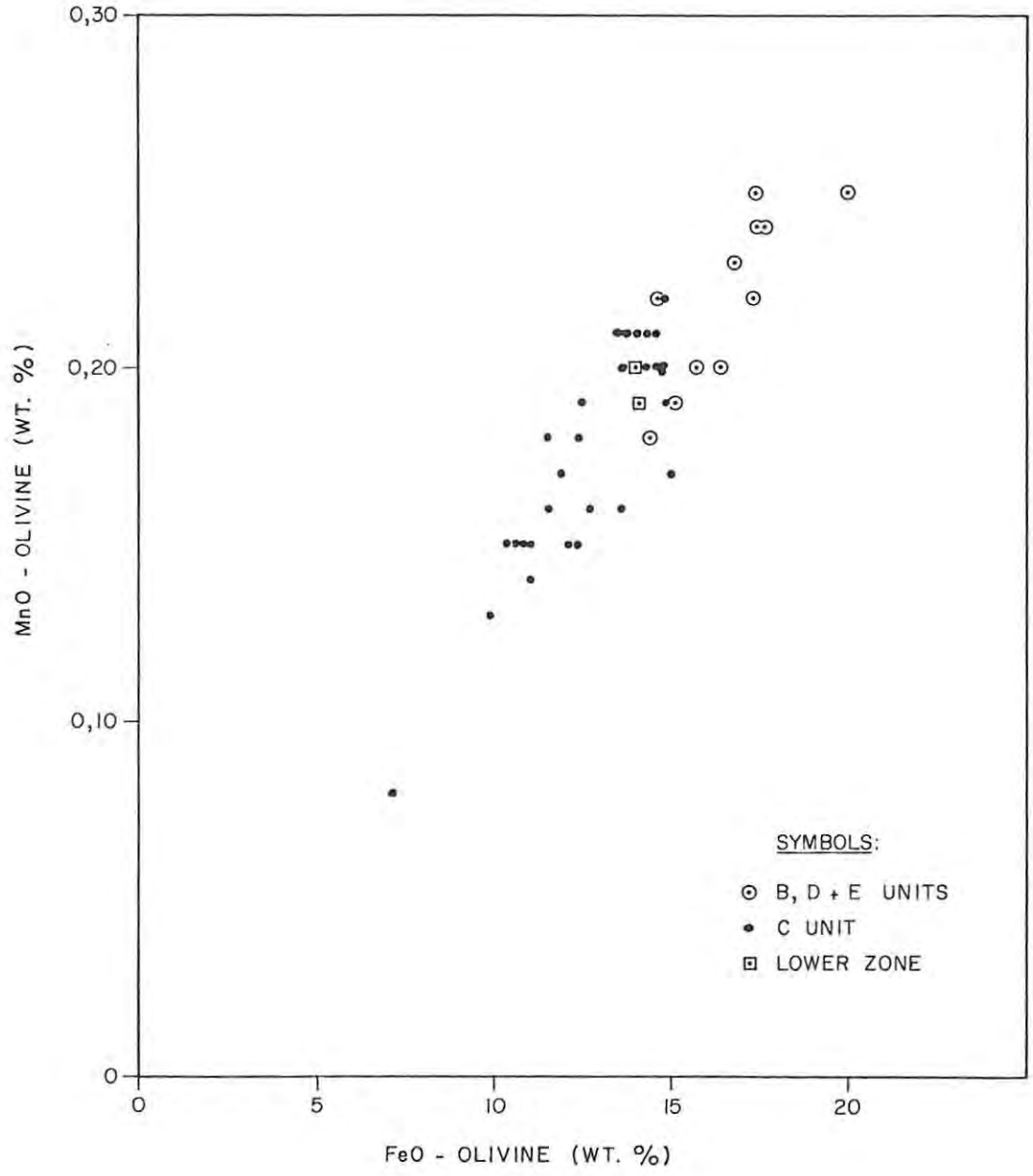

FIG. II PLOT OF MnO VERSUS FeO IN OLIVINE OF THE RUIGHOEK PYROXENITE SUCCESSION. CONCENTRATIONS EXPRESSED IN WEIGHT PER CENT.

olivine in fine-grained, granular-textured bronzitites such as samples 125 and 139 does not appear to be related to late-stage replacement processes. Hence, an investigation of these occurrences was included in the analytical programme in order to establish, for example, whether the olivine is in equilibrium with the coexisting orthopyroxene or whether the grains represent occult or "tramp" xenocrysts.

A comparison of the ranges of MMF (olivine) ratios and NiO contents with those of olivine grains in the C unit is given in Figs. 12(A) and (B). Whereas NiO contents are generally comparable with chromite-rich associations (samples 01, 07 and 331 are the exceptions), the range of MMF ratios is from 0,783 to 0,847. However, there is an excellent compositional correspondence between olivine in the immediate footwall of the LG 1 chromitite (sample 286) and in the immediate hanging-wall of the LG 3 chromitite layer (sample 213 B). Though this may be reconciled on the basis that both occurrences represent equivalent mineralogical environments, the similarity between analyses 139 and 254 A is anomalous.

5.2.1.3 SUMMARY

The salient features arising from the above may be summarized as follows:

1. Relative to juxtaposed olivine-rich layers, olivine grains in chromite-rich rocks are significantly enriched in magnesium. This is associated with higher Ni contents in most instances and finer grain-sizes.

2. A pronounced cryptic variation is evident in juxtaposition to chromite-rich layers and this contrasts with the compositional homogeneity of olivine-rich domains. Within the immediate footwall rocks of the LG 4 chromitite layer, for example (on the scale of a polished thin-section orientated parallel to the core axis), a rise in MMF (olivine) ratios with increasing stratigraphic height is linked to an increase in chromite modal abundance. However, there is no unequivocal evidence to suggest

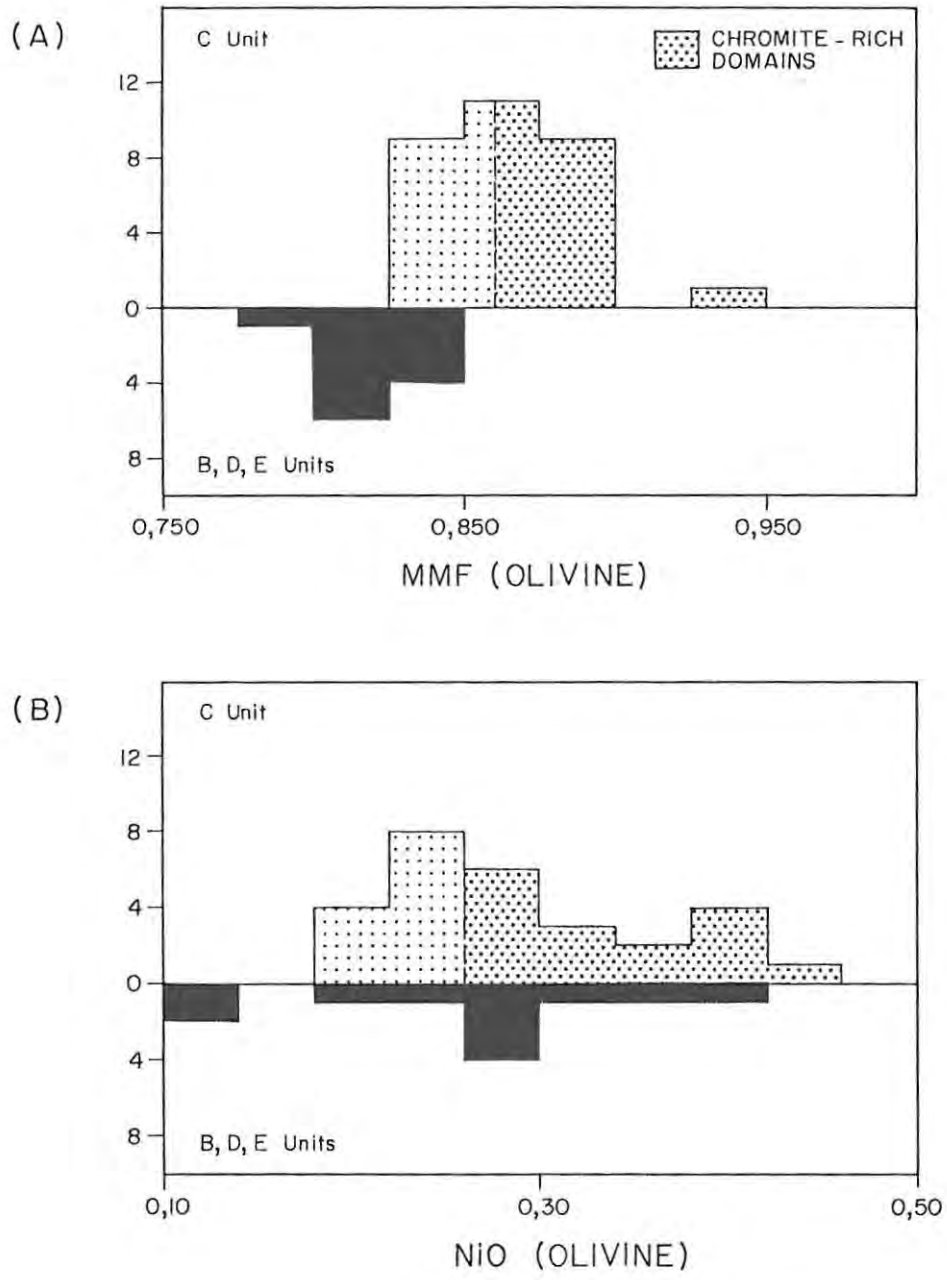

FIG. 12 (A)

PLOT DEPICTING SPREAD OF OLIVINE MMF RATIOS IN THE B, D AND E UNITS RELATIVE TO SAMPLES FROM THE C UNIT.

(B)

SPREAD OF NiO (OLIVINE) CONCENTRATIONS.

that the cryptic variation is a smooth function of stratigraphic position rather than the modal olivine/chromite ratio. Abrupt variations in the latter parameter (e.g., within the layered hanging-wall of the H chromitite layer) are linked to abrupt compositional changes, suggesting that grain-to-grain compositional changes with stratigraphic height in chromite-rich horizons may stem from subsolidus re-equilibration.

3. Individual olivine grains in chromite-rich environments depict pronounced core-rim compositional gradients. This is particularly true in domains where the modal proportion of olivine is subordinate to chromite.

4. The most nickeliferous olivine within the C_1 and C_3 subunits is found at the base of each subunit (marked by the first appearance of primocrystal olivine above a substantial thickness of bronzitite). The most magnesian compositions, however, do not occur in these basal, olivine-bearing layers.

5. The concentration of nickel in olivine declines with increasing stratigraphic height in the C_1 and C_3 subunits. Reversals in this trend occur at the level of the I and LG 4 chromitite layers in the C_3 subunit.

These compositional trends are evident in Fig. 13(A), which is a plot of NiO versus MgO in olivine. Included in the figure are two ideal curves linking the compositions of incremental batches of olivine crystals produced by fractional crystallization of olivine from hypothetical initial magmas. These curves were derived via a manipulation of the formulations of Roeder and Emslie (1970), Roeder (1974) and Hart and Davis (1978). Theoretical fractionation curve (A) is representative of an initial magma in equilibrium with olivine in the basal olivine-chromitite layer of the C_3 subunit (analysis 200 A, Table 2). Curve (B), however, links derivative olivine cumulates produced by fractionation of a parental Bushveld magma proposed by Davies et al. (1980). From the distribution of data points relative to the latter curve, it would seem that fractionation of this putative parental magma to the Bushveld complex could not have produced the range of observed olivine compositions in the C

unit. However, the coherency between fractionation curve (A) and many of the data points suggests that olivine in olivine-rich rocks of the C unit may have been derived by fractionation of a common parent magma. It is notable that olivine within the Lower Zone granular harzburgite KA 571 also falls within this group, whereas olivine in the pentlandite-bearing poikilitic harzburgite KA 622 shows a substantially depleted NiO content. Furthermore, olivine crystals in chromite-rich layers adjacent to the LG 4 chromitite define a unique population that requires a parent magma with a higher initial Mg/Fe^{2+} ratio than curve (A). This may, however, be an artifact of a process such as subsolidus re-equilibration of olivine and chromite. Consider the relationship between analyses 180, 177 C, 177 B and 177 A, for example. From the disposition of these data points relative to fractionation curve (A) in Fig. 13(A), a systematic trend deviating towards more ultramafic compositions is apparent. It is impossible to gauge whether the latter is indicative in part of a reversal in the fractionation trend caused by mixing of chemically distinct magmas (e.g., fractionated residua and parental magma), or is wholly attributable to subsolidus re-equilibration processes. There is some indication, however, that at least two compositionally different magmas contributed to the crystal pile of the C_1 subunit. Samples 258 and 254 A, representative of the basal 7 metres of the C_1 subunit, yield a population in Fig. 13(A) that is distinct from data points pertaining to the upper, olivine-rich portion of the subunit (samples 247, 245 and 238). Whereas the latter subset conforms very closely to fractionation curve (A), olivine in the basal olivine-bronzitite succession may have crystallized from a magma of different lineage.

Fig. 13(B) is an equivalent NiO versus MgO construction depicting the compositional variation of olivine in the B, D and E units. Analyses of olivine grains adjacent to the bounding contacts of the LG 3 chromitite are also shown. Olivine fractionation curve (C) represents an initial magma composition in equilibrium with the nickeliferous olivine occurrence in the footwall bronzitite of the LG 3 chromitite layer (analysis 214 A). It is evident from the figure that the observed olivine compositions may be genetically related to a common parent magma that differed in composition from

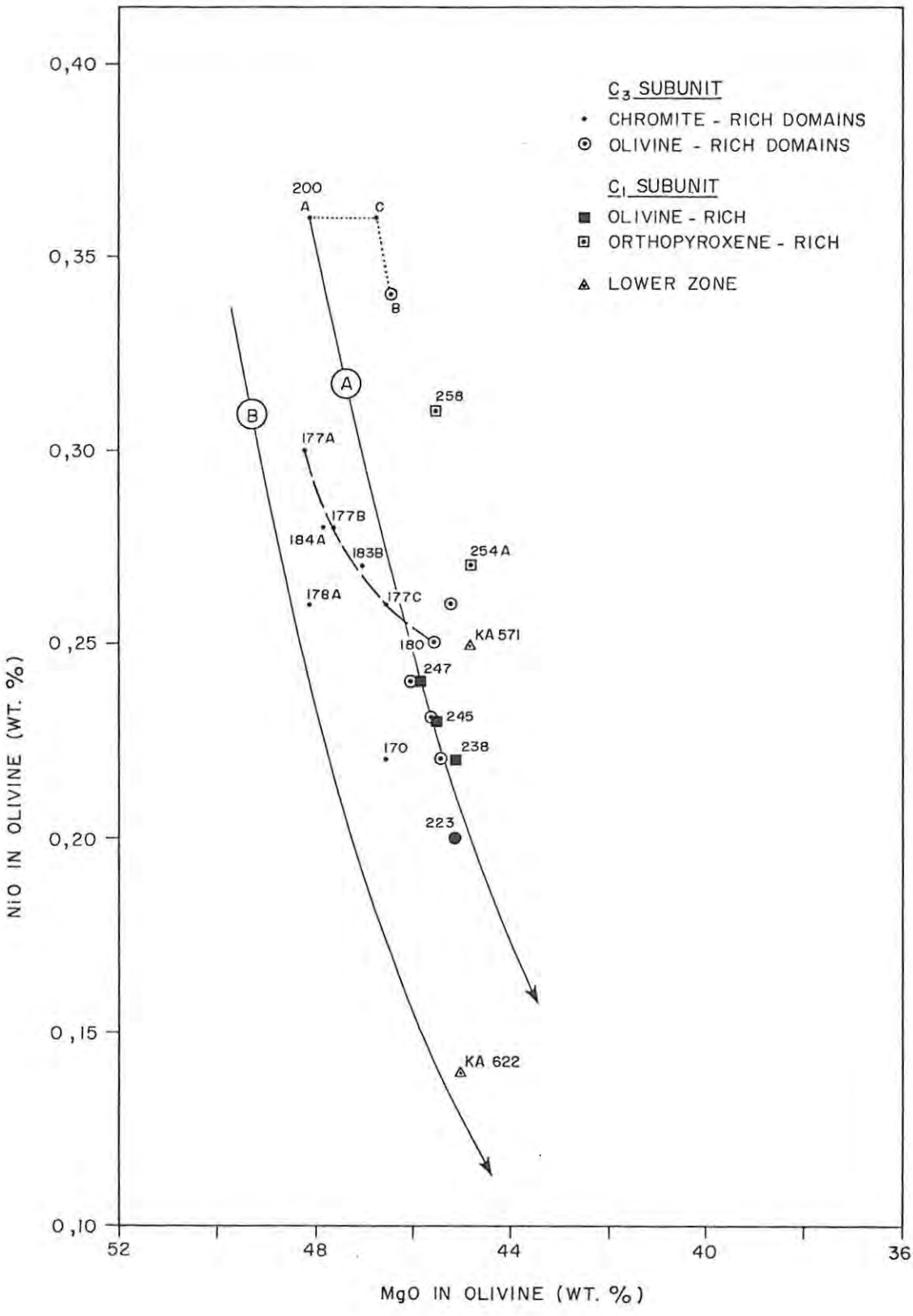

FIG 13(A) PLOT OF THE WEIGHT PER CENT ABUNDANCES OF NiO VERSUS MgO FOR OLIVINE WITHIN THE C UNIT. FRACTIONATION CURVES (A) AND (B) REPRESENT SUCCESSIVE OLIVINE COMPOSITIONS IN CUMULATES PRODUCED BY FRACTIONATION OF ASSUMED INITIAL MAGMAS IN A CLOSED SYSTEM. THE COMPOSITIONAL DISTINCTION BETWEEN CHROMITE - RICH AND OLIVINE - RICH DOMAINS IS EMPHASIZED IN THE FIGURE.

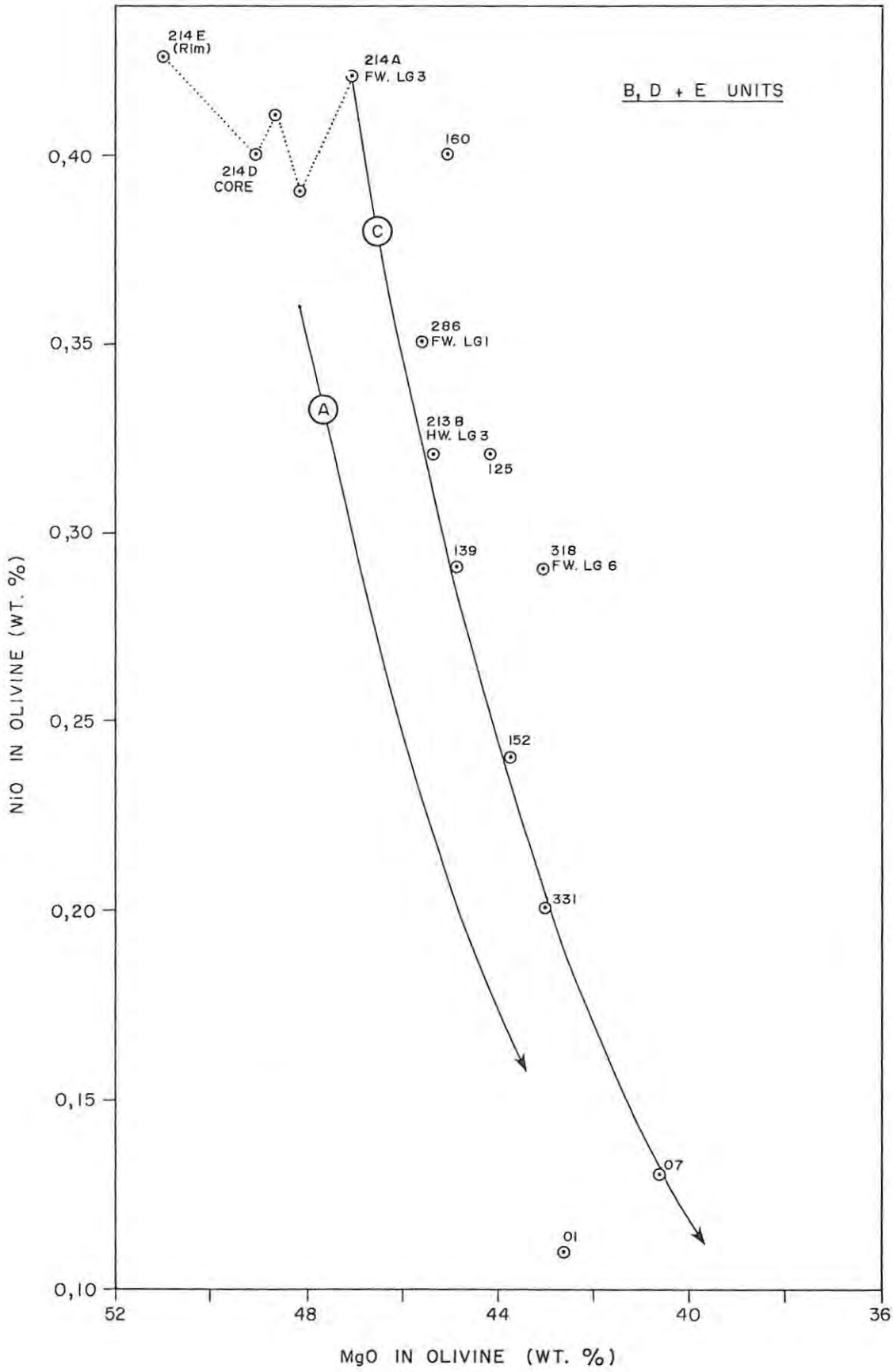

FIG 13 (B) PLOT DEPICTING THE RELATIONSHIP BETWEEN OLIVINE COMPOSITIONS IN THE B, D AND E UNITS AND THEORETICAL OLIVINE FRACTIONATION CURVE (C). THE COMPOSITIONAL VARIATION OF OLIVINE WITHIN THE FOOTWALL LEADER CHROMITITE OF THE LG 3 LAYER IS INCLUDED TO ILLUSTRATE THE PRONOUNCED MgO-ENRICHMENT IN CHROMITE-RICH DOMAINS.

the parental magma to the C_3 subunit. Intuitively this would seem to be reasonable, but a perplexing issue is raised. An olivine occurrence at the immediate hanging-wall contact of the LG 3 chromitite has also been noted on the farm Zwartkop, some distance to the north-east (von Gruenewaldt and Worst, 1986). It is therefore anomalous that a genetic relationship should exist between olivine in sample 213 B and olivine in the ultramafic pegmatite assemblages 152, 331 and 07, since there is unequivocal macroscopic evidence of late-stage replacement of layered rocks at these levels. Furthermore, olivine grains within olivine-bronzitites in the basal portion of the C_2 subunit (samples 254A and 258) display NiO contents and MMF ratios which conform to hypothetical fractionation curve (C). In summation, the disposition of data points in Figs. 13(A) and (B) suggests that the variation of NiO and $Mg/(Mg + Fe^{2+})$ in olivine of dunites is distinct from olivine grains intergrown with orthopyroxene in bronzitites and olivine-bronzitites. This may be attributed to subsolidus equilibration between olivine and orthopyroxene within the latter environment.

5.2.2 ORTHOPYROXENE

Orthorhombic orthopyroxene falls within the inosilicate structural group. The structure is characterized by continuous chains of linked SiO_4 tetrahedra, each chain of composition $(SiO_3)_n$. The chains are linked laterally by (Mg, Fe^{2+}) atoms in octahedral M1 positions and in distorted, 6- to 8-fold coordinated M2 sites. Other cations such as Ca, Na, Al, Ti, Fe^{3+} and Cr generally occupy less than 10 per cent of these M1, M2 positions. Most of the Al^{3+} within orthopyroxene is present as a proxy for tetrahedral Si^{4+}. In order to maintain charge balance, substitution of Al^{3+} for Si^{4+} in the lattice must be compensated by substitution of Cr^{3+}, Al^{3+}, Ti^{4+} or Fe^{3+} into M1, M2, positions (Campbell and Borley, 1974). A generalized formula for orthopyroxene may be given as $(Mg, Fe^{2+})\ SiO_3$.

Pressure imposes a control on the Al content of orthopyroxene and this relationship has served as a potential geobarometer of equilibration conditions in the garnet- and spinel-peridotite stability fields (Obata, 1976; Presnall, 1976). Alternative

interpretations have been presented, however, suggesting that the Al_2O_3 content of orthopyroxene is more applicable as a geothermometer (Fujii, 1976). Experimental studies on synthetic orthopyroxenes have shown that the distribution coefficient for Cr between orthopyroxene and silicate liquid (D^{Cr}) is dependent on the temperature and fO_2 conditions of the melt (Irving, 1978). For example, D^{Cr} declines with decreasing fO_2 at a given temperature, and rises with decreasing temperature at a given fO_2. This temperature dependence of D^{Cr} stems from the relative proportion of octahedral sites available in the silicate liquid and the favourable stabilization of Cr^{3+} in M1 pyroxene sites. A sympathetic correlation between Cr^{3+} and Al^{3+} contents in pyroxenes has been observed in synthetic systems, suggesting that coupled chromium-aluminium substitution occurs in pyroxenes (Schreiber and Haskin, 1976). The entry of Al and Cr may be treated as the substitution of a Tschermak-type molecule (Mg, Fe^{2+}, Al, Cr)(Si, Al)O_3 for (Mg,Fe^{2+})SiO_3 (Eales and Marsh, 1983). Maintenance of charge balance thus requires that $Al^{tet} = Al^{oct} + Cr^{oct}$, and it follows that the atomic Al/Cr ratio in octahedral orthopyroxene sites may be expressed as:

$$(Al/Cr)^{oct} = [(Al/Cr)^{total} - 1]/2$$ (Eales and Marsh, op. cit.)

Hence, $(Al/Cr)^{oct}$ can be computed directly from the analytical data, thereby minimizing the conventional reliance on superior orthopyroxene analyses to assess the proportion of Al^{VI}.

Microprobe analyses of orthopyroxene crystals from 65 stratigraphic positions in the Ruighoek Pyroxenite are presented in Table 4. This tabulation includes analyses of orthopyroxene in four samples of the Groenfontein Harzburgite subzone and analyses of reaction-replacement orthopyroxene in a few olivine-bearing samples. Unless otherwise specified in the key to Table 4, each analysis represents a mean composition based on at least three determinations per sample and, in certain instances, as many as twelve determinations. Furthermore, the analyses are representative of intracrystalline domains well removed from (a) occluded chromite grains (unless stipulated in the key), and (b) domains showing coarse lamellae or blebs of exsolved clinopyroxene. The microprobe beam was defocussed to a diameter of 20 - 25 microns in order to obtain an approximation of the "bulk"

TABLE 4 MICROPROBE ANALYSES OF ORTHOPYROXENES DRILL CORE ZS 7

SAMPLE	01	11	28	32	39	43	50	61	70	71
SIO2	55.94	55.62	56.29	55.87	55.90	55.60	55.27	55.38	55.27	55.25
TIO2	.12	.11	.09	.12	.10	.11	.09	.13	.14	.12
AL2O3	1.37	1.29	1.00	1.15	1.08	1.20	1.21	1.23	1.25	1.17
FEO	11.23	11.52	10.80	11.40	11.40	11.18	11.20	12.01	12.01	12.02
MNO	.25	.23	.23	.23	.24	.24	.24	.25	.26	.23
MGO	30.04	29.19	30.72	29.80	29.99	29.74	30.06	29.10	29.22	29.20
CAO	1.27	1.73	.91	1.36	1.07	1.36	1.20	1.48	1.23	1.59
CR2O3	.53	.51	.51	.50	.45	.50	.50	.50	.52	.53
	100.75	100.20	100.55	100.43	100.23	99.93	99.77	100.08	99.90	100.11
				CATIONS	NUMBER OF OXYGENS = 6					
SI	1.9645	1.9691	1.9742	1.9701	1.9732	1.9691	1.9615	1.9669	1.9656	1.9633
TI	.0032	.0029	.0024	.0032	.0027	.0029	.0024	.0035	.0037	.0032
AL	.0567	.0538	.0413	.0478	.0449	.0501	.0506	.0515	.0524	.0490
FE2	.3298	.3411	.3168	.3362	.3365	.3311	.3324	.3567	.3572	.3572
MN	.0074	.0069	.0068	.0069	.0072	.0072	.0072	.0075	.0078	.0069
MG	1.5724	1.5403	1.6059	1.5663	1.5779	1.5699	1.5901	1.5405	1.5489	1.5466
CA	.0478	.0656	.0342	.0514	.0405	.0516	.0456	.0563	.0469	.0605
CR	.0147	.0143	.0141	.0139	.0126	.0140	.0140	.0140	.0146	.0149
	3.9966	3.9940	3.9957	3.9958	3.9954	3.9959	4.0038	3.9969	3.9972	4.0016
MMF	.826	.818	.835	.823	.824	.825	.827	.811	.812	.812
Al/Cr	3.85	3.76	2.92	3.43	3.56	3.57	3.61	3.67	3.58	3.28

SAMPLE	78	79	83	90	95	104	117	125	128 C	128 R
SIO2	55.16	55.05	55.33	55.09	55.38	55.55	55.36	55.40	55.44	55.10
TIO2	.10	.10	.10	.09	.09	.08	.10	.08	.08	.12
AL2O3	1.39	1.48	1.38	1.38	1.18	1.25	1.31	1.27	1.32	.81
FEO	10.88	10.89	10.66	10.75	10.72	10.98	10.90	10.13	10.66	10.93
MNO	.24	.24	.24	.25	.23	.24	.24	.22	.25	.25
MGO	29.54	29.71	29.94	29.81	29.58	29.66	30.34	30.49	30.13	30.28
CAO	1.66	1.40	1.50	1.34	1.57	1.50	1.48	1.27	1.35	.66
CR2O3	.56	.61	.55	.52	.58	.54	.55	.53	.56	.37
	99.53	99.48	99.70	99.23	99.33	99.80	100.28	99.39	99.79	98.52
				CATIONS	NUMBER OF OXYGENS= 6					
SI	1.9618	1.9581	1.9614	1.9623	1.9708	1.9690	1.9543	1.9639	1.9627	1.9744
TI	.0027	.0027	.0027	.0024	.0024	.0021	.0027	.0021	.0021	.0032
AL	.0583	.0620	.0577	.0579	.0495	.0522	.0545	.0531	.0551	.0342
FE2	.3236	.3239	.3160	.3202	.3190	.3255	.3218	.3003	.3156	.3275
MN	.0072	.0072	.0072	.0075	.0069	.0072	.0072	.0066	.0075	.0076
MG	1.5660	1.5751	1.5820	1.5827	1.5690	1.5670	1.5964	1.6110	1.5899	1.6173
CA	.0633	.0534	.0570	.0511	.0599	.0570	.0560	.0482	.0512	.0253
CR	.0157	.0172	.0154	.0146	.0163	.0151	.0154	.0149	.0157	.0105
	3.9985	3.9996	3.9994	3.9990	3.9939	3.9952	4.0081	4.0001	3.9998	4.0000
MMF	.828	.829	.833	.831	.831	.828	.832	.842	.834	.831
Al/Cr	3.71	3.6	3.74	3.96	3.03	3.45	3.53	3.56	3.5	3.25

TABLE 4 (cont.)

SAMPLE	134 R	134(150)	134(450)	134(850)	139 A	139 B	155 C	155 R	164	183B
SIO2	55.90	55.73	55.62	55.55	55.58	55.51	55.62	55.62	55.76	56.71
TIO2	.12	.12	.12	.11	.09	.09	.10	.14	.10	.12
AL2O3	.90	.94	1.08	1.14	1.57	1.27	1.06	1.04	1.20	1.08
FEO	10.92	11.04	10.94	10.85	9.72	9.83	10.60	10.76	10.54	8.30
MNO	.23	.23	.25	.25	.22	.22	.23	.20	.22	.17
MGO	30.73	30.51	30.11	30.11	30.77	30.93	30.22	30.98	30.19	32.33
CAO	.86	.93	1.33	1.34	1.76	1.52	1.34	.83	1.44	1.47
CR2O3	.53	.53	.52	.55	.56	.52	.51	.46	.54	.46
	100.19	100.03	99.97	99.90	100.27	99.89	99.68	100.03	99.99	100.64
				CATIONS	NUMBER OF OXYGENS = 6					
SI	1.9700	1.9689	1.9675	1.9660	1.9525	1.9574	1.9699	1.9623	1.9683	1.9679
TI	.0032	.0032	.0032	.0029	.0024	.0024	.0027	.0037	.0027	.0031
AL	.0374	.0391	.0450	.0476	.0650	.0528	.0442	.0432	.0499	.0442
FE2	.3218	.3262	.3236	.3211	.2856	.2899	.3140	.3175	.3111	.2409
MN	.0069	.0069	.0075	.0075	.0065	.0066	.0069	.0060	.0066	.0050
MG	1.6142	1.6066	1.5876	1.5884	1.6111	1.6257	1.5953	1.6291	1.5884	1.6722
CA	.0325	.0352	.0504	.0508	.0662	.0574	.0508	.0314	.0545	.0547
CR	.0148	.0148	.0145	.0154	.0156	.0145	.0143	.0128	.0151	.0126
	4.0007	4.0009	3.9995	3.9996	4.0049	4.0066	3.9982	4.0060	3.9966	4.0006
MMF	.833	.831	.83	.831	.849	.848	.835	.836	.836	.874
Al/Cr	2.52	2.64	3.1	3.09	4.16	3.64	3.09	3.37	3.3	3.5

SAMPLE	184A	184B>500	184B.440	184B. 65	184B. 45	184B. 15	184B. 10	203 C	203 R	205 C
SIO2	57.00	56.97	56.87	56.99	57.01	57.24	57.47	55.58	55.57	55.68
TIO2	0.00	.09	.10	.12	.10	.11	.12	.09	.12	.10
AL2O3	.81	1.04	.98	.85	.79	.78	.69	1.14	1.06	1.17
FEO	7.12	8.15	8.04	7.46	7.14	7.02	6.88	9.85	9.81	9.89
MNO	.20	.18	.15	.18	.16	.15	.17	.21	.25	.21
MGO	33.01	32.40	33.09	33.75	33.90	34.08	34.16	31.16	31.24	30.85
CAO	1.60	1.68	.93	.63	.64	.68	.52	1.29	.92	1.29
CR2O3	.40	.44	.39	.36	.40	.53	.54	.54	.49	.52
	100.14	100.95	100.55	100.34	100.14	100.59	100.55	99.86	99.46	99.71
				CATIONS	NUMBER OF OXYGENS = 6					
SI	1.9775	1.9702	1.9695	1.9713	1.9731	1.9718	1.9777	1.9594	1.9643	1.9651
TI	0.0000	.0023	.0026	.0031	.0026	.0028	.0031	.0024	.0032	.0027
AL	.0331	.0424	.0400	.0347	.0322	.0317	.0280	.0474	.0442	.0487
FE2	.2066	.2357	.2329	.2158	.2067	.2022	.1980	.2904	.2900	.2919
MN	.0059	.0053	.0044	.0053	.0047	.0044	.0050	.0063	.0075	.0063
MG	1.7070	1.6701	1.7081	1.7401	1.7488	1.7499	1.7522	1.6374	1.6460	1.6228
CA	.0595	.0622	.0345	.0233	.0237	.0251	.0192	.0487	.0348	.0488
CR	.0110	.0120	.0107	.0098	.0109	.0144	.0147	.0151	.0137	.0145
	4.0005	4.0003	4.0026	4.0034	4.0027	4.0023	3.9978	4.0070	4.0036	4.0007
MMF	.892	.876	.88	.889	.894	.896	.898	.849	.85	.847
Al/Cr	3	3.53	3.73	3.54	2.95	2.2	1.9	3.13	3.22	3.35

TABLE 4 (cont.)

SAMPLE	205 R	208 C	208 REM	208 EX	208 EX	211 C	211 R	213B	214A.1	214A.2
SIO2	55.78	55.67	55.67	54.88	55.48	55.97	56.01	55.79	55.91	56.08
TIO2	.12	.10	.14	.11	.11	.07	.12	.14	.09	.08
AL2O3	.69	1.19	1.13	1.89	1.56	1.12	1.07	1.15	1.08	.97
FEO	9.84	9.97	10.52	11.33	11.45	10.15	10.30	9.98	9.75	9.04
MNO	.24	.22	.24	.23	.25	.22	.21	.21	.20	.20
MGO	31.20	31.07	30.75	29.82	30.13	30.92	31.51	30.46	31.08	31.65
CAO	.80	1.11	.84	.72	.69	1.13	.76	1.95	1.52	1.43
CR2O3	.29	.48	.47	.71	.66	.53	.54	.53	.53	.47
	98.96	99.81	99.76	99.69	100.33	100.11	100.52	100.21	100.16	99.92
				CATIONS	NUMBER OF OXYGENS = 6					
SI	1.9792	1.9627	1.9667	1.9484	1.9569	1.9682	1.9618	1.9637	1.9644	1.9678
TI	.0032	.0027	.0037	.0029	.0029	.0019	.0032	.0037	.0024	.0021
AL	.0289	.0494	.0470	.0791	.0649	.0464	.0442	.0477	.0447	.0401
FE2	.2920	.2940	.3108	.3364	.3378	.2985	.3017	.2938	.2865	.2653
MN	.0072	.0066	.0072	.0069	.0075	.0066	.0062	.0063	.0060	.0059
MG	1.6501	1.6327	1.6192	1.5780	1.5841	1.6206	1.6450	1.5980	1.6276	1.6554
CA	.0304	.0419	.0318	.0274	.0261	.0426	.0285	.0735	.0572	.0538
CR	.0081	.0134	.0131	.0199	.0184	.0147	.0150	.0147	.0147	.0130
	3.9991	4.0033	3.9995	3.9991	3.9985	3.9994	4.0055	4.0014	4.0035	4.0035
MMF	.849	.847	.838	.824	.824	.844	.845	.845	.85	.861
Al/Cr	3.55	3.68	3.58	3.97	3.52	3.15	2.94	3.24	3.04	3.08

SAMPLE	214A.3	215	215 R	221	223D	225 C	225 R	238 C	238 R	249 C
SIO2	56.13	55.81	55.85	56.15	55.84	55.90	55.65	55.59	55.45	56.32
TIO2	.07	.08	.13	.09	.09	.10	.15	.05	.14	.09
AL2O3	.73	1.14	.89	1.18	1.20	1.16	.90	1.24	1.25	1.18
FEO	8.67	9.49	9.82	9.17	9.29	9.87	10.37	9.23	9.41	9.28
MNO	.17	.21	.19	.22	.18	.21	.22	.22	.22	.22
MGO	32.46	31.19	31.27	31.76	31.74	31.05	31.08	31.05	31.41	31.82
CAO	.94	1.27	.84	1.23	1.13	1.22	.50	1.34	1.07	1.16
CR2O3	.38	.51	.36	.49	.43	.54	.48	.53	.39	.49
	99.55	99.70	99.35	100.29	99.90	100.05	99.35	99.25	99.34	100.56
				CATIONS	NUMBER OF OXYGENS = 6					
SI	1.9707	1.9660	1.9737	1.9631	1.9606	1.9653	1.9710	1.9655	1.9593	1.9639
TI	.0018	.0021	.0035	.0024	.0024	.0026	.0040	.0013	.0037	.0024
AL	.0302	.0473	.0371	.0486	.0497	.0481	.0376	.0517	.0521	.0485
FE2	.2546	.2796	.2902	.2681	.2728	.2902	.3072	.2729	.2781	.2706
MN	.0051	.0063	.0057	.0065	.0054	.0063	.0066	.0066	.0066	.0065
MG	1.6987	1.6377	1.6472	1.6551	1.6611	1.6271	1.6408	1.6364	1.6543	1.6539
CA	.0354	.0479	.0318	.0461	.0425	.0460	.0190	.0508	.0405	.0433
CR	.0105	.0142	.0101	.0135	.0119	.0150	.0134	.0148	.0109	.0135
	4.0070	4.0011	3.9992	4.0034	4.0063	4.0005	3.9995	3.9999	4.0055	4.0027
MMF	.869	.854	.85	.86	.858	.848	.842	.857	.856	.859
Al/Cr	2.87	3.33	3.67	3.6	4.17	3.2	2.8	3.49	4.77	3.59

TABLE 4 (cont.)

SAMPLE	249 R	254A	258B(1)	258B(2)	259	265 C	265 R	271	280	286A
SIO2	56.31	55.99	55.74	55.57	55.63	55.39	55.39	55.55	55.61	55.21
TIO2	.12	.07	.12	.09	.12	.09	.14	.09	.10	.11
AL2O3	1.15	1.18	1.29	1.29	1.21	1.16	1.06	1.21	1.22	1.07
FEO	9.31	9.44	9.31	9.79	10.22	9.95	9.89	10.65	10.30	10.57
MNO	.24	.22	.22	.22	.22	.23	.22	.24	.23	.22
MGO	31.90	31.60	31.18	30.99	30.97	30.25	30.85	30.52	30.45	30.70
CAO	.96	1.00	1.68	.97	1.04	1.66	.98	1.20	1.35	.83
CR2O3	.40	.44	.49	.56	.59	.55	.53	.54	.54	.49
	100.39	99.94	100.03	99.48	100.00	99.28	99.06	100.00	99.80	99.20
				CATIONS	NUMBER OF OXYGENS = 6					
SI	1.9657	1.9652	1.9584	1.9633	1.9601	1.9665	1.9667	1.9617	1.9649	1.9632
TI	.0032	.0018	.0032	.0024	.0032	.0024	.0037	.0024	.0027	.0029
AL	.0473	.0488	.0534	.0537	.0502	.0485	.0444	.0504	.0508	.0448
FE2	.2718	.2771	.2736	.2893	.3011	.2954	.2937	.3145	.3044	.3143
MN	.0071	.0065	.0065	.0066	.0066	.0069	.0066	.0072	.0069	.0066
MG	1.6599	1.6532	1.6329	1.6320	1.6265	1.6008	1.6327	1.6065	1.6037	1.6272
CA	.0359	.0376	.0632	.0367	.0393	.0631	.0373	.0454	.0511	.0316
CR	.0110	.0122	.0136	.0156	.0164	.0154	.0149	.0151	.0151	.0138
	4.0019	4.0025	4.0049	3.9996	4.0034	3.9991	3.9999	4.0032	3.9995	4.0045
MMF	.859	.856	.856	.849	.843	.844	.847	.836	.84	.838
Al/Cr	4.3	4	3.92	3.44	3.06	3.14	2.97	3.33	3.36	3.24

SAMPLE	290	297 C	297(R50)	297(RIM)	KA.410	KA.571	KA.622	KA.729
SIO2	55.41	55.45	55.41	55.60	55.96	55.98	56.26	55.90
TIO2	.10	.10	.16	.14	.08	.10	.08	.08
AL2O3	1.17	1.10	1.09	.77	1.16	1.24	1.53	1.36
FEO	10.42	10.47	10.78	10.73	10.24	9.52	9.71	11.67
MNO	.23	.22	.23	.21	.22	.21	.18	.24
MGO	30.64	30.63	30.58	31.07	30.86	31.03	31.43	30.45
CAO	1.24	1.48	.92	.76	1.46	1.51	1.76	.59
CR2O3	.53	.54	.49	.34	.50	.52	.60	.46
	99.74	99.99	99.66	99.62	100.48	100.11	101.55	100.75
				CATIONS	NUMBER OF OXYGENS = 6			
SI	1.9605	1.9591	1.9632	1.9687	1.9636	1.9650	1.9505	1.9631
TI	.0027	.0027	.0043	.0037	.0021	.0026	.0021	.0021
AL	.0488	.0458	.0455	.0321	.0480	.0513	.0625	.0563
FE2	.3083	.3094	.3194	.3177	.3005	.2795	.2815	.3427
MN	.0069	.0066	.0069	.0063	.0065	.0062	.0053	.0071
MG	1.6159	1.6131	1.6149	1.6398	1.6140	1.6235	1.6242	1.5939
CA	.0470	.0560	.0349	.0288	.0549	.0568	.0654	.0222
CR	.0148	.0151	.0137	.0095	.0139	.0144	.0164	.0128
	4.0050	4.0078	4.0029	4.0067	4.0034	3.9995	4.0079	4.0003
MMF	.839	.839	.834	.837	.843	.853	.852	.823
Al/Cr	3.29	3.03	3.32	3.37	3.45	3.56	3.81	4.39

KEY TO TABLE 4

E unit	:	01	- 71
D_2 subunit:		78	- 83
D_1 subunit:		90	- 164
C_3 subunit:		183B	- 184B.10
C_2 subunit:		203	- 225R
C_1 subunit:		238C	- 258B(1)
B unit	:	258B(2)	- 297(RIM)
LOWER ZONE:		KA.410	- KA.729

Analyses representative of core-domains, with (C) and (R) used to denote core and rim, respectively, in certain samples. Distance in microns from rim of crystal is shown by 134(150), for example. Position of microprobe beam relative to the boundary of an occluded chromite grain is portrayed as 184B > 500 (distance in microns).

01 : Granular-textured chromite bronzitite with olivine-bearing domains; hanging-wall of LG 7 chromitite layer. Similar olivine-bearing domains are found in the laminated footwall (i.e., interleaved chromitite and granular-textured bronzitite layers) of the massive ore.

11 : Coarse-grained bronzitite with net-textured pyrrhotite as the only interstitial phase.

28 : Granular-textured bronzitite adjacent to a chromitite lens (refer to Fig. 8(G)).

32 : Thin chromite bronzitite layer; coarse-grained orthopyroxene crystals with chromite in the interstices.

39 : Granular-textured bronzitite with localized olivine-bearing domains which appear to represent ultramafic pegmatite assemblages.

43 : Polygonal mosaic of medium- to fine-grained crystals with a trace modal content of small chromite grains and "interstitial" chromite (refer to Fig. 45B).

50 : As in sample 40. Plagioclase is not present in these bronzitites.

61 : Adcumulate-textured bronzitite showing a degree of deuteric oxidation (i.e., oxide-charged orthopyroxene crystals). Plagioclase and clinopyroxene modal contents are low.

70 : Mesocumulate-textured, feldspathic bronzitite. Chromite is conspicuous in thin section.

71 : As in sample 70, but slightly finer-grained and with less mesostasis; near base of E unit.

78 : Granular-textured bronzitite some 1,5 m below the LG 6A chromitite layer, with a low modal chromite content.

79 : As in sample 78 (about 1,9 m below the LG 6A).

83 : As in samples 78 and 79, but with a higher chromite content (refer to Fig. 43B); ca. 5 m below the LG 6 chromitite layer and 1,7 m above the base of the D_2 subunit.

90 : Granular-textured bronzitite with plagioclase and clinopyroxene in poorly annealed cavities.

95 : Similar to sample 90.

104 : Medium-grained, meso- to adcumulate-textured bronzitite with feldspathic mesostasis. The modal chromite content is very low (refer to Fig. 8C(iv)).

117 : Granular-textured bronzitite with plagioclase in poorly-annealed cavities.

125 : Granular-textured bronzitite showing two small grains of olivine in the thin section and oxide-charged orthopyroxene crystals (refer to Fig. 43C). Crystals showing no inclusions were selected for analysis.

128 : Coarse- to medium-grained, adcumulate-textured bronzitite with plagioclase (sodic), amphibole, mica and quartz comprising the mesostasis (low modal proportion).

134 : Mesocumulate-textured and feldspathic bronzitite (refer to Fig. 8C(i)) with a trace chromite content. Analyses are representative of a core-rim analytical traverse within a single crystal bounded by well-formed faces. Seventy second integration times were used on peak and background for each element; Ti, Cr and Al contents at each beam position represent the average of 3 x 70 seconds counting times.

139 : Granular-textured bronzitite with one small grain of olivine in the thin section. No intercumulus silicate phases are present. Analysis (A) represents a core composition of a grain with anomalously high Al_2O_3, CaO and Cr_2O_3 contents, whereas analysis (B) is representative of the average of 3 juxtaposed grains (whole-rock analysis (Table 34) yields 1,27% Al_2O_3, 1,72% CaO, 0,60% Cr_2O_3 and Mg-number of 0,847).

155 : Coarse-grained, adcumulate-textured bronzitite (refer to Fig. 8C(ii)).

164 : As in sample 155.

183B : Reaction-replacement orthopyroxene in chromite dunite; hanging-wall of the I chromitite layer.

184A : Reaction-replacement orthopyroxene in an olivine-rich inclusion within the I chromitite layer. TiO_2 not analyzed.

184B : Reaction-replacement orthopyroxene with inclusions of olivine and chromite. Analyses are representative of a compositional profile from > 500 microns to 10 microns of a chromite grain boundary. Chromitiferous poikilitic harzburgite in the footwall of the I chromitite layer.

203 : Adcumulate-textured bronzitite with a conspicuous modal proportion of intercumulus plagioclase. Mica and quartz are a minor component of the mesostasis. Sample located 3,3 m below the H chromitite layer, which marks the top of the C_2 subunit.

205 : Adcumulate-textured bronzitite with intercumulus plagioclase.

208 : Adcumulate-textured bronzitite with intercumulus plagioclase and sporadic oikocrysts of clinopyroxene (transmitting green light).
208 REM = small chadacryst in clinopyroxene
208 EX = exsolved lamellae in clinopyroxene
208 = average composition of core-domains of five crystals intergrown with plagioclase.

211 : Meso- to adcumulate-textured, fairly chromitiferous bronzitite with plagioclase, mica and quartz represented in the mesostasis.

213B : Adcumulate-textured, plagioclase-bearing bronzitite separated from the abrupt, top contact of the LG 3 chromitite layer by a thin zone of poikilitic harzburgite.

214A : Granular-textured and chromitiferous bronzitite in the immediate footwall of the LG 3 leader layer (refer to Fig. 8(J)). Nickeliferous olivine crystals represent a minor component of the rock. Analyses 1 to 3 are of polygonal grains in increasing juxtaposition to the chromite-rich domain.

215 : Laths of orthopyroxene in adcumulate-textured bronzitite showing a feldspathic mesostasis.

221 : Bronzitite domain interleaved with olivine-bronzitite layers. Sample located 3,2 m below the LG 3 chromitite and 1,2 m above granular-textured dunite in sample 223.

223D : Reaction-replacement orthopyroxene in fine-grained, granular-textured dunite.

225 : Adcumulate-textured bronzitite showing a low modal proportion of mesostasis (comprising sodic plagioclase, mica, quartz and amphibole: some of the latter may be pseudomorphic after clinopyroxene). Nickeliferous sulphides (partially altered to magnetite) and graphite are visible in polished section.

238 : Orthopyroxene intergrown with olivine in granular harzburgite (i.e., both are cumulus phases). Sample located some 0,25 m above the E chromitite layer, and is representative of the first appearance of orthopyroxene crystals above a succession of olivine-chromite cumulate rocks. The mesostasis comprises plagioclase plus clinopyroxene.

249 : Orthopyroxene in olivine-bronzitite below a succession of dunite, some 6,7m above the base of the C_1 subunit.

254A : Orthopyroxene in olivine-bronzitite. Numerous opx crystals are charged with opaque and amber-coloured oxide inclusions (e.g., refer to Fig. 27C), with the latter being a Cr-spinel. These inclusions are generally confined to the core-domains of orthopyroxene crystals and may have arisen in response to some oxidation-exsolution process, thus accounting for lower Cr contents in the pyroxene host.

258B(1): Orthopyroxene intergrown with olivine at the base of the C_1 subunit; no intercumulus silicate phases are present.

258B(2): Adcumulate-textured bronzitite exhibiting intercumulus plagioclase plus minor mica and quartz. Graphite platelets are conspicuous in thin section (refer to Fig. 25C). Analysis numbers (1) and (2) derived from the same section orientated parallel to the drill core axis. Fo content of the olivine crystals is 84,9 mol. %.

259 : Adcumulate-textured bronzitite with a mesostasis composed of plagioclase + amphibole + mica + quartz.

265 : Adcumulate-textured bronzitite with a feldspathic mesostasis (refer to Fig. 8A(i)).

271 : Laths of orthopyroxene in adcumulate-textured bronzitite (refer to Fig. 8A(ii)).

280 : Medium- to coarse-grained, adcumulate-textured bronzitite, with plagioclase + minor mica comprising the intercumulus silicate fraction.

286A : Adcumulate-textured bronzitite in the footwall of the LG 1 chromitite layer.

290 : Adcumulate-textured bronzitite with intercumulus plagioclase plus minor clinopyroxene.

297 : Analyses of the core of an orthopyroxene crystal (297C), 50 microns from the rim

(297(R50)), and rim-domain (RIM). The latter is representative of a thin selvage which borders most orthopyroxene crystals intergrown with plagioclase, and which exhibits no exsolution lamellae of clinopyroxene.

BOREHOLE KA 5

KA 410 Medium-grained, meso- to adcumulate-textured bronzitite; mesostasis composed predominantly of plagioclase.

KA 571 Granular harzburgite.

KA 622 Poikilitic harzburgite (sulphide-bearing).

KA 729 Medium-grained, meso- to adcumulate-textured bronzitite.

The harzburgites exhibit (a) coarser chromite particle sizes, and (b) substantially higher modal chromite contents than the bronzitites.

composition. The question of whether the analyses should be distributed over a large population of grains within a sample, or confined to a few grains assumed to be representative of the sample, remains a moot point. The approach adopted here is as follows. Two grains in a sample were selected and if the initial measurements showed a good correspondence, one or two additional analyses were obtained of these grains. However, a number of other grains were selected for analysis if the compositional difference was significant.

The degree to which a single analysis is representative of a sample population may be gauged from the following data. Six analyses spread over core domains of five grains were determined using a focussed beam. Another grain was selected at random from the assemblage on the following day, but in this instance a defocussed beam was employed. These data are presented in an abridged form in Table 5.

TABLE 5 :

SPREAD IN MICROPROBE ANALYSES OF ORTHOPYROXENE CRYSTALS IN A BRONZITITE SAMPLE EMPLOYING FOCUSSED AND DEFOCUSSED BEAMS

	A1	A2	B	C	D	E	$\bar{X}_{A,E}$	F
TiO_2	0,16	0,17	0,14	0,17	0,17	0,17	0,16	0,14
Al_2O_3	1,17	1,28	1,23	1,22	1,06	1,11	1,17	1,15
CaO	0,91	1,56	1,30	1,49	1,31	1,06	1,27	1,17
Cr_2O_3	0,49	0,52	0,55	0,55	0,48	0,50	0,51	0,53
MMF	0,842	0,841	0,843	0,843	0,845	0,841	0,842	0,840

A - E: Analyses employing a focussed (10 microns) beam

$\bar{X}_{A,E}$: Mean of analyses A - E

F : Defocussed beam (25 microns); single analysis

MMF : $Mg/(Mg + Fe^{2+})$ in orthopyroxene

A log through the study section, with relevant microprobe data, is presented in Fig. 14. Horizontal bars drawn through data points depict core-rim compositional relationships, with the disposition of arrowhead symbols indicating the rim compositions. Analyses of reaction-replacement orthopyroxene are excluded from Fig. 14 at this juncture, as are data points representing orthopyroxene in chromite-rich domains in juxtaposition to the LG 3, LG 6 and LG 6A chromitite layers. The plot is therefore representative of orthopyroxene grains within macroscopically homogeneous bronzitites depicting an accessory to minor modal abundance of chromite, and of cumulus orthopyroxene within olivine-bronzitites and granular harzburgites in the C unit. Some salient features that emerge from these data are (a) the pronounced rise in mol. per cent En in orthopyroxene (En = 100 Mg/(Mg + Fe^{2+})) upward through the B unit, ultimately reaching a high value within the C_1 subunit, (b) the irregular decline in En content with increasing stratigraphic height in subunits above the C_1 subunit, and (c) the uniform Cr_2O_3 content in orthopyroxene within the succession.

5.2.2.1 ORTHOPYROXENE IN THE B UNIT

The compositional variation of orthopyroxene in the B unit was determined at eight stratigraphic positions spread over 49,8 metres. The En content of orthopyroxene core-domains varies from a high value of 84,9 mol. per cent (analysis 258 B/2) at the top contact of the unit to minimum values of 83,4 - 83,9 mol. per cent below the LG 1 chromitite layer. The composition of orthopyroxene in sample 271, however, appears to be anomalously low ($En_{83,6}$) with respect to its stratigraphic position (Fig. 14). Cr_2O_3 contents in core-domains appear to show a sympathetic variation with En contents, increasing from an average of 0,52 wt. per cent below the LG 1 chromitite to 0,56 - 0,59 wt. per cent in the extreme upper portion of the unit. Al_2O_3 abundances vary between 1,07 wt. per cent (in the immediate, fairly feldspathic and coarse-grained footwall bronzitite of the LG 1 chromitite) and 1,29 wt. per cent, with an average abundance of 1,16 wt. per cent (n = 30). An irregular rise in Al content with stratigraphic height is suggested by the data. The average atomic

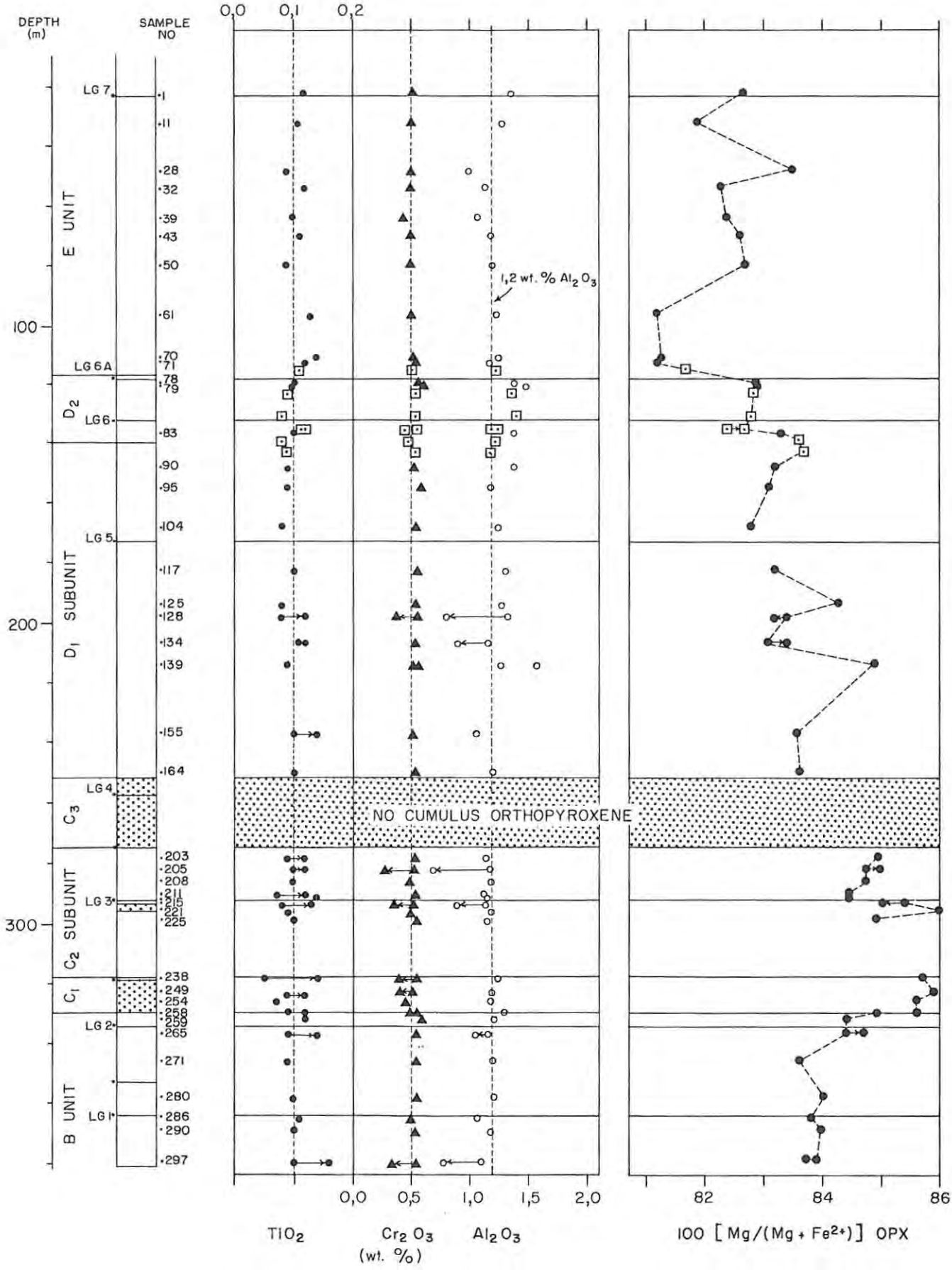

FIG. 14 PLOT OF ORTHOPYROXENE MICROPROBE DATA VERSUS STRATIGRAPHIC POSITION IN DRILL CORE ZS 7. ZONAL CHANGES WITHIN ORTHOPYROXENE CRYSTALS ARE DENOTED VIA THE SENSE OF ARROWHEAD SYMBOLS. DATA POINTS DEPICTED BY (⊡) SYMBOLS ARE OF SAMPLES FROM DRILL CORE ZS 3.

Al/Cr is 3,20, with minimum and maximum values of 3,03 and 3,44, respectively.

An evaluation of core-rim compositional variation at two stratigraphic positions highlighted the following relationship: relative to core-domains, rim compositions adjacent to plagioclase-bearing interstices are depleted in CaO, Al_2O_3 and Cr_2O_3. This is well illustrated in sample 297, and to a lesser degree in sample 265. However, the former displays higher atomic Al/Cr (rim), whereas orthopyroxene in the latter sample shows a decline in this ratio. TiO_2, on the other hand, is enriched by ca. 0,05 wt. per cent in the marginal domains. The zonal decrease in Al_2O_3 and CaO, and zonal increase in TiO_2, is consistent with the contemporaneous *in situ* crystallization of zonal orthopyroxene growth structures and plagioclase in a restricted melt volume. The zonal decline in Al/Cr in sample 265 is thus induced by preferential entry of Al into plagioclase, whereas the observed zonal increase in Al/Cr in sample 297 may be reconciled in terms of (a) the nucleation of clinopyroxene and phlogopite, which are fairly abundant at this level as intercumulus silicate phases intergrown with plagioclase, and (b) the lower modal abundance of plagioclase. Representative microprobe analyses of clinopyroxene and phlogopite are presented in subsequent tabulations.

5.2.2.2 ORTHOPYROXENE IN THE C_1 SUBUNIT

A pronounced increase in the En content of orthopyroxene is evident immediately above the first appearance of olivine at the base of the C_1 subunit. This is noted on the scale of a polished thin section (258 B), with orthopyroxene of composition $En_{85,6}$ above a 1 cm thick olivine-rich layer (analysis 258 B/1) and orthopyroxene of composition $En_{84,9}$ below the layer (analysis 258 B/2). Textural differences between the domains are equally pronounced, with a granular intergrowth of olivine and orthopyroxene in the upper domain quite distinct from the underlying, plagioclase-bearing and coarser-grained bronzitite typical of the B unit. Futhermore, a sympathetic rise in atomic Al/Cr from 3,44 to 3,92 is noted and can

be attributed to a decline in Cr_2O_3 contents from 0,56 to 0,49 wt. per cent across this layer of dunite. The respective concentrations of Al_2O_3 and Cr_2O_3 within numerous grains were checked, and the compositional change to lower Cr_2O_3 in the upper olivine-bearing domain, with Al_2O_3 remaining essentially constant, was found to be reproducible. The concentration of NiO in orthopyroxene was determined in the latter domain (these data are not presented in Table 4) but no detectable change was observed. The measured abundances of 0,06 - 0,10 wt. per cent NiO are equivalent to those of grains in the juxtaposed bronzitite, and of grains in the bronzitite above and below the LG 1 chromitite layer (i.e., samples 280 and 290, respectively).

Sample 249 is representative of the stratigraphic level at which orthopyroxene disappears as a liquidus phase to be replaced by olivine and a weak modal abundance of chromite. Orthopyroxene of composition $En_{85,9}$ is present here, and data pertaining to core-rim relationships indicate a zonal rise in Al/Cr and TiO_2, and a decline in CaO. Similar zonal changes were noted in samples 254 A and 238, for example. In sample 254 A, measured Al/Cr ratios of rim-domains adjacent to olivine crystals are typically in the following range:

1. 5,18 (1,04% Al_2O_3; 0,30% Cr_2O_3),
2. 5,98 (1,49% Al_2O_3; 0,37% Cr_2O_3), and
3. 7,07 (0,95% Al_2O_3; 0,20% Cr_2O_3).

The modal abundance of intercumulus silicate phases in samples 238, 249 and 254 A is low and, where present, plagioclase is subordinate to clinopyroxene. It would seem, therefore, that unique zonal growth structures in orthopyroxene may stem from the order of nucleation of plagioclase and clinopyroxene in the interstitial melt. Nucleation and growth of primocrystal olivine should induce a sympathetic enrichment of Cr and Al in the residual magma, implying that the Cr_2O_3 - depleted core-domains of orthopyroxene crystals in the C_1 subunit, relative to the B unit, are the result of diffusive homogenization of chromium-poor zonal structures. That this feature is not as apparent in B unit bronzitites may be due to the following:

1. The higher modal abundance of orthopyroxene in the B unit, in conjunction with substantially coarser orthopyroxene grain-sizes (i.e., the proportion of Cr-depleted, secondary overgrowth is small relative to the volume of primocrystal orthopyroxene).

2. Preferential partitioning of Al into intercumulus plagioclase effectively enhances the activity of residual Cr^{3+} in the interstitial magma.

3. A lower modal abundance of chromite is present in the B unit. This, however, is not supported by petrographic observations.

Finally, it was noted in chapter 5.2.2.1 that a mild enrichment in Cr_2O_3 content accompanied the rise in mol. per cent En in orthopyroxene upward through the B unit. This trend of increasing enstatite content continues through the C_1 subunit to the stratigraphic level of sample 249, but the concentration of Cr_2O_3 in orthopyroxene appears to reach a maximum of 0,59 wt. per cent in the bronzitite below the first appearance of olivine (sample 259 located 1,8 metres below the contact), followed by a significant decline with increasing stratigraphic height to 0,44 wt. per cent within the C_1 subunit (sample 254 A). Atomic Al/Cr, however, shows a sympathetic cryptic change from 3,06 to 4,00 through this interval, and data will be presented in the subsequent text showing a sympathetic rise in atomic Al/Cr of associated chromite. It is therefore evident that subscription to subliquidus, secondary growth processes as the major factor inducing compositional variation in orthopyroxene may be invalid.

5.2.2.3 ORTHOPYROXENE IN THE C_2 SUBUNIT

Representative analyses of orthopyroxene within the upper 23 metres of the C_2 subunit are given in Table 4 (samples 203 to 255). These are based on a total of 52 microprobe analyses spread over ten samples. Sample 225 represents the lowermost of the latter and is located 2,1 metres below the layered, olivine-bearing succession in the footwall of the LG 3 chromitite. This sample is representative of coarse-grained bronzitites at this stratigraphic level which

display adcumulus textures and a relatively high modal abundance of intercumulus amphibole and mica. The five samples above the LG 3 chromitite layer are essentially adcumulate-textured bronzitites, characterized by a predominance of intercumulus plagioclase plus large clinopyroxene oikocrysts and sporadic, phlogopite-rich domains. With the exception of samples 214 A and 211, all of these samples depict low modal concentrations of chromite.

Compositional changes in relation to stratigraphic height are illustrated in Fig. 14. Orthopyroxene of composition $En_{84,5}$ occurs within 1 cm of the thin, poikilitic harzburgite zone in the immediate hanging-wall of the LG 3 chromitite. It is not known whether the CaO content of 1,9 wt. per cent is representative as only a single determination was made using a defocussed beam (analysis 213 B). In contrast, the composition of orthopyroxene within granular-textured and olivine-bearing bronzitite in the footwall of the leader chromitite layer is $En_{85,0}$ at a point 2 cm below the chromitite, $En_{86,1}$ approximately 10 mm below and $En_{86,9}$ at the basal contact (sample 214A). The upper grain boundary of the latter crystal is mantled by a chain of chromite grains (the thin section was cut parallel to the drill core axis). With increasing modal percent chromite and/or increasing proximity to the chromitite contact, the following compositional changes are evident from the data (analyses 214A.1 - 3):

1. Al_2O_3 declines from 1,08 to 0,73 wt. per cent.
2. Cr_2O_3 declines from 0,53 to 0,38 wt. per cent.
3. CaO declines from 1,52 to 0,94 wt. per cent.
4. MnO declines from 0,20 to 0,17 wt. per cent.
5. TiO_2 may decline from ca. 0,09 to 0,07 wt. per cent, but a greater number of analyses are required to substantiate this.

Samples 221 and 223 D are representative of olivine-bearing bronzitite and dunite, respectively, within the 2 m thick zone of olivine-bearing cumulates below the LG 3 chromitite layer. The orthopyroxene in sample 223 D is of the reaction-replacement type and the composition of $En_{85,8}$ is similar to that of cumulus orthopyroxene in sample 221 ($En_{86,0}$) which is stratigraphically above sample 223 D.

The atomic Al/Cr ratios, and concentrations of Al_2O_3 and Cr_2O_3, are equivalent to those measured in the basal portion of the C_1 subunit. Relative to adjacent bronzitites, it would seem that orthopyroxene in olivine-bearing domains is characterized by higher atomic Al/Cr ratios.

Above the LG 3 chromitite layer, the composition of orthopyroxene changes from $En_{84,5}$ in the immediate hanging-wall to $En_{84,9}$ at a position 3,2 m below the top of the subunit. Within the 7,4 m thick stratigraphic interval encompassed by samples 203, 205 and 208, a subtle, reciprocal cryptic variation in Al_2O_3 and Cr_2O_3 contents may be present. This is emphasized by atomic Al/Cr ratios which decline from 3,68 to 3,13 with increasing stratigraphic height. With the exception of sample 214 A, the data depicted in Fig. 14 indicate that the antipathetic Al_2O_3 - Cr_2O_3 relationship is reproduced above and below the LG 3 chromitite layer. The latter may, however, be an artifact of sample distribution and/or the comparison of orthopyroxene in mineralogically distinct environments. With respect to the concentration of Cr_2O_3 in orthopyroxene above and below the LG 3 chromitite, no Cr_2O_3-depletion is evident in the immediate hanging-wall: abundances of 0,53 wt. per cent are depicted within 2 cm of the top contact (analysis 213 B) and within 2 cm of the footwall leader chromitite layer (analysis 214 A.1).

Analyses of two exsolved orthopyroxene blebs within a large clinopyroxene oikocryst in sample 208 are given in Table 4. Analysis 208 REM is representative of a small, relict chadacryst of cumulus orthopyroxene hosted by the oikocryst, whereas 208 C is an average core-composition of juxtaposed well-formed grains intergrown with intercumulus plagioclase. The sequence 208 C - 208 REM - 208 EX may therefore correspond to compositional changes resulting from progressively lower equilibration temperatures. Apart from a decline in the MMF ratio (from 0,847 to 0,824) and CaO content (from 1,11 to 0,70 wt. per cent), there is a marked rise in Al_2O_3 and Cr_2O_3 contents. By virtue of the ability of clinopyroxene to accommodate appreciable levels of Cr and Al (representative analyses of clinopyroxene in the study section will be presented in a subsequent section), the implied saturation of this late-stage mineral with respect to Cr is anomalous. However, it would seem from textural

evidence that, specific to this occurrence and certain horizons in the B unit, nucleation of intercumulus clinopyroxene kept apace with resorption of cumulus orthopyroxene and intercumulus plagioclase. Available Al and Cr would thus be augmented by a contribution from the pre-existing mineral assemblage. Zonal structures in orthopyroxene and chromite of non-replaced domains should therefore reflect the influence of plagioclase nucleation and not the more complex affects of clinopyroxene (± plagioclase) nucleation.

Data pertaining to core-rim compositional changes in five samples are available in Table 4. The following features emerge from the data:

1. Rim compositions are enriched by 0,1 - 0,2 mol. per cent En in samples 203, 205 and 208, but are depleted by 0,4 - 0,6 mol. per cent En in samples 215 and 225.
2. Rim domains show a lime depletion of 0,37 - 0,49 wt. per cent in the upper four samples (average 0,41 wt. per cent), and a depletion of 0,72 wt. per cent in sample 225.
3. TiO_2 is enriched by 0,02 to 0,05 wt. per cent in the marginal zones.
4. Al_2O_3 and Cr_2O_3 are depleted in the rims (sample 211 is the exception), but atomic Al/Cr can increase or decrease relative to the core-compositions.

The lowest measured rim abundances of Al_2O_3 and Cr_2O_3 were 0,69 and 0,29 wt. per cent, respectively, for a lobate protrusion on the apex of an orthopyroxene grain intergrown with plagioclase (sample 205). This extension presumably reflects a zone of accelerated, secondary growth. Hence, the higher Al/Cr ratio of this rim (3,55), relative to the average of the core domains (3,35), can be attributed to a more rapid depletion of chromium in a restricted melt volume.

5.2.2.4 ORTHOPYROXENE IN THE C_3 SUBUNIT

Analyses 183 B, 184 A and 184 B are representative of reaction-replacement orthopyroxene within chromite-rich rocks associated with the I chromitite layer (see Table 4). The compositions in these environments were determined for two reasons: firstly, to contrast

the composition of large, orthopyroxene oikocrysts with cumulus orthopyroxene in adjacent units, and secondly, to investigate compositional gradients in proximity to chromite-rich domains.

Analyses 183 B and 184 B > 500 (i.e., more than 500 microns from the nearest chromite grain boundary) indicate compositions of $En_{87,4}$ and $En_{87,6}$, respectively. The concentration of Al_2O_3 (1,06 wt. per cent) and Cr_2O_3 (0,45 wt. per cent) is slightly lower than in orthopyroxene of the C_2 subunit and B unit, with the Al/Cr ratio of 3,51 slightly higher than the average. Analysis 184 A is representative of orthopyroxene intergrown with olivine in a silicate inclusion within the I chromitite layer. The orthopyroxene is of composition $En_{89,2}$ and depicts atomic Al/Cr of 3,00. With increasing proximity to occluded chromite grains, however, pronounced compositional changes are evident. Within sample 184 B, for example, the original olivine grain boundaries are marked by the disposition of large, euhedral chromite grains. Olivine remnants commonly occur in the centres of these mantled silhouettes. A microdomain showing a lower abundance of chromite grains and clinopyroxene exsolution lamellae was selected for the analytical traverse, which was from 440 to 10 microns of the euhedral face of a chromite grain. It is clear from the data that there is a pronounced increase in mol. per cent En on nearing the boundary from $En_{88,0}$ to a minimum boundary condition in the region of $En_{89,6}$. This trend is linked to a decline in Al_2O_3 and CaO contents and a rise in Cr_2O_3. The fluorescence effect of Cr in the adjacent chromite is anticipated to be minimal at these distances.

5.2.2.5 ORTHOPYROXENE IN THE D UNIT

Approximately 150 analyses were carried out on orthopyroxene from a wide range of textural environments in the D unit. Thirteen bronzitite samples were selected from drill core ZS 7, with a maximum sample spacing of 23 m, and nineteen samples from ZS 3 drill core. The maximum sample spacing of the latter was 8 m. A selection of the analytical data is presented in Fig. 14, with a more comprehensive depiction of the compositional variation through the D_2 subunit shown in Fig. 16. Tables 4 and 6 provide a tabulation of the analytical data pertaining to drill cores ZS 7 and ZS 3, respectively.

Orthopyroxene of composition $En_{83,6}$ occurs within 2,5 metres of the base the D_1 subunit (sample 164), and the data display a gross irregular decrease in enstatite content with increasing stratigraphic height to a composition of $En_{82,8}$ in the footwall of the LG 6A chromitite layer (sample 78). Al_2O_3 contents show a progressive rise with increasing stratigraphic height from 1,20 to approximately 1,40 wt. per cent. Cr_2O_3 abundances vary between 0,51 and 0,61 wt. per cent, with higher concentrations more prevalent in the D_2 subunit. TiO_2 abundances are typically in the range 0,08 - 0,10 wt. per cent. Reversals in the trend of declining En content are evident from the disposition of data points in Fig. 14. For example, fine-grained orthopyroxene, intergrown with a trace modal abundance of olivine in sample 139, is enriched by 1,9 mol. per cent En relative to the coarse-grained, feldspathic assemblage of sample 134. Furthermore, the En content rises with increasing stratigraphic height above the LG 5 chromitite, reaching a high value of approximately 83,6 mol. per cent at the top of the D_1 subunit, then declines sharply to 82,3 mol. per cent in the basal portion of the D_2 subunit. The geometric relationships of this compositional trend are similar to those of the orthopyroxene crystallinity profile presented in Fig. 8(C), which shows a progressive decline in grain-size above the LG 5 chromitite layer, followed by an abrupt increase some 7m below the LG 6 chromitite layer. A conspicuous rise in the modal abundance of chromite and intercumulus plagioclase is also evident in the basal portion of the D_2 subunit.

Cryptic zonal structures were observed in large orthopyroxene crystals within coarse-grained, meso- and adcumulate-textured bronzitites of the D_1 subunit. Sample 134, which is a mesocumulate-textured, feldspathic bronzitite, is cited here as an example. Fig. 15(A) illustrates the textural environment of the selected grain and the orientation of the analytical traverse relative to an apical crystal face. The relevant data are presented in Table 4 and the analytical precision can be judged from a comparison of duplicate analyses given in Table 1. Fig. 15(B) summarizes the compositional changes plotted against proximity to the well-formed crystal face. It is clear from the data points that zonal decreases in Al^{3+} and Ca^{2+} cations are associated with reciprocal increases in the

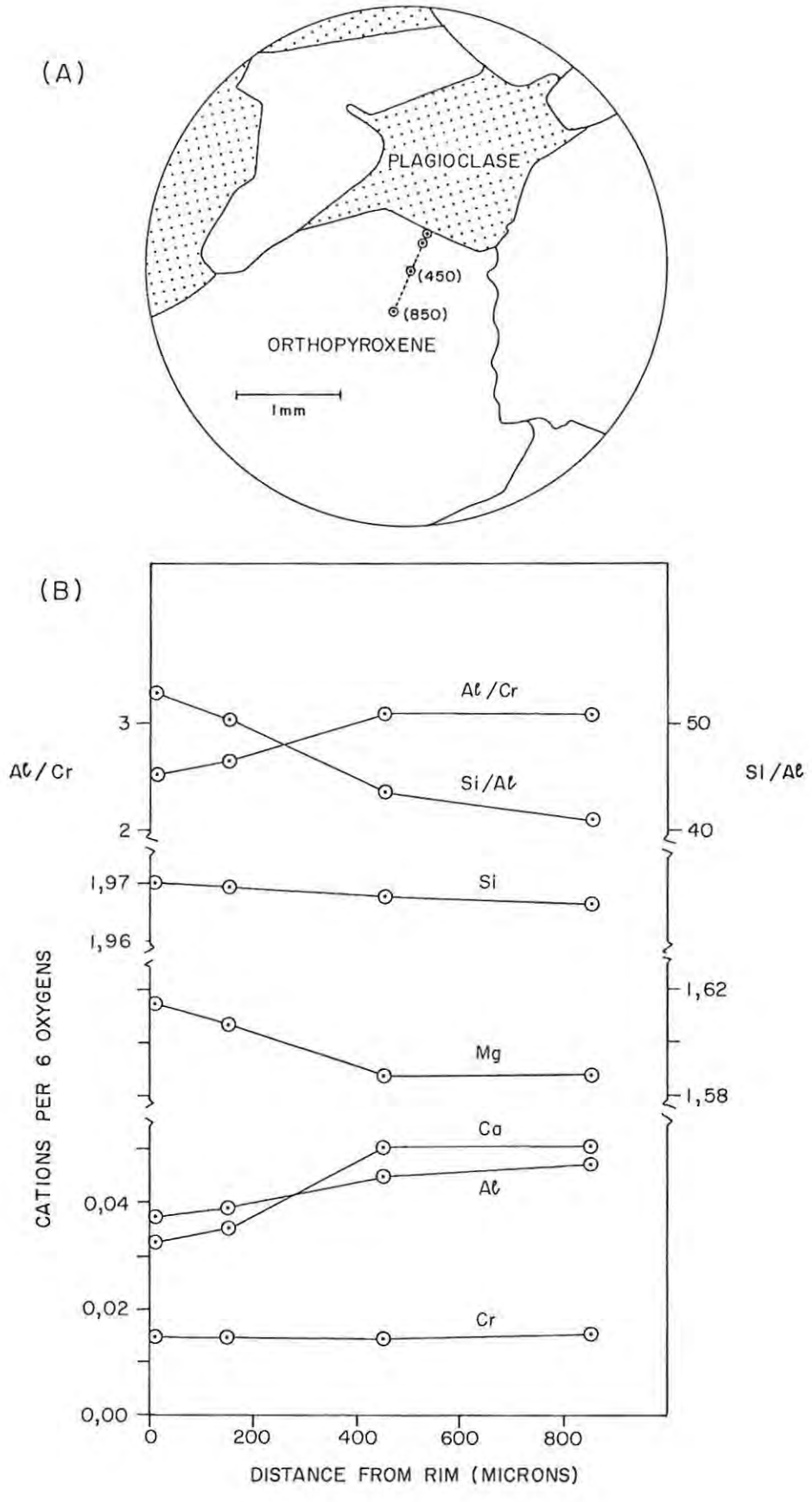

FIG. 15 (A) TEXTURAL ENVIRONMENT OF ANALYZED GRAIN IN SAMPLE 134; (B) PLOT OF COMPOSITIONAL PARAMETERS VERSUS DISTANCE FROM RIM, SHOWING ZONAL CHANGES AS THE RIM-DOMAIN IS APPROACHED.

proportions of Si and Mg cations. No zonal depletion of Cr^{3+} cations is evident and atomic Al/Cr declines from 3,09 to 2,52. The cryptic rise in atomic Si/Al (from 41,3 to 52,6) is also a notable feature. However, a rim composition within sample 128 (coarse-grained, adcumulate-textured bronzitite showing orthopyroxene intergrown with minor amphibole, mica, quartz and plagioclase) indicates a sympathetic depletion in Al, Ca and Cr. Sample 128 is located 8,4 m stratigraphically above 134, near the top of a 13 m thick horizon of coarse-grained bronzitite which encompasses both samples. Adcumulate textures and a higher relative modal content of hydrous silicate phases are prevalent within the upper portion of this horizon. The compositional differences between orthopyroxene rim-domains at the two stratigraphic levels may therefore be attributed to (a) the nature and relative abundance of intercumulus silicate phases, and/or (b) ingress of volatile-enriched, Cr-depleted residual melt from lower, solidifying layers contributing to the adcumulus growth processes. Orthopyroxene crystallinity measurements show an abrupt transition to annealed, finer-grained assemblages within 3 m of sample 128 (Fig. 8C), and orthopyroxene of composition $En_{84,2}$ is depicted in these essentially anchimonomineralic bronzitites (sample 125), contrasting with a composition of $En_{83,4}$ in sample 128. Furthermore, no chemical zonation in orthopyroxene crystals is evident in the fine-grained assemblages. Hence, the data suggest that the coarse-grained cumulate rocks may have cooled through a greater subliquidus temperature interval. The magnitude of the latter may be a function of the melt/crystal ratio, i.e., the bulk composition of the system liquid + crystals. In order to substantiate some of the above, consider the following arithmetic exercise. The size of the zoned orthopyroxene crystal in sample 134 cited above measures 3,2 x 1,88 mm. Assuming that the width of the zonal structure is 0,3 mm (Fig. 15(B)) and the grain shape approximates to an ellipsoid, the calculated volume of the structure is 3,7 mm^3 or 62 per cent of the 5,9 mm^3 total crystal volume. In contrast, typical grain-sizes in sample 125 are 1,27 x 0,93 mm, giving a calculated volume of 0,57 mm^3 per crystal. Hence, fine-grained samples 125 and 139 may be representative of an intraformational chill facies with little intercumulus liquid relative to coarse-grained samples 128, 134 and 155, which must have been immersed within a relatively larger volume of intercumulus melt

in order to achieve the significant degree of zonal overgrowth observed.

With respect to the D_2 succession, drill core ZS 3, microprobe analyses of orthopyroxene given in Table 6 are representative of the following mineralogical environments:

1. Bronzite-chromitite (thin sections 303 A, 304 A, and portions of 303 C, 315 and 317 C).
2. Chromitiferous granular-textured bronzitite (thin sections 302 A, 303 C, 314, 317 A, 318 A and 318 B).
3. Granular-textured bronzitite with a dissemination to weak dissemination of chromite (thin sections 315, 323 and 325).
4. Feldspathic, mesocumulate-textured bronzitite with disseminated chromite (thin sections 300 and 320).
5. Granular-textured bronzitite with trace modal chromite content (thin sections 304 B, 304 C, 305, 306 and 308).

Samples 325 and 323 from the upper 3 m of the D_1 subunit depict orthopyroxene of composition $En_{83,6}$. This parameter declines to $En_{82,3}$ at the + 4 m level (Fig. 16), which is within a horizon of medium-grained, feldspathic bronzitite. The relevant compositional profile shown in Fig. 16 is based on the assumption that this composition is representative of these feldspathic rocks. The granular-textured bronzitite in the footwall of the LG 6 chromitite has been partially replaced by olivine-bearing ultramafic pegmatite (analysis 318 B/2), but large areas of the residual, original assemblage yield a composition of $En_{82,9}$.

Orthopyroxene within the chromite-rich, layered hanging-wall of the LG 6 chromitite shows a pronounced increase in mol. per cent En relative to chromite-poor domains. Analysis 317 C/2 is representative of a cumulus orthopyroxene grain in a bronzite-chromitite layer. With increasing proximity to the grain boundary, the composition rises from $En_{84,8}$ (core) to $En_{85,9}$ (rim). This is coupled to a decline in Al_2O_3, MnO, CaO and mild enrichment in Cr_2O_3 content. However, an orthopyroxene-rich layer less than 1 cm above the latter (317 C/1) shows a composition of $En_{83,4}$ in the

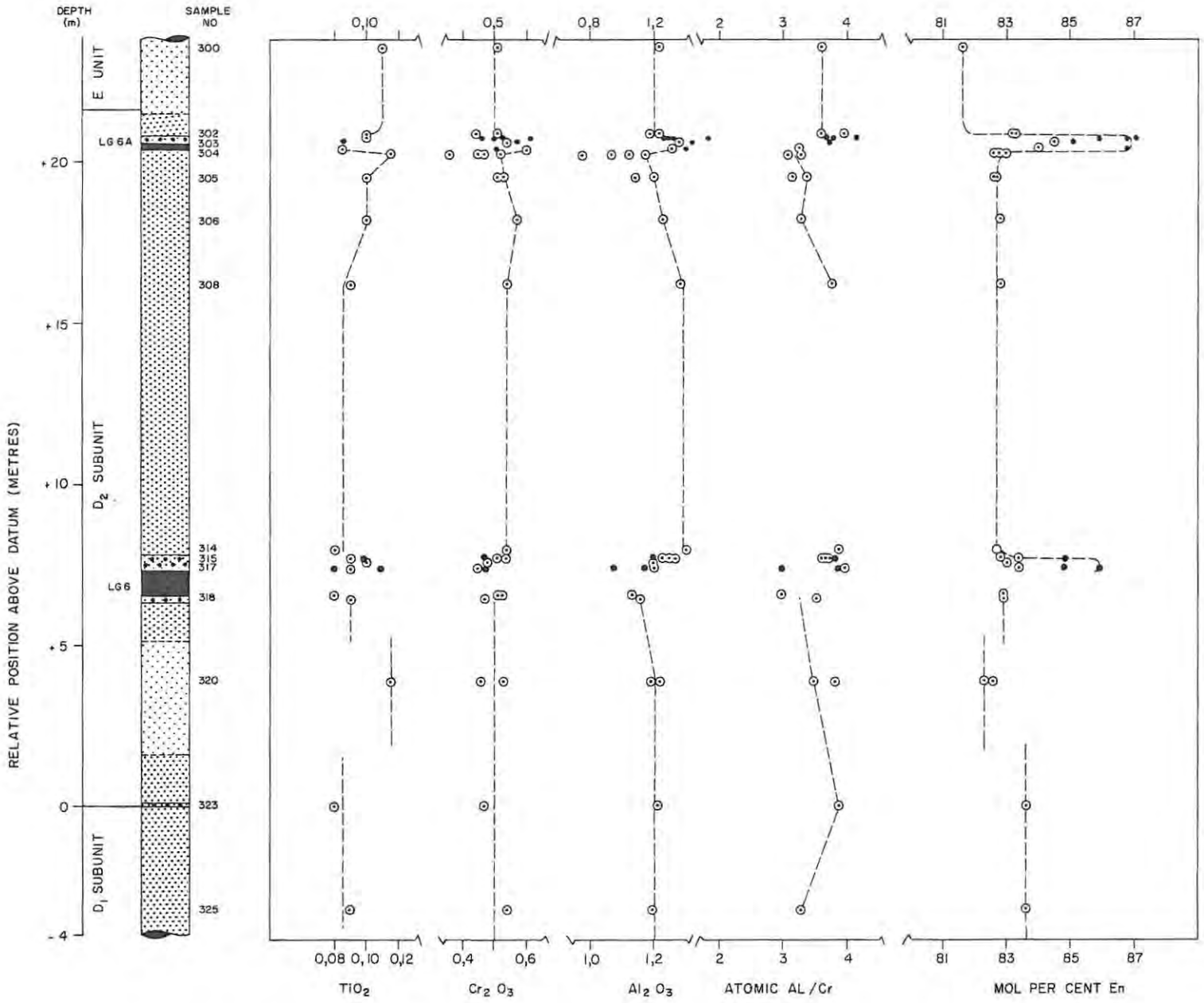

FIG. 16 LOG OF THE D_2 SUBUNIT (DRILL CORE ZS 31), WITH ANALYTICAL DATA PERTAINING TO ORTHOPYROXENE.

TABLE 6 MICROPROBE ANALYSES OF ORTHOPYROXENE: DRILL CORE IS 3

SAMPLE	300	302A C	302A R	303A C	303A C	303A R	303A R	303C C	303C C	304A C
SIO2	55.36	55.82	56.02	55.52	55.34	56.05	55.96	55.47	55.32	56.64
TIO2	.11	.10	.10	.11	.09	.10	.10	.08	.09	.09
AL2O3	1.23	1.23	1.17	1.28	1.54	1.27	1.31	1.43	1.35	1.40
FEO	11.80	10.82	10.94	9.16	8.98	8.43	8.60	9.21	9.94	8.61
MNO	.26	.26	.26	.21	.21	.22	.20	.23	.22	.21
MGO	29.50	30.27	30.79	30.80	30.80	32.09	31.81	30.85	30.60	31.89
CAO	1.21	1.51	.88	1.39	1.78	.85	1.06	1.46	.89	1.79
CR2O3	.51	.51	.44	.46	.61	.50	.53	.57	.54	.51
	99.98	100.52	100.60	98.93	99.35	99.51	99.57	99.30	98.95	101.14
				CATIONS	NUMBER OF OXYGENS = 6					
SI	1.9652	1.9635	1.9658	1.9682	1.9559	1.9659	1.9644	1.9611	1.9656	1.9607
TI	.0029	.0026	.0026	.0029	.0024	.0026	.0026	.0021	.0024	.0023
AL	.0515	.0510	.0484	.0535	.0641	.0525	.0542	.0596	.0565	.0571
FE2	.3503	.3183	.3210	.2716	.2654	.2473	.2525	.2723	.2954	.2493
MN	.0078	.0077	.0077	.0063	.0063	.0065	.0059	.0069	.0066	.0062
MG	1.5609	1.5870	1.6104	1.6275	1.6225	1.6776	1.6644	1.6257	1.6206	1.6455
CA	.0460	.0569	.0331	.0528	.0674	.0319	.0399	.0553	.0339	.0664
CR	.0143	.0142	.0122	.0129	.0170	.0139	.0147	.0159	.0152	.0140
	3.9990	4.0013	4.0013	3.9957	4.0011	3.9983	3.9986	3.9990	3.9962	4.0014
MMF	.816	.832	.833	.856	.859	.871	.868	.856	.845	.868
Al/Cr	3.6	3.59	3.96	4.14	3.77	3.77	3.68	3.74	3.71	4.07

SAMPLE	304A C	304B C	304B R	304C C	304C C	305 C	305 R	305 P 1	305 P 2	305 P 3
SIO2	56.02	55.24	55.39	55.37	55.53	55.27	55.49	55.38	55.46	55.58
TIO2	.08	.11	.11	.12	.11	.10	.10	.09	.09	.10
AL2O3	1.31	1.14	.93	1.04	.75	1.20	1.08	1.53	1.35	1.22
FEO	10.41	10.89	11.04	11.25	11.12	11.21	11.28	11.01	10.94	11.00
MNO	.25	.28	.26	.25	.28	.25	.25	.26	.22	.25
MGO	30.70	29.99	30.27	30.05	30.15	29.97	30.45	30.13	30.32	29.98
CAO	1.30	1.13	.79	.99	.70	1.34	.82	1.86	1.51	1.87
CR2O3	.60	.52	.45	.47	.36	.53	.51	.56	.55	.56
	100.67	99.30	99.24	99.54	99.00	99.87	99.98	100.82	100.44	100.56
				CATIONS	NUMBER OF OXYGENS = 6					
SI	1.9627	1.9666	1.9719	1.9683	1.9808	1.9607	1.9636	1.9478	1.9546	1.9590
TI	.0021	.0029	.0029	.0032	.0030	.0027	.0027	.0024	.0024	.0027
AL	.0541	.0478	.0390	.0436	.0315	.0502	.0450	.0634	.0561	.0507
FE2	.3050	.3242	.3287	.3344	.3317	.3326	.3338	.3238	.3225	.3242
MN	.0074	.0084	.0078	.0075	.0085	.0075	.0075	.0077	.0066	.0075
MG	1.6032	1.5914	1.6062	1.5922	1.6030	1.5847	1.6061	1.5795	1.5928	1.5750
CA	.0488	.0431	.0301	.0377	.0268	.0509	.0311	.0701	.0570	.0706
CR	.0166	.0146	.0127	.0132	.0102	.0149	.0143	.0156	.0153	.0156
	3.9999	3.9992	3.9994	4.0001	3.9954	4.0041	4.0041	4.0104	4.0073	4.0052
MMF	.84	.83	.83	.826	.828	.826	.827	.829	.831	.829
Al/Cr	3.25	3.27	3.07	3.3	3.08	3.36	3.14	4.06	3.66	3.25

TABLE 6 (cont.)

SAMPLE	305 P 4	306	308	314	315 1	315 2	315 3	315 4	315 5	317A
SIO2	55.83	55.22	55.33	55.50	55.66	55.66	55.29	55.53	55.37	55.50
TIO2	.07	.10	.09	.08	.10	.09	.08	.08	.09	.10
AL2O3	.92	1.25	1.36	1.40	1.19	1.25	1.30	1.33	1.30	1.19
FEO	11.25	11.05	11.03	11.23	9.79	10.65	11.13	11.14	11.04	10.97
MNO	.24	.25	.25	.25	.22	.22	.25	.26	.26	.23
MGO	30.76	29.98	29.91	30.26	30.70	30.20	30.16	30.12	29.93	30.22
CAO	.52	1.02	1.41	.81	1.42	1.43	1.02	1.30	1.49	1.31
CR2O3	.41	.57	.54	.54	.47	.51	.52	.54	.54	.48
	100.00	99.44	99.92	100.07	99.55	100.01	99.75	100.30	100.02	100.00
				CATIONS	NUMBER OF OXYGENS = 6					
SI	1.9717	1.9639	1.9601	1.9610	1.9669	1.9655	1.9608	1.9599	1.9603	1.9630
TI	.0019	.0027	.0024	.0021	.0027	.0024	.0021	.0021	.0024	.0027
AL	.0383	.0524	.0568	.0583	.0496	.0520	.0543	.0553	.0542	.0496
FE2	.3323	.3287	.3268	.3318	.2893	.3145	.3301	.3288	.3269	.3245
MN	.0072	.0075	.0075	.0075	.0066	.0066	.0075	.0078	.0078	.0069
MG	1.6192	1.5892	1.5793	1.5937	1.6171	1.5896	1.5943	1.5846	1.5794	1.5932
CA	.0197	.0389	.0535	.0307	.0538	.0541	.0388	.0492	.0565	.0496
CR	.0114	.0160	.0151	.0151	.0131	.0142	.0146	.0151	.0151	.0134
	4.0016	3.9993	4.0015	4.0002	3.9991	3.9990	4.0026	4.0028	4.0026	4.0028
MMF	.829	.828	.828	.827	.848	.834	.828	.828	.828	.83
Al/Cr	3.35	3.27	3.76	3.86	3.78	3.66	3.71	3.66	3.58	3.7

SAMPLE	317C 1	317C 2C	317C 2R	318A	318B 1	318B 2	320 C	320 R	323	325
SIO2	55.53	55.91	56.42	55.26	55.76	55.98	55.39	55.10	55.33	55.16
TIO2	.08	.11	.08	.07	.09	.09	.12	.11	.08	.09
AL2O3	1.20	1.14	.94	1.06	1.11	.92	1.24	1.18	1.22	1.19
FEO	10.76	9.78	9.18	11.10	11.00	10.70	11.47	11.11	10.53	10.48
MNO	.25	.21	.19	.23	.24	.25	.26	.25	.25	.25
MGO	30.34	30.85	31.62	30.27	30.13	30.64	30.08	29.76	30.19	30.14
CAO	1.48	1.54	1.01	1.60	1.55	1.26	1.33	1.25	1.22	1.23
CR2O3	.45	.44	.47	.53	.47	.34	.53	.46	.47	.54
	100.09	99.98	99.91	100.12	100.35	100.18	100.42	99.22	99.29	99.08
				CATIONS	NUMBER OF OXYGENS = 6					
SI	1.9616	1.9674	1.9770	1.9568	1.9663	1.9722	1.9566	1.9655	1.9665	1.9651
TI	.0021	.0029	.0021	.0019	.0024	.0024	.0032	.0030	.0021	.0024
AL	.0500	.0473	.0388	.0442	.0461	.0382	.0516	.0496	.0511	.0500
FE2	.3179	.2878	.2690	.3287	.3244	.3153	.3388	.3314	.3130	.3122
MN	.0075	.0063	.0056	.0069	.0072	.0075	.0078	.0076	.0075	.0075
MG	1.5975	1.6181	1.6515	1.5977	1.5837	1.6090	1.5838	1.5824	1.5993	1.6005
CA	.0560	.0581	.0379	.0607	.0586	.0476	.0503	.0478	.0465	.0469
CR	.0126	.0122	.0130	.0148	.0131	.0095	.0148	.0130	.0132	.0152
	4.0050	4.0000	3.9950	4.0118	4.0017	4.0016	4.0070	4.0002	3.9992	3.9999
MMF	.834	.848	.859	.829	.829	.836	.823	.826	.836	.836
Al/Cr	3.96	3.87	2.98	2.98	3.51	4.02	3.48	3.81	3.87	3.28

KEY TO TABLE 6

E unit : 300
D_2 subunit: 302 - 323
D_1 subunit: 325

300 : Bronzitite with conspicuous chromite content and feldspathic mesostasis (refer to Fig. 20(A)).

302A : Chromitiferous bronzitite (refer to Fig. 20(B)).

303A, 303C: Chromite bronzitite and bronzite-chromitite layers in the hanging-wall of the LG 6A layer (refer to Figs. 20(C) and (D)). Sample numbers include grain number and whether core(C) - or rim(R)-domains.

304A : Grain 1C is representative of a crystal in the chromite-rich, gradational footwall of the LG 6A layer, whereas grain 2C is representative of a silicate-rich domain at the immediate footwall contact (refer to Fig. 19(A)).

304B, 304C: Granular-textured bronzitites with plagioclase in poorly annealed cavities (refer to Figs. 19(B) and (C)).

305 : Fine-grained, granular-textured bronzitite (analyses 305 C and R) hosting a large idiomorphic crystal of orthopyroxene (analyses P1(core) to P4(rim). Refer to Figs. 18 and 19(D).

306, 308 : Granular-textured bronzitite.

314 : Chromitiferous, granular-textured bronzitite.

315 : Chromitiferous granular-textured bronzitite overlying a thin bronzite-chromitite layer (refer to Fig. 17). Analysis (1) represents an average composition of 3 crystals in juxtaposition to the chromite-rich domain, and (2) to (5) are of individual grains.

317A : Chromite bronzitite in hanging-wall of LG 6 chromitite layer.

317C : Grain (1) is depicted in a chromite bronzitite layer, whereas grain (2) is in a bronzite-chromitite layer.

318A : Chromitiferous, granular-textured bronzitite, with localized domains of olivine-bearing ultramafic pegmatite.

318B : As in 318(A), but located 16 cm below (A); footwall of the LG 6 chromitite layer. Analysis 318B (2) is representative of reaction-replacement orthopyroxene with the beam positioned in juxtaposition to an aggregate of chromite grains.

320 : Plagioclase-bearing, adcumulate-textured bronzitite.

323 : Chromitiferous, granular-textured bronzitite in juxtaposition to a chromite bronzitite layer marking the base of the D_2 subunit.

325 : Granular-textured bronzitite with isolated grains of olivine.

constituent grains, and it is noted that Cr_2O_3 contents (0,45 wt. per cent) and atomic Al/Cr (3,96) are equivalent to those of the orthopyroxene core-domains in the juxtaposed chromite-rich environments. Furthermore, it is evident from the disposition of data points in Fig. 16 that the Cr_2O_3 content rises from 0,44 to 0,54 wt. per cent with increasing stratigraphic height through the gradational hanging-wall. By virtue of the inadequate sample density, it is impossible to state whether the progressive Cr_2O_3-enrichment is a smooth, reciprocal function of the decline in bulk modal abundance of chromite. However, some substantiative evidence is afforded within sample 315, which is representative of the uppermost chromite-rich domain above the LG 6 chromitite layer. This bronzite-chromitite layer and 2,0 cm of the overlying granular-textured bronzitite were sampled in a thin section cut parallel to the drill core axis. Fig. 17 is a representation of the latter, showing the relative positions of the analyzed orthopyroxene crystals with microprobe data. The relevant analyses are available in Table 6 (analyses 315/1 - 315/5). The following features emerge from an inspection of the figure:

1. The En content of orthopyroxene is higher ($En_{84,8}$) adjacent to the chromitite than in the overlying bronzitite ($En_{82,8}$). Furthermore, the composition of $En_{82,8}$ is depicted within 10 mm of the chromite-rich environment.
2. The Al_2O_3 content rises from 1,19 wt. per cent to a pervasive abundance of 1,30 wt. per cent within the bronzitite.
3. The Cr_2O_3 content rises from 0,47 wt. per cent to a concentration of 0,54 wt. per cent some 15 mm above the chromitite.

The trend of constant or rising Cr_2O_3 contents with increasing stratigraphic height appears to be evident up to the position of sample 306 at the + 18 m level (Fig. 16). The concentration of Al_2O_3 in orthopyroxene similarly increases through the hanging-wall of the LG 6 and it would seem that orthopyroxene in the exceptionally fine-grained, annealed bronzitites separating the LG 6 and LG 6A chromitite layers is more aluminous (1,36 - 1,46 wt. per cent) than in the footwall succession (ca. 1,20 wt. per cent). The bronzitites exposed between the two chromitite layers show only a trace modal abundance of chromite, but chromite reappears as a more conspicuous

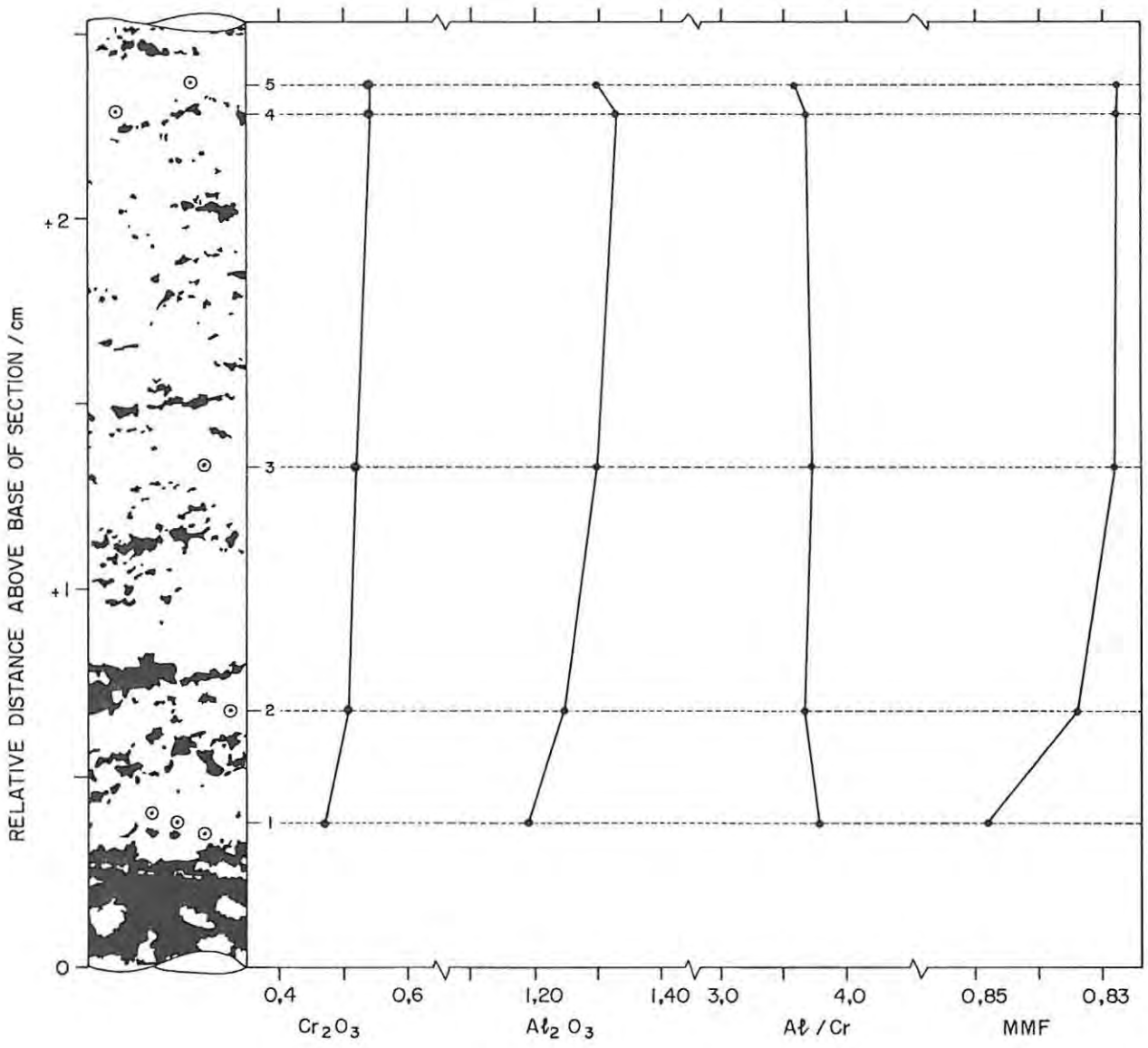

FIG. 17 LOG OF THIN SECTION 315 SHOWING (a) POSITIONS OF ANALYZED ORTHOPYROXENE CRYSTALS AND (b) VARIATION OF Cr_2O_3, Al_2O_3 (wt %), ATOMIC Al/Cr, AND $Mg/(Mg + Fe^{2+})$ OF ORTHOPYROXENE IN RELATION TO STRATIGRAPHIC HEIGHT. LOG REDRAWN FROM PHOTOGRAPH OF THIN SECTION. THE BRONZITE-CHROMITITE LAYER AT THE BASE OF THE SECTION IS 32 cm ABOVE THE LG 6 CHROMITITE.

phase in the upper 1 cm of this homogeneous succession. This occurrence is preceded by two unusual features: (a) the appearance of large, euhedral chromite grains intergrown with plagioclase or clinopyroxene in poorly annealed cavities (thin section 304 C), and (b) a single occurrence of an exceptionally large, euhedral orthopyroxene crystal within a fine-grained assemblage, some 90 cm below the LG 6A chromitite (Fig. 18). The results of a core-rim analytical traverse across this crystal are presented in Table 6 (analyses 305 P/1 - 305 P/4) and may be contrasted with the composition of the associated fine-grained orthopyroxene (analyses 305 C and 305 R).

An apparent decline in Al_2O_3 contents is indicated within 5 m of the basal contact of the LG 6A chromitite layer (Fig. 16). A minimum value of 1,04 wt. per cent was measured in sample 304 C, approximately 14 cm below the LG 6A chromitite, associated with 0,47 - 0,52 wt. per cent Cr_2O_3. There is a cryptic rise in Al and Cr with increasing stratigraphic height above this level, culminating in a concentration of 1,31 wt. per cent Al_2O_3 and 0,68 wt. per cent Cr_2O_3 in the immediate footwall bronzitite (analysis 304 A/2). A sympathetic rise in En content from 82,6 mol. per cent (304 C) to 84,0 mol. per cent is evident, and in CaO content. Similarly, disseminated orthopyroxene within the overlying bronzite-chromitite layer (analysis 304 A/1) is more magnesian ($En_{86,8}$) and more calcian (1,79 wt. per cent CaO). Photographs of thin sections 304 A, B, C and 305 are presented in Figs. 19(A) to (D), illustrating the relative modal proportion of chromite in each domain and in relation to the basal contact of the LG 6A chromitite layer.

The magnesian character of orthopyroxene in chromite-rich domains is emphasized by data pertaining to the hanging-wall succession of the LG 6A chromitite (thin sections 302 A, 303 A and 303 C). However, recognition of cryptic changes with increasing stratigraphic height is complicated by abrupt changes in modal chromite/orthopyroxene ratios and orthopyroxene grain-sizes and, in contrast to the footwall succession, the presence of modal intercumulus plagioclase (the latter increases in modal abundance with stratigraphic height above the basal chromite-rich environments and sample 300 is cited as a typical example). The data make no pretence, therefore, of being a

comprehensive representation. Accordingly, attention is restricted to the variation of Cr_2O_3 and Al_2O_3 in order to facilitate a comparison with analytical data pertaining to orthopyroxene in the hanging-wall of the LG 6 chromitite. Table 7 provides relevant data drawn from the analyses reported in Table 6, arranged in order of stratigraphic position. Figs. 20(A) to (D) present photographs of the thin sections with the respective positions of the analyzed grains shown.

TABLE 7:

VARIATION OF Al_2O_3 AND Cr_2O_3 IN ORTHOPYROXENE OF THE LG 6A HANGING-WALL SUCCESSION

ANALYSIS No	MINERALOGICAL DOMAIN	Al_2O_3%	Cr_2O_3%
300	Feldspathic bronzitite	1,28	0,51
302 A (Core)	Chromitiferous bronzitite	1,23	0,51
302 A (Rim)		1,17	0,44
303 A1 (Core)	Chromite bronzitite	1,28	0,46
303 A2 (Core)	Bronzite-chromitite	1,54	0,61
303 A2 (Rim)		1,27	0,50
303 C2 (Core)	Chromitiferous Bronzitite	1,35	0,54
303 C1 (Core)	Bronzite-chromitite	1,43	0,57

Orthopyroxene rim-compositions were determined in the chromite-rich environment of 303 A to assess whether the marginal domains were relatively enriched in Cr_2O_3. The latter contents were found to be equivalent or slightly depleted relative to core-domains and, in conjunction with a similar zonal distribution in sample 302 A, it

FIG. 18 : Photomicrograph showing a large, euhedral orthopyroxene crystal, with a minimum diameter of 10mm, in a granular-textured and fine-grained bronzitite (sample 305; 80cm below LG 6A chromitite layer). Microprobe analyses of the large crystal are denoted 305P 1(CORE) - 305P 4(RIM) in Table 6, and indicate a zonal decline in atomic Al/Cr with constant MMF ratio.

FIGS. 19(A) to (D): Photomicrographs illustrating the rise in modal chromite content with increasing stratigraphic height in the footwall of the LG 6A chromitite layer (drill core ZS 3). All sections were photographed with plane polarized transmitted light, and are orientated parallel to the drill core axis.

(A): Thin section 304(A): immediate footwall of the LG 6A massive chromite ore, showing layering defined in terms of the modal chromite/orthopyroxene ratio. Intercumulus plagioclase (+ minor biotite) is present in the bronzitite at the base of the section.

(B): Thin section 304(B): bronzitite immediately below section 304(A).

(C): Thin section 304(C): bronzitite 10 - 12 cm below the base of section 304(A).

(D): Thin section 305: Granular-textured bronzitite with plagioclase in poorly annealed cavities, some 85 cm below base of section 304(A).

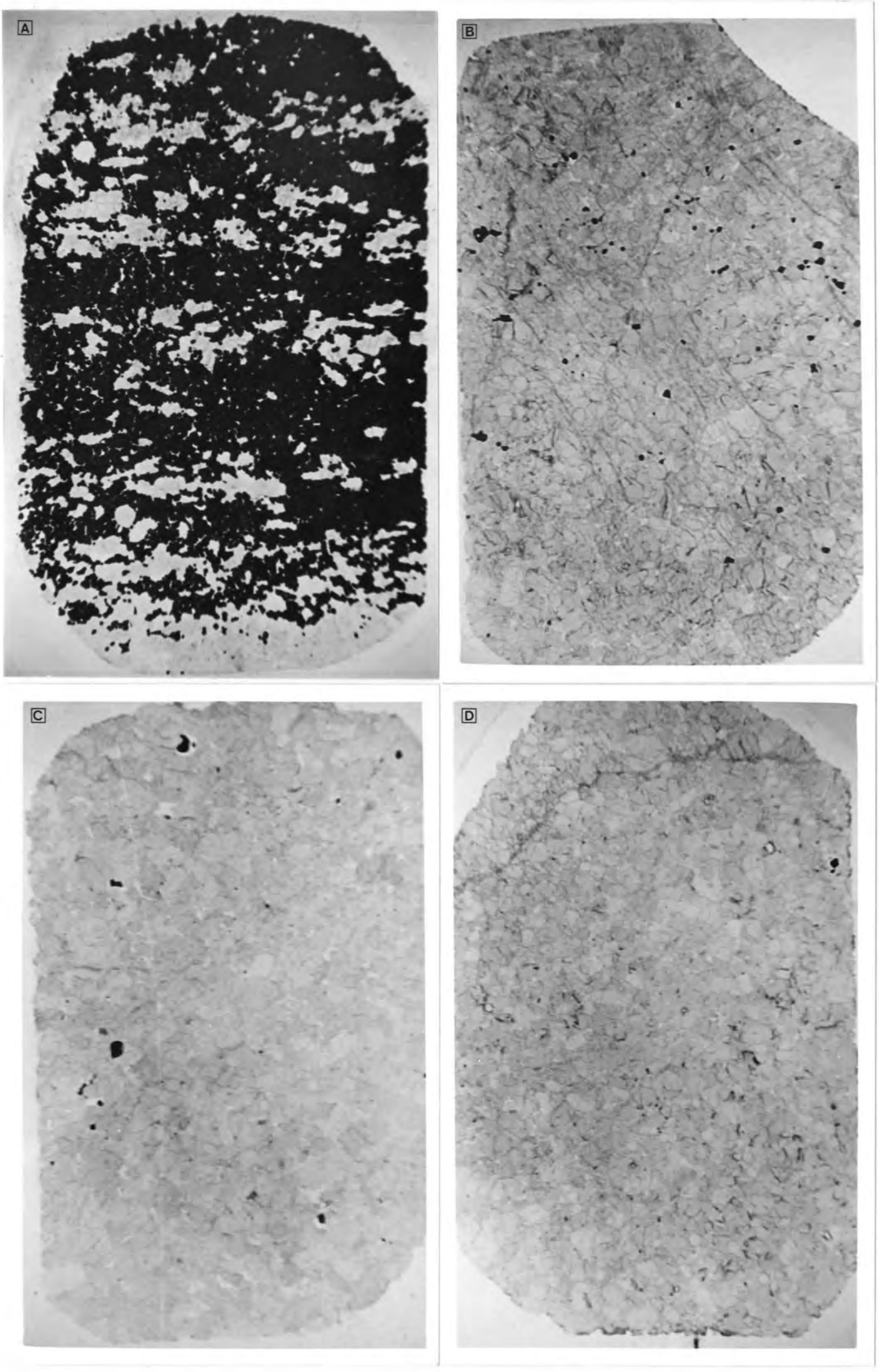
A
B
C
D

FIGS. 20(A) to (D): Photomicrographs illustrating the irregular decline in modal chromite content with increasing stratigraphic height in the gradational hanging-wall of the LG 6A chromitite layer (drill core ZS 3).

(A): Thin section 300: chromitiferous and feldspathic, mesocumulate-textured bronzitite, some 3 m above the LG 6A chromitite layer. Intercumulus plagioclase is conspicuous in thin section, and intergrown chromite grains exhibit exsolved needles and rods of rutile. Intercumulus clinopyroxene (minor) poikilitically encloses rounded chadacrysts of orthopyroxene and occludes orientated rods of an opaque spinel.

(B): Thin section 302(A): chromitiferous bronzitite with low mesostasis volume, 27 cm above the LG 6A chromitite.

(C): Thin section 303(A): chromite bronzitite and bronzite-chromitite layers, 9cm above the massive chromite ore.

(D): Thin section 303(C): chromitiferous bronzitite and bronzite-chromitite assemblages in the immediate hanging-wall of the LG 6A chromitite layer.

SYMBOL:

● positions of analyzed orthopyroxene crystals

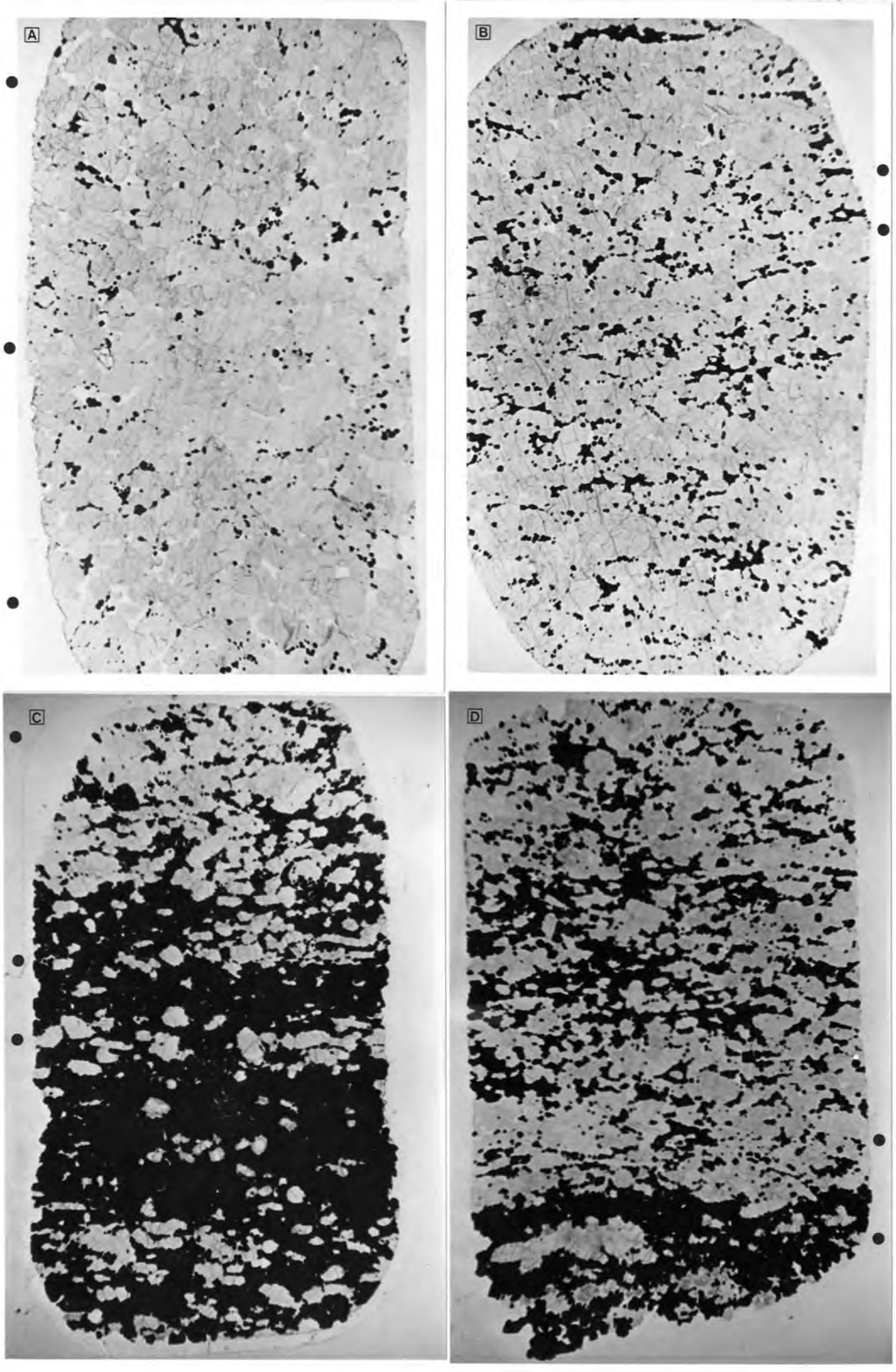
A
B
C
D

would seem that the concentration of Cr_2O_3 in orthopyroxene core-domains has not been augmented by the diffusion of Cr from circumjacent chromite. Hence, the data suggest (Table 7) that a series of cyclical variations are superimposed on a broad trend of declining Al_2O_3 and Cr_2O_3 with increasing stratigraphic height through the chromite-rich interval. Furthermore, Al_2O_3 contents appear to reach and maintain a fairly constant value (ca. 1,25 wt. per cent) in the overlying orthopyroxene-richer layers, whereas Cr_2O_3 may rise initially from a low value of ca. 0,46 wt. per cent to a constant value of 0,51 wt. per cent. An extremely comprehensive analytical programme is required to ensure that these trends are not an artifact of sample distribution or subsolidus re-equilibration between orthopyroxene and chromite. A sample spacing on the scale of millimetres may afford a means of circumventing these problems. Nonetheless, the data would indicate that a gross trend of rising Al_2O_3 and Cr_2O_3 with increasing stratigraphic height is evident through the gradational hanging-wall of the LG 6 chromitite, whereas these parameters decline through the equivalent succession of the LG 6A chromitite layer. A feature which should not be overlooked is the reappearance of minor intercumulus plagioclase some 4m below the basal contact of the LG 6A chromitite (sample 308) and within centimetres of the upper contact (sample 303, for example). Furthermore, the textural differences between the respective hanging-wall bronzitites are pronounced (refer to the crystallinity profile in Fig. 8(D)). Hence, the contrasting compositional trends may reflect changes in the crystallization and chemical conditions of the magma and not subsolidus re-equilibration processes. The latter would act to produce equivalent compositional trends that are a function of the gradational decline in whole-rock chromite abundance above the chromitite layers. With reference to Fig. 16, however, it is evident that cryptic changes in minor element contents within orthopyroxene (e.g., Ti) are also linked to petrographic parameters such as modal plagioclase content. The question which thus arises is: are the textural changes in response to thermal fluctuations in the magma (therefore also compositional changes in the magma and phases crystallizing from it) or do the cryptic compositional changes merely reflect varying degrees of subliquidus equilibration with residual melt (as achieved by in situ secondary growth followed by diffusive homogenization)? The present study is not in a position to

yield an answer at this juncture, but consideration should be given to both queries by virtue of the pronounced crystallinity gradients exposed within the D_2 subunit in the studied section, and the link between composition and modal proportion mesostasis noted in bronzitites of the D_1 subunit.

5.2.2.6 ORTHOPYROXENE IN THE E UNIT

Bronzitites of the E unit were sampled at ten stratigraphic positions in drill core ZS 7 and one position in drill core ZS 3 (sample 300). The variation of TiO_2, Cr_2O_3, Al_2O_3 contents and $Mg/(Mg + Fe^{2+})$ ratios through the succession is graphically illustrated in Fig. 14. Samples 61, 70 and 71 are representative of medium- to coarse-grained orthopyroxene crystals intergrown with plagioclase, clinopyroxene and amphibole. A low modal abundance of chromite characterizes the succession above the level of sample 70, but an elongate chromitite lens (with a high void volume) is depicted in sample 28. Samples 39, 43 and 50 are representative of orthopyroxene adcumulates showing very low modal proportions of intercumulus silicate phases in poorly annealed cavities. These assemblages are, however, coarser-grained than the granular-textured bronzitites of the D unit. Sample 32 is representative of a thin chromite-orthopyroxene cumulate layer some 30 m below the LG 7 chromitite, and sample 11 depicts coarse-grained orthopyroxene intergrown with an intimate mixture of hexagonal and monoclinic pyrrhotite (as an interstitial phase). The latter is indicative of the decomposition of a magmatic, monosulphide solid solution during arrested cooling. No other interstitial phases are present in the assemblage. Sample 01 is representative of a granular-textured bronzitite in the hanging-wall of the LG 7 chromitite layer. The respective microprobe analyses are reported in Table 4. It should be noted that olivine of a seemingly ultramafic pegmatite association is depicted in samples 01 and 39.

A trend of declining En content is noted through the lower 6 m of the E unit (Fig. 14), reaching an apparent minimum of 81,1 mol. per cent at the stratigraphic level of sample 61. A reversal to more magnesian compositions is evident at some position between samples 61

and 50, where orthopyroxene of composition $En_{82,7}$ is present. This is followed by a gradational decline to a composition of $En_{82,3}$ in sample 32. Approximately 1 cm above the chromitite lens in sample 28, however, a composition of $En_{83,5}$ is depicted. The bronzitite at this level is composed of a fine- to medium-grained, polygonal assemblage of annealed orthopyroxene grains. Small, euhedral chromite grains are conspicuous in thin section. It should be recalled that the stratigraphic interval between samples 32 and 28 is marked by a pronounced rise in orthopyroxene crystallinity (Fig. 8E). Furthermore, MgO-enriched compositions were only observed in immediate juxtaposition to the chromitite lens. Hence, there is no basis for rejecting the analysis on the grounds that it may be spurious: the magnitude of the increase (1,2 mol. per cent En) is comparable to that noted in the lower portion of the D_1 subunit.

Orthopyroxene of composition $En_{81,8}$ is depicted in sample 11, some 21 m above sample 28. A notable feature is that the stratigraphic separation between the LG 6A chromitite and sample 61 (the level at which an apparent minimum composition of 81,1 mol. per cent En was recorded) is 22 m. Furthermore, the composition of $En_{81,8}$ is consistent with the probable continuation of the compositional trend through samples 50 to 32 and, from an inspection of Fig. 14, of the generalized compositional change throughout the D and E units. It is therefore anticipated that a reversal to more magnesian composition may be depicted between the stratigraphic level of sample 11 and the LG 7 chromitite layer. This is substantiated in part by a composition of $En_{82,6}$ in the hanging-wall of the chromitite layer.

The minor oxides TiO_2, Cr_2O_3 and Al_2O_3 do not show a significant variation through the E unit, although the sample distribution is wholly unsuitable for purposes other than a comparison with lower units. This is available in Fig. 14. The average Cr_2O_3 content of 0,51 wt. per cent does not differ from that of orthopyroxene within the underlying units, nor does the average Al_2O_3 content of 1,20 wt. per cent differ substantially. The average TiO_2 abundance of 0,11 wt. per cent is, however, slightly higher. Exclusion of sample 39 from the data set, by virtue of possible compositional perturbations stemming from the partial replacement by ultramafic pegmatite, has a negligible effect on these averages.

5.2.2.7 SUMMARY

Broader Conclusions

Mean Al_2O_3, Cr_2O_3 and MMF values of cumulus orthopyroxene within the respective subunits of the Ruighoek Pyroxenite are presented in Table 8. These data are exclusive of orthopyroxene rim-compositions and of orthopyroxene in chromite-rich domains.

TABLE 8:

AVERAGE Al_2O_3, Cr_2O_3 CONTENTS AND MMF RATIOS OF ORTHOPYROXENE WITHIN SUBUNITS OF THE RUIGHOEK PYROXENITE

SUBUNIT	B	C_1	C_2	D_1	D_2	E
Al_2O_3	1,16	1,22	1,15	1,24	1,30	1,20
Cr_2O_3	0,53	0,48	0,52	0,54	0,54	0,51
MMF	0,841	0,857	0,848	0,835	0,828	0,821

Al_2O_3, Cr_2O_3: wt. per cent
MMF : $Mg/(Mg + Fe^{2+})$

The microprobe data reported in the preceding text compare favourably with the partial analyses of McDonald (1967), and Fig. 7 of that publication, showing the variation of FeO in orthopyroxene as a function of stratigraphic height on farm Ruighoek, can be compared with Fig. 14 of the present study. Furthermore, the variation in the enstatite content of orthopyroxene with stratigraphic height and the absolute En contents are consistent with those observed by Cameron (1980) in the central sector of the Eastern Bushveld Complex. Certain implications of the latter are significant. For example, (1) differences in the number and nature of chromitite layers within the

Ruighoek Pyroxenite relative to the Mooihoek Pyroxenite are not a function of a compositionally distinct magma crystallizing under different P,T conditions. However, (2) it is evident from the data pertaining to the Lower Zone samples (Table 4, samples KA 410, 571, 622, 729), that no clear distinction is afforded purely on the basis of orthopyroxene chemistry. The composition of orthopyroxene within sample KA 410 ($En_{84,3}$; 1,16 wt. per Al_2O_3; 0,50 wt. per cent Cr_2O_3) is equivalent to the mean of the B unit, and orthopyroxene within the granular harzburgite samples KA 571 and ZS 7 238 (i.e., near the top of the C_1 subunit) yields comparable Al_2O_3, Cr_2O_3 and enstatite contents. Hence, if it is postulated that orthopyroxene within the Lower Critical Zone is saturated with respect to chromium, this must also apply to the Groenfontein Harzburgite subzone. The present study has shown that (3) relative to core-domains, the outer rims of well-formed, cumulus orthopyroxene grains in feldspathic assemblages may show depletion in Al, Ca and Cr, but higher atomic Cr/Al ratios and Ti abundances. In conjunction with petrographic observations of large chromite grains within embayments on these margins, or smaller grains occluded within the marginal domains, (4) the data are consistent with the continued growth of orthopyroxene after nucleation of intercumulus plagioclase had commenced. A further compositional change is (5) the higher En content of the rim-domains. This feature is inconsistent with the normal fractionation path of a melt, but can be reconciled in terms of a progressive increase in the Fe^{3+}/Fe^{2+} ratio of the residual melt. However, no titanomagnetite is present in the plagioclase-bearing interstices, which were commonly seen to be charged with a random distribution of rutile rods and needles. Furthermore, (6) orthopyroxene in chromite-rich domains is significantly enriched in MgO relative to adjacent silicate-rich layers. One compositional profile on nearing a chromite-orthopyroxene grain boundary indicated higher MMF ratios and Cr abundances and a progressive depletion in Al content, but Cr-depleted rim-compositions were recorded in chromite-rich domains in the hanging-wall of the LG 6A chromitite layer.

MMF Ratios

The overall decline in the orthopyroxene MMF ratio with increasing stratigraphic height in the Ruighoek Pyroxenite succession conforms to normal progressive fractionation of a magma. A pronounced reversal of the sense of this trend is evident in proximity to the LG 2 chromitite layer. The compositions of orthopyroxene within the upper 7 metres of the B unit and lower 7 metres of the C_1 subunit are intermediate between the minimum B unit composition of $En_{83,6}$ and the maximum of $En_{85,9}$ measured midway through the C_1 subunit. The microprobe data emphasize a similar but less pronounced trend in the upper portion of the D_1 subunit. However, due to the compositional homogeneity of fine-grained bronzitites within the LG 6 - LG 6A succession ($En_{82,8}$ - $En_{83,0}$), no clear lineage is evident between orthopyroxene depicted in the basal portion of the D_2 subunit ($En_{83,6}$) and in the overlying E unit ($En_{81,2}$). Data pertaining to other fine-grained, granular-textured assemblages in the D and E units may also seem to be aberrational but are consistent with the premise that the compositions of successive, fine-grained orthopyroxene assemblages approximate to liquidus compositions, thereby defining a liquid line of descent.

Cr Depletion

The question of whether there is evidence of Cr-depletion immediately above a chromitite layer is of particular relevance to this study. However, microprobe data reported here do not point to a consistent relationship. For example, orthopyroxene above and below the LG 3 chromitite, which is bounded by sharp contacts, shows a composition of 0,53 wt. per cent Cr_2O_3. In contrast, an increase from 0,44 to 0,54 wt per cent Cr_2O_3 was measured through the gradational hanging-wall of the LG 6 chromitite, whereas a step-wise depletion was observed through that of the LG 6A chromitite. In both instances, however, restored levels of Cr_2O_3, typical of concentrations in the adjacent bronzitites, were noted some 20 - 30 cm above the massive chromite ore. Furthermore, the magnitude of the compositional change is comparable with that

observed in the basal portion of the C_1 subunit, where the sense of the compositional variation of orthopyroxene is equally perplexing. Consider, for example, the following proposal: the rise in mol. per cent En with increasing stratigraphic height through the upper portion of the B unit, and into the C_1 subunit, may be indicative of partial liquid mixing at the base of a new influx with residual magma that is in equilibrium with more Fe-rich orthopyroxene. Given this situation, a sympathetic rise in orthopyroxene Cr_2O_3 contents is to be anticipated. However, the opposite is observed within the olivine-bronzitites of the C_1 subunit, where a trend of Cr_2O_3-depletion is evident. A high value of 0,59 wt per cent Cr_2O_3 is actually observed some 2 m below the first appearance of olivine (or 2,5 m above the LG 2 chromitite) and no change in the modal abundance of chromite is associated with these features. Hence, the minor Cr-depletion trend noted within orthopyroxene in the LG 6A gradational hanging-wall cannot be viewed as unequivocal evidence for chromite crystallization from a restricted melt volume. Considerations of this nature will be examined in relevant sections of the subsequent text.

CALCULATED TEMPERATURES

Final temperatures of equilibration can be calculated from the compositions of coexisting ortho- and clinopyroxene (Wood and Banno, 1973; Wells, 1977). The single pyroxene geothermometer of Mercier (1980) was employed in this study to calculate temperatures and these results are reported in Table 9, together with temperature estimates based on the two-pyroxene geothermometer of Wells (op. cit.). The single pyroxene geothermometer is particularly useful in that it facilitates an evaluation of zonal structures in orthopyroxene crystals. Use of the Wells geothermometer is dependent on the assumption that the coexisting Ca-rich and Ca-poor pyroxenes are in equilibrium. This may not be the case in the Ruighoek Pyroxenite, where intercumulus clinopyroxene is seen to have resorbed cumulus orthopyroxene grains to varying degrees. Hence, the calculated temperatures are dependent on the selection of representative pyroxene pairs. For example, juxtaposed rim compositions of ortho- and clinopyroxene should approximate to minimum equilibration

TABLE 9:

CALCULATED EQUILIBRIUM TEMPERATURES FOR COEXISTING PYROXENES BASED ON THE MERCIER AND WELLS GEOTHERMOMETERS

SAMPLE	MMF (opx)	T°C (MERCIER)		T°C (WELLS)
		opx	cpx	
E UNIT				
01	0,826	1 165		
11	0,818	1 259		
28	0,835	1 086		
32	0,823	1 185		
39	0,824	1 125		
43	0,825	1 186		
50	0,827	1 152		
61	0,811	1 211	1 016	945
70	0,812	1 160	1 035	961
71	0,812	1 229		
300	0,816	1 155		
D_2 SUBUNIT				
302A	0,832	1 213 (1 078)		
303A	0,857	1 228 (1 072)		
303C	0,845	1 203		
304A	0,840	1 214		
304B	0,830	1 138		
304C	0,826	1 107	1 053	950
305	0,826	1 180	1 017	950 (899)
305 P1	0,829	1 273 (Core)		
305 P2	0,831	1 210		
305 P4	0,829	980 (Rim)		
306	0,828	1 114	1 031	974 (915)
308	0,828	1 194		
314	0,827	1 064	1 052	991 (933)
315	0,828	1 203	1 056	977
317A	0,830	1 175	1 052	986
317C	0,841	1 215		
318	0,829	1 224	1 073	1 002 (969)
320	0,823	1 176 (1 166)	1 078	1 009

TABLE 9: (continued)

SAMPLE	MMF (opx)	T°C (MERCIER)		T°C (WELLS)
		opx	cpx	
323	0,836	1 158	1 038	924* (985)
325	0,836	1 159	1 029	974
78	0,828	1 243		
79	0,829	1 192		
83	0,833	1 212		
D_1 SUBUNIT				
90	0,831	1 183	1 064	975
95	0,831	1 226		
104	0,828	1 213		
117	0,832	1 204		
125	0,842	1 167		
128	0,834	1 182 (1 024)		
134 (850)	0,831	1 179 (Core)		
134 (450)	0,830	1 178		
134 (150)	0,831	1 091		
134 R	0,833	1 074 (Rim)		
139	0,848	1 235		
155	0,835	1 181 (1 066)		
164	0,836	1 200		
C_2 SUBUNIT				
203	0,849	1 167 (1 089)		
205	0,847	1 169 (1 059)	1 038	965
208	0,847	1 131	1 130	1 047
208 EX	0,824	1 045	997	920
211	0,844	1 135 (1 048)		
213B	0,845	1 293		
214A 1	0,850	1 212		
215	0,854	1 165 (1 069)		
221	0,860	1 156	1 031	962
223 D	0,858	1 135 (secondary opx)		
225	0,848	1 153 (977)		

TABLE 9: (continued)

SAMPLE	MMF (opx)	T°C (MERCIER) opx	T°C (MERCIER) cpx	T°C (WELLS)
C_1 SUBUNIT				
238	0,857	1 180		
249	0,859	1 139 (1 096)		
254A	0,856	1 106		
258B 1	0,856	1 245	1 055	963
B UNIT				
259	0,843	1 115		
265	0,844	1 242 (1 104)		
271	0,836	1 150		
280	0,840	1 182		
286A	0,838	1 068		
290	0,839	1 158		
297	0,839	1 204 (1 047)		
LOWER ZONE				
KA 410	0,843	1 202		
KA 571	0,853	1 212		
KA 622	0,852	1 250		
KA 729	0,823	1 002		

T°C (Mercier) Single pyroxene geothermometer of Mercier (1980)

opx: 1 213 (1 078)

- 1 213: Temperature calculation based on core composition
- (1 078): Temperature calculation based on rim composition

cpx: Temperature calculation based on composition of intercumulus clinopyroxene

T°C (Wells) Two-pyroxene geothermometer of Wells (1977)

950 (899)

- 950: Temperature calculation based on composition of orthopyroxene core and core-domain of intercumulus clinopyroxene
- (899): Temperature calculation based on composition of orthopyroxene core and exsolved clinopyroxene bleb

924* (985)

- 924*: Temperature calculation based on composition of clinopyroxene margin and orthopyroxene core

temperatures, whereas calculations based on spatially removed core compositions may deviate from the minimum (zoning is pronounced within intercumulus clinopyroxene). In order to assess the above, calculated temperatures based on exsolved clinopyroxene blebs within well-formed orthopyroxene crystals are included in Table 9.

Calculations based on the Mercier geothermometer and orthopyroxene core-compositions yield the following average crystallization temperatures:

1. E unit 1 173°C
2. D_2 subunit 1 180°C
3. D_1 subunit 1 197°C
4. C_2 subunit 1 171°C
5. C_1 subunit 1 167°C
6. B unit 1 159°C

Calculated temperatures derived for rim-compositions are on average 105°C lower, suggesting that orthopyroxene crystallized over a temperature interval of this magnitude. However, the procedure is very sensitive to the calcium content of the orthopyroxene (refer to samples 134 and 305 in Table 9, for example). If nucleation of plagioclase induced the CaO-depleted nature of the rim-domains, the temperature differential noted above bears no relationship to crystallization temperatures. Similarly, progressively lower calculated temperatures are indicated for calcium-depleted zonal structures in proximity to chromite (not presented in Table 9). Temperatures based on the compositions of intercumulus clinopyroxene grains vary between 1 025 and 1 066°C, with an average of 1 052°C. The latter is 122°C lower than the average calculated temperature of 1 174°C derived from orthopyroxene core-compositions. Fig. 21 is a plot of calculated temperature versus MMF (orthopyroxene) and although these is a substantial spread in the data points, the locus or bulk average (MMF = 0,835; 1 174°C) for the Ruighoek Pyroxenite is consistent with the two-pyroxene temperature relationship derived by Hulbert (1983) for the Rustenburg Layered Suite south of Potgietersrus:

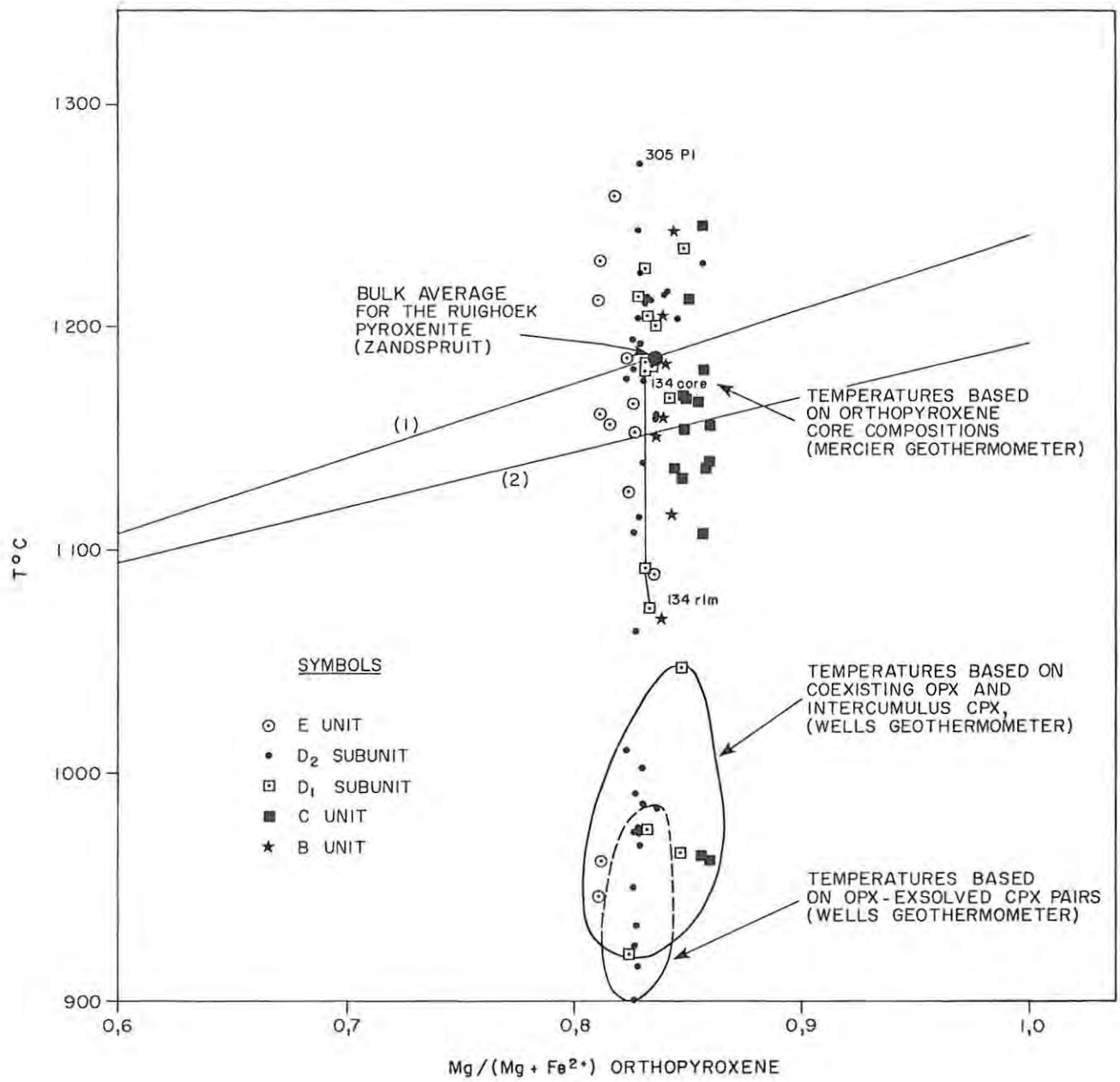

FIG. 21 CALCULATED TEMPERATURE VS MMF (OPX) FOR (i) ORTHOPYROXENES AND (ii) COEXISTING PYROXENES FROM THE RUIGHOEK PYROXENITE. CURVE (1) WAS CONSTRUCTED ACCORDING TO THE EXPRESSION $T°C = 333,46 \left(x \frac{OPX}{Mg}\right) + 907,6$, AND CURVE (2) ACCORDING TO $T°C = 245,99 \left(x \frac{OPX}{Mg}\right) + 946,00$, DERIVED BY HULBERT (1983) FOR THE RUSTENBURG LAYERED SUITE SOUTH OF POTGIETERSRUS AND FOR THE EASTERN AND WESTERN BUSHVELD COMPLEX, RESPECTIVELY.

$$T = 333,46\ (X_{Mg})^{opx} + 907,6$$

Calculated temperatures based on the two-pyroxene Wells geothermometer vary between 1 047 and 920°C, with a mean of 970°C. The lower calculated temperatures may stem from analytical errors (i.e., CaO in clinopyroxene too high) or may reflect equilibration to lower blocking temperatures. The latter consideration may account for the wide range in calculated temperatures resulting from both geothermometers (Fig. 21). The average calculated temperature of five orthopyroxene-exsolved clinopyroxene pairs is 940°C and, by virtue of the intimate intergrowth of these phases and implied equilibrium conditions, may reflect a minimum blocking temperature.

5.3 INTERCUMULUS SILICATE PHASES

5.3.1 ORTHOPYROXENE AS A REPLACING PHASE

Analyses of reaction-replacement orthopyroxene in poikilitic harzburgites are available in Table 4, and the compositional variation has been briefly discussed in section 5.2.2.4. The major occurrence of this secondary silicate phase is within the C_3 subunit, particularly in the immediate footwall of the LG 4 and I chromitite layers. Characteristically, no other intercumulus silicate phases are present in these domains where extensive replacement of olivine has occurred. In a few instances, however, anhedral clinopyroxene is observed within large, structurally continuous oikocrysts of reaction-replacement orthopyroxene (e.g., within polished section 177A). This texture is suggestive of olivine replacement after clinopyroxene had crystallized as an intercumulus phase between cumulus olivine grains and points to upward migration of residual melt, with the reaction $Mg_2SiO_4 + SiO_2 = Mg_2Si_2O_6$ going almost to completion in domains beneath impermeable, chromite-rich layers.

The enstatite content of reaction-replacement orthopyroxene is generally one to two mol. per cent higher than the forsterite content of coexisting olivine grains, irrespective of mineralogical environment. For example, olivine of composition $Fo_{84,4}$ is associated with reaction-replacement orthopyroxene of composition

$En_{85,8}$ in sample 223 D (layered dunite in the C_2 subunit), and $Fo_{81,6}$ olivine is associated with $En_{83,6}$ orthopyroxene in an ultramafic pegmatite replacement assemblage below the LG 6 chromitite layer.

5.3.2 CLINOPYROXENE

Clinopyroxene displays a high capacity for chromium and represents an effective scavenger of Cr in basaltic systems. With the exception of the lower portion of the Critical Zone of the Rustenburg Layered Suite south of Potgietersrus, chromite is not found in association with gabbronoritic rocks of the eastern and western Bushveld Complex. The composition of clinopyroxene in layered rocks has been found to vary as a function of the modal proportion of clinopyroxene (Nwe, 1975; McBirney and Noyes, 1979; Wilson, 1982). Furthermore, many studies on lava samples and dynamic crystallization experiments have shown that the composition of clinopyroxene is sensitive to the crystallization order of the minerals separating from a melt. Plagioclase, in particular, can influence the abundance of Al^{3+} in clinopyroxene by virtue of accommodating the Ca-Tschermak molecule, $Ca\ Al_2\ SiO_6$.

Clinopyroxene occurs in small amounts as an intercumulus mineral in the Ruighoek Pyroxenite succession. Within the granular-textured bronzitites of the D and E units, clinopyroxene occupies poorly annealed cavities and is commonly stoped to varying degrees along polygonal orthopyroxene grain boundaries. These minor occurrences are generally optically zoned and depict fine-scale, exsolution lamellae of Ca-poor pyroxene. Within feldspathic bronzitites, however, clinopyroxene commonly occurs as large, green oikocrysts, poikilitically enclosing chadacrysts of orthopyroxene and, in some instances, remnants of intercumulus plagioclase. Chromite also occurs as an occluded phase. Partial to complete amphibolitization is common and the oikocrysts display broad exsolution lamellae or blebs of orthopyroxene. Minute oxide inclusions, depicting a schiller structure, were only observed in the D_2 subunit and basal portion of the E unit (drill core ZS 3). These appear to be stubby rods and platelets of magnetite.

Microprobe analyses of clinopyroxene are presented in Table 10. These data are representative of the following associations:

1. Clinopyroxene as an exsolved phase within cumulus orthopyroxene.
2. Clinopyroxene as an intercumulus mineral in granular-textured and feldspathic bronzitites.
3. Clinopyroxene as an intercumulus mineral in granular harzburgite, and within chromitiferous poikilitic harzburgite.

Descriptions of the respective microdomains are available in the key to Table 10. The $Mg/(Mg + Fe^{2+})$ ratio of clinopyroxene varies between a low value of 0,871 for an intercumulus grain intergrown with plagioclase in sample 61 (E unit), and a high value of 0,917 for a domain some 50 microns from an occluded chromite grain (chromitiferous poikilitic harzburgite sample 177 A). A pronounced chemical zonation is noted in proximity to occluded chromite grains, with a rise in the MMF ratio of clinopyroxene indicated on nearing chromite grain boundaries. Zoning also occurs within intercumulus grains depicted in silicate-rich rocks, and the margins adjacent to orthopyroxene grain boundaries indicate slightly higher MMF ratios (0,002 - 0,011 mol. fraction). Similarly, clinopyroxene filling poorly annealed cavities in granular-textured bronzitites is less Fe-rich than larger grains in adjacent, coarser-grained bronzitite (compare, for example, analyses 320 and 323).

The MMF ratio of exsolved clinopyroxene is higher than that of the coexisting intercumulus phase (refer to samples 305 and 306), which generally shows a degree of resorption of the cumulus orthopyroxene framework. Furthermore, it is evident from the data that there is a positive correlation of MMF (clinopyroxene) and the MMF ratio of the coexisting orthopyroxene. A similar correlation of MMF (clinopyroxene) and MMF (olivine) is suggested (samples 177 A and 238).

The clinopyroxenes contain 1,19 to 2,34 wt. per cent Al_2O_3 and 0,70 to 1,13 wt. per cent Cr_2O_3, with average contents of 1,73 wt. per cent Al_2O_3 and 0,92 wt. per cent Cr_2O_3. These averages are based on 44 microprobe analyses and the calculated standard deviations are 0,29 and 0,12, respectively. The abundances of Al and Cr are clearly higher than in coexisting orthopyroxene, but the lower average atomic

TABLE 10 MICROPROBE ANALYSES OF CLINOPYROXENE

SAMPLE	61 (1)	61 (2)	61 (3)	70 (1)	70 (2)	83	90	115	205	208 (1)
SIO2	52.91	53.05	53.23	52.89	52.76	53.27	53.21	52.98	53.24	53.13
TIO2	.37	.30	.25	.40	.28	.20	.19	.19	.26	.23
AL2O3	2.34	1.96	1.62	1.81	2.33	1.81	1.86	1.39	1.75	2.27
FEO	4.15	4.29	4.15	3.90	4.26	3.84	3.94	3.73	3.62	4.14
MNO	.13	.15	.14	.11	.13	.13	.14	.13	.12	.14
MGO	16.03	16.36	16.21	16.49	16.24	17.14	16.99	17.15	16.89	17.40
CAO	22.74	22.21	22.40	22.38	22.02	22.21	22.22	22.52	22.45	21.24
NA2O	.30	.36	.31	.41	.36	0.00	.49	.29	.37	.38
CR2O3	1.12	.97	.88	.97	1.13	.96	.89	.70	1.02	1.10
	100.09	99.65	99.19	99.36	99.51	99.56	99.93	99.08	99.72	100.03
				CATIONS		NUMBER OF OXYGENS = 6				
SI	1.9361	1.9478	1.9619	1.9464	1.9395	1.9507	1.9459	1.9534	1.9491	1.9371
TI	.0102	.0083	.0069	.0111	.0077	.0055	.0052	.0053	.0072	.0063
AL	.1009	.0848	.0704	.0785	.1009	.0781	.0802	.0604	.0755	.0975
FE2	.1270	.1317	.1279	.1200	.1310	.1176	.1205	.1150	.1108	.1262
MN	.0040	.0047	.0044	.0034	.0040	.0040	.0043	.0041	.0037	.0043
MG	.8743	.8953	.8905	.9045	.8898	.9356	.9261	.9425	.9217	.9456
CA	.8915	.8737	.8846	.8824	.8673	.8714	.8706	.8896	.8806	.8297
NA	.0213	.0256	.0222	.0293	.0257	0.0000	.0347	.0207	.0263	.0269
CR	.0324	.0282	.0256	.0282	.0328	.0278	.0257	.0204	.0295	.0317
	3.9977	4.0002	3.9943	4.0038	3.9987	3.9908	4.0133	4.0113	4.0044	4.0054
MMF	.873	.871	.874	.882	.871	.888	.885	.891	.892	.882
% En	46.09	46.99	46.68	47.35	47.03	48.51	48.2	48.3	48.09	49.62
% Fs	6.91	7.16	6.94	6.46	7.13	6.31	6.49	6.1	5.97	6.84
% Wo	47	45.85	46.38	46.19	45.84	45.18	45.31	45.6	45.94	43.54
Al/Cr	3.11	3	2.75	2.78	3.07	2.8	3.12	2.96	2.56	3.07

SAMPLE	208 (2)	221	258	290 (1)	290 (2)	290 (3)	290 (4)	177A (1)	177A (2)	184B
SIO2	53.50	53.79	53.41	53.10	53.08	53.01	53.20	54.07	54.12	53.51
TIO2	.24	.26	.16	.29	.26	.29	.29	.15	.18	.22
AL2O3	2.14	1.74	1.19	1.59	1.63	1.64	1.49	1.75	1.43	1.53
FEO	3.62	3.27	3.36	3.13	3.83	3.99	3.47	3.10	2.83	3.33
MNO	.14	.12	.12	.11	.13	.16	.13	.11	.11	.10
MGO	16.49	17.24	17.34	16.77	17.22	17.33	16.86	17.51	17.43	17.90
CAO	22.82	22.76	22.45	23.03	22.12	21.54	22.52	22.47	22.62	21.95
NA2O	.49	.31	.41	.34	.33	.21	.44	.37	.43	0.00
CR2O3	1.12	.75	.76	.95	.89	.93	.83	.87	.82	.92
	100.56	100.24	99.20	99.31	99.49	99.10	99.23	100.40	99.97	99.46
				CATIONS		NUMBER OF OXYGENS = 6				
SI	1.9440	1.9541	1.9627	1.9512	1.9480	1.9508	1.9565	1.9578	1.9668	1.9551
TI	.0066	.0071	.0044	.0080	.0072	.0080	.0080	.0041	.0049	.0060
AL	.0916	.0745	.0515	.0689	.0705	.0711	.0646	.0747	.0612	.0659
FE2	.1100	.0993	.1033	.0962	.1176	.1228	.1067	.0939	.0860	.1018
MN	.0043	.0037	.0037	.0034	.0040	.0050	.0040	.0034	.0034	.0031
MG	.8931	.9335	.9498	.9185	.9420	.9506	.9242	.9450	.9441	.9748
CA	.8884	.8859	.8839	.9067	.8698	.8493	.8873	.8717	.8807	.8593
NA	.0345	.0218	.0292	.0242	.0235	.0150	.0314	.0260	.0303	0.0000
CR	.0322	.0215	.0221	.0276	.0258	.0271	.0241	.0249	.0236	.0266
	4.0048	4.0016	4.0107	4.0047	4.0084	3.9996	4.0069	4.0014	4.0011	3.9926
MMF	.89	.903	.902	.905	.889	.885	.896	.91	.917	.905
% En	47.11	48.56	48.94	47.72	48.72	49.31	48.08	49.37	49.32	50.27
% Fs	6.03	5.36	5.51	5.17	6.29	6.63	5.76	5.08	4.67	5.41
% Wo	46.86	46.08	45.55	47.11	44.99	44.06	46.16	45.55	46.01	44.32
Al/Cr	2.84	3.46	2.33	2.49	2.73	2.62	2.68	3	2.59	2.47

TABLE 10 (cont.)

SAMPLE	238	304C	305 (1)	305 (2)	306 (1)	306 (2)	314 (1)	314 (2)	315 (1)	315 (2)
SIO2	52.85	53.39	53.40	53.16	53.10	53.08	53.10	53.36	53.57	53.56
TIO2	.23	.22	.18	.18	.18	.15	.19	.21	.18	.19
AL2O3	2.12	1.34	1.64	1.86	1.95	2.02	2.17	1.94	1.57	1.69
FEO	3.52	4.22	4.08	3.78	4.10	3.74	3.94	3.87	3.27	4.02
MNO	.17	.15	.14	.14	.14	.13	.17	.13	.12	.12
MGO	16.89	16.84	16.66	16.52	16.64	16.29	16.39	16.68	17.51	17.03
CAO	21.79	22.48	22.21	23.22	21.91	22.65	22.39	21.50	22.46	22.57
NA2O	.44	.38	.50	.49	.46	.47	.55	.45	.40	.35
CR2O3	1.00	.73	.86	1.10	.99	1.08	1.12	.92	.90	.82
	99.01	99.75	99.67	100.45	99.47	99.61	100.02	99.06	99.98	100.35
				CATIONS	NUMBER OF OXYGENS = 6					
SI	1.9452	1.9586	1.9580	1.9397	1.9503	1.9481	1.9422	1.9613	1.9522	1.9508
TI	.0064	.0061	.0050	.0049	.0050	.0041	.0052	.0058	.0049	.0052
AL	.0920	.0579	.0709	.0800	.0844	.0874	.0935	.0840	.0674	.0725
FE2	.1083	.1295	.1251	.1153	.1259	.1148	.1205	.1190	.0997	.1224
MN	.0053	.0047	.0043	.0043	.0044	.0040	.0053	.0040	.0037	.0037
MG	.9266	.9208	.9105	.8985	.9109	.8911	.8935	.9138	.9511	.9245
CA	.8593	.8836	.8726	.9078	.8622	.8907	.8774	.8467	.8770	.8808
NA	.0314	.0270	.0355	.0347	.0328	.0334	.0390	.0321	.0283	.0247
CR	.0291	.0212	.0249	.0317	.0287	.0313	.0324	.0267	.0259	.0236
	4.0036	4.0093	4.0069	4.0169	4.0046	4.0051	4.0091	3.9935	4.0103	4.0083
MMF	.895	.876	.879	.886	.878	.885	.881	.884	.905	.883
% En	48.78	47.5	47.61	46.65	47.86	46.89	47.11	48.52	49.24	47.87
% Fs	5.98	6.92	6.76	6.21	6.85	6.25	6.63	6.53	5.35	6.53
% Wo	45.24	45.58	45.63	47.14	45.29	46.86	46.26	44.95	45.41	45.6
Al/Cr	3.16	2.73	2.84	2.52	2.94	2.79	2.88	3.14	2.6	3.07

SAMPLE	317 (1)	317 (2)	318A (1)	318A (2)	318A (3)	318A (4)	318A (5)	318A (6)	320 (1)	320 (2)
SIO2	53.49	53.51	53.90	53.31	53.80	53.44	53.53	53.53	53.40	53.52
TIO2	.14	.14	.13	.14	.14	.14	.13	.13	.26	.28
AL2O3	1.58	1.63	1.36	1.38	1.54	1.59	1.33	1.45	1.78	1.83
FEO	3.90	4.09	3.50	4.08	3.84	3.90	3.52	4.08	3.97	4.39
MNO	.12	.14	.13	.12	.13	.15	.12	.13	.12	.16
MGO	16.58	16.95	17.27	17.20	16.95	16.80	17.20	17.63	16.58	16.95
CAO	22.51	21.97	22.17	21.87	22.22	22.18	22.27	21.60	22.09	21.49
NA2O	.44	.40	.41	.37	.46	.49	.45	.32	.48	.48
CR2O3	.88	.86	.81	.75	.96	.94	.82	.84	.92	.90
	99.64	99.69	99.68	99.22	100.04	99.63	99.37	99.71	99.60	100.00
				CATIONS	NUMBER OF OXYGENS = 6					
SI	1.9612	1.9593	1.9685	1.9611	1.9622	1.9589	1.9637	1.9576	1.9573	1.9542
TI	.0039	.0039	.0036	.0039	.0038	.0039	.0036	.0036	.0072	.0077
AL	.0683	.0703	.0585	.0598	.0662	.0687	.0575	.0625	.0769	.0788
FE2	.1196	.1252	.1069	.1255	.1171	.1196	.1080	.1248	.1217	.1341
MN	.0037	.0043	.0040	.0037	.0040	.0047	.0037	.0040	.0037	.0049
MG	.9061	.9251	.9401	.9431	.9214	.9179	.9405	.9610	.9058	.9225
CA	.8843	.8619	.8675	.8620	.8683	.8711	.8753	.8463	.8675	.8407
NA	.0313	.0284	.0290	.0264	.0325	.0348	.0320	.0227	.0341	.0340
CR	.0255	.0249	.0234	.0218	.0277	.0272	.0238	.0243	.0267	.0260
	4.0037	4.0034	4.0015	4.0074	4.0033	4.0067	4.0081	4.0068	4.0008	4.0028
MMF	.883	.881	.897	.882	.887	.884	.897	.885	.881	.873
% En	47.35	48.27	49	48.76	48.22	47.97	48.79	49.64	47.71	48.5
% Fs	6.44	6.76	5.78	6.68	6.34	6.5	5.8	6.65	6.6	7.31
% Wo	46.21	44.97	45.22	44.56	45.44	45.53	45.41	43.71	45.69	44.19
Al/Cr	2.67	2.82	2.5	2.74	2.38	2.52	2.41	2.57	2.88	3.03

KEY TO TABLE 10

DRILL CORE ZS 7

E UNIT

61 (1) Exsolved bleb in a coarse orthopyroxene (opx) grain; average of two analyses determined on successive days.

61 (2) Core-domain of intercumulus grain which abuts against interstitial plagioclase in one quadrant; one of few grains which did not show partial amphibolitization and orthopyroxene exsolution lamellae.

61 (3) Margin of 61 (2), adjacent to a convex orthopyroxene grain boundary. Partial resorbtion is indicated in thin section.

70 (1) Small intergranular bleb on opx-opx grain boundary and may be representative of an externally exsolved grain or a rim domain. Larger clinopyroxene grains showed pervasive amphibolitization along cleavage planes and were not selected for analysis.

70 (2) Exsolved bleb in core-domain of large opx crystal (showing coarse clinopyroxene lamellae).

D_2 SUBUNIT

83 Average of 2 small grains occupying poorly annealed cavities. In both instances, the clinopyroxene is stoped along polygonal opx grain boundaries. A smaller number of incomplete triple junctions are plagioclase-bearing. Na_2O not analyzed.

D_1 SUBUNIT

90 Average of 3 small intercumulus grains filling incomplete opx triple junctions. Textural relationships are similar to those in sample 83.

115 Core-domain of small intercumulus grain in a polygonal opx framework. Limited resorbtion of the adjacent opx has occurred.

C_2 SUBUNIT

205 Average of 2 analyses of an intercumulus grain which is stoped along opx grain boundaries. Resorbtion of adjacent opx is minor. The zone selected for analysis shows a minimum development of fine opx exsolution lamellae. The abundance of cpx in the rock is very subordinate to that of intercumulus plagioclase.

208 (1) Average of 2 analyses of a homogeneous domain within a large oikocryst hosting a number of strongly resorbed, cumulus opx remnants. The oikocryst possesses a distinctive green colour in plane polarized light and has domains showing coarse opx lamellae. Amphibolitization of the margins and sporadic intragranular areas is common. Curved cpx-plagioclase grain boundaries are depicted in common interstices. Sub-rounded chromite grains are an occluded phase (analyses available).

208 (2) Average of 2 analyses with the electron beam positioned immediately adjacent to a coarse opx lamellae (analysis 208 EX in Table 4).

221 Average of 3 analyses of an intercumulus grain in planar contact with plagioclase in one quadrant (analysis available; Table 11). Core-rim compositions of an occluded chromite grain are given.

B UNIT

258 Top of B unit (associated with chromite analyses denoted 258 B) some 2 cm below first appearance of cumulus olivine. The analysis represents a clinopyroxene oikocryst enclosing resorbed opx grains. Associated intercumulus silicate phases are plagioclase, mica, amphibole and quartz.

290 (1) Oikocryst enclosing mildly resorbed opx grains. Beam-position removed from zones of exsolved opx lamellae.

290 (2) Same grain as above, but beam straddling opx lamellae-rich zone.

290 (3) Core-domain of a second intercumulus grain.

290 (4) Rim-composition of 290 (3).

C_3 SUBUNIT

177A(1) Anhedral grain poikilitically enclosing large, euhedral chromite grains and intergrown with reaction-replacement orthopyroxene. Electron beam positioned $\pm$ 400 microns from nearest chromite grain. Chromitiferous poikilitic harzburgite; immediate footwall of LG 4 chromitite layer.

177A(2) Average of 2 analyses of same grain but beam positioned 50 microns from the chromite grain boundary mentioned above (refer to chromite analyses 177 A/5 and 6).

184 B Anhedral intercumulus grain occluding euhedral chromite grains. Beam positioned 550 microns from nearest chromite. Chromitiferous poikilitic harzburgite; immediate footwall of I chromitite layer. Na_2O not analyzed.

238 Coarse, anhedral grain with an occluded opx crystal but interstital to rounded olivines. Average of 2 analyses from a domain exhibiting a weak development of very fine exsolution lamellae of opx. Granular harzburgite in hanging-wall of E chromitite layer.

DRILL CORE ZS 3

D_2 SUBUNIT

304 C Average of 2 analyses of a small oikocryst in the fine-grained footwall bronzitite of the LG 6A chromitite, poikilitically enclosing two partially resorbed opx crystals and one large, slightly rounded chromite grain (analysis 304 C/5). Plagioclase is the only other intercumulus phase present, filling a small number of poorly annealed cavities. Beam positions well removed from the chromite grain boundary.

305 (1) Average of three analyses of the centre of an intercumulus grain. In addition to a minor abundance of plagioclase in poorly annealed cavities, trace amounts of mica are present.

305 (2) Exsolved bleb in centre of adjacent bronzite crystal.

306 (1) Intercumulus grain in granular, chromite-poor bronzitite. Fairly extensive resorbtion and stoping has occurred. Only plagioclase and clinopyroxene are depicted in poorly annealed interstices.

306 (2) Exsolved bleb in orthopyroxene lath. Average of 3 analysis.

314 (1) Exsolved bleb in opx crystal showing polygonal grain boundaries.

314 (2) Fine-grained intercumulus clinopyroxene with minor resorbtion of adjacent opx and stoping along polygonal grain boundaries. Clinopyroxene is the only intercumulus silicate in this fine-grained, chromitiferous bronzitite (hanging-wall of the LG 6 chromitite) and occupies poorly annealed interstices.

315 (1) Intercumulus clinopyroxene depicted in the immediate hanging-wall of a thin chromite leader to the LG 6 chromitite. One half of this grain is in contact with annealed chromitite and the other is in contact with the overlying fine-grained, chromite-bearing granular bronzitite. The clinopyroxene has stoped along the annealed opx grain boundaries.

315 (2) Intercumulus grain occupying a poorly annealed cavity in the overlying granular bronzitite (ca. 2 cm above). Some resorbtion of the adjacent orthopyroxene has occurred. Two small chromite grains are enclosed within this clinopyroxene grain (analyses 315/6 and 7). No plagioclase is present in the rock.

317 (1) Margin of an oikocryst which has stoped along polygonal orthopyroxene grain boundaries. There is some development of fine orthopyroxene exsolution lamellae and orientated oxide platelets (schiller structure) within the central region of this grain. No plagioclase is present. Gradational hanging-wall of LG 6 chromitite.

317 (2) Microprobe beam (diameter 20 microns) placed over lamellae-rich zone in centre of same grain.

318A(1) Intercumulus grain adjacent to aggregated chromite; adjacent to olivine-bearing domain of an ultramafic pegmatite replacement lens. Footwall of LG 6 chromitite layer.

318A(2) Core-domain of intercumulus grain.

318A(3) Average of 2 analyses of an exsolved bleb in an orthopyroxene grain.

318A(4) Exsolved bleb in the centre of an orthopyroxene grain adjacent to the host of 318A (3).

318A(5) Margin of intercumulus grain which poikilitically encloses two coarse chromite grains. Beam positioned approximately 200 microns from nearest chromite.

318A(6) Centre of latter grain which is removed from orthopyroxene or chromite.

320 (1) Margin of a large, optically zone oikocryst in a plagioclase-bearing bronzitite. Clinopyroxene is very subordinate to the abundance of plagioclase. Orthopyroxene remnants and minor chromite are poikilitically enclosed within this clinopyroxene grain.

320 (2) Centre of the latter oikocryst. Orientated oxide platelets and orthopyroxene exsolution lamellae are depicted in the core regions of this grain.

D_1 SUBUNIT

323 (1) Exsolved bleb in polygonal orthopyroxene grain.

323 (2) Centre of small intercumulus grain in poorly annealed cavity which has stoped along some polygonal grain boundaries. Optical zoning from margin to core is evident. Opx is the only intercumulus phase present here.

325 (1) Centre of small intercumulus grain in a poor-annealing cavity.

325 (2) Small, isolated bleb on orthopyroxene-orthopyroxene grain boundary: may be an externally exsolved granule as one of the adjacent opx's is transected by a kink plane which intersects the bleb. No plagioclase, mica or amphibole is present in this rock.

Al/Cr of 2,80 equates with atomic Al/Cr of orthopyroxene rim-domains intergrown with plagioclase. The highest absolute abundances of Al_2O_3 and Cr_2O_3 are associated with exsolved clinopyroxene blebs in cumulus orthopyroxene crystals (refer to analyses 61/1, 70/2 and 323/1, for example). High concentrations were also noted in a clinopyroxene oikocryst within sample 208 (2,20 wt. per cent Al_2O_3; 1,11 wt. per Cr_2O_3), associated with anomalously high concentrations of Al_2O_3 and Cr_2O_3 within intimately intergrown orthopyroxene lamellae. These features thus serve as a potential demonstration of the diminished solubility of Al and Cr within both pyroxenes at lower temperatures. Clinopyroxene within olivine-bearing successions of the C_2 and C_1 subunits shows higher atomic Al/Cr (3,31), which is consistent with the higher Al/Cr of coexisting orthopyroxene. However, it would seem that a significant decline in this ratio may occur in proximity to chromite-rich domains (as shown by analyses 177 A/1 and 177 A/2).

The abundance of TiO_2 in clinopyroxene varies between 0,13 and 0,40 wt. per cent. Concentrations of greater than 0,20 wt. per cent are, with few exceptions, restricted to occurrences in plagioclase-bearing bronzitites. This is true for both exsolved and intercumulus clinopyroxene within a given sample. The clinopyroxenes contain 0,21 to 0,55 wt. per cent Na_2O and averaged contents indicate that clinopyroxene in granular-textured bronzitites, i.e., in rocks with low modal abundances of intercumulus silicate phases, is Na_2O-enriched ($x = 0,42$; $s = 0,07$) relative to more feldspathic bronzitites ($x = 0,36$; $s = 0,07$, where x = mean content in wt. % and s = standard deviation). All of the above features point to the influence of plagioclase nucleation in a restricted melt volume.

An estimate of the Fe^{3+} content of a pyroxene can be made by employing the charge balance equation of Cameron and Papike (1981):

$$^{VI}Al^{3+} + Cr^{3+} + 2Ti^{4+} + Fe^{3+} = {}^{IV}Al^{3+} + Na^{+}$$

Fig. 22 is a plot of these compositional parameters derived for a selection of microprobe data. The proportion of Al^{3+} cations in octahedral pyroxene sites was calculated from structural formulae, with the Na cation abundance in orthopyroxene regarded as zero. It

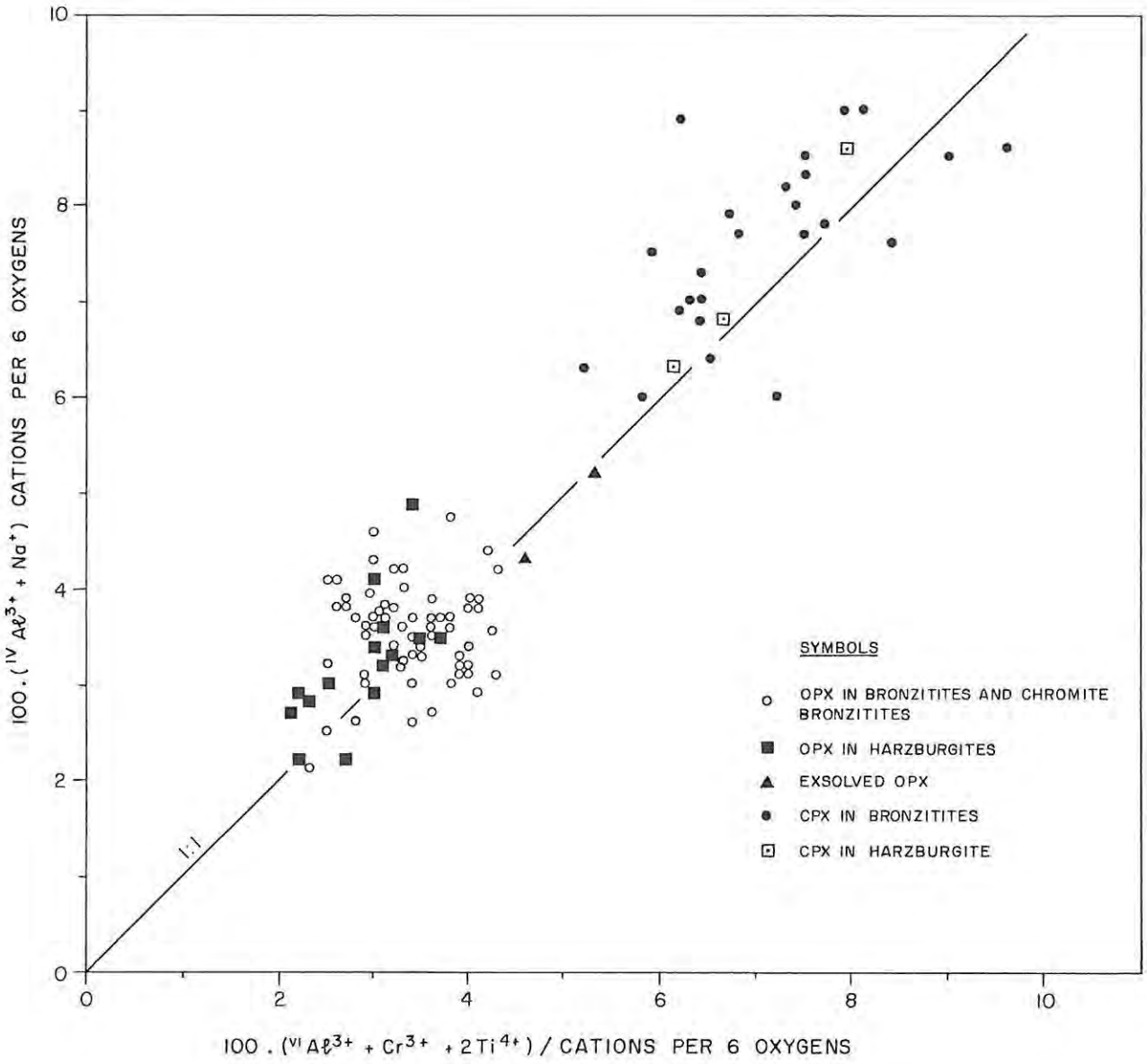

FIG.22 PLOT OF 100.($^{IV}Al^{3+}$ + Na^{+}) VERSUS 100.($^{VI}Al^{3+}$ + Cr^{3+} + 2 Ti^{4+}) FOR ORTHO- AND CLINOPYROXENES, RUIGHOEK PYROXENITE, INDICATING ADHERENCE TO THE CHARGE BALANCE EQUATION OF CAMERON AND PAPIKE (1981). THE 1:1 RELATIONSHIP IS THE IDEAL SOLUTION TO THE EQUATION:

$$^{VI}Al^{3+} + Cr^{3+} + 2Ti^{4+} + Fe^{3+} = {}^{IV}Al^{3+} + Na^{+}$$

is evident from the data points that (a) clinopyroxene displays a greater capacity for the minor elements, and (b) the distribution of these elements between the two pyroxenes adheres rigorously to the constraints of charge balance. Though a scatter of data points about the ideal 1:1 charge balance relationship is portrayed, there is clearly no provision for significant amounts of Na and Fe^{3+} in orthopyroxene of the study section, irrespective of mineralogical environment. However, the locus of clinopyroxene data points suggests that minor levels of Fe^{3+} are present within the Ca-rich pyroxene phase.

5.3.3 PLAGIOCLASE

Low temperature plagioclase feldspars are members of the tectosilicate structural group and are classified chemically in terms of the binary system Ca Al_2 Si_2O_8 (anorthite) - Na Al Si_3O_8 (albite). Minor concentrations of the potassium molecule KAl Si_3O_8 are generally present in solid solution. The chemical substitution mechanism between the anorthite and albite end-members is of the form Na Si = Ca Al at high temperatures, but a modification of the structural state occurs under conditions of slow cooling. This can give rise to an intimate intergrowth of structural types depending on the bulk composition of the homogeneous high temperature phase (for example, peristerite or Böggild structures).

Plagioclase within the Rustenburg Layered Suite exhibits ubiquitous chemical zoning (Kruger, 1983), which thus necessitates the use of a defocussed microprobe beam in order to obtain a meaningful estimate of the bulk composition. A beam diameter of 20 to 30 microns was employed in the present study and the compositions cited in Table 11 are averages of core-, intermediate- and rim-domains (unless specified).

Plagioclase is an intercumulus phase in the study section but its modal proportion never exceeds ca. 10 per cent. It is most abundant within the coarser-grained bronzitites of the B unit, C_2 subunit and basal portion of the E unit. Chromite is a common inclusion and, unlike clinopyroxene-filled interstices, no reaction relationship

between orthopyroxene and plagioclase or chromite and plagioclase was noted in the Ruighoek Pyroxenite succession. However, orthopyroxene corona structures, nucleated on chromite, were observed within plagioclase-filled interstices in a Lower Zone harzburgite sample.

Minute, randomly orientated oxide inclusions within plagioclase are a common feature in the study section. These occur as rods and needles and do not represent a schiller structure. The inclusions are most common within plagioclase core-domains, where their presence is indicated under medium-power magnification by cellular, optically inhomogeneous patches. The high reflectivity, anisotropism and internal reflections (reddish to amber) suggest that these inclusions are rutile.

The most calcian plagioclase (An_{88}) in the studied section is intergrown with olivine in the C_1 subunit (sample 254 A, Table 11), and the most sodic is An_{02} in a micropegmatite-bearing bronzitite near the base of the D_1 subunit (sample 160). No systematic cryptic variation is evident from the incomplete study, largely due to the compositional variation observed within individual samples; the microprobe analyses reported in Table 12 are representative of the range observed in sample 290, a plagioclase- bearing bronzitite below the LG 1 chromitite layer.

TABLE 11 MICROPROBE ANALYSES OF PLAGIOCLASE

SAMPLE	70	90	115	160	160	197D	203	205	208	211
SIO2	50.30	51.55	50.29	58.41	64.80	48.09	48.30	48.24	48.50	62.03
AL2O3	31.36	30.05	30.78	25.89	18.77	33.17	32.38	31.96	32.86	23.82
CAO	14.62	12.78	14.36	7.55	.12	16.05	15.69	15.60	15.79	5.17
NA2O	3.20	4.15	3.27	7.36	3.22	2.40	2.48	2.69	2.47	8.87
K2O	.07	.08	.09	.08	11.44	0.00	0.00	.13	.08	0.00
	99.55	98.61	98.79	99.29	98.35	99.71	98.85	98.62	99.70	99.89
				CATIONS	NUMBER OF OXYGENS = 8					
SI	2.3014	2.3702	2.3174	2.6271	2.9908	2.2067	2.2328	2.2387	2.2241	2.7522
AL	1.6911	1.6284	1.6717	1.3724	1.0210	1.7939	1.7641	1.7481	1.7760	1.2456
CA	.7167	.6296	.7090	.3638	.0059	.7891	.7771	.7757	.7758	.2458
NA	.2839	.3700	.2922	.6418	.2882	.2135	.2223	.2420	.2196	.7630
K	.0041	.0047	.0053	.0046	.6736	0.0000	0.0000	.0077	.0047	0.0000
	4.9971	5.0029	4.9955	5.0099	4.9795	5.0032	4.9963	5.0122	5.0001	5.0066
				ANORTHITE PERCENT						
AN AL/SI	69.63	62.93	67.91	37.26	2.08	79.34	76.65	75.81	77.59	24.61
AN CA/NA	71.34	62.69	70.45	36.01	.61	78.70	77.76	75.65	77.57	24.36
AN SI	69.86	62.98	68.26	37.29	.92	79.33	76.72	76.13	77.59	24.78
AN AL	69.11	62.84	67.17	37.24	2.10	79.39	76.41	74.81	77.60	24.56
AN CA	71.67	62.96	70.90	36.38	.59	78.91	77.71	77.57	77.58	24.58
AN NA	71.20	62.53	70.26	35.36	3.83	78.65	77.77	75.03	77.57	23.70
AVE AN	70.47	62.82	69.16	36.59	1.69	79.05	77.17	75.83	77.58	24.43

SAMPLE	215	221	225	254A	258	265	280	280	290	320
SIO2	50.25	47.47	60.58	45.70	51.95	48.27	48.49	52.46	51.02	47.53
AL2O3	30.27	33.10	24.38	34.58	29.71	33.18	31.93	29.48	31.07	33.09
CAO	13.84	16.58	5.88	18.13	12.79	16.26	15.84	12.22	13.52	15.96
NA2O	3.63	2.02	8.19	1.29	4.20	2.23	2.65	4.50	3.61	2.21
K2O	.10	.09	.13	0.00	.14	.08	.06	.13	.19	.04
	98.09	99.26	99.16	99.70	98.79	100.02	98.97	98.79	99.41	98.83
				CATIONS	NUMBER OF OXYGENS = 8					
SI	2.3314	2.1921	2.7138	2.1107	2.3846	2.2087	2.2422	2.4040	2.3313	2.2001
AL	1.6552	1.8015	1.2872	1.8824	1.6073	1.7894	1.7401	1.5922	1.6733	1.8052
CA	.6880	.8204	.2822	.8972	.6290	.7972	.7848	.6000	.6619	.7915
NA	.3265	.1809	.7114	.1155	.3738	.1978	.2376	.3998	.3198	.1983
K	.0059	.0053	.0074	0.0000	.0082	.0047	.0035	.0076	.0111	.0024
	5.0072	5.0002	5.0020	5.0058	5.0028	4.9978	5.0083	5.0036	4.9975	4.9976
				ANORTHITE PERCENT						
AN AL/SI	66.41	80.66	28.69	88.85	61.23	79.09	75.34	59.45	67.02	80.10
AN CA/NA	67.42	81.50	28.19	88.59	62.22	79.74	76.50	59.56	66.67	79.77
AN SI	66.86	80.79	28.62	88.93	61.54	79.13	75.78	59.60	66.87	79.99
AN AL	65.52	80.15	28.72	88.24	60.73	78.94	74.01	59.22	67.33	80.52
AN CA	68.80	82.04	28.22	89.72	62.90	79.72	78.48	60.00	66.19	79.15
AN NA	66.75	81.38	28.12	88.45	61.80	79.75	75.89	59.26	66.91	79.93
AVE AN	66.96	81.09	28.43	88.80	61.74	79.39	76.00	59.51	66.83	79.91

KEY TO TABLE 11

70 Average of 4 core- and 2 rim-compositions; 6,8 metres above base of E unit. Coarse-grained bronzitite.

90 Average of 4 analyses of grains in small interstices. Granular-textured bronzitite; 8,2 metres below top of D_1 subunit.

115 Average of 2 analyses of grains in poorly annealed cavities. Granular bronzitite; 6,2 metres below LG 5 chromitite, D_1 subunit.

160 Plagioclase and micropegmatite associated with medium-grained bronzitite; 8,2 metres above base of D_1 subunit. Adjacent domains within the drill core sample are olivine-bearing.

197 D Plagioclase-bearing dunite; 2 metres above base of C_3 subunit. Na_2O not analyzed.

203 Bronzitite; 3,2 metres below top of C_2 subunit. Plagioclase is intergrown with red mica.

205 Bronzitite; 7,2 metres below top of C_2 subunit.

208 Bronzitite; 10,5 metres below top of C_2 subunit. Average of 8 analyses.

211 Bronzitite; 15 metres below top of C_2 subunit. Plagioclase intergrown with red mica and quartz.

215 Bronzitite; 90 centimetres below LG 3 chromitite layer. C_2 subunit.

221 Plagioclase intergrown with magnesian orthopyroxene in olivine-bearing succession; 3,1 metres below LG 3 chromitite. C_2 subunit.

225 Coarse-grained, adcumulate bronzitite; 6,5 m below LG 3 chromitite. C_2 subunit.

254 A Olivine-bronzitite, 4,3 metres above base of C_1 subunit.

258 Bronzitite with intercumulus plagioclase, mica, amphibole and quartz. Top of B unit.

265 Bronzitite; 7,2 metres below top of B unit.

280 Bronzitite; 28,5 metres below top of B unit. The more sodic composition is of a grain adjacent to red mica.

290 Bronzitite; 4,4 metres below LG 1 chromitite layer.

320 Drill core ZS 3. Medium-grained bronzitite; 2,8 metres below LG 6 chromitite layer.

TABLE 12:

COMPOSITIONAL VARIATION OF PLAGIOCLASE WITHIN SAMPLE 290, B UNIT

GRAIN No.	1	2	3
SiO_2	50,12	51,24	51,43
Al_2O_3	32,07	31,22	30,84
CaO	14,59	13,72	13,21
Na_2O	3,10	3,51	3,87
K_2O	0,17	0,23	0,30
TOTAL	100,05	99,92	99,65
% An	71,68	67,24	64,94

Oxide contents determined by microprobe analysis and expressed in wt. per cent.

1-2: Average compositions of core-domains
3: Average compositions of rim-domains

5.3.4 MICA

Micas are a subgroup of the phyllosilicate structural group, which includes the chlorite group and clay minerals. The varieties depicted in rock assemblages of the Ruighoek Pyroxenite succession are trioctrahedral micas of the general formula $X_2\ Y_6\ Z_8\ O_{20}\ (OH)_4$, where X is mainly potassium, Y is mainly Mg and Fe but includes Al, Cr and Ti, and Z is Si or Al. Since (OH) group cannot be determined by microprobe analysis, the formula can be given as $X_2\ Y_6\ Z_8\ O_{20}$ or $K_2O\ .\ 6(Mg,\ Fe^{2+})\ O\ .\ 6\ SiO_2\ .\ Al_2O_3$.

The microprobe analyses presented in Table 13 are representative of red, pleochroic mica which occurs as an intercumulus phase in feldspathic bronzitites and coarse-grained, adcumulate-textured bronzitites. However, the occurrence is not pervasive and certain

rocks depict a higher modal proportion (for example, sample 211 in the C_2 subunit). The grain-size never exceeds the dimensions of a single interstice, which is generally shared by quartz. Where mica is intergrown with plagioclase, the latter is generally more sodic than in adjacent layers (refer to analyses 211, 225 and 280; Table 11). Mica very rarely occurs in fine-grained, granular-textured bronzitites.

The mica is a titanian phlogopite (Mg/Fe > 2:1), and microprobe analyses of mica from three geologically separate areas are given in Table 13 for comparison. Phlogopite within the studied section commonly hosts large chromite grains as an occluded phase and it will be shown in a subsequent section that preferential partitioning of Al and Ti into the mica induces lower Al and Ti contents (but higher Cr) in the encapsulated spinel grains.

TABLE 13:

MICROPROBE ANALYSES OF INTERCUMULUS MICA

SAMPLE NO.	165	225	280	A	B	C
SiO_2	39,45	38,59	39,26	38,73	39,35	39,14
TiO_2	2,27	3,61	3,78	5,59	5,32	4,96
Al_2O_3	14,18	13,88	13,81	13,19	13,79	15,36
FeO	4,77	4,94	5,23	6,64	8,60	2,67
MnO	0,02	0,04	0,03			0,04
MgO	22,57	21,81	21,21	19,18	17,71	22,42
Na_2O	0,41	0,52	0,47	0,59		1,24
K_2O	5,73	8,28	9,03	9,18	9,17	8,14
Cr_2O_3	1,81	1,92	1,87	1,36	1,33	1,66
NiO	0,81	0,16	0,20			
TOTAL	92,02	93,75	94,89	94,66	95,27	95,63

All Fe as FeO

KEY:

165 : Basal portion of D_1 subunit. Coarse-grained, adcumulate-textured bronzitite with a very low void volume.

225 : C_2 subunit coarse-grained, adcumulate-textured bronzitite. Amphibole and sodic plagioclase are additional intercumulus silicate phases.

280 : B unit; plagioclase-bearing bronzitite.

A : Red, titanian phlogopite from the Insizwa Intrusion, Transkei (Eales, 1980).

B : Mica in the Merensky cyclic unit, Rustenburg district (Kruger, 1983; sample M 4).

C : Phlogopite in bronzitite, upper part of E unit. Eastern Bushveld Complex (Cameron, 1980; Table I).

The average atomic Al/Cr of mica in samples 165, 225 and 280 is 11,16 (s = 0,54). Based on the consideration that these titanian micas represent late-stage crystallization products of residual melt, the NiO contents of 0,16 to 0,20 wt. per cent seem anomalously high. However, these abundances are consistent with the significant levels of Cr_2O_3 (Fig. 23 and Table 13), which are in the range 1,80 to 1,95 wt. per cent and thus exceed the Cr_2O_3 contents of cumulus orthopyroxene and intercumulus clinopyroxene.

5.3.5 AMPHIBOLE

The amphibole minerals have an inosilicate atomic structure and are characterized chemically in terms of the following structural formula: $WX_2\ Y_5\ Z_8\ O_{22}\ (OH)_2$, where W is known as the vacant site. The latter site is occupied by Na in certain of the calcium amphiboles, of which hornblende is an important member. Amphibole is a common late-stage, accessory phase in coarse-grained, adcumulate-textured bronzitites and some mesocumulate-textured, feldspathic bronzitites of the studied section, in which it can occur as a deuteric alteration product of pyroxenes and as a crystallization product of late-stage, magmatic residua. Idiomorphism is commonly displayed in domains where intergrown with quartz and micropegmatite

but sector zoning was observed in only one sample (254 A; C_1 subunit). Actinolitic amphibole (uralite) is ubiquitous as a replacement phase of the pyroxenes, particularly intercumulus clinopyroxene. The mineral is characterized in thin section by a light green to tan pleochroism. A fibrous amphibole variety is often intimately intergrown with sulphide and oxide selvages. This is well developed in portions of the C_2 subunit (for example, in sample 225 and at the top of the subunit where a minor abundance of base metal sulphides is present) and within a silicate-parting of the laminated LG 5 chromitite layer. The fine-grained, granular-textured bronzitites of the D unit are devoid of amphibole, but uralite is common within the coarser-grained adcumulate-textured bronzitites of the E unit. Apart from a limited abundance of uralite along cleavage planes of coarse-grained orthopyroxene crystals, and of intergrown clinopyroxene exsolution lamellae, the modal abundance and grain-size of intercumulus amphibole is subordinate to that of plagioclase and clinopyroxene. Idiomorphic amphibole is rare and the grain-sizes are small.

Microprobe analyses of amphibole are presented in Table 14. It is evident from the data that the concentrations of Ti, Al and Cr are intermediate between the respective contents in clinopyroxene and titanian phlogopite (Fig. 23). The average atomic Al/Cr is 5,34 ($n = 8$; $s = 0,43$).

TABLE 14:

MICROPROBE ANALYSES OF AMPHIBOLE

SAMPLE NO.	70	115	165	184A	225(1)	225(2)
SiO_2	52,21	52,23	51,57	44,86	52,22	52,22
TiO_2	0,35	0,30	0,56	1,12	0,35	0,38
Al_2O_3	4,69	4,29	4,89	10,98	3,61	5,17
FeO	4,63	3,83	3,69	3,62	3,54	3,73
MnO	0,07	0,09	0,06	0,06	0,07	0,09
MgO	20,00	21,05	20,65	18,05	22,08	20,28
CaO	12,13	12,36	12,03	11,68	12,29	12,21
Na_2O	0,83	0,63	0,89	2,46	0,77	0,71
K_2O	0,23	0,25	0,38	0,00	0,36	0,10
Cr_2O_3	1,37	1,12	1,38	2,55	0,93	1,68
NiO	0,08	0,12	0,10	0,00	0,05	0,04
TOTAL	96,59	96,27	96,20	95,38	96,27	96,61

All Fe as Feo

KEY:

70 Core of anhedral, intercumulus grain; E unit.

115 Deuteric alteration product of intracrystalline domain within orthopyroxene (n = 2). D_1 subunit.

165 Core of anhedral, intercumulus grain within coarse-grained, adcumulate-textured bronzitite (n = 2); D_1 subunit.

184 A Subgrain of amphibole within large oikocryst of reaction-replacement orthopyroxene; olivine-bearing silicate lens in I chromitite layer, C_3 subunit.

225(1) Core of large, intercumulus grain intergrown with sodic plagioclase. Large bleb of base metal sulphide (+ magnetite) associated with the interstice.

225(2) Core of second grain in an adjacent interstice. Presence of interstitial sulphides and graphite platelets are an unusual feature of this bronzitite.

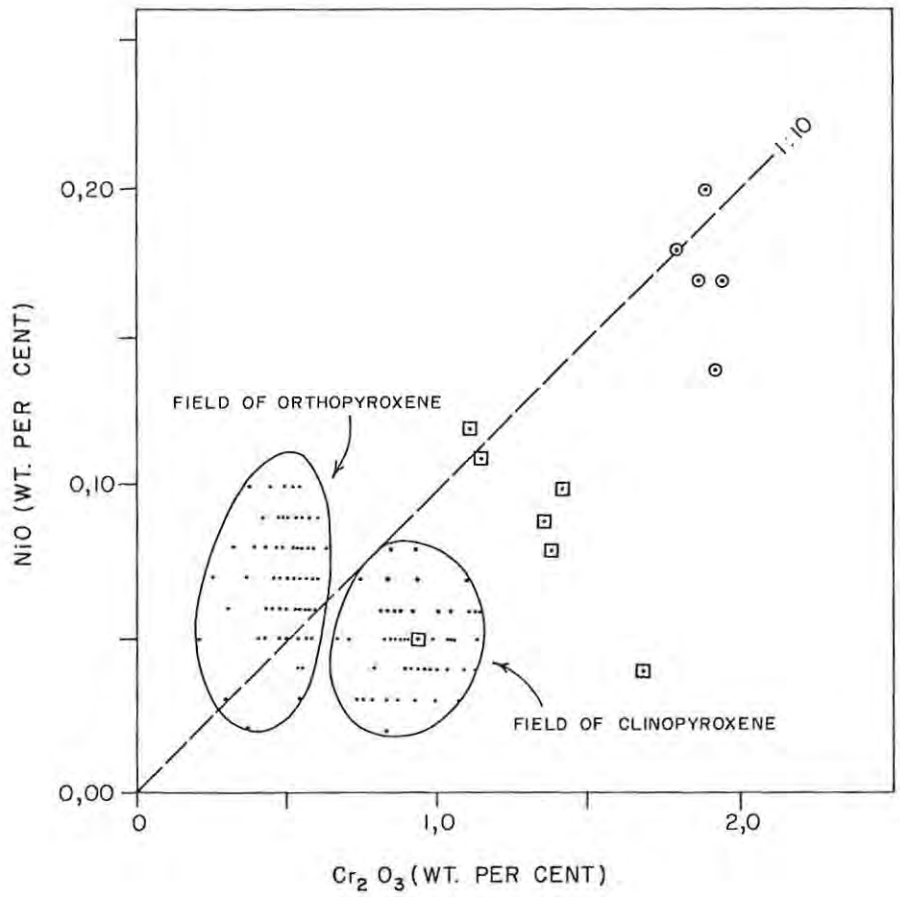

FIG. 23 CONCENTRATION OF NiO PLOTTED AGAINST Cr_2O_3 FOR (a) ORTHOPYROXENES, (b) CLINOPYROXENE, (c) AMPHIBOLE AND (d) TITANIAN PHLOGOPITE. DATA POINTS REPRESENT 150 SELECTED MICROPROBE ANALYSES. THE LINE WITH 1:10 SLOPE WAS CONSTRUCTED FOR DIAGRAMMATIC PURPOSES, BUT ILLUSTRATES THE RELATIVE ABUNDANCE OF Ni AND Cr IN FERROMAGNESIAN SILICATE PHASES OF THE RUIGHOEK PYROXENITE. SYMBOLS: ⊙ TITANIAN PHLOGOPITE ; ⊡ AMPHIBOLE.

5.3.6 SILICATE INCLUSIONS WITHIN CHROMITE

A number of authors have described silicate inclusions in chromite grains and, in most instances, these reports have been pertinent to chromite from chromitite layers. For example, McDonald (1965) described rounded to subrounded inclusions in chromite from the chromitite layers of the Ruighoek Pyroxenite on the farm Ruighoek. Inclusions have also been noted in chromite of the chromitite deposits at Nietverdiend, Western Transvaal (Kruparz and Van Rensburg, 1965), within chromitite layers of the Stillwater Complex (Jackson, 1966) and within the UG 2-like chromitite layer south of Potgietersrus (Hulbert, 1983). Similarly, Irvine (1975) described mono- and bimineralic inclusions, granitic in composition, within chromite of the Muskox intrusion, and olivine inclusions occur within chromite of podiform chromitite (Lehmann, 1983). In contrast, Donaldson and Brown (1977) report MgO-rich melt inclusions within euhedral Cr-Al spinel grains in a sample of oceanic tholeiite. Recent proposals invoke sintering of a porous chromite aggregate at sustained near-liquidus temperatures to account for these features within chromitite layers (Hulbert, op cit.), a concept that is advocated here (referred to as grain annealing in section 4.2 of the present text). However, it is difficult to apply this reasoning to dispersed chromite grains which may be wholly or partially occluded by cumulus orthopyroxene and olivine crystals in silicate-rich domains.

Samples 215 and 221, representative of magnesian bronzitites in the footwall of the LG 3 chromitite layer, depict a low abundance of small chromite grains carrying silicate inclusions. The grains selected for analysis show a single, spherical silicate inclusion toward the centre, varying between 30 and 80 microns in diameter. The results of a cursory microprobe examination are presented in Table 15.

TABLE 15:

MICROPROBE ANALYSES OF SILICATE INCLUSIONS WITHIN CHROMITE

SAMPLE No.	215		221			
	A1	A2	A1	B1	B2	B3
SiO_2	80,86	78,94	46,89	56,91	34,43	51,5
TiO_2	0,10	0,11	0,95	0,20	0,13	0,40
Al_2O_3	3,78	4,19	14,31	3,47	2,27	5,43
FeO	1,37	0,89	5,76	1,89	6,51	4,21
MnO	0,02	0,05	N.A.	0,02	0,07	0,09
MgO	3,96	5,59	19,13	29,78	36,42	25,63
CaO	0,07	0,08	0,42	0,14	0,55	5,84
Na_2O	0,18	0,34	2,92	0,91	0,05	0,83
Cr_2O_3	3,21	1,56	1,68	0,50	0,96	0,88
NiO	0,01	0,03	0,12	0,10	0,03	0,07
TOTAL	93, 56	91,78	92,18	93,92	81,42	94,88

N.A.: Not analyzed. All Fe as FeO

KEY:

215 A1 - A2: Spherical silicate inclusion of 30 micron-diameter within anhedral, intergranular chromite grain (ca. 275 microns in diameter); associated chromite analysis denoted 215/6.

221 A1: 40-micron inclusion within 230 micron-diameter, intergranular chromite grain. The associated chromite analysis is denoted 221/6.

221 B1 - B3: Three beam positions within an 80 micron-diameter inclusion, hosted by an intergranular chromite grain of 250 x 280 micron diameter. Both A and B inclusions carry a spinel phase. The associated analysis of the host chromite grain is 221/4.

A defocussed electron beam (ca. 25 micron diameter) was employed in order to measure approximate bulk compositions. Unfortunately, the host chromite contributed to the count rates and, with respect to analyses 215 A1 and A2 in particular, the analyses cited in Table 15 cannot be regarded as representative. However, it is evident from the data that quartz, mica and amphibole compositions are depicted: these may be daughter products from the breakdown of orthopyroxene. The compositional variation of inclusion 221 B is indicative of an intergrowth of these phases and the magnesian character is to be anticipated by virtue of the proximity to chromite.

Silicate inclusions are present in chromite grains which are partially or wholly occluded by orthopyroxene. However, they are more frequent within intergranular chromite grains and are a very common feature in olivine-bearing assemblages (silicate inclusions are also a typical feature of intergranular chromite in some intrusive dunite bodies of the Upper Critical Zone (R Scoon, pers. comm.)). This is well illustrated at the base of the C_1 subunit and within the uppermost stratigraphic levels of the B unit, where some unusual chromite morphologies are depicted. Only one occurrence of olivine occluded by chromite was observed. This occurrence is in the footwall of the LG 6 chromitite, drill core ZS 3, where an olivine inclusion is in optical continuity with a large oikocryst of replacement olivine (associated with an ultramafic pegmatite replacement assemblage). This is therefore indicative of a penetrative structure and suggests that annealing of intergranular chromite aggregrates can occur in silicate-rich environments. However, inspection of numerous polished thin sections has shown that most silicate inclusions are not penetrative features. Hence, it is incorrect to attribute the hydrous silicate assemblages of many silicate inclusions to wetting of porous chromite structures by late-stage melt. Porous chromite structures are rare and their occurrence is restricted to certain granular-textured bronzitites of the D and E units. Fig. 24(A) is tendered as an example, with the proviso that this feature may be a resorption texture and not a primary growth form.

Chromite morphologies akin to mantle and spherical chromite occur within the uppermost few centimetres of the B unit (mantle and

spherical chromite-types are described by Hulbert and von Gruenewaldt (1980)). These chromite grains are large (0,3 mm) and only occur as an intergranular phase, commonly intergrown with plagioclase. Spherical chromite often encloses mica and no intracrystalline chromite-chromite grain boundaries are evident (Fig. 24(B)). The occlusion of smaller silicate inclusions is a typical feature. An example of a pseudo-mantle chromite is shown in Fig. 24(C), where the presence of at least one intracrystalline grain boundary is of significance. Rutile is ubiquitous within this composite chromite grain as an exsolved phase and as externally exsolved granules. Furthermore, a few stubby rutile needles, nucleated on the chromite grain boundaries, project into the circumjacent plagioclase and also occur within two of the silicate inclusions. These features were noted for other chromite grains of differing morphologies, but unattached rutile was not observed as inclusions within intercumulus plagioclase. The degree of chromite anhedralism within the sample appears to be a function of grain-size and the number of silicate inclusions: subrounded chromite is smaller with few inclusions, whereas anhedral chromite is coarser with a higher number of inclusions. Arrested suturing of intergranular chromite is a common feature, but it is clear from Fig. 24(D) that this process cannot wholly account for the disposition and incidence of silicate inclusions. Hence, the interpretation favoured here is as follows. The chromite morphologies are not primary, in situ growth forms, but result from annealing of fine-grained aggregated chromite with a component of secondary, inclusion-free growth to yield planar interfaces. There is no valid reason for stipulating that annealing is only feasable in a compacting crystal mush: the process may initiate during a period of suspension or long-range settling of a porous chromite aggregate, and the resultant densification may influence the rate of settling. However, as suggested by Young (1984), the silicate inclusions may be representative of residual liquid droplets (derived from the footwall) not miscible with a more primitive, supernatant melt.

To summarize, silicate inclusions within dispersed chromite grains may stem from annealing of chromite aggregates while settling through a liquid column or during compaction of the crystal pile. The latter regime cannot, however, account for spherical silicate inclusions

FIGS. 24(A) to (F): Photomicrographs of chromite grains with contrasted morphologies and silicate inclusions.

(A): Porous grain (dark brown in transmitted light) resident in a triple junction of polygonal orthopyroxene crystals within a granular-textured bronzitite (sample 125; D_1 subunit). The textural features may be indicative of resorbtion, prior to encapsulation, of a grain which initially contained a high number of silicate inclusions. A point of interest is that a trace occurrence of olivine crystals (i.e., one crystal within this thin section) is exposed within the fine-grained bronzitite. Microprobe analysis shows the chromite grain to be enriched in Mg and Al relative to grains with usual morphologies in underlying, coarse-grained and adcumulate-textured bronzitites. A photomicrograph of an equivalent granular-textured bronzitite host is presented in Fig. 8C(iii), and a microprobe analysis of the chromite grain is given in Table 26 (analysis 125/1). Section photographed with plane polarized transmitted light. The longer dimension of the grain measures 60 microns.

(B): Spherical morphological type with mica as the occluded phase (the highly reflective material is a remnant of graphite coating), and representative of an intergranular grain between orthopyroxene crystals (sample 258; top of the B unit). The diameter of the chromite grain is 300 microns. Silicate minerals within the small, spherical silicate inclusions (less than 30 microns in diameter) are usually mica and quartz. Section photographed with plane polarized reflected light.

(C): Grain with a pseudo-mantle morphology showing (i) straight intracrystalline grain boundaries, (ii) well-formed, smooth planar boundaries, and (iii) silicate inclusions. The grain abuts against orthopyroxene crystals on three sides, with intercumulus plagioclase feldspar (low relief, light grey) enclosed within the incomplete termination. This chromite grain is depicted in a microdomain adjacent to (B). Note that rutile rods within the chromite are not resolved under the magnification used, which is the same as in (B). Section photographed with reflected light.

A

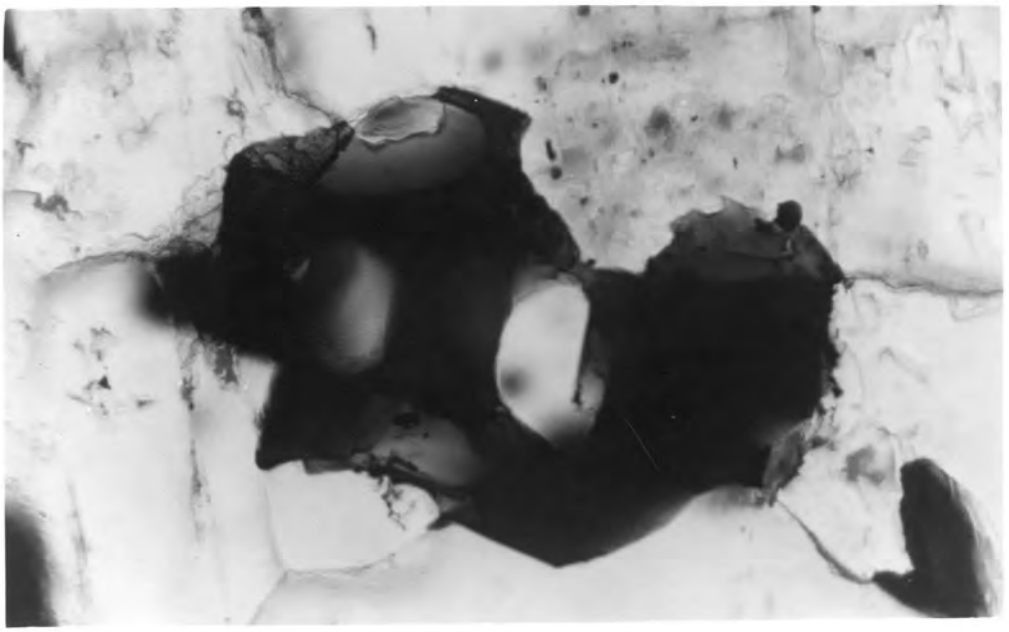

B

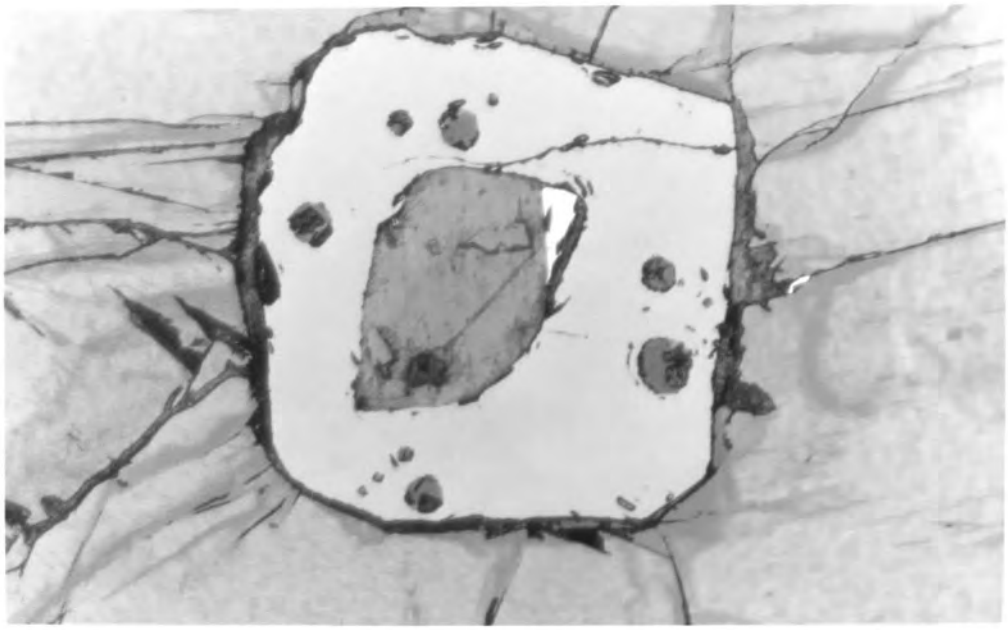

C

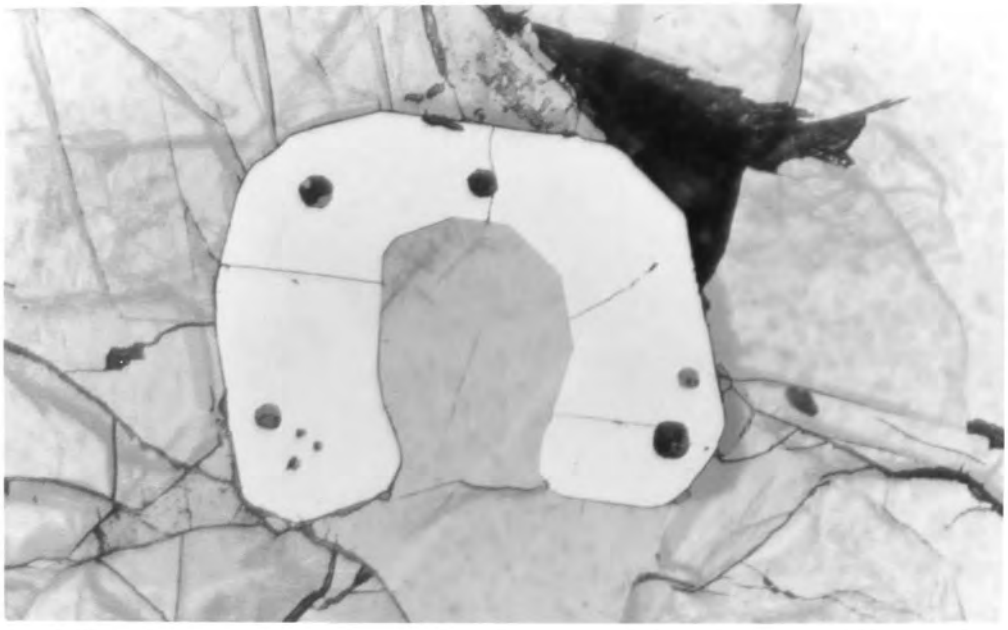

FIGS. 24(D): Aggregate of intergranular grains in an olivine-bronzitite near the base of the C_1 subunit (sample 255). Note the irregular grain boundaries, incidence of silicate inclusions and occurrence of a small, equant grain (bottom left) with a spherical silicate inclusion. Section photographed with reflected light.

(E): Equant, welded grains showing a high incidence of spherical inclusions of varying sizes, and enclosed in a structurally continuous grain of reaction-replacement orthopyroxene. Chromitiferous poikilitic harzburgite in the hanging-wall of chromite dunite and olivine-chromitite lithologies (C_2 subunit, sample 222; within 4 m of the basal contact of the LG 3 chromitite layer). Section photographed in transmitted light. Scale 5cm = 0,25mm.

(F): Small grain, with a diameter of 100 microns, welded against a larger, equant grain with a diameter of 210 microns. Reflected light microscopy reveals no grain boundary separating the two grains, both of which are encapsulated within a well-formed orthopyroxene lath (C_2 subunit, sample 215; footwall of the LG 3 chromitite layer). The silicate assemblage within the larger silicate inclusion comprises mica and quartz. Section photographed with plane polarized transmitted light. Chromite grains with silicate inclusions are generally seen near the footwall contacts of chromitite layers and in association with the appearance of olivine as a cumulus phase. They are very rare in the interiors of chromitite layers (where advanced degrees of grain annealing are indicated) and in isomodal, homogeneous units of rock. These observations are relevant to Young's (1984) proposal (refer to p. 107 of the present text).

Ⓓ

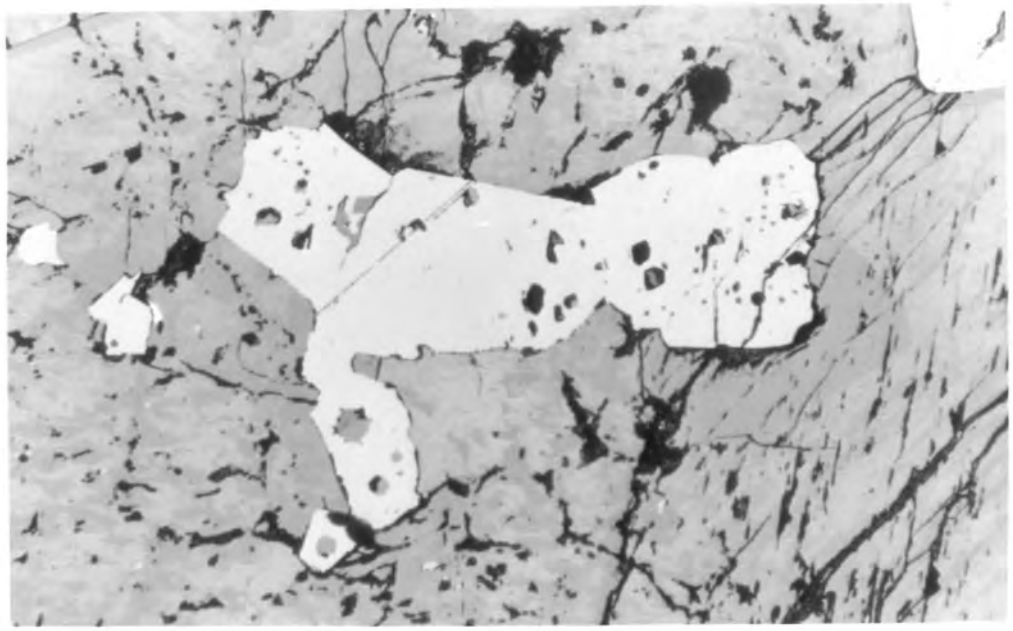

Ⓔ

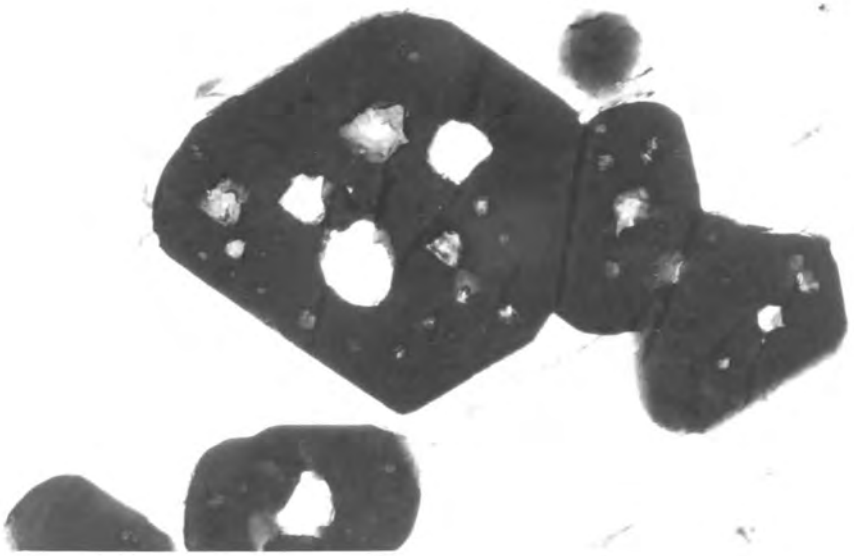

Ⓕ

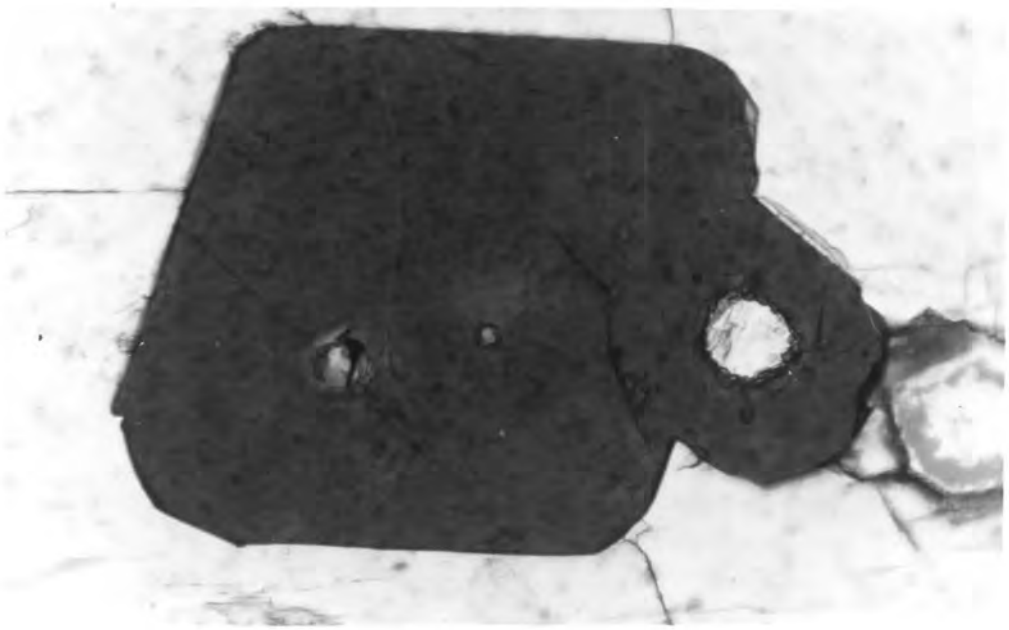

within subrounded chromite occluded by cumulus silicate phases, nor does it account for the morphology depicted in Fig. 24(E). Furthermore, inclusion-charged grains are (a) confined to olivine-bearing horizons of the Ruighoek Pyroxenite succession, and (b) exhibit lower Cr/Al ratios than grains in the pyroxenite units. These data will be presented in the subsequent text. Finally, attention is drawn to the textural relationship depicted in Fig. 24(F), which shows two welded chromite grains occluded within the core-domain of an orthopyroxene crystal. The smaller chromite grain is 100 microns in diameter and hosts a 30 micron silicate inclusion composed of a mica + quartz intergrowth. The larger grain is 210 microns in diameter and hosts a number of small inclusions. If the mica + quartz intergrowth is regarded as an orthopyroxene breakdown product, the textural relationship displayed by the smaller grain can be regarded as substantiative evidence for the nucleation of chromite on silicate crystallites. Hence, the number of silicate inclusions within the larger chromite grain may be indicative of the number of small grains which welded to yield a coarser product. This is quite plausible if the relative volumes are considered. For example, the calculated volume of the larger chromite grain is 9 times that of the smaller and three silicate inclusions are visible in the plane of the thin section. Thus two considerations which arise from the above are: (a) aggregation and annealing processes must be near completion prior to encapsulation within a well-formed orthopyroxene crystal, and (b) unless each small chromite grain is of the same composition, a wide spectrum of intermediate compositions may ultimately result from diffusive homogenization.

5.3.7 OTHER PHASES

Occurrences of graphite, base metal sulphides, rutile, magnetite, ilmenite, ferritchromite, micropegmatite, quartz, bastite, magnesite and serpentine minerals are depicted within the study section. Serpentine is a pervasive constituent of the olivine-rich C_1 and C_3 subunits and is associated with trails of magnetite granules released by oxidation of olivine. It is not clear whether the serpentinization is of deuteric or meteoric origin. Campbell (1975), for example, has discounted deuteric serpentinization of olivine

cumulates in the Jimberlana Intrusion, Western Australia, by virtue of the adcumulate texture of the rocks. Where serpentinization has reached advanced stages in dunites of the C_1 and C_3 subunits, alteration of chromite to ferritchromite is common along grain boundaries and fractures, and chromite is partially pseudomorphed by sulphides in a few samples (Fig. 25A). Nickel and Hudson (1976) describe chromian valleriite pseudomorphs of Cr-spinel in the Nepean and Perseverance Ni-Fe sulphide deposits, Western Australia, in which chromite is intergrown with sulphides in the main ore zones. Similarly, intergrowths in the C unit of the studied section may stem from hydrothermal reactions.

Chromite is also prone to alteration where replacement of layered bronzitite by ultramafic pegmatite assemblages has occurred. The example cited in Fig. 25(B) is from drill core ZS3 at the stratigraphic level of sample 331 within the D_1 subunit: a circumjacent zone of ferritchromite is disposed about a subrounded chromite grain, and the thin silicate selvage between the two spinel phases is a common feature. The ferritchromite is porous and a sulphide phase is often depicted within the silicate voids. The host pegmatite assemblage comprises olivine-orthopyroxene-magnesite-amphibole, and the magnesite occurrence may attest to a replacement phenomenon associated with the ingress of a CO_2-rich fluid. In contrast, non-porous ferritchromite is developed along annealed chromite grain boundaries in the gradational footwall of the LG 7 chromitite layer, where shearing parallel to the plane of layering has fractured the chromite.

GRAPHITE

Graphite is a trace constituent within bronzitites in the upper 2 metres of the B unit, occuring as elongate flakes up to 2,5 mm in length. These grains are penetrative structures, cross-cutting well-formed orthopyroxene grain boundaries (Fig. 25C) and the following textural features suggest that graphite crystallized as a primary magmatic phase:

FIGS. 25(A) to (C): Photomicrographs illustrating alteration of chromite, and graphite platelets within bronzitite.

(A): Intimate intergrowth of sulphide (higher reflectivity) and chromite in serpentinized dunite above the I chromitite layer, C_3 subunit (sample 183A). Section photographed with plane polarized reflected light. Scale 5cm = 0,25mm.

(B): Pseudomorphic alteration of chromite to ferritchromite (higher reflectivity) in an ultramafic pegmatite assemblage, drill core ZS 3 (D_1 subunit, sample 331). Scale 5cm = 0,25mm.

(C): Graphite platelets (acicular, opaque) in an adcumulate-textured, chromite-bearing bronzitite. The microdomain is within 10 mm of the first appearance of cumulus olivine crystals marking the base of the C_1 subunit. Micro-brecciation of the bronzitite is linked to serpentini-zation of olivine in adjacent domains, but no fracture control on graphite distribution is evident. Section photographed with transmitted light under crossed nicols. Scale 5cm = 2mm.

Ⓐ

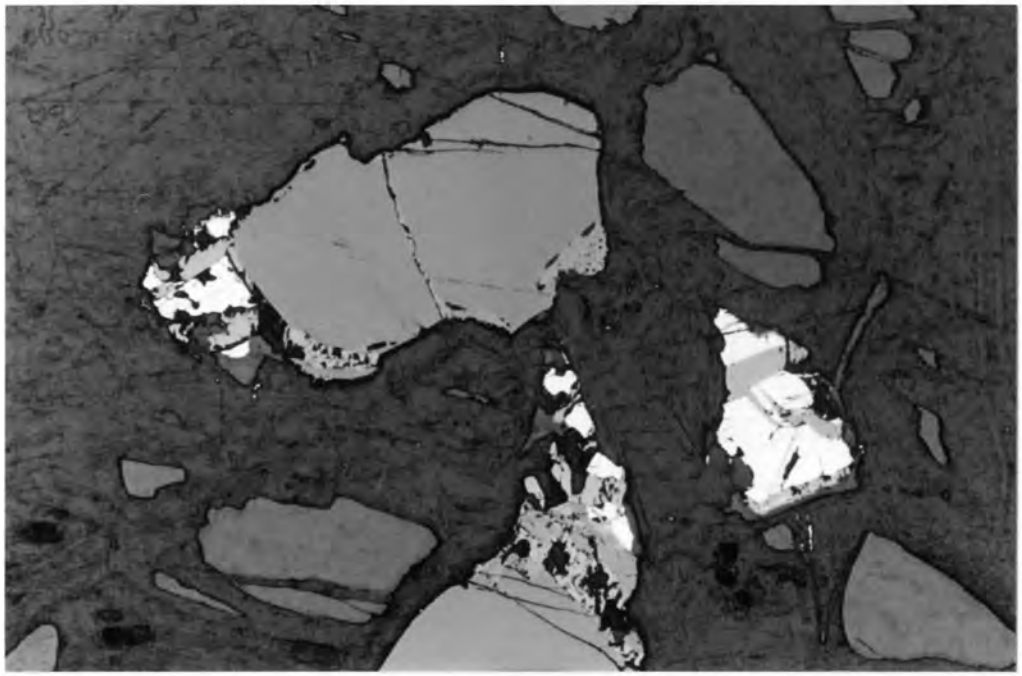

Ⓑ

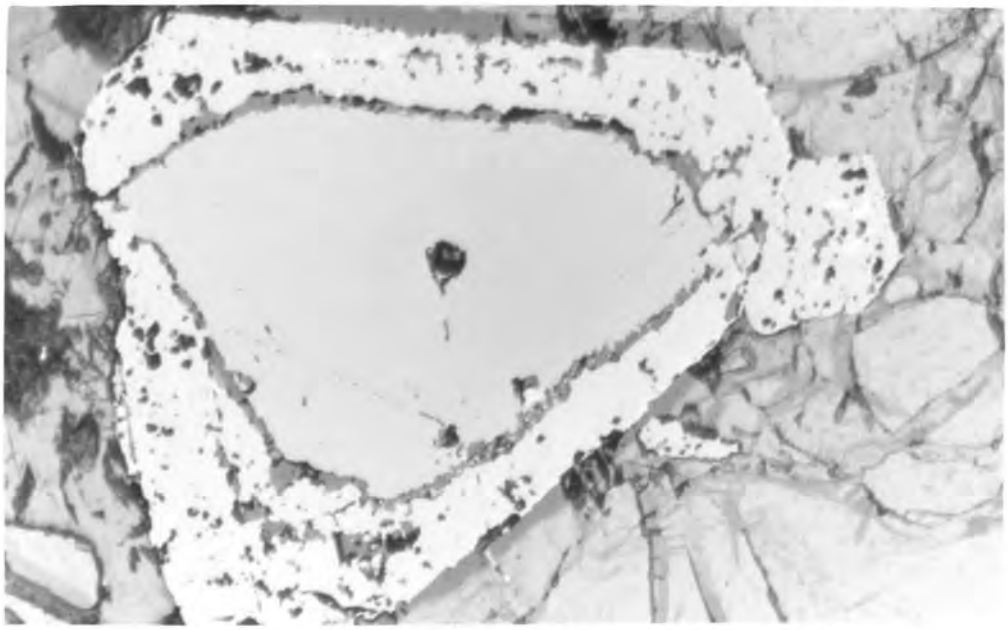

Ⓒ

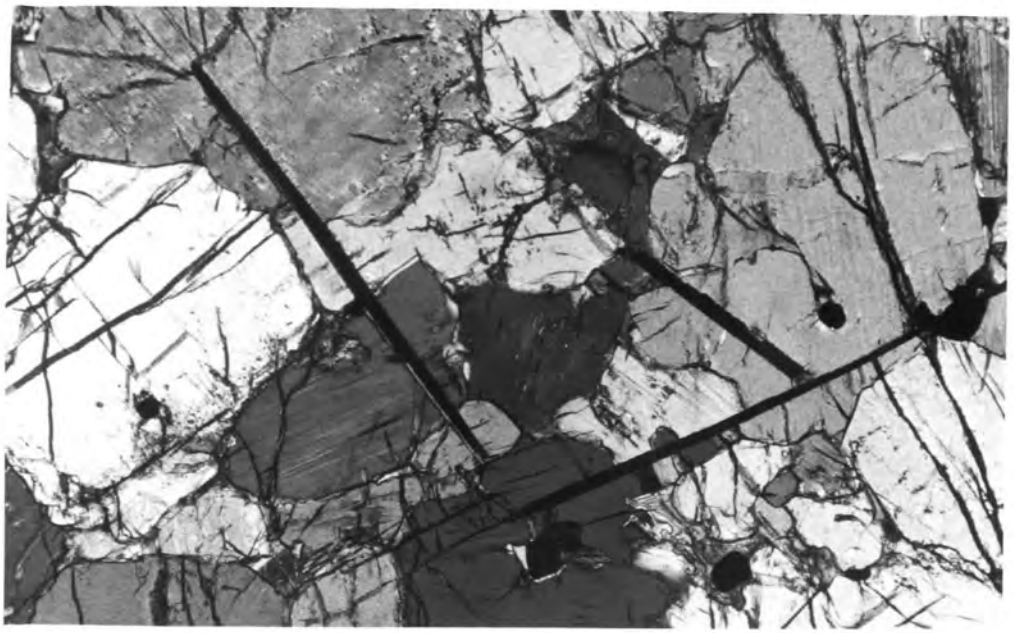

1. No alteration of the juxtaposed orthopyroxene host and intercumulus plagioclase is evident, suggesting that the disposition of graphite grains is not fracture-controlled.
2. The highest abundance is reached within 1 centimetre of the first cumulus olivine grains marking the base of the C_1 subunit (the latter show alteration to serpentine along fractures).
3. No graphite occurs in association with or above the first olivine grains. This is irreconcilable with fracture-control of graphite distribution as these features are observed on the scale of a thin section.

Eckstrand (1975) has proposed that oxidation of olivine in the presence of an aqueous phase can produce a strongly reducing environment. Operation of such a process to account for the graphite occurrence can be discounted in terms of the unaltered nature of the adjacent bronzitite and the low modal abundance of olivine. Furthermore, graphite is not observed within serpentinized dunites in the C_1 and C_3 subunits. The textural features therefore suggest that graphite nucleation preceded that of orthopyroxene in the bronzitite layers at the top of the B unit, and presaged the appearance of nickeliferous olivine as a primary liquidus phase. Merkle and Hatton (1983) have reported magmatic graphite above the MG 2 chromitite layer on the same property (i.e., the farm Zandspruit), and postulate that this feature (in association with an increase in whole-rock sulphide content) may be indicative of an irruption of new magma at this stratigraphic level. Supportive evidence for the notion that graphite occurrences within the studied section are not fortuitously disposed is given by modal occurrences in adcumulate-textured bronzitite below the layered, olivine-bearing succession within the C_2 subunit (sample 225), and in samples 28 and 149 in the E unit and D_1 subunit, respectively. With reference to Fig. 14, it is noted that all these samples are at stratigraphic levels at which a cryptic rise in orthopyroxene MMF ratios is evident. Other notable features are that (a) nickeliferous sulphides are present at trace levels within sample 225 (a relationship analogous to that documented by Merkle and Hatton (1983)), and (b) chromite grains within magnesian, olivine-bearing assemblages in the C_1 and C_2 subunits are charged with spherical silicate inclusions. It will be shown in the subsequent text that chromite in these mineral assemblages yields

Al_2O_3-rich and Fe_2O_3-poor compositions, i.e., a chemistry which experimentally has been correlated with reducing redox conditions (Ulmer, 1969; Buntin et al., 1983). Furthermore, it will be shown that (a) the Fe^{3+} content of chromite within the ZS7 drill core section is maintained at low levels, and (b) significant increases in Fe^{3+} content with increasing stratigraphic height can occur through a homogeneous succession of chromite-poor bronzitite and, paradoxically, not be mirrored within the equivalent succession of an adjacent drill core section. It should be stressed, however, that the implications of these data require an appropriate assessment of the textural observations and analytical data which have been presented above.

RUTILE

Rutile occurrences within the Mooihoek and Ruighoek Pyroxenite successions have been described by Cameron (1979) and McDonald (1967), respectively. Similar occurrences are found in silicate-rich rocks of drill cores ZS3 and ZS7, where rutile is observed in the following textural environments:

1. As crystallographically orientated lamellae in chromite.
2. As external granules on chromite grain boundaries.
3. As a random distribution of needles and rods intergrown with intercumulus plagioclase in bronzitites.

In contrast to these rather pervasive occurrences, only a single grain was observed within the Lower Group chromitite layers (Fig. 26(A)). The latter is interstitial to polygonal-textured, annealed grains within the LG 6A chromitite, drill core ZS7, and is intergrown with ilmenite (this was the only ilmenite occurrence noted). Varieties (1) and (2) are products of subsolidus exsolution (Fig. 26(B)) and are more abundant in feldspathic bronzitites. The intracrystalline concentration is not uniform within individual grains, nor between grains within a thin section. However, exsolved rutile is only seen within chromite grains occluded by plagioclase or within intergranular particles adjacent to plagioclase-bearing domains. Small chromite grains occluded by orthopyroxene, or grains

Ⓐ

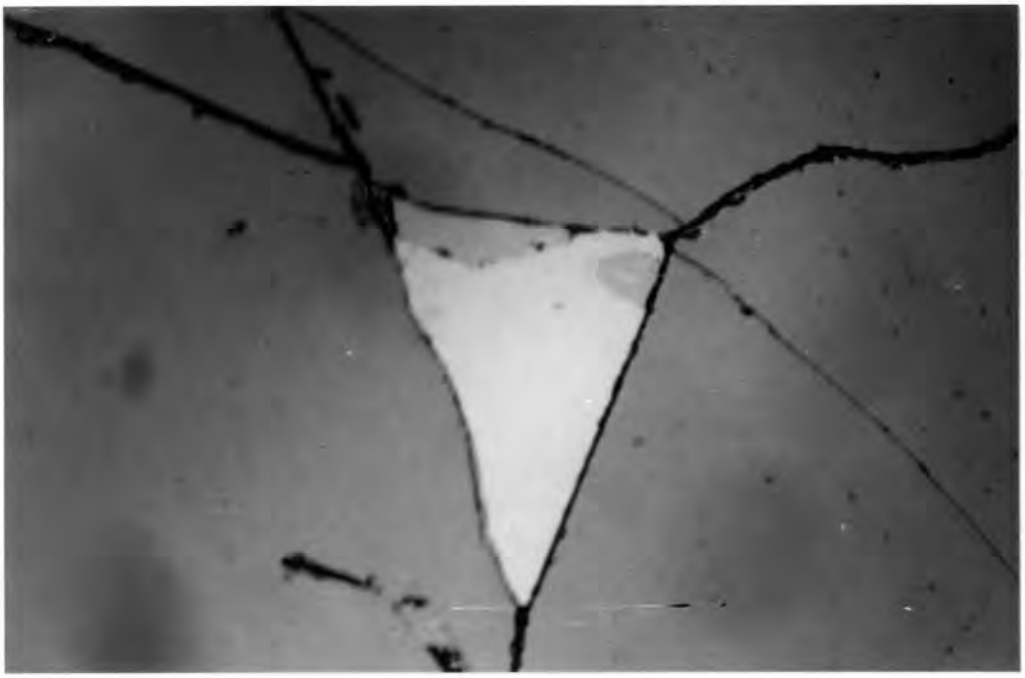

Ⓑ

FIGS. 26(A) and (B): Photomicrographs of rutile occurrences within the studied section. Both sections photographed with plane polarized reflected light.

(A): Intergranular rutile (white, highly reflective) intergrown with ilmenite (light grey) in an annealed assemblage of large, polygonal chromite grains (dark grey) within the LG 6A chromitite layer (drill core ZS 7). Tonal variations stem from imperfections in the negative, and the pitted nature of the chromite represents poor polishing. The assemblage shown is the only occurrence of rutile and ilmenite noted within the LG chromitite layers of the studied section. Scale 5cm = 62 microns.

(B): Crystallographically orientated rutile lamellae (white) within a large chromite grain (400 microns in diameter) enclosed in intercumulus plagioclase (dark grey). A photomicrograph of the bronzitite host is presented in Fig. 8C(iv) (D_1 subunit, sample 104; hanging-wall of the LG 5 chromitite layer). Rutile is not present within chromite grains in the juxtaposed granular-textured bronzitites. Scale 5cm = 62 microns.

within granular-textured bronzitites, do not exhibit exsolved rutile. Furthermore, occurrences of acicular rutile crystals within intercumulus plagioclase are confined to certain adcumulate- and mesocumulate- textured bronzitites of the B unit and C_2 and D_1 subunits. Acicular crystals were not observed within plagioclase-bearing rocks of the E unit and D_2 subunit and within plagioclase grains filling poorly annealed cavities in granular- textured bronzitites. Rutile of any form was not observed within adcumulate-textured olivine- bronzitites, dunites and harzburgites of the C_1 and C_3 subunit, nor within the Lower Zone samples exposed in borehole KA5.

The textural features cited above support the notion that Ti-saturation in chromite is linked to the nucleation of plagioclase in the interstitial melt volume. This is manifested by two features in particular: (a) where a single chromite grain occupies a plagioclase-filled interstice, exsolved rutile is more prevalent, and (b) exsolved rutile is not present within chromite grains intergrown with titanian phlogopite. Hence, the TiO_2 content of chromite is not anticipated to vary as a smooth function of stratigraphic height by virtue of the interplay of factors such as these and subsolidus equilibration processes.

SULPHIDES

A systematic study of base metal sulphide occurrences was not made but the following observations warrant mention. Sulphides are a very rare constituent of the chromitite layers and are wholly absent in domains comprising large, polygonal chromite grains. A thin chromitite stringer in sample 07 (E unit) represents one exception, but the high sulphide content at this stratigraphic level appears to be linked to the juxtaposition of an olivine-rich, ultramafic pegmatite assemblage. Trace abundances of pyrrhotite are found within certain silicate-rich horizons, generally as small, irregular grains intergrown with intercumulus silicate phases. Chalcopyrite and pentlandite are intergrown with pyrrhotite in a few instances, suggestive of the decomposition of a monosulphide solid solution.

More rarely, microscopic inclusions of pyrrhotite occur within orthopyroxene in granular-textured bronzitites. Comparatively higher sulphide abundances are found in the upper portion of the B unit, in bronzitites underlying the olivine-bearing succession within the C_2 subunit and in the upper portion of the C_2 subunit. Certain adcumulate-textured and micropegmatite-bearing bronzitites near the base of D_1 subunit are host to sulphides, but these occurrences are very sporadic. Weak disseminations of sulphides occur sporadically within two horizons of the E unit, viz., from 41 to 74 metres below the LG 7 chromitite layer (samples 41 to 62) and within 18 metres of the LG 7 (samples 5 to 26). Although some of these occurrences are associated with olivine-bearing bronzitites and may thus reflect a degree of replacement by ultramafic pegmatite assemblages, it is of interest that there is a correspondence between these sulphide-bearing intervals and measured fluctuations in orthopyroxene crystallinity (refer to Fig. 8E). A comprehensive study of the sulphide modal variation in relation to stratigraphic position within these horizons may serve to elucidate this apparent relationship.

Other than trace occurrences of a pyrite-oxide intergrowth within serpentine, sulphide occurrences within the C_1 and C_3 subunits are restricted to small blebs occluded by reaction-replacement orthopyroxene. No primary magmatic sulphides were observed in adjacent olivine-rich domains, suggesting that magmatic sulphur was introduced via late-stage melt. Resorption of olivine crystals would re-introduce nickel into the melt or, by virtue of the siliceous melt composition and envisaged stagnant conditions imposed by the adcumulate textures, nickel may effectively be enriched in relict olivine ahead of the replacement front (a process akin to zone refining). It is not known whether the sulphide blebs are nickeliferous, but the concentration of NiO in reaction-replacement orthopyroxene (0,03 to 0,07 wt. per cent) is equivalent to that of orthopyroxene within granular harzburgites and bronzitites.

5.4 CHROMITE

The section which follows (pp. 113 - 151) presents in detail the observations and analytical data that constitute the focus of the

present study. A summary of the conclusions appears on pp. 148 - 151 but this section stresses (a) compositional variations of chromite grains within paragenetically different environments, (b) compositional changes with stratigraphic height, (c) the effects of reaction with late-stage liquids, (d) subsolidus equilibration with ferromagnesian silicates, and (e) the significance of variations in TiO_2.

The relatively simple general formula of the spinel group $A[B_2]O_4$, belies the compositionally diverse and complex array of spinellids found in natural and synthetic systems. The spinel structure is based on a cubic close-packed array of oxygen anions, with each unit cell containing 8 divalent cations in a total of 64 tetrahedral sites and 16 trivalent cations in a total of 32 octahedral sites. Hence, spinel sensu stricto can be written as $Mg_8\ Al_{16}\ O_{32}$. The inverse spinel structure, of which ulvöspinel is a member, has the general formula $B[AB]O_4$, where one half of the B cations are in octahedral sites with A cations. In terms of octahedral site preference energies (OSPE), this condition arises when A cations (such as Fe^{2+} and Ni^{2+}) have a higher OSPE than B cations (Burns, 1970). The Fe^{3+} cation, with zero OSPE, can form both normal and inverse spinels, whereas Cr^{3+} will only form normal spinels by virtue of the exceptionally high OSPE. Natural solid solutions of Cr-bearing spinels can be characterized in terms of the formula $(Mg, Fe^{2+})O.(Cr, Al, Fe^{3+})_2O_3$, and a method of graphical representation of the compositional variations is afforded by the trigonal spinel prism of Stevens (1944).

Though the partitioning of Mg and Fe^{2+} between Cr-spinel and basaltic magma is understood, the behaviour of trivalent Cr, Al and Fe is problematical. For example, a trend of declining $Mg/(Mg + Fe^{2+})$ ratios is manifested with progressively lower liquidus temperatures (Hill and Roeder, 1974; Akella et al., 1976; Fisk and Bence, 1980), whereas variable $(Al/Cr)^{spinel}$ ratios at constant temperature and pressure have been noted in natural peridotite assemblages (Sinton, 1977). Furthermore, subsolidus re-equilibration between Cr-spinels and associated ferromagnesian silicate phases serves to substantially depress the MMF (spinel) ratio (Jackson, 1969; Roeder et al., 1979; Wilson, 1982), whereas only limited diffusion of Cr into

orthopyroxene has been noted (Wilson, op cit.,). However, Eales and Reynolds (1983) and Eales (1985) have demonstrated a pronounced sensitivity of $(Al/Cr)^{spinel}$ to plagioclase nucleation in the Bushveld Complex. The Al/Cr ratio is seen to increase as the associated MMF ratio declines from high values to a cation ratio of approximately 0,450, whereupon nucleation of primocrystal plagioclase at the base of the Upper Critical Zone imposes a coupled trend of declining Al/Cr with a further decrease in MMF (spinel).

The influence of oxygen fugacity on spinel chemistry has received considerable attention (for example, by Irvine (1965), Speidel and Osborn (1967) and Ulmer (1969)). In essence, spinels enriched in magnetite or magnesioferrite end-members form under oxidizing magmatic conditions, whereas spinels enriched in $FeCr_2O_4$ and $FeAl_2O_4$ should reflect relatively reducing conditions. In addition, opposing changes in the MMF ratio can result depending on the fO_2 conditions attending subsolidus re-equilibration processes. It is believed that the redox conditions of the magma impose a control on the abundance of crystallizing chromite, and it has been proposed that periodic increases in fO_2 culminate in the formation of chromitite layers within the Lower Critical Zone (Snethlage and von Gruenewaldt, 1977; Snethlage and Klemm, 1978). Cameron and Desborough (1969) and Cameron (1975) make recourse to fO_2 fluctuations to account for higher Al_2O_3, Mg/Fe and Cr/Fe in chromite within chromitite layers of the Eastern Bushveld Complex. However, the analytical data reported by Cameron (1977) indicate that, relative to chromite within juxtaposed silicate-rich rocks, chromite within chromitite layers is depleted in the Fe_2O_3 component, while Cr_2O_3 remains essentially constant. This feature contradicts the anticipated increase of Fe^{3+} in spinel with higher ambient fO_2, as shown experimentally by Roeder (1982).

Wilson (1982) investigated the compositional variation of chromite within ultramafic rocks of the Zimbabwean Great Dyke and found that small grains occluded by orthopyroxene or olivine were enriched in Cr and Fe^{2+} relative to larger occluded grains within the same thin section. Intermediate grain-sizes were seen to be associated with intermediate compositions. These features were attributed to the influence of surface area/mass ratios of chromite grains during in

situ crystallization and subsolidus re-equilibration. It is envisaged that a small chromite grain, in equilibrium with a limited volume of magma, will be Cr-enriched relative to a larger grain in equilibrium with an equivalent melt volume. Within the subsolidus field, diffusive exchange of Fe^{2+} and Mg would induce a greater departure from primary compositions in small grains by virtue of the higher surface area/mass ratio. These compositional trends are not evident in chromite grains occluded by intercumulus silicate phases, a feature taken to be indicative of variable degrees of reaction with residual melt. It is important to note, however, that clinopyroxene is generally an abundant intercumulus phase within the lower cyclic units of the Great Dyke and crystallized before plagioclase (Bichan, 1969; Wilson, *op. cit.*). In summation it may therefore be concluded that the composition of chromite is influenced by any combination of magma composition, temperature and sequence of crystallization, oxygen fugacity, modal abundance of chromite, reaction with late-stage melt and subsolidus re-equilibration. Clearly, indiscriminate use of the electron microprobe will not assist in an evaluation of the above.

Some 650 microprobe analyses were obtained of chromite grains within a variety of textural and mineralogical environments in the studied section. These analyses are presented in Tables 22 to 29, which include (a) structural formulae calculated on the basis of 32 oxygens, (b) a selection of cation ratios, and (c) chromite grain-size measurements. The nature of the enclosing silicate phase, denoted "HOST", and the mineralogical assemblage, denoted "ROCK TYPE", are conveyed via numeric characters (see key for Tables 22 to 29). The diameter of the analyzing beam was generally 10 microns but was adjusted to suit various needs. For example, difficulties were experienced in attempting to estimate the bulk TiO_2 content of chromite showing exsolved rutile lamellae by virtue of two reasons: firstly, an inhomogeneous distribution of lamellae within grains, and secondly, the rutile lamellae are optically indistinguishable beneath the conductive graphite coating. An estimation of core-rim compositional relationships was complicated by the observation that core-domains of large grains may depict a high abundance of intimately intergrown rutile, whereas the marginal-domains are typically devoid of lamellae and show externally exsolved rutile

granules. Use of a broad beam commonly resulted in inferior analyses and the procedure finally adopted employed a 20 micron diameter beam, positioned in a structurally homogeneous area of the grain, in order to obtain a provisional total analysis (i.e., of Cr, Fe, Mg, et cetera). The concentrations of Ti were then determined at five other positions and averaged. It should be stressed, therefore, that the chromite analyses are strictly representative of subsolidus equilibrium compositions; an inordinate number of analyses would be required of each grain to ascertain the bulk, near-solidus levels of Ti.

Instrumental problems imposed a 20 micron limit on the minimum grain-size suitable for analysis. Attempts to refine the beam diameter to below 10 microns resulted in severe shape distortions leading to spurious analyses. Hence, spinel occurrences which could not be studied were (a) minute, facetted octahedra transmitting amber to reddish-brown light, (b) anhedral platelets transmitting pale green to amber light and (c) a trace occurrence of exsolved platelets within olivine (sample 184A; C_3 subunit), orientated parallel to the olivine c-axis and transmitting brown light (Fig. 27A). The latter are less than 5 microns in width but can be up to 0,25 mm in length, and an attempted microprobe analysis indicated a composition of at least 22 wt. per cent Cr_2O_3. The spinel octahedra, usually 10 microns in diameter, are a common feature of the D_1 subunit where they occur as inclusions within coarse- and fine-grained orthopyroxene crystals. These may represent grains isolated from the magma at an early stage, but this is inconsistent with the observation that crystals of less than 10 microns can occur within 0,05 mm of grains which are greater than 300 microns in diameter and which are indented within orthopyroxene grain boundaries (Fig. 27B). Furthermore, clusters of minute octahedra or prisms can be seen in juxtaposition to larger grains (> 60 microns), all of which are wholly enclosed within orthopyroxene core- or marginal-domains. This bimodal grain-size distribution may therefore be indicative of mixing of two populations of chromite, viz., very small crystals that grew in situ from a limited melt volume and larger crystals (> 60 microns) that settled through a substantial liquid column. An alternative explanation, and one that is favoured here by virtue of the perfect idiomorphism, is that the small octahedra represent a suspension of

FIGS. 27(A) to (C): Photomicrographs of chromite particles which could not be analyzed with the electron microprobe by virtue of the exceptionally small sizes. However, Cr-count rates well in excess of background were recorded where the particles were exposed in polished surfaces. All sections photographed with transmitted light.

(A): Crystallographically orientated lamellae of Cr-spinel within a large olivine crystal. The latter is exposed within an olivine/reaction-replacement orthopyroxene inclusion in the I chromitite layer (C_3 subunit, sample 184A), and represents the only occurrence of this type in the studied section. Scale 5cm = 0,25mm.

(B): Facetted octahedron of chromite (diameter of 10 microns) in juxtaposition to a chromite grain with a diameter of 300 microns. The latter is deeply indented in an orthopyroxene grain boundary, whereas the small particle is wholly within orthopyroxene. Grains of this size were never recognised as inclusions in intercumulus silicate phases (D_1 subunit, sample 147). Two other octahedra are visible deeper into the section which is about 35 microns in thickness. These small crystals are very rarely seen with reflected light.

(C): Granule of amber-coloured spinel in orthopyroxene within an olivine-bronzitite(C_1 subunit, sample 255). Juxtaposition of rods or trails of opaque oxide granules are a sympathetic feature. Scale 5cm = 62 microns.

Ⓐ

Ⓑ

Ⓒ

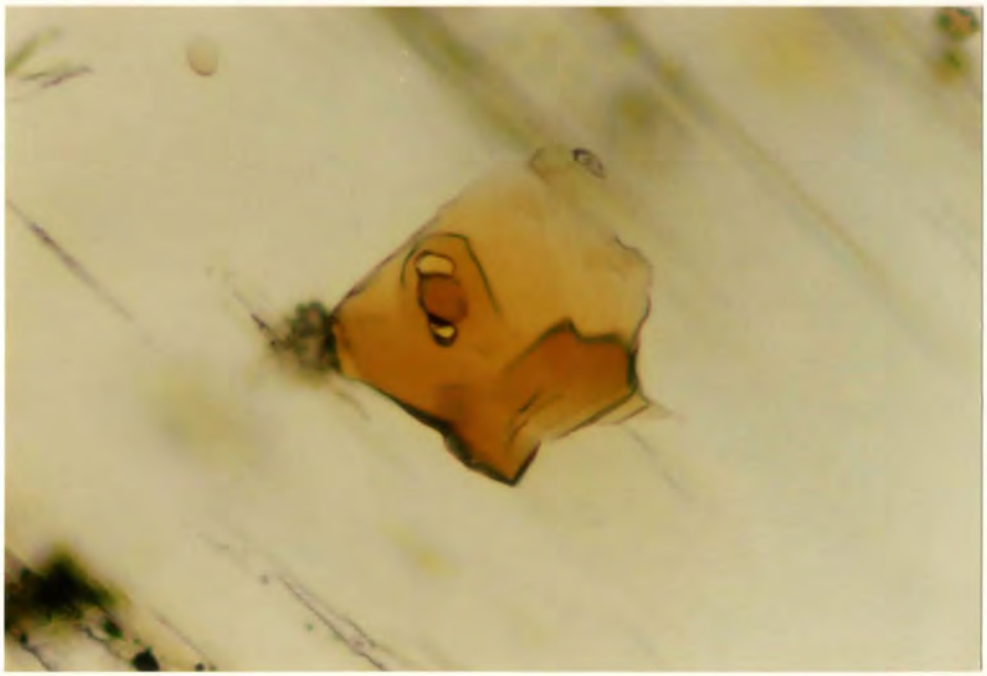

intratelluric spinel carried into the magma chamber. The reddish-brown transmitted colour may be regarded as being indicative of chromiferous spinels (Eales and Reynolds, 1983). Similar occurrences are found within the upper 7 metres of the B unit (i.e., above and below the LG 2 chromitite) and in the footwall bronzitites of the LG 1 and LG 3 chromitite layers. These small spinel crystals were not observed as inclusions within olivine of the C_1 and C_3 subunits but anhedral spinel platelets, transmitting pale green to amber light, occur along cleavage planes of well-formed orthopyroxene crystals within olivine-bronzitites of the C_1 subunit (Fig. 27C). These are commonly associated with opaque spinel granules and droplets. Olivine and orthopyroxene crystals with no spinel inclusions occur in adjacent domains, and these textural features suggest that the translucent spinel stems from deuteric oxidation processes. Reaction-replacement orthopyroxene is also commonly charged with inclusions of opaque and translucent spinels.

5.4.1 CHROMITE IN CHROMITITE LAYERS

All of the Lower Group chromitite layers and associated minor layers were sampled, with the exception of the LG 1 and LG 6 (drill core ZS7) chromitite layers. A complete intersection of the LG 6A chromitite (ZS7) was made available for study, whereas only chip samples of the other LG chromitites were collected from the base of each layer. Most of the analytical work was completed at the University of Cape Town, thus necessitating an interlaboratory check. A selection of duplicate microprobe analyses is presented in Table 16. Relative to the operating conditions employed at the University of Cape Town, duplicate analyses at Rhodes showed consistently higher Mg and Al, and lower FeO (total). The discrepancies are, however, acceptable and no restrictions can be imposed when relating this data to that of chromite grains within silicate-rich rocks, the bulk of which were analyzed at Rhodes University.

A quartz crystal was employed at the University of Cape Town for the determination of MnO contents, resulting in Cr K_β spectral line interference on the Mn peak position. The standard correction

procedure adopted is: MnO = MnO* - 0,01 [Cr_2O_3], where MnO* and Cr_2O_3 are derived from the microprobe data and are expressed in weight per cent. The standard operating conditions at Rhodes University utilize a LiF crystal for the determination of manganese, and it is evident from Table 16 that a consistent discrepancy of 0,15 wt. per cent MnO is depicted. Hence, where the same material was analyzed on a different occasion at Rhodes or further analyses were generated to supplement data acquired at the University of Cape Town, the following correction factor was adopted: MnO = MnO* - 0,003 [Cr_2O_3]. This procedure has, however, a negligible effect on the calculated cation abundances and cation ratios (for example, the proportion of Cr cations increases by 0,01 if this system is used).

By virtue of the limited sample material available, it was necessary to evaluate the degree to which a chip sample is representative of a given chromitite layer and to assess the compositional variation of chromite within a single polished section. Analytical data for chromite within an orientated polished section of the LG 2 chromitite layer are presented in Table 17, and a graphical representation of the grain-to-grain compositional and textural variation is given in Fig. 28. No chemical zoning of chromite grains was detected in this massive chromite ore, though pronounced variations in grain-size and -shape are evident. However, there is a suggestion of subtle compositional changes with stratigraphic position which may correlate with textural environment. Accordingly, it was decided to standardize the selection of micro-domains within the chromitite chip samples, in view of which domains showing polygonal, annealed grains were selected for analysis.

Table 18 presents average microprobe analyses of chromite within chromitite layers of the Ruighoek Pyroxenite succession, including minor layers in juxtaposition to the LG 3, LG 5 and LG 6 chromitite layers. Cr_2O_3 contents rise from 50,88 wt. per cent within the C chromitite to an apparent maximum of 55,84 wt. per cent within the thin leader layer below the LG 3 chromitite layer. An irregular decline in Cr_2O_3 with increasing stratigraphic height is evident above this level to a concentration of 48,15 wt. per cent within the LG 7 chromitite. It is notable, however, that a pronounced rise to

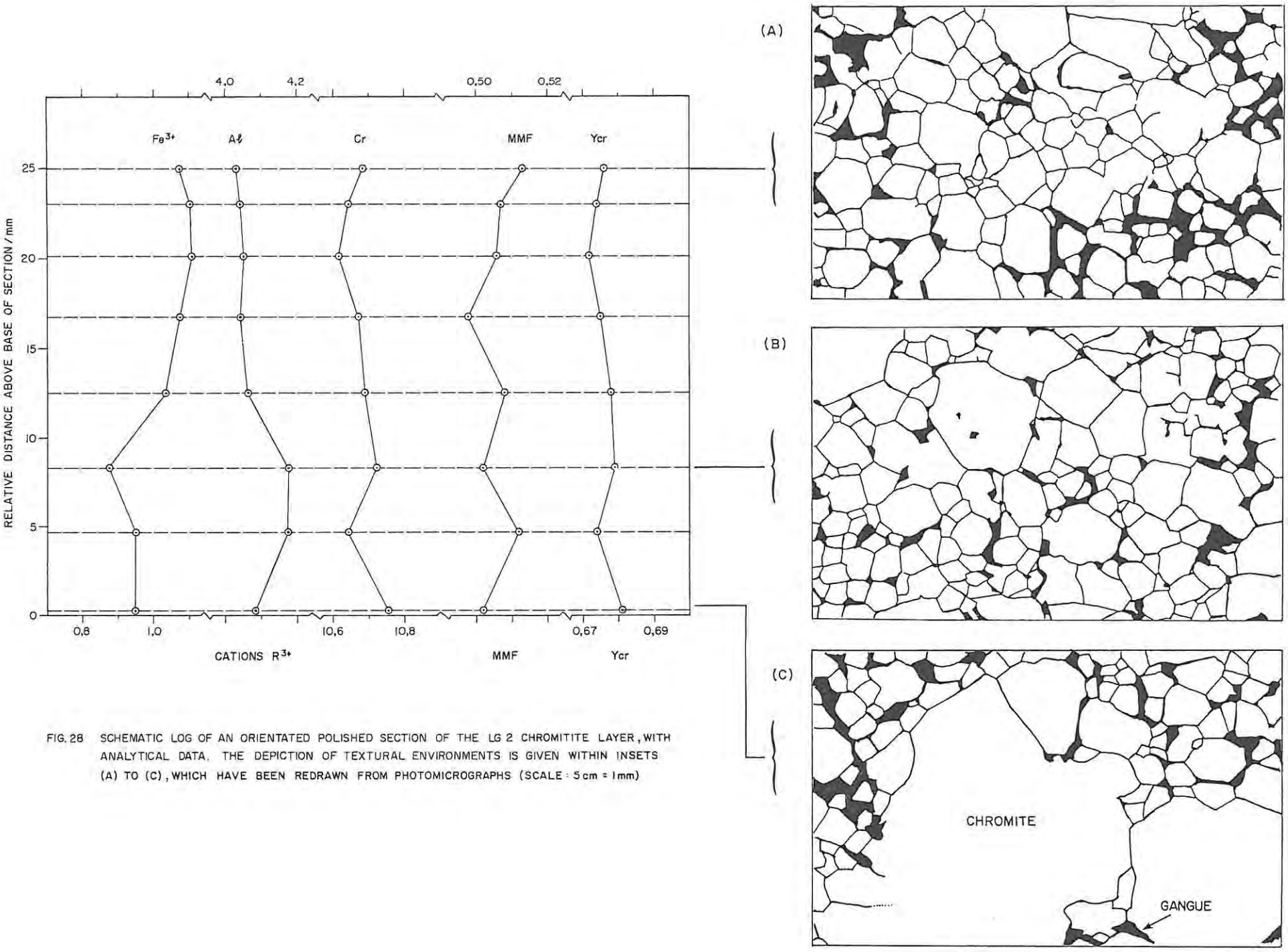

FIG. 28 SCHEMATIC LOG OF AN ORIENTATED POLISHED SECTION OF THE LG 2 CHROMITITE LAYER, WITH ANALYTICAL DATA. THE DEPICTION OF TEXTURAL ENVIRONMENTS IS GIVEN WITHIN INSETS (A) TO (C), WHICH HAVE BEEN REDRAWN FROM PHOTOMICROGRAPHS (SCALE : 5 cm = 1 mm)

TABLE 16: DUPLICATE MICROPROBE ANALYSES OF CHROMITE WITHIN THE LG 6A CHROMITITE LAYER (DRILL CORE ZS 7)

Analysis	A	B	C	D	E	F	G
TiO_2	1,03	0,99	1,03	0,99	1,06	1,07	1,07
Cr_2O_3	49,56	49,05	49,91	49,95	49,83	49,33	49,48
Al_2O_3	15,49	15,91	15,01	16,21	15,43	16,70	16,74
Fe_2O_3	2,48	2,83	1,83	2,10	1,59	1,96	2,14
FeO	21,41	20,99	21,06	20,60	21,13	20,18	20,61
MgO	8,69	9,00	8,66	9,43	8,70	9,67	9,59
MnO	0,40	0,55	0,34	0,49	0,40	0,56	0,52
TOTAL	**99,06**	**99,32**	**97,84**	**99,77**	**98,14**	**99,47**	**100,15**
$Mg/(Mg+Fe^{2+})$	0,419	0,433	0,422	0,449	0,423	0,460	0,453
^{Y}Cr	0,660	0,649	0,674	0,656	0,670	0,648	0,647
OXIDATION RATIO	0,094	0,108	0,072	0,084	0,063	0,080	0,085

A - B: Duplicate analyses at (A) University of Cape Town and (B) Rhodes University
C - D: Duplicate analyses at (C) University of Cape Town and (D) Rhodes University
E - F - G: Duplicate analyses at (E) University of Cape Town and (F - G) Rhodes University (the latter on successive days)

Fe speciation calculated on the assumption of stoichiometry

$^{Y}Cr = Cr/(Cr + Al + Fe^{3+})$

Oxidation Ratio $= Fe^{3+}/(Fe^{3+} + Fe^{2+}_{tot})$

TABLE 17: MICROPROBE ANALYSES OF CHROMITE WITHIN A 2,5 cm SECTION OF THE LG 2 CHROMITITE LAYER, ORIENTATED PARALLEL TO THE DRILL CORE AXIS (SAMPLE FROM BASE OF LAYER)

Analysis No.	1	2	3	4	5	6	7	8
TiO_2	,53	,57	,56	,54	,52	,55	,52	,52
Cr_2O_3	52,03	51,25	51,97	52,04	51,86	51,50	51,27	51,47
Al_2O_3	13,26	13,49	13,59	13,27	13,19	13,19	13,06	13,03
Fe_2O_3	4,82	4,82	4,47	5,29	5,50	5,65	5,58	5,43
FeO	18,31	17,91	18,38	18,25	18,56	18,24	18,06	17,84
MgO	10,39	10,56	10,41	10,59	10,37	10,52	10,45	10,56
MnO	,22	,19	,22	,17	,17	,17	,19	,22
TOTAL	99,56	98,79	99,60	100,15	100,17	99,82	99,13	99,07

CATIONS PER 32 OXYGENS

Ti	,104	,112	,110	,105	,102	,108	,103	,103
Fe^{2+}	,104	,112	,110	,105	,102	,108	,103	,103
Cr	10,756	10,645	10,722	10,690	10,673	10,620	10,647	10,687
Al	4,086	4,176	4,179	4,063	4,046	4,054	4,042	4,032
Fe^{3+}	,949	,953	,879	1,035	1,077	1,110	1,103	1,074
Fe^{2+}	3,901	3,822	3,902	3,861	3,938	3,872	3,865	3,817
Mg	4,049	4,135	4,049	4,101	4,023	4,089	4,091	4,134
Mn	,048	,042	,048	,037	,037	,037	,042	,048
MMF	,502	,512	,502	,508	,498	,506	,507	,513
Y_{Cr}	,681	,674	,679	,677	,675	,672	,674	,676
Y_{Al}	,258	,264	,264	,257	,256	,256	,255	,255
$Y_{Fe^{3+}}$	,060	,060	,055	,065	,068	,070	,069	,068
FFF	,191	,195	,179	,207	,210	,218	,217	,215
	Relative distance above base of section /mm							
	0,3	4,7	8,3	12,5	16,7	20,1	23,0	25,0

Cations calculated from microprobe data on assumption of stoichiometry and assigning of Ti to the ulvöspinel molecule.

1 - 8: Core-domains
Analyzed at the University of Cape Town. The concentration of MnO is corrected for Cr K_β spectral line interference according to the relationship:

MnO = MnO* - 0,01[Cr_2O_3], where MnO* and Cr_2O_3 are expressed in wt. per cent.

MMF = $Mg/(Mg + Fe^{2+}_{total})$
Y_{Cr} = $Cr/(Cr + Al + Fe^{3+})$
Y_{Al} = $Al/(Cr + Al + Fe^{3+})$
$Y_{Fe^{3+}}$ = $Fe^{3+}/(Cr + Al + Fe^{3+})$
FFF = $Fe^{3+}/(Fe^{3+} + Fe^{2+}_{total})$
= Oxidation ratio

54,36 wt. per cent Cr_2O_3 occurs within a chromitite lens at the level of sample 28 in the E unit. Furthermore, the Fe_2O_3 content of grains within the LG 6A chromitite, drill core ZS3, is significantly higher (7,86 wt. per cent) than is measured in the equivalent ZS7 exposure (2,36 wt. per cent). With the exception of the LG 2 chromitite layer, Fe_2O_3 contents of chromite within chromitite layers exposed in drill core ZS7 are substantially less than 4,0 wt. per cent. Fe_2O_3 contents decline from 5,20 wt. per cent within the LG 2 to an apparent minimum of 1,31 wt. per cent within the LG 4 chromitite. There is an irregular rise above this level, with 2,74 wt. per cent Fe_2O_3 recorded within the chromitite lens in sample 28. TiO_2 contents decline from 0,78 wt. per cent within the C chromitite to 0,46 wt. per cent within the LG 3, followed by an irregular increase through the C_3, D_1 and D_2 subunits to a concentration of 1,03 wt. per cent within the LG 6A chromitite (drill core ZS7). The TiO_2 content of the LG 7 chromitite (1,02 wt. per cent) is very similar to the latter. Relative to the LG 2 (ZS7), LG 6 (ZS3) and LG 6A (ZS3) chromitite layers, it is evident from the data that chromite within the chromitite layers displays high Cr- and Al-contents and low Fe^{3+} contents.

A log of the Ruighoek Pyroxenite succession, showing analytical data pertaining to chromite within chromitite layers, is presented in Fig. 29. The reciprocal variation of Cr and Al in drill core ZS7, with Fe^{3+} remaining at low concentrations, indicates that charge balance and stoichiometry in the chromite solid solution is preserved via substitution of Al and Cr. However, this does not apply to the ZS3 drill core exposure of the LG 6A chromitite, where substitution of Fe^{3+} for Al is evident. The latter is coupled to an increase in the MMF ratio, a feature that is also manifested at the level of the LG 2 chromitite layer. Though stoichiometry may be maintained in different ways, there is a broad decline in the Y_{Cr} ratio (Y_{Cr} = $Cr/(Cr + Al + Fe^{3+})$) with increasing stratigraphic height, with maxima at the LG 3, LG 4 and sample 28 horizons. The MMF ratios rise irregularly with increasing stratigraphic height from 0,435 within the C chromitite to 0,558 within the I chromitite layer, then decline through the D and E units. Excluding sample 28, which shows a sympathetic increase of Cr content and MMF ratio, an overall trend of increasing Al content is evident through successive chromitite

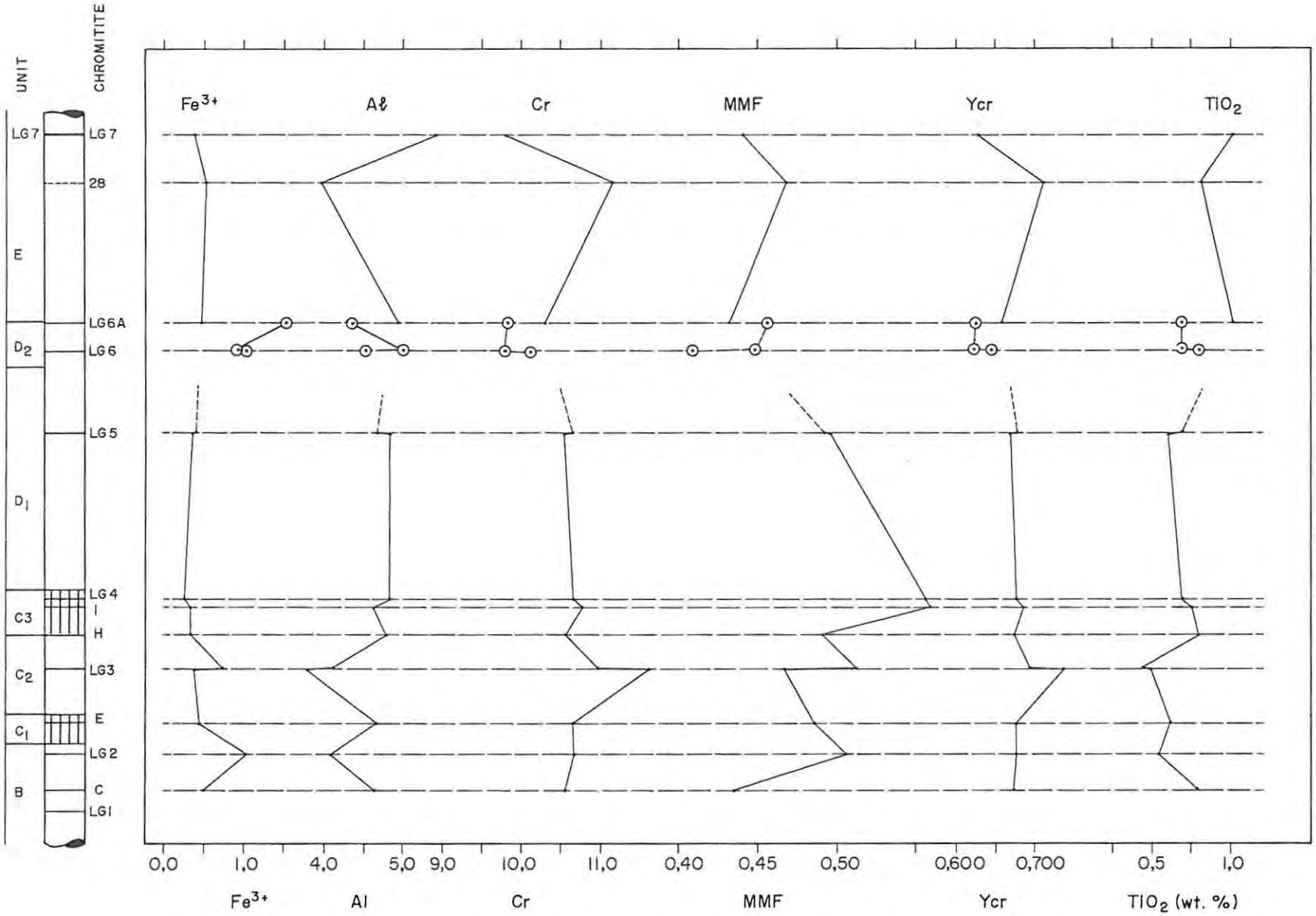

FIG. 29 LOG OF THE RUIGHOEK PYROXENITE SUCCESSION WITH ANALYTICAL DATA PERTAINING TO THE COMPOSITIONAL VARIATION OF CHROMITE WITHIN CHROMITITE LAYERS.

SYMBOLS: • DRILL CORE ZS7 ; ⊙ DRILL CORE ZS3

TABLE 18: AVERAGE COMPOSITION OF CHROMITE WITHIN THE LOWER GROUP CHROMITITE LAYERS AND ASSOCIATED MINOR LAYERS.

Layer	C	LG 2	E	LG 3 Leader	LG 3	H	I	LG 4
Drill Core	ZS7	ZS7	ZS7	ZS7	ZS7	ZS7	ZS7	ZS7
n	4	8	4	2	3	9	2	2
TiO_2	0,78	0,54	0,61	0,49	0,46	0,79	0,75	0,68
Cr_2O_3	50,88	51,67	51,85	55,84	53,29	51,67	52,85	52,47
Al_2O_3	15,01	13,26	15,29	12,16	13,40	15,73	15,18	15,96
Fe_2O_3	2,52	5,20	2,24	1,93	3,75	1,68	1,67	1,31
FeO	20,78	18,19	19,00	19,41	17,82	18,99	16,61	16,60
MgO	8,98	10,48	10,12	9,50	10,52	10,30	11,80	11,67
MnO	0,36	0,19	0,35	0,37	0,48*	0,33	0,13	0,35
NiO	n.a.	n.a.	n.a.	n.a.	0,09	n.a.	n.a.	0,10
TOTAL	98,31	99,53	99,46	99,70	99,81	99,49	98,99	99,14
CATIONS PER 32 OXYGENS								
Ti	0,153	0,106	0,119	0,097	0,090	0,154	0,145	0,131
Fe^{2+}	0,153	0,106	0,119	0,097	0,090	0,154	0,145	0,131
Cr	10,552	10,680	10,641	11,641	10,972	10,565	10,772	10,654
Al	4,640	4,085	4,678	3,780	4,110	4,793	4,617	4,830
Fe^{3+}	0,499	1,023	0,438	0,384	0,735	0,329	0,324	0,254
Fe^{2+}	4,406	3,872	4,006	4,183	3,791	3,952	3,430	3,436
Mg	3,512	4,084	3,914	3,734	4,083	3,972	4,534	4,467
Mn	0,081	0,043	0,077	0,082	0,105	0,073	0,028	0,076
Ni	-	-	-	-	0,019	-	-	0,021
MMF	0,435	0,506	0,486	0,467	0,512	0,491	0,558	0,556
Y_{Cr}	0,672	0,676	0,675	0,736	0,693	0,673	0,685	0,676
Y_{Al}	0,295	0,258	0,296	0,239	0,259	0,305	0,293	0,306
$Y_{Fe^{3+}}$	0,031	0,064	0,027	0,023	0,046	0,020	0,020	0,016
FFF	0,098	0,204	0,095	0,082	0,159	0,074	0,083	0,066

TABLE 18 (Continued):

Layer	LG 5 FW	LG 5	LG 6	LG 6 HW	LG 6A	LG 6A	SAMPLE 28	LG 7
Drill Core	ZS7	ZS7	ZS3	ZS3	ZS3	ZS7	ZS7	ZS7
n	4	8	4	2	3	9	2	2
TiO_2	0,61	0,69	0,80	0,69	0,69	1,03	0,81	1,02
Cr_2O_3	51,56	51,97	48,59	47,82	47,70	49,75	54,36	48,15
Al_2O_3	15,88	15,27	14,62	16,40	14,16	15,76	13,03	17,83
Fe_2O_3	1,87	2,04	5,19	4,78	7,86	2,36	2,74	2,08
FeO	18,59	18,82	21,66	20,33	20,03	21,05	19,67	20,95
MgO	10,29	10,26	8,42	9,33	9,47	9,03	9,72	9,41
MnO	0,34	0,37	0,36	0,58*	0,39	0,38	0,56*	0,34
NiO	0,07	n.a.	n.a.	n.a.	n.a.	n.a.	n.a.	n.a.
TOTAL	99,21	99,42	99,64	99,93	100,30	99,36	100,89	99,78
CATIONS PER 32 OXYGENS								
Ti	0,118	0,135	0,158	0,134	0,136	0,201	0,158	0,197
Fe^{2+}	0,118	0,135	0,158	0,134	0,136	0,201	0,158	0,197
Cr	10,553	10,659	10,117	9,793	9,832	10,280	11,161	9,808
Al	4,843	4,669	4,537	5,006	4,350	4,849	3,987	5,412
Fe^{3+}	0,366	0,399	1,028	0,932	1,544	0,464	0,536	0,383
Fe^{2+}	3,908	3,949	4,614	4,270	4,232	4,398	4,114	4,339
Mg	3,971	3,969	3,305	3,602	3,680	3,516	3,762	3,588
Mn	0,106	0,081	0,080	0,127	0,087	0,083	0,123	0,072
Ni	0,013	-	-	-	-	-	-	-
MMF	0,496	0,492	0,409	0,449	0,457	0,432	0,468	0,441
Y_{Cr}	0,669	0,677	0,645	0,622	0,625	0,659	0,711	0,628
Y_{Al}	0,307	0,296	0,289	0,318	0,277	0,310	0,254	0,346
$Y_{Fe^{3+}}$	0,023	0,025	0,065	0,059	0,098	0,029	0,034	0,024
FFF	0,083	0,089	0,177	0,174	0,261	0,091	0,111	0,077

Cations calculated from microprobe data on assumption of stoichiometry and assigning of Ti to the ulvöspinel molecule.

MnO = MnO* - 0,01[Cr_2O_3]

n.a. = Not analyzed

n = Number of analyses

MB3AAL

layers. The pattern of TiO_2 variation is very similar to that of Al (Fig. 29).

C CHROMITITE LAYER

Table 19 presents microprobe analyses of chromite within the 1,5 cm thick C chromitite layer. The chromitite occurs at a stratigraphic position in the B unit where there is an abrupt increase in orthopyroxene crystallinity (Fig. 8A); the footwall contact is sharp but the hanging-wall is gradational over 10 mm. These features are summarized in Fig. 30(A), which includes analytical data plotted in relation to stratigraphic height. It is evident from data points representative of chromite within the chromitite layer that the proportions of Cr, Al and Fe^{3+} cations are linked to the MMF ratios, with the highest Cr content and lowest MMF ratio depicted at the top contact. Representative photomicrographs of the lower, middle and upper domains of the chromitite are given in Fig. 30(B). These show that a higher interstitial volume occurs towards the contacts, associated with arrested grain annealing textures. The sympathetic disposition of the MMF data points suggests, therefore, that some degree of reaction with late-stage melt or subsolidus re-equilibration may have occurred. The latter is confirmed in part by the composition of a 70 micron chromite grain occluded by orthopyroxene in the hanging-wall bronzitite. The MMF ratios of large chromite grains close to the upper contact are intermediate compositions, but this is not reflected in the Cr- and Al-contents. Of particular interest is the decline in TiO_2 from 0,83 wt. per cent at the base to 0,66 wt. per cent at the top contact, linked to an increase in the oxidation ratio ($Fe^{3+}/(Fe^{3+} + Fe^{2+})$). It is difficult to reconcile these subtle compositional trends in terms of long-range settling of crystals, deposition from density flows, or crystallization from an unrestricted volume of magma. Rather, the data suggests that equilibrium was maintained with a restricted melt volume at the base of a liquid column.

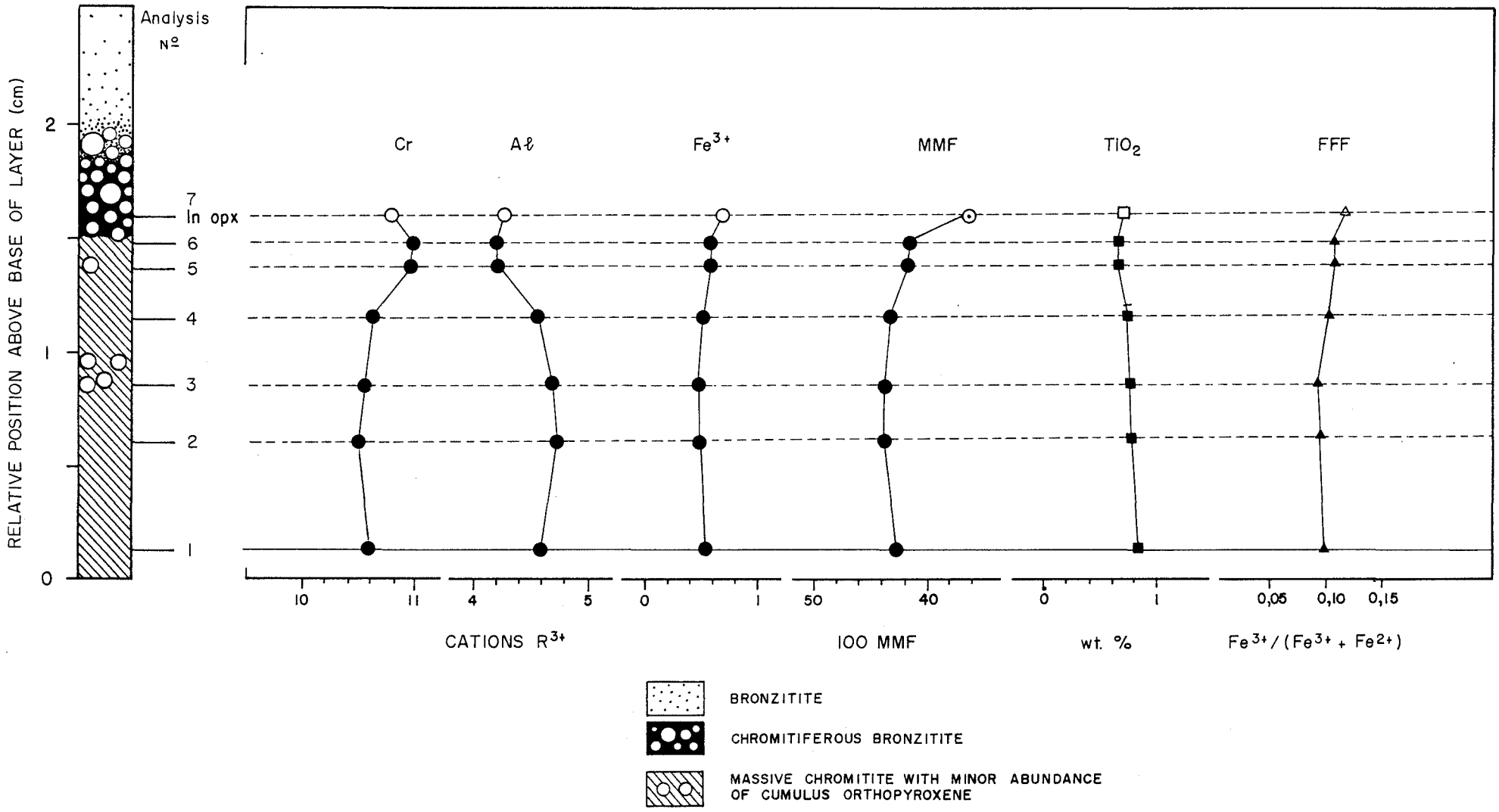

FIG. 30(A) LOG OF THE C CHROMITITE LAYER (B UNIT), WITH ANALYTICAL DATA.

FIG. 30(B): Photomicrographs of (i) upper, (ii) middle and (iii) basal textural environments within an orientated section of the C chromitite layer, B unit (sample 276). Photographed with plane polarized reflected light under low power magnification. (5cm = 1mm). The intercumulus silicate phase is orthopyroxene (light grey).

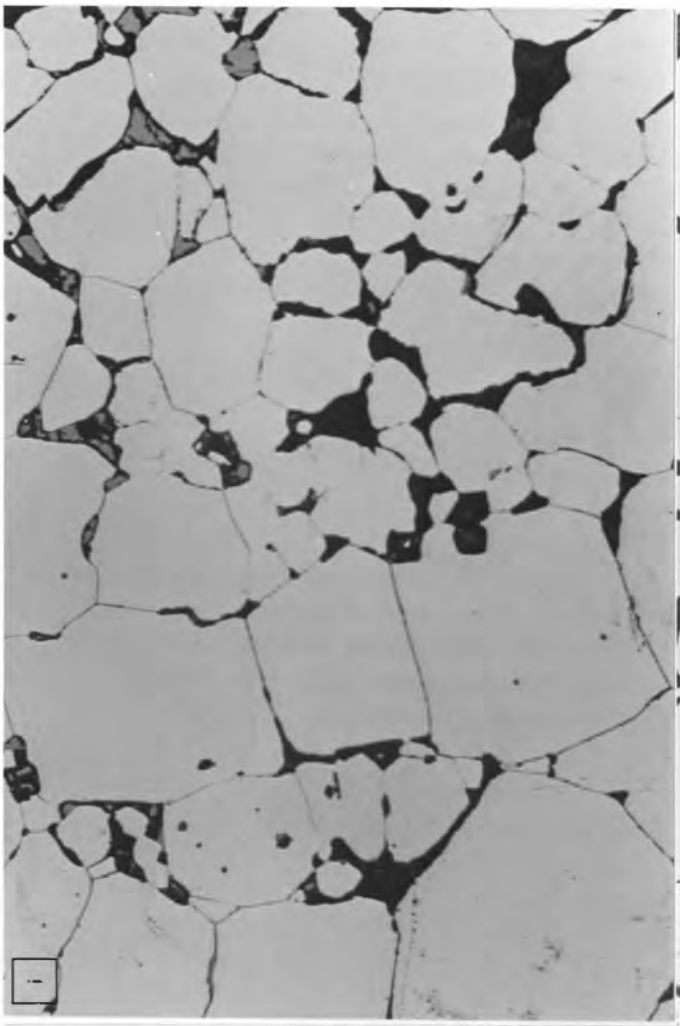

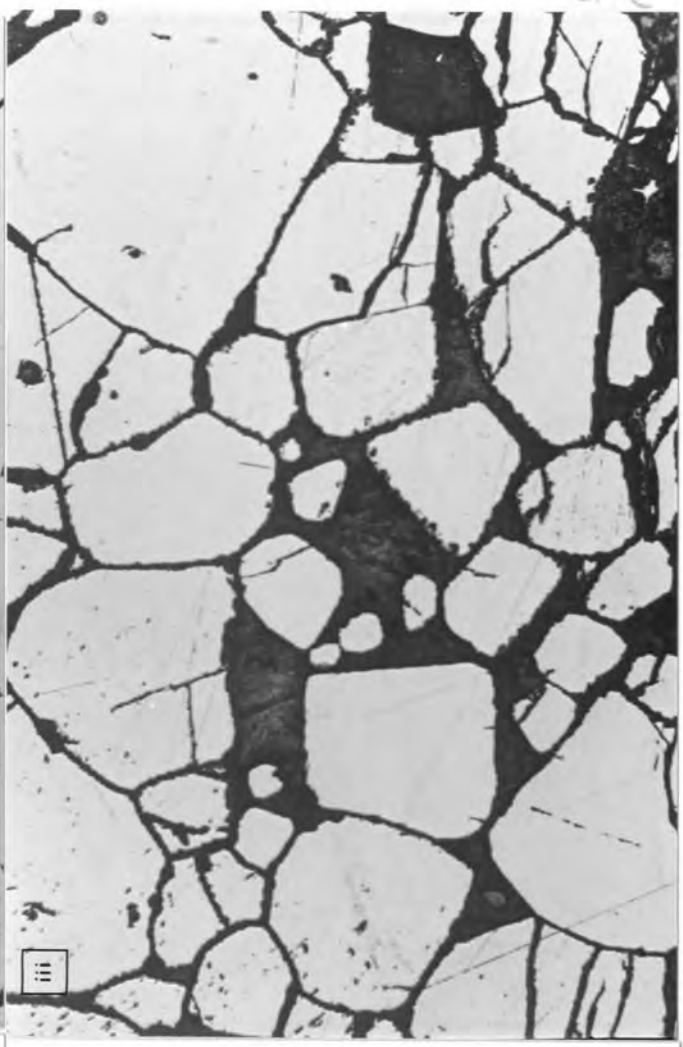

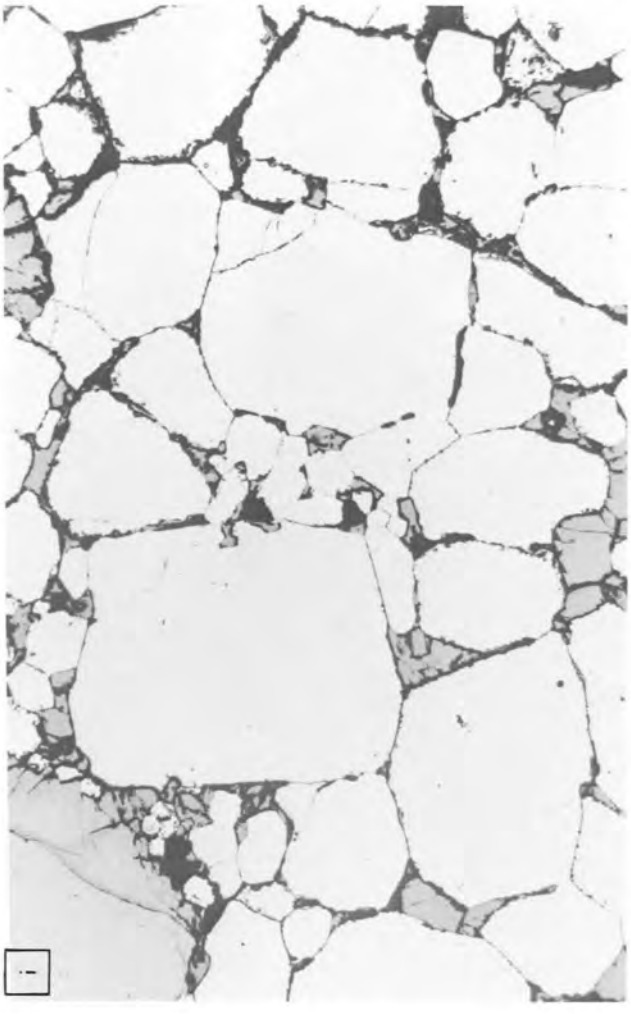

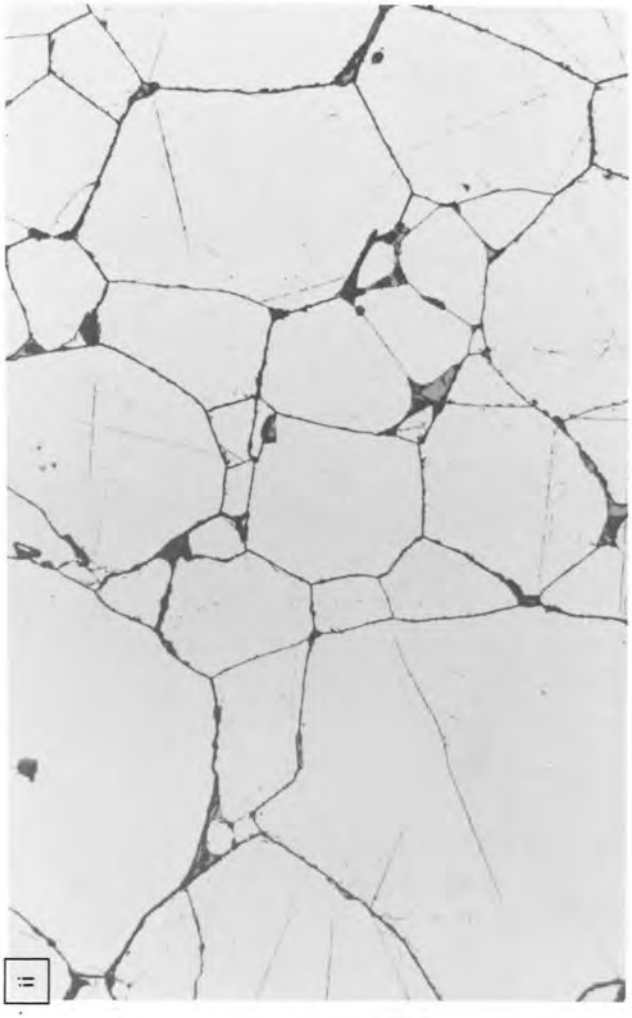

TABLE 19: MICROPROBE ANALYSES OF CHROMITE WITHIN THE C CHROMITITE LAYER, B UNIT

Analysis No.	1	2	3	4	5	6	7
TiO_2	,83	,78	,77	,74	,67	,66	,70
Cr_2O_3	50,98	50,65	50,67	51,22	52,41	52,52	51,06
Al_2O_3	14,85	15,30	15,14	14,76	13,46	13,46	13,52
Fe_2O_3	2,57	2,42	2,39	2,71	2,87	2,88	3,34
FeO	21,09	20,64	20,60	20,80	21,14	21,22	22,86
MgO	8,84	9,09	9,03	8,97	8,55	8,53	7,40
MnO	,36	,36	,38	,36	,37	,36	,37
TOTAL	99,52	99,24	98,98	99,56	99,47	99,63	99,25

CATIONS PER 32 OXYGENS

Ti	,163	,153	,152	,145	,133	,131	,140
Fe^2	,163	,153	,152	,145	,133	,131	,140
Cr	10,573	10,491	10,531	10,614	10,963	10,972	10,788
Al	4,590	4,723	4,690	4,558	4,196	4,191	4,257
Fe^3	,508	,477	,474	,535	,572	,573	,672
Fe^2	4,463	4,370	4,376	4,415	4,544	4,559	4,968
Mg	3,456	3,549	3,538	3,504	3,372	3,36	2,947
Mn	,079	,079	,084	,079	,082	,080	,083
MMF	,427	,439	,438	,434	,418	,417	,365
Y_{Cr}	,674	,668	,670	,675	,696	,697	,686
Y_{Al}	,292	,301	,298	,290	,266	,266	,270
Y_{Fe^3}	,032	,030	,030	,034	,036	,036	,042
FFF	,099	,095	,094	,104	,109	,108	,116
	Distance above base of layer/cm						
	0,12	0,58	0,84	1,13	1,35	1,46	1,58

1 - 5: Polygonal chromite grains within the chromitite
6: Euhedral chromite grain at contact with overlying bronzitite
7: 70 Micron diameter chromite grain occluded by a well-formed orthopyroxene crystal

H CHROMITITE LAYER

Table 20 summarizes the compositional variation of chromite within the H chromitite layer and overlying olivine-bearing assemblages in relation to stratigraphic height. Cr_2O_3 contents decline from 52,40 wt. per cent at the base to 49,89 wt. per cent at the top of this 4 cm thick, massive chromitite layer. This is linked to a reciprocal increase in Al_2O_3 contents from 15,08 wt. per cent to 17,64 wt. per cent, and a rise in Fe_2O_3 contents from 1,62 wt. per cent to 2,10 wt. per cent. MMF ratios rise from 0,484 at the base to 0,509 at the top of the layer. Perturbations in these trends are evident within the overlying silicate-rich rocks, which may reflect subsolidus re-equilibration with the coexisting silicate phases and reaction with late-stage melt (reaction-replacement orthopyroxene is a pervasive constituent from the +5 to +6 cm level). The analytical data are depicted in Fig. 31, which shows a columnar log of the studied interval.

Though the proportions of Cr, Al and Fe^{3+} cations are linked to the MMF ratios, the sense of the cryptic variation is opposite to that seen in the C chromitite layer, viz., the highest Cr and lowest MMF ratio are depicted at the base of the chromitite layer. From an inspection of the analytical data presented in Table 20, it is clear that the decline in Cr contents with increasing stratigraphic height is balanced by a reciprocal increase in Al contents, with the $Y_{Fe^{3+}}$ ratio remaining essentially constant. However, as noted in the C chromitite layer, TiO_2 contents decline irregularly from 0,85 wt. per cent at the base to 0,63 wt. per cent at the top of the layer. Similarly, there is an increase in oxidation ratios with increasing stratigraphic height, becoming more pronounced at the level immediately preceding the first appearance of olivine within the C_3 subunit. This feature is irreconcilable with the proposal that a rise in fO_2 stimulates copious nucleation of chromite in a basaltic magma. Furthermore, it is evident from the data points that the trend of declining Cr with increasing stratigraphic height is reversed at the +5 cm level, where a thin olivine-chromitite layer is depicted. The Cr_2O_3 content of chromite within this layer (52,21 wt. per cent) is equivalent to that of chromite near the base of the chromitite layer.

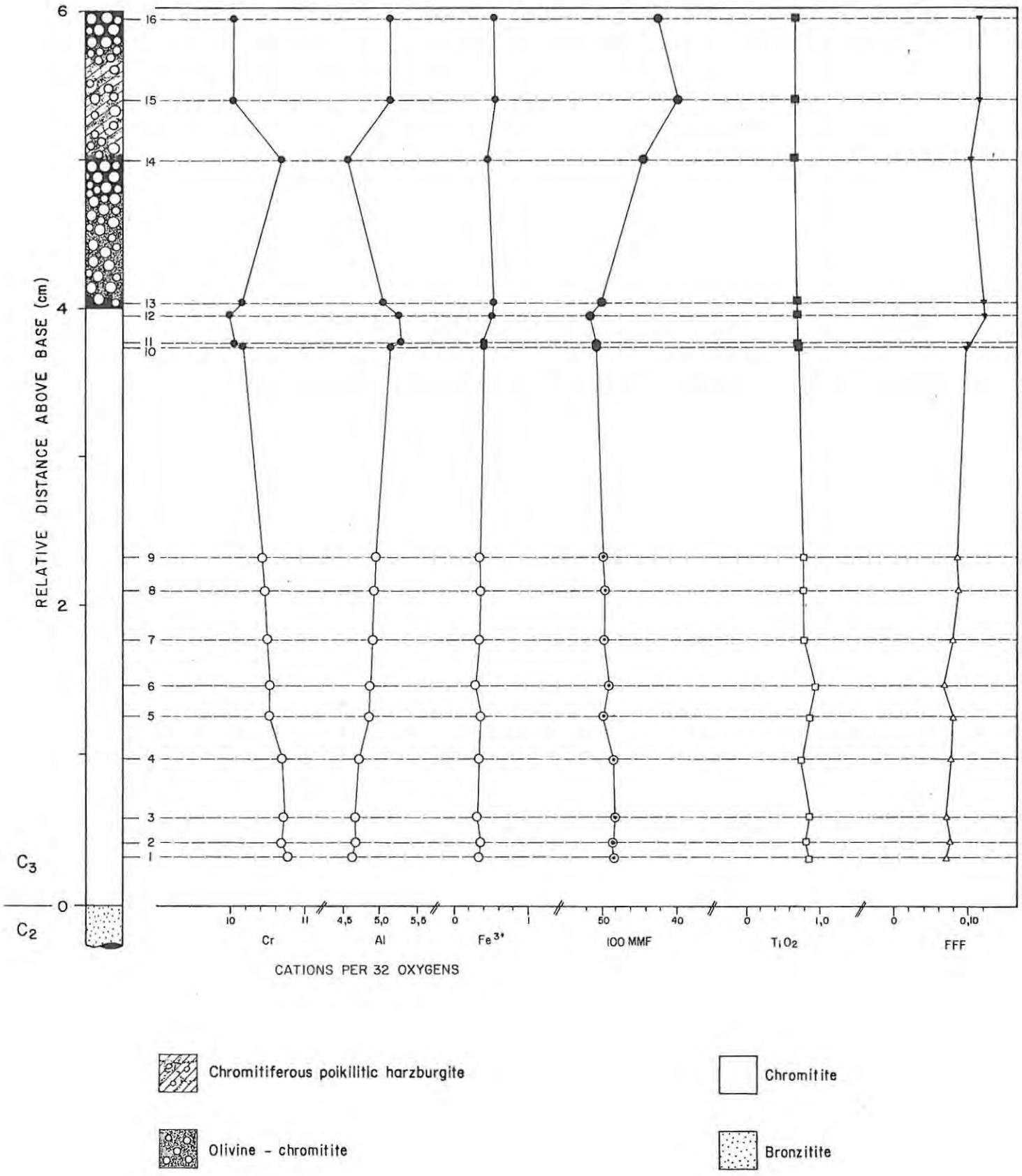

FIG. 31 LOG OF H CHROMITITE LAYER (AT THE BASE OF THE C_3 SUBUNIT) WITH ANALYTICAL DATA.

CLOSED SYMBOLS: ANALYZED AT RHODES UNIVERSITY
OPEN SYMBOLS : ANALYZED AT THE UNIVERSITY OF CAPE TOWN

TABLE 20: MICROPROBE ANALYSES OF CHROMITE WITHIN THE H CHROMITITE LAYER, BASE OF C_3 SUBUNIT, AND OF CHROMITE IN THE OVERLYING OLIVINE-CHROMITE CUMULATE LAYER

Analysis No.	1	2	3	4	5	6	7	8
TiO_2	,85	,80	,83	,73	,82	,91	,76	,73
Cr_2O_3	52,40	52,06	52,14	52,04	51,32	51,40	51,32	51,06
Al_2O_3	15,08	15,29	15,29	15,39	15,90	15,97	16,16	16,14
Fe_2O_3	1,62	1,74	1,56	1,66	1,77	1,48	1,70	1,84
FeO	19,23	19,14	19,30	19,07	18,77	19,05	18,77	18,74
MgO	10,14	10,17	10,10	10,14	10,46	10,35	10,46	10,42
MnO	,34	,33	,31	,35	,31	,35	,36	,33
TOTAL	99,66	99,53	99,53	99,38	99,35	99,51	99,53	99,26
	CATIONS PER 32 OXYGENS							
Ti	,165	,156	,161	,142	,159	,176	,147	,141
Fe^{2+}	,165	,156	,161	,142	,159	,176	,147	,141
Cr	10,742	10,674	10,695	10,680	10,490	10,496	10,462	10,439
Al	4,608	4,672	4,674	4,707	4,844	4,860	4,910	4,918
Fe^{3+}	,317	,340	,306	,326	,346	,289	,331	,358
Fe^{2+}	4,005	3,995	4,025	3,999	3,900	3,938	3,900	3,911
Mg	3,919	3,931	3,906	9,923	4,031	3,984	4,020	4,016
Mn	,074	,072	,068	,076	,067	,076	,078	,072
MMF	,484	,486	,482	,486	,498	,491	,498	,497
Y_{Cr}	,685	,680	,682	,679	,668	,670	,666	,664
Y_{Al}	,294	,297	,298	,299	,308	,310	,312	,312
Y_{Fe^3}	,020	,021	,019	,020	,022	,018	,021	,022
FFF	,070	,075	,068	,072	,078	,065	,075	,081
	Distance above base of layer/cm							
	0,32	0,42	0,58	0,97	1,26	1,46	1,76	2,09

TABLE 20 (Continued):

Analysis No.	9	10	11	12	13	14	15	16
TiO_2	,73	,66	,63	,63	,62	,58	,59	,58
Cr_2O_3	51,35	50,72	49,89	49,48	50,25	52,21	49,20	49,54
Al_2O_3	16,39	17,24	17,64	17,52	16,82	15,04	17,04	17,08
Fe_2O_3	1,83	2,06	2,10	2,64	2,68	2,49	3,01	2,88
FeO	18,85	18,51	18,40	18,11	18,71	20,51	22,32	21,47
MgO	10,52	10,78	10,73	10,92	10,51	9,22	8,30	8,85
MnO	,35	,50*	,49*	,47*	,47*	,49*	,55*	,54*
TOTAL	100,02	100,47	99,88	99,77	100,06	100,54	101,01	100,94

CATIONS PER 32 OXYGENS

Ti	,140	,126	,121	,121	,119	,113	,114	,112
Fe^{2+}	,140	,126	,121	,121	,119	,113	,114	,112
Cr	10,410	10,190	10,055	9,982	10,170	10,695	10,017	10,053
Al	4,952	5,162	5,299	5,268	5,074	4,592	5,171	5,166
Fe^{3+}	,354	,396	,404	,508	,517	,487	,584	,558
Fe^{2+}	3,902	3,809	3,803	3,745	3,887	4,331	4,694	4,497
Mg	4,021	4,083	4,077	4,153	4,010	3,561	3,186	3,386
Mn	,076	,108	,106	,101	,102	,107	,120	,117
MMF	,498	,509	,509	,517	,500	,444	,398	,423
Y_{Cr}	,662	,647	,638	,633	,645	,678	,635	,637
Y_{Al}	,315	,327	,336	,334	,321	,291	,327	,327
Y_{Fe^3}	,022	,025	,025	,032	,032	,030	,037	,035
FFF	,080	,091	,093	,116	,114	,098	,108	,107
	Distance above base of layer/cm							
	2,32	3,72	3,76	3,94	4,03	4,99	5,40	5,95

1 - 11: Polygonal chromite grains in the chromitite
12: Large grain at top contact; no annealed texture (110 microns in diameter)
13: Euhedral intergranular chromite grain at level of first appearance of olivine
14: Chromite in mantle around olivine crystal
15: Euhedral chromite grain in reaction-replacement orthopyroxene; silicate-rich domain
16: Chromite (500 microns in diameter) in mantle around olivine crystal
1 - 9: Analyzed at University of Cape Town
10 - 16 Analyzed at Rhodes University
MnO = MnO* - 0,01[Cr_2O_3]

It should be stressed that the H chromitite layer marks the transition from meso- and adcumulate-textured feldspathic bronzitites to adcumulate-textured dunites in which no cumulus orthopyroxene is present. Hatton and von Gruenewaldt (1984) have proposed that the C_3 subunit crystallized from a new irruption of ultramafic magma emplaced near the base of the existing liquid column. They envisage that mixing of the new influx with pyroxenitic liquid in the chamber ultimately induced the crystallization of olivine and chromite from the hybrid melt. If the new influx of magma was injected at the floor, however, a degree of liquid mixing with fractionated, Cr-depleted melt may occur at the base (Eales and Reynolds, 1985). Hence, chromite with intermediate compositions would crystallize from the thin basal zone of hybrid magma and should ultimately show a compositional change to relatively Cr_2O_3-enriched compositions with increasing stratigraphic height. However, the opposite is observed within the H chromitite layer and its immediate hanging-wall. Although the Cr-depletion trend may be indicative of crystallization from a restricted melt volume, it will be shown in the subsequent text that the compositional changes mentioned above are in fact intermediate between Cr_2O_3-rich chromite compositions within the C_2 subunit bronzitites and Cr_2O_3-depleted compositions within the overlying dunites of the C_3 subunit.

LG 6A CHROMITITE LAYER

Table 21 presents the compositional variation of chromite within the LG 6A chromitite layer (drill core ZS7) in relation to stratigraphic height. Fig. 32 provides a depiction of the analytical data and the major features stressed here are (a) the subdued compositional variation within massive chromite domains, and (b) the compositional differences between weakly disseminated chromite in silicate partings and polygonal chromite within the massive domains. It is evident from the data that the MMF ratio of chromite occluded by reaction-replacement orthopyroxene (analysis 10 in Table 21) is higher than in the juxtaposed massive ore, a particularly anomalous feature, whereas the MMF ratio of chromite occluded by olivine (analysis 17) is drastically depressed. Furthermore, these changes are linked to a

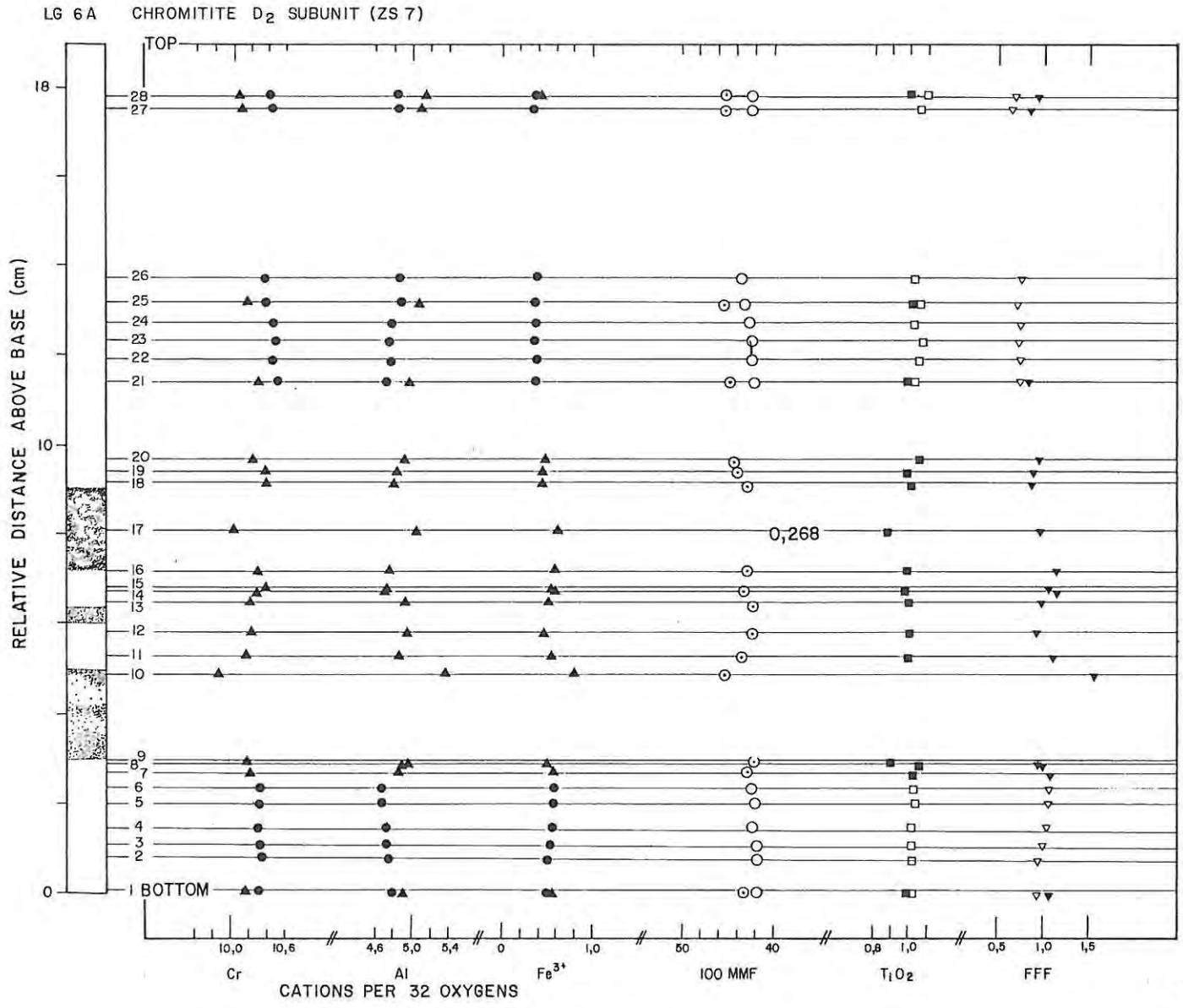

Chromite - Bronzitite (+ Pegmatitic Olivine)

Chromitite

SYMBOLS:	Cr	Aℓ	Fe^{3+}	MMF	TiO_2	FFF
RHODES	▲	▲	▲	⊙	■	▼
UNIV. OF CAPE TOWN	●	●	●	○	□	▽

FIG. 32 LOG OF LG 6A CHROMITITE (DRILL CORE ZS 7), WITH ANALYTICAL DATA.

TABLE 21: MICROPROBE ANALYSES OF CHROMITE WITHIN THE LG 6A CHROMITITE LAYER (DRILL CORE ZS7)

Analysis	1	2	3	4	5	6	7	8	9	10	11	12	13	14
TiO_2	1,03	1,03	1,02	1,02	1,04	1,03	1,03	1,06	,90	n.a.	,99	1,00	1,00	,96
Cr_2O_3	49,56	49,93	49,40	49,66	49,81	49,77	49,60	49,61	49,34	47,82	49,67	49,67	49,58	49,36
Al_2O_3	15,49	15,37	15,17	15,31	15,18	15,14	15,76	15,96	16,11	17,56	15,99	16,08	16,03	15,37
Fe_2O_3	2,48	2,52	2,67	2,83	2,91	2,92	2,89	2,61	2,49	4,11	2,95	2,42	2,61	2,98
FeO	21,41	21,53	21,32	21,35	21,50	21,39	21,25	21,37	21,39	20,07	21,11	21,36	21,49	20,88
MgO	8,69	8,68	8,62	8,77	8,71	8,74	8,97	9,02	8,73	9,40	9,13	8,93	8,87	8,96
MnO	0,40	0,41	0,38	0,38	0,39	0,38	,39	,32	,41	n.a.	,41	,41	,39	,37
NiO	n.a.	n.a.	n.a.	n.a.	n.a.	n.a.	,07	n.a.	,05	n.a.	,05	n.a.	n.a.	n.a.
TOTAL	99,06	99,47	98,58	99,32	99,54	99,37	99,96	99,95	99,42	98,96	100,30	99,87	99,97	98,88
	CATIONS PER 32 OXYGENS													
Ti	0,203	0,203	0,202	0,201	0,205	0,203	,201	,207	,177	-	,193	,195	,195	,190
Fe^{2+}	0,203	0,203	0,202	0,201	0,205	0,203	,201	,207	,177	-	,193	,195	,195	,190
Cr	10,302	10,348	10,332	10,302	10,325	10,331	10,20	10,189	10,194	9,820	10,163	10,208	10,188	10,265
Al	4,799	4,748	4,729	4,734	4,690	4,684	4,830	4,886	4,961	5,375	4,877	4,926	4,910	4,764
Fe^{3+}	0,491	0,497	0,533	0,560	0,574	0,578	,567	,511	,491	,805	,574	,475	,511	,591
Fe^{2+}	4,505	4,517	4,516	4,485	4,509	4,495	4,422	4,437	4,498	4,360	4,377	4,449	4,478	4,404
Mg	3,406	3,392	3,399	3,430	3,404	3,420	3,478	3,493	3,401	3,639	3,522	3,460	3,436	3,513
Mn	0,089	0,091	0,085	0,084	0,087	0,084	,086	,070	,091	-	,090	,090	,086	,082
Ni	-	-	-	-	-	-	-	-	-	-	-	-	-	-

MMF	0,419	0,418	0,418	0,422	0,419	0,421	0,429	0,429	0,421	0,454	0,435	0,426	0,423	0,433
Y_{Cr}	0,660	0,663	0,662	0,660	0,662	0,662	0,653	0,653	0,651	0,613	0,650	0,654	0,652	0,657
Y_{Al}	0,307	0,304	0,303	0,303	0,300	0,300	0,309	0,313	0,317	0,335	0,312	0,315	0,314	0,305
$Y_{Fe^{3+}}$	0,031	0,031	0,034	0,035	0,036	0,037	0,036	0,032	0,031	0,050	0,036	0,030	0,032	0,037
FFF	0,094	0,095	0,101	0,106	0,108	0,109	0,109	0,099	0,095	0,155	0,111	0,092	0,098	0,113
	Distance above base of layer/cm													
	0,05	0,83	1,14	1,43	1,99	2,40	2,72	2,94	2,97	5,01	5,27	5,79	6,45	6,68

Analysis	15	16	17	18	19	20	21	22	23	24	25	26	27	28
TiO_2	,98	,99	,88	1,01	,98	1,06	1,03	1,06	1,07	1,03	1,06	1,03	1,06	1,09
Cr_2O_3	50,37	50,18	47,56	50,55	50,21	49,95	49,91	49,74	49,92	49,91	49,93	49,92	49,83	49,69
Al_2O_3	15,35	15,51	16,01	15,72	15,64	16,13	15,01	15,18	15,16	15,31	15,73	15,72	15,43	15,46
Fe_2O_3	2,73	3,06	3,16	2,28	2,26	2,46	1,83	1,88	1,81	1,90	1,76	1,95	1,59	1,73
FeO	21,10	21,30	26,49	21,31	20,78	20,88	21,06	20,99	21,03	20,96	21,03	20,81	21,13	21,13
MgO	9,03	9,03	5,47	9,05	9,18	9,36	8,66	8,75	8,77	8,83	8,98	9,09	8,70	8,76
MnO	,36	,40	,44	,37	,38	,35	,34	,37	,35	,38	,34	,38	,40	,37
NiO	,05	n.a.	,08	n.a.	n.a.	,07	n.a.	n.a.	n.a.	n.a.	n.a.	n.a.	n.a.	n.a.
TOTAL	99,97	100,47	100,09	100,29	99,43	100,26	97,84	97,97	98,11	98,32	98,83	98,90	98,14	98,23
	CATIONS PER 32 OXYGENS													
Ti	,195	,190	,192	,193	,176	,197	,192	,206	,213	,204	,209	,203	,211	,216
Fe^{2+}	,195	,190	,192	,193	,176	,197	,192	,206	,213	,204	,209	,203	,211	,216
Cr	10,188	10,265	10,370	10,281	9,998	10,358	10,360	10,199	10,471	10,438	10,365	10,351	10,441	10,397
Al	4,910	4,764	4,710	4,736	5,016	4,801	4,810	4,909	4,739	4,772	4,867	4,858	4,819	4,821
Fe^{3+}	,511	,591	,536	,597	,634	,446	,445	,480	,361	,379	,348	,385	,318	,346
Fe^{2+}	4,478	4,404	4,405	4,424	5,716	4,422	4,345	4,305	4,452	4,433	4,409	4,362	4,473	4,461
Mg	3,436	3,513	3,505	3,488	2,168	3,496	3,571	3,603	3,468	3,481	3,514	3,553	3,437	3,456
Mn	,086	,082	,079	,088	,099	,081	,084	,076	,078	,085	,075	,084	,089	,082
Ni	-	-	,010	-	,017	-	-	,014	-	-	-	-	-	-
MMF	,432	,430	,268	,430	,440	,444	,422	,426	,426	,428	,432	,437	,423	,424
Y_{Cr}	,664	,658	,638	,663	,663	,654	,674	,670	,672	,669	,665	,663	,670	,667
Y_{Al}	,301	,303	,320	,307	,308	,314	,302	,305	,304	,306	,312	,311	,309	,309
$Y_{Fe^{3+}}$	,034	,038	,040	,028	,028	,030	,023	,024	,023	,024	,022	,024	,029	,022
FFF	,104	,114	,097	,088	,089	,096	,072	,074	,071	,075	,070	,077	,063	,068
	Distance above base of layer/cm													
	6,77	7,18	8,07	9,13	9,34	9,63	11,35	11,86	12,27	12,67	13,08	13,66	17,45	17,78

All analyses are representative of core-domains.

1 - 6: Analyzed at University of Cape Town (polished section B3)
7 - 20: Analyzed at Rhodes (polished section B2 and B1)
21 - 28: Analyzed at University of Cape Town (polished section MID and TOP)
9: Adjacent to silicate parting in chromitite. Grains show numerous silicate inclusions at this level
10: Euhedral grain occluded by large orthopyroxene oikocryst within ultramafic pegmatite assemblage
17: Subrounded grain occluded by large olivine oikocryst within ultramafic pegmatite assemblage

All other analysis are of polygonal chromite grains within annealed domains. n.a. Not analyzed

The uppermost portion of the chromitite (polished section "TOP") shows microbrecciation and alteration of chromite to ferritchromite along grain boundaries and cracks.

relative rise in Al and Fe^{3+} cations and depletion in Cr. Adjacent chromite grains within the massive ore depict compositions intermediate between these extremes and those of chromite removed from the lithological contacts. Orthopyroxene and olivine within the silicate parting are related to an ultramafic pegmatite assemblage which has not disrupted the fine-scale layering of the original orthopyroxene-chromite parting; parallel chromite stringers are continuous through large olivine crystals showing strain deformation lamellae. The cryptic trends adjacent to these replaced domains suggest that chromite reacted with a high-temperature metasomatic fluid, and subsequent diffusive homogenization of the zonal structures induced intermediate bulk compositions. Ingress of the fluid into the massive chromite assemblage is probably facilitated by the higher, residual interstitial volume adjacent to the contacts, where the efficacy of annealing is impaired.

By virtue of the level of analytical precision attained at the respective Universities, no long-term, cryptic compositional changes can be said to be unequivocally indicated within this exposure of the LG 6A chromitite layer (Fig. 32). However, there is a suggestion of small-scale, cyclic variations in the proportions of Cr, Al and Fe^{3+} cations, which are linked to variations in the MMF ratios. For example, there is a progressive decline in Cr and increase in Al cations and MMF ratios through the +11 to +14 cm interval. The proportion of Fe^{3+} cations is, however, remarkably constant ($x = 0{,}370$; $s = 0{,}013$). A similar trend is evident within the +9 to +10 cm interval, but the compositional change in the basal 2 cm of the chromitite reflects Fe^{3+} cations proxying for Al^{3+} cations in the chromite lattice, with Cr^{3+} contents and MMF ratios remaining constant. The reciprocal relationship between the proportions of Al^{3+} and Fe^{3+} cations at this level is clearly illustrated by the Y_{Al} and $Y_{Fe^{3+}}$ ratios, which are presented in Table 21 (analyses 1 to 6). These systematic variations cannot be attributed to factors such as instrumental drift, for example. The specimen current was continuously monitored during analyses and preselected chromite grains were analyzed at random from two different polished sections mounted side by side.

Silicate partings within the LG 6A chromitite layer are minor lensoid structures of restricted lateral extent. In conjunction with the compositional variability of chromite within and adjacent to the ultramafic pegmatite assemblages, it is therefore suggested that the pattern of variation within the +3 to +9 cm interval does not reflect the magmatic conditions attending initial crystallization. The subtle increase in TiO_2 contents, from 1,02 wt. per cent (s = 0,016; n = 7) at the base of the layer to 1,07 wt. per cent (s = 0,001; n = 6) at the top, is somewhat anomalous in terms of the depletion trends noted in the C and H chromitite layers. However, the occurrence of interstitial rutile intergrown with ilmenite at the +12 cm level (Fig. 26(A)), within a zone of massive chromite ore, suggests that Ti-saturation of chromite was maintained during formation of the LG 6A chromitite at this location. Analysis of a chip sample of the LG 6A chromitite in drill core ZS3 indicates an average TiO_2 content of 0,69 wt. per cent, associated with an oxidation ratio of 0,261. The latter is more than double that of the ZS7 exposure, which declines from an average of 0,103 (n = 7) in the basal portion of the chromitite to an average of 0,077 at the top (n = 6). Given that the textural and mineralogical environments of chromite within the LG 6A chromitite layer are identical in both exposures, the discrepancy in oxidation ratios is thus wholly anomalous. Subsolidus re-equilibration with silicate phases can clearly be discounted, and it must thus follow that the compositional differences point to the influence of some fluid phase (i.e., either a primary magmatic feature or fumarolic ingress and migration of some other derivative under contrasting redox conditions). With respect to the notions that (a) the oxidation ratio of chromite within massive ore domains reflects the fO_2 conditions attending crystallization, and (b) periodic increases in fO_2 trigger copious nucleation of chromite to yield anchimonomineralic chromitite layers, the analytical data thus yield no supportive evidence of either. Hence, at this juncture, suffice it to conclude that there appears to be some evidence of a bottom crystallization mechanism, with nutrients drawn from a limited volume of magma adjacent to the crystalline floor.

To summarize, detailed analytical traverses through chromitite layers from different subunits facilitate recognition of (a) vertical

compositional gradients in two thinner layers that differ in sense but span the thickness of the layer, and (b) a stacked series of compositional gradients in a thicker chromitite layer. These gradients are defined in terms of variations in MMF ratios, TiO_2 contents and in the proportions of Cr, Al and Fe^{3+} cations. The subtle, grain-to-grain compositional changes are regarded as being irreconcilable with mechanisms such as long-range settling of chromite crystals or deposition from density currents to account for the origin of chromitite layers in the Ruighoek Pyroxenite. Furthermore, the study has shown that lateral changes in chromite composition can occur within a given chromitite layer, at least at the level of the LG 6A chromitite. It is not known whether smooth, horizontally disposed compositional gradients also exist, i.e., a situation which would be consistent with the down-dip accretion model of Irvine et al. (1983). However, a mechanism which may account for this feature is upward, fumarolic migration of hydrogen-enriched residual melt through the crystal mush in geologically localized areas (for example, as proposed by Buntin et al. (1983) to account for the reduced chemistry of spinels within pothole structures in the Merensky Reef footwall).

5.4.2 CHROMITE IN SILICATE - RICH ROCKS

5.4.2.1 CHROMITE WITHIN THE B UNIT

Table 22 presents microprobe analyses of chromite within silicate-rich domains of the B unit. Fig. 33 depicts a log of the succession and shows the variation of the oxides TiO_2, Al_2O_3 and Cr_2O_3, and of the MMF ratio, in relation to stratigraphic height. Data pertaining to chromite within the LG 2 and C chromitite layers are also shown. Features portrayed here are (a) the high degree of compositional diversity of chromite within silicate-rich domains relative to chromite within chromitite layers, and relative to cryptic changes with stratigraphic height, (b) the higher MMF ratios of chromite within chromitite layers, (c) the antipathetic relationship between Al_2O_3- and Cr_2O_3-contents, with higher TiO_2 contents linked to high Cr_2O_3 contents, and (d) chromite occluded by cumulus orthopyroxene is

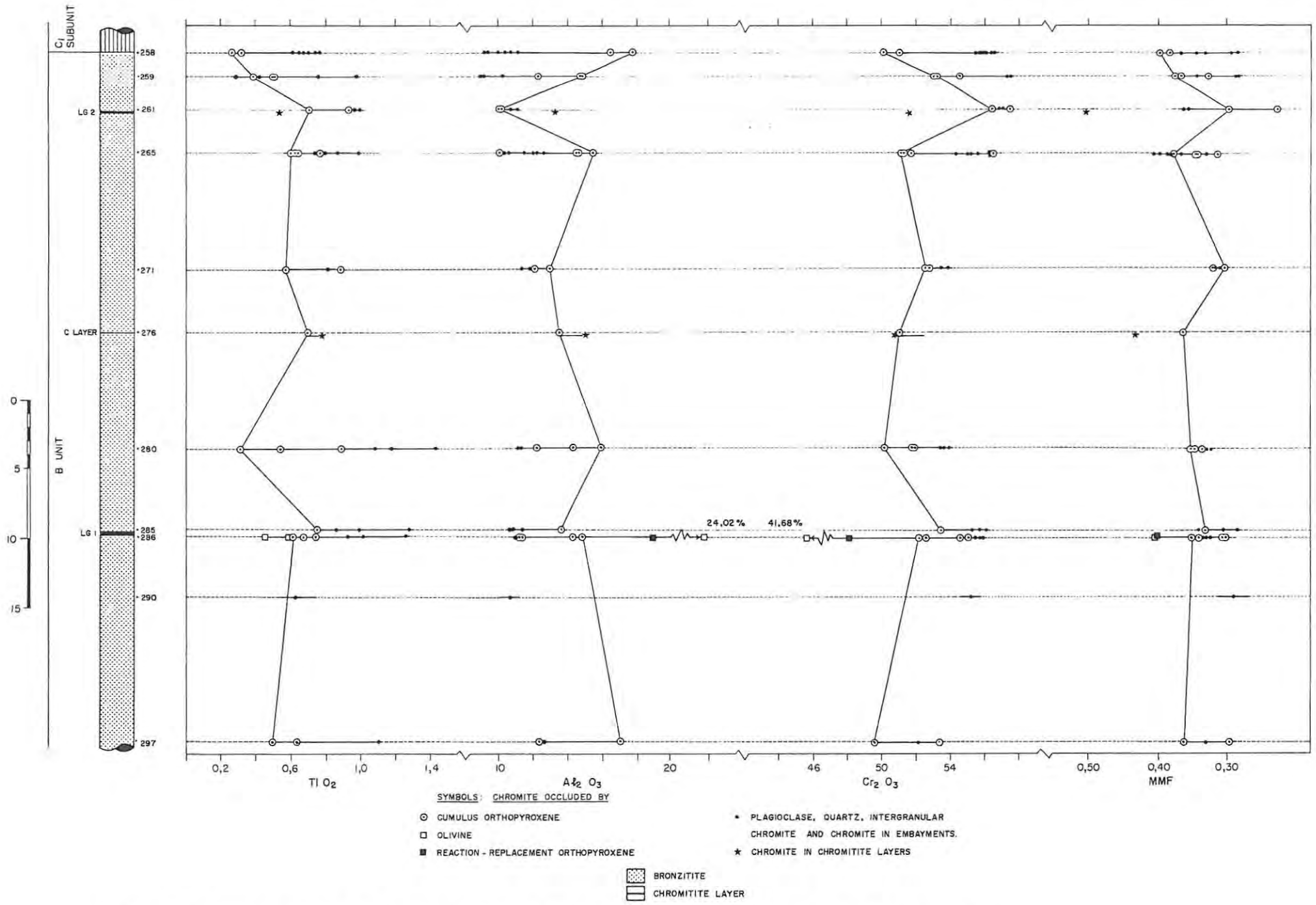

FIG. 33 LOG OF THE B UNIT SUCCESSION, WITH CHROMITE ANALYTICAL DATA. COMPOSITIONAL PROFILES LINK GRAINS OCCLUDED IN ORTHOPYROXENE.

depleted in Cr_2O_3 relative to chromite intergrown with intercumulus silicate phases (with the exception of sample 261). The main objective of the subsequent text is to illustrate the relative influence of grain-size and textural environment on chromite chemistry. In this spirit, attention is drawn to specific examples.

Sample 297 is a plagioclase-bearing bronzitite hosting accessory chromite, some 15 metres below the LG 1 chromitite layer. Plagioclase is the predominant intercumulus silicate phase and is intergrown with a number of chromite grains which are larger than those occluded by orthopyroxene. This relationship is found throughout the succession of layered rocks, with chromite crystals of intermediate grain-sizes commonly found encapsulated within the rim-domains of well-formed orthopyroxene crystals. The domain selected for analysis shows a chromite grain, 80 microns in diameter, enclosed within the core-domain of an orthopyroxene crystal, a 60 micron diameter grain occluded within the rim-domain of the same crystal and another, 200 microns in diameter, intergrown with plagioclase in a juxtaposed interstice. The analytical results, denoted 297/1, 2 and 3, respectively, are presented in Table 22, and the salient features may be summarized as follows:

Number	1	2	3
TiO_2	0,49	0,63	1,10
Cr_2O_3	49,61	53,42	52,19
Al_2O_3	16,97	12,34	12,61
MMF	0,362	0,297	0,334
Cr/Al	1,96	2,90	2,78
HOST	opx core	opx rim	plag

These data are representative of core-domains within the chromite grains. It is evident that the grain intergrown with plagioclase, and the grain occluded within the rim of the orthopyroxene crystal, is enriched in TiO_2 and Cr_2O_3 relative to the grain depicted in the

orthopyroxene core-domain. The MMF ratio of the latter is higher, a feature which is generally observed in the B unit (Fig. 33).

Fig. 34 depicts typical textural environments of chromite grains within sample 265, which is a more feldspathic bronzitite some 2,8 metres below the LG 2 chromitite layer. As is the case with most chromite-poor bronzitites, only a few small chromite grains are enclosed within orthopyroxene; the majority are generally greater than 200 microns in diameter and are intergrown with plagioclase. It is evident from the textural relationships portrayed in Fig. 34 that substantial in situ secondary growth of orthopyroxene has occurred, resulting in chromite grains being indented in cupolas or embayments on the pyroxene grain boundaries. Furthermore, the sympathetic configuration of the orthopyroxene and juxtaposed chromite grain boundaries indicates that in situ secondary enlargement of both crystalline phases must have taken place contemporaneously to produce these textures, i.e., both chromite and orthopyroxene competed for available nutrients in the interstitial melt. Microprobe analyses of chromite within these environments are presented in Table 22 and are denoted 265/1 to 265/10. Cr_2O_3 contents range from 51,31 wt. per cent for chromite occluded by orthopyroxene (analysis 265/3) to 56,37 wt. per cent for a grain with a diameter of 340 microns and intergrown with plagioclase (analysis 265/10). Analysis 265/4 is a special case and will be discussed later. Grain-sizes of chromite intergrown with plagioclase vary between 110 and 340 microns, with the larger grains tending to be more anhedral. The average measured grain-size of chromite occluded within orthopyroxene is 60 microns, with ca. 90 microns representing the upper limit. The analyses are representative of core compositions and two features are evident from the data. Firstly, consider the data pertaining to chromite occluded by orthopyroxene (analysis 265/1 to 265/3). The 60 micron diameter crystals have lower MMF ratios (0,345) than an 80 micron diameter crystal (0,379), whereas the concentrations of Cr_2O_3 and Al_2O_3 are comparable. The second case, of chromite intergrown with plagioclase, shows the opposite: small grains have higher MMF ratios and Al_2O_3 contents relative to larger grains. The grain-size measurements represent minimum diameters of a given crystal and should not be regarded as accurate: problems arise from the orientation of the crystal, the component of anhedralism and

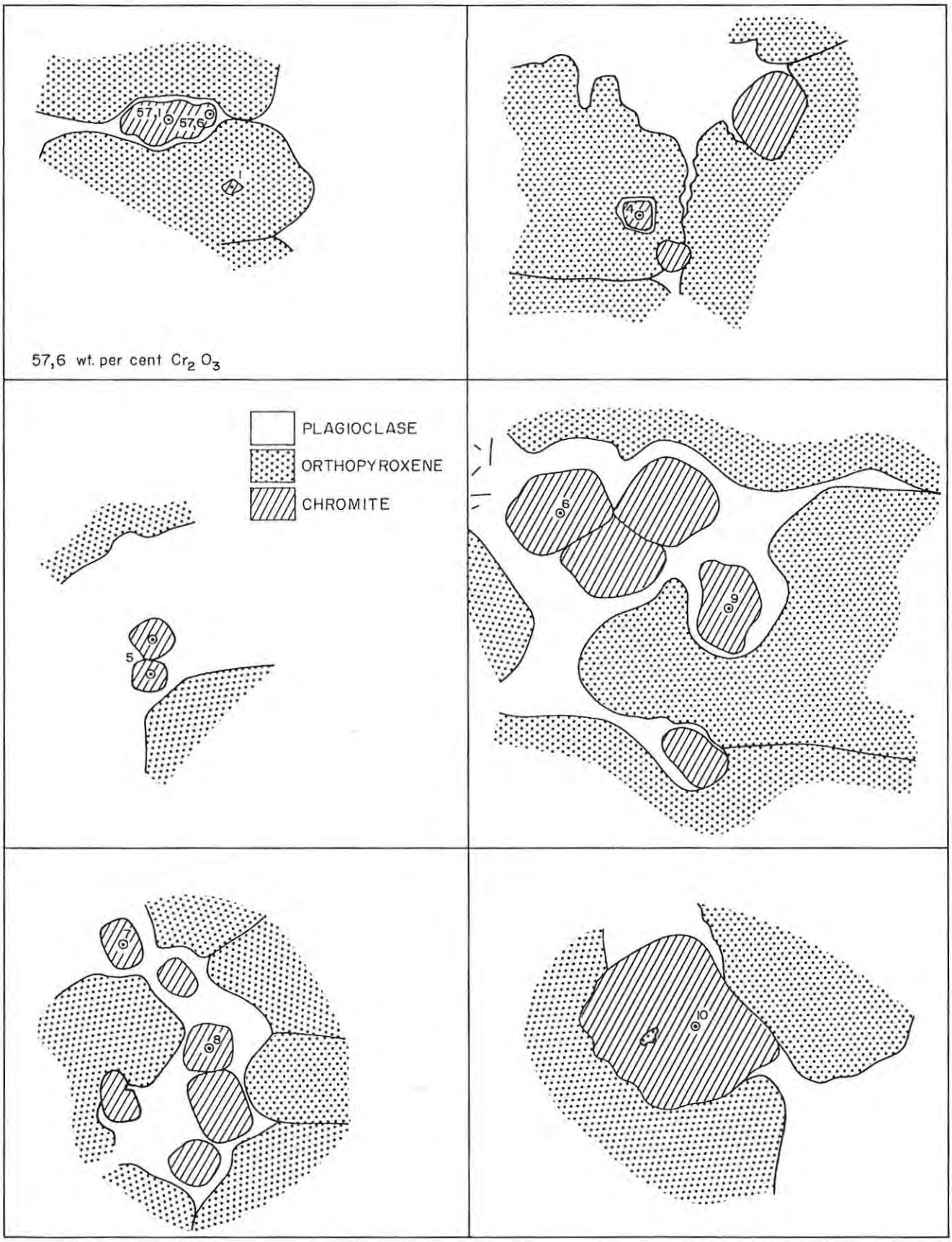

FIG. 34 ILLUSTRATION OF THE RELATIVE GRAIN-SIZES AND TEXTURAL ENVIRONMENTS OF ANALYZED CHROMITE GRAINS IN SAMPLE 265 (B UNIT 337,5 METRES DEPTH). [4] ANALYSIS NUMBER (SEE TABLE 22) ; ⊙ POSITION OF ELECTRON BEAM ; [>/] ACICULAR NEEDLES OF RUTILE OR TITANOMAGNETITE IN PLAGIOCLASE.

sectioning effects in larger crystals. For example, analysis 265/4 is representative of a rounded chromite grain showing a circumjacent selvage of plagioclase and wholly enclosed within the apical domain of a well-formed orthopyroxene crystal. In view of the textural variants depicted in Fig. 34, this feature is clearly indicative of a chromite grain residing in an embayment and does not reflect reaction between chromite and orthopyroxene with plagioclase as the product. Hence, analysis 265/4 is regarded here as being representative of the rim-domain of a large crystal residing in the intercumulus volume.

In an attempt to reconcile the compositional variation depicted in Fig. 33, attention was given to the following arithmetic exercise. Firstly, it was assumed that a Cr_2O_3 content of ca. 50 wt. per cent, shown by chromite grains enclosed within orthopyroxene core-domains, is representative of early-formed grains that were isolated from melt via encapsulation. Secondly, it was assumed that chromite grains with a protracted residence time in the interstitial magma receive additional growth increments until such time as dearth of nutrients, or encapsulation by intercumulus silicate phases, preclude further growth. Thirdly, in order to simplify the modelling procedure, it was assumed that successive growth increments are of constant Cr_2O_3 content and that diffusive homogenization within grains may eliminate zonal structures. The latter is confirmed in part by the present investigation which detected very subtle compositional gradients in large chromite grains occluded by plagioclase, mica and quartz. Relict zonal structures in small chromite grains were not detected. The assumption of constant Cr_2O_3 content is undoubtedly incorrect by virtue of the restricted melt volume, unless a hiatus in crystallization ensures that efficient communication with the supernatant liquid column is maintained. Fig. 35(A) portrays a theoretical asymptotic curve representing the compositional path of a chromite grain, with an initial Cr_2O_3 content of 50 wt. per cent, receiving successive growth increments (with a Cr_2O_3 content of 58 wt. per cent) followed by grain homogenization. Two important features arise from this exercise: (a) a limiting bulk composition is approached after the initial grain-size has doubled, i.e., the volume (V_o) has risen by a factor of eight, and (b) the bulk volume of the chromite grain ultimately imposes a compositional buffer. Fig. 35(B) depicts the disposition of measured data points relative to ideal

asymptotic relationships between Cr_2O_3 content and grain-size. Curve (A) represents successive increments of chromite containing 57 wt. per cent Cr_2O_3 and curve (B) those with 55 wt. per cent Cr_2O_3. The agreement with these curves suggests, therefore, that the model is applicable, viz., grain growth proceeds via successive increments of Cr_2O_3-enriched chromite, followed by grain homogenization. It is advocated here that enhancement of the activity of chromium in the interstitial melt by nucleation of plagioclase accounts for (a) accelerated chromite growth rates, and (b) the Cr-enriched compositions of chromite intergrown with plagioclase and the margins of orthopyroxene crystals. Confirmation is found in the higher TiO_2 contents (Fig. 33), zonal rises in Ti and Cr/Al towards the rims of some large chromite grains and the more restricted compositional variation of chromite in samples with a low modal abundance of plagioclase (e.g., sample 271). Within the feldspathic and chromitiferous bronzitite hanging-wall of the LG 2 chromitite layer (sample 261; Fig. 8A(iii)), analyses of two chromite grains occluded in a lobate extension of an orthopyroxene crystal indicate Cr_2O_3 contents of 56,51 and 57,51 wt. per cent, linked to MMF ratios of 0,229 and 0,299, respectively. These grains are approximately 140 microns in diameter and the compositional correspondence with plagioclase-hosted chromite (analysis 261/3) suggests that these grains were encapsulated after nucleation of plagioclase. Subsequent subsolidus re-equilibration with the orthopyroxene host, in conjunction with a higher $FeCr_2O_4$-component inherited prior to encapsulation, induced a marked decline in the MMF ratios.

The reactivity of chromite to its host environment can be illustrated by two further examples. Chromite occluded by intercumulus quartz (analysis 259/5) yields an analysis of 0,28 wt. per cent TiO_2, 57,52 wt. per cent Cr_2O_3 and an MMF ratio of 0,289. Quartz is intergrown with red, titanian phlogopite in this particular interstice, but the latter is not in contact with the chromite grain (which does not host exsolved rutile). In this instance, therefore, it is evident that the Ti content is less than that of small grains occluded in orthopyroxene and is substantially less than the Ti content of grains intergrown with plagioclase (refer to Fig. 33). However, the most

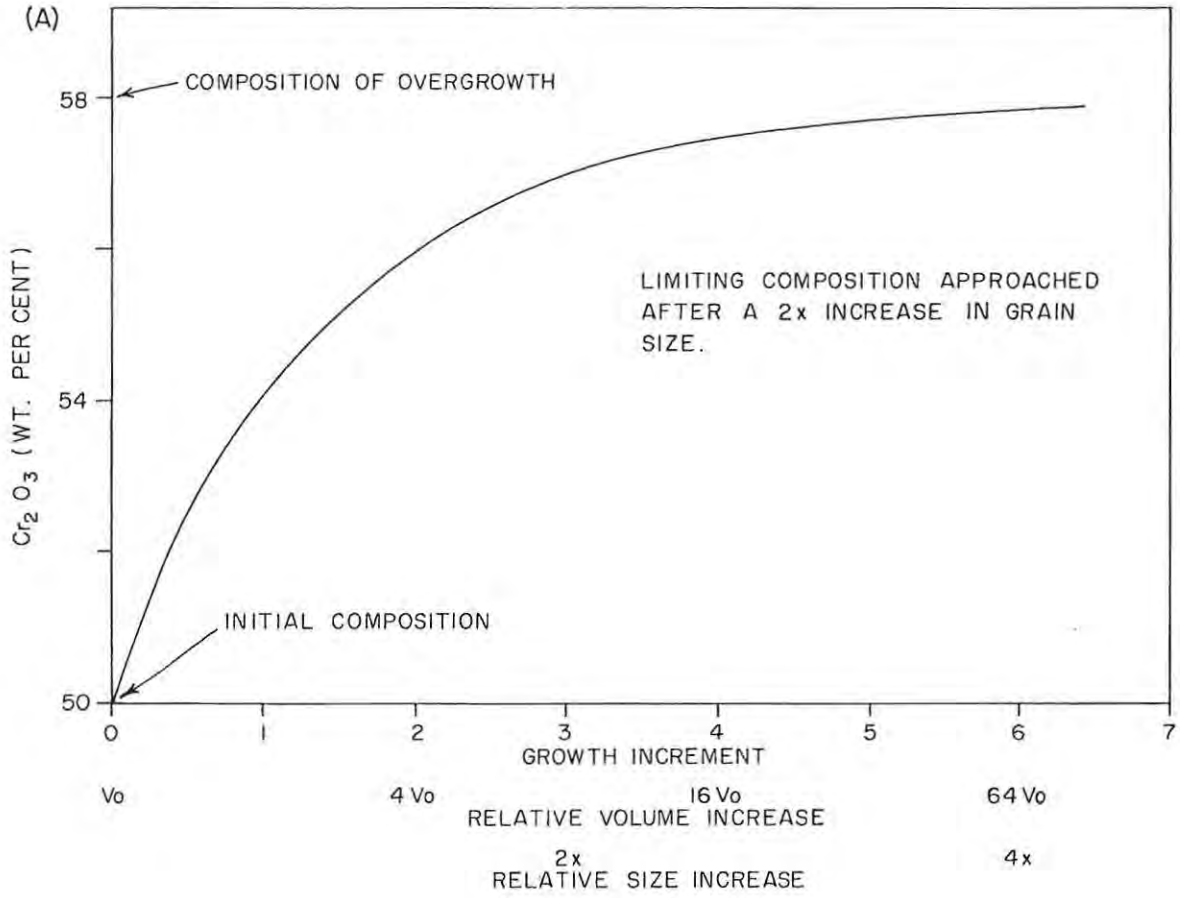

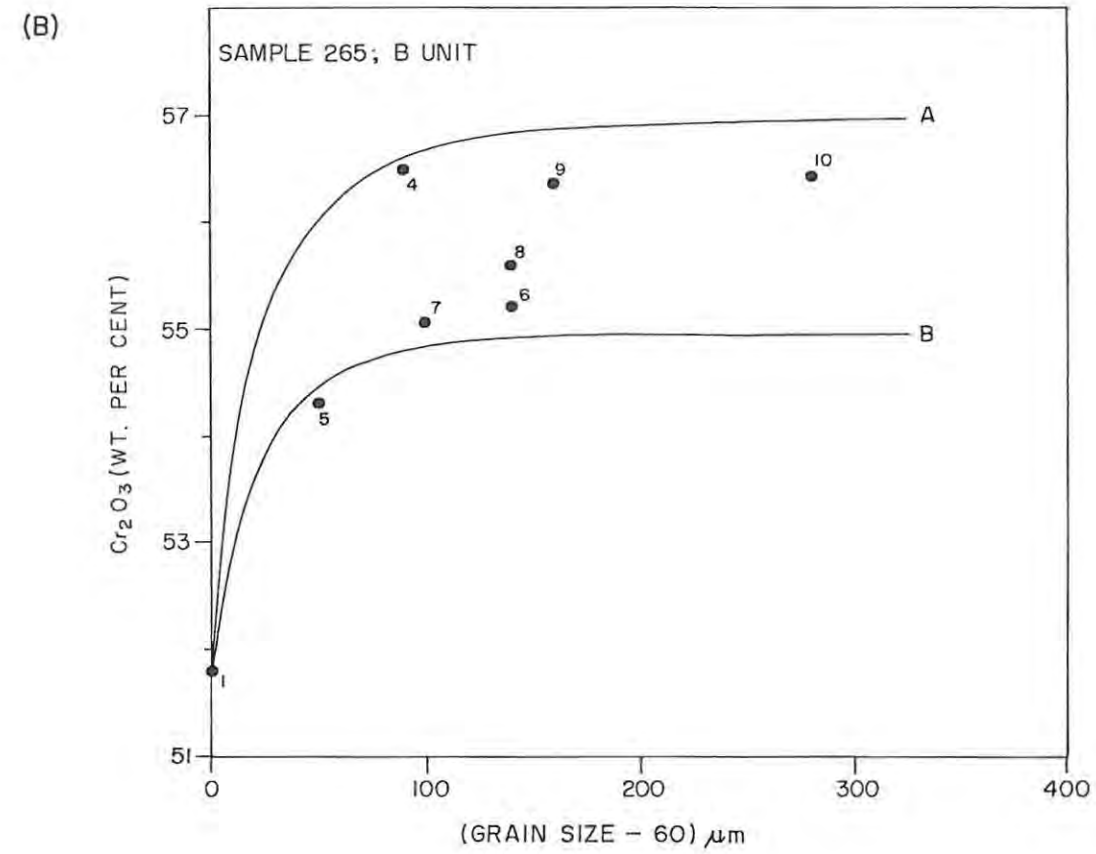

FIG. 35 PLOT OF Cr_2O_3 CONTENT IN CHROMITE AGAINST GRAIN-SIZE SHOWING (A) A HYPOTHETICAL ASYMPTOTIC RELATIONSHIP DEFINING GRAIN GROWTH ACHIEVED BY INCREMENTS OF Cr_2O_3-ENRICHED CHROMITE, AND (B) DISPOSITION OF DATA POINTS RELATIVE TO HYPOTHETICAL CURVES A AND B. SYMBOL: ($\bullet^{10}$) MICROPROBE ANALYSIS NUMBER

pronounced compositional changes occur within the thin zone of poikilitic harzburgite at the immediate footwall contact of the LG 1 chromitite layer (sample 286A). The Al_2O_3 content of grains occluded by olivine is 24,02 wt. per cent (analysis 286A/5), whereas the Al_2O_3 contents of chromite occluded by cumulus orthopyroxene and interumulus plagioclase within the juxtaposed bronzitite are 13,51 and 11,09 wt. per cent, respectively. Chromite occluded by reaction-replacement orthopyroxene (analysis 286/6) shows an intermediate composition of 18,84 wt. per cent Al_2O_3. These aluminous compositions are linked to higher MMF ratios (Fig. 33 and Table 22) and, in terms of the comparable compositional changes observed within silicate partings in the LG 6A chromitite layer, may reflect reaction with magnesian fluids of a pegmatite lineage. Paradoxically, equivalent compositional changes are concomitant with the appearance of cumulus olivine in the layered succession.

5.4.2.2 CHROMITE WITHIN THE C_1 SUBUNIT

Chromite associated with the first appearance of cumulus olivine at the base of the C_1 subunit depicts a cryptic transition to compositions enriched in the $MgAl_2O_4$-component. Microprobe analyses of chromite within the C_1 subunit are presented in Table 23. Fig. 36 provides a summary of the within-sample variation in TiO_2- and Al_2O_3-contents, and MMF ratios, and of the variation in relation to stratigraphic height. The following features are evident from the disposition of data points in Fig. 36 and inspection of Table 23:

1. Al_2O_3 contents of grains occluded by cumulus orthopyroxene rise to ca. 17 wt. per cent in the uppermost portion of the B unit and remain at this abundance through the C_1 subunit. However, associated MMF ratios rise with increasing stratigraphic height to an average value of 0,452 at the level of sample 249.
2. Al_2O_3 contents of grains occluded by olivine vary between 17,44 and 21,21 wt. per cent. No clear relationship between grain-size and Al_2O_3 content is evident.
3. MMF ratios of grains occluded by olivine are lower than for grains of comparable grain-size occluded by coexisting orthopyroxene.

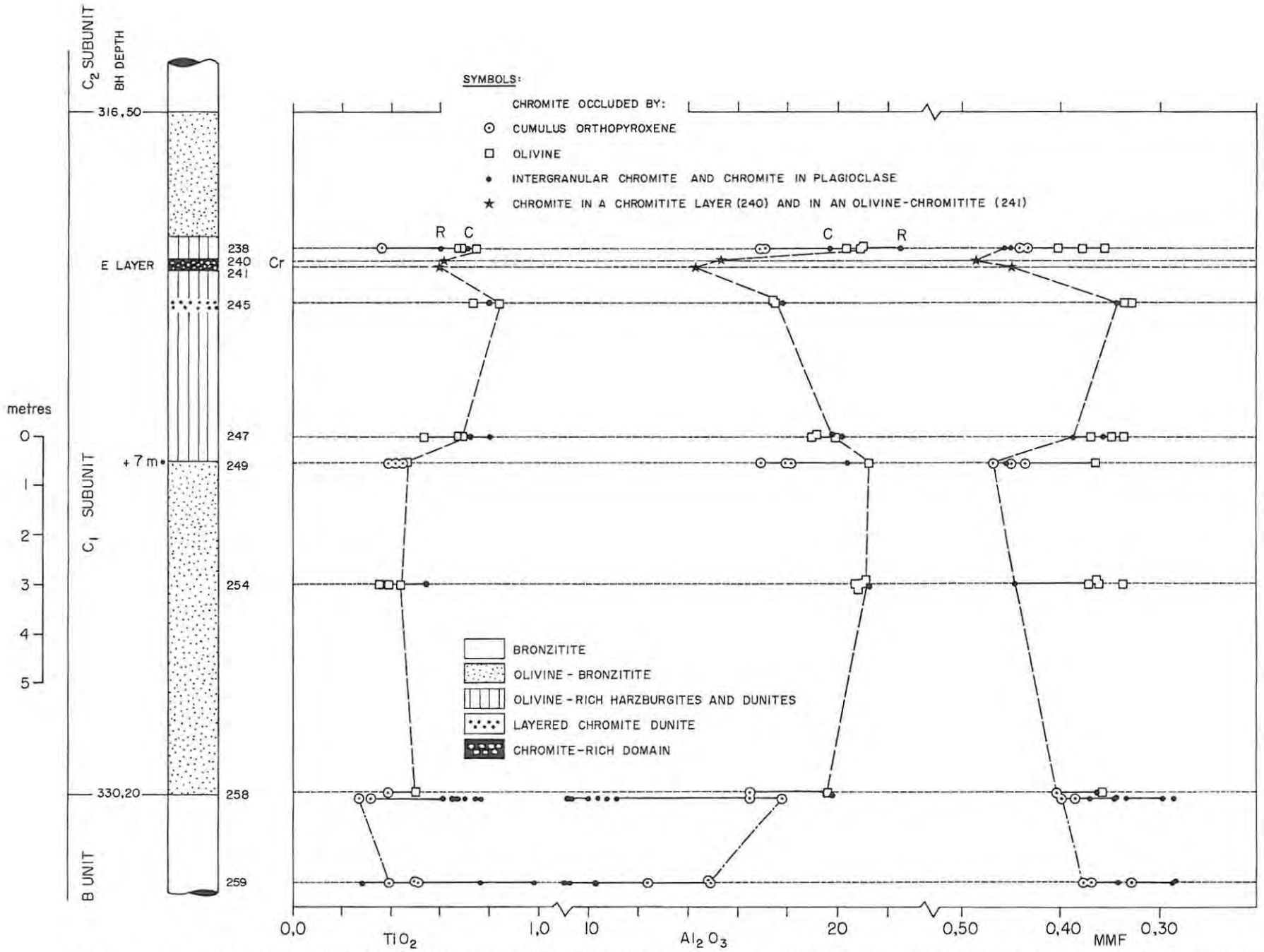

FIG. 36 LOG OF THE C_1 SUBUNIT SUCCESSION, WITH CHROMITE ANALYTICAL DATA. OXIDE CONTENTS EXPRESSED IN WT. %; C = CORE, R = RIM.

4. MMF ratios of coarse-grained chromite that is intergranular to olivine (i.e., located between olivine crystals with no intercumulus silicate phase present) are higher than for smaller occluded grains.
5. Chromite occluded by intercumulus plagioclase within a granular harzburgite (sample 238) is not enriched in Cr_2O_3 relative to chromite enclosed in cumulus orthopyroxene and olivine, but depicts a zonal rise in Al_2O_3 content. The MMF ratio is higher than for grains enclosed in the cumulus silicate phases.
6. Grains associated with chromitiferous rocks of the E chromitite horizon are significantly depleted in Al_2O_3 relative to chromite within the adjacent silicate-rich rocks. Fe_2O_3 contents are slightly lower (average of 1,95 wt. per cent) than in chromite from adjacent olivine-rich domains ($x = 2,17$ wt. per cent; $n = 10$), but stoichiometry is maintained primarily in terms of a reciprocal variation of Al and Cr contents.
7. Al_2O_3 contents of grains occluded by olivine rise from 19,56 wt. per cent at the base of the unit to 21,21 wt. per cent near the +7 metre level, then decline to 17,45 wt. per cent within 70 centimetres of the E chromitite layer. A further rise to 20,68 wt. per cent Al_2O_3 is evident in the harzburgite above the chromitite layer. A notable feature is the sympathetic variation in MMF ratios and Al_2O_3 contents within silicate-rich domains.
8. Grains occluded by orthopyroxene exhibit lower TiO_2 contents than grains occluded by coexisting olivine crystals.

The average Fe_2O_3 contents of chromite occluded by olivine and orthopyroxene crystals are 2,20 and 2,11 wt. per cent, respectively. These are slightly higher than the average Fe_2O_3 content of 1,95 wt. per cent displayed by coarse-grained chromite within chromite-rich rocks (samples 240 and 241). Chromite grains occluded by the cumulus silicate phases are generally less than 100 microns in diameter, with coarser grain-sizes depicted within the rim-domains. Grain-sizes coarser than ca. 200 microns are very rarely enclosed within olivine and orthopyroxene, but may be indented to varying degrees. Inclusions of chromite are more common in orthopyroxene than in olivine and, within olivine-orthopyroxene cumulate assemblages, the latter feature can be attributed to the relatively coarser grain-size of orthopyroxene. Intercumulus plagioclase and

clinopyroxene are generally not present in the granular- and adcumulate-textured assemblages which characterize the C_1 subunit.

Chromite grain-sizes within sample 241, representative of an olivine-chromitite assemblage in the footwall of the E chromitite layer, vary between 200 and 250 microns and annealed textures are only locally depicted (Fig. 37A). This contrasts with the overlying massive assemblage in which grain diameters vary between 600 and 1 000 microns (Fig. 37B). Primary grain-sizes are indicated in domains with a higher silicate content by euhedral grains 100 microns in diameter. Dispersed olivine crystals within the olivine-chromitite are 1 mm in diameter, whereas diameters of 2 to 4 mm are represented in the hanging-wall chromite dunite and footwall poikilitic harzburgite. The preponderance of relatively small chromite grains in the 8 cm thick olivine-chromitite layer (sample 241) is anomalous with respect to the gradational modal transition to 4 cm of chromite dunite, followed by an abrupt transition to large annealed grains within the overlying, thin chromitite layer, and points to arrested densification. Chains of chromite grains with a subvertical orientation may be depicted (Fig. 37C), recommending heterogeneous nucleation of chromite on a basal substratum of chromite crystals as a potential mechanism of origin (arborescent growth-forms within the UG 1 and UG 2 chromitite layers have been documented by Eales and Reynolds (1985)). A cursory examination of the latter assemblage by microprobe analysis showed a constant Al/Cr ratio of 0,401 through a vertical interval of 1 centimetre, whereas the Al/Cr ratio of chromite within the overlying chromitite was noted to rise from 0,429 to 0,446 with increasing stratigraphic height. Other than this apparent cryptic rise in Al/Cr from bottom to top of the chromite-rich horizon, which encompasses or may represent the E chromitite layer, a feature which clearly emerges from the data is the reciprocal relationship between modal chromite content and the Al/Cr ratio of chromite. For example, the Al/Cr ratio of grains within sample 245 (which exhibits a rhythmic and fine-scale repetition of dunite and chromite dunite layers) is 0,556, whereas weakly disseminated grains in olivine-rich sample 247 yield an average Al/Cr ratio of 0,650. Within silicate-rich domains, however, a dependence on the nature of the occluding silicate phase is also evident.

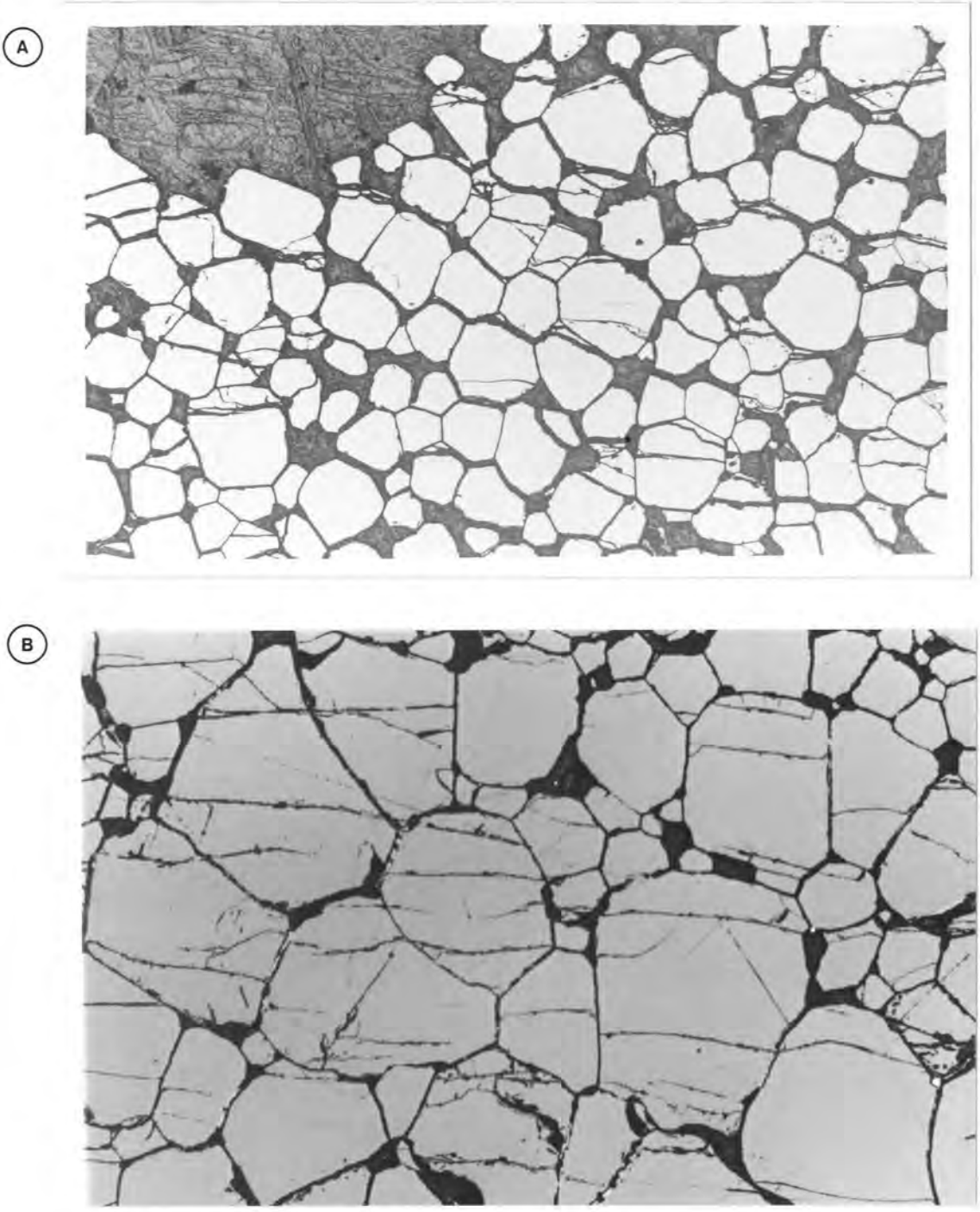

FIGS. 37(A) to (C): Photomicrographs of chromite within and in juxtaposition to the E chromitite layer, C_1 subunit. All sections photographed with plane polarized reflected light and the same degree of magnification. Scale 5cm = 1mm.

(A): Grains within an olivine-chromitite in the immediate footwall of the E layer (though this may represent the basal portion of the chromitite) exhibiting a low degree of grain annealing. Particle sizes are in the range 200 - 250 microns (sample 241).

(B): Advanced degrees of grain annealing within a massive domain of the E layer. Olivine crystals, or serpentine pseudomorphs, are not present; the mesostasis is represented by serpentine minerals. Coarse particle sizes within this domain vary between 600 and 1 000 microns, with smaller grains depicted in areas showing arrested annealing (thin section 240).

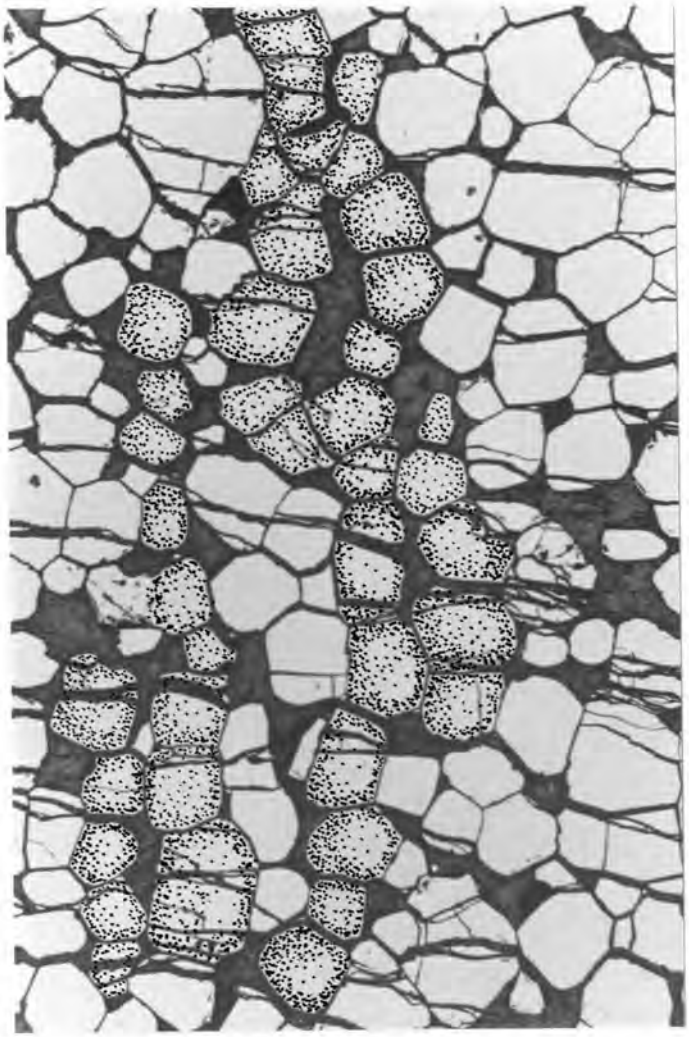

FIG. 37 (C): Putative arborescent or chain-like structures (growth-forms) linking individual grains (emphasized) within the olivine- chromitite layer shown in (A). The mesostasis is composed of serpentinized bastite. Preservation of this texture may be linked to arrested grain annealing, implied by the higher intercumulus space relative to other chromite-rich domains.

MB4AAD

It may be recalled that cumulus orthopyroxene crystals coexisting with olivine depict rim-compositions of higher Al/Cr ratios, stemming primarily from lower Cr_2O_3 contents. This zonal Cr-depletion trend is also manifested in the associated chromite. Samples 249 and 238 are cited here as examples. Chromite that is interstitial to cumulus orthopyroxene in sample 249 (analysis 249/5) exhibits a rim Al/Cr ratio of 0,664, whereas the Al/Cr ratio of chromite occluded by orthopyroxene is 0,531. Chromite intergrown with plagioclase in sample 238 (analysis 238/6) depicts core and rim Al/Cr ratios of 0,632 and 0,715, respectively, whereas orthopyroxene hosted grains show an average ratio of 0,510. Problematically, these rim compositions approximate to Al/Cr ratios of grains occluded by olivine.

5.4.2.3 CHROMITE WITHIN THE C_2 SUBUNIT

Table 24 presents microprobe analyses of chromite within 10 samples from the C_2 subunit. Compositional features indicated by the data are as follows:

1. Chromite occluded by olivine is enriched in Al_2O_3 (analyses 223/1, 223/2 and 213B/7).
2. Chromite occluded by orthopyroxene is depleted in TiO_2 and Cr_2O_3 relative to coarser-grained crystals intergrown with plagioclase.
3. Relative to chromite marking the abrupt upper contact of the LG 3 chromitite layer (analysis 213B/1), grains occluded by plagioclase and cumulus orthopyroxene in the immediately overlying bronzitite are enriched in Cr_2O_3 but exhibit lower MMF ratios.
4. Cr_2O_3- and TiO_2-contents of chromite enclosed in core-domains of orthopyroxene crystals are generally slightly lower than the contents depicted in larger grains encapsulated within rim-domains. The MMF ratios of the latter may be lower.
5. Subdued zonal increases of Cr content are depicted in chromite grains intergrown with plagioclase, mica and quartz.
6. Rim-domains of grains intergrown with mica and quartz are substantially depleted in TiO_2 relative to the cores.

Figs. 38(A) to (C) present a graphical summary of some of the abovementioned features. The data are consistent with the empirical model developed earlier, viz., that in situ growth of chromite is achieved contemporaneously with the nucleation of plagioclase in the residual melt volume. This would not apply to mica and quartz, which are late-stage crystallization products. The zonal rise in Cr content and depletion in Ti shown by grains in these domains (e.g., sample 211) is therefore adjudged to be the combined influence of (a) earlier nucleation of plagioclase, (b) reaction with intercumulus melt, and (c) preferential partitioning of Al and Ti into titanian phlogopite at subsolidus temperatures. The latter is emphasized by the magnitude of the compositional gradient (for example, from 0,97 wt. per cent TiO_2 in a core domain to 0,43 wt. per cent in the rim; analysis 211/6); more efficient grain homogenization by diffusion at higher temperatures would tend to flatten the gradient. A slight decline in TiO_2 content was noted in the rims of chromite grains intergrown with plagioclase in sample 203. However, this is more pronounced in sample 211 (analysis 211/5), where chromite is intergrown with a more sodic plagioclase. In samples such as 203, and 265 in the B unit, trace abundances of rutile needles intergrown with plagioclase may account for the absence of exsolved rutile lamellae in plagioclase-hosted chromite grains and the restricted range in TiO_2 contents.

In summation, small chromite grains occluded within cores of cumulus orthopyroxene crystals in a particular sample indicate (a) TiO_2-poor compositions (0,18 to 0,50 wt. per cent), and (b) Al_2O_3-enriched compositions relative to larger grains intergrown within orthopyroxene rims, and relative to substantially larger grains intergrown with intercumulus plagioclase. Cryptic, within-sample trends of rising Cr and Ti are linked to declining MMF ratios, but Fe_2O_3 contents are constant at low levels irrespective of textural environment or proximity to the LG 3 chromitite layer (Fig. 39). Chromite occluded by olivine within the thin poikilitic harzburgite zone above the LG 3 chromitite is identical in composition to analysis 286A/5, which is representative of Al_2O_3-enriched chromite occluded by olivine in the immediate footwall of the LG 1 chromitite layer. However, chromite occluded by olivine in the chromitiferous bronzitite footwall of the LG 3 leader chromitite (analysis 214A/8)

is only mildly depleted in Cr_2O_3 (50,56 wt. per cent) relative to chromite enclosed within adjacent orthopyroxene grains (52,72 to 54,60 wt. per cent; analyses 214A/5 and 6). The MMF ratios of the latter chromite grains average 0,405, whereas that of chromite intergrown with olivine is 0,325. Within the hanging-wall of the LG 3 chromitite layer, chromite grains occluded by olivine and reaction-replacement orthopyroxene yield MMF ratios of 0,411 and 0,453, respectively, which are intermediate between those of chromite at the top contact of the LG 3 (0,480) and dispersed chromite in the overlying bronzitite (0,389 to 0,362).

Fig. 39 is a plot of measured MMF ratios and proportions of Cr, Al and Fe^{3+} cations in relation to stratigraphic height. Horizontal bars drawn through mean data points for the H chromitite layer are representative of the spread of measured values. Compositional profiles shown in the figure link mean compositons of chromite grains occluded within orthopyroxene. The proportion of Cr in orthopyroxene-hosted grains rises with increasing stratigraphic height from 9,72 cations in sample 223 to an average of 11,37 cations in sample 211, coupled to a decline in MMF ratios from 0,438 to 0,325. Bronzitites above the stratigraphic level of sample 211, which is an adcumulate-textured, medium- to coarse-grained bronzitite with intercumulus plagioclase, mica and quartz, depict a minor abundance of chromite and are more feldspathic. A decline in Cr contents with increasing stratigraphic height is suggested above sample 205, linked to a rise in the proportion of Al cations and in the MMF ratio (i.e., trends which are manifested in the H chromitite layer at the top of the C_2 subunit). The sense of the cryptic change of the latter ratio therefore mirrors the rise in mol. per cent En in orthopyroxene (Fig. 14).

The Cr_2O_3 content of chromite at the abrupt, upper contact of the LG 3 chromitite is 51,96 wt. per cent (analysis 213B/1), which is similar to the content in grains occluded by reaction-replacement orthopyroxene some 2 mm above the contact (analysis 213B/6). These large orthopyroxene oikocrysts depict remnants of olivine and poikilitically enclose the heavy dissemination of chromite marking the top contact of the LG 3. Hence, the apparent decline in Cr_2O_3 contents from 55,84 wt. per cent in the footwall leader layer to

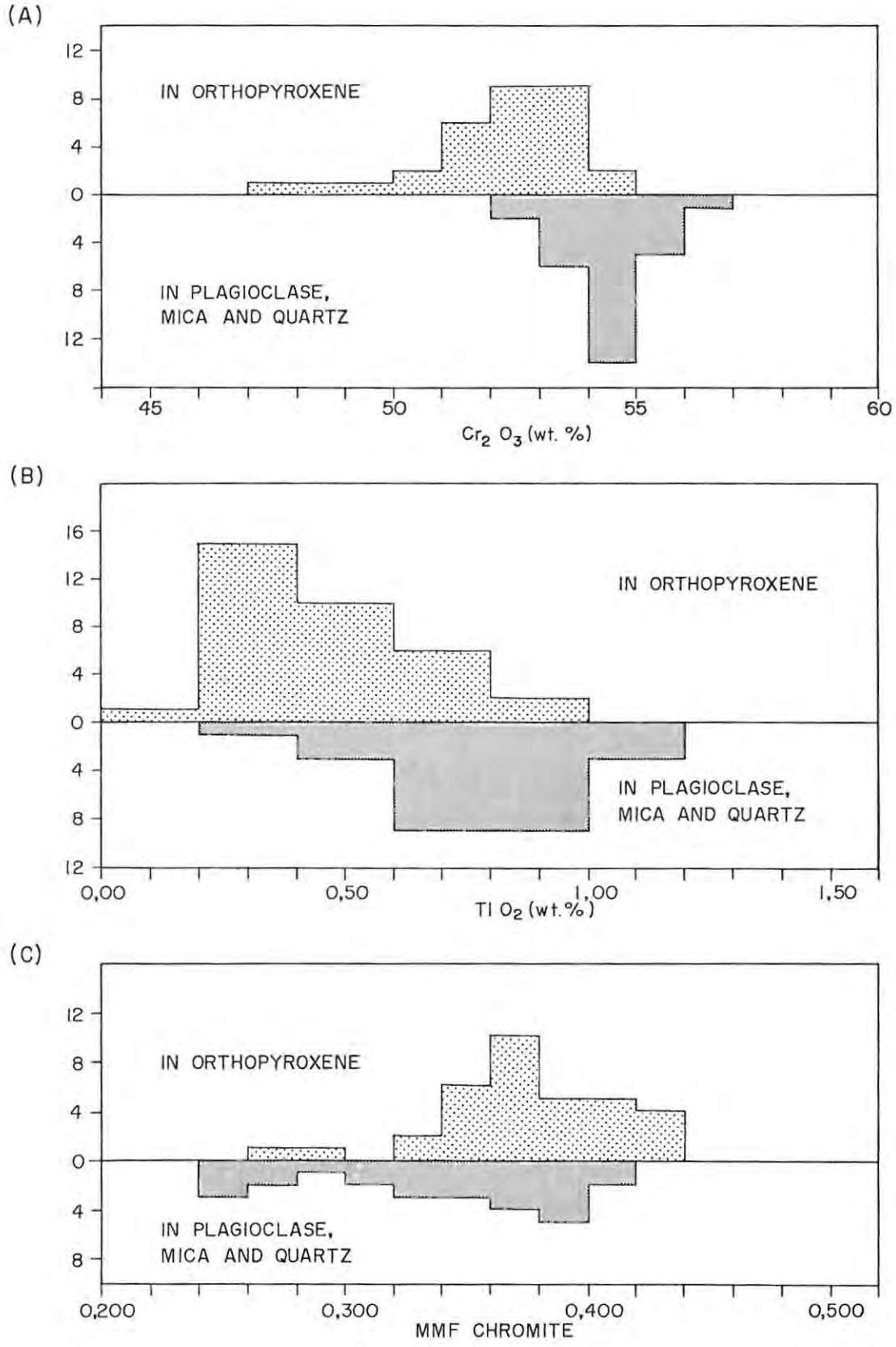

FIG. 38 PLOT SHOWING SPREAD OF (a) Cr_2O_3 CONTENTS, (b) TiO_2 CONTENTS, AND (c) MMF RATIOS IN WEAKLY DISSEMINATED CHROMITE GRAINS WITHIN BRONZITITES OF THE C_2 SUBUNIT.

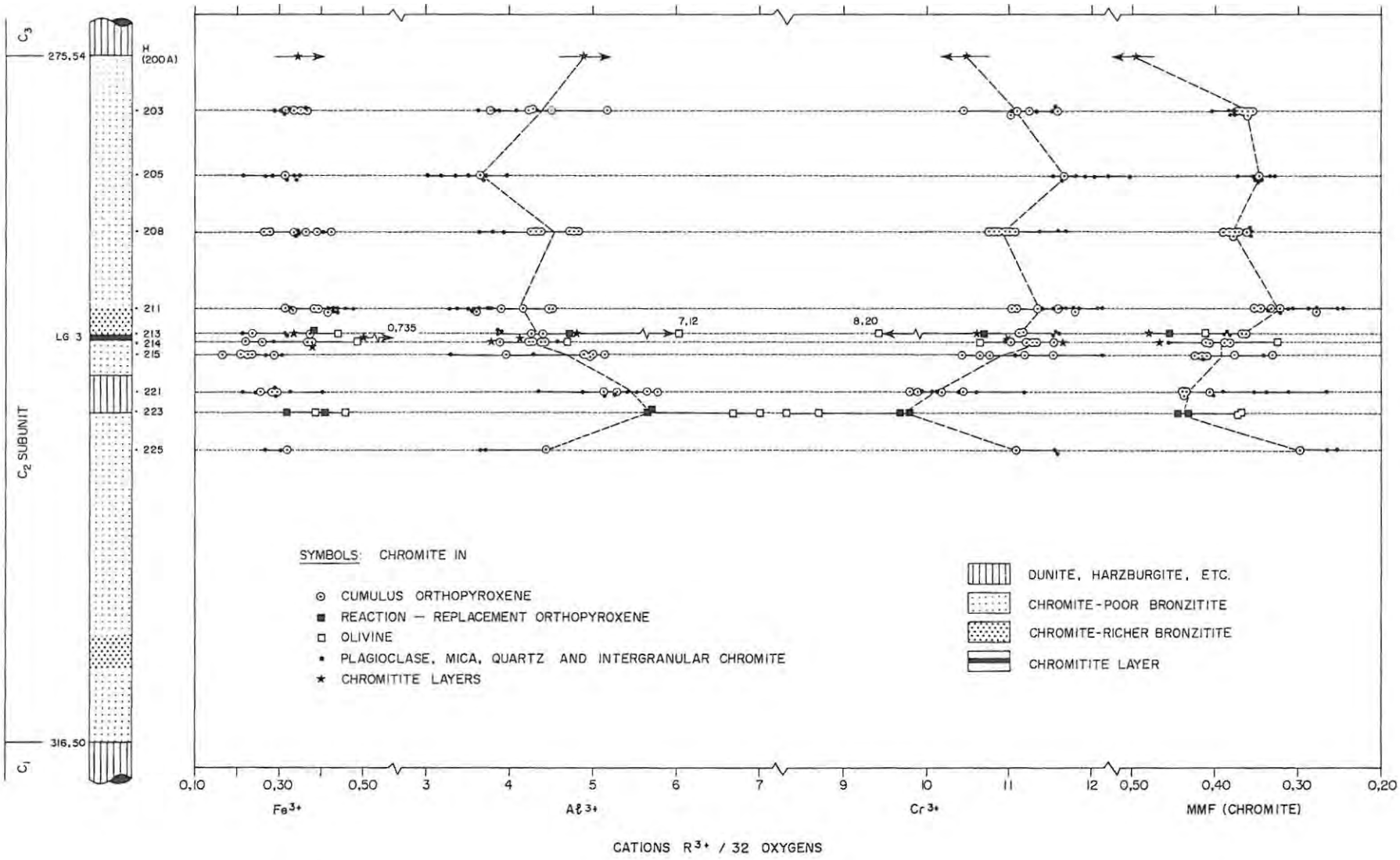

FIG 39 LOG OF THE C_2 SUBUNIT SHOWING (a) WITHIN-SAMPLE COMPOSITIONAL VARIATION OF CHROMITE, AND (b) COMPOSITIONAL VARIATION IN RELATION TO STRATIGRAPHIC HEIGHT. THE SENSE OF CRYPTIC CHANGES IN THE H CHROMITITE LAYER, WITH INCREASING STRATIGRAPHIC HEIGHT, IS PORTRAYED VIA ARROWHEAD SYMBOLS. THE COMPOSITIONAL PROFILES LINK AVERAGE VALUES FOR GRAINS OCCLUDED WITHIN ORTHOPYROXENE.

51,96 wt. per cent at the top of the LG 3 chromitite may not be representative of a primary cryptic trend attending crystallization: microprobe analysis of grain-to-grain cryptic changes in the LG 3 chromitite layer is required to assess this consideration.

5.4.2.4 CHROMITE WITHIN THE C_3 SUBUNIT

Microprobe analyses of chromite within dunites, poikilitic harzburgites and chromite-rich assemblages of the C_3 subunit are presented in Table 25. A log of the C_3 subunit is presented in Fig. 40, which shows a plot of MMF ratios and the proportions of Fe^{3+} and Cr cations in relation to stratigraphic height. Cr_2O_3 contents vary between 45,10 and 54,33 wt. per cent, with concentrations in excess of 50 wt. per cent restricted to chromite-rich domains. TiO_2 contents vary between 0,25 and 1,03 wt. per cent, with a mean concentration of 0,69 wt. per cent for the subunit ($n = 67$; $s = 0,15$). MMF ratios vary between 0,329 and 0,558, and are linked to (a) the modal proportion of chromite, and (b) the nature of the occluding silicate phase. Furthermore, small chromite grains occluded by olivine have lower MMF ratios than larger grains. The MMF ratios of coarse, intergranular chromite grains are consistently higher than those of grains occluded by olivine, but the MMF ratios of the rim-domains are comparable (analyses 180/3 and 4 are representative of core and rim compositions, respectively). Intergranular chromite grains are generally enriched in Al_2O_3 relative to smaller grains occluded by olivine. With the exception of sample 172, small chromite grains occluded by olivine are slightly enriched in Cr_2O_3 relative to larger grains found towards the rims of olivine grains. Hence, with the achievement of extended growth periods, as evinced by coarser-grain sizes and textural environment, a trend of increasing Al_2O_3 content is evident in adcumulate-textured, olivine-rich rocks.

Chromite grains occluded by olivine in the C_3 subunit are generally subrounded; euhedral habits are rarely observed. Intergranular chromite within adcumulate-textured dunites, which are essentially anchimonomineralic assemblages of coarse-grained, polygonal olivine crystals, is characterized by subhedral to anhedral shapes and

generally occurs at olivine triple-junctions. This feature suggests that migration of olivine grain boundaries occurred, facilitating the expulsion of trapped residual melt. Subvertical alignment of olivine crystals is also evident within the lower portion of the subunit. Many of the large, intergranular chromite grains depict silicate inclusions and relict, intracrystalline grain boundaries, indicative of a mosaic of annealed grains. Anomalously large chromite grains showing no annealing textures occur, however, in some feldspathic poikilitic harzburgite lenses. For example, analysis 196D/1 is representative of the core composition of a grain measuring 2,0 x 3,0 mm in diameter, but it should be noted that these are very rare. In contrast, chromite grains in the chromitiferous footwall rocks of the I and LG 4 chromitite layers are euhedral and measure ca. 300 microns in diameter (Fig. 41). These grains occur as heavy disseminations which silhouette olivine crystals, and the large grain-sizes cannot be attributed to annealing processes. In juxtaposed olivine-chromitite layers, however, annealing has induced grain-sizes of up to 1,2 mm (thin section 177A). Hence, the larger grain-sizes, euhedralism and higher Cr_2O_3-contents attending the copious appearance of chromite in these footwall environments point to crystallization from a Cr-undepleted magma. Though the available analytical data do not allow for the unequivocal recognition of cryptic compositional changes in the layered, chromitiferous rocks associated with the I and LG 4 chromitite layers, it is evident from the data that (a) chromite in the immediate footwall rocks is enriched in Cr relative to chromite in the respective hanging-wall layers, and (b) the Cr contents of grains within the chromitite layers are of intermediate abundances.

The proportion of Fe^{3+} cations is higher within grains in olivine-rich assemblages than in chromite-rich domains, and is higher in grains occluded by olivine (Fig. 40). A degree of deuteric oxidation of olivine is thus implied (Eales et al., 1984). Furthermore, it is evident from the data that an increase in the modal proportion of chromite is not linked to a rise in the $Fe^{3+}/(Fe^{3+} + Fe^{2+})$ ratio: the absolute magnitude of the latter is comparable to that of chromite within the pyroxenite subunits.

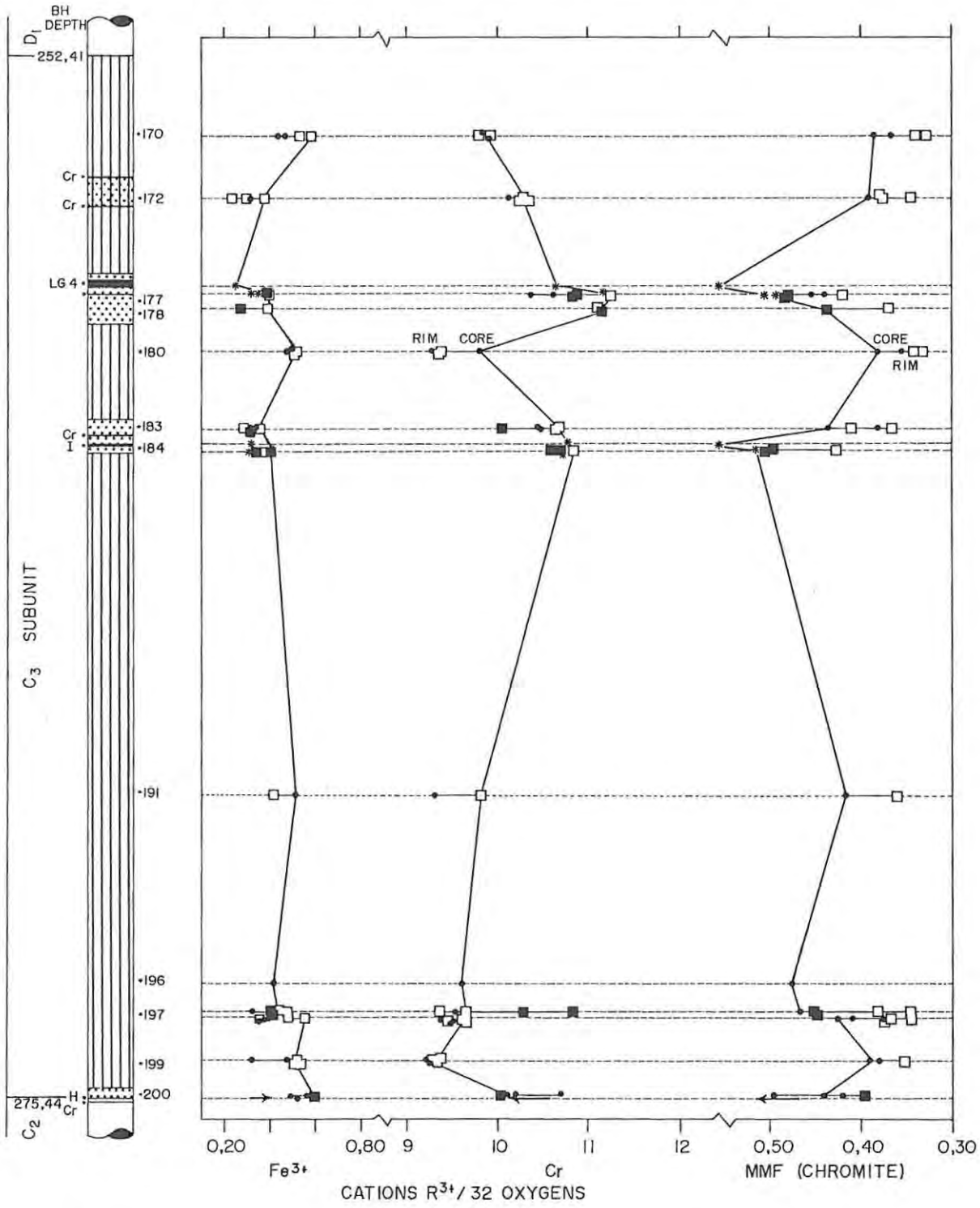

FIG. 40 LOG OF THE C_3 SUBUNIT SHOWING (a) WITHIN-SAMPLE COMPOSITIONAL VARIATION OF CHROMITE, AND (b) COMPOSITIONAL VARIATION IN RELATION TO STRATIGRAPHIC HEIGHT. SYMBOLS: CHROMITE IN

- □ OLIVINE
- ■ REACTION-REPLACEMENT ORTHOPYROXENE
- • PLAGIOCLASE, CLINOPYROXENE & INTERGRANULAR CHROMITE
- * CHROMITITE LAYERS

CHROMITE-POOR DUNITE AND HARZBURGITE

CHROMITE-RICH DOMAINS

Cr CHROMITITE LAYERS

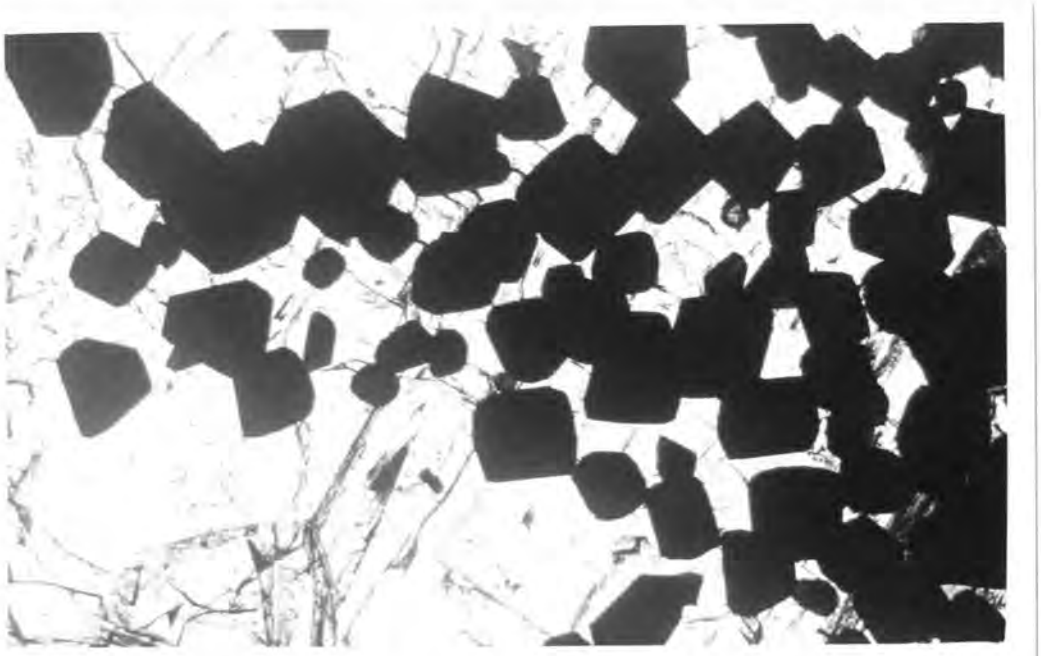

FIG. 41: Photomicrograph of a chromitiferous poikilitic harzburgite layer in the footwall of the LG 4 chromitite, illustrating the heavily disseminated, equant and coarse nature (± 300 microns) of chromite grains depicted in circumjacent silhouettes about olivine crystals. Some 80 to 100 per cent of the latter has been replaced by orthopyroxene, which is structurally continuous with the orthopyroxene crystal encapsulating the chromite grains. These textural features point to (i) a high liquid/olivine ratio, (ii) reaction- replacement at early stages of compaction, i.e., during or prior to impingement and annealing of chromite to yield an impermeable assemblage (domains showing annealed interstitial aggregates of chromite also exhibit very limited degrees of replacement of olivine), and (ii) upward migration of magmatic residua not in equilibrium with olivine resident in the chromite-rich domain.

5.4.2.5 CHROMITE WITHIN THE D SUBUNIT

Table 26 presents microprobe analyses of chromite within the D_1 and D_2 subunits exposed in drill core ZS 7. The within-sample variations of (a) MMF ratios, and (b) proportions of Fe^{3+} and Cr cations per formula unit are summarized in Fig. 42, which shows a log of the succession. The range of Cr_2O_3 contents is from 40,76 to 57,30 wt. per cent: the former concentration is representative of a 20 micron-diameter grain occluded by a polygonal, fine-grained orthopyroxene crystal (analysis 125/2), whereas the latter is representative of a 40 micron-diameter grain occluded within the marginal-domain of a large orthopyroxene crystal in a mesocumulate-textured, feldspathic assemblage (analysis 134/2). Cr_2O_3 contents decline irregularly with increasing stratigraphic height from an average composition of 52,28 wt. per cent in the basal, coarse-grained adcumulate bronzitites (Fig. 43(A)) to an average of 48,74 wt. per cent in proximity to the LG 6A chromitite layer, where granular-textured bronzitites are depicted (Fig. 43(B)). This cryptic trend might be linked with the gross rise in orthopyroxene crystallinity with increasing stratigraphic height (refer to Fig. 8C). Chromite grains associated with olivine-bearing microdomains in sample 160 (analyses 160/3 and 4) are enriched in Al_2O_3 relative to chromite intergrown with orthopyroxene. Furthermore, grains which are intergranular to olivine show a zonal decline in Cr_2O_3 from 48,36 wt. per cent to 43,62 wt. per cent. The latter composition is similar to that of smaller grains wholly enclosed within olivine crystals (Cr_2O_3 content of 43,99 wt. per cent). A feature which clearly emerges from Fig. 42 is the large variation in Cr_2O_3 content of grains depicted within the bronzitites bounded by samples 139 and 125. For example, a subhedral chromite grain in sample 125 displays a composition of 40,76 wt. per cent Cr_2O_3 (analysis 125/2), whereas the average content in two grains in sample 128, with diameters of 70 microns and occluded by coarse-grained orthopyroxene, is 56,45 wt. per cent Cr_2O_3 (analyses 128/1 and 2). Chromite within samples 125 and 139 is typically subhedral to anhedral, and analyses 125/1 and 2 are representative of translucent grains, transmitting amber to reddish-brown light. Many of the orthopyroxene crystals are charged with similar inclusions, in conjunction with trains of opaque granules (Fig. 43(C)). A trace and

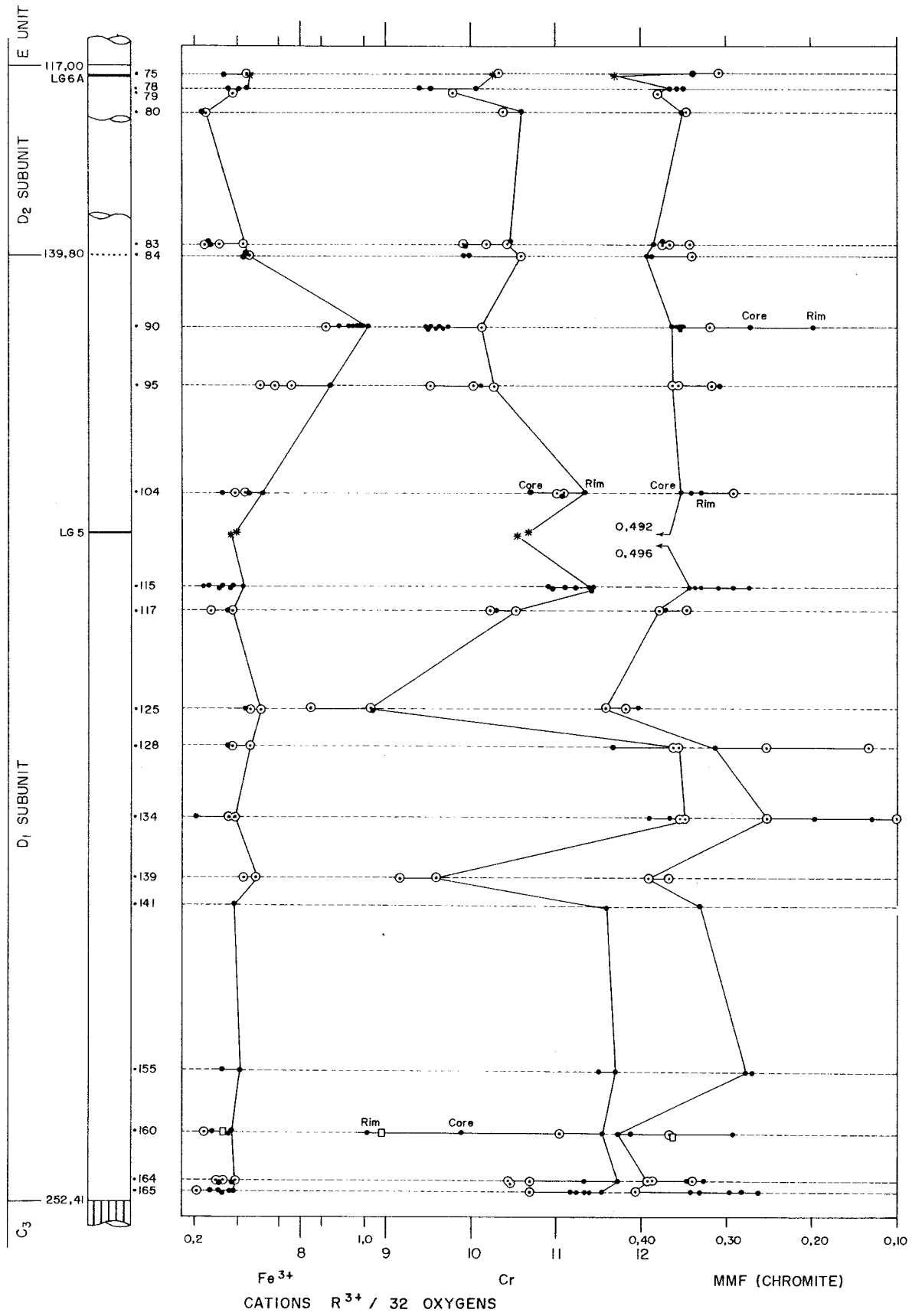

FIG. 42 LOG OF THE D UNIT SHOWING (a) THE WITHIN - SAMPLE COMPOSITIONAL VARIATION OF CHROMITE, AND (b) COMPOSITIONAL VARIATION IN RELATION TO STRATIGRAPHIC HEIGHT. SYMBOL USAGE IS AS DENOTED IN PREVIOUS DIAGRAMS.

FIG. 43(A): Textural features of a coarse-grained, adcumulate-textured bronzitite exposed in the basal portion of the D_1 subunit (sample 165). Section cut normal to the drill core axis and photographed with transmitted light under crossed nicols. Field of view measures 2,5 by 1,7cm.

43(B): Granular-textured bronzitite near the base of the D_2 subunit (sample 83), showing a polygonal mosaic of orthopyroxene crystals. Note the very much smaller particle sizes of chromite grains relative to Fig. 43(A). Photographed with transmitted light under crossed nicols. The field of view is the same as (A) above. Section cut normal to the drill core axis.

43(C): Photomicrograph of the central portion of an oxide-charged orthopyroxene crystal within a granular-textured bronzitite (D_1 subunit, sample 125). These features are (i) not a pervasive characteristic of all granular-textured bronzitites (e.g., the assemblage shown in (B) above), (ii) are rarely displayed within coarser-grained rocks, and (iii) are more prevalent within bronzitites which host a minor abundance of olivine crystals. Section photographed with transmitted light. (Scale 5cm = 0,25mm).

(A)

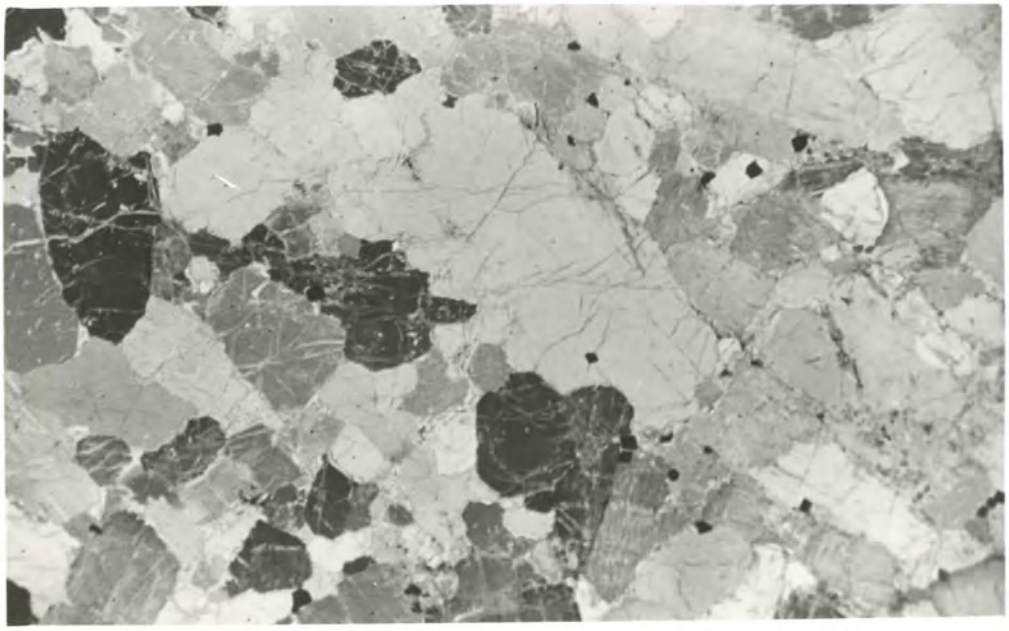

(B)

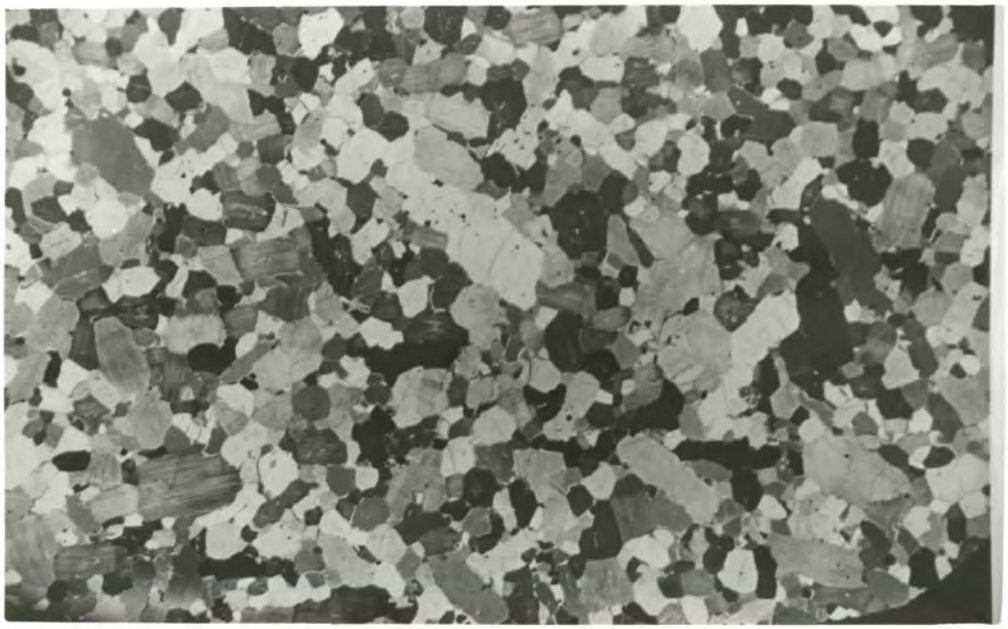

(C)

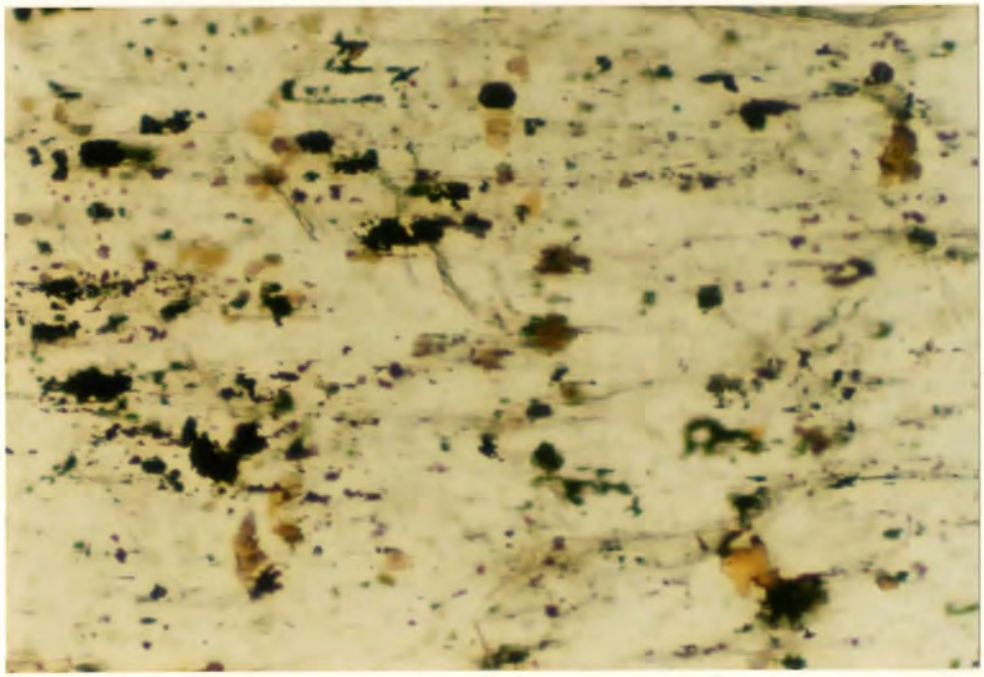

sporadic occurrence of olivine crystals is also associated with these fine-grained, granular-textured bronzitites.

TiO_2 contents vary between 0,16 and 1,62 wt. per cent. The latter concentration is representative of a rutile-bearing grain intergrown with plagioclase in sample 134. The average TiO_2 content of grains occluded by orthopyroxene within the unit is 0,43 wt. per cent ($n = 28$; $s = 0,16$), whereas that of chromite intergranular to orthopyroxene and intergrown with plagioclase is 0,63 ($n = 26$; $s = 0,15$) and 1,02 wt. per cent ($n = 11$; $s = 0,27$), respectively. The variation of TiO_2 in relation to stratigraphic height is addressed in the subsequent text. Fe_2O_3 contents indicate a restricted variation between ca. 1,00 and 2,80 wt. per cent, but a trend of rising Fe_2O_3 with increasing stratigraphic height is depicted above the LG 5 chromitite layer, culminating in a high mean value of 4,72 wt. per cent within sample 90 (a bronzitite depicting a bimodal grain-size distribution, interstitial clinopyroxene and a trace abundance of plagioclase in poorly annealed cavities). The modal abundance of chromite remains at accessory levels throughout the interval bounded by the LG 5 chromitite layer and the chromite bronzitite layer marking the base of the D_2 subunit (sample 84, Fig. 42). Inspection of the chromite compositional parameters Y_{Cr}, Y_{Al} and $Y_{Fe}{}^{3+}$ for samples 90, 95 and 104 (Table 26) indicates that $Fe^{3+} \rightleftharpoons Cr$ is the principal substitution mechanism, whereas the composition of chromite within the other 20 samples indicates a reciprocal range of Cr and Al. This feature thus accounts for the cryptic decline in Cr content with increasing stratigraphic in the upper portion of the D_1 subunit.

MMF ratios of chromite within orthopyroxene-rich rocks of the unit vary between 0,440 and 0,100, and are broadly linked to the proportions of Al and Cr cations. A comparison of samples 125 and 134 serves as an extreme example. It is evident from the data points depicted in Fig. 42 that cryptic compositional changes in relation to stratigraphic height are a function of the grain-size of the host bronzitite and the modal proportion of intercumulus silicate phases. Sample 164, for example, is a coarse-grained bronzitite depicting a fairly sodic intercumulus plagioclase. The Cr_2O_3 content of a chromite grain with a diameter of 50 microns and occluded by

orthopyroxene is 50,94 wt. per cent (analysis 164/1), whereas a 500 micron-diameter grain intergrown with plagioclase depicts a zonal rise in Cr_2O_3 to a rim composition of 54,48 wt. per cent (analysis 164/3). The latter feature is linked to a zonal decline in MMF ratio from 0,345 to 0,329. Within granular-textured bronzitites, however, small grains occluded by orthopyroxene tend to be enriched in Cr_2O_3 relative to coarser, intergranular grains. Secondly, rim compositions of the latter (i.e., in juxtaposition to orthopyroxene with no residual film of an intercumulus silicate phase) indicate lower TiO_2 contents and substantially depressed MMF ratios (e.g., analysis 90/6, where the MMF ratio of a rim-domain is 0,198, whereas that of the core is 0,272).

5.4.2.6 CHROMITE WITHIN THE E UNIT

Microprobe analyses of chromite within bronzitites of the E unit and within an ultramafic pegmatite assemblage are presented in Table 27. Fig. 44 depicts a log of the succession, with MMF ratios and the proportions of Fe^{3+} and Cr cations per formula unit plotted in relation to stratigraphic height. Average compositions of chromite within the LG 6A and LG 7 chromitite layers, and within the chromitite lens in sample 28, are also shown. Relative to the latter environments, accessory chromite within the bronzitites shows lower MMF ratios and, significantly, the proportions of Fe^{3+} and Cr cations in grains occluded by orthopyroxene are comparable to the proportions in polygonal grains within chromitite layers. This feature lends no support to the notion that Al partitions into occluded chromite grains at subsolidus temperatures due to the diminished solubility of Al in orthopyroxene, but microprobe analyses of exsolved clinopyroxene within orthopyroxene crystals indicate compositions enriched in Al_2O_3 relative to intercumulus clinopyroxene (section 5.3.2). Chromite grains encapsulated within large, well-formed orthopyroxene crystals, which generally depict a greater abundance of clinopyroxene lamellae and blebs relative to granular-textured orthopyroxene grains, are generally rimmed by a halo of clinopyroxene (Fig. 45A). A circumjacent, lamellae-free zone is usually observed within the orthopyroxene host, indicating that the chromite-orthopyroxene interface served as a low energy nucleation

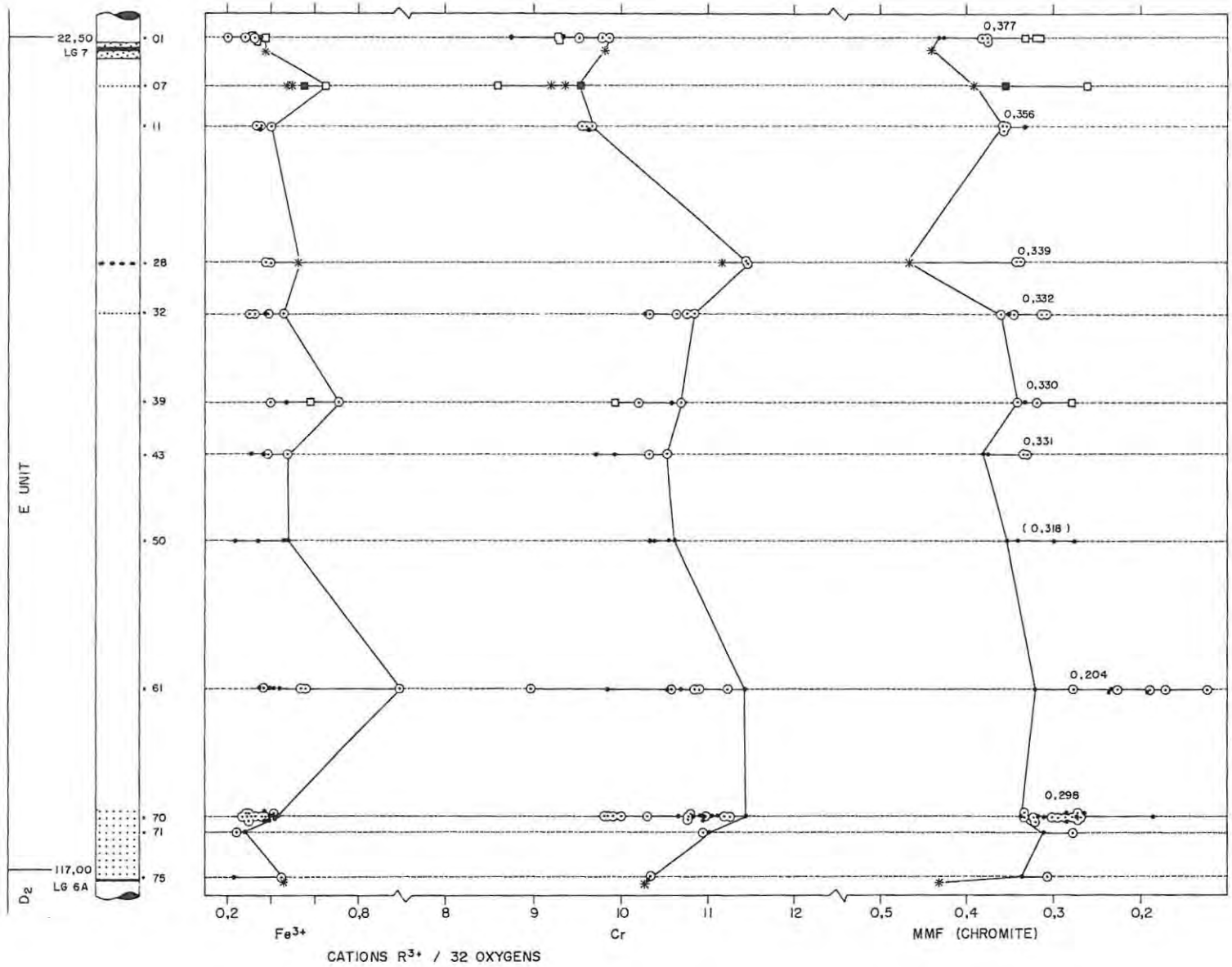

FIG. 44 LOG OF THE E UNIT SHOWING (a) WITHIN- SAMPLE COMPOSITIONAL VARIATION OF MMF RATIOS AND THE PROPORTIONS OF Fe^{3+} AND Cr CATIONS IN CHROMITE, AND (b) COMPOSITIONAL VARIATION IN RELATION TO STRATIGRAPHIC HEIGHT. SYMBOL USAGE IS AS DENOTED IN PREVIOUS DIAGRAMS.
MMF = 0,298 : WITHIN-SAMPLE AVERAGE MMF RATIO OF CHROMITE OCCLUDED BY ORTHOPYROXENE.

site for clinopyroxene. Analyses 70/1 to 70/4 were carried out in order to evaluate the compositional influence of clinopyroxene on small chromite grains with a high surface area/mass ratio. Core compositions were measured of grains with (a) no clinopyroxene halo (analysis 70/1), (b) a partial halo (analysis 70/2), and (c) a complete 360° halo (analyses 70/3 and 4). It is evident from the data that no consistent pattern emerges. Hence, without recourse to rim compositions of these small chromite grains, this question cannot be answered since there is an overriding relationship between composition and textural environment in sample 70. For example, grains encapsulated within the margins of orthopyroxene crystals yield average TiO_2- and Cr_2O_3-contents of 1,02 and 51,05 wt. per cent, respectively, whereas grains within core-domains yield concentrations of 0,63 wt. per cent TiO_2 and 48,34 wt. per cent Cr_2O_3. The former compositions tend towards those of intergranular chromite grains and grains intergrown with plagioclase (x = 1,21 wt. per cent TiO_2 and 51,18 wt. per cent Cr_2O_3).

Sample 61 is another example of a bronzitite which may have undergone a degree of deuteric oxidation. There is a fairly pervasive distribution of opaque spinel granules and many of the medium-grained orthopyroxene crystals are charged with anhedral spinel granules which transmit amber light. Analysis 61/1 is representative of these Al_2O_3-enriched spinels and a notable feature is the low MMF ratio of 0,173. This contrasts with the magnesian character noted for a seemingly equivalent occurrence in sample 125. The Cr_2O_3 content of a larger, opaque and equant grain within the same orthopyroxene crystal is 49,79 wt. per cent (analysis 61/2), linked to an MMF ratio of 0,226. It should be stressed that, whereas (a) only an accessory abundance of chromite is depicted in sample 61, and (b) the rock is an adcumulate-textured bronzitite with a low abundance of intercumulus silicate phases, chromite at this stratigraphic level is compositionally equivalent to grains within sample 70, which is conspicuously more feldspathic and chromite-rich. For example, the average Cr_2O_3 content of grains encapsulated in orthopyroxene core-domains is 49,74 wt. per cent, and 51,28 wt. per cent for grains occluded in rim-domains.

It is evident from the orthopyroxene crystallinity profiles of the D and E units, depicted in Figs. 8(C) and 8(E), respectively, that a broad similarity exists between them, viz., an overall trend of increasing crystallinity with increasing stratigraphic height, followed by a progressive and more abrupt decline in this physical parameter in the footwall rocks of the LG 6 and LG 7 chromitite layers. The coarse-grained interval bounded by samples 128 and 134 in the D_1 subunit shows a transition from feldspathic, mesocumulate-textured rocks to adcumulate-textured rocks with increasing stratigraphic height. The chemical composition of chromite in these rocks is characterized by high Cr_2O_3 contents and a wide range of low MMF ratios. Within the overlying, granular-textured bronzitites (e.g., from sample 115 to 125), chromite depicts a textural variation which can be described as "interstitial". These textures are also a ubiquitous feature of a 14 m thick interval bounded by samples 43 and 53 in the E unit, of which Fig. 45(B) is a typical example (analyses 43/3, 43/4 and 50/2 in Table 27 are representative of the latter habit in the E unit and may be compared with analysis 117/3). It may thus be of significance that the following features are observed within both the E and D units:

1. There is a gradation from coarse-grained, mesocumulate-textured bronzitite to coarse-grained, adcumulate-textured bronzitite over a comparable stratigraphic thickness in both units.
2. Deuteric oxidation of cumulus orthopyroxene is indicated in the adcumulate-textured assemblages and immediately overlying, granular-textured assemblages.
3. Interstitial chromite morphologies are exposed in granular-textured bronzitites above the coarse-grained, adcumulate bronzitites.
4. There is an 89 m vertical separation between the level of sample 134 and the LG 6A chromitite, and between the level of sample 71 and the LG 7 chromitite layer.

Potentially, therefore, these similarities point to a duplication of magmatic conditions attending crystallization within the E unit without, however, reproducing layers analogous to the LG 5 and LG 6 chromitite layers.

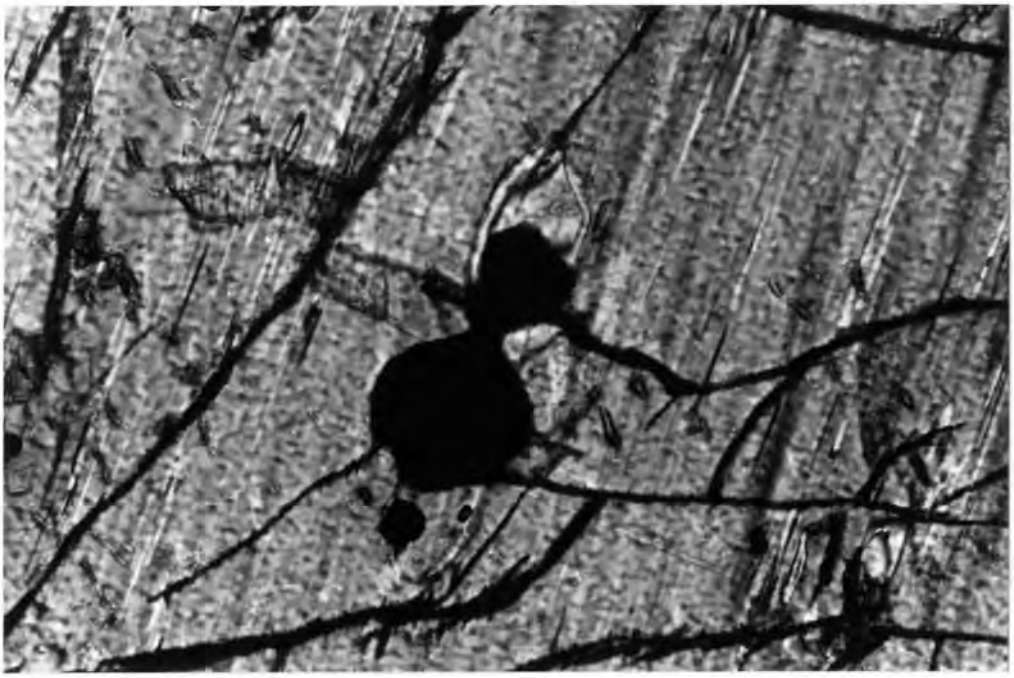

FIG. 45(A): Partial halo of exsolved clinopyroxene nucleated on the grain boundary of a small chromite grain occluded within the core of an orthopyroxene crystal (E unit, sample 70). Section photographed with transmitted light under crossed nicols. The smaller of the chromite grains is 50 microns in diameter. It should be noted that the occurrence of spherical to ellipsoidal blebs of clinopyroxene in juxtaposition to small encapsulated chromite grains is a textural feature common to the entire studied section.

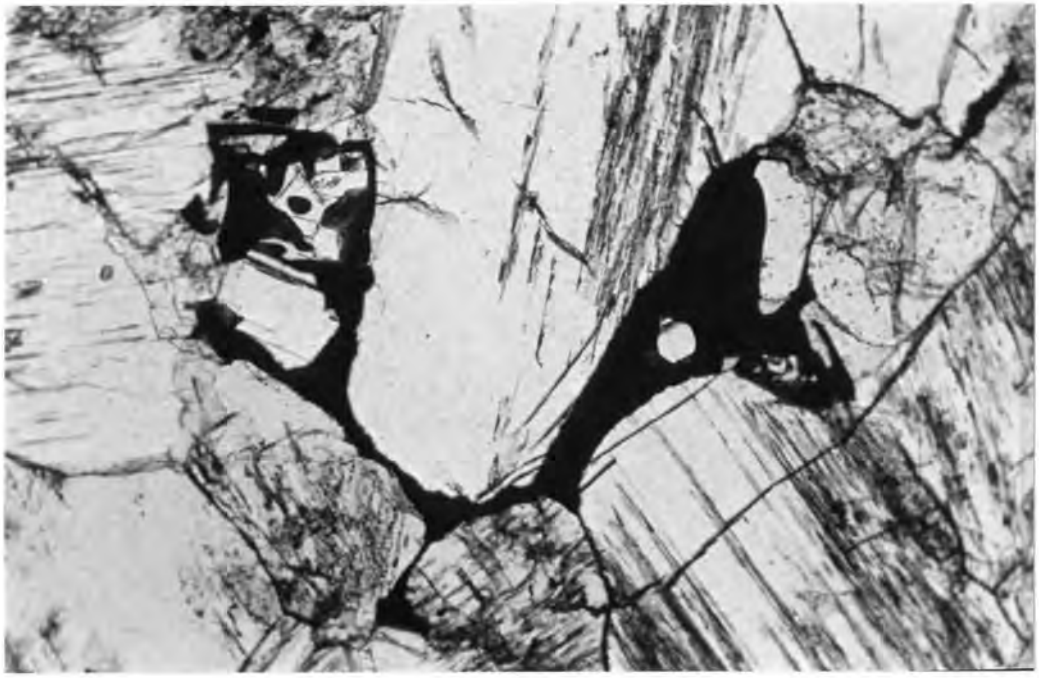

45(B): Interstitial chromite within a medium-grained, granular-textured bronzitite (E unit, sample 50). Note the correspondence between the chromite grain (reflected light microscopy yields no evidence of intracrystalline grain boundaries) and what is described in the present text as a "poorly annealed cavity". Finer-grained bronzitites depicting advanced degrees of annealing or foam texture do not display this feature, thus indicating that it is not a recrystallization phenomenon. Section photographed with transmitted light. Scale 5cm = 1mm.

Sample 39 is composed of a polygonal, annealed mosaic of orthopyroxene crystals and depicts a minor abundance of large olivine grains (2 to 4 mm in diameter), with associated pyrrhotite. The latter is confined to domains within and adjacent to the olivine grains and the textures are indicative of localized replacement by ultramafic pegmatite. Oxidation of the primary orthopyroxene assemblage is evinced by inclusions of opaque and translucent spinel granules. Chromite grains occluded by olivine crystals are slightly larger than within the adjacent bronzitite, but the Cr_2O_3 content of the former (47,59 wt. per cent; analysis 39/4) is only mildly depleted relative to a content of 49,98 wt. per cent for grains occluded in primary orthopyroxene. In contrast, extensive replacement by an olivine-sulphide assemblage is depicted in sample 07. Fig. 46(A) serves to illustrate the relative abundance of secondary sulphides in a 3 mm thick chromitite stringer and Fig. 46(B) illustrates the localized oxidation of chromite to an Fe-rich spinel of higher reflectivity. The Cr_2O_3 content of annealed grains within the stringer is 46,32 wt. per cent (analysis 07/1), whereas that of chromite occluded by olivine in juxtaposed replaced domains is 41,72 wt. per cent (analysis 07/2). Sample 11, however, is a primary magmatic assemblage of orthopyroxene, pyrrhotite and accessory chromite. The mean Cr_2O_3 content of chromite at this stratigraphic level is 46,71 wt. per cent. Measurements of orthopyroxene crystallinity exposed a progressive increase in orthopyroxene grain-size from the level of sample 28 to the LG 7 chromitite layer, and a sympathetic decline in chromite modal abundance is noted. Within 1 metre of the basal contact of the LG 7 chromitite, however, there is a dramatic rise in orthopyroxene crystallinity and a number of thin chromitite layers are depicted. Sample 01 is a granular-textured bronzitite some 88 cm above the LG 7 chromitite, and shows a weak dissemination of chromite grains and patches of replacement olivine. The Cr_2O_3 content of small chromite grains occluded by orthopyroxene is 47,32 wt. per cent (analyses 01/1 and 01/3), whereas chromite occluded by olivine yields an average composition of 45,31 wt. per cent (analyses 01/5 and 01/7). It should be stressed that the modal abundance of olivine is less than 2 per cent and the occurrences are localized. Analyses 01/1 and 01/3 are of occluded grains well removed from olivine-bearing domains and no fracturing of the host orthopyroxene is exposed. It is thus

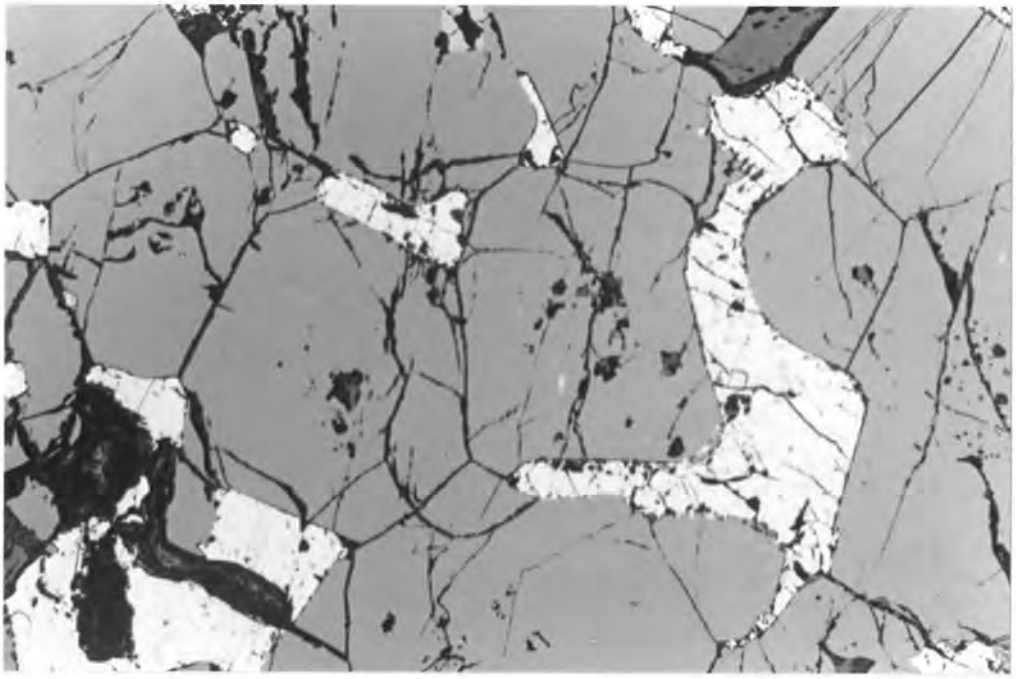

FIG. 46(A): Pyrrhotite intergrown with chromite (grey) in a thin chromite stringer exposed at the stratigraphic level of sample 07 (E unit). The sulphide phase appears to have replaced the earlier silicate gangue, and is linked to an olivine-rich ultramafic pegmatite which has replaced the original bronzitite on both sides of the stringer. Photographed with plane polarized reflected light. Scale 5cm = 1mm.

46(B): Oxidation of chromite within the stringer to ferritchromite (higher reflectivity) along polygonal grain boundaries and triple junctions. Photographed with reflected light. The magnification is 4 times that used in (A). A lobate sulphide grain (centre, right) is visible in the field of view.

unlikely that a fluid phase of a replacement lineage gained access to these grains. In summation, it is suggested that the cryptic changes in Cr_2O_3 content through the upper 60 metres of the sampled section reflect a primary compositional trend and are not a function of secondary reactions and equilibration. The latter are linked to distinctive mineralogical environments and analyses of grains in these domains can be grouped as a subset which is not pertinent to this study. Thus, Cr_2O_3 contents rise from an average of 49,36 wt. per cent within samples 50, 43 and 39 to 54,28 wt. per cent at the stratigraphic level of sample 28, with an intermediate composition of 50,69 wt. per cent in sample 32. The latter is representative of annealed grains within a coarse-grained chromite bronzitite layer. The Cr_2O_3 content of chromite declines with increasing stratigraphic height above sample 28 to ca. 46 wt. per cent in the footwall of the LG 7 chromitite, followed by a reversal to 48,15 wt. per cent within the LG 7 chromitite layer (microprobe analyses of chromite within the thin and numerous leader chromitite layers below the LG 7 massive ore were not carried out). This measured decline in Cr_2O_3 content through a 20 m thick stratigraphic interval, linked to a decline in modal chromite abundance, is irreconcilable with crystallization from a thick vertical column of magma.

Average MMF ratios of chromite grains occluded by orthopyroxene within individual samples are given in Fig. 44. The disposition of data points indicates an overall increase in this parameter with stratigraphic height, from an average of 0,274 within the basal 20 m of the unit to 0,377 above the LG 7 chromitite layer. To a degree, this is consistent with the measured cryptic variation in the enstatite content of orthopyroxene through the E unit (Fig. 14), and the rise in crystallinity of the sample population with increasing stratigraphic height (refer to Fig. 8E). The proportion of Al cations in chromite shows a reciprocal variation with Cr, irrespective of mineralogical or textural environment.

5.4.2.7 CHROMITE WITHIN THE D_2 SUBUNIT, DRILL CORE ZS 3

Table 28 presents microprobe analyses of chromite within bronzitites, chromitiferous bronzitites, bronzite-chromitites and chromitite layers of the D_2 subunit exposed in drill core ZS 3. Fig. 47 shows a log of the succession and summarizes the within- and between-sample variation of MMF ratios and the proportions of Cr, Al and Fe^{3+} cations. Features portrayed in the figure indicate (a) higher MMF ratios within chromite-rich domains, (b) a progressive rise in the proportion of Fe^{3+} cations with increasing stratigraphic height, from 0,372 cations per formula unit at the base of the subunit to 1,75 cations per formula unit in samples adjacent to the LG 6A chromitite layer, (c) a reciprocal variation of Al and Cr below the LG 6 chromitite layer, (d) proxying of Fe^{3+} for Al cations in samples above the LG 6 chromitite, in conjunction with a reciprocal variation of Al and Cr, and (e) a rise in Al content at the stratigraphic level of the LG 6A chromitite layer, linked to a reciprocal decline in Cr and Fe^{3+} contents.

MMF ratios of chromite grains occluded by orthopyroxene in bronzitites decline with stratigraphic height from 0,363 at the base of the subunit to 0,247 at a level 90 cm below the LG 6A chromitite layer (i.e., within sample 305 which depicts the exceptionally large, idiomorphic orthopyroxene crystal hosted by a fine-grained, granular-textured bronzitite illustrated in Fig. 18). The ratio rises to 0,380 within 1 mm of the basal contact of the LG 6A chromitite, and a further decline to 0,266 is evident within bronzitites at the base of the E unit. Samples 300 and 301 are chromitiferous, feldspathic bronzitites and chromite intergrown with plagioclase depicts extensive subsolidus exsolution of rutile lamellae. The estimated average TiO_2 content of the latter grains is 1,24 wt. per cent but, as illustrated by analysis 301/1, a wide range of contents can be measured. Fig. 48 is a photomicrograph of a chromite aggregate within sample 301, and analysis 301/3 is representative of the constituent, annealed grains which show extensive exsolution of rutile in core-domains and along polygonal grain boundaries. The MMF ratio of 0,350 is anomalously low in terms of the large volume of the aggregate, as is the estimated TiO_2 content of 1,22 wt. per cent anomalous, and no obvious compositional correlation with chromite

within the gradational hanging-wall of the LG 6A chromitite is evident (e.g., analyses 303A/1 and 2).

The cryptic variation in the proportion of Fe^{3+} cations (Fig. 47) lends no support to the proposals of Snethlage and von Gruenewaldt (1977) and Snethlage and Klemm (1978) that an increase in fO_2 of approximately 1,0 log unit may stimulate copious nucleation of chromite. By using the relationship of Wilson (1982), for example, calculation indicates that the cryptic decline in Fe^{2+}/Fe^{3+} ratios from sample 314 to 305 may be in response to a rise in fO_2 of 4,0 log units, but the host rocks remain feebly chromitic. Furthermore, the proportion of Fe^{3+} cations in chromite within the LG 6 chromitite is higher than in the bounding rocks, whereas chromite within the LG 6A chromitite exhibits a mild depletion in this component relative to grains within the juxtaposed bronzitite. The pattern of cryptic variation at the level of the LG 6A chromitite is comparable with that documented by Cameron (1975 and 1977) for chromitite layers in the Mooihoek Pyroxenite, viz., chromite within chromitite layers is enriched in MgO and Al_2O_3. However, the reciprocal decline in Cr_2O_3 content does not conform to Cameron's studies, which indicate a reciprocal decline in Fe_2O_3 with Cr_2O_3 contents remaining essentially constant.

The variation of MMF ratios against Al and Cr contents as a function of grain-size was investigated in sample 308. Four grains occluded within an orthopyroxene crystal were selected for analysis and extended counting times were employed. The data are summarized in Fig. 49, in conjunction with the results of an equivalent investigation carried out on sample 32 from the E unit of drill core ZS 7. It is evident from the data points that (a) smaller grains exhibit higher Cr contents and lower MMF ratios, (b) the proportion of Fe^{3+} cations remains constant, and (c) the rise in Al with increasing grain-size is linked to an increase in the MMF ratio. This relationship between composition and grain-size is consistent with Wilson's (1982) studies. It should be stressed, however, that the compositional diversity of chromite within feldspathic assemblages of the Ruighoek Pyroxenite stems from the above-mentioned relationship and the subsequent Cr-enrichment trend imposed by the nucleation of plagioclase. However, the analytical data reveal that

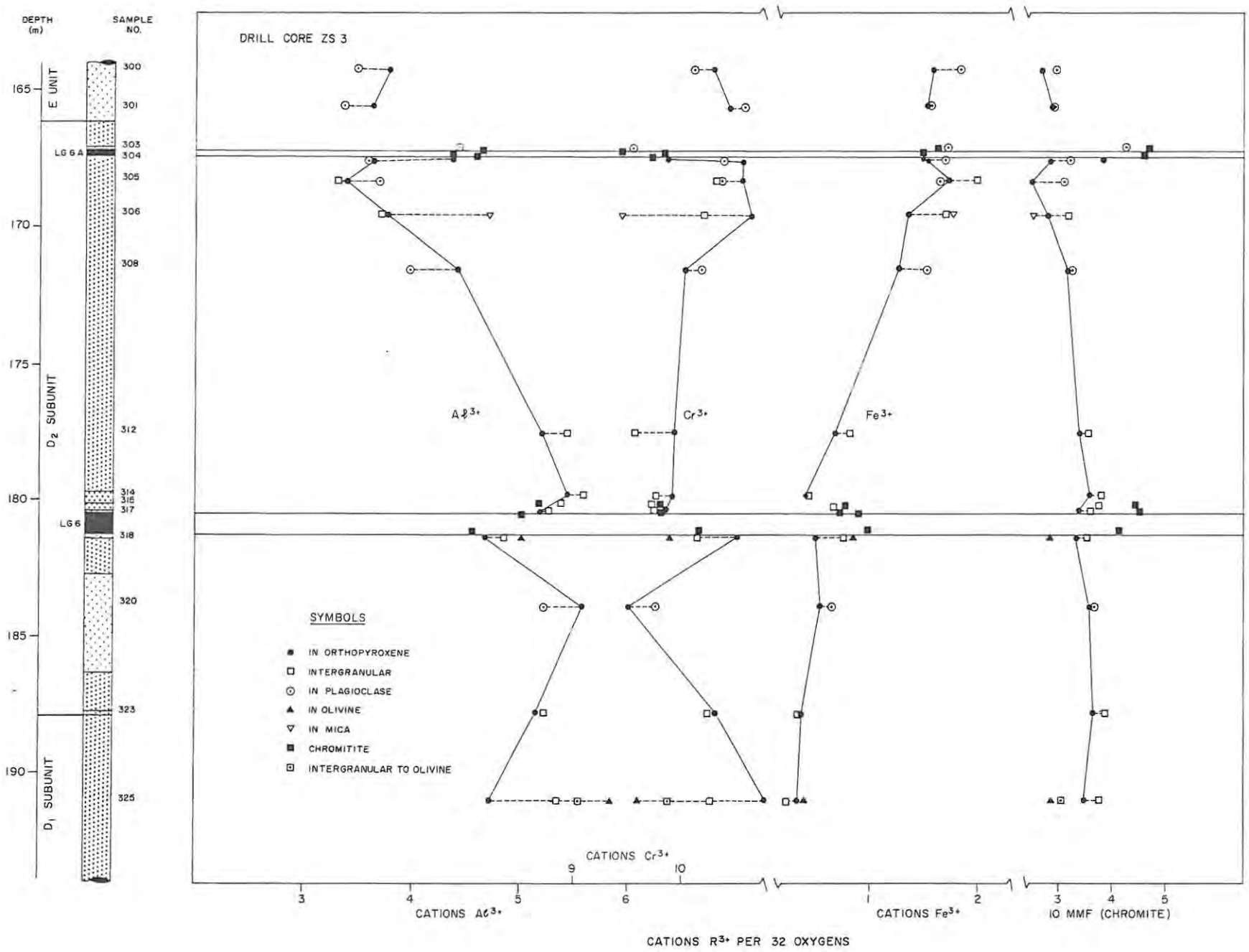

FIG. 47 LOG OF THE D_2 SUBUNIT, WITH ANALYTICAL DATA.

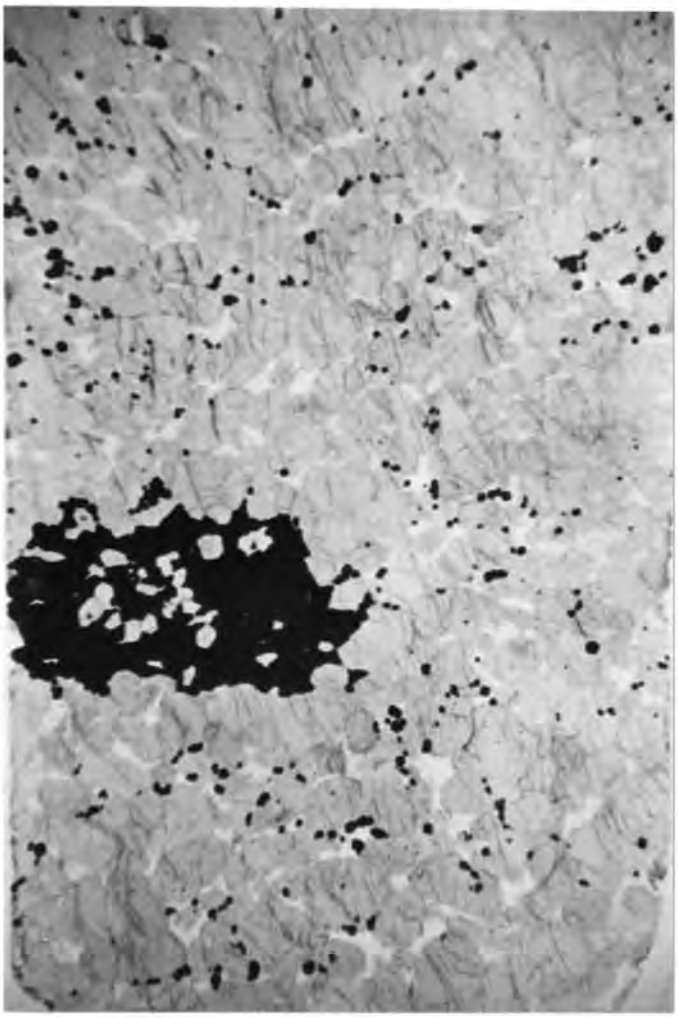

FIG. 48: Photomicrograph of a chromitiferous, feldspathic bronzitite exposed 1,5m above the LG 6A chromitite layer in drill core ZS 3 (sample 301). The thin section is orientated parallel to the drill core axis and shows an anomalous, annealed aggregate of chromite grains as an inclusion within the bronzitite. Note the smaller size of orthopyroxene crystals within the aggregate relative to crystals represented in the bronzitite. Microprobe analysis of chromite grains within the aggregate yield an average MMF ratio and TiO_2 content of 0,350 and 1,22%, respectively, which are representative of evolved conditions relative to chromite within the LG 6A layer (MMF ratio of 0,457 and TiO_2 content of 0,69%). The section has been photographed in plane polarized transmitted light (field of view measures 3 by 2cm). Exsolved rutile is a conspicuous feature within this sample.

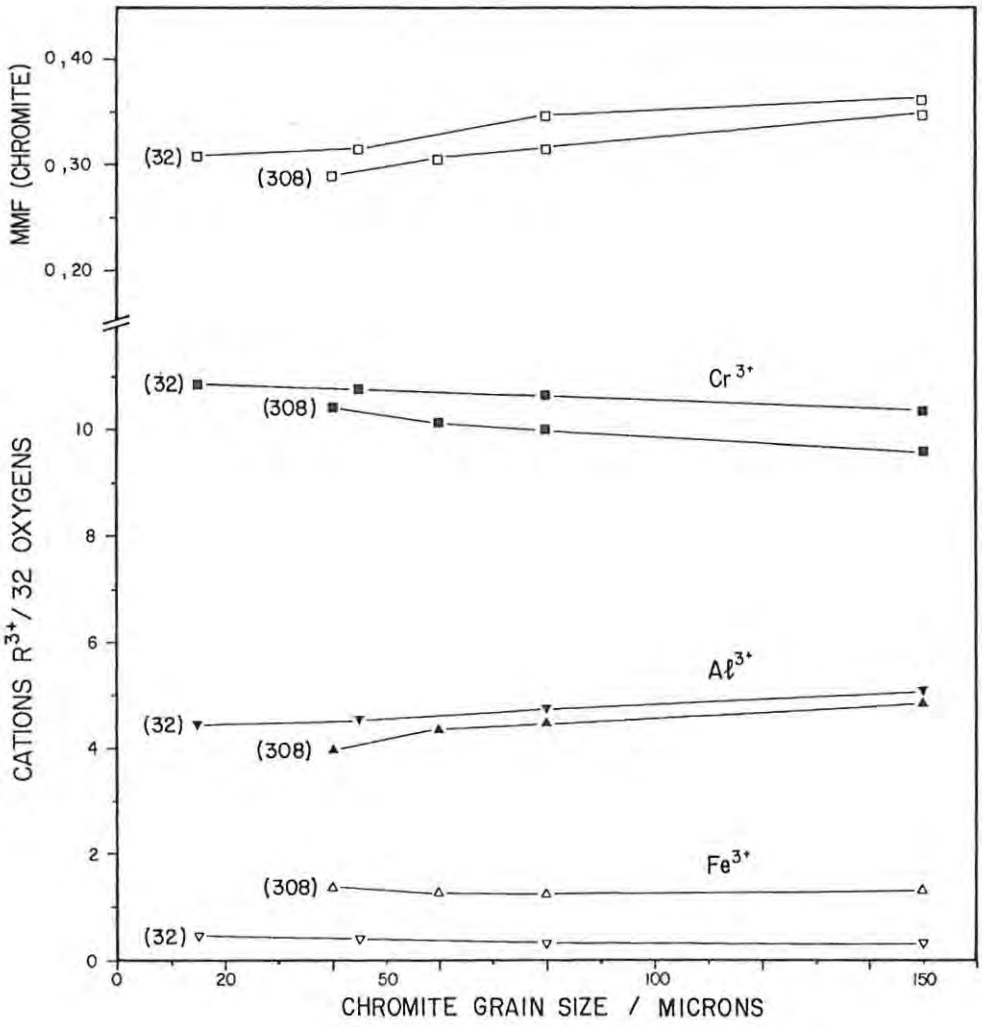

FIG. 49 COMPOSITIONAL VARIATION OF ORTHOPYROXENE HOSTED CHROMITE GRAINS AS A FUNCTION OF CHROMITE GRAIN SIZE, FOR SAMPLES 32 (E UNIT, ZS 7) AND 308 (D_2 SUBUNIT, ZS 3)

the latter trend is not manifested in granular-textured bronzitites: a feature which points to isolation of these assemblages from interstitial magma at an early stage of crystallization.

5.4.2.8 CHROMITE WITHIN THE LOWER ZONE

Microprobe analyses of chromite within 4 samples from drill core KA 5 are presented in Table 29. Cr_2O_3 contents of grains within bronzitite samples denoted 410 and 729 are higher (48,93 to 52,75 wt. per cent) than in the harzburgites (39,44 to 47,67 wt. per cent). Fe_2O_3 contents are substantially higher than determined in drill core ZS 7, varying between 5,73 and 10,60 wt. per cent. Relative to the B unit of the studied section, chromite within the KA 5 bronzitite samples is enriched in Fe_2O_3 and depleted in Al_2O_3, with comparable Cr_2O_3 contents. It will be shown in a subsequent section, however, that the variation of Al and Cr is systematically linked to MMF ratios and is in accordance with the relationships observed in the Ruighoek Pyroxenite.

5.4.2.9 SUMMARY

The present investigation has shown that (1) MMF ratios of polygonal chromite grains within chromitite layers are higher than in disseminated or accessory grains in juxtaposed silicate-rich domains. (2) Secondly, subtle cryptic changes in MMF ratios with stratigraphic height were measured within chromitite layers, systematically linked to variations in the proportions of Cr and Al cations, whereas (3) chromite within silicate-rich environments shows an irregular cryptic variation in relation to stratigraphic height. Though the latter may result from varying degrees of reaction with late-stage melt and subsolidus re-equilibration with coexisting ferromagnesian silicate phases, it is evident from the data that the proportions of Cr and Al cations are linked to variations in MMF ratios within individual samples. This stems from two relationships between composition and grain-size, both of which indicate higher Cr contents coupled to lower MMF ratios. In summation, these are (4) grains isolated from the magma at an early stage by encapsulation in cumulus orthopyroxene

show a trend of increasing Al and Mg with increasing grain-size, and (5) incremental in situ growth, contemporaneous with the nucleation of plagioclase, yields a trend of increasing Cr and Fe^{2+} with increasing grain-size. Though the former is subdued, it is significant that an equivalent cryptic trend of rising Al and Mg with increasing stratigraphic height was measured within the H chromitite layer. The implications are (6) that efficient expulsion of interstitial melt from the chromite accumulation precluded subsequent open-system reactions, (7) a grain-size gradient of increasing size from bottom to top may have characterized the accumulation prior to densification and recrystallization, or (8) crystallization from a restricted volume of melt is indicated. The latter is favoured here since, as suggested by Wilson (1982), the trend of increasing Al with increasing grain-size, for small grains enclosed by cumulus silicate phases, points to crystallization from a restricted volume. The following mass balance consideration illustrates this equilibrium:

$$(1 - V_{xtl}) \cdot [Cr]_{melt} = V_{xtl} \cdot [Cr]_{xtl}$$

where V_{xtl} is the volume fraction of chromite and $[Cr]_{melt}$ is the concentration of chromium in the melt. $[Cr]_{xtl} \propto (1 - V_{xtl})/V_{xtl}$ and remains constant unless the absolute value of V_{xtl} is significant.

(9) The Y_{Al} ratio of chromite occluded by olivine crystals within granular harzburgites and olivine-bronzitites of the C_1 subunit is higher than for grains enclosed in coexisting cumulus orthopyroxene. For example, the average Y_{Al} ratio of the former association is 0,396, whereas that of the latter is 0,332. The corresponding average MMF ratios are 0,370 and 0,439, respectively. The average Y_{Al} ratio of intergranular chromite, including a grain intergrown with plagioclase, is 0,389 and these grains depict a zonal rise in atomic Al/Cr which is consistent with the measured zonal increase of Al/Cr in coexisting orthopyroxene. (10) The dissimilarity in the proportions of Al and Cr in chromite occluded by olivine and orthopyroxene cannot be resolved in terms of grain-size relationships or reaction with residual melt since (a) both silicate phases are the product of cotectic crystallization, and (b) reaction-replacement orthopyroxene is not depicted in these granular-textured rocks (in which intercumulus silicate phases are rarely present). Olivine is,

however, extremely anhedral and is typically "interstitial" to orthopyroxene in olivine-poor assemblages. Hence, it is advocated (11) that advanced migration of olivine grain boundaries during compaction resulted in occlusion of smaller intergranular chromite grains. The higher TiO_2 content of chromite enclosed in olivine, relative to orthopyroxene-hosted grains, is consistent with this conjecture, as is the subrounded habit. Migration of olivine grain boundaries would be inhibited in chromite-rich domains, and the data indicate that occluded grains in these environments are enriched in Cr_2O_3 relative to intergranular grains and crystals intergrown with clinopyroxene or reaction-replacement orthopyroxene. (12) Reaction with liquid, yielding Al_2O_3-rich compositions, is indicated in poikilitic harzburgite assemblages adjacent to the LG 1 and LG 3 chromitite layers. However, (13) chromite intergrown with reaction-replacement orthopyroxene in these domains, and in olivine-rich samples such as 197A and 223D, is enriched in Cr_2O_3 relative to grains occluded by olivine. Hence, (14) an alternative consideration to the above is the closed-system, ionic transfer of Cr from orthopyroxene to an aluminian chromite. This can be illustrated in terms of the following generalized reaction (after Eales and Reynolds, 1985):

(Al-spinel) + (Cr-Al bronzite) $\rightleftharpoons$ (Cr-spinel) + (Al-bronzite)

This relationship is consistent with the higher Cr content of smaller chromite grains enclosed in cumulus orthopyroxene due to the enhanced reactivity of small grains with a higher surface area/mass ratio. However, (15) the present investigation has shown that orthopyroxene may be enriched in Cr and Mg adjacent to occluded chromite grains, implying transfer of Al and Fe^{2+} into chromite with cooling (refer to section 5.2.2.4).

Fig. 50 is a plot of TiO_2 contents in chromite in relation to stratigraphic position. Features portrayed here are (16) the irregular decline in TiO_2 contents towards the top of the C_2 subunit, followed by an irregular rise with increasing stratigraphic height through the D and E units, (17) TiO_2 contents of polygonal chromite grains within chromitite layers are higher relative to small equant grains occluded by cumulus orthopyroxene in juxtaposed bronzitites,

and (18) larger grains intergrown with plagioclase, and grains which are intergranular to orthopyroxene, are enriched in TiO_2 relative to chromite enclosed in orthopyroxene or within chromitite layers (with the exception of the LG 6A and LG 7 chromitite layers). The latter feature (19) can be attributed to the influence of plagioclase nucleation and the inferred longer residence time of these grains in residual melt. Similarly (20), larger chromite grains enclosed in the rim domains of orthopyroxene crystals are enriched in TiO_2 relative to smaller grains removed from grain boundaries. However, observation (17) cited above is anomalous with respect to the contention that the compositions of chromite within chromitite layers approximate to primary liquidus compositions. The data suggests, therefore, (21) that ionic transfer of Ti from chromite to orthopyroxene occurs with cooling. Alternatively, the higher TiO_2 content of chromite within chromitite layers is intimately related to the magmatic conditions that stimulated and attended nucleation of chromite, as evinced by the grain-to-grain decline in TiO_2 through the C and H chromitite layers.

Average Y_{Cr} ratios of grains enclosed in core domains of orthopyroxene crystals within the respective units of the Ruighoek Pyroxenite are given in Table 30. Data pertaining to Lower Zone bronzitite samples and the LG chromitite layers are included in the tabulation.

Unlike titanium, it is evident from the tabulation (22) that there is a similarity between the relative proportion of Cr cations in orthopyroxene-hosted grains and chromite within chromitite layers, although this is not apparent where higher levels of Fe^{3+} cations are depicted (e.g., the LG 2 chromitite in drill core ZS7 and the LG 6A chromitite in drill core ZS3). This implies (23) that ionic transfer of Cr from orthopyroxene to chromite with cooling may not be of major significance in the studied section, but the relationship indicated in the tabulation is to be anticipated by virtue of the magnitude of $(D_{Cr})^{sp}$.

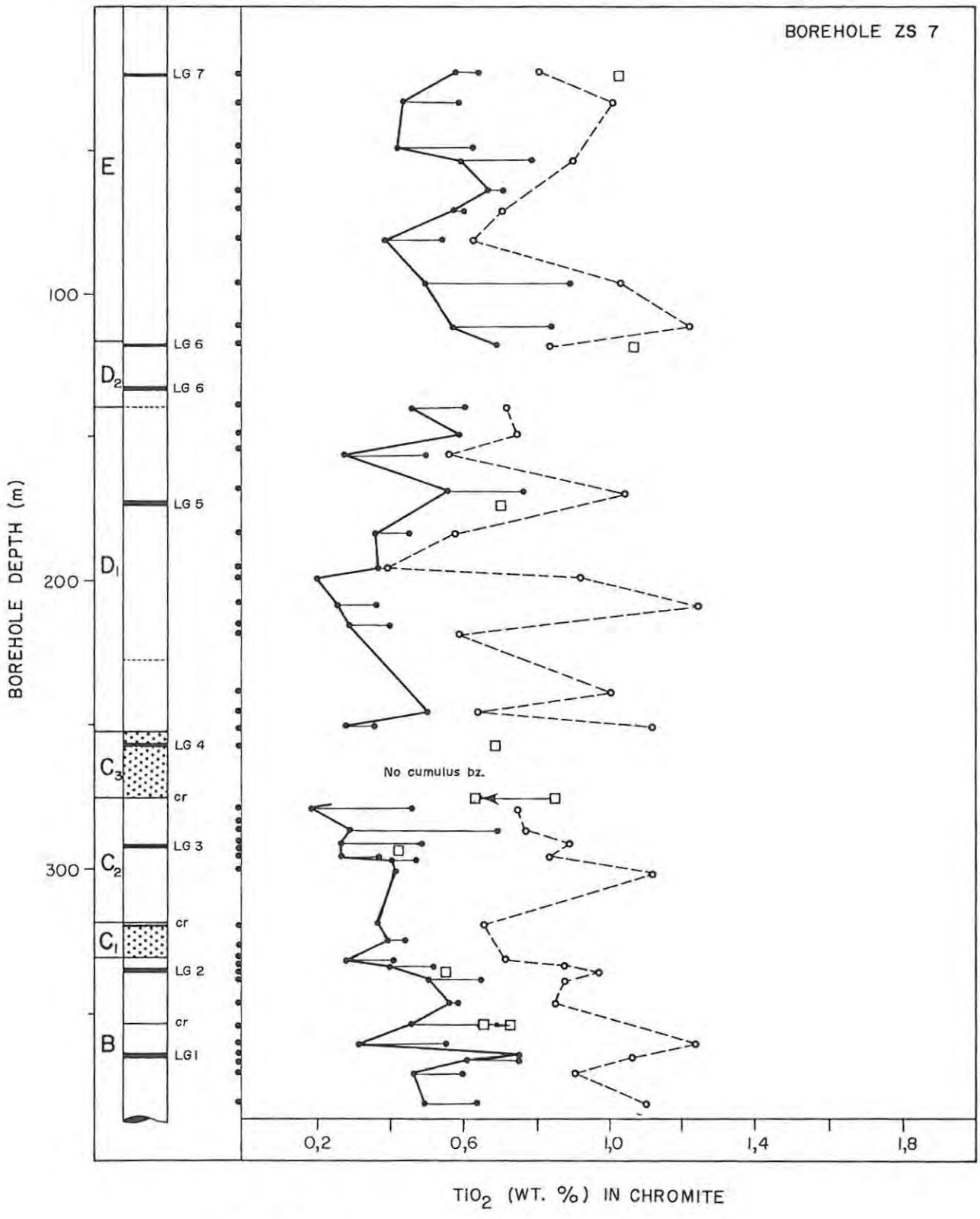

SYMBOLS:

- • SMALL GRAINS ENCLOSED IN CUMULUS BRONZITE
- ○ LARGE INTERGRANULAR CHROMITE AND/OR GRAINS ENCLOSED IN INTERSTITIAL PLAGIOCLASE (AVERAGE VALUES).
- □ CHROMITITES

FIG. 50 TiO_2 ABUNDANCE IN CHROMITE AS A FUNCTION OF STRATIGRAPHIC POSITION AND NATURE OF THE OCCLUDING SILICATE PHASE. HORIZONTAL BARS LINKING DATA POINTS REPRESENT VARIATION OBSERVED WITHIN INDIVIDUAL SAMPLES.

KEY TO TABLES 22 to 29

Cations calculated from original microprobe data on assumption of stoichiometry and assigning of Ti to ulvöspinel.

NiO = 0.00: not analyzed
Grain-size: minimum diameter in micrometres
MMF : $Mg/(Mg + Fe^{2+}_{total})$
FFF : $Fe^{3+}/(Fe^{3+} + Fe^{2+}_{total})$
Y(Cr) : Compositional parameter $Cr/(Cr + Al + Fe^{3+})$

HOST: identity of the encapsulating silicate phase

1 orthopyroxene
2 plagioclase
3 intergranular (i.e., no mesostasis present)
4 olivine
5 mica
6 micropegmatite/quartz
7 clinopyroxene
8 annealed aggregates or polygonal grains within chromitite layers
9 embayment in orthopyroxene (± selvage of plagioclase)

ROCK TYPE OR MICRODOMAIN

1 bronzitite
2 dunite
3 olivine-bronzitite
4 granular- or poikilitic harzburgite; ultramafic pegmatite
5 chromitite
6 olivine-chromitite
7 bronzite-chromitite
8 chromite bronzitite
9 chromite dunite

Core-rim pairs are denoted by the same analysis number, with the rim composition given as the second analysis.

Sample 184A : I chromitite layer
Sample 200 : H chromitite layer
Sample 258A : Analyses of grains within and above the first appearance of olivine at base of C_1 subunit (section = 258B)
Sample 258B : Uppermost, graphite-bearing bronzitite of the B unit
Sample 258B* : Sample 258, but section cut 15 cm below 258B (258B* = 258C)

Borehole depths of samples can be found in Appendix I.

Note: All sections cut parallel to the core axis, with exceptions being 50, 90, 115, 165, 208, 225, 280 and 290.

TABLE 22 MICROPROBE ANALYSES OF CHROMITE : UNIT B

SAMPLE	258B	258B★	258B	258B	258B	258B★	258B★	258B	259	259
ANALYSIS	1	2	3	4	5	6	7	8	1	2
TIO2	.32	.27	.61	.74	.67	.70	.65	.76	.51	.50
CR2O3	51.12	50.17	56.15	55.79	56.61	55.54	56.51	55.95	54.63	53.12
AL2O3	16.53	17.76	9.35	10.38	9.28	11.13	10.72	10.06	12.38	14.88
FE2O3	.64	.81	1.62	1.21	1.09	1.49	1.12	1.12	.96	.71
FEO	22.25	21.87	24.47	22.96	24.27	23.13	22.22	23.23	23.87	23.02
MGO	7.84	8.16	5.60	6.82	5.77	6.87	7.33	6.57	6.58	7.57
MNO	.44	.57	.49	.44	.43	.58	.56	.46	.29	.29
NIO	0.00	.08	0.00	0.00	0.00	.06	.08	0.00	0.00	0.00
TOTAL	99.14	99.70	98.30	98.35	98.12	99.50	99.20	98.15	99.22	100.10
					CATIONS PER 32 OXYGENS					
TI	.063	.053	.127	.152	.140	.142	.132	.157	.103	.099
FE2+	.063	.053	.127	.152	.140	.142	.132	.157	.103	.099
CR	10.625	10.301	12.342	12.090	12.448	11.867	12.089	12.186	11.659	11.048
AL	5.121	5.435	3.063	3.352	3.041	3.544	3.418	3.265	3.938	4.613
FE3+	.127	.158	.339	.251	.229	.304	.229	.232	.196	.141
FE2+	4.829	4.699	5.563	5.111	5.506	5.087	4.898	5.194	5.286	4.967
MG	3.072	3.159	2.320	2.786	2.392	2.767	2.956	2.698	2.648	2.968
MN	.097	.125	.115	.102	.101	.133	.128	.107	.066	.065
NI	0.000	.017	0.000	0.000	0.000	.013	.017	0.000	0.000	0.000
MMF	.385	.399	.289	.346	.297	.346	.370	.335	.329	.369
Y(CR)	.669	.648	.783	.770	.791	.755	.768	.776	.738	.699
Y(AL)	.322	.341	.194	.213	.193	.225	.217	.208	.249	.291
Y(FE3+)	.007	.009	.021	.016	.014	.019	.014	.014	.012	.008
FFF	.025	.032	.056	.045	.038	.054	.043	.041	.035	.027
GRAIN SIZE									80.	140.
HOST	1.	1.	9.	9.	3.	2.	2.	6.	1.	1.
ROCK TYPE	1.	1.	1.	1.	1.	1.	1.	1.	1.	1.

SAMPLE	259	259	259	259	261	261	261	265	265	265
ANALYSIS	2	3	4	5	1	2	3	1	2	3
TIO2	.39	.98	.76	.28	.71	.94	.99	.60	.63	.64
CR2O3	53.06	57.41	57.37	57.52	56.51	57.51	56.95	51.77	51.36	51.31
AL2O3	14.88	9.02	10.23	9.15	10.15	10.08	10.89	14.69	14.66	15.54
FE2O3	1.20	.93	.95	1.11	1.39	1.08	1.13	1.46	1.60	1.20
FEO	22.78	25.07	23.47	24.32	27.12	25.24	23.25	23.48	23.44	22.51
MGO	7.71	5.73	6.91	5.57	4.54	6.06	7.38	6.98	6.93	7.73
MNO	.28	.38	.33	.38	.55	.42	.44	.55	.56	.52
NIO	0.00	0.00	0.00	0.00	0.00	0.00	0.00	.08	.10	.08
TOTAL	100.31	99.53	100.02	98.34	100.98	101.33	101.03	99.61	99.29	99.54
					CATIONS PER 32 OXYGENS					
TI	.077	.203	.154	.058	.145	.189	.197	.120	.126	.127
FE2+	.077	.203	.154	.058	.145	.189	.197	.120	.126	.127
CR	11.007	12.479	12.243	12.650	12.165	12.210	11.969	10.870	10.822	10.684
AL	4.601	2.922	3.254	2.999	3.257	3.190	3.411	4.597	4.600	4.823
FE3+	.238	.194	.194	.233	.287	.220	.225	.292	4.322	.239
FE2+	4.922	5.563	5.144	5.601	6.030	5.479	4.974	5.096	5.099	4.832
MG	3.015	2.348	2.780	2.310	1.843	2.426	2.926	2.763	2.753	3.035
MN	.062	.088	.075	.089	.127	.095	.099	.124	.126	.116
NI	0.000	0.000	0.000	0.000	0.000	0.000	0.000	.017	.021	.017
MMF	.376	.289	.344	.289	.229	.299	.361	.346	.345	.379
Y(CR)	.694	.800	.780	.796	.774	.781	.766	.689	.687	.678
Y(AL)	.290	.187	.207	.188	.207	.204	.218	.291	.292	.306
Y(FE3+)	.015	.012	.012	.014	.018	.014	.014	.018	.020	.015
FFF	.035	.032	.035	.039	.044	.037	.041	.053	.058	.045
GRAIN SIZE								60	60	80
HOST	1.	9.	2.	6.	1.	1.	2.	1.	1.	1.
ROCK TYPE	1.	1.	1.	1.	1.	1.	1.	1.	1.	1.

TABLE 22 (cont.)

SAMPLE	265	265	265	265	265	265	265	271	271	271
ANALYSIS	4	5	6	7	8	9	10	1	2	3
TIO2	.77	.78	.74	.87	.78	.79	.99	.57	.89	.81
CR2O3	56.52	54.33	55.20	55.08	55.64	56.37	56.37	52.65	52.84	53.86
AL2O3	10.12	12.59	12.20	12.08	11.52	10.59	10.32	12.97	12.08	11.31
FE2O3	1.09	1.56	1.50	.80	1.10	1.24	1.09	1.53	2.24	1.99
FEO	24.02	21.30	21.60	21.91	22.01	22.32	23.76	24.62	24.28	24.17
MGO	6.21	8.28	8.11	7.83	7.68	7.34	6.62	6.09	6.45	6.33
MNO	.59	.52	.54	.57	.56	.61	.56	.26	.31	.32
NIO	.03	.07	.09	.03	.05	.06	.06	0.00	0.00	0.00
TOTAL	99.35	99.44	99.99	99.18	99.35	99.33	99.77	98.69	99.10	98.79
					CATIONS PER 32 OXYGENS					
TI	.158	.156	.148	.175	.157	.161	.201	.116	.181	.166
FE2+	.158	.156	.148	.175	.157	.161	.201	.116	.181	.166
CR	12.203	11.427	11.587	11.671	11.815	12.051	12.078	11.304	11.321	11.621
AL	3.257	3.947	3.817	3.815	3.646	3.374	3.296	4.150	3.858	3.637
FE3+	.224	.314	.300	.163	.224	.253	.223	.313	.458	.410
FE2+	5.329	4.584	4.650	4.736	4.787	4.889	5.184	5.475	5.323	5.351
MG	2.528	3.283	3.210	3.128	3.075	2.958	2.674	2.465	2.605	2.575
MN	.136	.117	.121	.129	.127	.140	.128	.060	.071	.074
NI	.006	.015	.019	.006	.011	.013	.013	0.000	0.000	0.000
MMF	.315	.409	.400	.389	.383	.369	.331	.305	.321	.318
Y(CR)	.778	.728	.737	.745	.753	.768	.774	.716	.724	.741
Y(AL)	.207	.251	.243	.243	.232	.215	.211	.263	.246	.232
Y(FE3+)	.014	.020	.019	.010	.014	.016	.014	.019	.029	.026
FFF	.039	.062	.058	.032	.043	.047	.039	.053	.076	.069
GRAIN SIZE	150	110	200	160	200	220	340	75.		110.
HOST	9.	2.	2.	2.	2.	9.	2.	1.	1.	2.
ROCK TYPE	1.	1.	1.	1.	1.	1.	1.	1.	1.	1.

SAMPLE	276	280	280	280	280	280	280	285B	285B	285B
ANALYSIS	1	1	2	3	4	5	6	1	2	3
TIO2	.70	.54	.31	.99	1.17	1.08	1.43	.75	.99	.86
CR2O3	51.06	51.85	50.22	51.92	53.87	53.65	53.53	53.41	55.70	56.15
AL2O3	13.52	14.28	15.90	12.23	11.15	11.24	11.21	13.60	10.81	10.64
FE2O3	3.34	1.70	1.78	2.59	1.32	1.50	1.35	1.70	1.43	1.89
FEO	22.86	23.62	23.09	23.10	23.62	23.61	23.71	24.34	25.57	24.89
MGO	7.40	6.78	7.09	6.94	6.58	6.55	6.73	6.83	5.77	6.19
MNO	.37	.52	.53	.57	.60	.55	.60	.46	.50	.50
NIO	0.00	.08	.03	.06	.06	.06	.07	0.00	0.00	0.00
TOTAL	99.25	99.38	98.95	98.41	98.38	98.25	98.63	101.20	100.78	101.12
					CATIONS PER 32 OXYGENS					
TI	.141	.108	.061	.202	.240	.222	.293	.148	.200	.173
FE2+	.141	.108	.061	.202	.240	.222	.293	.148	.200	.173
CR	10.788	10.946	10.544	11.150	11.651	11.616	11.535	11.144	11.873	11.908
AL	4.258	4.493	4.975	3.914	3.594	3.627	3.600	4.222	3.435	3.363
FE3+	.673	.343	.355	.530	.272	.311	.277	.337	.291	.382
FE2+	4.968	5.166	5.067	5.045	5.164	5.185	5.111	5.215	5.567	5.411
MG	2.948	2.698	2.800	2.809	2.683	2.673	2.734	2.682	2.319	2.475
MN	.084	.117	6.110	.131	.139	.127	.138	.103	.114	.113
NI	0.000	.017	9.000	.013	.013	.013	.015	0.000	0.000	0.000
MMF	.365	.338	.353	.348	.331	.330	.335	.333	.286	.307
Y(CR)	.686	.693	.664	.714	.750	.746	.748	.709	.761	.760
Y(AL)	.270	.284	.313	.251	.231	.233	.233	.268	.220	.214
Y(FE3+)	.042	.021	.022	.034	.017	.020	.018	.021	.018	.024
FFF	.116	.061	.064	.091	.048	.054	.048	.059	.047	.064
GRAIN SIZE	70.							60.		
HOST	1.	1.	1.	1.	2.	2.	2.	1.	2.	2.
ROCK TYPE	7.	1.	1.	1.	1.	1.	1.	1.	1.	1.

TABLE 22 (cont.)

SAMPLE	285B	286A	286A	286A	286A	286A	286A	290	297	297	297
ANALYSIS	4	1	2	3	4	5	6	1	1	2	3
TIO2	1.28	.67	.74	.61	1.20	.58	.45	.62	.49	.63	1.10
CR2O3	55.27	55.04	52.58	52.20	55.69	41.68	48.07	55.20	49.61	53.42	52.19
AL2O3	11.28	11.36	14.32	14.84	11.09	24.02	18.84	10.57	16.97	12.34	12.61
FE2O3	1.56	1.91	1.29	1.48	.89	2.33	1.97	1.23	1.54	1.65	2.35
FEO	24.02	24.62	24.00	23.56	24.15	22.60	22.22	24.42	23.24	24.70	23.92
MGO	7.05	6.17	6.98	7.16	6.77	8.70	8.35	5.68	7.40	5.88	6.76
MNO	.48	.46	.40	.50	.43	.50	.50	.60	.54	.63	.61
NIO	0.00	0.00	0.00	.07	.05	.10	.08	.05	0.00	0.00	0.00
TOTAL	100.94	100.24	100.31	100.42	100.28	100.52	100.48	98.37	99.79	99.25	99.54
					CATIONS PER 32 OXYGENS						
TI	.256	.136	.147	.121	.242	.109	.087	.128	.096	.128	.222
FE2+	.256	.136	.147	.121	.242	.109	.087	.128	.096	.128	.222
CR	11.635	11.731	10.988	10.861	11.824	8.253	9.750	12.047	10.268	11.460	11.087
AL	3.539	3.609	4.460	4.602	3.509	7.089	5.696	3.439	5.235	3.946	3.933
FE3+	.313	.389	.257	.295	.182	.440	.381	.257	.303	.337	.475
FE2+	5.093	5.416	5.160	5.065	5.181	4.626	4.682	5.511	4.992	5.477	5.154
MG	2.798	2.479	2.750	2.809	2.710	3.248	3.193	.338	2.888	2.378	2.707
MN	.108	.105	.089	.111	.098	.106	.109	.140	.120	.145	.139
NI	0.000	0.000	0.000	.015	.011	.020	.016	.011	0.000	0.000	0.000
MMF	.343	.308	.341	.351	.333	.406	.401	.292	.362	.297	.334
Y(CR)	.751	.745	.699	.689	.762	.522	.616	.765	.649	.727	.712
Y(AL)	.228	.229	.284	.292	.226	.449	.359	.218	.331	.250	.256
Y(FE3+)	.020	.024	.016	.018	.011	.027	.024	.016	.019	.021	.030
FFF	.055	.065	.046	.053	.032	.085	.073	.043	.056	.056	.081
GRAIN SIZE		40.	70.	90.	180.	240.			80.	60.	200.
HOST	2.	1.	1.	1.	2.	4.	1.	3.	1.	1.	2.
ROCK TYPE	1.	1.	1.	1.	1.	1.	1.	1.	1.	1.	1.

TABLE 23 MICROPROBE ANALYSES OF CHROMITE : SUBUNIT C1

SAMPLE	238	238	238	238	238	238	238	240	241B	245B
ANALYSIS	1	2	3	4	5	6	6	1	1	1
TIO2	.67	.74	.69	.36	.36	.70	.60	.61	.60	.84
CR2O3	44.41	45.25	44.01	49.59	49.73	46.40	44.71	51.85	53.15	47.11
AL2O3	20.88	20.26	20.91	17.06	16.98	19.68	21.46	15.29	14.31	17.44
FE2O3	2.19	2.22	2.21	1.91	2.42	2.00	2.11	2.24	1.57	2.19
FEO	24.03	22.29	23.11	20.58	20.44	20.52	20.47	19.00	20.16	24.27
MGO	7.47	8.50	7.93	8.89	9.08	9.46	9.66	10.12	9.25	6.89
MNO	.54	.54	.52	.53	.57	.57	.58	.35	.35	.49
NIO	0.00	0.00	0.00	0.00	0.00	0.00	0.00	0.00	0.00	0.00
TOTAL	100.19	99.81	99.38	98.93	99.59	99.34	99.60	99.46	99.39	99.23
					CATIONS PER 32 OXYGENS					
TI	.129	.143	.134	.071	.070	.135	.114	.119	.119	.166
FE2+	.129	.143	.134	.071	.070	.135	.114	.119	.119	.166
CR	9.006	9.168	8.959	10.235	10.197	9.400	8.959	10.641	11.024	9.815
AL	6.311	6.118	6.345	5.248	5.189	5.942	6.409	4.678	4.425	5.416
FE3+	.423	.429	.428	.376	.473	.387	.403	.438	.310	.434
FE2+	5.026	4.636	4.843	4.424	4.364	4.263	4.226	4.006	4.304	5.184
MG	2.856	3.247	3.044	3.459	3.510	3.613	3.649	3.914	3.616	2.706
MN	.117	.117	.113	.117	.125	.124	.124	.077	.077	.109
NI	0.000	0.000	0.000	0.000	0.000	0.000	0.000	0.000	0.000	0.000
MMF	.356	.404	.379	.434	.441	.451	.456	.486	.450	.335
Y(CR)	.572	.583	.569	.645	.642	.597	.568	.675	.699	.626
Y(AL)	.400	.389	.403	.330	.327	.377	.406	.296	.280	.345
Y(FE3+)	.026	.027	.027	.023	.029	.024	.025	.027	.019	.027
FFF	.075	.082	.079	.077	.096	.080	.084	.095	.065	.075
GRAIN SIZE	90.	340.	120.	45.	100.	200.	200.			170.
HOST	4.	4.	4.	1.	1.	2.	2.	8.	8.	4.
ROCK TYPE	4.	4.	4.	4.	4.	4.	4.	5.	6.	2.

TABLE 23 (cont.)

SAMPLE	245B	247	247	249	249	249	249	249	254	254
ANALYSIS	2	1	2	1	2	3	4	5	1	1
TIO2	.80	.67	.72	.47	.45	.42	.39	.47	.39	.35
CR2O3	46.92	45.37	45.50	43.80	48.91	48.94	50.54	45.79	44.66	44.40
AL2O3	17.78	19.47	20.03	21.21	17.91	18.13	16.91	20.42	21.00	21.08
FE2O3	2.12	2.31	2.12	2.62	2.65	2.02	1.67	2.11	2.00	1.72
FEO	24.08	23.86	22.91	23.55	19.72	20.28	20.73	20.25	23.57	24.21
MGO	7.03	7.34	8.13	7.60	9.79	9.38	8.96	9.56	7.48	6.98
MNO	.48	.45	.46	.56	.56	.56	.55	.53	.54	.53
NIO	0.00	0.00	0.00	0.00	0.00	0.00	0.00	0.00	.06	.05
TOTAL	99.21	99.47	99.88	99.82	99.99	99.74	99.75	99.13	99.71	99.33
					CATIONS PER 32 OXYGENS					
TI	.158	.131	.139	.091	.087	.081	.076	.090	.075	.068
FE2+	.158	.131	.139	.091	.087	.081	.076	.090	.075	.068
CR	9.754	9.319	9.244	8.893	9.908	9.951	10.356	9.259	9.089	9.093
AL	5.509	5.964	6.065	6.418	5.407	5.494	5.165	6.154	6.370	6.435
FE3+	.419	.453	.411	.507	.511	.392	.327	.406	.389	.336
FE2+	5.137	5.057	4.785	4.969	4.139	4.282	4.418	4.241	4.999	5.178
MG	2.755	2.842	3.114	2.909	3.739	3.596	3.462	3.644	2.870	2.695
MN	.106	.099	.100	.122	.121	.122	.121	.115	.118	.116
NI	0.000	0.000	0.000	0.000	0.000	0.000	0.000	0.000	.012	.010
MMF	.342	.353	.387	.365	.469	.451	.435	.456	.361	.339
Y(CR)	.621	.591	.588	.562	.626	.628	.653	.585	.573	.573
Y(AL)	.351	.378	.385	.405	.341	.346	.325	.389	.402	.406
Y(FE3+)	.026	.028	.026	.032	.032	.024	.020	.025	.024	.021
FFF	.073	.079	.077	.091	.107	.082	.067	.085	.071	.060
GRAIN SIZE				70.	80.	110.	110.			
HOST	3.	4.	3.	4.	1.	1.	1.	3.	4.	4.
ROCK TYPE	2.	2.	2.	3.	3.	3.	3.	3.	3.	3.

SAMPLE	254	254	254	258A	258A	258A
ANALYSIS	2	2	3	1	2	3
TIO2	.44	.48	.54	.50	.50	.39
CR2O3	45.51	44.65	45.32	45.06	45.03	49.58
AL2O3	20.68	20.82	21.25	19.56	19.65	16.49
FE2O3	1.69	1.95	1.77	2.22	2.23	1.98
FEO	23.18	23.56	20.81	23.53	23.34	21.62
MGO	7.77	7.50	9.41	7.30	7.46	8.20
MNO	.54	.54	.50	.43	.39	.40
NIO	.06	.04	.07	0.00	0.00	0.00
TOTAL	99.88	99.54	99.67	98.60	98.60	98.66
				CATIONS PER 32 OXYGENS		
TI	.085	.093	.103	.098	.098	.077
FE2+	.085	.093	.103	.098	.098	.077
CR	9.242	9.106	9.097	9.329	9.309	10.330
AL	6.256	6.329	6.358	6.036	6.054	5.121
FE3+	.328	.379	.338	.437	.439	.393
FE2+	4.895	4.990	4.317	5.055	5.005	4.689
MG	2.975	2.884	3.561	2.849	2.908	3.221
MN	.117	.118	.107	.095	.086	.089
NI	.012	.008	.014	0.000	0.000	.403
MMF	.373	.361	.446	.356	.362	.403
Y(CR)	.584	.576	.576	.590	.589	.651
Y(AL)	.395	.400	.402	.381	.383	.323
Y(FE3+)	.020	.023	.021	.027	.027	.024
FFF	.061	.069	.071	.078	.079	.076
GRAIN SIZE						70.
HOST	4.	4.	3.	4.	3.	1.
ROCK TYPE	3.	3.	3.	3.	3.	3.

TABLE 24 MICROPROBE ANALYSES OF CHROMITE : SUBUNIT C2

SAMPLE	203	203	203	203	203	203	203	203	203	203
ANALYSIS	1	2	3	4	4	5	5	6	7	7
TIO2	.18	.45	.39	.85	.73	.83	.78	.67	.73	.71
CR2O3	50.15	53.29	52.45	52.74	54.24	52.57	54.35	55.50	53.83	54.42
AL2O3	16.61	13.43	14.37	13.47	11.84	13.76	12.15	11.45	12.97	12.07
FE2O3	1.59	1.74	1.58	1.68	1.81	1.52	1.43	1.60	1.55	1.80
FEO	22.48	23.00	22.85	22.80	22.68	21.53	22.19	22.21	22.30	22.11
MGO	7.51	7.10	7.24	7.48	7.21	8.19	7.61	7.56	7.69	7.64
MNO	.57	.58	.56	.56	.57	.58	.53	.53	.58	.58
NIO	0.00	0.00	0.00	0.00	0.00	0.00	0.00	0.00	0.00	0.00
TOTAL	99.09	99.60	99.44	99.58	99.09	98.99	99.05	99.53	99.65	99.34
					CATIONS PER 32 OXYGENS					
TI	.036	.090	.078	.170	.148	.166	.158	.135	.146	.143
FE2+	.036	.090	.078	.170	.148	.166	.158	.135	.146	.143
CR	10.452	11.244	11.025	11.098	11.570	11.051	11.547	11.782	11.328	11.535
AL	5.160	4.224	4.502	4.225	3.764	4.311	3.847	3.623	4.068	3.813
FE3+	.316	.351	.316	.337	.369	.305	.290	.324	.311	.365
FE2+	4.922	5.044	5.004	4.906	4.970	4.623	4.831	4.854	4.818	4.815
MG	2.951	2.824	2.869	2.968	2.900	3.246	3.048	3.026	3.051	3.053
MN	.127	.131	.126	.126	.130	.131	.121	.120	.131	.132
NI	0.000	0.000	0.000	0.000	0.000	0.000	0.000	0.000	0.000	0.000
MMF	.373	.354	.360	.368	.361	.403	.379	.377	.380	.381
Y(CR)	.656	.710	.695	.708	.736	.705	.736	.749	.721	.734
Y(AL)	.323	.266	.284	.269	.239	.275	.245	.230	.258	.242
Y(FE3+)	.019	.022	.019	.021	.023	.019	.018	.020	.019	.023
FFF	.059	.064	.058	.062	.067	.059	.054	.061	.059	.068
GRAIN SIZE	60.	70.	50.	130.	130.	220.	220.		90.	90.
HOST	1.	1.	1.	1.	1.	2.	2.	2.	2.	2.
ROCK TYPE	1.	1.	1.	1.	1.	1.	1.	1.	1.	1.

SAMPLE	205A	205A	205A	205A	205A	208	208	208	208	208
ANALYSIS	1	2	2	3	4	1	2	3	4	4
TIO2	.89	.67	.59	.93	1.03	.33	.29	.34	.68	.61
CR2O3	54.01	55.36	56.32	54.52	54.47	51.97	52.02	51.59	52.58	52.39
AL2O3	11.35	11.28	9.81	11.67	12.58	15.14	15.20	15.45	13.52	13.79
FE2O3	1.52	1.21	1.65	1.32	.33	1.68	1.40	1.60	1.94	2.12
FEO	22.98	22.92	23.02	22.96	22.56	22.20	22.22	21.98	22.90	22.62
MGO	6.85	6.91	6.55	7.09	7.52	7.73	7.64	7.86	7.27	7.49
MNO	.56	.55	.57	.58	.58	.54	.56	.52	.56	.51
NIO	.05	.08	.07	.07	.06	.06	.04	.09	.05	.04
TOTAL	98.22	98.98	98.58	99.15	99.14	99.65	99.38	99.43	99.51	99.58
					CATIONS PER 32 OXYGENS					
TI	.183	.137	.122	.189	.208	.065	.058	.067	.136	.122
FE2+	.183	.137	.122	.189	.208	.065	.058	.067	.136	.122
CR	11.667	11.871	12.237	11.640	11.543	10.831	10.871	10.749	11.087	11.011
AL	3.654	3.604	3.177	3.713	3.973	4.703	4.734	4.798	4.249	4.320
FE3+	.313	.249	.341	.269	.068	.334	.279	.317	.391	.425
FE2+	5.070	5.062	5.170	4.998	4.851	4.829	4.856	4.777	4.973	4.909
MG	2.790	2.793	2.682	2.854	3.004	3.037	3.010	3.088	2.890	2.968
MN	.129	.126	.132	.133	.132	.120	.125	.116	.126	.115
NI	.011	.018	.016	.015	.013	.013	.008	.019	.011	.008
MMF	.346	.349	.335	.354	.372	.382	.379	.389	.361	.371
Y(CR)	.746	.754	.776	.745	.741	.682	.684	.677	.705	.698
Y(AL)	.234	.228	.201	.238	.255	.296	.298	.302	.270	.274
Y(FE3+)	.020	.015	.021	.017	.004	.021	.010	.019	.024	.026
FFF	.056	.045	.060	.049	.013	.063	7.050	.061	.071	.077
GRAIN SIZE										
HOST	1.	3.	3.	2.	2.	1.	1.	1.	1.	1.
ROCK TYPE	1.	1.	1.	1.	1.	1.	1.	1.	1.	1.

TABLE 24 (cont.)

SAMPLE	208	208	208	208	208	208	211	211	211	211
ANALYSIS	5	6	7	8	9	10	1	2	2	3
TIO2	.70	.78	.71	.81	.86	.51	.28	.32	.29	.26
CR2O3	52.41	53.67	54.48	54.86	54.93	55.14	54.16	52.63	52.66	53.14
AL2O3	14.01	12.45	11.98	11.44	11.76	11.87	12.20	14.43	14.26	13.06
FE2O3	1.83	1.99	1.66	1.71	1.15	1.21	1.95	1.64	1.58	1.87
FEO	22.40	22.97	22.79	22.84	23.80	24.20	23.71	23.15	23.30	23.41
MGO	7.70	7.19	7.16	7.13	6.62	6.19	6.30	7.06	6.90	6.51
MNO	.53	.60	.57	.57	.61	.59	.63	.61	.56	.61
NIO	.06	.05	.09	.09	.10	.06	0.00	0.00	0.00	0.00
TOTAL	99.65	99.71	99.44	99.46	99.83	99.77	99.23	99.85	99.56	98.86
					CATIONS PER 32 OXYGENS					
TI	.139	.157	.143	.164	.174	.103	.057	.064	.058	.053
FE2+	.139	.157	.143	.164	.174	.103	.057	.064	.058	.053
CR	10.980	11.357	11.581	11.690	11.688	11.770	11.595	11.034	11.089	11.354
AL	4.375	3.927	3.795	3.633	3.730	3.777	3.893	4.509	4.476	4.159
FE3+	.366	.402	.337	.348	.233	.246	.398	.328	.318	.382
FE2+	4.827	4.985	4.981	4.986	5.183	5.361	5.313	5.072	5.134	5.283
MG	3.041	2.868	2.869	2.865	2.656	2.491	2.543	2.791	2.739	2.622
MN	.119	.136	.130	.130	.139	.135	.144	.137	.126	.140
NI	.013	.011	.019	.019	.022	.013	0.000	0.000	0.000	0.000
MMF	.379	.358	.358	.357	.331	.313	.321	.352	.345	.331
Y(CR)	.698	.724	.737	.746	.746	.745	.729	.695	.698	.714
Y(AL)	.278	.250	.241	.231	.238	.239	.245	.284	.281	.261
Y(FE3+)	.023	.025	.021	.022	.014	.015	.025	.020	.020	.024
FFF	.068	.072	.061	.063	.041	.043	.069	.060	.057	.067
GRAIN SIZE							35.	50.	50.	40.
HOST	1.	3.	2.	2.	7.	7.	1.	1.	1.	1.
ROCK TYPE	1.	1.	1.	1.	1.	1.	1.	1.	1.	1.

SAMPLE	211	211	211	211	211	211	211	211	211	213B
ANALYSIS	4	5	5	6	6	7	7	8	8	1
TIO2	.48	.76	.32	.97	.43	.88	.43	.96	.44	.68
CR2O3	54.59	54.63	56.09	53.46	55.14	53.78	54.64	54.19	56.02	51.96
AL2O3	11.20	11.36	10.46	11.87	10.92	11.29	11.15	11.82	10.20	15.75
FE2O3	2.01	2.17	2.09	2.15	2.32	2.09	2.23	1.60	2.02	1.72
FEO	25.25	23.60	23.45	26.55	26.36	25.38	24.79	24.68	24.00	19.35
MGO	5.35	6.68	6.32	5.09	4.76	5.52	5.60	6.20	5.99	10.04
MNO	.67	.65	.67	.71	.72	.67	.68	.65	.68	.40
NIO	0.00	0.00	0.00	0.00	0.00	0.00	0.00	0.00	0.00	0.00
TOTAL	99.56	99.85	99.40	100.80	100.65	99.61	99.52	100.11	99.35	99.91
					CATIONS PER 32 OXYGENS					
TI	.098	.154	.065	.197	.088	.180	.088	.194	.090	.132
FE2+	.098	.154	.065	.197	.088	.180	.088	.194	.090	.132
CR	11.784	11.643	12.082	11.398	11.851	11.585	11.782	11.535	12.115	10.608
AL	3.604	3.608	3.358	3.772	3.498	3.625	3.583	3.750	3.288	4.792
FE3+	.415	.440	.429	.436	.475	.430	.458	.326	.416	.335
FE2+	5.668	5.167	5.279	5.792	5.905	5.603	5.566	5.363	5.400	4.048
MG	2.177	2.684	2.567	2.046	1.929	2.242	2.277	2.488	2.442	3.864
MN	.155	.148	.155	.162	.166	.155	.157	.148	.157	.087
NI	0.000	0.000	0.000	0.000	0.000	0.000	0.000	0.000	0.000	0.000
MMF	.274	.335	.324	.254	.243	.279	.287	.309	.307	.480
Y(CR)	.745	.741	.761	.730	.748	.740	.744	.738	.765	.674
Y(AL)	.228	.229	.211	.241	.221	.231	.226	.240	.207	.304
Y(FE3+)	.026	.028	.027	.027	.029	.027	.028	.020	.026	.021
FFF	.067	.076	.074	.067	.073	.069	.074	.055	.070	.074
GRAIN SIZE	100.	170.	170.	440.	440.	200.	200.	250.	250.	
HOST	1.	2.	2.	5.	5.	6.	6.	6.	6.	8.
ROCK TYPE	1.	1.	1.	1.	1.	1.	1.	1.	1.	5.

TABLE 24 (cont.)

SAMPLE	213B	213B	213B	213B	213B	213B	213B	214A	214A	214A
ANALYSIS	2	3	4	4	5	6	7	1	2	3
TIO2	.41	.53	.80	.83	.77	.60	.61	.49	.45	.38
CR2O3	52.68	53.38	54.65	54.66	54.71	51.72	41.11	55.84	53.59	53.88
AL2O3	13.47	14.09	12.26	12.31	12.29	15.38	23.95	12.16	14.03	13.64
FE2O3	1.85	1.19	1.31	1.32	1.05	1.95	2.31	1.93	1.10	1.13
FEO	22.62	22.90	22.23	22.29	21.97	20.18	22.43	19.41	22.32	22.14
MGO	7.23	7.46	7.74	7.80	7.86	9.37	8.79	9.50	7.74	7.70
MNO	.45	.44	.46	.40	.39	.35	.34	.37	.40	.40
NIO	0.00	0.00	0.00	0.00	0.00	0.00	0.00	0.00	0.00	0.00
TOTAL	98.71	99.99	99.46	99.61	99.04	99.56	99.55	99.70	99.64	99.28
					CATIONS PER 32 OXYGENS					
TI	.082	.105	.160	.166	.155	.117	.115	.097	.089	.076
FE2+	.082	.105	.160	.166	.155	.117	.115	.097	.089	.076
CR	11.193	11.161	11.551	11.531	11.595	10.657	8.204	11.641	11.221	11.340
AL	4.266	4.391	3.863	3.870	3.882	4.723	7.123	3.780	4.379	4.279
FE3+	.375	.237	.264	.265	.212	.384	.440	.384	.221	.228
FE2+	5.001	4.961	4.811	4.807	4.771	4.283	4.620	4.183	4.855	4.854
MG	2.896	2.941	3.084	3.102	3.141	3.640	3.307	3.734	3.056	3.056
MN	.102	.098	.104	.090	.088	.077	.072	.082	.090	.090
NI	0.000	0.000	0.000	0.000	0.000	0.000	0.000	0.000	0.000	0.000
MMF	.362	.367	.382	.384	.389	.452	.411	.467	.381	.382
Y(CR)	.706	.706	.736	.736	.739	.676	.520	.736	.709	.715
Y(AL)	.269	.278	.246	.247	.247	.299	.451	.239	.276	.270
Y(FE3+)	.023	.015	.016	.016	.013	.024	.027	.023	.013	.014
FFF	.068	.044	.050	.050	.041	.080	.085	.082	.042	.044
GRAIN SIZE	50.	70.	200.	200.		70.				
HOST	1.	1.	2.	2.	2.	1.	4.	8.	1.	1.
ROCK TYPE	1.	1.	1.	1.	1.	1.	1.	5.	1.	1.

SAMPLE	214A	214A	214A	214A	214A	215	215	215	215	215
ANALYSIS	4	5	6	7	8	1	2	3	4	5
TIO2	.42	.44	.48	.54	.51	.31	.26	.33	.36	.71
CR2O3	53.69	54.60	52.72	52.83	50.56	50.60	51.53	51.23	53.21	53.96
AL2O3	13.58	12.34	14.22	14.67	14.90	16.72	15.73	16.13	14.36	12.42
FE2O3	1.28	1.87	1.86	1.45	2.42	1.47	1.18	1.14	.83	1.02
FEO	21.97	21.23	21.51	19.79	24.36	21.45	20.92	20.75	22.26	23.67
MGO	7.79	8.13	8.25	9.39	6.59	8.37	8.36	8.63	7.55	6.58
MNO	.41	.41	.42	.40	.29	.48	.55	.49	.51	.54
NIO	0.00	0.00	0.00	0.00	0.00	.06	.06	.06	.06	.05
TOTAL	99.14	99.02	99.46	99.07	99.64	99.46	98.59	98.76	99.14	98.96
					CATIONS PER 32 OXYGENS					
TI	.084	.088	.095	.106	.102	.061	.052	.065	.072	.144
FE2+	.084	.088	.095	.106	.102	.061	.052	.065	.072	.144
CR	11.311	11.553	11.011	10.962	10.637	10.445	10.764	10.647	11.189	11.542
AL	4.264	3.892	4.427	4.537	4.672	5.144	4.897	4.996	4.500	3.960
FE3+	.257	.378	.371	.287	.486	.289	.235	.226	.167	.209
FE2+	4.813	4.664	4.657	4.237	5.321	4.624	4.572	4.497	4.879	5.212
MG	3.094	3.243	3.249	3.674	2.614	3.257	3.292	3.381	2.993	2.653
MN	.092	.093	.094	.089	.065	.106	.123	.109	.115	.124
NI	0.000	0.000	0.000	0.000	0.000	.012	.013	.013	.013	.011
MMF	.387	.405	.406	.458	.325	.410	.415	.425	.376	.331
Y(CR)	.714	.730	.696	.694	.673	.657	.677	.670	.705	.734
Y(AL)	.269	.245	.280	.287	.295	.323	.308	.314	.283	.252
Y(FE3+)	.016	.023	.023	.018	.030	.018	.014	.014	.010	.013
FFF	.049	.073	.072	.061	.082	.058	.048	.047	.032	.037
GRAIN SIZE		75.	80.							
HOST	1.	1.	1.	3.	4.	1.	1.	1.	1.	1.
ROCK TYPE	1.	1.	1.	1.	1.	1.	1.	1.	1.	1.

TABLE 24 (cont.)

SAMPLE	215	215	215	215	221	221	221	221	221	221
ANALYSIS	6	6	7	8	1	1	2	3	4	4
TIO2	.86	.62	.77	.81	.46	.40	.61	.42	.62	.64
CR2O3	54.78	55.98	55.91	52.57	47.98	48.29	49.56	51.04	48.17	50.27
AL2O3	11.66	10.25	10.20	13.60	19.00	18.49	17.29	16.85	17.36	15.47
FE2O3	1.20	1.78	1.25	1.50	1.32	1.52	1.43	1.28	1.43	1.48
FEO	24.85	24.44	23.02	21.00	20.84	20.57	21.77	20.62	23.87	24.70
MGO	6.00	5.90	6.68	8.39	9.05	9.05	8.39	9.06	6.89	6.26
MNO	.58	.57	.57	.54	.47	.50	.54	.51	.56	.53
NIO	.06	.06	.06	.06	.04	.05	.08	.05	.04	.08
TOTAL	100.00	99.60	98.46	98.48	99.17	98.88	99.68	99.83	98.95	99.43
					CATIONS PER 32 OXYGENS					
TI	.175	.127	.159	.163	.089	.078	.119	.082	.123	.128
FE2+	.175	.127	.159	.163	.089	.078	.119	.082	.123	.128
CR	11.696	12.082	12.126	11.094	9.787	9.897	10.184	10.445	10.062	10.589
AL	3.710	3.297	3.297	4.278	5.777	5.648	5.296	5.140	5.405	4.857
FE3+	.244	.366	.259	.302	.258	.298	.281	.251	.286	.297
FE2+	5.439	5.454	5.123	4.527	4.408	4.383	4.614	4.382	5.153	5.378
MG	2.415	2.401	2.731	3.338	3.480	3.497	3.250	3.496	2.714	2.486
MN	.133	.132	.132	.122	.103	.110	.119	.112	.125	.120
NI	.013	.013	.013	.013	.008	.010	.017	.010	.008	.017
MMF	.300	.300	.340	.415	.436	.439	.407	.439	.339	.311
Y(CR)	.747	.767	.773	.708	.618	.625	.646	.659	.638	.672
Y(AL)	.237	.209	.210	.272	.365	.356	.336	.324	.343	.308
Y(FE3+)	.015	.023	.016	.019	.016	.018	.017	.015	.018	.018
FFF	.041	.061	.046	.060	.054	.062	.056	.053	.051	.051
GRAIN SIZE										
HOST	3.	3.	2.	2.	1.	1.	1.	1.	3.	3.
ROCK TYPE	1.	1.	1.	1.	1.	1.	1.	1.	1.	1.

SAMPLE	221	221	221	221	221	221	223	223	223	225	225	225	225
ANALYSIS	4	5	6	7	7	8	1	2	3	1	2	3	4
TIO2	.38	.63	.56	.51	.44	.64	.67	.62	.64	.41	.46	1.05	1.18
CR2O3	47.41	48.93	50.27	50.34	53.35	53.26	42.82	41.31	48.04	51.85	54.63	53.02	53.67
AL2O3	17.75	17.18	16.70	16.68	13.36	13.88	22.05	23.31	18.60	13.93	10.93	11.40	11.53
FE2O3	2.01	1.64	1.23	1.11	1.22	1.05	1.98	2.37	1.61	1.57	1.46	1.50	1.29
FEO	26.30	23.54	21.72	21.07	21.93	21.92	23.53	23.57	20.58	24.64	25.70	26.18	26.11
MGO	5.37	7.27	8.29	8.57	7.51	7.88	7.72	7.85	9.29	5.88	4.88	4.98	5.31
MNO	.58	.54	.52	.54	.58	.53	.50	.50	.47	.58	.57	.56	.54
NIO	.04	.06	.06	.07	.07	.08	.07	.06	.07	.06	.03	.03	.07
TOTAL	99.85	99.80	99.36	98.90	98.47	99.24	99.34	99.59	99.31	98.92	98.66	98.73	99.70
						CATIONS PER 32 OXYGENS							
TI	.075	.124	.110	.100	.089	.128	.129	.119	.124	.083	.096	.217	.242
FE2+	.075	.124	.110	.100	.089	.128	.129	.119	.124	.083	.096	.217	.242
CR	9.915	10.127	10.392	10.429	11.341	11.188	8.689	8.315	9.789	11.077	11.943	11.551	11.553
AL	5.533	5.300	5.145	5.150	4.233	4.346	6.669	6.993	5.649	4.436	3.561	3.702	3.699
FE3+	.401	.325	.243	.220	.248	.211	.382	.454	.313	.320	.304	.312	.265
FE2+	5.744	5.031	4.641	4.518	4.843	4.743	4.923	4.901	4.314	5.486	5.843	5.817	5.705
MG	2.117	2.837	3.231	3.347	3.010	3.121	2.954	2.979	3.569	2.368	2.011	2.045	2.155
MN	.130	.120	.115	.120	.132	.119	.109	.108	.103	.133	.133	.131	.124
NI	.008	.013	.013	.015	.015	.017	.014	.012	.014	.013	.007	.007	.015
MMF	.266	.354	.404	.420	.378	.390	.368	.372	.445	.298	.252	.253	.265
Y(CR)	.625	.643	.658	.660	.717	.710	.552	.527	.621	.699	.755	.742	.744
Y(AL)	.349	.336	.326	.326	.267	.276	.424	.444	.359	.280	.225	.237	.238
Y(FE3+)	.025	.020	.015	.013	.015	.013	.024	.028	.019	.020	.019	.020	.017
FFF	.064	.059	.048	.045	.047	.041	.070	.082	.065	.054	.048	.049	.042
GRAIN SIZE							65.	50.	140.				
HOST	3.	3.	3.	7.	7.	2.	4.	4.	1.	1.	2.	2.	2.
ROCK TYPE	1.	1.	1.	1.	1.	1.	2.	2.	2	1.	1.	1.	1.

TABLE 25 MICROPROBE ANALYSES OF CHROMITE : SUBUNIT C3

SAMPLE	170	170	170	170	172A	172A	172A	172A	LG4	LG4
ANALYSIS	1	2	3	4	1	2	3	4	1	1
TIO2	.72	.44	.68	.76	.70	.65	.68	.70	.68	.68
CR2O3	47.99	47.34	48.12	47.65	48.91	49.28	50.27	48.90	52.02	52.47
AL2O3	17.03	17.72	17.39	17.70	16.30	16.76	16.96	17.17	16.37	15.96
FE2O3	2.61	2.94	2.36	2.26	1.83	1.47	1.17	1.56	1.77	1.31
FEO	24.57	24.01	22.52	23.27	23.69	22.70	22.95	22.34	16.48	16.60
MGO	6.79	6.96	7.98	7.63	7.03	7.72	7.89	8.08	11.90	11.67
MNO	.47	.50	.49	.50	.45	.47	.44	.42	.35	.35
NIO	0.00	.05	.04	0.00	0.00	0.00	0.00	0.00	.10	.10
TOTAL	100.19	99.97	99.59	99.77	98.92	99.05	100.36	99.17	99.67	99.15
					CATIONS PER 32 OXYGENS					
TI	.142	.086	.133	.149	.139	.128	.132	.137	.130	.131
FE2+	.142	.086	.133	.149	.139	.128	.132	.137	.130	.131
CR	9.942	9.787	9.923	9.821	10.258	10.252	10.317	10.120	10.482	10.654
AL	5.258	5.460	5.345	5.437	5.095	5.197	5.188	5.296	4.917	4.830
FE3+	.516	.580	.465	.444	.367	.292	.229	.307	.340	.254
FE2+	5.244	5.166	4.781	4.925	5.117	4.867	4.850	4.754	3.383	3.436
MG	2.652	2.713	3.103	2.965	2.781	3.028	3.053	3.152	4.521	4.467
MN	.104	.111	.108	.110	.101	.104	.096	.093	.075	.076
NI	0.000	.010	.008	0.000	0.000	0.000	0.000	0.000	.020	.021
MMF	.329	.340	.387	.368	.346	.377	.379	.391	.562	.556
Y(CR)	.632	.618	.630	.625	.652	.651	.655	.643	.666	.676
Y(AL)	.334	.345	.339	.346	.324	.330	.329	.336	.312	.306
Y(FE3+)	.032	.036	.029	.028	.023	.018	.014	.019	.021	.016
FFF	.087	.099	.086	.080	.065	.055	.043	.059	.088	.066
GRAIN SIZE	70.	90.			75.	125.	180.			
HOST	4.	4.	3.	3.	4.	4.	4.	3.	8.	8.
ROCK TYPE	2.	2.	2.	2.	9.	9.	9.	9.	5.	5.

SAMPLE	177A	177A	177A	177A	177A	177A	178A	178A	180	180
ANALYSIS	1	2	3	4	5	6	1	2	1	2
TIO2	.64	.67	.63	.62	.51 *	.54	.59	.63	.65	.73
CR2O3	53.41	54.09	52.84	52.69	51.65	50.81	54.05	54.33	45.91	45.68
AL2O3	13.14	13.69	14.64	14.74	15.96	16.78	13.84	14.20	19.18	19.17
FE2O3	1.97	1.61	1.93	2.01	1.57	1.55	1.99	1.37	2.66	2.68
FEO	20.89	18.25	19.16	19.05	20.52	20.14	23.11	20.74	24.78	24.46
MGO	8.53	10.39	9.95	10.02	9.08	9.41	7.67	9.11	6.92	7.14
MNO	.44	.37	.39	.39	.50	.50	.47	.45	.42	.42
NIO	0.00	0.00	0.00	0.00	.07	.09	0.00	0.00	.04	0.00
TOTAL	99.02	99.08	99.54	99.53	99.86	99.83	101.73	100.83	100.56	100.28
					CATIONS PER 32 OXYGENS					
TI	.128	.131	.123	.121	.100	.105	.115	.122	.126	.142
FE2+	.128	.131	.123	.121	.100	.105	.115	.122	.126	.142
CR	11.230	11.194	10.881	10.842	10.608	10.378	11.130	11.144	9.385	9.347
AL	4.118	4.222	4.493	4.520	4.886	5.109	4.248	4.341	5.844	5.846
FE3+	.395	.318	.378	.394	.307	.303	.391	.268	.518	.522
FE2+	4.519	3.863	4.050	4.026	4.359	4.248	4.919	4.378	5.233	5.153
MG	3.381	4.054	3.863	3.887	3.516	3.624	2.978	3.523	2.667	2.754
MN	.099	.082	.086	.085	.110	.109	.104	.099	.092	.092
NI	0.000	0.000	0.000	0.000	.015	.019	0.000	0.000	.008	0.000
MMF	.421	.503	.480	.483	.440	.454	.371	.439	.332	.342
Y(CR)	.713	.711	.690	.688	.671	.657	.705	.707	.595	.594
Y(AL)	.261	.268	.285	.286	.309	.323	.269	.275	.371	.372
Y(FE3+)	.025	.020	.024	.025	.019	.019	.024	.017	.032	.033
FFF	.078	.073	.083	.086	.064	.065	.072	.056	.088	.089
GRAIN SIZE			60.	120.	290.	290.			100.	120.
HOST	4.	8.	1.	1.	7.	7.	4.	1.	4.	4.
ROCK TYPE	6.	6.	4.	4.	4.	4.	6.	4.	2.	2.

TABLE 25 (cont.)

SAMPLE	180	180	183B	183B	183B	183B	183B	184A	184A	184B
ANALYSIS	3	4	1	2	3	4	5	1	2	1
TIO2	.78	.60	.69	.76	.79	.79	.72	.75	.62	.69
CR2O3	47.98	45.66	51.02	51.05	50.61	50.03	48.99	52.85	54.30	51.72
AL2O3	17.99	19.91	15.06	15.38	15.93	15.70	17.44	15.18	14.01	14.42
FE2O3	2.13	2.10	1.79	1.43	1.64	1.69	1.59	1.67	2.11	1.91
FEO	23.05	23.94	23.03	21.65	20.86	22.54	20.94	16.61	18.27	20.82
MGO	7.98	7.43	7.52	8.53	9.07	7.86	9.12	11.80	10.54	8.76
MNO	.43	.44	.33	.12	.27	.34	.25	.13	.53	.27
NIO	0.00	0.00	0.00	0.00	0.00	0.00	0.00	0.00	0.00	0.00
TOTAL	100.35	100.09	99.44	98.93	99.18	98.96	99.05	98.99	100.39	98.59
					CATIONS PER 32 OXYGENS					
TI	.151	.116	.137	.150	.155	.157	.140	.145	.120	.137
FE2+	.151	.116	.137	.150	.155	.157	.140	.145	.120	.137
CR	9.803	9.309	10.672	10.636	10.458	10.456	10.066	10.772	11.086	10.839
AL	5.478	6.050	4.695	4.776	4.906	4.891	5.341	4.611	4.263	4.504
FE3+	.415	.408	.356	.285	.323	.337	.311	.324	.410	.381
FE2+	4.832	5.048	4.960	4.622	4.406	4.826	4.411	3.430	3.827	4.478
MG	3.074	2.856	2.965	3.350	3.533	3.097	3.533	4.534	4.057	3.461
MN	.094	.096	.073	.026	.059	.076	.055	.028	.116	.060
NI	0.000	0.000	0.000	0.000	0.000	0.000	0.000	0.000	0.000	0.000
MMF	.381	.356	.367	.412	.436	.383	.436	.558	.506	.428
Y(CR)	.624	.590	.678	.677	.666	.666	.640	.685	.703	.689
Y(AL)	.349	.383	.298	.304	.312	.311	.339	.293	.270	.286
Y(FE3+)	.026	.025	.022	.018	.020	.021	.019	.020	.026	.024
FFF	.076	.073	.065	.056	.066	.063	.064	.083	.094	.076
GRAIN SIZE									160.	
HOST	3.	3.	4.	4.	3.	3.	1.	8.	1.	4.
ROCK TYPE	2.	2.	9.	9.	9.	9.	9.	5.	5.	6.

SAMPLE	184B	184B	184B	191	191	196D	197A	197A	197A	197A
ANALYSIS	2	3	4	1	2	1	1	2	3	4
TIO2	.74	.69	.68	.68	.49	.84	.85	.87	.94	.44
CR2O3	51.81	51.39	51.86	47.20	45.48	47.13	46.34	45.28	47.06	52.33
AL2O3	15.32	15.40	15.37	17.84	19.59	18.72	17.94	19.09	19.20	14.82
FE2O3	1.60	2.04	1.73	2.06	2.65	2.12	2.30	2.17	1.65	2.04
FEO	17.96	18.36	18.69	23.43	21.53	19.70	24.06	22.83	20.23	20.04
MGO	10.73	10.50	10.32	7.48	8.74	10.12	7.19	8.02	9.99	9.33
MNO	.24	.22	.25	.26	.26	.19	.23	.26	.16	.21
NIO	0.00	0.00	0.00	0.00	0.00	0.00	0.00	0.00	0.00	0.00
TOTAL	98.41	98.60	98.91	98.95	98.74	98.82	98.92	98.53	99.24	99.22
					CATIONS PER 32 OXYGENS					
TI	.145	.135	.133	.134	.095	.162	.168	.170	.180	.086
FE2+	.145	.135	.133	.134	.095	.162	.168	.170	.180	.086
CR	10.685	10.595	10.677	9.801	9.313	9.587	9.642	9.352	9.526	10.844
AL	4.709	4.732	4.716	5.521	5.979	5.676	5.563	5.877	5.792	4.577
FE3+	.314	.400	.340	.407	.516	.410	.457	.428	.319	.403
FE2+	3.774	3.869	3.939	5.013	4.568	4.077	5.128	4.819	4.152	4.307
MG	4.172	4.081	4.005	2.928	3.374	3.881	2.820	3.123	3.812	3.645
MN	.053	.048	.055	.057	.057	.041	.051	.057	.034	.046
NI	0.000	0.000	0.000	0.000	0.000	0.000	0.000	0.000	0.000	0.000
MMF	.515	.504	.495	.362	.419	.477	.347	.384	.468	.453
Y(CR)	.680	.673	.678	.623	.589	.611	.615	.597	.609	.685
Y(AL)	.299	.300	.299	.351	.378	.362	.355	.375	.370	.289
Y(FE3+)	.020	.025	.021	.025	.032	.026	.029	.027	.020	.025
FFF	.074	.090	.077	.073	.099	.088	.079	.079	.068	.084
GRAIN SIZE										
HOST	8.	1.	1.	4.	3.	2.	4.	4.	2.	1.
ROCK TYPE	6.	4.	4.	2.	2.	4.	2.	2.	2.	2.

TABLE 25 (cont.)

SAMPLE	197A	197D	197D	197D	197D	197D	197D	199	199	199
ANALYSIS	5	1	2	3	4	5	6	1	2	3
TIO2	.50	.99	.87	1.03	1.02	.95	.77	.55	.39	.45
CR2O3	49.81	46.23	46.68	45.93	46.35	46.46	45.98	45.10	45.87	45.95
AL2O3	16.69	17.70	18.57	18.48	18.81	19.10	19.82	19.56	19.80	19.55
FE2O3	2.13	2.80	1.78	2.43	2.02	1.85	1.81	2.66	2.62	2.71
FEO	20.36	24.13	23.43	23.35	23.47	21.58	22.15	23.85	23.93	24.01
MGO	9.31	7.26	7.73	7.91	7.94	9.05	8.67	7.41	7.45	7.40
MNO	.20	.28	.30	.22	.28	.24	.29	.22	.30	.31
NIO	0.00	0.00	0.00	0.00	0.00	0.00	0.00	0.00	0.00	0.00
TOTAL	99.01	99.40	99.36	99.36	99.89	99.23	99.49	99.35	100.36	100.39
					CATIONS PER 32 OXYGENS					
TI	.097	.195	.170	.201	.198	.184	.148	.107	.075	.087
FE2+	.097	.195	.170	.201	.198	.184	.148	.107	.075	.087
CR	10.260	9.586	9.610	9.451	9.477	9.469	9.346	9.271	9.335	9.362
AL	5.124	5.470	5.698	5.668	5.732	5.802	6.005	5.993	6.006	5.937
FE3+	.418	.552	.349	.477	.393	.358	.350	.520	.507	.525
FE2+	4.340	5.099	4.933	4.882	4.877	4.469	4.614	5.079	5.076	5.089
MG	3.615	2.838	3.000	3.068	3.060	3.477	3.322	2.871	2.858	2.842
MN	.044	.062	.066	.048	.061	.052	.063	.048	.065	.067
NI	0.000	0.000	0.000	0.000	0.000	0.000	0.000	0.000	0.000	0.000
MMF	.448	.348	.370	.376	.376	.427	.410	.356	.356	.354
Y(CR)	.649	.614	.613	.605	.607	.605	.595	.587	.589	.591
Y(AL)	.324	.350	.363	.363	.367	.371	.382	.379	.378	.375
Y(FE3+)	.026	.035	.022	.030	.025	.022	.022	.032	.032	.033
FFF	.086	.094	.064	.085	.071	.071	.068	.091	.089	.092
GRAIN SIZE								150.		
HOST	1.	4.	4.	4.	3.	2.	2.	4.	4.	4.
ROCK TYPE	2.	2.	2.	2.	2.	2.	2.	2.	2.	2.

SAMPLE	199	199	200B	200B	200B	200B	200B	200B	200B	200B
ANALYSIS	4	5	1	2	3	4	5	6	7	8
TIO2	.45	.25	.58	.59	.58	.62	.63	.63	.66	.73
CR2O3	45.81	45.46	49.54	49.20	52.21	50.25	49.48	49.89	50.72	51.35
AL2O3	20.80	20.57	17.08	17.04	15.04	16.82	17.52	17.64	17.24	16.39
FE2O3	1.63	2.42	2.88	3.01	2.49	2.68	2.64	2.10	2.06	1.83
FEO	22.89	23.00	21.47	22.32	20.51	18.71	18.11	18.40	18.51	18.85
MGO	8.25	8.00	8.85	8.30	9.22	10.51	10.92	10.73	10.78	10.52
MNO	.25	.25	.54	.55	.49	.47	.47	.49	.50	.35
NIO	0.00	0.00	0.00	0.00	0.00	0.00	0.00	.07	0.00	0.00
TOTAL	100.08	99.96	100.94	101.02	100.55	100.06	99.78	99.96	100.48	100.03
					CATIONS PER 32 OXYGENS					
TI	.086	.048	.112	.114	.113	.119	.121	.121	.126	.140
FE2+	.086	.048	.112	.114	.113	.119	.121	.121	.126	.140
CR	9.252	9.218	10.053	10.017	10.695	10.170	9.982	10.055	10.190	10.410
AL	6.261	6.217	5.166	5.171	4.592	5.074	5.268	5.299	5.162	4.952
FE3+	.313	.467	.558	.584	.487	.517	.508	.404	.396	.354
FE2+	4.804	4.887	4.497	4.694	4.331	3.887	3.745	3.803	3.809	3.902
MG	3.141	3.058	3.386	3.186	3.561	4.010	4.153	4.077	4.083	4.021
MN	.054	.054	.117	.120	.107	.102	.101	.106	.108	.076
NI	0.000	0.000	0.000	0.000	0.000	0.000	0.000	.014	0.000	0.000
MMF	.391	.382	.423	.398	.444	.500	.517	.509	.509	.498
Y(CR)	.584	.579	.637	.635	.678	.645	.633	.638	.647	.662
Y(AL)	.395	.390	.327	.327	.291	.321	.334	.336	.327	.315
Y(FE3+)	.019	.029	.035	.037	.030	.032	.032	.025	.025	.022
FFF	.060	.086	.107	.108	.098	.114	.116	.093	.091	.080
GRAIN SIZE	99.		500.							
HOST	3	3.	3.	1.	3.	3.	3.	8.	8.	8.
ROCK TYPE	2	2.	6.	4.	6.	6.	5.	5.	5.	5.

TABLE 25 (cont.)

SAMPLE	200B	200B	200B	200B	200B	200B	200B	200B
ANALYSIS	9	10	11	12	13	14	15	16
TIO2	.73	.76	.91	.82	.73	.83	.80	.85
CR2O3	51.06	51.32	51.40	51.32	52.04	52.14	52.06	52.40
AL2O3	16.14	16.16	15.97	15.90	15.39	15.29	15.29	15.08
FE2O3	1.84	1.70	1.48	1.77	1.66	1.56	1.74	1.62
FEO	18.74	18.77	19.05	18.77	19.07	19.30	19.14	19.23
MGO	10.42	10.46	10.35	10.46	10.14	10.10	10.17	10.14
MNO	.33	.36	.35	.31	.35	.31	.33	.34
NIO	0.00	0.00	0.00	0.00	0.00	0.00	0.00	0.00
TOTAL	99.26	99.54	99.51	99.36	99.39	99.53	99.53	99.67
				CATIONS PER 32 OXYGENS				
TI	.141	.147	.176	.159	.142	.161	.156	.165
FE2+	.141	.147	.176	.159	.142	.161	.156	.165
CR	10.439	10.462	10.496	10.490	10.680	10.695	10.674	10.742
AL	4.918	4.910	4.860	4.844	4.707	4.674	4.672	4.608
FE3+	.358	.331	.289	.346	.326	.306	.340	.317
FE2+	3.911	3.900	3.938	3.900	3.999	4.025	3.996	4.005
MG	4.016	4.020	3.984	4.031	9.923	3.906	3.932	3.919
MN	.072	.078	.076	.067	.076	.068	.072	.074
NI	0.000	0.000	0.000	0.000	0.000	0.000	0.000	0.000
MMF	.497	.498	.491	.498	.486	.482	.486	.484
Y(CR)	.664	.666	.670	.668	.679	.682	.680	.685
Y(AL)	.312	.312	.310	.308	.299	.298	.297	.294
Y(FE3+)	.022	.021	.018	.022	.020	.019	.021	.020
FFF	.081	.075	.065	.078	.072	.068	.075	.070
GRAIN SIZE								
HOST	B.	B.	B.	B.	B.	B.	B.	B.
ROCK TYPE	5.	5.	5.	5.	5.	5.	5.	5.

TABLE 26 MICROPROBE ANALYSES OF CHROMITE : UNIT D (ZS 7)

SAMPLE	78	78	78	79	80	80	83	83	83	83	84	84	84
ANALYSIS	1	2	3	1	1	2	1	2	3	4	1	2	3
TIO2	.43	.45	.45	.55	.62	.62	.59	.59	.68	.61	.66	.75	.79
CR2O3	45.91	48.46	46.56	47.24	50.45	51.45	48.46	47.55	50.32	49.33	50.68	49.31	49.23
AL2O3	19.66	17.45	19.34	18.29	16.72	16.20	16.39	18.07	16.12	16.78	15.03	17.49	17.73
FE2O3	2.28	1.81	2.08	1.93	1.30	1.21	2.16	1.26	1.30	1.34	2.30	2.34	2.25
FEO	23.67	23.58	23.36	22.70	24.15	24.03	22.71	22.67	22.68	22.21	23.99	22.86	23.11
MGO	7.37	7.13	7.54	7.83	7.17	7.25	7.36	7.61	7.63	7.81	6.94	8.31	8.27
MNO	.54	.53	.57	.41	.39	.43	.54	.53	.55	.56	.40	.35	.34
NIO	0.00	0.00	0.00	0.00	0.00	0.00	.11	.07	.12	.14	0.00	0.00	0.00
TOTAL	99.86	99.41	99.90	98.95	100.81	101.20	98.33	98.35	99.41	98.79	100.01	101.42	101.72
					CATIONS PER 32 OXYGENS								
TI	.084	.089	.087	.108	.121	.121	.118	.117	.135	.121	.131	.144	.151
FE2+	.084	.089	.087	.108	.121	.121	.118	.117	.135	.121	.131	.144	.151
CR	9.392	10.063	9.523	9.767	10.376	10.563	10.192	9.905	10.472	10.280	10.595	9.982	9.932
AL	5.995	5.401	5.896	5.636	5.125	4.957	5.138	5.610	5.000	5.212	4.683	5.277	5.331
FE3+	.445	.358	.406	.380	.255	.237	.434	.251	.259	.267	.458	.452	.432
FE2+	5.039	5.091	4.967	4.857	5.133	5.099	4.936	4.878	4.858	4.777	5.174	4.752	4.780
MG	2.843	2.791	2.908	3.052	2.780	2.806	2.918	2.989	2.994	3.068	2.735	3.171	3.145
MN	.118	.118	.125	.091	.085	.094	.122	.118	.123	.125	.089	.075	.073
NI	0.000	0.000	0.000	0.000	0.000	0.000	.023	.015	.025	.030	0.000	0.000	0.000
MMF	.356	.350	.365	.380	.346	.349	.366	.374	.374	.385	.340	.393	.389
Y(CR)	.593	.636	.601	.618	.658	.670	.646	.628	.665	.652	.673	.635	.632
Y(AL)	.378	.341	.372	.357	.325	.314	.325	.355	.317	.330	.297	.335	.339
Y(FE3+)	.028	.022	.025	.024	.016	.015	.027	.015	.016	.016	.029	.028	.027
FFF	.079	.064	.074	.071	.046	.043	.079	.047	.049	.051	.079	.084	.080
GRAIN SIZE				120.	110.		120.						
HOST	3.	3.	3.	1.	1.	3.	1.	1.	3.	3.	1.	3.	3.
ROCK TYPE	1.	1.	1.	1.	1.	1.	1.	1.	1.	1.	1.	1.	1.

TABLE 26 (cont.)

SAMPLE	90	90	90	90	90	90	90	95	95	95
ANALYSIS	1	2	3	4	5	6	6	1	2	3
TIO2	.64	.65	.76	.68	.80	.58	.36	.16	.49	.27
CR2O3	48.05	45.74	46.20	46.79	45.63	45.71	45.43	46.65	48.17	48.68
AL2O3	15.23	16.81	16.55	16.57	17.03	16.51	16.41	19.43	16.42	15.97
FE2O3	4.08	5.00	4.81	4.45	4.70	5.01	4.75	2.64	3.30	2.89
FEO	24.36	23.35	23.57	23.18	23.57	26.11	28.17	23.35	23.34	24.22
MGO	6.42	7.23	7.17	7.40	7.26	5.49	3.91	7.48	7.22	6.32
MNO	.53	.53	.56	.52	.50	.57	.63	.52	.49	.56
NIO	.09	.11	.11	.12	.10	.06	.04	0.00	0.00	0.00
TOTAL	99.40	99.43	99.74	99.71	99.60	100.05	99.71	100.24	99.44	98.92
					CATIONS PER 32 OXYGENS					
TI	.128	.129	.150	.134	.158	.116	.073	.031	.097	.054
FE2+	.128	.129	.150	.134	.158	.116	.073	.031	.097	.054
CR	10.135	9.530	9.613	9.720	9.480	9.599	9.678	9.516	10.045	10.281
AL	4.788	5.220	5.133	5.131	5.274	5.167	5.211	5.908	5.104	5.027
FE3+	.820	.992	.953	.880	.930	1.002	.965	.514	.657	.583
FE2+	5.308	5.018	5.039	4.960	5.024	5.685	6.277	5.009	5.052	5.357
MG	2.553	2.840	2.813	2.898	2.844	2.173	1.570	2.877	2.839	2.517
MN	.120	.118	.125	.116	.111	.128	.144	.114	.109	.127
NI	.019	.023	.023	.025	.021	.013	.009	0.000	0.000	0.000
MMF	.319	.355	.351	.362	.354	.272	.198	.363	.355	.317
Y(CR)	.643	.605	.612	.617	.604	.608	.610	.597	.635	.646
Y(AL)	.304	.331	.326	.326	.336	.327	.329	.370	.322	.316
Y(FE3+)	.052	.063	.060	.055	.059	.063	.060	.032	.041	.036
FFF	.131	.161	.155	.147	.152	.147	.131	.092	.113	.097
GRAIN SIZE	35.			80.	250.	200.		70.	90.	30.
HOST	1.	2.	2.	7.	7.	3.	3.	1.	1.	1.
ROCK TYPE	1.	1.	1.	1.	1.	1.	1.	1.	1.	1.

SAMPLE	95	104	104	104	104	104	LG5	LG5	109A	109A
ANALYSIS	4	1	1	2	2	2	1	2	1	2
TIO2	.55	.75	.55	.99	.81	1.31	.69	.70	.58	.61
CR2O3	47.93	51.57	51.95	50.98	53.19	51.91	51.99	51.95	51.66	51.54
AL2O3	15.37	13.43	13.29	13.99	12.34	12.75	15.24	15.31	15.67	15.94
FE2O3	4.18	1.91	2.15	2.62	2.25	1.65	2.03	2.05	2.06	1.83
FEO	24.69	25.02	24.89	23.46	23.50	24.11	18.80	18.84	18.30	18.57
MGO	6.21	5.85	5.83	7.21	6.85	6.68	10.26	10.27	10.43	10.31
MNO	.58	.59	.59	.59	.59	.59	.37	.37	.48	.49
NIO	0.00	0.00	0.00	0.00	0.00	0.00	0.00	0.00	.05	.07
TOTAL	99.51	99.13	99.25	99.85	99.53	99.00	99.39	99.50	99.23	99.37
					CATIONS PER 32 OXYGENS					
TI	.110	.152	.112	.198	.164	.266	.134	.136	.113	.119
FE2+	.110	.152	.112	.198	.164	.266	.134	.136	.113	.119
CR	10.109	11.025	11.104	10.702	11.306	11.077	10.670	10.648	10.586	10.544
AL	4.831	4.279	4.234	4.377	3.910	4.055	4.662	4.677	4.786	4.860
FE3+	.839	.390	.438	.525	.456	.335	.397	.401	.402	.358
FE2+	5.400	5.507	5.515	5.014	5.120	5.177	3.948	3.950	3.855	3.901
MG	2.469	2.358	2.349	2.854	2.745	2.688	3.970	3.968	4.029	3.977
MN	.131	.135	.135	.133	.134	.135	.081	.081	.105	.107
NI	0.000	0.000	0.000	0.000	0.000	0.000	0.000	0.000	.010	.014
MMF	.309	.294	.294	.353	.341	.330	.492	.492	.503	.497
Y(CR)	.640	.702	.703	.685	.721	.716	.678	.677	.671	.668
Y(AL)	.306	.272	.268	.280	.249	.262	.296	.297	.303	.308
Y(FE3+)	.053	.024	.027	.033	.029	.021	.025	.025	.025	.022
FFF	.132	.064	.072	.091	.079	.057	.088	.089	.091	.081
GRAIN SIZE	85.	110.		500.						
HOST	3.	1.	1.	2.	2.	2.	8.	8.	8.	8.
ROCK TYPE	1.	1.	1.	1.	1.	1.	5.	5.	5.	5.

TABLE 26 (cont.)

SAMPLE	109A	109A	109A	109A	109A	109A	109A	109A	115	115
ANALYSIS	3	4	5	6	7	8	9	10	1	1
TIO2	.63	.61	.62	.62	.64	.63	.62	.67	.64	.61
CR2O3	51.43	51.60	50.98	50.09	49.26	49.36	49.86	49.69	52.77	50.89
AL2O3	16.11	15.78	16.30	16.36	17.12	17.11	16.92	16.83	12.74	14.10
FE2O3	1.65	1.95	1.68	1.90	1.80	1.88	1.55	1.84	1.15	1.61
FEO	18.85	18.64	19.52	22.05	21.45	21.15	21.57	21.24	24.62	24.30
MGO	10.16	10.26	9.75	8.16	8.56	8.75	8.49	8.73	5.78	6.15
MNO	.49	.48	.47	.53	.51	.53	.52	.50	.58	.49
NIO	.08	.07	.08	.04	.08	.08	.07	.07	.08	.05
TOTAL	99.41	99.40	99.40	99.76	99.43	99.49	99.61	99.58	98.36	98.21
					CATIONS PER 32 OXYGENS					
TI	.122	.119	.121	.122	.125	.123	.121	.131	.131	.124
FE2+	.122	.119	.121	.122	.125	.123	.121	.131	.131	.124
CR	10.520	10.565	10.450	10.345	10.142	10.144	10.262	10.218	11.398	10.914
AL	4.912	4.816	4.980	5.036	5.254	5.241	5.190	5.158	4.102	4.507
FE3+	.323	.382	.329	.374	.353	.368	.305	.361	.237	.330
FE2+	3.958	3.920	4.112	4.697	4.548	4.476	4.576	4.491	5.494	5.390
MG	3.918	3.961	3.768	3.177	3.323	3.390	3.294	3.385	2.354	2.487
MN	.107	.105	.103	.117	.112	.117	.115	.110	.134	.112
NI	.017	.014	.017	.008	.017	.017	.015	.015	.017	.011
MMF	.489	.495	.470	.397	.415	.424	.412	.422	.294	.310
Y(CR)	.667	.670	.663	.656	.644	.643	.651	.649	.724	.692
Y(AL)	.311	.305	.316	.319	.333	.332	.329	.327	.260	.286
Y(FE3+)	.020	.024	.020	.023	.022	.023	.019	.072	.015	.020
FFF	.073	.086	.072	.072	.070	.074	.060	0.000	.040	.056
GRAIN SIZE										
HOST	8.	8.	8.	8.	8.	8.	8.	8.	3.	3.
ROCK TYPE	5.	5.	5.	8.	8.	8.	8.	8.	1.	1.

SAMPLE	115	115	115	117	117	117	125	125	125	128
ANALYSIS	2	3	4	1	2	3	1	2	3	1
TIO2	.55	.73	.58	.35	.44	.57	.36	.38	.36	.19
CR2O3	52.05	53.49	51.43	50.13	49.59	49.71	43.56	40.76	43.83	55.79
AL2O3	13.33	12.27	14.14	15.85	17.34	16.64	21.74	24.37	21.84	9.26
FE2O3	2.13	1.88	1.60	1.90	1.41	1.85	2.40	2.69	2.35	2.19
FEO	23.41	23.33	23.58	23.34	22.63	22.81	21.65	21.17	22.24	28.99
MGO	6.69	6.78	6.62	6.98	7.78	7.68	8.69	9.34	8.41	2.52
MNO	.55	.59	.56	.55	.57	.57	.49	.50	.57	.73
NIO	.05	.08	.09	0.00	0.00	0.00	0.00	0.00	0.00	0.00
TOTAL	98.76	99.15	98.61	99.11	99.77	99.83	98.90	99.21	99.60	99.67
					CATIONS PER 32 OXYGENS					
TI	.112	.148	.117	.070	.086	.112	.069	.072	.069	.040
FE2+	.112	.148	.117	.070	.086	.112	.069	.072	.069	.040
CR	11.105	11.417	10.952	10.522	10.223	10.281	8.829	8.115	8.843	12.390
AL	4.239	3.903	4.488	4.958	5.328	5.130	6.568	7.231	6.567	3.065
FE3+	.432	.383	.325	.380	.277	.364	.464	.510	.452	.464
FE2+	5.172	5.119	5.195	5.114	4.850	4.879	4.573	4.388	4.678	6.771
MG	2.691	2.728	2.658	2.762	3.024	2.995	3.321	3.506	3.199	1.055
MN	.126	.135	.128	.124	.126	.126	.106	.107	.123	.174
NI	.011	.017	.019	0.000	0.000	0.000	0.000	0.000	0.000	0.000
MMF	.337	.341	.333	.347	.379	.375	.417	.440	.402	.134
Y(CR)	.703	.727	.694	.663	.645	.651	.556	.511	.557	.778
Y(AL)	.268	.248	.284	.312	.336	.325	.414	.456	.414	.192
Y(FE3+)	.027	.024	.020	.023	.017	.023	.029	.032	.028	.029
FFF	.075	.067	.057	.068	.053	.068	.090	.102	.086	.063
GRAIN SIZE				40.	110.			20.	60.	70.
HOST	3.	3.	3.	1.	1.	3.	1.	1.	3.	1.
ROCK TYPE	1.	1.	1.	1.	1.	1.	1.	1.	1.	1.

TABLE 26 (cont.)

SAMPLE	128	128	134	134	134	139	139	141	155	155
ANALYSIS	2	3	1	2	3	1	2	1	1	1
TIO2	.20	.91	.25	.35	1.24	.39	.28	.58	1.00	.55
CR2O3	57.12	54.60	56.27	57.30	55.39	44.21	46.36	54.99	52.75	54.07
AL2O3	9.52	11.32	9.05	9.27	9.57	20.29	18.85	12.10	12.39	11.65
FE2O3	1.83	1.79	1.82	1.71	.59	2.16	2.47	1.88	2.01	1.62
FEO	25.58	24.37	30.38	25.82	29.27	22.99	22.18	23.92	25.85	25.36
MGO	4.84	6.28	1.90	4.89	3.22	7.49	7.91	6.68	5.54	5.35
MNO	.67	.65	.47	.47	.41	.52	.52	.57	.63	.58
NIO	0.00	0.00	0.00	0.00	0.00	0.00	0.00	0.00	0.00	0.00
TOTAL	99.77	99.92	100.15	99.82	99.70	98.05	98.58	100.72	100.18	99.18
					CATIONS PER 32 OXYGENS					
TI	.041	.185	.052	.072	.260	.077	.055	.116	.203	.113
FE2+	.041	.185	.052	.072	.260	.077	.055	.116	.203	.113
CR	12.445	11.662	12.508	12.487	12.210	9.156	9.590	11.589	11.248	11.687
AL	3.091	3.604	2.998	3.011	3.144	6.263	5.812	3.801	3.938	3.753
FE3+	.381	.364	.386	.355	.126	.427	.488	.378	.409	.333
FE2+	5.855	5.322	7.091	5.881	6.565	4.960	4.800	5.217	5.629	5.685
MG	1.988	2.529	.796	2.009	1.338	2.925	3.085	2.654	2.227	2.180
MN	.156	.149	.111	.109	.096	.115	.115	.129	.144	.134
NI	0.000	0.000	0.000	0.000	0.000	0.000	0.000	0.000	0.000	0.000
MMF	.252	.314	.100	.252	.163	.367	.388	.332	.276	.273
Y(CR)	.781	.746	.787	.787	.788	.577	.603	.734	.721	.740
Y(AL)	.194	.230	.188	.189	.203	.395	.365	.241	.252	.237
Y(FE3+)	.023	.023	.024	.022	.008	.026	.030	.023	.026	.021
FFF	.060	.062	.051	.056	.018	.078	.091	.066	.065	.054
GRAIN SIZE	70.	200.	60.	40.		20.	25.			
HOST	1.	6.	1.	1.	3.	1.	1.	3.	6.	6.
ROCK TYPE	1.	1.	1.	1.	1.	1.	1.	1.	1.	1.

SAMPLE	160	160	160	160	160	164	164	164	164	164	165	165	165
ANALYSIS	1	2	3	4	4	1	2	2	3	3	1	2	3
TIO2	.58	.50	.65	.62	.59	.36	.34	.27	1.16	1.09	.52	.91	.29
CR2O3	43.99	51.98	53.15	48.36	43.62	50.94	50.68	50.50	53.29	54.48	51.46	52.96	53.38
AL2O3	21.49	14.27	11.81	18.32	22.15	15.28	16.76	16.68	12.11	10.91	15.85	12.57	12.36
FE2O3	1.69	1.21	1.76	1.46	1.89	1.94	1.51	1.67	1.88	1.54	1.08	1.30	1.78
FEO	23.44	22.37	24.52	21.11	22.00	23.60	22.23	22.18	23.69	23.91	21.55	24.97	25.52
MGO	7.68	7.32	5.73	8.90	8.70	6.84	8.01	7.93	7.03	6.60	8.31	5.90	5.11
MNO	.52	.58	.62	.52	.49	.56	.54	.54	.43	.41	.48	.55	.59
NIO	.09	.06	.04	.04	.13	0.00	0.00	0.00	0.00	0.00	.07	.07	.04
TOTAL	99.49	98.30	98.29	99.33	99.57	99.53	100.08	99.77	99.59	98.95	99.32	99.24	99.07
						CATIONS PER 32 OXYGENS							
TI	.112	.101	.134	.121	.113	.072	.066	.053	.234	.223	.103	.185	.059
FE2+	.112	.101	.134	.121	.113	.072	.066	.053	.234	.223	.103	.185	.059
CR	8.938	11.037	11.543	9.890	8.773	10.689	10.429	10.430	11.317	11.734	10.678	11.348	11.533
AL	6.508	4.516	3.823	5.584	6.640	4.779	5.140	5.135	3.833	3.502	4.902	4.014	3.980
FE3+	.329	.245	.365	.285	.362	.389	.297	.329	.381	.317	.215	.266	.367
FE2+	4.926	4.925	5.501	4.446	4.569	5.168	4.773	4.793	5.087	5.225	4.627	5.475	5.773
MG	2.942	2.930	2.346	3.431	3.299	2.706	3.108	3.088	2.815	2.680	3.251	2.383	2.081
MN	.113	.132	.144	.114	.105	.126	.119	.119	.098	.095	.107	.126	.136
NI	.019	.013	.009	.008	.026	0.000	0.000	0.000	0.000	0.000	.015	.015	.009
MMF	.368	.368	.293	.429	.413	.340	.391	.389	.345	.329	.407	.296	.263
Y(CR)	.566	.698	.733	.628	.556	.674	.657	.656	.728	.754	.676	.726	.726
Y(AL)	.412	.285	.243	.354	.420	.301	.323	.323	.246	.225	.310	.256	.250
Y(FE3+)	.020	.015	.023	.018	.022	.024	.018	.020	.024	.020	.013	.017	.023
FFF	.061	.046	.060	.058	.071	.069	.057	.063	.066	.055	.043	.044	.059
GRAIN SIZE						50.	220.		500.		80.		
HOST	4.	1.	3.	3.	3.	1.	1.	1.	2.	2.	1.	3.	5.
ROCK TYPE	1.	1.	1.	1.	1.	1.	1.	1.	1.	1.	1.	1.	1.

TABLE 27 MICROPROBE ANALYSES OF CHROMITE : UNIT E

SAMPLE	01	01	01	01	01	01	01	01	LG.7	LG.7
ANALYSIS	1	2	3	4	5	6	7	8	1	2
TIO2	.64	.57	.58	.80	.65	.73	.74	.70	1.03	1.02
CR2O3	46.34	47.76	47.87	46.12	45.24	45.45	45.24	43.54	48.14	48.46
AL2O3	19.30	18.99	18.32	20.10	20.07	20.04	20.10	22.27	17.87	17.82
FE2O3	1.70	1.02	1.44	1.71	1.91	1.63	1.67	1.83	1.67	1.72
FEO	22.82	23.01	22.92	21.30	25.36	25.19	24.74	21.57	21.36	20.90
MGO	7.89	7.80	7.74	9.15	6.52	6.68	6.93	9.14	9.14	9.44
MNO	.53	.52	.50	.55	.56	.54	.53	.48	.29	.34
NIO	0.00	0.00	0.00	0.00	0.00	0.00	0.00	0.00	0.00	0.00
TOTAL	99.23	99.68	99.37	99.74	100.32	100.27	99.96	99.54	99.50	99.70
					CATIONS PER 32 OXYGENS					
TI	.125	.111	.114	.154	.126	.142	.144	.133	.200	.197
FE2+	.125	.111	.114	.154	.126	.142	.144	.133	.200	.197
CR	9.512	9.781	9.864	9.313	9.255	9.291	9.257	8.728	9.833	9.864
AL	5.904	5.796	5.626	6.050	6.119	6.106	6.129	6.654	5.440	5.406
FE3+	.334	.201	.282	.330	.373	.318	.326	.350	.325	.333
FE2+	4.830	4.874	4.883	4.397	5.363	5.307	5.211	4.442	4.416	4.302
MG	3.053	3.012	3.007	3.484	2.515	2.575	2.673	3.455	3.520	3.623
MN	.116	.114	.110	.119	.123	.118	.116	.103	.063	.074
NI	0.000	0.000	0.000	0.000	0.000	0.000	0.000	0.000	0.000	0.000
MMF	.381	.376	.375	.433	.314	.320	.332	.430	.432	.446
Y(CR)	.603	.619	.625	.593	.587	.591	.589	.554	.630	.632
Y(AL)	.374	.367	.356	.385	.388	.388	.390	.422	.348	.346
Y(FE3+)	.021	.012	.017	.021	.023	.020	.020	.022	.020	.021
FFF	.063	.038	.053	.067	.063	.050	.057	.071	.065	.069
GRAIN SIZE	40.	50.	50.		50.	80.	135.	200.		
HOST	1.	1.	1.	3.	4.	4.	4.	7.	8.	8.
ROCK TYPE	8.	8.	8.	8.	8.	8.	8.	8.	5.	5.

SAMPLE	LG.7	LG.7	07	07	07	11	11	11	11	28
ANALYSIS	3	4	1	2	3	1	2	2	3	1
TIO2	1.02	1.01	1.10	.85	1.04	.58	.55	.43	1.00	.81
CR2O3	47.67	48.35	46.32	41.72	46.31	46.61	46.49	47.08	46.67	54.36
AL2O3	17.64	17.98	19.06	21.02	18.25	19.25	18.97	18.95	18.35	13.03
FE2O3	2.76	1.76	2.58	3.17	2.56	1.73	2.08	1.81	1.79	2.74
FEO	21.02	20.94	22.99	27.22	23.96	23.67	23.70	23.63	24.65	19.67
MGO	9.35	9.45	8.33	5.44	7.44	7.41	7.30	7.30	6.96	9.72
MNO	.35	.34	.55	.56	.54	.53	.54	.54	.53	.56
NIO	0.00	0.00	.07	0.00	0.00	0.00	0.00	0.00	0.00	0.00
TOTAL	99.81	99.83	101.00	99.98	100.10	99.78	99.63	99.75	99.95	100.89
					CATIONS PER 32 OXYGENS					
TI	.197	.195	.211	.166	.203	.113	.108	.084	.196	.158
FE2+	.197	.195	.211	.166	.203	.113	.108	.084	.196	.158
CR	9.711	9.823	9.348	8.592	9.508	9.554	9.562	9.673	9.619	11.161
AL	5.356	5.445	5.733	6.452	5.585	5.881	5.815	5.803	5.637	3.987
FE3+	.536	.340	.497	.622	.501	.338	.407	.355	.352	.536
FE2+	4.332	4.306	4.697	5.764	5.001	5.020	5.050	5.053	5.178	4.114
MG	3.591	3.620	3.169	2.112	2.880	2.864	2.831	2.828	2.704	3.762
MN	.076	.074	.119	.123	.119	.116	.119	.119	.117	.123
NI	0.000	0.000	.014	0.000	0.000	0.000	0.000	0.000	0.000	0.000
MMF	.442	.445	.392	.262	.356	.358	.354	.355	.334	.468
Y(CR)	.622	.629	.600	.548	.609	.605	.605	.611	.616	.711
Y(AL)	.343	.348	.368	.411	.358	.372	.368	.366	.361	.254
Y(FE3+)	.034	.021	.031	.039	.032	.021	.025	.022	.022	.034
FFF	.105	.070	.091	.094	.087	.061	.073	.064	.061	.111
GRAIN SIZE				70.	130.	100.	100.	70.		
HOST	8.	8.	8.	4.	1.	1.	1.	1.	3.	8.
ROCK TYPE	5.	5.	5.	4.	4.	1.	1.	1.	1.	5.

TABLE 27 (cont.)

SAMPLE	28	28	32	32	32	32	32	39	39	39
ANALYSIS	2	3	1	2	3	4	5	1	2	3
TIO2	.41	.62	.59	.75	.78	.71	.93	.68	.70	.66
CR2O3	54.25	54.24	50.97	50.96	50.91	49.79	49.61	48.69	51.28	51.08
AL2O3	12.78	12.39	14.08	14.43	15.19	16.52	16.15	15.40	14.89	15.19
FE2O3	1.91	1.97	2.29	1.94	1.68	1.59	1.92	3.58	2.01	2.37
FEO	23.59	23.55	24.54	24.56	23.78	23.33	23.90	24.56	23.93	24.29
MGO	6.75	6.85	6.12	6.33	7.03	7.43	7.23	6.46	6.95	6.84
MNO	.61	.60	.64	.62	.60	.58	.57	.61	.56	.61
NIO	0.00	0.00	0.00	0.00	0.00	0.00	0.00	0.00	0.00	0.00
TOTAL	100.31	100.22	99.23	99.60	99.97	99.95	100.32	99.98	100.33	101.04
					CATIONS PER 32 OXYGENS					
TI	.082	.124	.119	.151	.155	.140	.183	.135	.139	.130
FE2+	.082	.124	.119	.151	.155	.140	.183	.135	.139	.130
CR	11.436	11.454	10.836	10.764	10.629	10.309	10.270	10.204	10.694	10.581
AL	4.015	3.900	4.462	4.543	4.727	5.098	4.983	4.810	4.628	4.690
FE3+	.384	.397	.463	.391	.334	.314	.380	.714	.399	.468
FE2+	5.179	5.137	5.401	5.339	5.098	4.971	5.052	5.310	5.142	5.193
MG	2.683	2.727	2.453	2.521	2.767	2.900	2.822	2.552	2.733	2.671
MN	.138	.136	.146	.140	.134	.129	.126	.137	.125	.135
NI	0.000	0.000	0.000	0.000	0.000	0.000	0.000	0.000	0.000	0.000
MMF	.337	.341	.307	.314	.345	.362	.350	.319	.341	.334
Y(CR)	.722	.727	.687	.685	.677	.655	.656	.648	.680	.672
Y(AL)	.253	.247	.283	.289	.301	.324	.318	.305	.294	.297
Y(FE3+)	.024	.025	.029	.024	.021	.019	.024	.045	.025	.029
FFF	.068	.070	.077	.066	.059	.057	.067	.115	.070	.080
GRAIN SIZE	70.	60.	15.	45.	80.	150.		45.	80.	
HOST	1.	1.	1.	1.	1.	1.	1.	1.	1.	3.
ROCK TYPE	1.	1.	8.	8.	8.	8.	8.	1.	1.	1.

SAMPLE	39	43	43	43	43	50	50	61	61	61
ANALYSIS	4	1	2	3	4	1	2	1	2	3
TIO2	.74	.57	.59	.65	.76	.67	.37	.49	.88	1.01
CR2O3	47.59	49.24	50.21	48.05	47.32	50.38	48.44	42.40	49.79	50.50
AL2O3	16.78	15.90	15.58	17.94	18.46	15.62	15.92	18.89	14.29	13.65
FE2O3	2.90	2.41	1.94	1.60	1.89	1.15	2.38	4.43	2.66	1.80
FEO	26.15	24.06	24.03	22.85	23.01	23.16	24.65	29.44	27.62	28.72
MGO	5.71	6.68	6.74	7.76	7.88	7.17	5.93	3.47	4.55	3.79
MNO	.62	.61	.59	.55	.53	.53	.56	.59	.64	.63
NIO	0.00	0.00	0.00	0.00	0.00	.06	.06	0.00	0.00	0.00
TOTAL	100.50	99.48	99.69	99.41	99.86	98.75	98.32	99.71	100.44	100.11
					CATIONS PER 32 OXYGENS					
TI	.147	.114	.117	.127	.148	.134	.075	.098	.178	.206
FE2+	.147	.114	.117	.127	.148	.134	.075	.098	.178	.206
CR	9.917	10.322	10.514	9.913	9.696	10.601	10.314	8.961	10.579	10.848
AL	5.212	4.968	4.863	5.516	5.638	4.899	5.052	5.950	4.525	4.370
FE3+	.577	.482	.388	.315	.370	.231	.484	.891	.540	.369
FE2+	5.618	5.223	5.207	4.860	4.839	5.023	5.479	6.484	6.032	6.320
MG	2.243	2.640	2.661	3.018	3.044	2.844	2.380	1.383	1.823	1.535
MN	.138	.137	.132	.121	.116	.119	.128	.133	.146	.145
NI	0.000	0.000	0.000	0.000	0.000	.013	.013	0.000	0.000	0.000
MMF	.280	.330	.333	.377	.379	.355	.300	.173	.226	.190
Y(CR)	.631	.654	.666	.629	.617	.673	.650	.567	.676	.696
Y(AL)	.331	.314	.308	.350	.359	.311	.318	.376	.289	.280
Y(FE3+)	.036	.030	.024	.020	.023	.014	.030	.056	.034	.024
FFF	.090	.082	.067	.059	.069	.042	.080	.119	.079	.053
GRAIN SIZE	110.	75.	50.					20.	70.	90.
HOST	4.	1.	1.	3.	3.	3.	3.	1.	1.	1.
ROCK TYPE	1.	1.	1.	1.	1.	1.	1.	1.	1.	1.

TABLE 28 MICROPROBE ANALYSES OF CHROMITE : UNITS E AND D (29 3)

SAMPLE	300	300	300	300	301	301	301	301	303A	303A
ANALYSIS	1	2	3	3	1	1	2	3	1	2
TIO2	.72	1.15	1.58	1.10	4.00	1.15	.85	1.22	.71	.65
CR2O3	47.39	46.87	46.45	46.65	48.83	50.09	48.94	48.44	45.57	45.70
AL2O3	11.70	10.04	11.23	11.11	9.88	10.66	11.42	12.02	14.15	15.06
FE2O3	8.02	9.66	8.64	9.34	3.34	8.07	7.87	8.33	8.86	8.61
FEO	25.73	25.77	25.05	24.57	28.52	25.83	25.35	23.93	20.90	19.63
MGO	5.25	5.28	6.25	6.18	5.48	5.92	5.84	7.26	8.66	9.66
MNO	.45	.45	.40	.47	.44	.50	.48	.43	.43	.40
NIO	0.00	0.00	0.00	0.00	0.00	0.00	0.00	0.00	0.00	0.00
TOTAL	99.27	99.22	99.61	99.42	100.50	102.22	100.75	101.63	99.28	99.71
					CATIONS PER 32 OXYGENS					
TI	.148	.239	.323	.226	.818	.230	.172	.242	.141	.127
FE2+	.148	.239	.323	.226	.818	.230	.172	.242	.141	.127
CR	10.269	10.242	9.986	10.060	10.508	10.565	10.430	10.117	9.537	9.425
AL	3.779	3.270	3.598	3.571	3.168	3.351	3.627	3.741	4.414	4.629
FE3+	1.655	2.009	1.769	1.918	.685	1.621	1.597	1.656	1.766	1.690
FE2+	5.751	5.719	5.375	5.379	5.675	5.532	5.543	5.045	4.486	4.155
MG	2.145	2.175	2.533	2.512	2.223	2.354	2.346	2.858	3.417	3.756
MN	.104	.105	.092	.108	.101	.112	.109	.096	.096	.088
NI	0.000	0.000	0.000	0.000	0.000	0.000	0.000	0.000	0.000	0.000
MMF	.266	.267	.307	.309	.255	.290	.291	.350	.424	.467
Y(CR)	.653	.659	.650	.646	.731	.679	.666	.652	.606	.598
Y(AL)	.240	.210	.234	.229	.220	.215	.231	.241	.280	.294
Y(FE3+)	.105	.129	.115	.123	.047	.104	.102	.106	.112	.107
FFF	.219	.252	.237	.254	.095	.219	.218	.238	.276	.282
GRAIN SIZE	50.	80.	290.	290.					280.	
HOST	1.	2.	2.	2.	2.	2.	1.	3.	2.	8.
ROCK TYPE	1.	1.	1.	1.	1.	1.	1.	1.	7.	5.

SAMPLE	L66A	304A	304A	304A	304A	304A	304A	304A	304B	304B
ANALYSIS	1	1	2	2	3	4	5	6	1	2
TIO2	.69	.58	1.05	.77	.17	.68	.69	.68	.58	.86
CR2O3	47.70	47.22	47.99	48.38	46.22	48.74	47.00	46.78	47.71	47.95
AL2O3	14.16	14.02	12.26	11.99	10.96	13.95	15.01	15.19	11.26	10.88
FE2O3	7.86	7.79	8.06	8.24	9.82	7.35	8.16	8.21	9.11	9.33
FEO	20.03	22.53	24.33	23.85	29.98	20.85	20.35	20.12	24.34	24.37
MGO	9.47	7.75	6.74	6.83	2.02	9.06	9.57	9.67	5.94	6.24
MNO	.39	.40	.48	.38	.40	.39	.29	.37	.56	.47
NIO	0.00	0.00	0.00	0.00	0.00	0.00	0.00	0.00	.13	.11
TOTAL	100.30	100.30	100.91	100.44	99.58	101.03	101.07	101.02	99.64	100.22
					CATIONS PER 32 OXYGENS					
TI	.136	.115	.210	.155	.035	.132	.133	.131	.118	.175
FE2+	.136	.115	.210	.155	.035	.132	.133	.131	.118	.175
CR	9.832	9.857	10.112	10.244	10.238	10.019	9.585	9.531	10.278	10.271
AL	4.350	4.362	3.850	3.784	3.618	4.274	4.562	4.612	3.615	3.473
FE3+	1.544	1.549	1.616	1.661	2.071	1.439	1.584	1.592	1.869	1.904
FE2+	4.232	4.860	5.214	5.187	6.990	4.402	4.256	4.204	5.430	5.348
MG	3.680	3.050	2.677	2.726	.843	3.511	3.679	3.714	2.413	2.520
MN	.087	.089	.108	.086	.090	.085	.063	.080	.129	.108
NI	0.000	0.000	0.000	0.000	0.000	0.000	0.000	0.000	.028	.024
MMF	.457	.380	.330	.337	.107	.436	.455	.461	.303	.313
Y(CR)	.625	.625	.649	.652	.642	.636	.609	.605	.652	.656
Y(AL)	.277	.276	.247	.241	.227	.271	.290	.293	.229	.222
Y(FE3+)	.098	.098	.103	.105	.130	.091	.100	.101	.118	.121
FFF	.261	.237	.229	.237	.227	.240	.265	.268	.251	.256
GRAIN SIZE										
HOST	8.	1.	2.	2.	5.	8.	8.	8.	3.	2.
ROCK TYPE	5.	1.	1.	1.	1.	7.	5.	5.	1.	1.

TABLE 28 (cont.)

SAMPLE	304B	304C	304C	304C	304C	304C	304C	304C	304C	305
ANALYSIS	3	1	2	2	2	3	4	5	5	1
TIO2	.89	.64	.81	.75	.77	.74	.50	.51	.71	.74
CR2O3	47.78	48.80	49.22	49.49	49.22	48.24	48.98	47.18	48.19	48.07
AL2O3	11.86	11.27	10.27	10.71	10.49	10.10	12.40	11.78	10.84	10.34
FE2O3	7.99	7.63	8.72	8.01	8.54	9.75	7.41	9.31	8.60	8.50
FEO	24.01	25.13	23.93	24.04	24.14	24.38	23.27	24.14	24.65	25.91
MGO	6.45	5.50	6.36	6.29	6.22	5.95	6.88	6.15	5.79	4.78
MNO	.52	.54	.49	.53	.53	.54	.47	.53	.50	.59
NIO	.09	.11	.12	.10	.12	.11	.11	.07	.08	.14
TOTAL	99.59	99.63	99.93	99.93	100.03	99.81	100.03	99.67	99.37	99.07
					CATIONS PER 32 OXYGENS					
TI	.181	.131	.165	.153	.157	.152	.100	.104	.146	.154
FE2+	.181	.131	.165	.153	.157	.152	.100	.104	.146	.154
CR	10.224	10.539	10.588	10.628	10.578	10.432	10.384	10.123	10.436	10.539
AL	3.784	3.628	3.293	3.428	3.360	3.255	3.918	3.767	3.499	3.379
FE3+	1.628	1.570	1.787	1.638	1.747	2.008	1.496	1.901	1.773	1.774
FE2+	5.256	5.611	5.281	5.310	5.331	5.425	5.119	5.375	5.502	5.854
MG	2.604	2.239	2.580	2.547	2.520	2.426	2.750	2.488	2.364	1.976
MN	.119	.125	.113	.122	.122	.125	.107	.122	.116	.138
NI	.020	.024	.026	.022	.026	.024	.024	.015	.018	.031
MMF	.323	.280	.321	.317	.314	.303	.345	.312	.295	.247
Y(CR)	.653	.670	.676	.677	.674	.665	.657	.641	.664	.671
Y(AL)	.241	.230	.210	.218	.214	.207	.248	.238	.223	.215
Y(FE3+)	.103	.099	.114	.104	.111	.127	.094	.120	.112	.113
FFF	.230	.214	.247	.230	.241	.264	.222	.257	.238	.227
GRAIN SIZE	250.	100.					300.			100.
HOST	2.	1.	2.	2.	2.	2.	7.	7.	7.	1.
ROCK TYPE	1.	1.	1.	1.	1.	1.	1.	1.	1.	1.

SAMPLE	305	305	306	306	306	306	306	306	308	308
ANALYSIS	2	3	1	2	2	3	4	4	1	2
TIO2	.87	.68	.50	.90	.87	.57	.14	.13	.66	.57
CR2O3	47.71	48.38	49.14	47.64	47.06	44.86	43.88	45.08	48.56	48.07
AL2O3	10.27	11.52	11.65	11.36	11.74	15.13	15.62	14.04	12.35	13.91
FE2O3	9.89	8.33	6.81	8.35	8.72	7.99	8.88	9.18	6.66	6.30
FEO	24.38	24.39	25.06	24.40	24.21	23.70	26.09	26.62	25.04	24.85
MGO	6.04	6.12	5.43	6.10	6.25	6.83	5.23	4.68	5.72	6.13
MNO	.55	.52	.54	.51	.52	.48	.50	.52	.59	.59
NIO	.10	.13	.11	.11	.13	.12	.07	.08	0.00	0.00
TOTAL	99.82	100.08	99.25	99.38	99.50	99.69	100.41	100.34	99.58	100.43
					CATIONS PER 32 OXYGENS					
TI	.179	.138	.103	.184	.178	.114	.028	.026	.135	.114
FE2+	.179	.138	.103	.184	.178	.114	.028	.026	.135	.114
CR	10.303	10.352	10.633	10.267	10.105	9.432	9.252	9.617	10.420	10.135
AL	3.306	3.674	3.757	3.649	3.757	4.741	4.909	4.464	3.950	4.371
FE3+	2.034	1.698	1.403	1.715	1.782	1.599	1.782	1.865	1.360	1.265
FE2+	5.391	5.384	5.635	5.380	5.322	5.159	5.793	5.981	5.550	5.430
MG	2.459	2.469	2.215	2.479	2.530	2.707	2.079	1.882	2.314	2.437
MN	.127	.119	.125	.118	.120	.108	.113	.119	.136	.133
NI	.022	.028	.024	.024	.028	.026	.015	.017	0.000	0.000
MMF	.306	.308	.278	.308	.315	.339	.263	.238	.289	.305
Y(CR)	.658	.658	.673	.657	.645	.598	.580	.603	.662	.642
Y(AL)	.211	.233	.238	.233	.240	.300	.308	.279	.251	.277
Y(FE3+)	.130	.107	.088	.109	.113	.101	.111	.116	.086	.080
FFF	.267	.235	.196	.235	.244	.232	.234	.236	.193	.185
GRAIN SIZE			40.			350.	250.	250.	40.	60.
HOST	3.	2.	1.	3.	3.	2.	5.	5.	1.	1.
ROCK TYPE	1.	1.	1.	1.	1.	1.	1.	1.	1.	1.

TABLE 28 (cont.)

SAMPLE	308	308	308	312	312	312	314	314	314	315
ANALYSIS	3	4	5	1	2	3	1	2	3	1
TIO2	.63	.63	.78	.46	.44	.48	.49	.49	.55	.72
CR2O3	47.97	46.69	47.42	47.67	47.92	46.25	48.05	47.49	47.50	47.69
AL2O3	14.29	15.79	12.37	16.76	16.78	17.64	17.16	18.02	18.22	16.91
FE2O3	6.24	6.72	7.71	3.80	3.41	4.27	2.36	2.11	2.31	3.98
FEO	24.71	23.99	24.26	24.17	24.22	23.75	23.58	23.16	22.84	20.61
MGO	6.39	7.16	6.27	6.89	6.83	7.24	7.05	7.41	7.81	9.15
MNO	.57	.59	.56	.42	.40	.41	.51	.53	.45	.48
NIO	0.00	0.00	0.00	0.00	0.00	0.00	.08	.07	.10	.12
TOTAL	100.81	101.58	99.38	100.18	100.00	100.05	99.29	99.29	99.79	99.66
					CATIONS PER 32 OXYGENS					
TI	.125	.123	.159	.091	.087	.094	.097	.096	.107	.139
FE2+	.125	.123	.159	.091	.087	.094	.097	.096	.107	.139
CR	10.044	9.599	10.158	9.886	9.956	9.545	10.009	9.830	9.755	9.776
AL	4.460	4.838	3.950	5.181	5.196	5.426	5.328	5.560	5.577	5.165
FE3+	1.245	1.316	1.574	.751	.674	.841	.469	.417	.452	.779
FE2+	5.349	5.095	5.339	5.213	5.236	5.092	5.100	4.976	4.856	4.330
MG	2.523	2.775	2.532	2.694	2.675	2.817	2.769	2.892	3.024	3.538
MN	.128	.130	.128	.093	.089	.091	.114	.117	.099	.106
NI	0.000	0.000	0.000	0.000	0.000	0.000	.017	.015	.021	.025
MMF	.315	.347	.315	.336	.334	.351	.347	.363	.378	.441
Y(CR)	.637	.609	.647	.624	.629	.603	.633	.622	.618	.621
Y(AL)	.283	.307	.251	.327	.328	.343	.337	.352	.353	.328
Y(FE3+)	.079	.083	.100	.047	.042	.053	.029	.026	.028	.049
FFF	.185	.201	.222	.124	.112	.139	.082	.075	.083	.148
GRAIN SIZE	80.	150.		55.	80.		40.	180.	225.	
HOST	1.	1.	2.	1.	1.	3.	1.	1.	3.	8.
ROCK TYPE	1.	1.	1.	1.	1.	1.	1.	1.	1.	7.

SAMPLE	315	315	315	315	315	315	315	317A	317A	317A
ANALYSIS	2	2	3	4	5	6	7	1	2	3
TIO2	.61	.56	.64	.67	.62	.50	.45	.65	.62	.70
CR2O3	46.64	46.63	47.07	47.16	47.34	46.55	45.29	47.06	47.18	46.89
AL2O3	17.74	17.85	17.16	17.15	17.01	17.88	18.82	16.68	16.61	16.95
FE2O3	3.19	3.55	3.49	3.62	3.65	3.24	3.63	3.69	3.72	3.72
FEO	23.66	23.00	23.10	22.36	22.62	23.43	23.09	24.16	23.89	23.39
MGO	7.19	7.64	7.47	7.98	7.80	7.25	7.51	6.74	6.90	7.32
MNO	.49	.49	.52	.51	.49	.50	.52	.54	.50	.51
NIO	.10	.11	.12	.11	.10	.10	.11	.11	.10	.10
TOTAL	99.62	99.83	99.58	99.57	99.64	99.45	99.43	99.64	99.53	99.58
					CATIONS PER 32 OXYGENS					
TI	.120	.110	.126	.132	.122	.098	.088	.129	.123	.139
FE2+	.120	.110	.126	.132	.122	.098	.088	.129	.123	.139
CR	9.656	9.604	9.757	9.743	9.792	9.643	9.331	9.820	9.846	9.739
AL	5.474	5.480	5.301	5.281	5.244	5.521	5.779	5.188	5.167	5.246
FE3+	.629	.696	.689	.713	.720	.639	.713	.734	.740	.736
FE2+	5.063	4.902	4.940	4.756	4.829	5.036	4.945	5.204	5.152	5.001
MG	2.807	2.967	2.919	3.108	3.042	2.832	2.917	2.652	2.715	2.866
MN	.109	.108	.115	.113	.108	.111	.115	.121	.112	.112
NI	.021	.023	.025	.023	.021	.021	.023	.023	.021	.020
MMF	.351	.371	.365	.388	.380	.355	.366	.332	.339	.357
Y(CR)	.612	.608	.619	.619	.621	.610	.589	.623	.625	.619
Y(AL)	.347	.347	.336	.335	.332	.349	.365	.329	.327	.333
Y(FE3+)	.039	.044	.043	.045	.045	.040	.045	.046	.047	.046
FFF	.108	.121	.119	.127	.127	.110	.124	.121	.123	.124
GRAIN SIZE	130.	150.	750.			100.	140.	100.	100.	
HOST	3.	3.	3.	3.	3.	7.	7.	1.	1.	3.
ROCK TYPE	1.	1.	1.	1.	1.	1.	1.	8.	8.	8.

TABLE 28 (cont.)

SAMPLE	317C	LG6	318A	318A	318A	318A	318A	318A	318A	318A
ANALYSIS	1	1	1	2	3	3	4	4	5	5
TIO2	.69	.80	.54	.55	.58	.62	.58	.61	.59	.63
CR2O3	47.82	48.59	49.24	49.97	49.22	48.33	45.76	45.13	48.76	48.16
AL2O3	16.40	14.62	15.19	15.09	15.25	15.75	16.43	16.68	15.86	16.54
FE2O3	4.78	5.19	3.20	2.90	3.74	3.84	4.98	4.98	3.59	3.39
FEO	20.33	21.66	24.36	24.42	23.42	23.56	25.54	26.25	23.48	22.99
MGO	9.33	8.42	6.40	6.47	7.15	7.08	5.81	5.37	7.16	7.55
MNO	.58	.36	.53	.51	.48	.52	.52	.53	.57	.53
NIO	0.00	0.00	.08	.08	.09	.08	.07	.06	.08	.10
TOTAL	99.93	99.64	99.55	99.99	99.93	99.79	99.69	99.61	100.10	99.90
					CATIONS PER 32 OXYGENS					
TI	.134	.158	.108	.110	.115	.123	.116	.122	.117	.124
FE2+	.134	.158	.108	.110	.115	.123	.116	.122	.117	.124
CR	9.793	10.117	10.372	10.483	10.279	10.089	9.621	9.514	10.139	9.975
AL	5.006	4.537	4.769	4.718	4.747	4.900	5.149	5.241	4.916	5.106
FE3+	.932	1.028	.642	.579	.744	.765	.998	1.000	.711	.670
FE2+	4.270	4.614	5.321	5.309	5.058	5.080	5.565	5.733	5.049	4.913
MG	3.602	3.305	2.542	2.559	2.815	2.786	2.303	2.134	2.807	2.948
MN	.127	.080	.120	.115	.107	.116	.117	.120	.127	.118
NI	0.000	0.000	.017	.017	.019	.017	.015	.013	.017	.021
MMF	.449	.409	.318	.320	.352	.348	.288	.267	.352	.369
Y(CR)	.622	.645	.657	.664	.651	.640	.610	.603	.643	.633
Y(AL)	.318	.289	.302	.299	.301	.311	.326	.332	.311	.324
Y(FE3+)	.059	.065	.040	.036	.047	.048	.063	.063	.045	.042
FFF	.174	.177	.105	.096	.125	.128	.149	.145	.121	.117
GRAIN SIZE			60.	65.	180.	180.	180.	180.	210.	210.
HOST	8.	8.	1.	1.	3.	3.	4.	4.	7.	7.
ROCK TYPE	5.	5.	8.	8.	8.	8.	8.	8.	8.	8.

SAMPLE	318A	318A	318A	318B	318B	318B	318B	318B	320	320
ANALYSIS	5	6	7	1	2	3	4	5	1	2
TIO2	.66	.54	.63	.61	.64	.66	.65	.62	.64	.90
CR2O3	47.83	50.19	47.79	50.65	49.70	48.48	47.66	48.11	45.49	46.12
AL2O3	16.75	13.98	16.12	14.22	15.05	15.84	15.37	15.47	18.35	17.62
FE2O3	3.40	4.06	4.19	2.99	2.99	3.52	4.05	4.00	2.75	3.03
FEO	22.83	23.31	23.08	23.75	23.54	23.37	25.84	25.35	23.41	23.76
MGO	7.69	7.00	7.46	6.75	6.98	7.21	5.51	5.95	7.17	7.18
MNO	.49	.51	.51	.52	.51	.53	.61	.53	.52	.53
NIO	.10	.07	.07	.10	.09	.09	.07	.06	.10	.10
TOTAL	99.76	99.66	99.86	99.60	99.50	99.69	99.76	100.10	98.44	99.25
					CATIONS PER 32 OXYGENS					
TI	.130	.108	.124	.122	.128	.131	.131	.124	.127	.178
FE2+	.130	.108	.124	.122	.128	.131	.131	.124	.127	.178
CR	9.900	10.577	9.929	10.683	10.436	10.111	10.078	10.107	9.492	9.585
AL	5.168	4.391	4.992	4.470	4.710	4.925	4.844	4.844	5.707	5.458
FE3+	.672	.815	.829	.602	.598	.700	.816	.801	.547	.600
FE2+	4.869	5.088	4.949	5.177	5.103	5.027	5.650	5.511	5.042	5.047
MG	3.001	2.781	2.922	2.684	2.763	2.835	2.197	2.357	2.821	2.813
MN	.109	.115	.113	.117	.115	.119	.138	.119	.116	.118
NI	.021	.015	.015	.021	.019	.018	.015	.013	.021	.021
MMF	.375	.348	.365	.336	.345	.354	.275	.294	.353	.349
Y(CR)	.629	.670	.630	.678	.662	.642	.640	.641	.602	.612
Y(AL)	.328	.278	.317	.283	.299	.312	.307	.307	.362	.349
Y(FE3+)	.042	.051	.052	.038	.037	.044	.051	.050	.034	.038
FFF	.118	.135	.140	.101	.102	.119	.123	.124	.095	.103
GRAIN SIZE	210.		450.	160.	160.		100.	200.	80.	90.
HOST	7.	3.	3.	1.	1.	3.	4.	4.	1.	1.
ROCK TYPE	8.	8.	8.	8.	8.	8.	8.	8.	1.	1.

TABLE 28 (cont.)

SAMPLE	320	320	320	320	323	323	323	323	323	323
ANALYSIS	3	4	5	6	1	2	3	4	4	5
TIO2	.88	1.13	.97	.89	.49	.52	.44	.44	.52	.57
CR2O3	45.92	47.11	46.75	46.05	50.88	49.48	48.06	52.25	49.48	49.78
AL2O3	17.86	16.50	16.52	17.17	15.86	16.36	17.28	14.09	16.27	16.43
FE2O3	2.79	3.07	3.07	3.42	1.02	2.05	2.62	2.29	2.21	1.61
FEO	23.43	23.74	23.14	23.05	23.35	23.05	22.56	22.82	22.52	22.53
MGO	7.34	7.26	7.34	7.47	7.07	7.38	7.68	7.30	7.71	7.70
MNO	.48	.51	.53	.51	.52	.49	.52	.53	.44	.50
NIO	.13	.11	.11	.12	.09	.07	.09	.08	.07	.11
TOTAL	98.83	99.43	98.43	98.69	99.28	99.41	99.25	99.81	99.23	99.23
					CATIONS PER 32 OXYGENS					
TI	.174	.224	.194	.177	.097	.103	.087	.088	.103	.114
FE2+	.174	.224	.194	.177	.097	.103	.087	.088	.103	.114
CR	9.557	9.817	9.823	9.620	10.652	10.307	9.967	10.961	10.305	10.357
AL	5.540	5.125	5.174	5.346	4.949	5.079	5.341	4.405	5.050	5.096
FE3+	.554	.609	.615	.681	.203	.408	.517	.458	.439	.319
FE2+	4.985	5.010	4.949	4.918	5.073	4.977	4.862	4.977	4.860	4.844
MG	2.880	2.852	2.908	2.942	2.791	2.898	3.003	2.887	3.027	3.022
MN	.107	.114	.119	.114	.117	.109	.115	.119	.098	.111
NI	.027	.023	.023	.025	.019	.015	.019	.017	.015	.022
MMF	.358	.352	.361	.366	.350	.363	.377	.363	.378	.378
Y(CR)	.610	.631	.629	.614	.674	.652	.629	.692	.652	.656
Y(AL)	.354	.329	.331	.341	.313	.321	.337	.278	.319	.322
Y(FE3+)	.035	.039	.039	.043	.012	.025	.032	.028	.027	.020
FFF	.096	.104	.106	.117	.037	.074	.094	.082	.081	.060
GRAIN SIZE	180.	180.	220.	370.		40.	160.	200.	200.	
HOST	1.	2.	2.	2.	1.	1.	1.	3.	3.	3.
ROCK TYPE	1.	1.	1.	1.	1.	1.	1.	1.	1.	1.

SAMPLE	323	323	323	323	323	325	325	325	325	325	325	325
ANALYSIS	5	5	5	6	7	1	2	3	4	5	6	7
TIO2	.59	.59	.58	.43	.44	.42	.42	.48	.49	.49	.50	.50
CR2O3	49.14	49.20	46.50	47.36	48.95	51.04	51.86	50.36	49.45	46.24	45.68	47.17
AL2O3	17.71	16.99	19.67	18.19	16.98	14.67	14.03	16.25	17.26	18.54	18.97	17.79
FE2O3	1.41	1.90	1.86	2.46	2.49	2.02	2.00	1.30	1.15	1.89	2.09	2.00
FEO	22.42	21.96	21.62	22.85	22.95	23.31	23.57	22.84	22.68	25.90	25.76	25.15
MGO	8.04	8.17	8.68	7.68	7.55	6.83	6.64	7.45	7.65	5.68	5.82	6.10
MNO	.53	.51	.51	.48	.52	.58	.56	.51	.53	.54	.57	.52
NIO	.11	.11	.11	.06	.08	.05	.08	.06	.08	.08	.09	.08
TOTAL	99.96	99.44	99.53	99.51	99.96	98.93	99.17	99.26	99.30	99.36	99.49	99.32
					CATIONS PER 32 OXYGENS							
TI	.115	.116	.112	.084	.086	.084	.085	.095	.096	.097	.099	.099
FE2+	.115	.116	.112	.084	.086	.084	.085	.095	.096	.097	.099	.099
CR	10.079	10.162	9.454	9.760	10.110	10.798	10.993	10.501	10.247	9.657	9.504	9.860
AL	5.414	5.230	5.961	5.587	5.227	4.626	4.433	5.050	5.331	5.771	5.883	5.542
FE3+	.275	.375	.360	.483	.490	.407	.404	.258	.228	.376	.415	.399
FE2+	4.751	4.682	4.539	4.897	4.928	5.133	5.202	4.944	4.877	5.626	5.571	5.462
MG	3.109	3.182	3.327	2.984	2.940	2.724	2.654	2.929	2.989	2.237	2.283	2.404
MN	.116	.113	.111	.106	.115	.131	.127	.114	.118	.121	.127	.116
NI	.023	.023	.023	.012	.017	.011	.017	.013	.017	.017	.019	.017
MMF	.389	.398	.417	.374	.369	.343	.334	.367	.375	.280	.287	.301
Y(CR)	.639	.644	.599	.616	.638	.682	.694	.664	.648	.611	.601	.624
Y(AL)	.343	.331	.378	.352	.330	.292	.280	.319	.337	.365	.372	.351
Y(FE3+)	.017	.023	.022	.030	.030	.025	.025	.016	.014	.023	.026	.025
FFF	.053	.072	.071	.088	.089	.072	.071	.048	.043	.061	.068	.066
GRAIN SIZE				80.	170.	40.	35.			90.	80.	
HOST	3.	3.	3.	7.	7.	1.	1.	1.	3.	4.	4.	3.
ROCK TYPE	1.	1.	1.	1.	1.	1.	1.	1.	1.	1.	1.	1.

TABLE 29 MICROPROBE ANALYSES OF CHROMITE : LOWER ZONE (KA 5)

SAMPLE	410	410	410	410	410	410	571	571	571	571
ANALYSIS	1	2	3	4	5	5	1	2	3	4
TIO2	.57	.30	.27	.38	.22	.20	.72	.65	.54	.83
CR2O3	48.93	49.81	52.75	51.67	51.29	51.20	41.51	45.56	47.67	44.00
AL2O3	11.39	12.17	7.38	6.62	6.72	6.75	20.33	16.61	15.29	19.08
FE2O3	8.37	7.30	9.49	10.41	10.60	10.58	5.88	7.13	7.05	6.06
FEO	24.66	24.36	25.85	27.97	27.83	27.79	25.50	23.45	21.96	23.62
MGO	6.09	6.23	4.77	3.31	3.19	3.16	6.75	7.69	8.46	8.09
MNO	.42	.47	.53	.57	.62	.64	.35	.45	.40	.41
NIO	0.00	0.00	0.00	0.00	0.00	0.00	0.00	0.00	0.00	0.00
TOTAL	100.43	100.65	101.04	100.94	100.48	100.33	101.04	101.55	101.38	102.10
					CATIONS PER 32 OXYGENS					
TI	.115	.060	.056	.080	.046	.042	.139	.126	.105	.158
FE2+	.115	.060	.056	.080	.046	.042	.139	.126	.105	.158
CR	10.444	10.359	11.515	11.455	11.426	11.423	8.430	9.304	9.753	8.823
AL	3.623	3.845	2.401	2.187	2.231	2.245	6.154	5.056	4.662	5.702
FE3+	1.701	1.474	1.972	2.197	2.249	2.247	1.138	1.387	1.374	1.158
FE2+	5.453	5.403	5.913	6.481	6.512	6.518	5.339	4.941	4.649	4.853
MG	2.451	2.490	1.963	1.383	1.340	1.329	2.584	2.961	3.263	3.058
MN	.096	.107	.124	.135	.148	.153	.076	.098	.088	.088
NI	0.000	0.000	0.000	0.000	0.000	0.000	0.000	0.000	0.000	0.000
MMF	.305	.313	.247	.174	.169	.168	.320	.368	.407	.378
Y(CR)	.662	.664	.724	.723	.718	.717	.536	.590	.617	.562
Y(AL)	.229	.242	.151	.138	.141	.141	.391	.321	.295	.363
Y(FE3+)	.107	.092	.124	.138	.141	.141	.072	.088	.087	.073
FFF	.233	.212	.248	.250	.255	.255	.171	.214	.224	.187
GRAIN SIZE	50.				140.					
HOST	1.	1.	9.	5.	5.	5.	4.	1.	1.	2.
ROCK TYPE	1.	1.	1.	1.	1.	1.	4.	4.	4.	4.

SAMPLE	622	622	622	622	622	729	729	729	729	729	729	729	729
ANALYSIS	1	2	3	4	5	1	1	3	4	5	6	7	7
TIO2	.96	1.00	.80	.53	.29	.40	.20	.37	.48	.45	.35	.68	.67
CR2O3	42.36	39.44	40.63	41.53	39.70	51.06	49.29	50.21	49.03	49.93	52.07	51.69	51.63
AL2O3	16.81	18.43	17.65	20.58	21.92	10.47	11.42	12.07	12.33	11.74	8.48	7.87	7.77
FE2O3	7.12	8.38	8.54	5.73	6.30	5.84	7.82	6.24	6.62	6.21	7.25	7.71	7.97
FEO	25.77	25.34	25.48	22.23	22.80	25.19	25.01	24.74	24.56	24.65	26.15	26.90	26.88
MGO	5.95	6.42	6.20	8.44	8.08	5.17	5.49	5.92	6.02	5.83	4.38	4.11	4.10
MNO	.41	.41	.38	.38	.35	.45	.42	.41	.41	.43	.51	.44	.47
NIO	0.00	0.00	0.00	0.00	0.00	0.00	0.00	0.00	0.00	0.00	0.00	0.00	0.00
TOTAL	99.39	99.43	99.69	99.43	99.45	98.58	99.65	99.96	99.45	99.25	99.20	99.40	99.49
						CATIONS PER 32 OXYGENS							
TI	.192	.198	.158	.102	.055	.083	.041	.075	.097	.092	.073	.143	.141
FE2+	.192	.198	.158	.102	.055	.083	.041	.075	.097	.092	.073	.143	.141
CR	8.915	8.217	8.487	8.446	8.048	11.193	10.638	10.734	10.512	10.766	11.526	11.478	11.462
AL	5.273	5.723	5.495	6.238	6.624	3.421	3.673	3.846	3.940	3.773	2.798	2.605	2.571
FE3+	1.427	1.663	1.699	1.111	1.216	1.219	1.606	1.270	1.351	1.276	1.529	1.630	1.684
FE2+	5.547	5.387	5.473	4.681	4.835	5.757	5.669	5.520	5.472	5.531	6.051	6.175	6.172
MG	2.361	2.522	2.442	3.236	3.088	2.137	2.234	2.386	2.433	2.370	1.828	1.721	1.716
MN	.092	.091	.085	.083	.076	.106	.097	.094	.094	.099	.121	.105	.112
NI	0.000	0.000	.302	0.000	0.000	0.000	0.000	0.000	0.000	0.000	0.000	0.000	0.000
MMF	.291	.311	.302	.403	.387	.267	.281	.298	.304	.296	.229	.214	.213
Y(CR)	.570	.526	.541	.534	.506	.706	.668	.677	.665	.680	.727	.730	.729
Y(AL)	.337	.366	.350	.394	.416	.216	.230	.242	.249	.238	.176	.165	.163
Y(FE3+)	.091	.106	.108	.070	.076	.077	.100	.080	.085	.080	.096	.103	.107
FFF	.199	.229	.231	.188	.199	.172	.219	.184	.195	.185	.199	.205	.210
GRAIN SIZE		105.	70.	140.	50.	50.	90.	90.	80.				
HOST	4.	4.	3.	1.	1.	1.	1.	1.	1.	1.	9.	2.	2.
ROCK TYPE	4.	4.	4.	4.	4.	1.	1.	1.	1.	1.	1.	1.	1.

TABLE 30:

AVERAGE Cr_2O_3 CONTENTS AND Y_{Cr} RATIOS OF CHROMITE ENCAPSULATED IN ORTHOPYROXENE CORE DOMAINS

UNIT/SUBUNIT	Cr_2O_3 (%)	Y_{Cr}	n	s	Y_{Cr} CHROMITITE
E	49,56	0,656	24	0,035	LG 7 : 0,628
D_2 ZS7	49,22	0,657	2	-	LG 6A: 0,659
D_2 ZS3	48,17	0,642	23	0,024	LG 6A: 0,625
					LG 6 : 0,645
D_1	50,18	0,665	17	0,051	LG 5 : 0,677
C_2	52,22	0,690	25	0,027	LG 3 : 0,693
C_1	49,55	0,641	6	0,011	-
B	52,18	0,694	14	0,029	LG 2 : 0,676
LOWER ZONE	49,75	0,674	7	0,015	-

n = number of analyses

s = standard deviation on estimate of Y_{Cr}

6. WHOLE-ROCK GEOCHEMISTRY

6.1. INTRODUCTION

There is a fundamental difference between the geochemistry of rapidly cooled rocks and slowly cooled, adcumulate-textured bronzitites, viz., the whole-rock geochemistry of the latter is drastically removed from the primary magma composition. Absolute abundances of major and trace elements reflect the relative modal proportions of cumulus and intercumulus phases, and a meaningful interpretation of the data requires a series of correction procedures to yield, for example, the concentration of a selected element in orthopyroxene. However, the ratio of two elements in solid solution within orthopyroxene is, to a first approximation, independent of the modal proportion of orthopyroxene, and recognition of systematic changes in these ratios in relation to stratigraphic height can be reconciled in terms of fractionation of a chemically unique batch of magma. Hence, the determination of selected ratios affords a means of recognizing cyclic units within a macroscopically homogeneous succession of bronzitites and, by implication, irruption of compositionally distinct or derivative batches of magma.

The procedures adopted in the present study required an initial assessment of applicable correction factors for chromite-bearing assemblages. To this end, bimineralic assemblages of chromite + orthopyroxene and chromite + olivine, depicting a wide spread of modal chromite/silicate ratios, were selected in order to determine the levels of trace and minor elements in theoretically pure olivine, orthopyroxene and chromite. Similarly, feldspathic- and essentially anchimonomineralic- bronzitites were selected in order to quantify trace element abundances in plagioclase. Application of these data to rocks composed of orthopyroxene-chromite-plagioclase- ($\pm$ clinopyroxene) thus facilitated an estimate of selected element concentrations and inter-element ratios in orthopyroxene at various stratigraphic levels.

6.2 ANALYTICAL METHODS

All samples were prepared and analyzed in the Department of Geology at Rhodes University. The drill core samples were crushed in a primary jaw-crusher and then milled in a tungsten steel swing mill. Small chromite-rich samples were powdered in a Cr - steel swing mill. The swing mills were cleaned with a pure quartzite, washed and precontaminated prior to the preparation of each powder. All major and trace elements were analyzed on a Phillips PW 1410, semi-automatic, X-ray fluorescence spectrometer employing standard techniques used at Rhodes University (Marsh, 1979). The major and minor element oxides SiO_2, Al_2O_3, total iron as FeO, MnO, MgO, K_2O and P_2O_5 were analysed on glass fusion discs using the method of Norrish and Hutton (1969). The trace elements Sr, Rb, Y, Zr, Ba, Zn, Cu, Ni, Co, V and Sc, as well as Na, were determined on pressed powder briquettes. Cr_2O_3 was determined on glass discs and on briquettes. Full corrections were made for tube and spectral line interferences, instrumental drift, flow counter dead-time and background. Corrections for matrix effects were made using mass absorption coefficients calculated from (a) major element analyses (Heinrich, 1966), and (b) the Mo - Compton scatter method (Reynolds, 1967 and Nesbitt et al., 1976).

Complete fusion of chromite in chromitiferous samples was not achieved. Hence, a determination of chromium in powder briquettes was attempted under standard operating conditions and the analytical results are presented in Fig. 51, which is a plot of wt. per cent Cr_2O_3 versus measured net Cr-peak intensity. It is evident from the data points that (a) the relationship is non-linear, (b) estimates based on Mo-Compton mass absorption coefficients (hereinafter denoted MAC) are unrealistic at high concentrations and are consistently higher than estimates based on Heinrich MAC's except at concentrations of less that 0,6 wt. per cent, and (c) estimates based on Heinrich MAC's appear to fail due to the spurious major element analyses. However, calculation of MAC's using Heinrich values applied to a range of hypothetical whole-rock compositions, derived by calculation from estimates of modal percentages and microprobe data (eg., mixtures of chromite with 20, 40, 60 and 80 per cent olivine), did not yield values which differed significantly from MAC

values calculated from measured whole-rock analyses. The influence of the assigned MAC value on Cr_2O_3 estimates is shown in Fig. 52. A range of assigned MAC values for each sample was submitted to the data reduction computer program, and the results summarized in Fig. 52 clearly indicate a greater sensitivity of Cr_2O_3 estimates to MAC values in chromite-rich rocks. Furthermore, there is a linear relationship between the determined Mo-Compton Cr and vanadium MAC values, as shown in Fig. 53, since long-wavelength MAC's are calculated from the same analytical reading. Accordingly, the following correction procedure was adopted for samples which demonstrated a net Cr-peak intensity in excess of 10^5 counts per second:

(a) Employing Mo-Compton MAC values, a sample of the LG 2 chromitite gave the highest Cr_2O_3 abundance of 81,75 wt. per cent for the suite of samples. Based on an inspection of polished thin sections and a normalized microprobe analysis of 51,91 wt. per cent Cr_2O_3 for chromite within this chromitite layer, it was assumed that 50,00 wt. per cent Cr_2O_3 was an appropriate whole-rock abundance.

(b) The relative Cr_2O_3 abundance in other samples was calculated according to:

$$Cr_2O_3^* = (Cr_2O_3)^{rock} \times 50,00/81,75$$

(c) The Cr* mass absorption coefficients which would yield these $Cr_2O_3^*$ abundances were calculated from regression equations of the type shown in Fig. 52.

(d) Compatible V* - and Sc* - absorption coefficients were calculated, respectively, from the following equations:

(i) Mu V* = 1,286 Mu Cr* + 1,70

(ii) Mu Sc* = 2,164 Mu Cr* + 2,79

(e) Short-wavelength MAC's derived by Heinrich and Mo-Compton procedures were in good agreement, and measured Mo-Compton MAC values were employed in the data reduction.

Corrected Cr_2O_3 analyses based on this technique are depicted in Fig. 51 by open circle symbols and it is clear from the tabulation presented in Appendix IV that these estimates are in good agreement with duplicate analyses performed at a commercial laboratory. Furthermore, it should be stressed that the above procedure does not

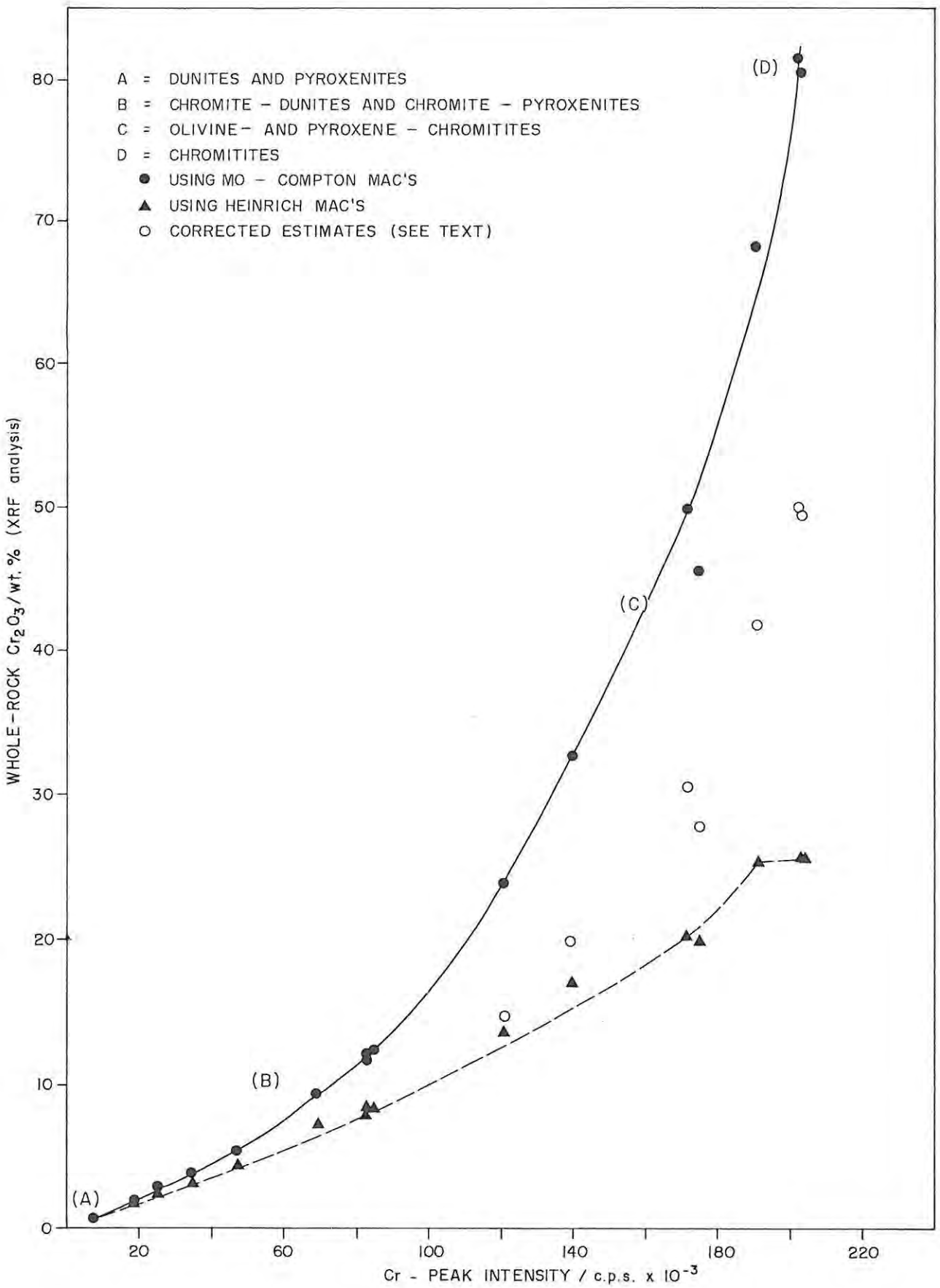

FIG. 51 PLOT OF WHOLE – ROCK Cr_2O_3 VERSUS Cr – PEAK INTENSITY SHOWING A NON–LINEAR RELATIONSHIP WHICH MAY BE ATTRIBUTED TO COUNT RATE AND/OR MASS ABSORBTION DIFFICULTIES.

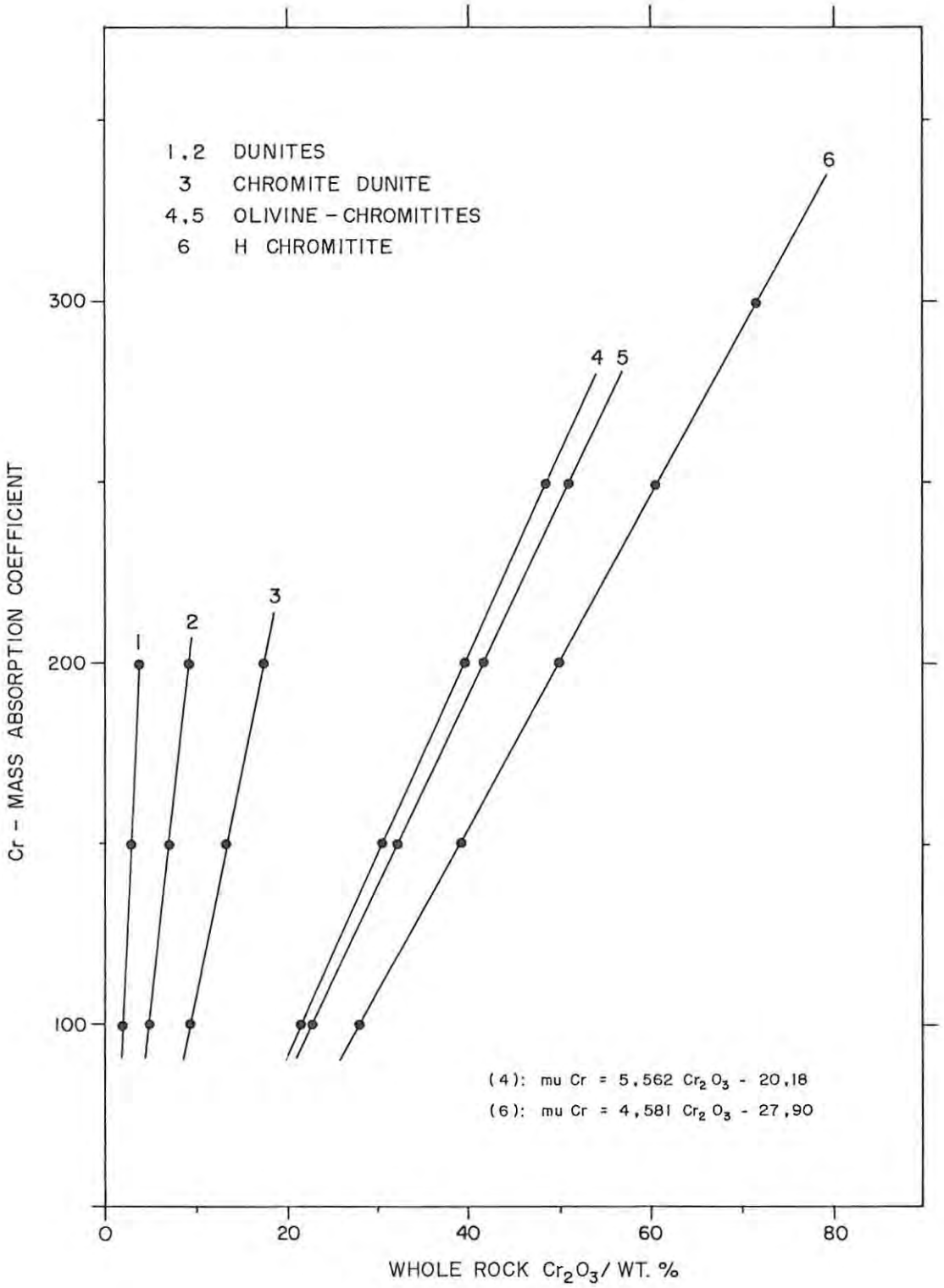

FIG. 52 HYPOTHETICAL Cr - MASS ABSORPTION COEFFICIENTS PLOTTED AGAINST DERIVED ESTIMATES OF WHOLE-ROCK Cr_2O_3 CONTENT FOR SELECTED OLIVINE-CHROMITE ASSEMBLAGES. WITH INCREASING MODAL CHROMITE CONTENT, IT IS EVIDENT THAT Cr_2O_3 ESTIMATES ARE INCREASINGLY SENSITIVE TO THE VALUE OF Cr - MAC EMPLOYED.

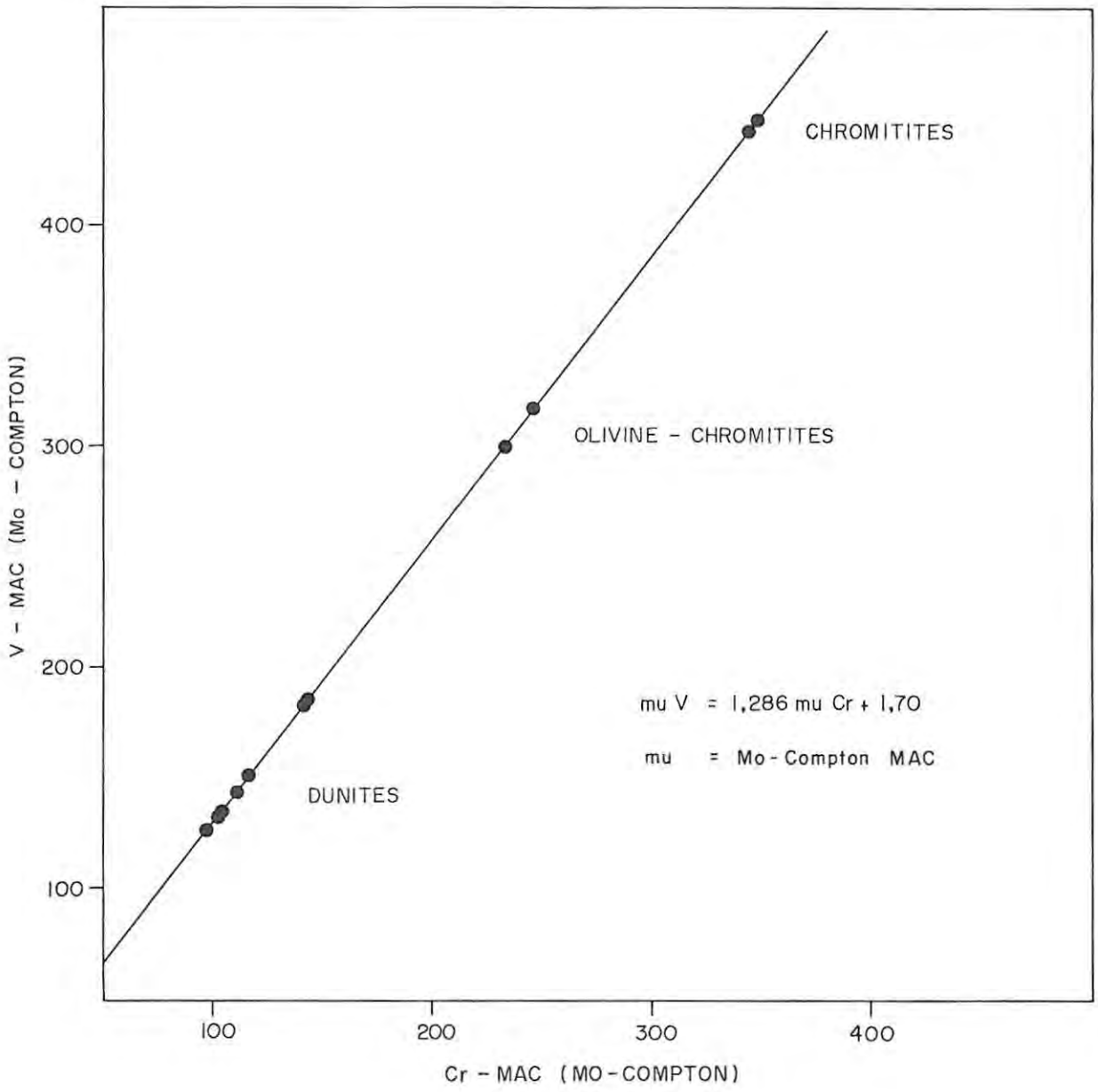

FIG 53 PLOT OF THE Mo – COMPTON V VERSUS Cr MASS ABSORBTION COEFFICIENT FOR SOME REPRESENTATIVE BRIQUETTED POWDERS. AN EQUIVALENT PLOT CAN BE CONSTRUCTED FOR Sc. THE LINEAR RELATIONSHIPS SHOWN AFFORD A MEANS OF CORRECTING THE V AND Sc RAW DATA TO GIVE ABUNDANCES COMPATIBLE WITH MORE REALISTIC WHOLE – ROCK $Cr_2 O_3$ LEVELS.

change whole-rock inter-element ratios of Cr, V and Sc. Fe_2O_3 was calculated in chromite-poor bronzitites and dunites of drill core ZS 7 as: $Fe_2O_3 = 0{,}001 \times FeO$, and as:

$$\frac{Fe_2O_3}{FeO}_{rock} = \frac{Fe_2O_3}{FeO}_{chromite} \times \left| \frac{Cr_2O_3^{rock} - Cr_2O_3^{opx}}{Cr_2O_3^{chromite}} \right|$$

in chromite-rich samples and samples depicting chromite with high Fe_2O_3 contents. The parameters Cr_2O_3 (chromite), Cr_2O_3 (opx) and $(Fe_2O_3/FeO)_{chromite}$ were obtained from microprobe data.

6.3 GEOCHEMISTRY OF THE D_2 SUBUNIT

Table 31 presents major and trace element analyses of 10 samples selected from drill core ZS 3. Samples 312 to 323 are representative of granular-textured chromite-orthopyroxene assemblages, with minor to trace proportions of clinopyroxene, whereas samples 300 to 308 are plagioclase-bearing. Cr_2O_3 abundances determined in fusion discs are presented with the tabulation of major element oxides, whereas the abundances determined on briquettes are given with the trace element analyses. A tabulation of Zn, Cu, Ni, Co, V, Sc and Cr_2O_3 analytical results based on Heinrich MAC values is available in Appendix V.

6.3.1 MAJOR ELEMENTS

Fig. 54(A) is a plot of whole-rock $Mg/(Mg + Fe^{2+})$ mol. ratios (hereinafter denoted Mg-number) versus Cr_2O_3 content. The latter is employed here as an index of the modal proportion of chromite, and the plotted values are estimates derived from briquettes, Mo-Compton MAC values and adjusted MAC's in the case of chromite-rich samples. There is a good agreement between the Mg-numbers and MMF (orthopyroxene) ratios of samples 304, 308, 312 and 323, attesting to the low modal abundances of chromite and clinopyroxene in these rocks. It is evident from the data points that Mg-numbers decline with increasing Cr_2O_3, but extrapolation to hypothetically pure chromite does not yield an acceptable MMF (chromite) ratio. This arises primarily from sample preparation and analytical difficulties,

TABLE 31:

WHOLE-ROCK ANALYSES; D_2 SUBUNIT (DRILL CORE ZS 3)

UNIT	E	D_2								
SAMPLE	300	304	308	312	314	316	317C	317c/o	318	323
SiO_2	52,02	54,61	55,67	54,86	53,18	36,82	9,25	30,30	47,12	54,02
TiO_2	0,17	0,11	0,09	0,09	0,10	0,28	0,53	0,30	0,15	0,09
Al_2O_3	3,82	1,78	1,60	1,53	1,79	6,71	13,87	7,01	3,13	1,61
Fe_2O_3	0,47	0,03	0,03	0,02	0,11	1,46	3,48	1,51	0,52	0,03
FeO	11,70	10,80	11,16	11,18	11,37	14,58	17,40	15,15	12,92	10,98
MnO	0,25	0,22	0,22	0,22	0,22	0,28	0,44	0,32	0,28	0,23
MgO	25,94	28,22	29,38	29,39	29,16	22,73	13,30	22,06	26,98	29,67
CaO	2,72	1,97	1,81	1,69	1,62	1,12	0,19	0,91	1,64	1,51
Na_2O	0,52	0,29	0,22	0,15	0,09	0,18	NA	NA	0,14	0,14
K_2O	-	0,03	-	-	-	-	-	-	-	-
P_2O_5	-	-	-	-	-	-	-	-	-	-
Cr_2O_3	2,44	0,59	0,68	0,71	1,93	10,79	28,97	15,82	5,34	1,70
L.O.I	0,82	1,11	0,88	1,04	0,89	0,67	1,24	1,88	0,88	0,61
TOTAL	100,87	99,76	101,74	100,88	100,46	95,62	88,67	95,29	99,10	100,59
Mg-no.	0,798	0,823	0,824	0,824	0,820	0,735	0,576	0,721	0,788	0,828
Sr	34,0	6,9	3,1	-	-	NA	NA	NA	NA	-
Rb	-	3,8	-	-	-	NA	NA	NA	NA	-
Y	3,1	3,2	3,2	2,7	-	NA	NA	NA	NA	2,3
Zr	3,0	6,7	2,3	2,2	-	NA	NA	NA	NA	-
Ba	18	-	-	NA	NA	NA	NA	NA	NA	-
Zn	93	68	78	73	89	255	579	305	138	75
Cu	22	12	15	9	11	22	23	18	25	7
Ni	547	552	572	565	529	662	746	774	850	581
Co	110	100	109	108	113	104	173	119	129	99
V	266	114	112	114	182	787	2812	1060	611	157
Sc	34	30	32	31	31	25	25	25	39	30
Cr_2O_3	3,06	0,68	0,81	0,83	2,30	14,66*	41,74*	19,98*	9,54*	1,84
BH DEPTH (m)	164,22	167,47	171,62	177,56	179,89	180,21	180,30	180,44	181,40	187,90

but it should be appreciated that the hypothetical relationship between Mg-number and whole-rock Cr_2O_3 content is non-linear since the MMF (chromite) - and MMF (orthopyroxene)- ratios rise with increasing modal abundance of chromite. Fig. 54(B) is a plot of whole-rock SiO_2 and Al_2O_3 versus Cr_2O_3 and, with the exception of sample 300 which is a chromitiferous, mesocumulate-textured feldspathic bronzitite, it is clear that (a) SiO_2 analyses can be used to estimate whole-rock modal abundances of chromite, and (b) extrapolation of the Al_2O_3 data yields mean Al_2O_3 (chromite) and Al_2O_3 (orthopyroxene) abundances for the subunit. For example, linear regression equation (3) permits calculation of a mean Al_2O_3 (orthopyroxene) content of 1,39 wt. per cent for an assigned value of 0,54 wt. per cent Cr_2O_3, which is in excellent agreement with the average of 1,38 wt. per cent Al_2O_3 determined by microprobe analysis within samples 308 and 314. If the plagioclase-bearing samples are excluded (as evinced by detectable levels of Sr), the derived linear regression equation is: $Al_2O_3 = 0{,}3076\ Cr_2O_3 + 1{,}098$ ($r = 0{,}9913$), yielding mean Al_2O_3 (orthopyroxene) concentrations of 1,24 to 1,27 wt. per cent for the microprobe determined range of 0,45 to 0,55 wt. per cent Cr_2O_3 in orthopyroxene (r denotes correlation coefficient). The variation of TiO_2 in samples 312 to 323 is defined in terms of: $TiO_2 = 0{,}011\ Cr_2O_3 + 0{,}076$ ($r = 0{,}9909$), and calculation yields 0,60 wt. per cent TiO_2 for an assigned value of 48,0 wt. per Cr_2O_3. This is in excellent agreement with microprobe data: the mean TiO_2- and Cr_2O_3 - contents of chromite within the succession bounded by samples 308 and 323 are 0,60 and 48,7 wt. per cent, respectively ($n = 76$). These consistencies indicate that the estimates of Cr_2O_3* in chromite-rich samples are reasonable. However, a point to be recognized is that significant errors would arise if olivine were present.

6.3.2 TRACE ELEMENTS

Fig. 55 shows the variation of V against Cr_2O_3, and the following equation is derived by regression analysis:

$$V = 49{,}814\ Cr_2O_3 + 76{,}32 \quad (r = 0{,}9976).$$

This relationship is exclusive of sample 317c, which depicts chromite enriched in V relative to chromite in orthopyroxene-rich rocks. The

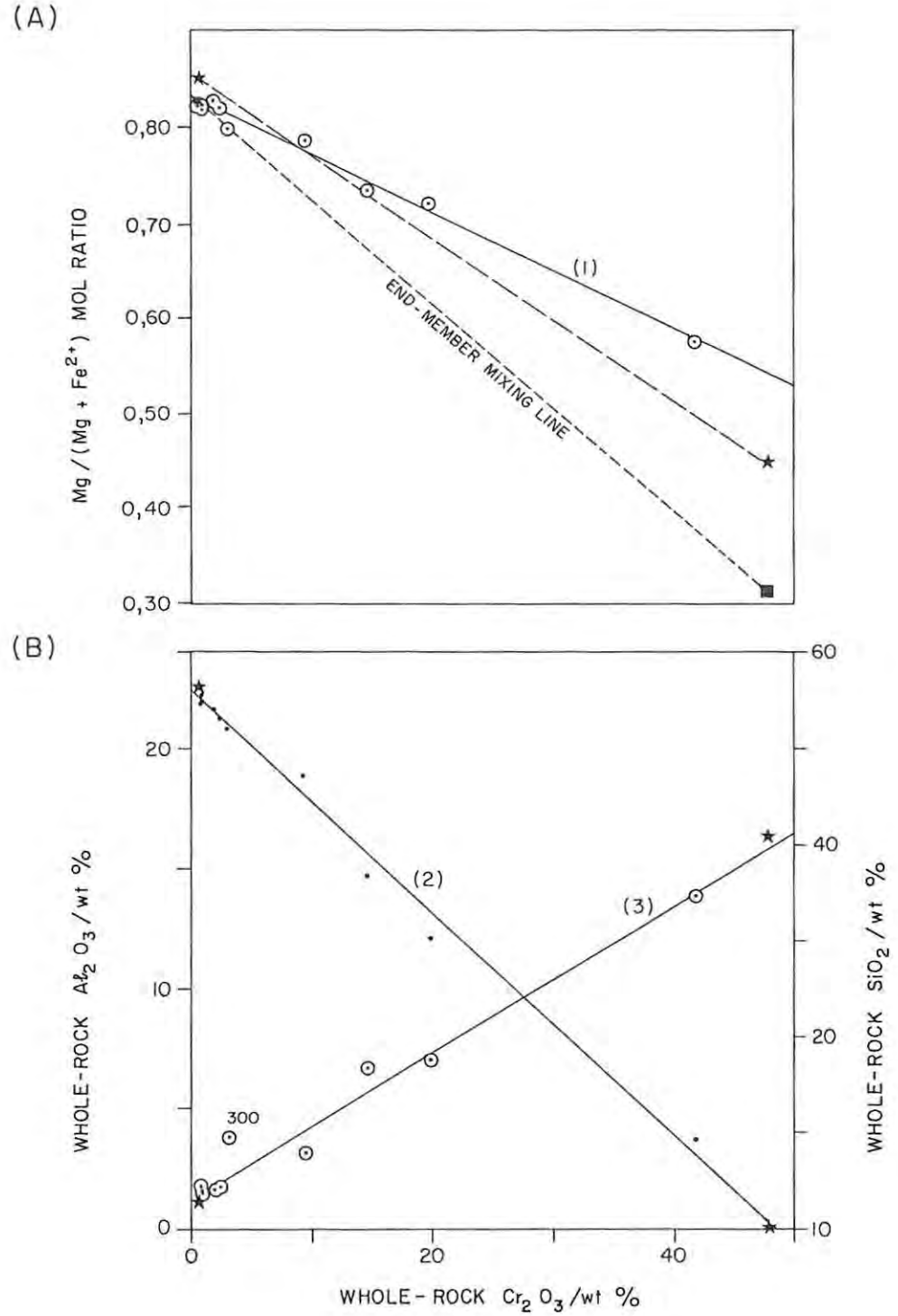

FIG 54 PLOT OF (A) WHOLE-ROCK $Mg/(Mg + Fe^{2+})$ MOL RATIO, AND (B) WHOLE-ROCK SiO_2 AND Al_2O_3 VERSUS WHOLE-ROCK Cr_2O_3.
SYMBOLS: • WHOLE ROCK SiO_2 ⊙ WHOLE ROCK Al_2O_3; ★ MICROPROBE DATA OF CHROMITE AND ORTHOPYROXENE WITHIN SAMPLE 317C, AND WITHIN SAMPLE 308 (■).

1. $Mg/(Mg + Fe^{2+}) = -0,00607\ Cr_2O_3 + 0,8333$ $(r = -0,9960)$
2. $SiO_2 = -1,1468\ Cr_2O_3 + 55,73$ $(r = -0,9953)$
3. $Al_2O_3 = 0,303\ Cr_2O_3 + 1,226$ $(r = 0,9917)$

(SAMPLE 300 IS EXCLUDED FROM LINEAR REGRESSION (3)).

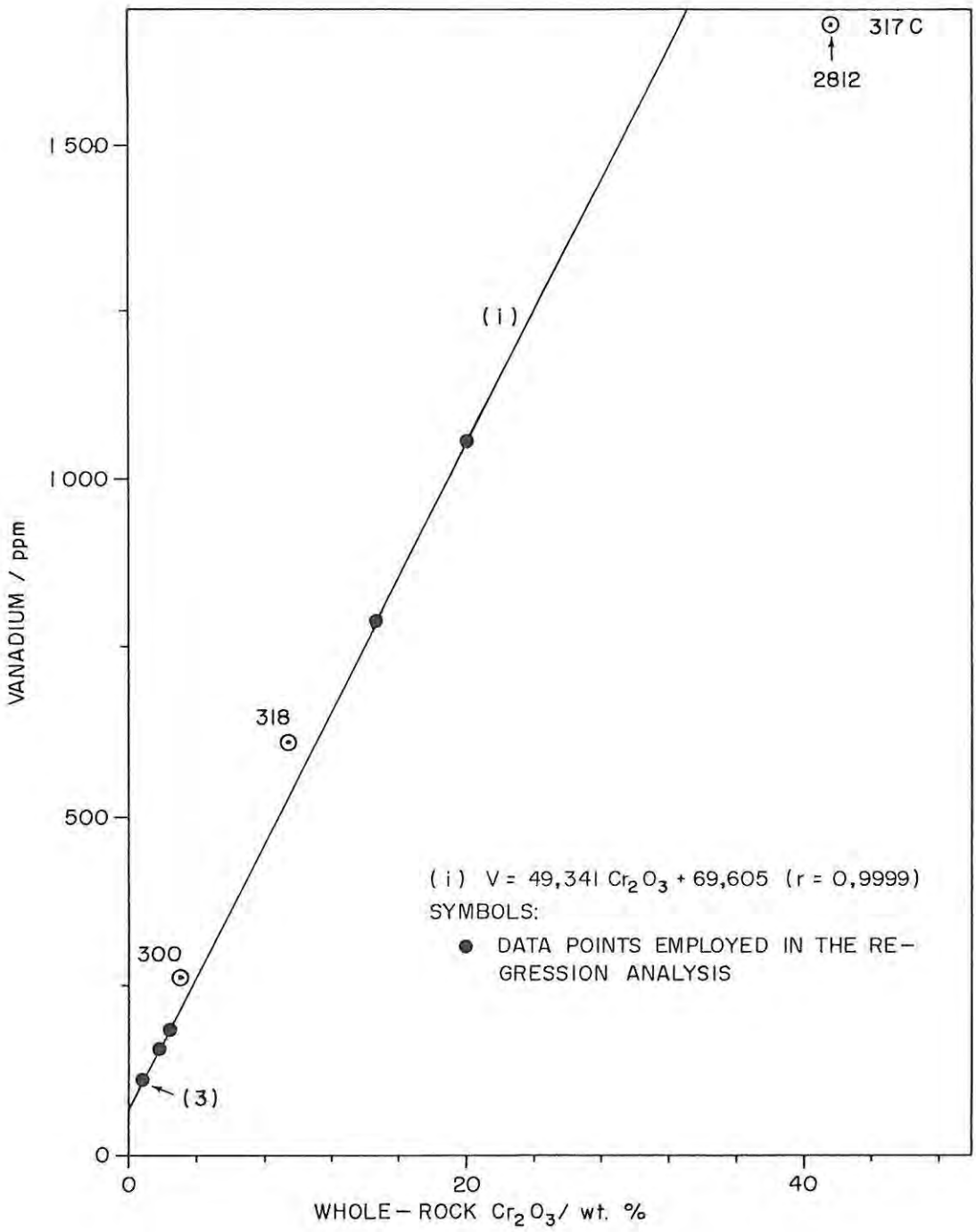

FIG. 55 PLOT OF WHOLE-ROCK V AGAINST Cr_2O_3, D UNIT (DRILL CORE ZS 3). REGRESSION ANALYSIS OF A SIX-POINT DATA SET (SEE TEXT) YIELDS 95 ppm V IN HYPOTHETICALLY PURE ORTHOPYROXENE AND 2438 ppm V (0,43 % V_2O_5) IN HYPOTHETICALLY PURE CHROMITE. THE DISPOSITION OF DATA POINTS SUGGESTS THAT CHROMITE IN GRANULAR-TEXTURED ROCKS DISPLAYS LOWER V CONTENTS THAN CHROMITE IN FELDSPATHIC ASSEMBLAGES (SAMPLE 300) AND IN CHROMITITE LAYERS (SAMPLE 317 C).

behaviour of V is therefore similar to Ti, which was also noted to be higher in chromite within chromitite layers. Sample 318 is similarly enriched in V relative to the estimated whole-rock Cr_2O_3 content, but this feature may be attributed to sample inhomogeneity: though care was taken to select a portion of sample 318 which did not depict lenses of ultramafic pegmatite, it is evident from the Ni content of 850 ppm that olivine was present in the sample. Furthermore, an anomalously high modal abundance of clinopyroxene is indicated by the Sc content of 39 ppm [Sc preferentially partitions into clinopyroxene (D_{Sc}^{cpx} = 3,1; Frey et al. (1978)] and would account for the excess of V (D_V^{cpx} = 1,5; Frey et al. (op. cit.)). Sample 318 is therefore neglected to suit the present purposes, as can samples 300 and 304 since (a) there is a conspicuous abundance of plagioclase and clinopyroxene in sample 300, and (b) minor amounts of plagioclase, clinopyroxene and biotite are depicted in sample 304. Hence, specific to a six-point data set comprising samples 308, 312, 314, 316, 317 c/o (i.e., a chromite bronzitite) and 323, the variation of V against Cr_2O_3 is given by the following equation:

$$V = 49{,}341\ Cr_2O_3 + 69{,}605 \quad (r = 0{,}9999)$$

Based on an average microprobe analysis of 0,52 wt. per cent Cr_2O_3 in orthopyroxene, the computed V content of orthopyroxene in the D_2 subunit is thus 95 ppm. Alternatively, the V content of chromite in bronzitites and chromite bronzitites is 2438 ppm, or 0,43 wt. per cent V_2O_5 (relative to an average Cr_2O_3 content of 48 wt. per cent). With respect to the bronzite-chromitite layer in the gradational hanging-wall of the LG 6 chromitite (sample number 317C), the estimated weight fraction of chromite in the whole-rock sample is 0,884 (based on microprobe and whole-rock Cr_2O_3 determinations and correction of the latter for a loss of ignition of 1,24 wt. per cent). Calculation thus yields an estimated V_2O_5 content in chromite of 0,58 wt. per cent within this layer. The contribution of V (opx) and Cr_2O_3 (opx) to this whole-rock analysis is negligible relative to experimental error. The regression equation given above affords a means of estimating the V content of orthopyroxene in chromite-orthopyroxene assemblages at other positions within the succession. The procedure is as follows:

1. The contribution of chromite to the whole-rock Cr_2O_3 analysis is derived from: $Cr_2O_3^{chr} = Cr_2O_3(rock) - Cr_2O_3(opx)$.
2. V in the chromite fraction is obtained by calculation from: $V^{chr} = 49,341\ Cr_2O_3^{chr}$.
3. V in orthopyroxene is obtained by subtraction: $V\ (opx) = V(rock) - V^{chr}$.

The variation of Zn, Cu, Ni, Co, and Sc against whole-rock Cr_2O_3 is shown in Fig. 56. It is evident from the data points that chromite is enriched in Zn, Cu, Ni and Co relative to orthopyroxene, but is depleted in Sc. With the exception of plagioclase-bearing samples 300, 304 and 318, the variation of Zn, Cu, Co and Sc against Cr_2O_3 is given by the following equations:

1. $Zn = 12,41\ Cr_2O_3 + 62,05 \quad (r = 0,9993)$
2. $Cu = 0,33\ Cr_2O_3 + 11,08 \quad (r = 0,8094)$
3. $Co = 1,46\ Cr_2O_3 + 100,61 \quad (r = 0,8938)$
4. $Sc = 0,17\ Cr_2O_3 + 30,50 \quad (r = -0,8299)$

Substitution of a Cr_2O_3 content of 0,52 wt. per cent thus yields 68 ppm Zn, 11 ppm Cu, 101 ppm Co and 30 ppm Sc in hypothetically pure orthopyroxene. Relative to an average Cr_2O_3 content in chromite of 48,0 wt. per cent, calculated contents in the spinel are 658 ppm Zn, 27 ppm Cu, 171 ppm Co and 22 ppm Sc. The variation of Ni is not systematically linked to Cr_2O_3 content. For example, Cr_2O_3 declines from 2,30 wt. per cent in sample 314 to 0,81 wt. per cent in sample 304, whereas Ni rises from 529 to 572 ppm. The analysis of 774 ppm Ni in sample 317 c/o is also not consistent with the anticipated variation (due to a trace occurrence of olivine). If this sample is excluded from the data set the variation of Ni against Cr_2O_3 is given by the equation:

$$Ni = 4,674\ Cr_2O_3 + 560,7 \quad (r = 0,9493),$$

and the calculated estimates of Ni in orthopyroxene and chromite are 563 ppm (0,07 % NiO) and 785 ppm (0,10 % NiO), respectively. These values are in excellent agreement with microprobe analyses. It is evident from the data, however, that correction factors for Ni, Cu, Co and Sc in chromite need not be applied to samples showing less than ca. 4 wt. per cent Cr_2O_3.

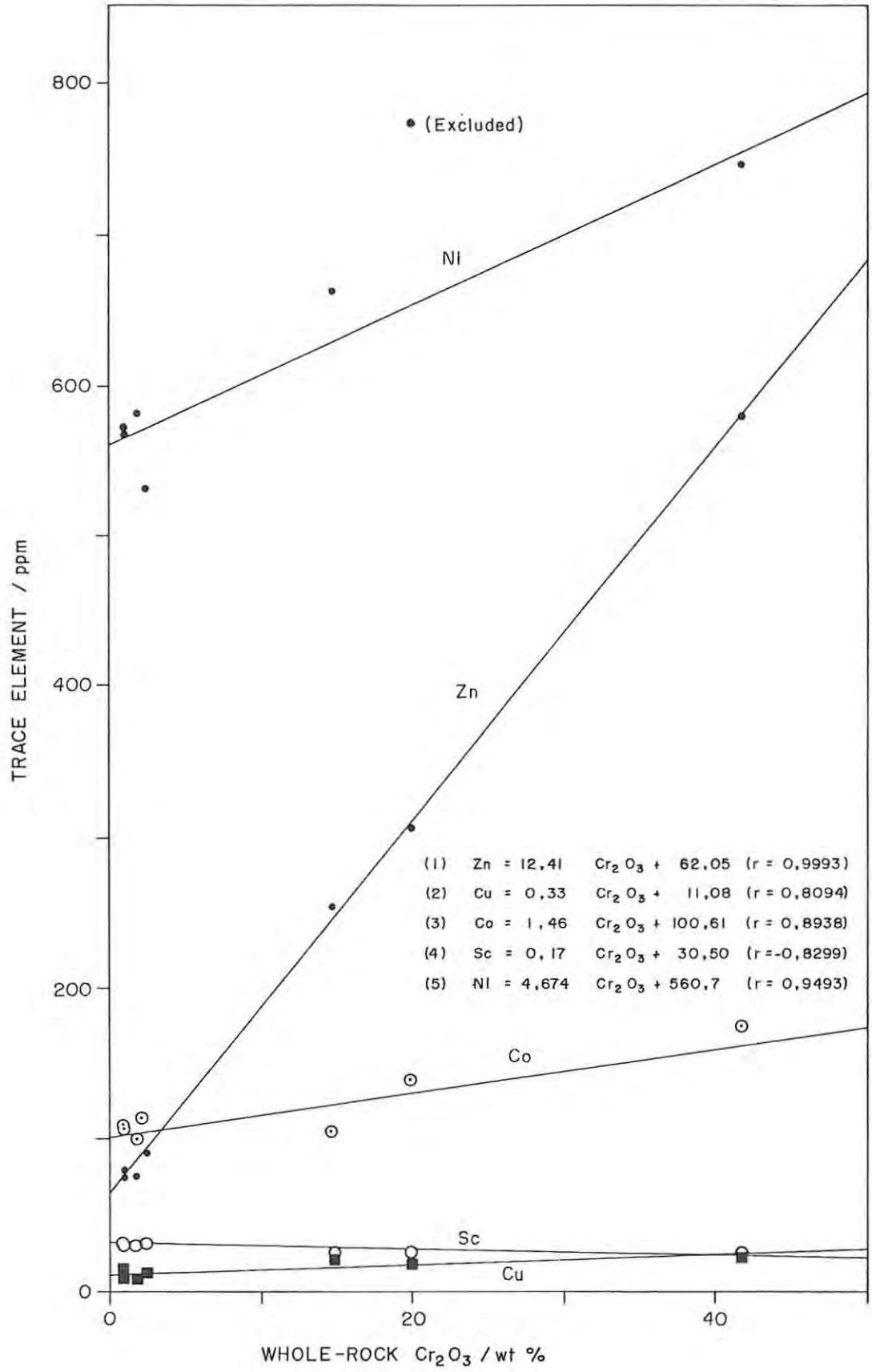

FIG 56 PLOT OF Zn, Cu, Ni, Co AND Sc VERSUS WHOLE-ROCK Cr_2O_3 FOR 7 SAMPLES OF THE D_2 SUBUNIT, DRILL CORE ZS 3.

The affinity of Sr for plagioclase is evinced by samples 300, 304 and 308. Sr rises from 3,1 ppm in sample 308 to 34,0 ppm in sample 300, linked to a rise in whole-rock Al_2O_3 and CaO. Ba was detected in sample 300 (18 ppm) and Rb in sample 304 (3,8 ppm). The Zr abundance of the latter is 6,7 ppm, consistent with the presence of red mica. Y was detected in 5 samples (x = 2,9 ppm) and Zr in four (x = 3,5 ppm). Nb was not detected in any samples throughout the studied section.

6.4 GEOCHEMISTRY OF THE C_1 AND C_3 SUBUNITS

Whole-rock analyses of 13 samples from the C_3 subunit and 3 samples from the C_1 subunit are presented in Table 32. A substantial loss of ignition was realized in these pervasively serpentinized rocks, and the trace element data presented in the tabulation have been recalculated on the basis of anhydrous conditions. Mo-Compton MAC values were employed in the correction of matrix effects. The assemblages selected for analysis ranged from adcumulate-textured dunites, with accessory levels of chromite, to olivine-chromitites and chromitites. Samples depicting cumulus or reaction-replacement orthopyroxene were not included in the data set.

6.4.1 MAJOR ELEMENTS

Calculated $Mg/(Mg + Fe^{2+})$ mol. ratios of chromite-poor dunites are in excellent agreement with microprobe estimates of Fo contents in olivine. Normalized SiO_2 contents vary between 41,05 and 4,06 wt. per cent, with the latter concentration being representative of the H chromitite layer. This may be regarded as an exaggerated concentration since complete fusion of the chromite fraction was not attained. CaO contents of the olivine-rich dunites vary between 0,06 and 0,44 wt. per cent, and are substantially higher than microprobe estimates of the lime content of olivine. In conjunction with Na_2O contents of up to 0,10 wt. per cent, this feature suggests that a minor intercumulus silicate fraction is present in some of the samples (though this is not evident in thin section). The influence of the modal proportion of chromite on whole-rock geochemistry is

TABLE 32:

WHOLE-ROCK ANALYSES: C_3 AND C_1 SUBUNITS

UNIT	C_3							
SAMPLE	170	172 A	172 B	175	177 A	177 B	178	180
SiO_2	32,82	29,44	31,78	33,61	17,48	33,23	29,57	33,42
TiO_2	0,04	0,13	0,08	0,02	0,25	0,11	0,11	–
Al_2O_3	0,85	3,67	2,08	0,51	7,51	5,65	2,85	0,08
Fe_2O_3	0,12	0,35	0,24	0,03	1,24	0,70	0,47	0,01
FeO	12,40	11,52	12,06	11,54	12,42	11,74	11,80	12,13
MnO	0,17	0,20	0,18	0,15	0,26	0,19	0,21	0,17
MgO	36,64	33,10	35,68	38,04	23,25	34,41	32,91	37,98
CaO	0,17	0,12	0,07	0,10	0,13	1,62	0,23	0,05
Na_2O	0,09	NA	0,06	0,08	NA	NA	NA	0,05
K_2O	–	–	–	–	–	0,04	–	–
P_2O_5	–	–	–	–	–	–	–	–
Cr_2O_3	1,32	4,62	3,47	1,05	12,60	4,79	4,65	0,32
L.O.I	13,79	10,29	12,38	14,96	6,54	10,49	10,54	15,13
TOTAL	94,41	93,44	98,08	100,09	81,68	102,87	93,34	99,34
Mg-no.	0,840	0,836	0,840	0,854	0,769	0,839	0,832	0,848
Zn	67	156	91	48	257	121	115	66
Cu	9	9	13	8	28	37	31	113
Ni	1721	1606	1632	1821	1259	1684	1660	2069
Co	159	186	162	163	134	174	170	180
V	80	510	225	46	958	362	346	27
Sc	6	11	8	6	16	9	11	4
Cr_2O_3	2,12	13,64	6,24	1,03	32,64	13,86	13,04	0,29
BH DEPTH (m)	254,15	255,56	255,64	256,10	257,76	257,90	258,10	259,00

TABLE 32 (Cont.):

UNIT	C_3					C_1		
SAMPLE	183 A	183 B	191	199	H CHROME	241	245	247
SiO_2	33,79	30,09	35,19	33,23	3,99	16,93	32,86	34,65
TiO_2	0,04	0,13	0,01	0,02	0,51	0,25	0,07	0,02
Al_2O_3	1,02	3,13	0,19	0,37	13,67	7,78	1,64	0,38
Fe_2O_3	0,11	0,45	0,01	0,02	1,59	1,33	0,12	0,03
FeO	11,45	11,26	11,28	12,36	15,90	13,35	12,41	11,44
MnO	0,18	0,20	0,16	0,16	0,44	0,32	0,20	0,17
MgO	38,76	34,05	38,72	36,91	11,79	23,38	36,03	38,25
CaO	0,18	0,41	0,29	0,23	0,48	0,03	0,07	0,38
Na_2O	NA	NA	0,06	0,10	NA	NA	NA	0,04
K_2O	-	-	-	0,02	-	-	-	-
P_2O_5	-	-	-	-	-	-	-	-
Cr_2O_3	1,84	3,61	0,22	0,44	31,65	17,92	3,36	0,57
L.O.I	11,50	9,46	14,34	16,37	1,71	6,66	12,71	13,81
TOTAL	98,87	92,79	100,47	100,23	81,73	87,95	99,47	99,74
Mg-no.	0,857	0,843	0,859	0,842	0,569	0,757	0,838	0,856
Zn	63	131	60	65	709	297	85	65
Cu	24	25	2	29	29	23	15	3
Ni	1787	1740	1787	1780	464	1314	1721	1721
Co	164	175	166	172	172	146	173	154
V	76	363	14	21	2830	961	125	41
Sc	6	11	6	5	18	13	8	7
Cr_2O_3	2,81	12,89	0,21	0,45	49,44	29,75	4,30	0,68
BH DEPTH (m)	260,63	260,73	267,77	274,99	275,52	319,62	320,28	322,04

. Fe_2O_3/FeO = 0,001 in olivine-rich rocks.
and $Fe_2O_3/FeO = (Fe_2O_3/FeO)^{CHROMITE} \times \frac{Cr_2O_3(ROCK)}{Cr_2O_3(CHROMITE)}$
in chromite-rich samples.

. NA = Not analyzed

. K_2O = 0,00 Below detection limit (denoted by (-) symbol)
. Mg-no. = Mg-number
= $Mg/(Mg + Fe^{2+})$ mol. ratio
. Trace element abundances, including Cr_2O_3, recalculated on the basis of anhydrous conditions

illustrated in Fig. 57, which shows a plot of normalized TiO_2 and Al_2O_3 versus Cr_2O_3. Absolute abundances of Cr_2O_3 range between 0,21 and 49,44 wt. per cent, but serve only as approximate indices of whole-rock chromite abundance since there is a pronounced cryptic variation of Cr_2O_3 (chromite) in relation to stratigraphic height. Hence, regression analysis of the data will yield mean concentrations. The variation of Al_2O_3 against Cr_2O_3 is given by the following equations:

1. Olivine-rich: $Al_2O_3 = 0,368\ Cr_2O_3 + 0,16$ $(r = 0,9919)$
2. Chromite-rich: $Al_2O_3 = 0,278\ Cr_2O_3 - 0,13$ $(r = 0,9937)$

An Al_2O_3 content of 0,16 wt. per cent in Cr-free olivine, serpentine and/or an intercumulus fraction, is indicated by equation (1). Significantly, the equations predict a higher Al_2O_3/Cr_2O_3 ratio in chromite grains within dunites. This is fully consistent with microprobe data, which yield average Al_2O_3/Cr_2O_3 (chromite) ratios of 0,41 and 0,29 for olivine-rich and chromite-rich domains, respectively. The variation of TiO_2 against Cr_2O_3 in dunites and chromite-rich rocks is given, respectively, by the following equations:

1. $TiO_2 = 0,0146\ Cr_2O_3 + 0,008$
2. $TiO_2 = 0,010\ Cr_2O_3 - 0,009$

Given that the Cr_2O_3 content of chromite in dunites varies between 45 and 47 wt. per cent (microprobe analysis), the former equation thus yields an average TiO_2 content of 0,68 wt. per cent in weakly disseminated chromite grains, which is in agreement with microprobe data.

6.4.2 TRACE ELEMENTS

Fig. 58(A) shows the variation of V against Cr_2O_3 and regression analysis of the data, with the exception of the H chromitite sample, yields the following equation:

$$V = 30,085\ Cr_2O_3 + 8,33\ (r = 0,9920)$$

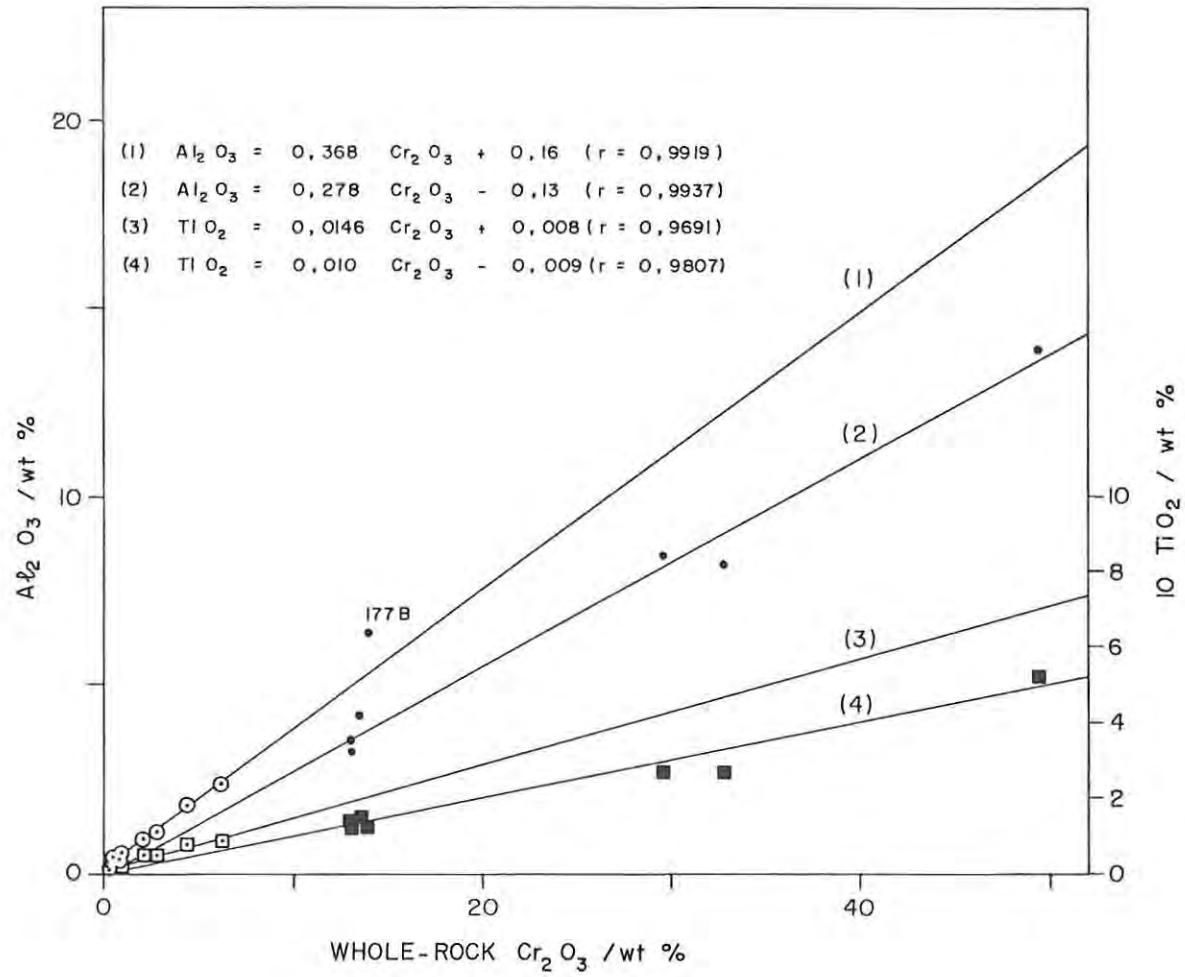

FIG 57 PLOT OF WHOLE-ROCK Al_2O_3 AND 10 x TiO_2 VERSUS Cr_2O_3 FOR OLIVINE–CHROMITE ASSEMBLAGES. Cr_2O_3 DETERMINED ON BRIQUETTES AND MO-COMPTON MAC VALUES WERE EMPLOYED TO CORRECT FOR MATRIX EFFECTS. EQUATION (2) IS EXCLUSIVE OF SAMPLE 177B.

SYMBOLS: ⊙ OLIVINE-RICH ROCKS
• CHROMITE-RICH ROCKS
— Al_2O_3
⊡ OLIVINE-RICH ROCKS
■ CHROMITE-RICH ROCKS
— TiO_2

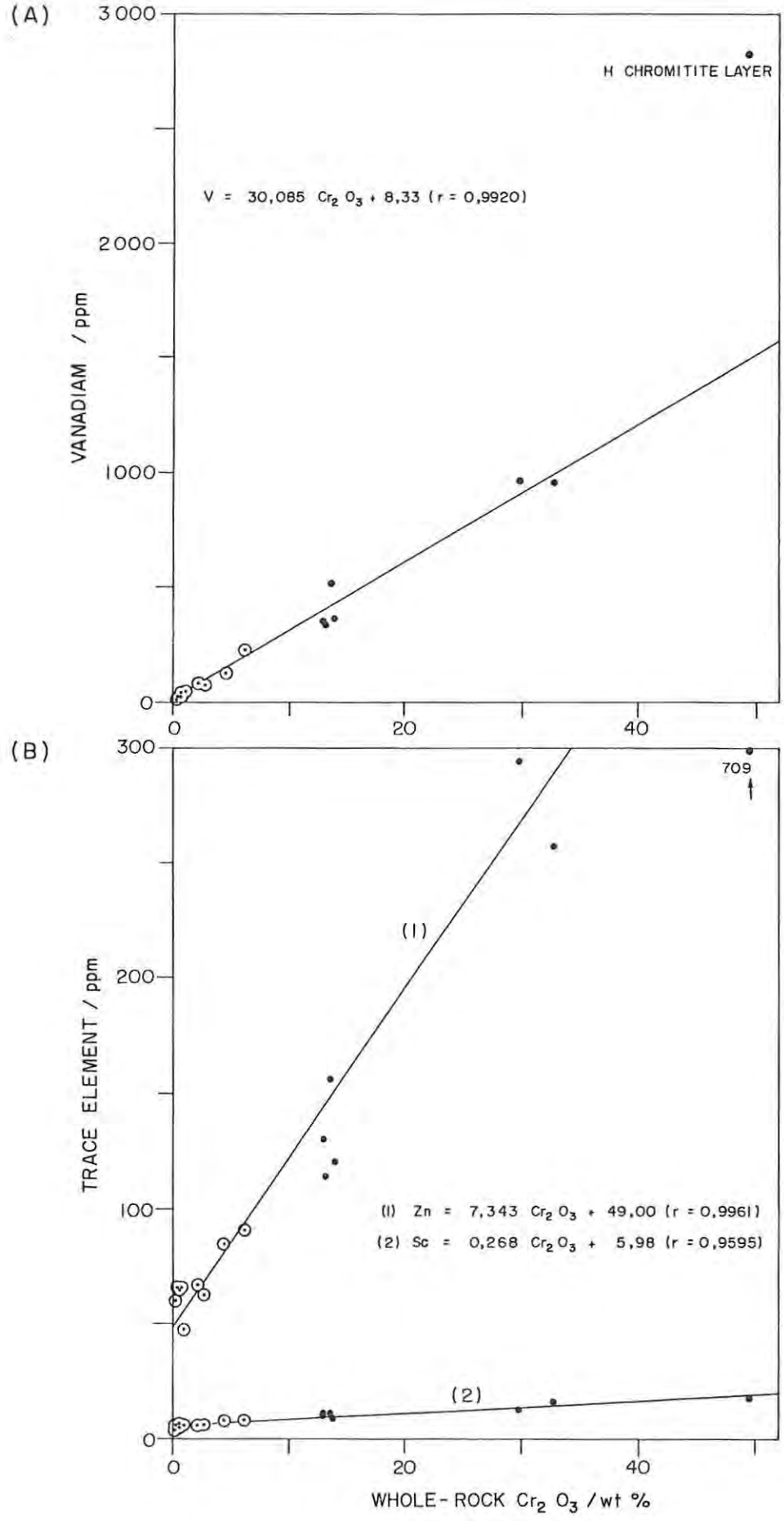

FIG. 58 PLOT OF (A) WHOLE ROCK VANADIUM, AND (B) Zn AND Sc VERSUS Cr_2O_3 FOR OLIVINE-CHROMITE ASSEMBLAGES IN THE C_1 AND C_3 SUBUNITS.

SYMBOLS: ⊙ OLIVINE-RICH; • CHROMITE-RICH
LINEAR EQUATIONS DERIVED BY REGRESSION ANALYSIS.

Hence, the mean V content of chromite-free olivine is 8 ppm, whereas that of the associated chromite containing 45 to 54 wt. per cent Cr_2O_3 is in the range 1360 to 1630 ppm. However, a more meaningful manipulation of the data is afforded if samples in stratigraphic juxtaposition are treated as separate subsets. For example, consideration of the subsets (a) hanging-wall of the LG 4 layer (i.e., samples 170 to 175), (b) footwall succession of the LG 4 layer (i.e., samples 177A to 183B), and (c) footwall succession of the E chromitite layer (i.e., samples 241 to 247) yields, respectively, the following equations by regression analysis:

1. $V = 36,960\ Cr_2O_3 + 2,45 \quad (r = 0,9996)$
2. $V = 28,978\ Cr_2O_3 - 9,45 \quad (r = 0,9975)$
3. $V = 32,091\ Cr_2O_3 + 4,16 \quad (r = 0,9995)$

It is thus evident from the data that (a) there is a significant cryptic variation in the V content of chromite, and (b) chromite with the highest V content (approximately 1780 ppm) is depicted in the hanging-wall succession of the LG 4 chromitite layer. However, these V contents are substantially lower than the measured 2830 ppm in the H chromitite layer, which is equivalent to the V content of chromite in the D_2 subunit (drill core ZS 3).

The variation of Zn and Sc against Cr_2O_3 is depicted in Fig. 58(B) and is given by the following equations:

1. $Zn = 7,343\ Cr_2O_3 + 49,00 \quad (r = 0,9661)$
2. $Sc = 0,268\ Cr_2O_3 + 5,98 \quad (r = 0,9595)$

Equation (2) is representative of all samples cited in Table 32, whereas equation (1) does not accommodate the high Zn content of the H chromitite layer. The mean Zn content of chromite-free olivine is thus 49 ppm, but regression analysis of data subsets stipulated above yields the following Zn contents in relation to stratigraphic position:

1. Hanging-wall LG 4: 43 ppm Zn in olivine
2. Footwall LG 4 : 49 ppm Zn in olivine
3. Footwall E layer : 55 ppm Zn in olivine

Cu varies between 2 and 29 ppm in the dunites, with sample 180 showing an anomalous concentration of 113 ppm due to a minor modal abundance of sulphides . The range in chromite-rich rocks is 9 to 37 ppm and it is evident from the data that the Cu contents of chromite and chromite-free olivine are ca. 29 and 3 ppm, respectively. Ni varies between 1721 and 1787 ppm (i.e., 0,22 and 0,23 % NiO) in chromite-poor dunites and these estimates are in excellent agreement with microprobe analyses. Similarly, the estimate of 464 ppm Ni in the H chromitite layer is consistent with a microprobe analysis of 0,07 wt. per cent NiO in the constituent chromite grains. A plot of whole-rock Ni versus Cr_2O_3 (Fig. 59) shows that (a) olivine within chromite-rich rocks is enriched in Ni, and (b) the Ni content of chromite intergrown with olivine varies between 400 and 550 ppm. The former observation was clearly indicated by the microprobe study of olivine. The Co content of the H chromitite layer is 172 ppm, which is equal to the extrapolated concentration in hypothetically pure chromite of the D_2 subunit (drill core ZS 3). Co varies between 154 and 180 ppm in dunites and, on the basis of Fig. 59, the whole-rock Ni/Co ratio should decline with increasing modal chromite abundance. A tabulation of Ni/Co ratios is presented in Table 33, from which it is evident that this trend is portrayed by samples which are in stratigraphic juxtaposition. Employing regression analysis the variation of Ni/Co against Cr_2O_3 is given by the following equations:

1. Samples 170-175 : $Ni/Co = -0,1968\ Cr_2O_3 + 11,30$ ($r = 0,9987$)
2. Samples 177A-183B: $Ni/Co = -0,0611\ Cr_2O_3 + 10,96$ ($r = 0,8540$)
3. Samples 241-245 : $Ni/Co = -0,0607\ Cr_2O_3 + 10,74$ ($r = 0,8840$)

The analysis indicates that (a) the Ni/Co ratio of chromite-free olivine varies between the narrow limits of 10,74 and 11,30, (b) the Ni/Co ratio of chromite is 7,84 and 7,86 in the footwall rocks of the LG 4 and E chromitite layers, respectively, and (c) chromite within the hanging-wall succession of the LG 4 layer has a mean Ni/Co ratio of 1,85.

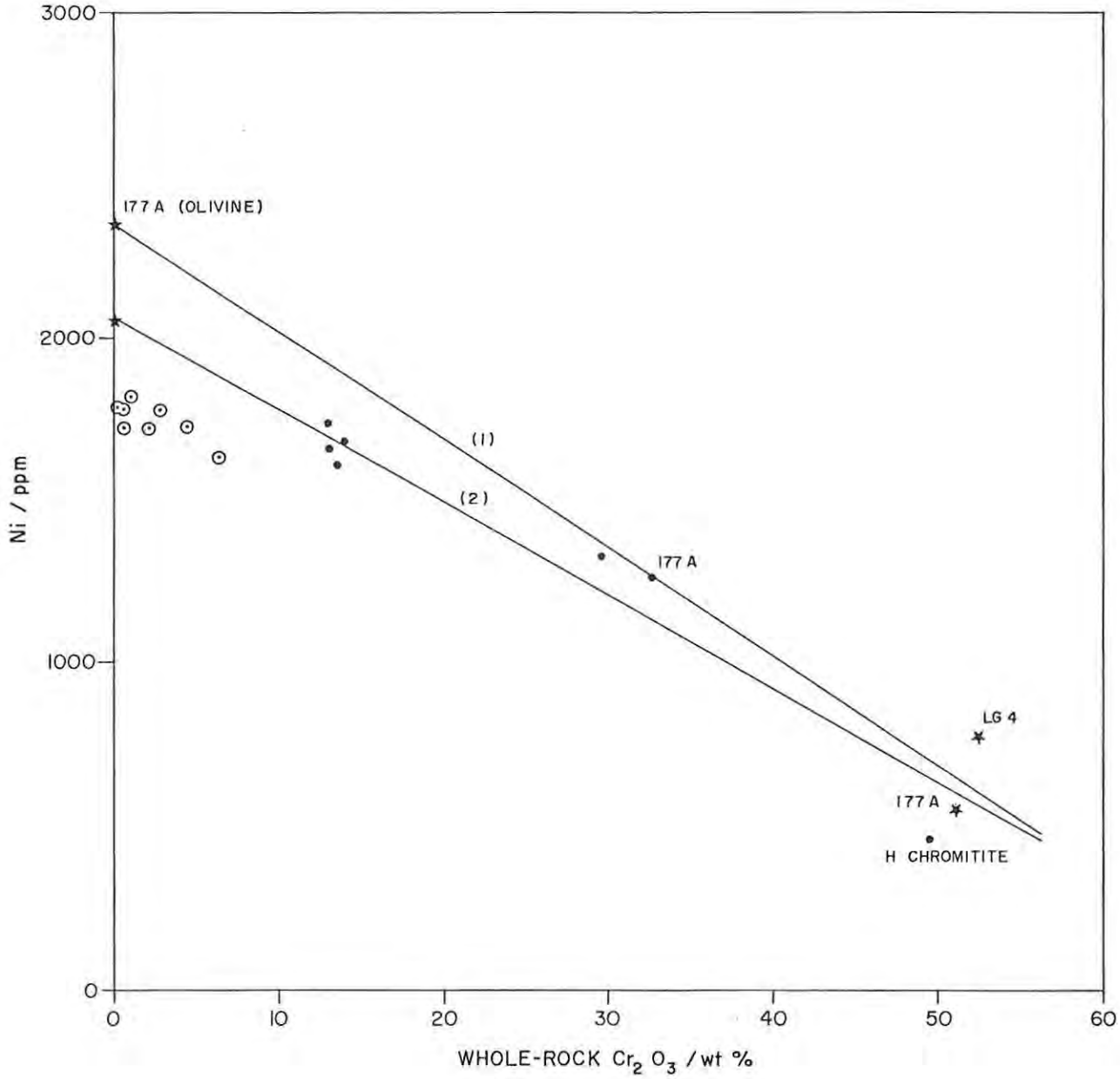

FIG. 59 PLOT OF WHOLE-ROCK Ni VERSUS Cr_2O_3 ; C_1 AND C_3 SUBUNITS. LINES (1) AND (2) REPRESENT VISUAL ESTIMATES LINKING MICROPROBE ANALYSES OF Ni IN OLIVINE AND WHOLE-ROCK Ni.

SYMBOLS: ⊙ DUNITES; • CHROMITE-RICH ROCKS; * MICROPROBE ANALYSES.

TABLE 33:

WHOLE-ROCK Ni/Co RATIOS AND EXTRAPOLATED $(Ni/Co)^{ol}$ AND $(Ni/Co)^{chr}$ RATIOS

SAMPLE	BH.DEPTH/m	Cr_2O_3	$(Ni/Co)^{ROCK}$	$(Ni/Co)^{ol}$	$(Ni/Co)^{chr}$
170	254,15	2,12	10,82		
172A	255,56	13,64	8,63	11,30	1,85
172B	255,64	6,24	10,07	(r = - 0,9987)	
175	256,10	1,03	11,17		
177A	257,76	32,64	9,39		
177B	257,90	13,86	9,69		
178	258,10	13,04	9,76	10,96	7,84
180[a]	259,00	0,29	11,49	(r = - 0,8540)	
183A	260,63	2,81	10,89		
183B	260,73	12,89	9,94		
191	267,77	0,21	10,76	10,76[b]	-
199	274,79	0,45	10,34	10,34	-
H	275,52	49,44	2,69		2,69
241	319,62	29,75	9,00	10,74	7,86
245	320,28	4,30	9,94	(r = - 0,8840)	
247	322,04	0,68	11,17		

180[a] : Data point not employed in regression analysis.

10,76[b] : Insufficient data points, but $(Ni/Co)^{rock}$ $(Ni/Co)^{ol}$.

$(Ni/Co)^{ol}$: Cr-free olivine

$(Ni/Co)^{chr}$: Calculated from regression equations using average Cr_2O_3 contents in chromite (microprobe analysis).

H : H chromitite layer.

6.5 GEOCHEMISTRY OF BRONZITITES WITHIN THE E, D, C AND B UNITS

Table 34 presents major and trace element analyses of (a) 34 bronzitite samples, (b) a 60 gram sample from the basal portion of the LG 2 chromitite layer, and (c) the Lower Zone bronzitite KA 410. The variation of major element oxides can be gauged from Fig. 60, which is a plot of whole-rock Al_2O_3 against MgO. It is evident from the disposition of data points that low modal proportions of plagioclase, chromite and clinopyroxene are present in the analyzed bronzitites. This is similarly evinced by the tabulated Mg-numbers in Table 34, which are generally in good agreement with microprobe estimates of orthopyroxene MMF ratios. It is thus possible to treat chromite-poor samples as bimineralic mixtures of orthopyroxene and intercumulus plagioclase, and an estimate of the contribution of plagioclase to the whole-rock Al_2O_3 content can be obtained from the following relationship:

$$Al_2O_3^{*} = Al_2O_3\ (rock) - \left[Al_2O_3\ (opx) \times \frac{MgO\ (rock)}{MgO\ (opx)} \right]$$

where Al_2O_3 (opx) and MgO (opx) are afforded by microprobe analyses. The ratio MgO(rock)/MgO(opx) serves as an index of the modal proportion of orthopyroxene and, with recourse to microprobe data, calculation readily yields the range of observed compositions.

6.5.1 STRONTIUM

Sr varies between less than 1 ppm and 51,4 ppm in the 35 analyzed bronzitites, associated with a range in Al_2O_3 contents of 1,16 to 3,50 wt. per cent. Ingestion of chromite was attained during fusion of these samples, and a minor correction for Al_2O_3 in the chromite fraction was made in terms of the following relationship:

$$Al_2O_3^{a}\ (chromite) = \frac{Al_2O_3\ (Chromite) \times Cr_2O_3\ (excess)}{Cr_2O_3\ (chromite)}$$

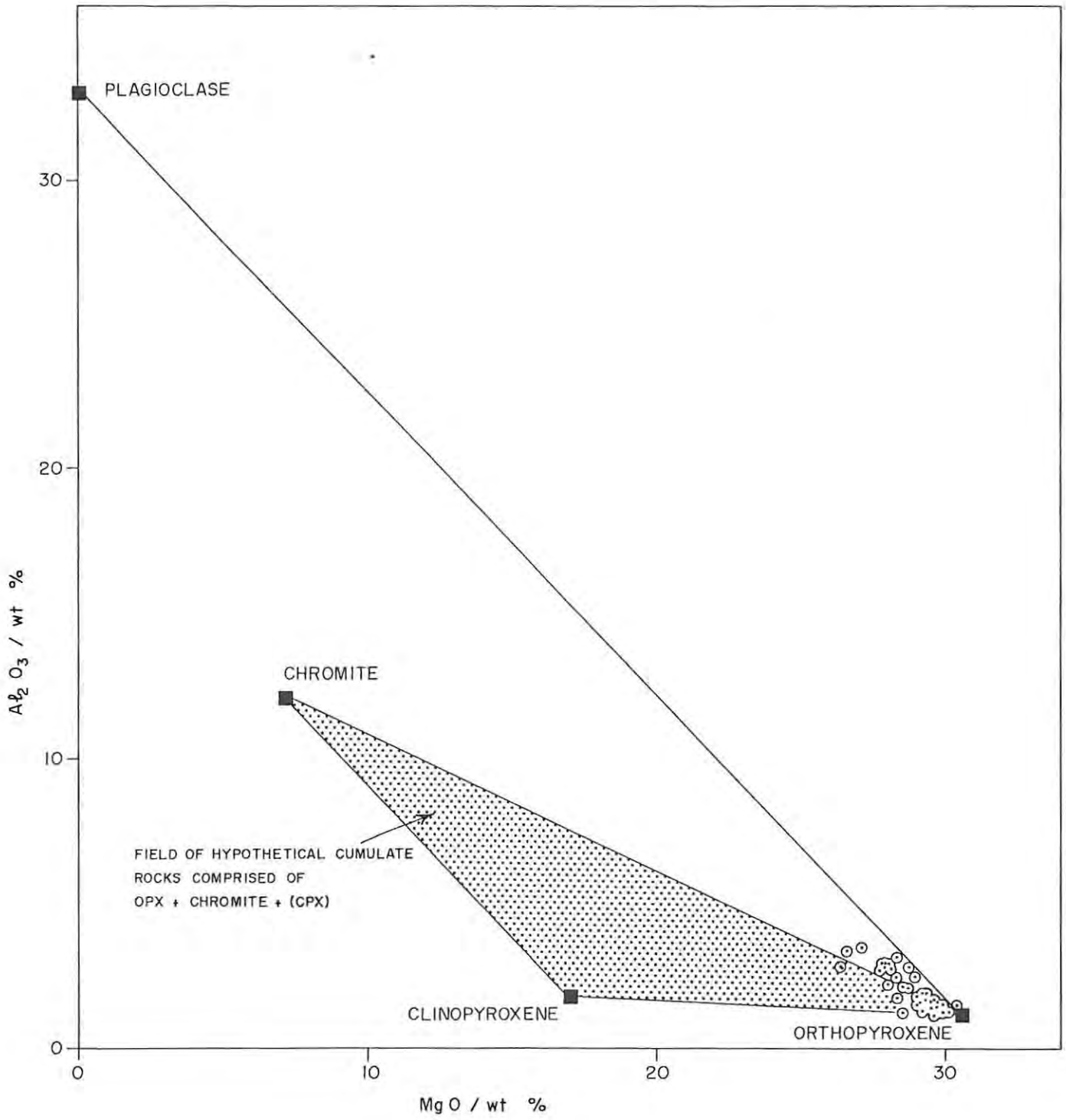

FIG. 60 PLOT OF Al_2O_3 VERSUS MgO FOR (⊙) E, D, C_2 AND B UNIT BRONZITITES, AND (■) SELECTED MICROPROBE ANALYSES OF ORTHOPYROXENE, CLINOPYROXENE, CHROMITE AND PLAGIOCLASE.

TABLE 34:

WHOLE-ROCK ANALYSES OF BRONZITITES (DRILL CORE ZS 7 AND KA 5)

UNIT	E			D_1		D_2						
SAMPLE	50	61	70	81	83	90	95	103	104	115	117	124
SiO_2	54,85	54,85	53,86	53,33	54,61	54,20	54,74	54,87	55,19	54,59	55,72	54,60
TiO_2	0,09	0,13	0,15	0,14	0,10	0,10	0,09	0,10	0,11	0,09	0,09	0,07
Al_2O_3	1,16	2,26	2,88	1,74	1,57	1,80	1,58	2,13	2,98	1,68	1,63	1,24
Fe_2O_3	0,01	0,01	0,02	0,04	0,01	0,02	0,01	0,01	0,01	0,01	0,01	0,01
FeO	11,24	11,15	11,35	11,93	10,80	10,89	10,81	10,43	10,45	10,39	10,33	9,94
MnO	0,22	0,25	0,26	0,25	0,23	0,22	0,25	0,23	0,23	0,21	0,23	0,23
MgO	29,62	28,03	26,41	28,35	29,88	29,02	29,09	28,68	27,80	29,29	29,73	29,91
CaO	1,50	2,30	2,57	1,72	1,72	1,97	1,76	2,22	2,54	1,88	1,91	1,64
Na_2O	0,10	0,19	0,40	0,17	0,16	0,18	0,11	0,31	0,50	0,20	0,10	0,12
K_2O	-	0,02	0,01	-	-	-	-	-	-	-	-	-
P_2O_5	-	-	0,02	-	-	-	-	-	-	-	-	-
Cr_2O_3	0,52	0,53	1,12	1,75	0,90	0,75	0,88	0,56	0,55	0,66	0,62	0,51
L.O.I	0,94	1,08	1,26	1,02	0,55	0,69	0,90	0,69	0,73	1,26	0,83	1,02
TOTAL	100,35	100,53	100,31	100,44	100,53	99,84	100,22	100,23	101,09	100,26	101,20	99,29
Mg-no.	0,824	0,817	0,805	0,809	0,831	0,826	0,827	0,830	0,825	0,834	0,836	0,842
Sr	-	16,2	24,8	3,0	2,5	6,2	3,0	14,5	31,2	6,8	5,3	-
Rb	-	-	-	-	-	-	-	-	-	-	-	-
Y	2,7	3,3	5,5	4,3	3,5	2,4	4,2	2,6	3,2	2,9	3,6	2,5
Zr	2,2	2,5	4,3	4,0	3,2	2,0	2,1	-	4,2	2,7	-	-
Ba	-	-	25	-	-	12	-	16	25	-	-	-
Zn	69	80	80	80	71	70	73	68	70	65	68	64
Cu	13	14	29	15	10	15	10	18	17	10	10	19
Ni	544	526	557	585	566	536	552	504	497	531	553	513
Co	101	101	102	102	102	100	100	101	98	95	99	99
V	128	134	204	231	134	119	114	109	117	108	124	108
Sc	30	32	32	31	31	29	28	28	27	27	26	25
Cr_2O_3	0,54	0,61	1,21	1,90	1,05	0,82	0,96	0,65	0,64	0,73	0,72	0,60
BH DEPTH (m)	79,56	96,51	111,22	135,25	138,20	148,08	155,32	166,78	168,20	179,65	182,43	192,77

KEY TO TABLES 31 and 33:

(-) symbol denotes not detected or less than lower limit of detection
Trace element abundances based on mass absorption coefficients derived from Heinrich values
L.O.I : Loss of ignition at 1 100°C
Mg-no. : $Mg/(Mg + Fe^{2+})$ mol. ratio
BH Depth: Taken at midpoint of sample

TABLE 34 (Cont.):

UNIT	D_2							C_2				
SAMPLE	133	134	139	155	161	164	165	201*	203	205 a	205 b	207
SiO_2	55,14	54,39	55,32	55,85	54,81	55,98	55,52		54,86	53,83	54,57	55,11
TiO_2	0,11	0,10	0,08	0,14	0,15	0,14	0,13	N	0,10	0,12	0,11	0,12
Al_2O_3	1,16	3,39	1,27	1,39	1,32	1,54	1,44	O	3,18	2,78	2,98	2,85
Fe_2O_3	0,01	0,01	0,01	0,01	0,02	0,01	0,01	T	0,01	0,04	0,02	0,01
FeO	10,29	9,81	9,69	10,37	10,52	10,67	10,54		9,37	9,67	9,37	9,32
MnO	0,22	0,22	0,22	0,22	0,21	0,21	0,18		0,19	0,20	0,20	0,18
MgO	28,48	26,60	30,10	29,53	29,24	29,02	29,71	A	28,54	28,11	27,97	28,69
CaO	1,91	2,80	1,72	1,02	1,09	1,22	1,25	N	2,57	2,41	2,72	2,47
NaO	0,15	0,31	0,12	0,20	0,17	0,29	0,25	A	0,39	0,29	0,35	0,40
K_2O	0,10	0,03	-	0,19	0,15	0,09	0,16	L	-	0,01	0,03	0,02
P_2O_5	-	-	-	-	-	0,02	-	Y	-	-	-	-
Cr_2O_3	0,52	0,48	0,53	0,48	0,83	0,72	0,69	Z	0,80	1,72	1,04	0,83
L.O.I	1,91	1,55	1,02	1,12	1,24	1,40	0,92	E	0,82	0,88	0,69	0,69
								D				
TOTAL	100,00	99,69	100,08	100,52	99,75	101,31	100,80		100,63	100,06	100,05	100,69
Mg-no.	0,831	0,828	0,847	0,835	0,832	0,828	0,834		0,843	0,838	0,842	0,846
Sr	-	46,0	-	3,0	-	9,8	9,5	7,9	42,9	29,3	39,9	37,7
Rb	6,3	4,5	-	8,7	8,7	7,0	6,3	3,1	-	-	-	-
Y	4,7	3,2	-	6,3	4,3	4,8	5,2	4,2	3,4	4,6	3,9	4,6
Zr	8,0	4,9	-	8,2	7,7	8,6	9,7	7,6	2,9	4,4	5,0	4,3
Ba	32	34	-	61	27	65	120	24	27	26	23	31
Zn	69	68	62	74	78	74	64	65	63	67	61	64
Cu	9	12	19	31	17	69	21	109	18	19	20	17
Ni	444	470	519	523	423	687	547	1324	505	516	491	513
Co	100	91	96	96	90	98	90	97	88	91	91	90
V	120	91	120	194	206	187	118	213	101	150	119	103
Sc	28	26	23	24	23	24	22	27	21	22	22	22
Cr_2O_3	0,61	0,53	0,60	0,55	1,07	0,78	0,76	0,88	0,87	1,90	1,20	0,91
BH DEPTH (m)	205,69	206,94	214,33	236,95	245,70	250,00	251,38	276,11	278,79	282,60	282,72	284,58

201* : Trace element data based on Mo-Compton mass absorption coefficients
205a, 205b: Full-core samples taken from opposite ends of an 18 cm drill core section, each of 7 cm
Samples 155, 164 and 201 are sulphide-bearing

TABLE 34 (Cont.):

UNIT	C_2				B								LOWER ZONE
SAMPLE	209	211	225	228	259	260	LG 2*	265	271	278	280	290	KA 410
SiO_2	53,84	53,58	55,68	56,05	55,81	55,71	2,34	53,93	54,74	54,15	54,64	55,60	55,17
TiO_2	0,13	0,13	0,13	0,11	0,12	0,11	0,38	0,11	0,10	0,10	0,12	0,12	0,13
Al_2O_3	2,82	2,95	1,64	1,50	2,07	1,58	12,16	2,73	1,92	3,50	2,46	2,55	3,04
Fe_2O_3	0,03	0,10	0,01	0,01	0,01	0,01	4,20	0,03	0,01	0,01	0,02	0,01	0,01
FeO	9,56	10,11	9,51	9,24	9,63	10,20	14,99	9,97	9,97	9,75	10,10	9,61	9,47
MnO	0,18	0,21	0,19	0,17	0,17	0,19	0,45	0,23	0,20	0,20	0,19	0,19	0,21
MgO	27,92	27,94	29,66	30,42	28,53	29,49	12,05	27,66	29,18	27,10	28,33	28,91	27,70
CaO	1,97	2,07	1,18	1,62	1,60	1,52	0,19	2,18	1,94	2,66	1,97	2,41	2,31
NaO	0,35	0,28	0,32	0,23	0,37	0,28	NA	0,33	0,30	0,40	0,32	0,35	0,60
K_2O	0,06	0,16	0,23	0,06	0,09	0,10	-	-	-	0,04	0,05	-	0,07
P_2O_5	-	0,02	-	-	-	-	-	-	-	-	-	-	-
Cr_2O_3	1,77	2,63	0,55	0,54	0,75	1,00	32,49	1,20	0,72	0,86	0,95	0,48	0,44
L.O.I	0,74	0,88	1,21	1,28	1,24	1,18	0,73	1,03	0,83	0,93	0,93	0,86	1,01
TOTAL	99,37	101,06	100,31	101,23	100,39	101,37	79,78	99,40	99,91	99,70	100,08	101,09	100,16
Mg-no.	0,839	0,831	0,847	0,854	0,840	0,837	0,588	0,831	0,839	0,832	0,833	0,843	0,839
Sr	27,2	25,4	8,8	7,6	28,6	10,1	NA	33,4	16,5	51,4	27,7	29,5	47,0
Rb	-	6,8	12,3	2,9	3,9	4,9	NA	-	-	2,7	1,9	-	4,0
Y	4,3	3,6	4,6	5,0	5,1	4,8	NA	2,7	3,1	3,6	5,2	4,3	2,9
Zr	6,7	10,8	8,7	6,8	8,3	8,3	NA	4,4	3,6	5,8	7,1	4,4	9,9
Ba	38	38	72	31	61	62	NA	27	17	42	32	23	40
Zn	66	83	64	58	66	70	485	70	69	70	63	62	63
Cu	19	20	25	18	17	15	25	16	18	18	12	14	30
Ni	515	517	468	494	518	517	850	514	524	530	561	512	718
Co	90	92	86	93	92	96	178	97	101	92	94	94	92
V	125	175	157	86	101	135	2528	108	96	97	97	95	91
Sc	21	21	22	21	24	25	26	24	25	24	25	25	23
Cr_2O_3	1,85	2,90	0,63	0,64	0,89	1,08	50,00	1,44	0,79	0,92	1,00	0,58	0,52
BH DEPTH (m)	287,51	290,48	298,86	303,42	332,03	333,44	334,78	337,52	345,95	356,19	358,75	369,37	410[1]

LG 2*: Trace element data based on Mo-Compton mass absorption coefficients (corrected)
NA : Not analyzed
410[1] : Depth in feet
Samples 225 and KA 410 are sulphide-bearing

where Cr_2O_3 (excess) = Cr_2O_3 (rock) - Cr_2O_3 (opx), and Al_2O_3- and Cr_2O_3 - (chromite) are given by microprobe analysis. Hence,

$$Al_2O_3{}^b = Al_2O_3 \text{ (rock)} - Al_2O_3{}^a \text{ (chromite)}$$
$$\approx Al_2O_3 \text{ (opx)} + Al_2O_3 \text{ (plagioclase)}$$

Fig. 61 depicts a plot of Sr versus $Al_2O_3{}^b$. It is evident from the disposition of data points that the variation of Sr against $Al_2O_3{}^b$ in the B and C units is distinct from the D and E units. Regression analysis of the data subsets yields the following equations:

1. B and C units : $Sr = 21{,}578\ Al_2O_3{}^b - 25{,}12$ ($r = 0{,}9969$)
2. D and E units : $Sr = 17{,}827\ Al_2O_3{}^b - 22{,}75$ ($r = 0{,}9978$)
3. D_2 subunit (ZS3): $Sr = 17{,}529\ Al_2O_3{}^b - 23{,}66$ ($r = 0{,}9999$)

Equation (1) is exclusive of samples 225 and 259, which depict higher modal abundances of mica and amphibole. Extrapolation to Sr-free orthopyroxene yields a mean Al_2O_3 content of 1,16 wt. per cent. This is in excellent agreement with the mean calculated from microprobe analyses (Table 8). Based on an average Al_2O_3 content of 31,5 wt. per cent in plagioclase (Table 11), the Sr content of intercumulus plagioclase in the B and C units may be calculated as 654 ppm. Equation (2) is exclusive of samples 164 and 165, which are micropegmatite-, mica-, and quartz-bearing, and sample 134. The variation of Sr against $Al_2O_3{}^b$ in the latter is more akin to that of bronzitites in the B and C units (Fig. 61). Extrapolation yields 1,27 wt. per cent Al_2O_3 in Sr-free orthopyroxene of the D and E units, which is equal to the average of 77 microprobe analyses, and 539 ppm Sr in hypothetically pure plagioclase. Within the upper portion of the D_2 subunit, drill core ZS3, and basal portion of the E unit (sample 300), extrapolation yields 1,35 wt. per cent Al_2O_3 in orthopyroxene and 528 ppm Sr in plagioclase. Hence, an estimate of the modal proportion of plagioclase in these rocks is given by the ratio Sr (rock)/Sr (plagioclase), hereby affording a means of correcting for the dilution of certain trace elements (e.g., V, Ni and Co) by the modal plagioclase content.

An alternative method of estimating the Sr content of pure plagioclase is shown in Fig. 62, which is a plot of whole-rock Sr

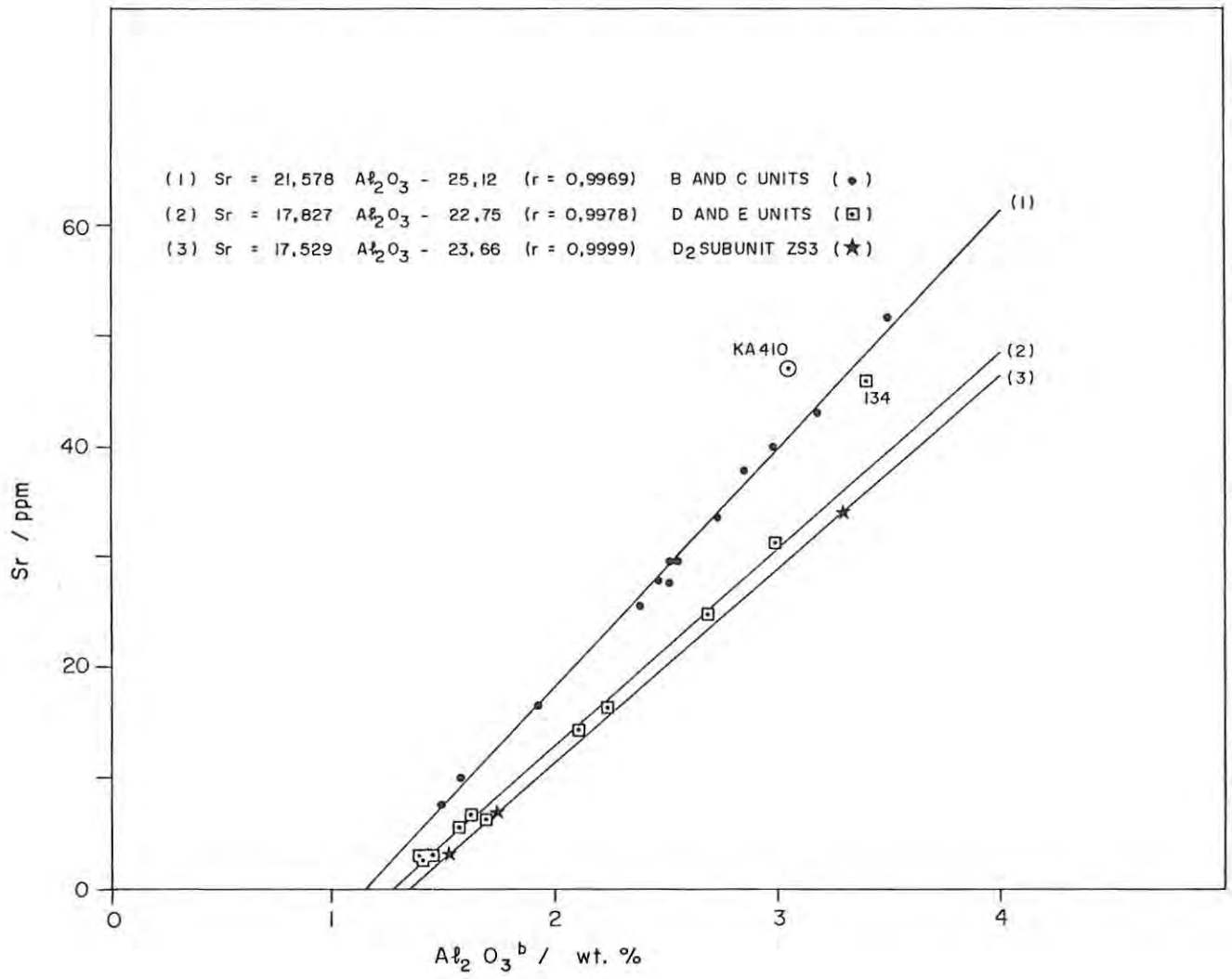

FIG. 61 PLOT OF WHOLE-ROCK Sr VERSUS $A\ell_2O_3{}^b$. THE ABSCISSA IS DEFINED BY $A\ell_2O_3{}^b = A\ell_2O_3$ (ROCK) - $A\ell_2O_3{}^a$ (CHROMITE), WHERE $A\ell_2O_3{}^a$ (CHROMITE) IS REPRESENTATIVE OF $A\ell_2O_3$ IN THE CHROMITE FRACTION OF THE ROCK. THIS CORRECTION WAS MADE FOR DATA POINTS CONFORMING TO REGRESSION LINES (2) AND (3), AND CERTAIN CHROMITIFEROUS BRONZITITES (e.g., SAMPLES 205a, 209, 211 AND 265) CONFORMING TO REGRESSION LINE (1). $A\ell_2O_3{}^a$ (CHROMITE) IS PARTICULARLY SIGNIFICANT AT LOW WHOLE-ROCK Sr CONTENTS. BASED ON AN AVERAGE $A\ell_2O_3$ CONTENT OF 31,5 wt. PER CENT IN PLAGIOCLASE, CALCULATION YIELDS (Sr / $A\ell_2O_3$) PLAGIOCLASE RATIOS OF (1) 20,7 , (2) 17,1 AND (3) 16,7 $\times 10^{-3}$, RESPECTIVELY.

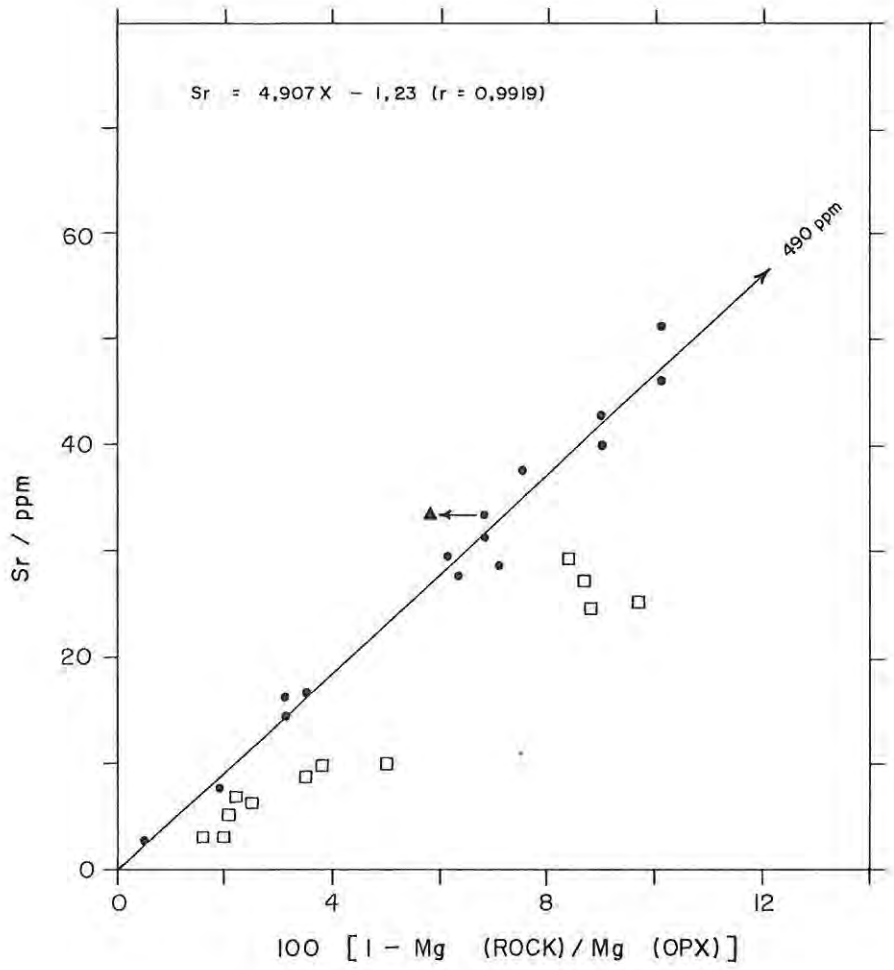

FIG. 62 PLOT OF WHOLE - ROCK Sr VERSUS 100 (1 − MgO (ROCK) / MgO (OPX)) FOR 27 BRONZITITE SAMPLES. THE ABSCISSA IS REPRESENTATIVE OF PERCENTAGE INTERCUMULUS PLAGIOCLASE; THE RATIO MgO (ROCK) / MgO (OPX) WAS CALCULATED FROM WHOLE - ROCK AND MICROPROBE ANALYSES NORMALIZED TO 100 %.

SYMBOLS: • DATA POINTS USED TO CALCULATE THE REGRESSION LINE

▲←• CORRECTION OF MgO (ROCK) FOR MgO IN CHROMITE FRACTION

$$MgO\left(\begin{smallmatrix}\text{SILICATE}\\ \text{FRACTION}\end{smallmatrix}\right) = MgO\ (\text{ROCK}) - MgO\ (\text{CHROMITE})\left[\frac{Cr_2O_3\ (\text{Rock}) - 0{,}52}{Cr_2O_3\ (\text{Chromite})}\right]$$

versus 100 x[1 - MgO (rock)/MgO (opx)]. The latter parameter is a measure of percentage plagioclase in an orthopyroxene-plagioclase sample, and it is evident from the plot that the highest modal abundance is slightly in excess of 10 per cent. Extrapolation of the indicated regression line, defined by 15 data points representative of samples within all the units, yields an apparent maximum Sr content of 490 ppm in plagioclase. Correction of whole-rock MgO for the contribution from chromite is significant in some samples (as illustrated by an arrowhead symbol in Fig. 62).

The above considerations may be summarized in terms of the $Sr/Al_2O_3^*$ ratio, where $Al_2O_3^*$ is an estimate of Al_2O_3 in the whole-rock plagioclase fraction (note that $Sr/Al_2O_3^* = x.10^{-3}$). Calculated ratios for individual samples are presented in Table 35, from which it is evident that $Al_2O_3^a$ (chromite) imposes a significant influence, particularly at low levels of Sr. It is clear from the tabulation that intercumulus plagioclase above the level of sample 134 in the D_1 subunit is characterized by a lower range of $Sr/Al_2O_3^*$ ratios. Samples with modal mica, amphibole and micropegmatite, such as 164, 165 and 259, yield anomalously high ratios. Similarly, the $Sr/Al_2O_3^*$ ratio of 23,6 x 10^{-3} for the Lower Zone bronzitite KA 410 is not strictly representative of the plagioclase fraction, since mica and amphibole are conspicuous in thin section. In summation, the Ruighoek Pyroxenite succession may be subdivided into two segments on the basis of distinctive whole-rock $Sr/Al_2O_3^*$ ratios, even though the modal proportion of plagioclase is extremely low.

6.5.2 NICKEL, COBALT, VANADIUM AND SCANDIUM

Table 36 presents estimates of Ni, Co, V and Sc in hypothetically pure orthopyroxene. These data have been corrected for (a) V in the whole-rock chromite fraction (employing the procedure outlined in section 6.3.2), and (b) dilution by plagioclase. Sc declines from 26 ppm in the B unit to 22 ppm in the C_2 subunit, then rises progressively through the D unit to 33 ppm in the basal portion of the E unit. This pattern of variation is summarized in Fig. 63, which is a plot of trace element abundances in hypothetically pure orthopyroxene in relation to stratigraphic height. It is evident

TABLE 35:

$MgO^{(rock)}/MgO^{(opx)}$ AND $Sr/Al_2O_3^*$ RATIOS OF BRONZITITES IN RELATION TO STRATIGRAPHIC POSITION

UNIT	SAMPLE	$\frac{MgO^{(rock)}}{MgO^{(opx)}}$	$Al_2O_3(opx) \times \frac{MgO^{(rock)}}{MgO^{(opx)}}$	$Al_2O_3{}^a$(chromite)	$Al_2O_3{}^*$	$Sr/Al_2O_3{}^* \times 10^{-3}$
	61	0,969	1,231	0,03	1,009	16,2
E	70	0,911	1,157	0,20	1,550	16,2
	300	0,878	1,186	0,52	2,114	16,2
	304	0,947	1,279	0,03	0,491	14,2
D_2	308	0,971	1,311	0,07	0,205	15,2
	83	0,996	1,265	0,16	0,145	17,3
	90	0,975	1,239	0,11	0,461	13,5
	95	0,983	1,249	0,13	0,210	14,4
	103	0,969	1,231	0,03	0,878	16,6
	104	0,932	1,183		1,786	17,6
D_1	115	0,978	1,242	0,05	0,397	17,3
	117	0,979	1,243	0,06	0,316	16,9
	134	0,892	1,133		2,316	20,2
	155	0,979	1,244		0,154	19,5
	164	0,962	1,221		0,319	30,7
	165	0,985	1,251		0,189	50,2
	203	0,910	1,055	0,08	2,054	21,0
	205a	0,904	1,049	0,28	1,473	20,1
	205b	0,898	1,042	0,14	1,817	22,1
C_2	207	0,921	1,069	0,09	1,691	22,4
	209	0,909	1,055	0,33	1,465	18,7
	211	0,896	1,039	0,54	1,365	18,8
	225	0,963	1,118		0,532	16,7
	228	0,980	1,137		0,363	21,2
	259	0,929	1,077	0,07	0,940	30,7
	260	0,950	1,102	0,11	0,358	28,4
	265	0,927	1,075	0,18	1,520	22,2
	271	0,964	1,119	0,06	0,758	21,8
B	278	0,8996	1,032	0,08	2,428	21,3
	280	0,9368	1,086	0,10	1,294	21,5
	290	0,9413	1,091		1,449	20,5
	KA 410	0,9097	1,055		2,005	23,6

$$Al_2O_3{}^* = Al_2O_3{}^{(rock)} - \left[\overline{Al_2O_3{}^a(\text{chromite})} + Al_2O_3(opx) \times \frac{\overline{MgO^{(rock)}}}{\overline{MgO^{(opx)}}}\right]$$

$Al_2O_3{}^a(\text{chromite}) = Al_2O_3(\text{chromite}) \times Cr_2O_3(\text{excess})/Cr_2O_3(\text{chromite})$
where $Cr_2O_3(\text{excess}) = Cr_2O_3(\text{rock}) - 0{,}52$

$Al_2O_3(opx)$: defined by extrapolation of regression lines given in Fig. 61

TABLE 36:

CONCENTRATION OF Ni, Co, Sc and V IN HYPOTHETICALLY PURE ORTHOPYROXENE (DRILL CORE ZS 7), AND INTERELEMENT RATIOS

UNIT	SAMPLE	Ni	Co	Sc	V	Ni/Co	Ni/Sc	Co/Sc	V/Co	V/Sc
	50	544	101	30	128	5,38	18,1	3,36	1,26	4,26
E	61	542	104	33	134	5,20	16,4	3,15	1,28	4,06
	70	583	106	33	178	5,46	17,4	3,18	1,67	5,39
	81	588	102	31	164	5,73	18,8	3,29	1,60	5,29
D_2	83	568	102	31	108	5,54	18,2	3,29	1,05	3,48
	90	542	101	29	106	5,36	18,4	3,44	1,04	3,65
	95	555	100	28	93	5,52	19,7	3,57	0,93	3,32
	103	518	103	28	106	4,99	18,0	3,60	1,02	3,78
	104	527	104	28	118	5,07	18,4	3,62	1,13	4,21
	115	537	96	27	99	5,58	19,6	3,51	1,03	3,66
	117	538	100	26	115	5,38	20,5	3,80	1,15	4,42
D_1	124	513	99	25	105	5,18	20,5	3,96	1,06	4,20
	133	444	100	28	116	4,44	15,8	3,57	1,16	4,14
	134	505	98	28	91	5,16	18,0	3,50	0,92	3,25
	139	519	96	23	120	5,40	22,5	4,17	1,25	5,21
	155	525	96	24	193	5,44	21,7	4,00	2,01	8,04
	161	423	90	23	179	4,70	18,3	3,91	1,98	7,78
	164	697	99	24	177	7,01	28,6	4,08	1,78	7,37
	165	555	91	22	108	6,07	24,8	4,09	1,18	4,90
	203	540	94	22	90	5,73	24,0	4,19	0,95	4,09
	205a	540	95	23	86	5,67	23,4	4,13	0,90	3,73
	205b	522	96	23	91	5,39	22,3	4,13	0,93	3,95
C_2	207	544	95	23	89	5,70	23,3	4,09	0,93	3,86
	209	537	94	22	62	5,72	24,5	4,28	0,65	2,81
	211	537	95	22	60	5,61	24,6	4,38	0,63	2,72
	225	474	87	22	154	5,44	21,2	3,90	1,77	7,00
	228	499	94	21	81	5,31	23,5	4,42	0,90	3,85
	259	541	96	25	87	5,63	21,5	3,83	0,90	3,48
	260	525	97	25	109	5,38	20,6	3,84	1,12	4,36
	265	541	102	25	66	5,29	21,4	4,04	0,64	2,64
	271	537	103	25	85	5,18	20,9	4,04	0,82	3,40
B	278	575	99	26	84	5,76	22,0	3,83	0,84	3,23
	280	585	98	26	77	5,96	22,4	3,76	0,78	2,96
	290	536	98	26	96	5,44	20,4	3,76	0,97	3,69
	KA 410	773	99	24	91	7,80	31,2	4,00	0,91	3,79

from the data points that Co and Ni display comparable patterns of variation, both of which depict an irregular rise in whole-rock content with increasing stratigraphic height through the D_1 subunit. The vanadium content of orthopyroxene declines from an average of 86 ppm in the B unit to an average of 80 ppm in the C_2 subunit (excluding sample 225), then rises to an average of 107 ppm in the interval bounded by samples 83 and 139 (in which a mild depletion in V with increasing stratigraphic height is suggested). A high vanadium content in late stage, intercumulus silicate phases (e.g., amphibole and micropegmatite) is evinced by samples 155, 161 and 164, in which estimates of vanadium in orthopyroxene are some 76 ppm higher than the average. Another notable feature is the higher Ni and V contents in samples 70 and 81, which are in stratigraphic juxtaposition to the D_2 subunit (Fig. 62). However, both of these rocks are substantially more chromitiferous than adjacent samples, and it is assumed here that the higher Ni and V contents stem from inadequate correction for this higher modal proportion. The higher abundances may, however, result in part from compositional differences since the microprobe study indicated higher TiO_2 contents in chromite within sample 70. The vanadium content of orthopyroxene in the lower portion of the E unit is about 130 ppm.

Deficiencies in the correction procedures adopted are only meaningful in mineralogically more complex samples such as 209 and 211, for example. Both of these bronzitites depict weakly disseminated chromite plus an intercumulus silicate fraction composed of plagioclase and titanian phlogopite. Hence, the depleted V content in hypothetically pure orthopyroxene of these samples (Table 36 and Fig. 63) follows from the assumption that chromite is the only other Cr- and V-bearing mineral phase present. Nonetheless, it is evident from Fig. 63 that the estimates of Sc, Co and Ni in orthopyroxene appear to be consistent with the geochemistry of other samples from the subunit. This lends considerable support to the reliability of the data.

Calculated Ni/Co, Ni/Sc, Co/Sc, V/Co and V/Sc ratios are presented in Table 36, and the variation of these ratios in relation to stratigraphic height is depicted in Fig. 64. Features portrayed here are (a) the stepped rise in V/Co ratios upward through the succession

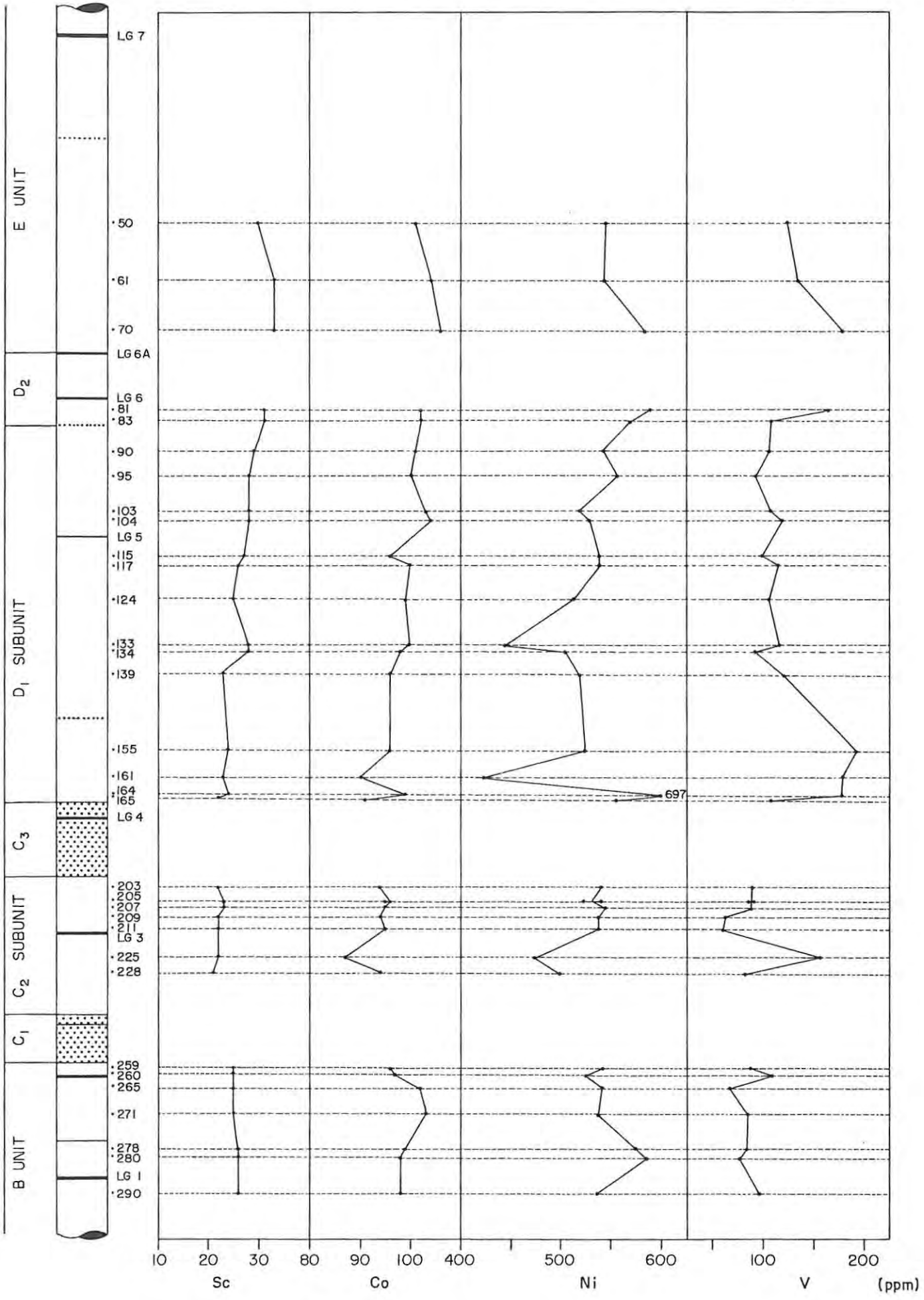

FIG. 63 VARIATION OF Sc, Co, NI AND V CONTENTS IN HYPOTHETICALLY PURE ORTHOPYROXENE IN RELATION TO STRATIGRAPHIC HEIGHT, DRILL CORE ZS 7. THE Ni ABUNDANCE OF 697 ppm IN SAMPLE 164 IS LINKED TO MODAL SULPHIDE CONTENT.

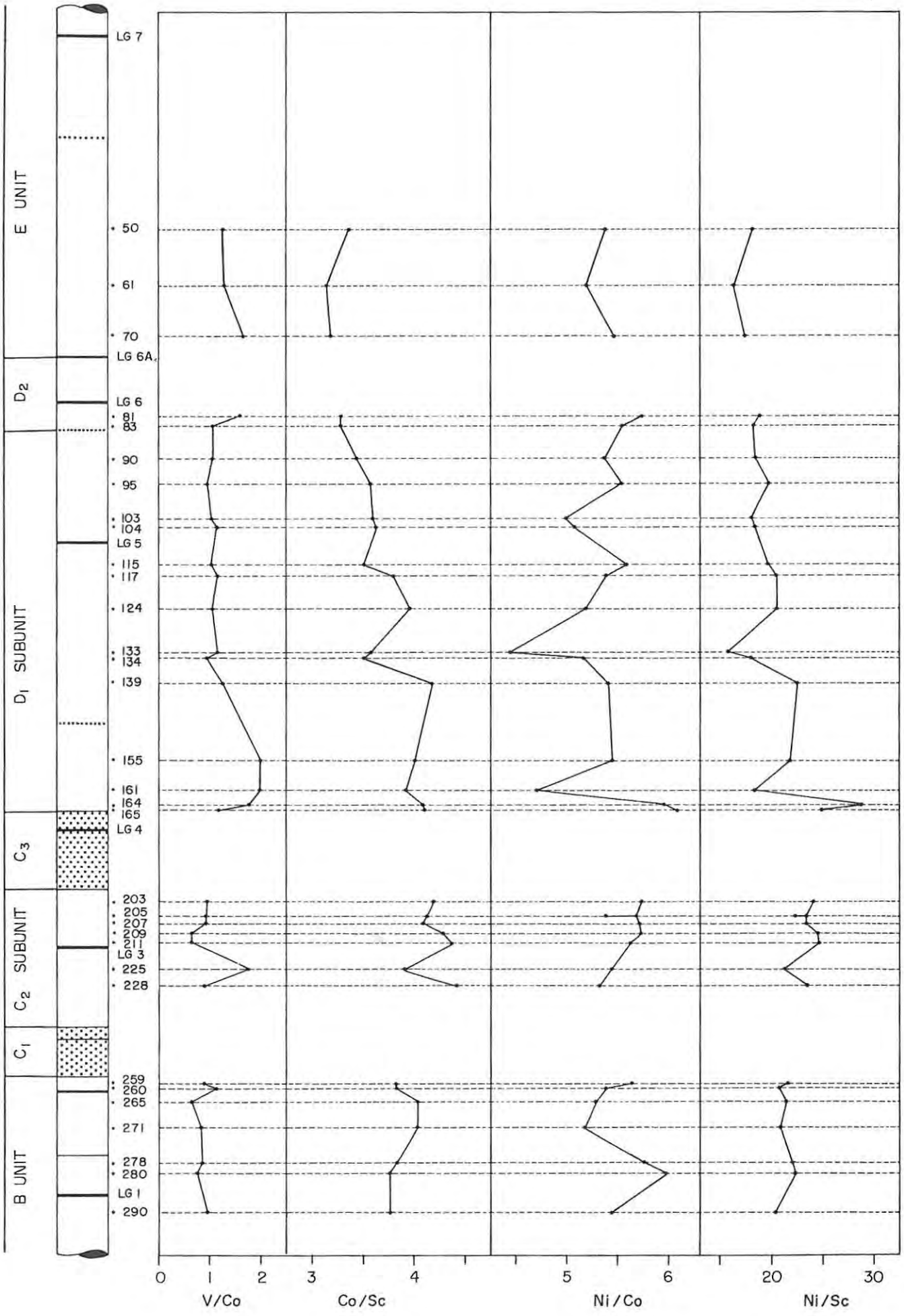

FIG. 64 VARIATION OF ORTHOPYROXENE V/Co, Co/Sc, Ni/Co AND Ni/Sc RATIOS IN RELATION TO STRATIGRAPHIC HEIGHT, DRILL CORE ZS 7.

(b) the rise in Co/Sc and Ni/Sc ratios from the B unit to the C_2 subunit, followed by a decline of these ratios through the D_1 subunit due to the progressive increase in the scandium content of orthopyroxene with increasing stratigraphic height, and (c) the rise in Ni/Co ratios with stratigraphic height in the bronzitites underlying the LG 6 and LG 5 chromitite layers. An equivalent variation of Ni/Co ratios adjacent to the LG 3, LG 2 and LG 1 chromitite layers is suggested by the data. These trends of rising Ni/Co ratios do not correlate with increments in copper contents and thus do not stem from increasing whole-rock sulphide contents. By virtue of the positive correlation between Sc and Co (Fig. 63), the V/Sc ratio also increases with stratigraphic height and, although there is some overlap of the ranges, average values for the units are as follows (disregarding samples 155, 161, 164 and 225):

1. E unit : 4,57
2. D_1 subunit: 4,11
3. C_2 subunit: 3,57
4. B unit : 3,39

However, the V/Sc ratio of orthopyroxene in the D_2 subunit of drill core ZS 3 is 3,16 (using extrapolated values of 95 ppm V and 30 ppm Sc in hypothetically pure orthopyroxene), representing either a potential reversal in the trend or laterally disposed compositional changes. The latter may result from the sensitivity of D^{opx} to fO_2: available experimental data suggest that D^{opx} declines in response to a rise in fO_2 (Irving, 1978). Hence, the lower V/Sc ratio indicated in drill core ZS 3 may reflect higher fO_2 of crystallization, which would be consistent with the higher Fe^{3+}/Fe^{2+} ratio of chromite in this succession relative to drill core ZS 7. Finally, examination of thin sections yields no evidence of a stepped or progressive increase in the modal proportion of clinopyroxene with stratigraphic height. Though the V/Sc ratio of clinopyroxene in the studied section is not known, data submitted by Kruger (1983) indicate a range of 3,75 to 6,60 (x = 5,09) for clinopyroxene separates from 8 whole-rock samples of the Upper Critical Zone, Rustenburg district. By virtue of the extremely low modal abundance of clinopyroxene in the studied section of the Ruighoek Pyroxenite, the rise in V/Sc ratios with increasing

stratigraphic height is therefore essentially independent of the modal orthopyroxene/clinopyroxene ratio.

6.5.3 INCOMPATIBLE ELEMENTS

Absolute whole-rock abundances of the incompatible elements Rb, Y, Zr and Ba are low, with highest concentrations observed in mica- and micropegmatite-bearing bronzitites. This is clearly illustrated by samples 155 to 165 in the basal portion of the D_1 subunit (Table 34). High concentrations of incompatible elements are indicated in the intercumulus silicate fraction of these samples by virtue of the low residual porosity. Considering the essentially anchimonomineralic character of the underlying dunites, and that of the overlying, granular-textured bronzitites, upward migration of later stage magmatic residua into these coarse-grained bronzitites would account for the high concentrations.

The influence of small amounts of mica and amphibole on whole-rock levels of Zr and Ba can be gauged from Figs. 65(A) and (B), which are plots of whole-rock Zr and Ba against Sr, respectively. Attention is confined to samples from the B unit and C_2 subunit since it was shown earlier (section 6.5.1) that the Sr content of plagioclase in these bronzitites could be regarded as a constant. The variation of Zr against Sr in samples with plagioclase as the predominant intercumulus silicate phase is given by the equation:

$$Zr = 0{,}0593\ Sr + 2{,}54 \quad (r = 0{,}9394)$$

Extrapolation yields 2,5 ppm Zr in Sr-free orthopyroxene and a Zr abundance of 41,3 ppm associated with hypothetically pure plagioclase (i.e., with a Sr content of 654 ppm). The average Ba/Sr ratio of the selfsame samples is 0,817 and calculation thus yields a Ba content of 534 ppm in hypothetically pure plagioclase. Hence, the average Ba/Zr ratio of plagioclase is 12,9, which is higher than the whole-rock average of 5,84 and the average of 6,32 for the other eight hydrous mineral-bearing samples in the data set. This is due to the detectable level of Zr in orthopyroxene.

Whole-rock Zr/Y ratios vary between 0,50 and 3,00 and appear to separate the succession into discrete segments. For example, the

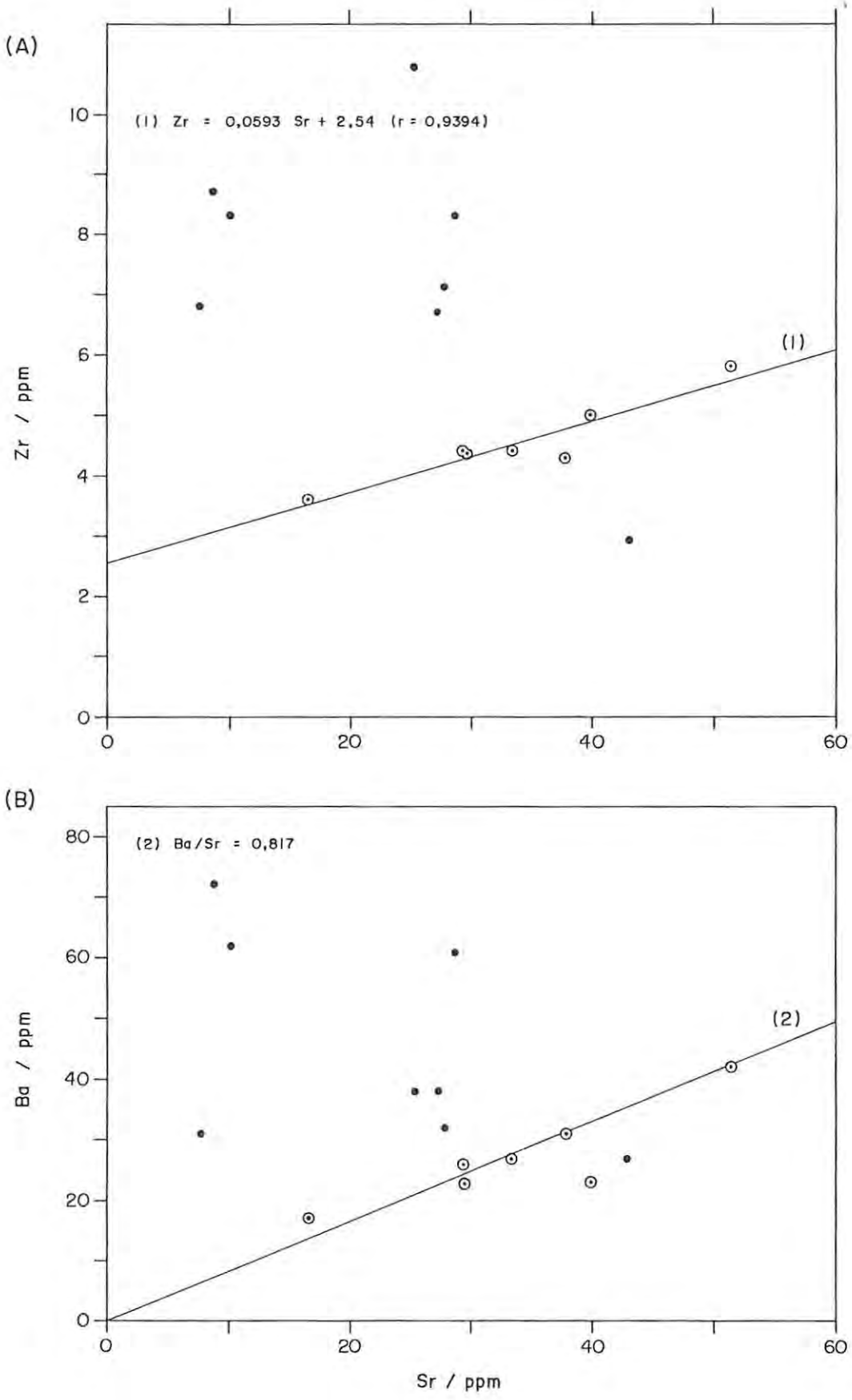

FIG 65 PLOT OF WHOLE-ROCK (A) Zr, AND (B) Ba VERSUS Sr FOR BRONZITITES IN THE C_2 SUBUNIT AND B UNIT.

SYMBOLS:
- ⊙ SAMPLES WITH PLAGIOCLASE AS PREDOMINANT INTERCUMULUS SILICATE PHASE (i.e. 205, 207, 265, 271, 278, AND 290)
- • SAMPLES WITH INTERCUMULUS PLAGIOCLASE PLUS SMALL AMOUNTS OF MICA AND AMPHIBOLE.

average Zr/Y ratios of the B unit and C_2 subunit are 1,44 (s = 0,26) and 1,47 (s = 0,70), respectively, whereas the coarse-grained bronzitites in the basal portion of the D_1 subunit, bounded by samples 133 and 165, yield an average ratio of 1,66 (s = 0,21). These values are higher than for the overlying succession, where average Zr/Y ratios of 0,87 (s = 0,28) and 0,78 (s = 0,03) are indicated in the upper portion of the D_1 subunit and E unit, respectively. With the exception of sample 304 in the immediate footwall of the LG 6A chromitite layer (Zr/Y ratio of 2,09), the average Zr/Y ratio of samples 300, 308 and 312 is 0,82.

6.6 SUMMARY

1. The relative abundances of compatible trace elements in hypothetically pure olivine, orthopyroxene and chromite, determined by extrapolation of whole-rock contents in bimineralic assemblages, can be summarized as follows:
   Zn: chromite (400 - 660ppm >> opx (60 - 80ppm) > ol (40 - 55ppm)
   Cu: chromite (28ppm) > opx (7 - 25ppm) > ol (3ppm)
   Ni: ol (>1 700ppm) >> chromite (400 - 785ppm) $\geq$ opx (440 - 585ppm)
   Co: chromite (170ppm) $\geq$ ol (155 - 180ppm) > opx (90 - 110ppm)
   V : chromite (1 360 - 2 800ppm) >> opx (65 - 130ppm) >> ol (<1ppm)
   Sc: opx (20 - 34ppm) $\geq$ chromite (18 - 22ppm) > ol (6ppm)

2. Bronzitites located stratigraphically above the coarse-grained assemblages in the D_1 subunit (i.e., above the level of sample 134) exhibit a distinctive range of $Sr/Al_2O_3^*$ ratios. This feature may be representative of crystallization from a chemically different magma (relative to parental magma(s) of the B unit and C_2 subunit). A point of interest is that this compositional change is linked to a transition from meso- and adcumulate-textured rocks to finer-grained, granular-textured bronzitites (refer to Figs. 8A and C).

3. Sc and Co in hypothetically pure orthopyroxene exhibit a minimum abundance within the C_2 subunit, then rise with increasing stratigraphic height. The vanadium contents of orthopyroxene in

the B unit and C_2 subunit are comparable (< 90 ppm), but are higher in the D_1 subunit (107 ppm) and E unit (ca. 130 ppm).

4. The Ni content of orthopyroxene does not exhibit a progressive decline with increasing stratigraphic height. This is particularly apparent within the D_1 subunit, where a progressive decline in orthopyroxene grain-size with increasing stratigraphic height (refer to Fig. 8C) is linked to an irregular rise in Ni contents. This progressive change to a more primitive value may therefore represent diminishing degrees of sub-liquidus equilibration with Ni-depleted intercumulus melt (a progressive rise in whole-rock sulphide content with increasing stratigraphic height is not manifested either in thin-section or via rising levels of Cu).

5. Co/Sc and Ni/Sc ratios in hypothetically pure orthopyroxene exhibit primitive values within the C_2 subunit, followed by a steady decline with increasing stratigraphic height through the overlying succession of bronzitites. Consanguinity of the C_2, D and E units is implied, but both ratios exhibit a discontinuity within the stratigraphic interval bounded by samples 124 and 139 (i.e., the succession of coarse-grained rocks interleaved between fine-grained, granular textured bronzitites some 35 metres below the LG 5 chromitite layer). This feature is also shown by a decline in the Ni/Co ratio, but no discontinuity in the V/Co ratio is manifested at this level.

With reference to Fig. 14, which depicts the variation in orthopyroxene MMF ratios in relation to stratigraphic height within the studied succession, it is evident that the variation in Ni/Sc ratios correlates with electron microprobe data (for example, relative to the B unit, a clear rise in orthopyroxene MMF and Ni/Sc ratios is portrayed within the C_2 subunit). This coherency thus facilitates the use of Ni/Sc ratios as indicators of reversals in cryptic variation, and suggests that the transition from the B unit to the C_2 subunit reports to a cryptic variation from evolved to geochemically more primitive character.

7. DETAILED ANALYSIS OF COMPOSITIONAL VARIATIONS IN CUMULUS PHASES.

A recurring theme within the preceding text is the apparent link between the mineral chemistry of coexisting cumulus phases, and the link between trivalent element contents in specific phases and variations in atomic $Mg/(Mg + Fe^{2+})$ ratios. A summary of these features is presented in the subsequent text, which includes sections dealing with the manipulation of chromite compositional parameters to yield calculated estimates of equilibration temperatures and fO_2.

7.1 COEXISTING ORTHOPYROXENE AND OLIVINE

The variation of $Mg/(Mg + Fe^{2+})$ in orthopyroxene against $Mg/(Mg + Fe^{2+})$ in olivine is depicted in Fig. 66. It is evident from the data that orthopyroxene compositions in the Ruighoek Pyroxenite and Groenfontein Harzburgite are systematically linked to X_{MgO} ratios of coexisting olivine crystals and, by implication, to the X_{MgO} ratio of parental magma. Significantly, the correlation encompasses reaction-replacement orthopyroxene of the C unit and olivine - orthopyroxene pairs within bronzitites of the D and E units.

The variation of measured values is not consistent with the equations derived by Morse (1979) and Scoon (1985), which relate the composition of the coexisting silicate phases (Fig. 66). Regression analysis of microprobe data for the studied section yields the following equation:

$$MMF\ (opx) = 0,906\ MMF\ (ol) + 0,091 \qquad (r = 0,9787)$$

Given that the distribution of Mg and Fe^{2+} between olivine and mafic magmas conforms to the relationship:
$K_D = (X_{FeO}/X_{MgO})^{ol}.(X_{MgO}/X_{FeO})^{liq} = 0,30$ (Roeder and Emslie, 1970), manipulation of measured values of X_{MgO} yields K_D (opx-melt) = $0,27 \pm 0,01$ (n = 14). This value is higher than the estimate of $0,26 \pm 0,01$ for the Hartley Complex of the Zimbabwean Great Dyke (Wilson, 1982), and Scoon's (1985) estimate of 0,256 for a variety of olivine-bearing Bushveld rocks.

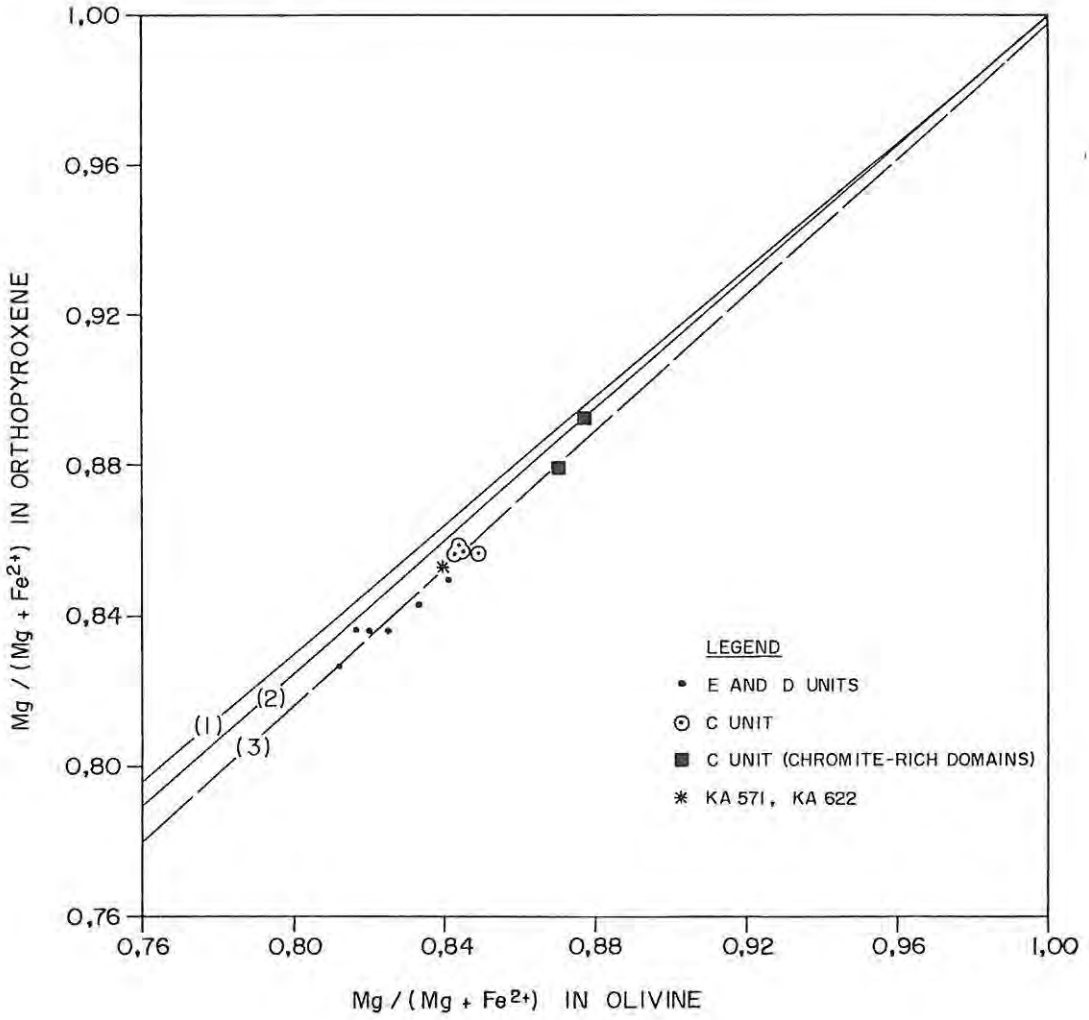

(1) : MMF (OPX) = 0,85 MMF (OLIVINE) + 0,15 (MORSE, 1979)
(2): MMF (OPX) = 0,875 MMF (OLIVINE) + 0,125 (SCOON, 1985)
(3): MMF (OPX) = 0,906 MMF (OLIVINE) + 0,091 (THIS STUDY)

FIG. 66 VARIATION OF $Mg/(Mg+Fe^{2+})$ IN ORTHOPYROXENE AGAINST THE $Mg/(Mg+Fe^{2+})$ RATIO OF COEXISTING OLIVINE.

The Fo content of olivine grains found in juxtaposition to the LG 1 and LG 3 chromitite layers (samples 213B, 214A and 286) is higher than the En content of cumulus orthopyroxene crystals in the immediately adjacent bronzitites. Microprobe measurements of reaction-replacement orthopyroxene depicted in the thin harzburgite layers were not carried out, but the anticipated composition in the footwall of the LG 1 chromitite layer, for example, is calculated to be $En_{85,7}$. This composition contrasts with the measured En content of 83,8 mol. per cent in the cumulus orthopyroxene crystals, and it is possible that the magnesian character of these anomalous, olivine-bearing assemblages may be representative of an MgO-enriched, interstitial melt expelled from the compacting chromitite layers. It follows from this consideration that a cryptic rise in MMF ratios of associated chromite grains may stem from this process; it will be shown in section 7.3 of the present text that MMF ratios of chromite grains and coexisting cumulus silicate phases correlate positively.

7.2 ALUMINIUM CONTENT OF ORTHOPYROXENE

Fig. 67 is a plot of aluminium in orthopyroxene versus the corresponding MMF ratios. These data are compared with microprobe analyses of orthopyroxene in the Lower Zone of the Eastern Bushveld Complex (Cameron, 1978) and in the Zimbabwean Great Dyke (Wilson, 1982), and it is clear from the disposition of data points that Al contents of orthopyroxene in the studied section are lower than in the latter occurrences. Furthermore, the negative correlation displayed by Wilson's data is not apparent in the bronzitites and olivine-bronzitites of the Ruighoek Pyroxenite, where a restricted range in Al contents is evident. With increasing proximity to the basal contact of the LG 3 leader chromitite layer, however, the grain-to-grain rise in the En content of cumulus orthopyroxene is linked to a decline in Al contents (sample 214A). Two additional features are portrayed in the figure. Firstly, the variation within bronzitites of the C_2 subunit conforms to this trend, albeit over a restricted range, and secondly, the sense of the variation within sample 214A is subparallel to (a) cryptic zonal changes adjacent to occluded chromite grains (as evinced by analyses denoted 184B), and (b) the correlation documented by Wilson (op. cit.).

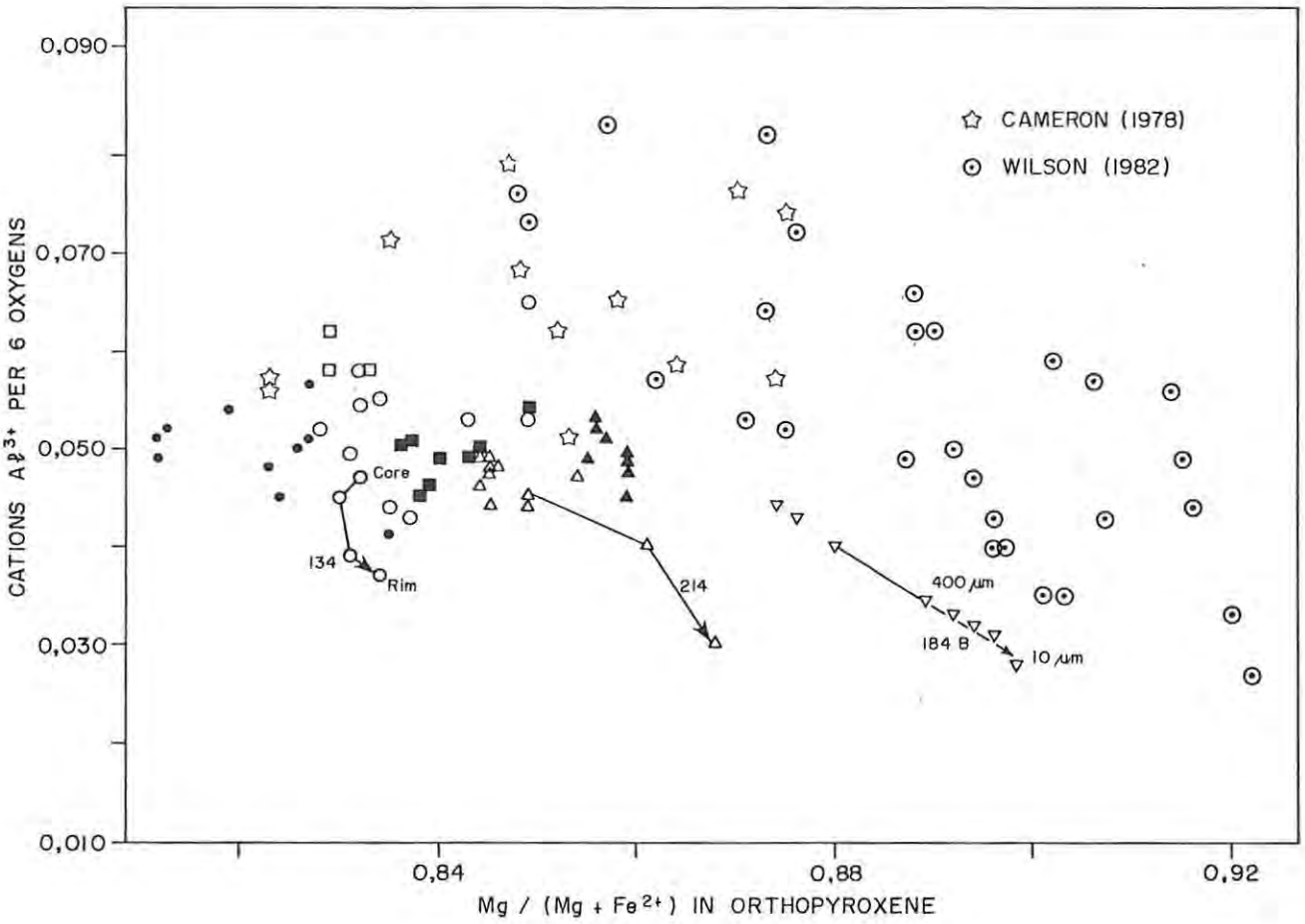

FIG. 67 VARIATION OF ALUMINIUM AGAINST Mg/(Mg + Fe^{2+}) IN ORTHOPYROXENE (DRILL CORE ZS 7). AVERAGE VALUES FOR SAMPLES ARE PLOTTED (UNLESS OTHERWISE SHOWN BY ARROWHEAD SYMBOLS LINKING INDIVIDUAL ANALYSES) AND ARE COMPARED WITH THE DATA OF CAMERON (1978) (FOR THE LOWER ZONE IN THE EASTERN BUSHVELD COMPLEX) AND OF (⊙) WILSON (1982) (FOR THE ZIMBABWEAN GREAT DYKE).

SYMBOLS:

(•) E UNIT; (□) D_2 SUBUNIT; (○) D_1 SUBUNIT; (▽) REACTION-REPLACEMENT ORTHOPYROXENE IN THE C_3 SUBUNIT; (△) C_2 SUBUNIT; (▲) C_1 SUBUNIT; (■) B UNIT.

SAMPLE 134 : CORE-RIM COMPOSITIONAL RELATIONSHIPS OF A SINGLE CRYSTAL, FELDSPATHIC BRONZITITE.

184 B : COMPOSITIONAL PROFILE ADJACENT TO AN OCCLUDED CHROMITE GRAIN (FOOTWALL OF THE I CHROMITITE LAYER).

214 : ANALYSES OF THREE CRYSTALS IN IMMEDIATE GRANULAR-TEXTURED FOOTWALL OF LG3 LEADER CHROMITITE (MMF (OPX) INCREASES TOWARDS THE CONTACT).

400 µm : MICRONS FROM CHROMITE GRAIN BOUNDARY.

The rise in Al contents with declining MMF ratios in the Great Dyke is linked to cryptic changes coincident with increasing stratigraphic height, i.e., normal fractionation processes. Hence, the compositional changes observed in the immediate footwall of the LG 3 leader chromitite layer may represent a reversal induced by fairly rapid liquid mixing at the base of a new influx of magma. Features such as the high Cr content of the leader chromitite and occurrence of juxtaposed nickeliferous olivine grains lend some support to this proposal. However, as illustrated by cryptic zonal changes adjacent to a euhedral chromite grain in sample 184B (Fig. 67), subsolidus re-equilibration of orthopyroxene and chromite could equally account for this apparent reversal, but is should be stressed that the decline in Al content is only manifested within 400 microns of chromite grain boundaries. In view of the corresponding rise in the MMF ratios of chromite grains, and decline in Al contents, it is advocated here that (a) the LG 3 leader chromitite layer is depicted in juxtaposition to the base of a cyclic unit, and (b) the nickeliferous olivine crystals within the granular-textured footwall rock may have nucleated in the putative influx prior to liquid mixing.

Core-rim compositional relationships in well-formed orthopyroxene crystals intergrown with plagioclase display a cryptic zonation of declining Al, with the MMF ratio remaining essentially constant (Fig. 67; sample 134). By implication, in situ secondary growth of orthopyroxene, followed by partial grain homogenization by diffusion, may account for the scatter that is evident in the data. This, however, is presumed to be a factor contributing to compositional diversity only in samples showing coarse-grained adcumulate textures or significant modal abundances of intercumulus plagioclase. These parameters do no characterize samples selected from the E unit and upper portion of the D unit. Hence, the restricted range of Al contents in orthopyroxene, linked to a somewhat greater range of MMF ratios, is possibly indicative of a restricted range of magma compositions.

Fig. 68 is an equivalent plot of Al contents versus MMF ratios for orthopyroxene in the D_2 subunit, drill core ZS 3. Though it was noted in the preceding text that orthopyroxene crystals within the

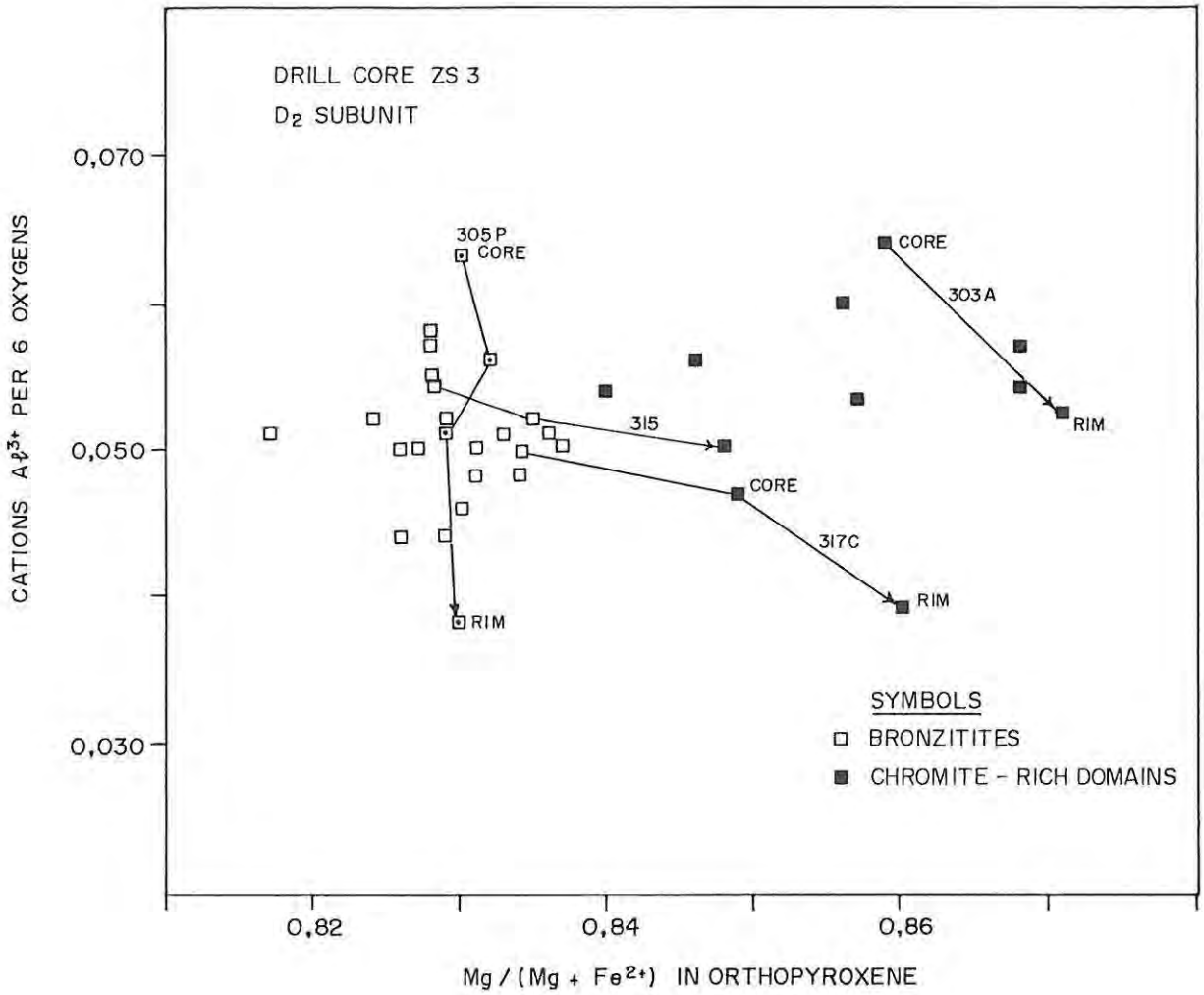

FIG. 68 VARIATION OF ALUMINIUM AGAINST $Mg/(Mg + Fe^{2+})$ IN ORTHOPYROXENE OF THE D_2 SUBUNIT, DRILL CORE ZS 3. THE RANGE IN $A\ell^{3+}$ CONTENTS OF ORTHOPYROXENE IN CHROMITE-RICH ENVIRONMENTS IS EQUIVALENT TO THE RANGE IN CHROMITE - POOR ENVIRONMENTS. CRYPTIC ZONAL STRUCTURES IN AN ORTHOPYROXENE PHENOCRYST, SAMPLE 305, ILLUSTRATE A TREND OF Aℓ-DEPLETION AT CONSTANT MMF RATIO.

footwall rocks of the LG 6 and LG 6A chromitite layers show lower Al_2O_3 contents, a negative correlation between Al and $Mg/(Mg + Fe^{2+})$ in orthopyroxene is not evident in the plot since a corresponding rise in Mg content was not detected. However, this trend is clearly illustrated by core-rim compositional changes within disseminated orthopyroxene crystals in chromite-rich domains (e.g., samples 303C and 317C). The main feature portrayed in the figure is that compositional diversity within the subunit stems from (a) zonal structures (as illustrated by zonal cryptic changes depicted within the orthopyroxene phenocryst in sample 305 and the disposition of other data points relative to this trend), (b) the rise in Al contents above the LG 6 chromitite layer, without a mandatory decline in MMF ratios, and (c) subsolidus re-equilibration with chromite in spinel-rich domains, which induces a substantial reduction in Al content of the juxtaposed silicate phase. By virtue of the latter observation, the irregular decline in Al contents of orthopyroxene with increasing stratigraphic height through the gradational hanging-wall of the LG 6A chromitite layer (refer to Table 7) points to a primary magmatic influence.

7.3 MMF RATIOS OF COEXISTING CHROMITE AND SILICATES

Fig. 69 is a plot of $Mg/(Mg + Fe^{2+})$ in chromite grains against the MMF ratio of the orthopyroxene or olivine host. A broad positive correlation is evident in the data although there is a considerable spread of chromite MMF ratios for a given MMF (silicate) ratio. The latter stems from (a) variable degrees of reaction with interstitial melt prior to encapsulation, (b) subsolidus re-equilibration with olivine and orthopyroxene, and (c) chromite grains enclosed in olivine crystals tend to be more Fe-rich than grains intergrown with orthopyroxene. This feature is also clearly displayed by microprobe analyses of mineral pairs in the Zimbabwean Great Dyke (Fig. 69).

The correlation of MMF (chromite) ratios and grain-size has been discussed in the preceding text. In summary, it was noted that larger grains occluded in the core-domains of well-formed olivine and orthopyroxene crystals yield higher MMF ratios than smaller grains within the same specimen. Secondly, the analytical data indicate

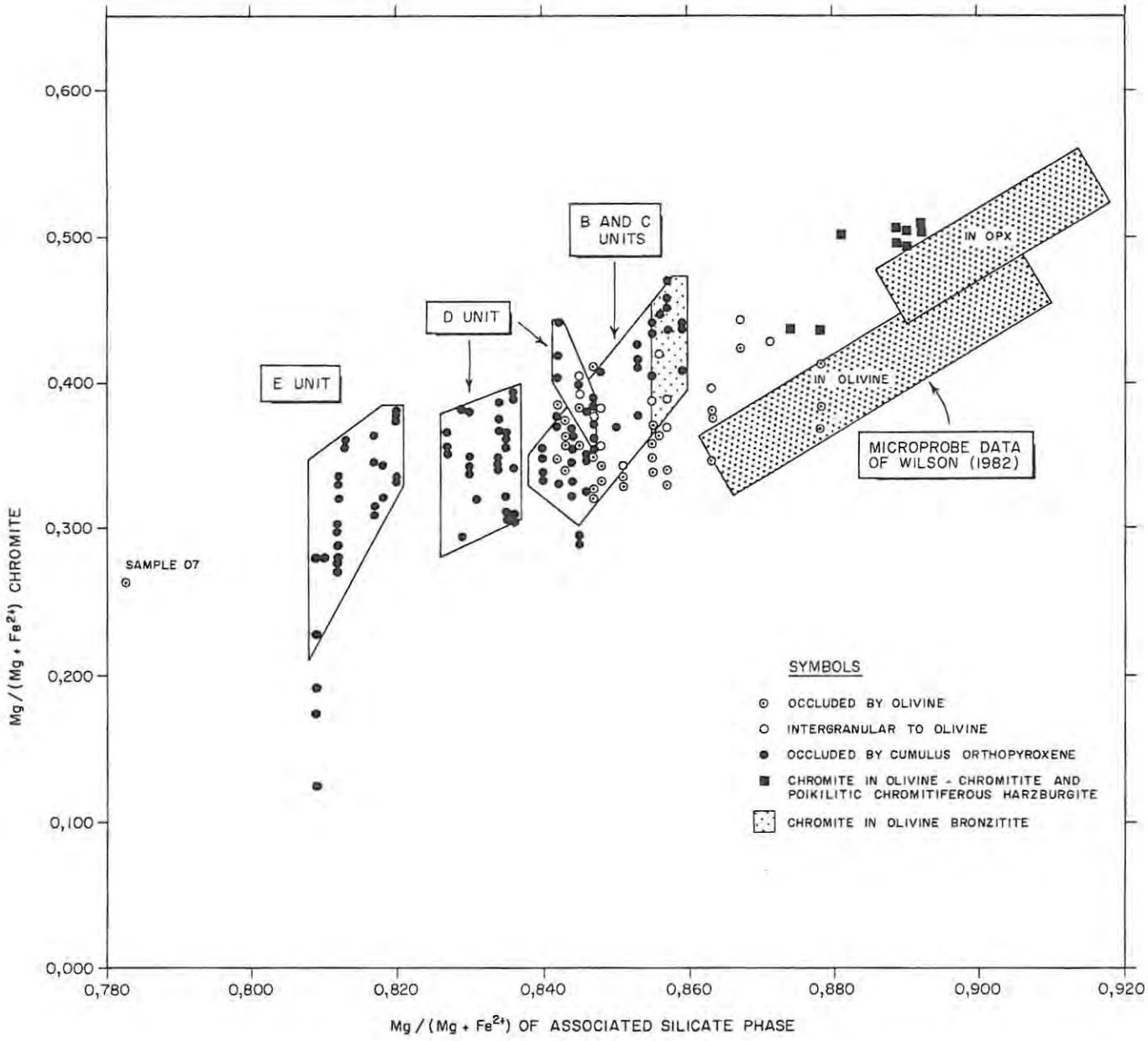

FIG. 69 VARIATION OF $Mg/(Mg + Fe^{2+})$ IN CHROMITE AGAINST $Mg/(Mg + Fe^{2+})$ IN COEXISTING ORTHOPYROXENE OR OLIVINE. DATA POINTS ARE REPRESENTATIVE OF CHROMITE GRAINS ENCLOSED IN THESE SILICATE PHASES (UNLESS SPECIFIED).

that the compositional variation of chromite is linked to the modal chromite/silicate ratio. This feature is summarized in Figs. 70(A) and (B), which depict the variation in chromite MMF ratios against whole-rock Cr_2O_3 contents of olivine-chromite and orthopyroxene-chromite assemblages, respectively. In conjunction with the observed links between composition and (a) nature of the occluding silicate phase, (b) grain-size, and (c) cryptic changes in the silicate phase as chromite grain boundaries are approached, the relationships displayed in Figs. 70(A) and (B) can be regarded as supportive evidence for the efficiency of subsolidus re-equilibration. It should be stressed, however, that the latter process induces a drastic rise of Fe^{2+} in weakly disseminated chromite grains, without disturbing the bulk composition of the silicate phases, whereas a marked rise of Mg in weakly disseminated orthopyroxene and olivine is achieved without measureably changing the Mg/Fe^{2+} ratio of the juxtaposed spinel (Roeder et al., 1979).

7.4 COMPOSITIONAL VARIATION OF CHROMITE

7.4.1. VARIATION IN Al AND Cr

The reciprocal variation in the proportions of Al and Cr cations in chromite within drill core ZS 7, irrespective of mineralogical environment, is summarized in Fig. 71. Regression analysis of the selected data yields a slope of -1,00, attesting to the constant level of Fe^{3+} cations. It is evident from the plot that (a) atomic Al/Cr ratios of chromite grains occluded by olivine, orthopyroxene and plagioclase fall into distinct ranges, and (b) the Al/Cr ratios of grains in silicate-rich assemblages are a reciprocal function of the Al content of the silicate host.

For purposes of clarity, data pertaining to chromite grains enclosed within the rim-domains of orthopyroxene crystals in feldspathic environments were omitted from Fig. 71. However, these indicate Al/Cr ratios intermediate between the respective loci of grains enclosed in orthopyroxene and plagioclase. Within the latter associations, atomic Al/Cr ratios are linked to the MMF ratios such

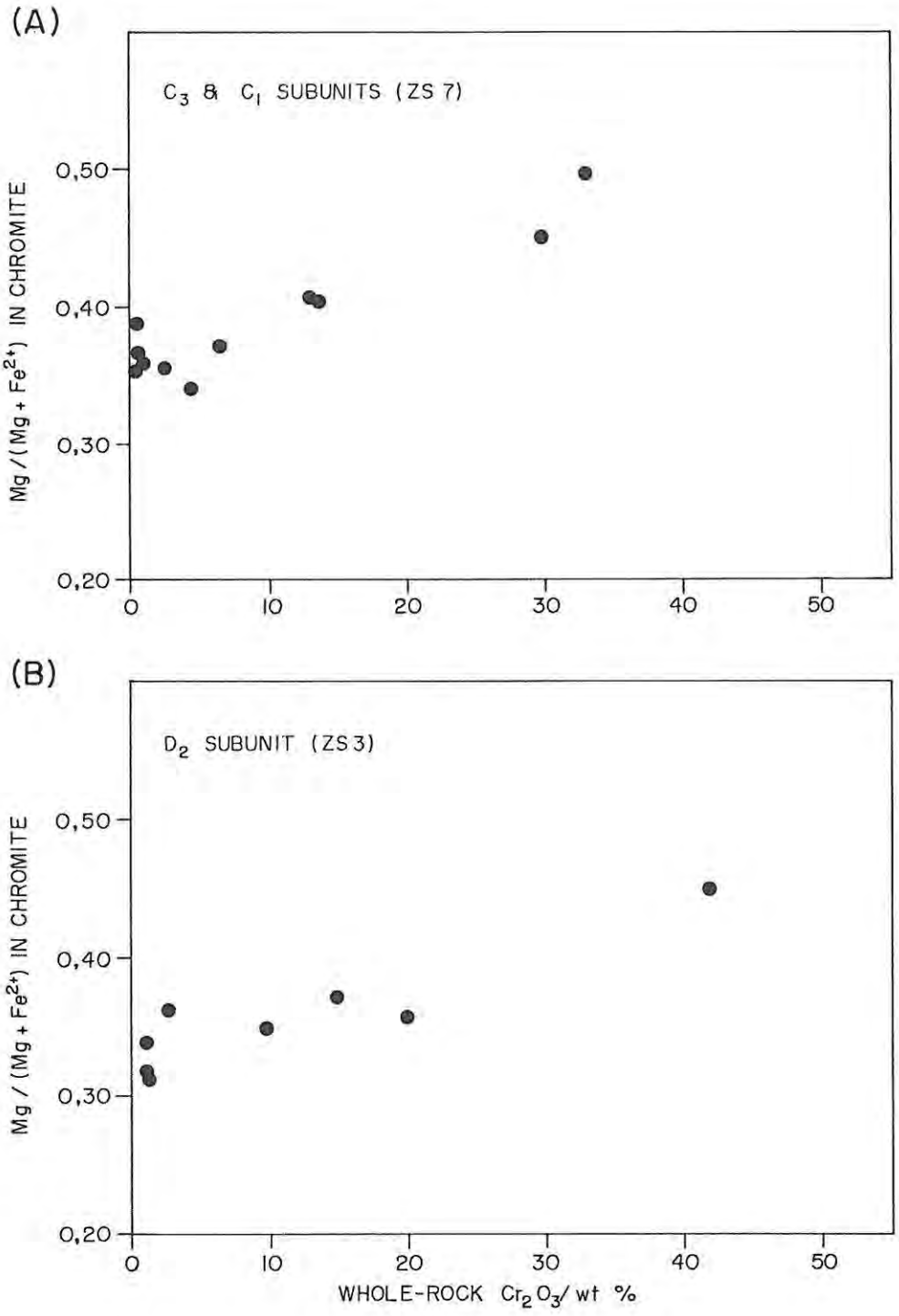

FIG. 70 VARIATION OF $Mg/(Mg+Fe^{2+})$ IN CHROMITE AGAINST WHOLE-ROCK Cr_2O_3 CONTENTS FOR (A) OLIVINE-CHROMITE ASSEMBLAGES AND (B) ORTHOPYROXENE-CHROMITE ASSEMBLAGES. CHROMITE MMF RATIOS (AVERAGE OF MICROPROBE ANALYSES) RISE WITH INCREASING MODAL PROPORTIONS OF CHROMITE.

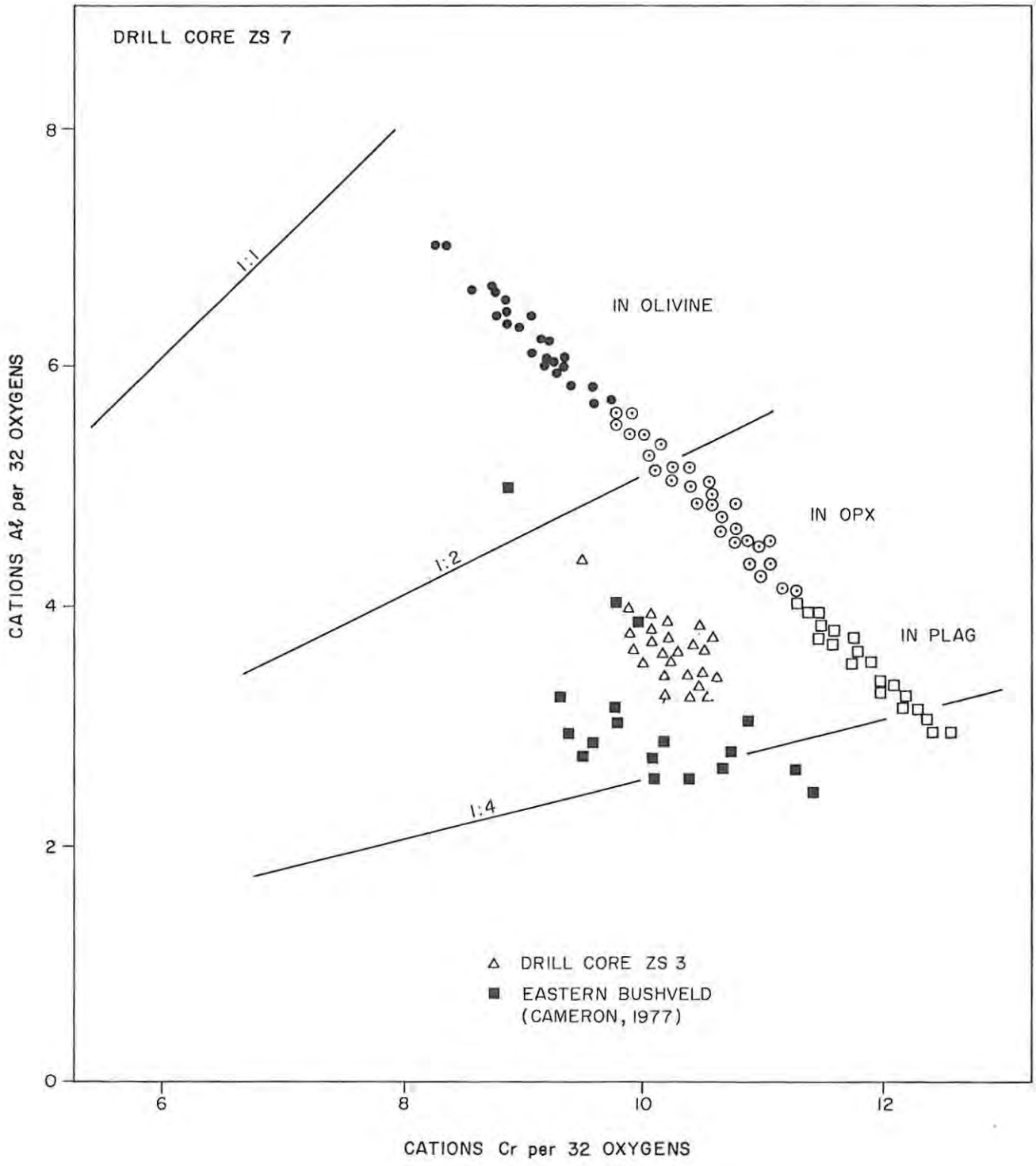

FIG. 71 CATIONS Al PER 32 OXYGENS PLOTTED AGAINST CATIONS Cr PER 32 OXYGENS FOR CHROMITE IN SILICATE-RICH ROCKS, DRILL CORE ZS7. ONLY A REPRESENTATIVE SELECTION OF THE DATA IS PLOTTED. COMPOSITIONS OF CHROMITE IN DRILL CORE ZS 3 AND THE CENTRAL SECTOR OF THE EASTERN BUSHVELD COMPLEX ARE PLOTTED TO ILLUSTRATE THE DIFFERENCES IN Fe^{3+}.

that Al/Cr declines with a decline in $Mg/(Mg + Fe^{2+})$. The range in Al/Cr ratios of chromite within chromitite layers overlaps that of grains occluded by orthopyroxene, with the exception of chromite within the LG 2 chromitite layer, for example, where higher proportions of Fe^{3+} and lower Al contents are indicated. The distinctive range in the proportions of Cr, Al and Fe^{3+} cations in chromite within the upper portion of the D_2 subunit in drill core ZS 3 is emphasized in Fig. 71. The data points are representative of chromite grains intergrown with plagioclase and orthopyroxene, and are compared with microprobe analyses of chromite in silicate-rich rocks from the Mooihoek Pyroxenite (Cameron, 1977). The range in Al/Cr ratios within the latter occurrences is subdued and, although the absolute Cr_2O_3 contents are substantially lower, overlaps the range in Al/Cr ratios depicted by chromite intergrown with plagioclase in drill core ZS 7. This feature stems from the higher proportion of Fe^{3+} cations and the maintenance of charge balance and stoichiometry by substitution of Fe^{3+} for Al cations, and Fe^{3+} for (Al, Cr) to a lesser degree. Whereas Cr^{3+} has a high octahedral site preference energy, Al and Fe^{3+} cations have zero OSPE in Cr-spinels and the differences noted above point to a higher activity of Fe^{3+} in the magmas from which the ZS 3 (D_2 subunit) and Mooihoek Pyroxenite successions crystallized.

7.4.2. VARIATION OF Al AGAINST $Mg/(Mg + Fe^{2+})$ IN CHROMITE

The observed link between MMF ratios and the proportions of Cr and Al cations in chromite grains is summarized in Figs. 72(A) to (D), which depict the variation of Al against $Mg/(Mg + Fe^{2+})$ in chromite. Fig. 72(A) is representative of chromite within chromitite layers exposed in drill core ZS 7, and includes data submitted by de Waal (1975). It is evident from the figure that the compositional relationship noted by Eales and Reynolds (1983) is manifested in both sets of analytical data, viz, the proportion of Al cations rises with a decline in MMF ratios from high values to ca. 0,450, followed by a decline in Al with a further decline in MMF ratios. Furthermore, it is evident from the disposition of data points pertaining to the ZS 7 succession that the compositional variation in relation to increasing stratigraphic height conforms roughly to this trend. Inconsistencies

are represented by the LG 4 and LG 3 leader chromitite layers, and the cryptic rise in Al with rising MMF ratios upward through the H chromitite layer. However, it is noted that the latter data points fall into discrete subsets which appear to span the compositional field between pyroxenite-hosted chromitite layers (e.g., the LG 5 chromitite) and the dunite-hosted LG 4 chromitite layer. This relationship would be wholly consistent with the occurrence of bronzitite below the H chromitite layer and magnesian dunite in the immediate hanging-wall. Upward percolation of late-stage residual melt from the underlying pyroxenite into the basal portion of the compacting chromitite layer, followed by equilibration, may account for the cryptic compositional changes, but the granular-textured nature of the footwall bronzitite militates against this notion. Impermeability of this assemblage is suggested by the mineralogical and evolved chemical characteristics of the underlying bronzitite (sample 201), which yields whole-rock trace element abundances of 7,9 ppm Sr, 3,1 ppm Rb, 7,6 ppm Zr, 24 ppm Ba, and 213 ppm V (chromite is an accessory constituent of the rock). Hence, it is advocated here that consideration should be given to the concept of varying degrees of magma mixing at the base of a liquid column as a potential control on chromite nucleation and its duration. This follows from the more conspicuous grain-to-grain compositional changes measured in the thin C and H chromitite layers (where a thin layer of hybrid magma is implied) relative to the extremely subdued cryptic changes measured within the thicker LG 6A chromitite (Fig. 71A).

Fig. 72(B) depicts the variation of Al against MMF ratios within the C_1 subunit, and it is clear from the data points that chromite grains in olivine-rich domains are enriched in Al and depleted in Mg relative to chromite-rich domains. Furthermore, olivine-hosted grains are enriched in Al and Fe^{2+} relative to grains enclosed in coexisting cumulus orthopyroxene. The MMF ratios of the latter are spread about an average of ca. 0,450, and this feature would seem to account for the Al-enriched nature of these grains relative to orthopyroxene-hosted grains in the B unit and C_2 subunit. A reciprocal variation of Al and Cr cations characterizes chromite within the C_1 subunit. For example, regression analysis of 29 data points yields a slope of -1,00 and a correlation coefficient of -0,993. Extrapolation of these data indicates average proportions of

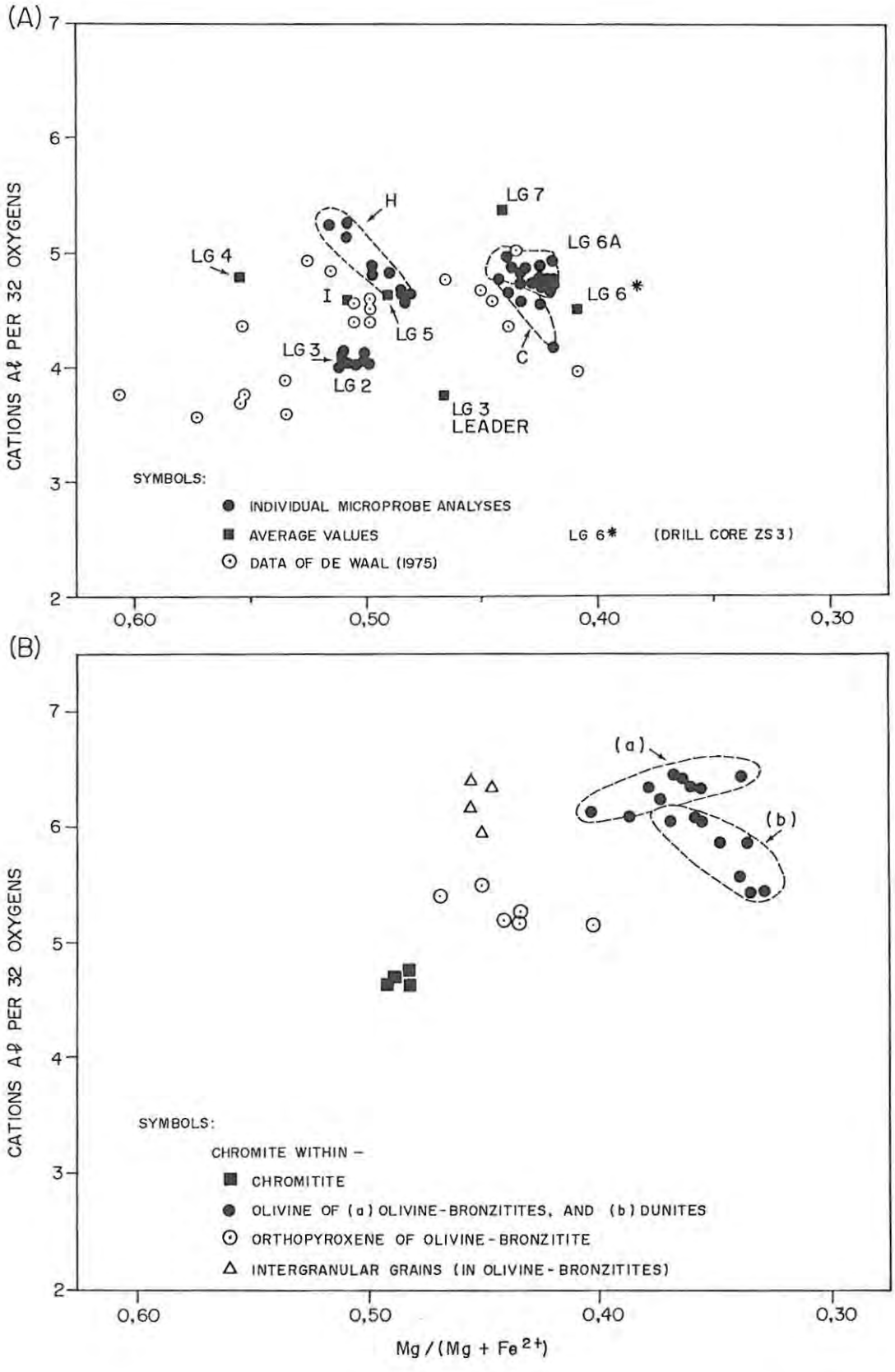

FIG. 72 CATIONS $A\ell^{3+}$ PER 32 OXYGENS PLOTTED AGAINST $Mg/(Mg + Fe^{2+})$ OF CHROMITE WITHIN (A) CHROMITITE LAYERS, AND (B) C_1 SUBUNIT (DRILL CORE ZS 7).

15,40 cations Al and 15,35 cations Cr in the hypothetically pure end-members $MgAl_2O_4$ and $FeCr_2O_4$, respectively. Incorporation of Fe^{3+} cations released by deuteric oxidation of olivine, or periodic fluctuations in fO_2, are thus not factors to be considered at this level of the studied section. Fig. 72(C) summarizes the variation within the C_2 subunit, and it is evident that chromite grains intergrown with silicate phases display (a) MMF ratios of less than 0,450, and (b) a decline in the proportion of Al cations with declining MMF ratios. These features are also evident within the D_1 subunit (Fig. 72D).

The influence of plagioclase nucleation and reaction with interstitial melt on chromite compositions can be assessed via Fig. 73, which depicts the variation in the proportions of Cr, Al and Fe^{3+} cations against chromite MMF ratios for grains intergrown with plagioclase in the B and C units. Relative to grains occluded by calcian plagioclase in the C_1 and C_3 subunits, displaying MMF ratios of $\pm$ 0,450, chromite intergrown with plagioclase in orthopyroxene-rich assemblages is depleted in Al and a positive correlation of Al contents and MMF ratios is indicated. By virtue of a similar correlation noted for chromite grains intergrown with orthopyroxene (e.g., Fig. 72C), and the restricted range of Al contents which overlaps that of chromite within chromitite layers (viz., 4 to 5 cations Al per 32 oxygen formula unit), the link between MMF ratios and Al contents in orthopyroxene-hosted chromite crystals stems from (a) subsolidus re-equilibration with the silicate host, causing a shift to lower MMF ratios, and (b) the residence time in the magma prior to encapsulation. The latter will be addressed in section 7.4.4 of the present text.

The correlation of Al with MMF ratios in bronzitite-hosted chromite grains is not dependent on the Fe_2O_3 content of the spinel. This is illustrated by samples KA 410 and 729 from the Groenfontein Harzburgite subzone (Fig. 74A), in which substitution of Fe^{3+} for Al with declining MMF ratios is clearly indicated by the microprobe data. This feature is also evident within the D_2 subunit of drill core ZS 3, and within Cameron's type-section of the Critical Zone in the Eastern Bushveld Complex (Fig. 74B). Relative to chromite within the ZS 7 drill core section, the microprobe data reported by Cameron

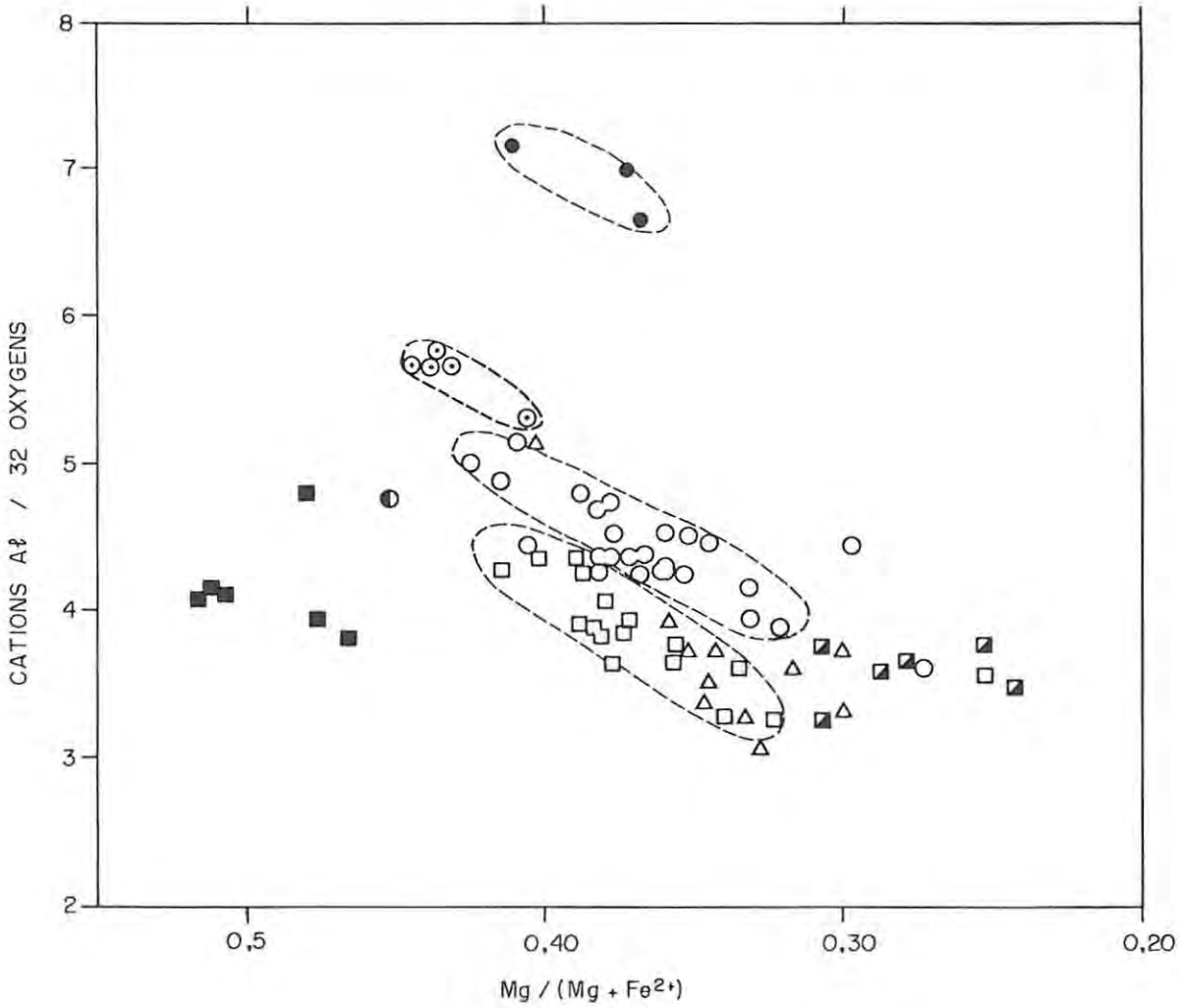

FIG. 72(C) CATIONS Al PER 32 OXYGENS PLOTTED AGAINST Mg / (Mg + Fe^{2+}) OF CHROMITE WITHIN THE C_2 SUBUNIT.

SYMBOLS:

■ CHROMITE WITHIN THE LG 3 AND LEADER CHROMITITE LAYERS.

CHROMITE OCCLUDED IN :

● OLIVINE

⊙ ORTHOPYROXENE WITHIN OLIVINE BRONZITITES

◐ REACTION - REPLACEMENT ORTHOPYROXENE (TOP CONTACT OF THE LG 3 CHROMITITE LAYER)

○ ORTHOPYROXENE WITHIN BRONZITITES

□ PLAGIOCLASE

◪ MICA OR QUARTZ

△ INTERGRANULAR CHROMITE

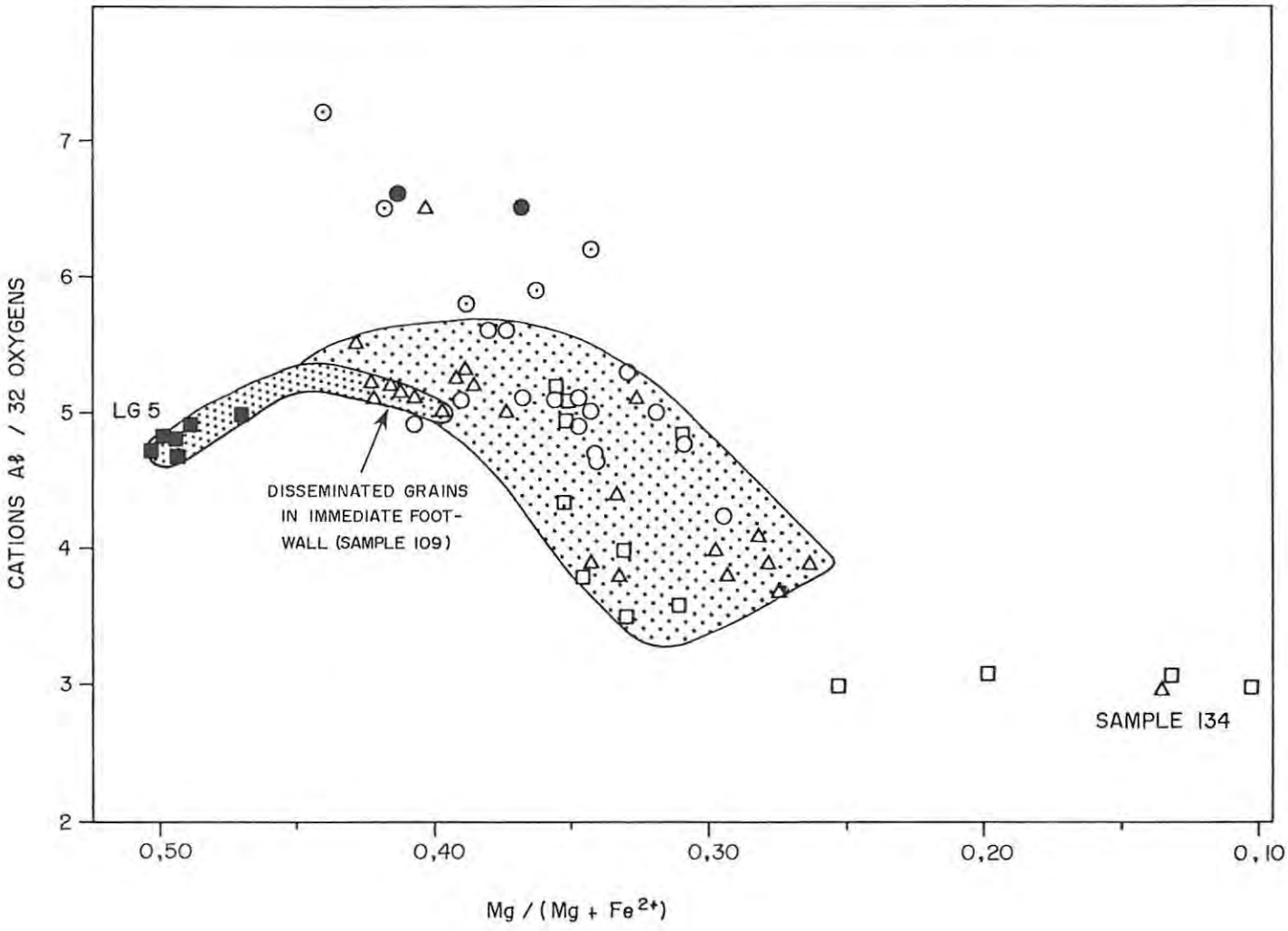

FIG. 72(D) CATIONS Aℓ PER 32 OXYGENS PLOTTED AGAINST Mg / (Mg + Fe^{2+}) OF CHROMITE WITHIN THE D_1 SUBUNIT.

SYMBOLS:

■ CHROMITE WITHIN THE LG 5 CHROMITITE LAYER

CHROMITE OCCLUDED IN:

- ● OLIVINE
- ⊙ ORTHOPYROXENE

] FINE-GRAINED, GRANULAR TEXTURED BRONZITITES AND OLIVINE-BEARING DOMAINS AT BASE OF SUBUNIT.

- ○ ORTHOPYROXENE IN BRONZITITES
- □ PLAGIOCLASE
- △ INTERGRANULAR CHROMITE

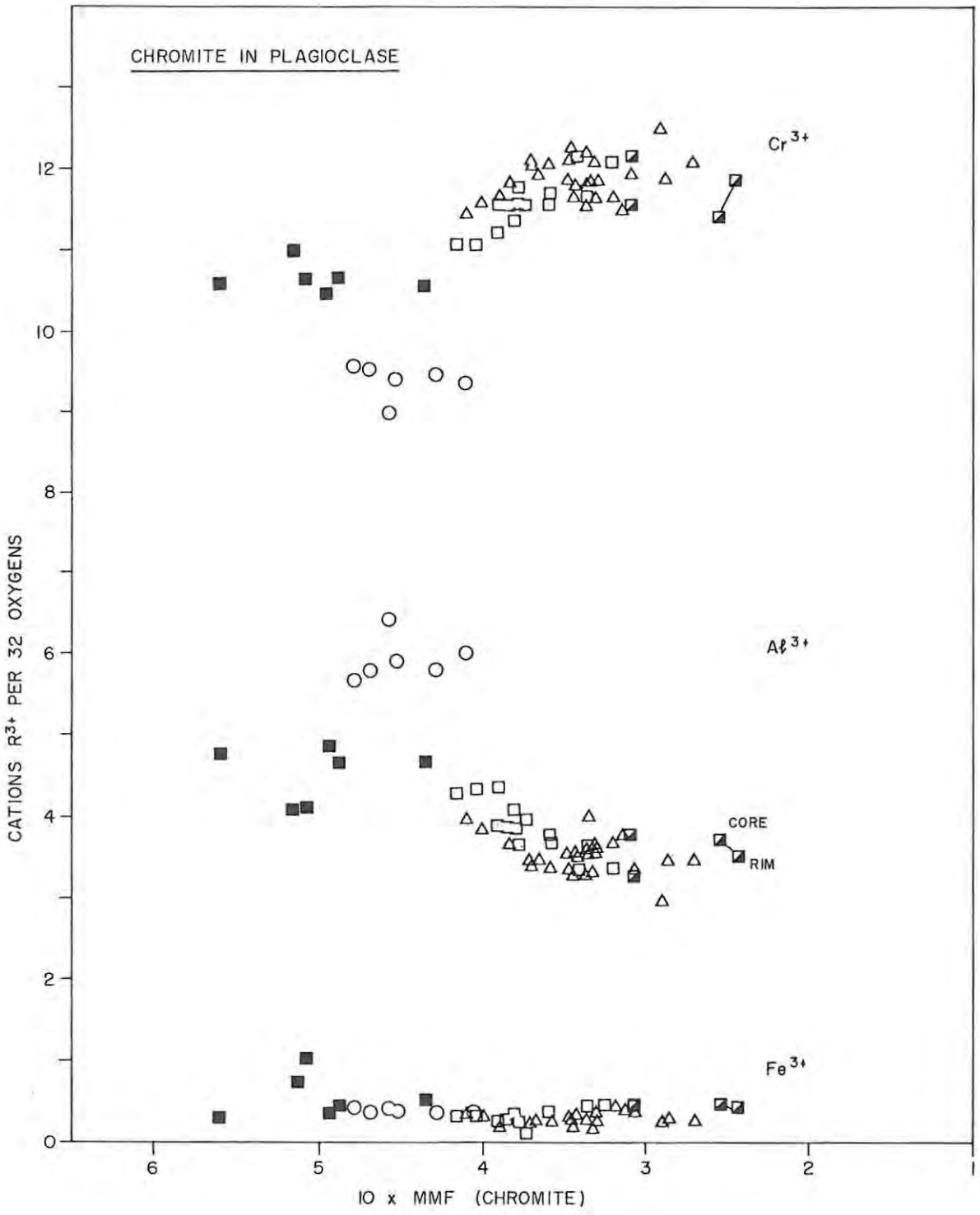

FIG. 73 VARIATION IN THE PROPORTIONS OF Cr, Aℓ AND Fe^{3+} CATIONS AGAINST 10xMMF (CHROMITE) RATIOS, FOR CHROMITE OCCLUDED BY INTERCUMULUS PLAGIOCLASE (#ZS7). RELATIVE TO CHROMITE GRAINS IN ADJACENT CHROMITITE LAYERS, GRAINS INTERGROWN WITH PLAGIOCLASE IN BRONZITITES OF THE B UNIT AND C_2 SUBUNIT ARE ENRICHED IN Cr AND DEPLETED IN Aℓ.

SYMBOLS:
- □ CHROMITE IN THE C_2 SUBUNIT
- ■ CHROMITE IN CHROMITITES
- ○ CHROMITE IN THE C_1 & C_3 SUBUNITS
- △ CHROMITE IN THE B UNIT
- ◪ GRAINS INTERGROWN WITH QUARTZ

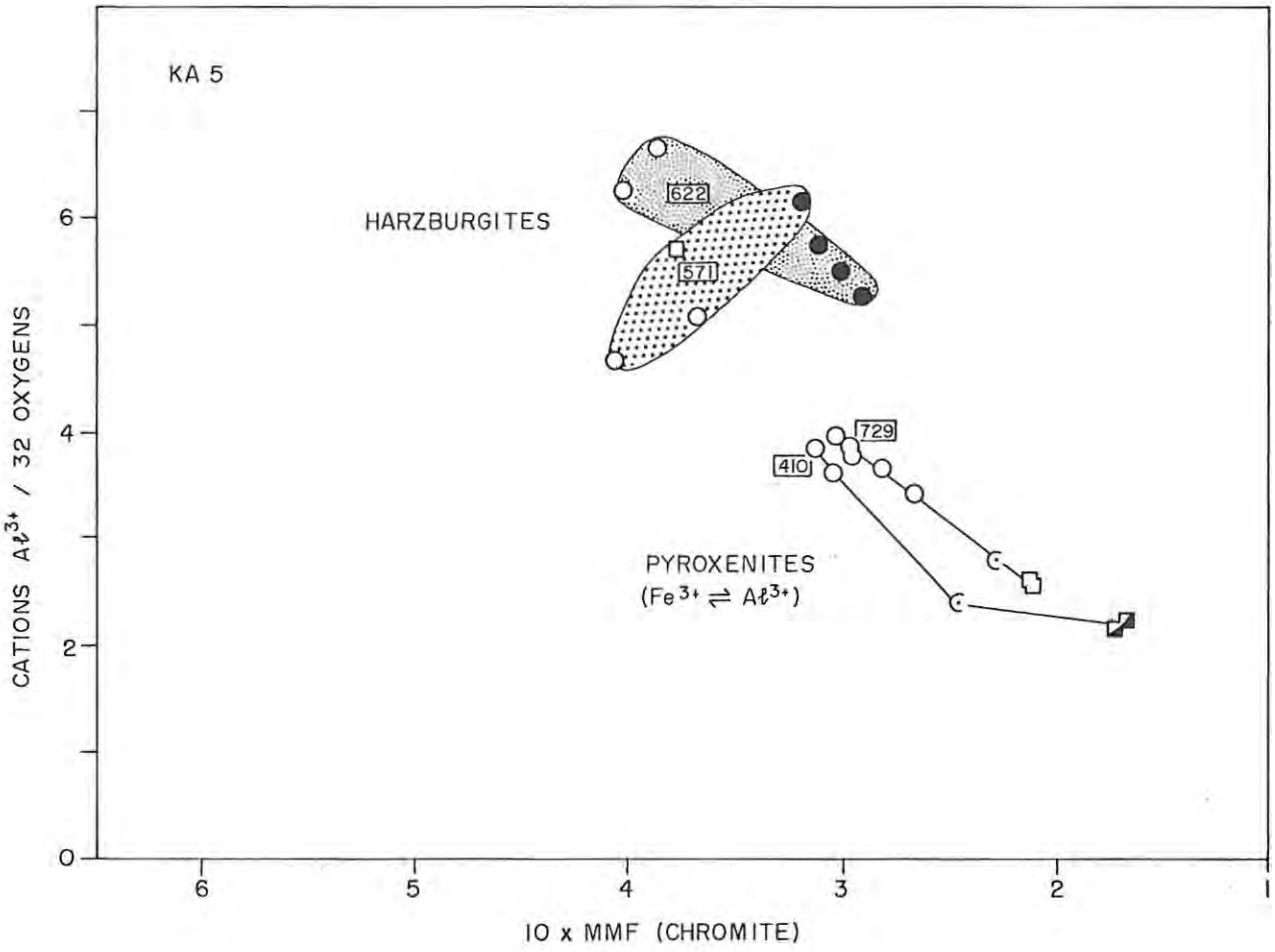

FIG. 74(A) VARIATION IN THE PROPORTION OF Aℓ CATIONS AGAINST IO x MMF (CHROMITE) RATIOS; GROENFONTEIN HARZBURGITE SUBZONE.

SYMBOLS: CHROMITE ENCLOSED IN

- ○ ORTHOPYROXENE
- ● OLIVINE
- ◔ EMBAYMENTS IN ORTHOPYROXENE
- ⌐ PLAGIOCLASE
- ◪ MICA

- 410 PYROXENITE
- 622 POIKILITIC HARZBURGITE
- 571 GRANULAR HARZBURGITE
- 729 PYROXENITE

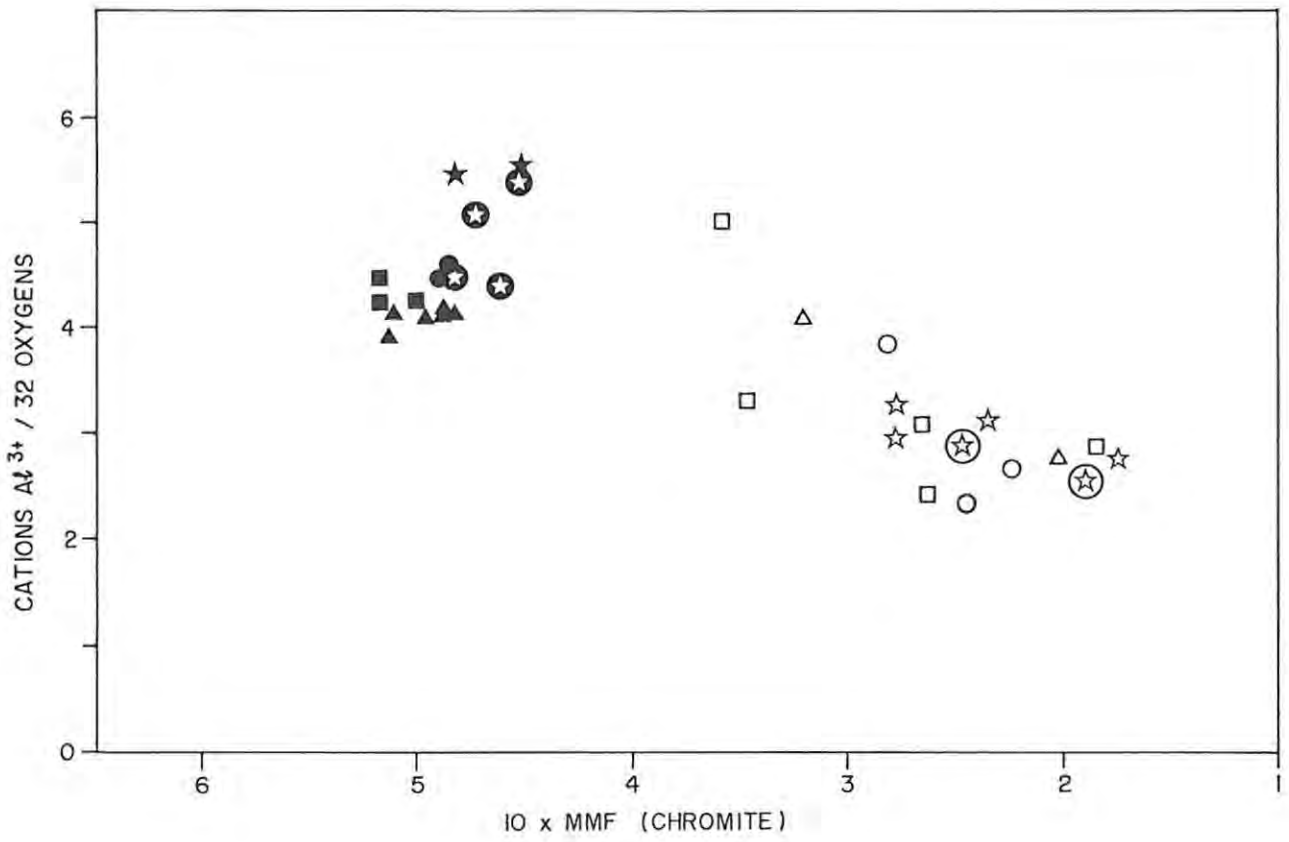

FIG. 74(B) DEPICTION OF CAMERON'S (1977) MICROPROBE DATA OF CHROMITE WITHIN THE B TO F UNITS OF THE CRITICAL ZONE IN THE EASTERN BUSHVELD COMPLEX. RELATIVE TO CHROMITE WITHIN CHROMITITE LAYERS, DISPERSED CHROMITE GRAINS IN SILICATE-RICH ENVIRONMENTS ARE ENRICHED IN Fe_2O_3 AND DEPLETED IN $Aℓ_2O_3$. WITHIN THE CHROMITITE LAYERS, WHERE MMF RATIOS IN EXCESS OF 0,450 ARE DEPICTED, A BETWEEN-LAYER CORRELATION OF RISING Aℓ CONTENT WITH DECLINING MMF RATIO IS EVIDENT.

SYMBOLS: CLOSED SYMBOLS = CHROMITE WITHIN CHROMITITE LAYERS.

- ☆ F UNIT
- ⊛ E UNIT
- ○ D UNIT
- □ C UNIT
- △ B UNIT

— MOOIHOEK PYROXENITE

(1977) indicate (a) chromite of comparable compositions within chromitite layers of the Mooihoek Pyroxenite, and (b) Al_2O_3-depleted compositions within silicate-rich domains, although the levels of Cr_2O_3 are comparable. In summation, it is evident that nucleation of intercumulus plagioclase can induce a compositional change of declining Al/Cr ratios linked to a decline in MMF ratios. This is achieved by (a) reciprocal substitution of Cr for Al, with Fe^{3+} remaining constant, or (b) substitution of Fe^{3+} for Al, with Cr remaining essentially constant. In geological areas where the latter relationship is depicted, chromite within chromitite layers is enriched in Al_2O_3 and depleted in Fe_2O_3 relative to juxtaposed silicate-rich environments. Furthermore, it would seem that lower Al contents and MMF ratios are displayed by disseminated chromite grains in these environments, whereas reciprocal substitution of Cr for Al ultimately yields a minimum Al content due to depletion of Cr in the residual melt volume (this is clearly illustrated in Fig. 73).

7.4.3 RELATIONSHIP BETWEEN $Y_{Fe^{3+}}$ AND $Mg/(Mg + Fe^{2+})$ IN CHROMITE

Based on theoretical considerations, Irvine (1965) concluded that a plot of the relative proportion of Fe^{3+} cations against the MMF ratio in Cr-spinels would reflect whether a particular assemblage of spinel crystals, in equilibrium with olivine and orthopyroxene, formed under increased or decreased fO_2 relative to another (at constant temperature). In principle, increased fO_2 within a magmatic system is reflected by a rise in the magnesioferrite ($MgFe_2O_4$) content of the Cr-spinel solid solution. In a plot of $Y_{Fe^{3+}}$ against MMF ratio, this is conveyed by a sympathetic rise in both parameters. Data pertaining to chromite within chromite- and silicate-rich domains of the B and C_2 units are summarized in Fig. 75. It is evident from the figure that polygonal chromite grains within the LG 2 and LG 3 chromitite layers may have formed under slightly higher fO_2 than chromite within (a) the C layer and LG 3 leader, and (b) bronzitites of the B unit and C_2 subunit. This distinction is not manifested within the C_1 and C_3 subunits, where a range of MMF ratios, linked to a diversity of textural and mineralogical environments, is depicted for an essentially constant level of Fe^{3+} cations. A notable feature

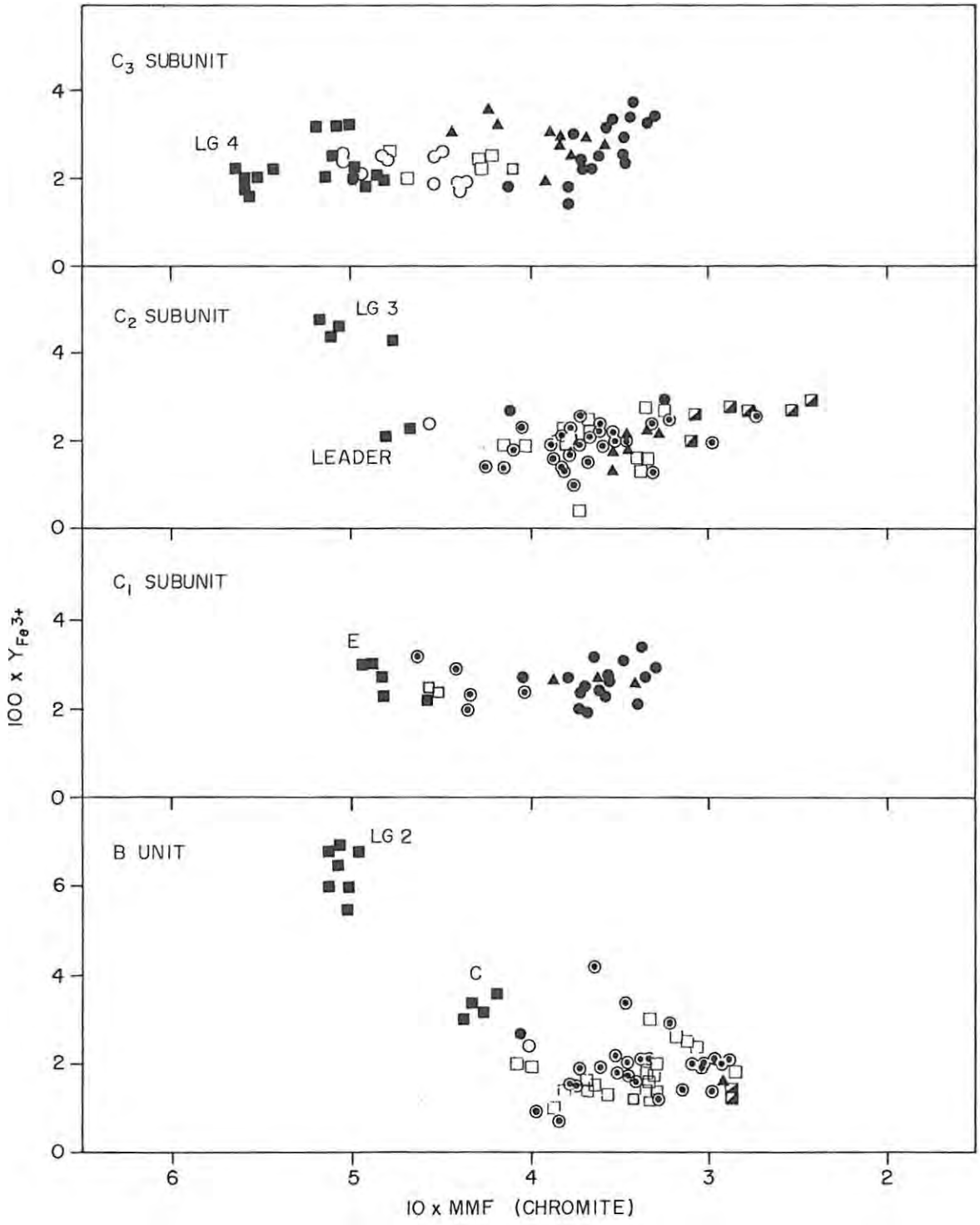

FIG. 75 PLOT OF THE CHROMITE COMPOSITIONAL PARAMETERS $Y_{Fe^{3+}}$ VERSUS MMF RATIO FOR THE B AND C UNITS, DRILL CORE ZS 7. DATA PERTAINING TO THE D AND E UNITS DEPICT A SIMILAR VARIATION.

SYMBOLS:

- ■ CHROMITITES
- ▲ INTERGRANULAR CHROMITE

CHROMITE ENCLOSED IN (⊙) ORTHOPYROXENE; (●) OLIVINE; (○) SECONDARY ORTHOPYROXENE; (□) PLAGIOCLASE; (◪) MICA OR QUARTZ

of the B unit and C_2 subunit is that intergranular chromite grains and grains intergrown with orthopyroxene, plagioclase, mica and quartz display comparable values of Y_{Fe}^{3+}. In general terms, a flat trajectory of rising Y_{Fe}^{3+} with declining MMF ratio is indicated by chromite grains intergrown with orthopyroxene and intercumulus silicate phases in the C_2 subunit. This feature may point to buffered fO_2 conditions in the interstitial melt volume.

The variation of Y_{Fe}^{3+} against MMF ratio in the D_2 subunit of drill core ZS 3 is summarized in Fig. 76. The main feature portrayed in the figure is that the compositional variation of chromite within silicate-rich domains, in relation to increasing stratigraphic height, is linked to a steep trajectory of rising Y_{Fe}^{3+} with declining MMF ratio. This path is subparallel to the theoretically derived oxygen isobars of Irvine (1965) (a depiction of these is available in Eales et al. (1980)), and is subparallel to the evolutionary path displayed by Cr-spinels during later stages of crystallization. It should be stressed, however, that this trajectory is not linked to a cryptic trend of Cr-depletion. By virtue of the between- and within- borehole chemical differences noted above, some considerable doubt is raised as to the importance of increased fO_2 in the formation of chromitite layers.

7.4.4 VARIATION OF TiO_2 AGAINST $Mg/(Mg + Fe^{2+})$ IN CHROMITE

It is timeous at this juncture to reiterate some salient features arising from the present investigation of TiO_2 in chromite as a function of textural and mineralogical environments. Firstly, grain-to-grain microprobe analyses of chromite within the H chromitite layer illustrate a cryptic decline in TiO_2 content upward through the layer, linked to a rise in MMF ratio. Secondly, it was clearly revealed at a number of stratigraphic levels that the TiO_2 contents of small chromite grains, occluded in core domains of well-formed orthopyroxene crystals, are lower than the contents of polygonal chromite grains within chromitite layers. However, the MMF ratios of the former are substantially lower: a feature attributed to advanced subsolidus re-equilibration with the orthopyroxene host. Thirdly, larger chromite grains indented or wholly occluded within

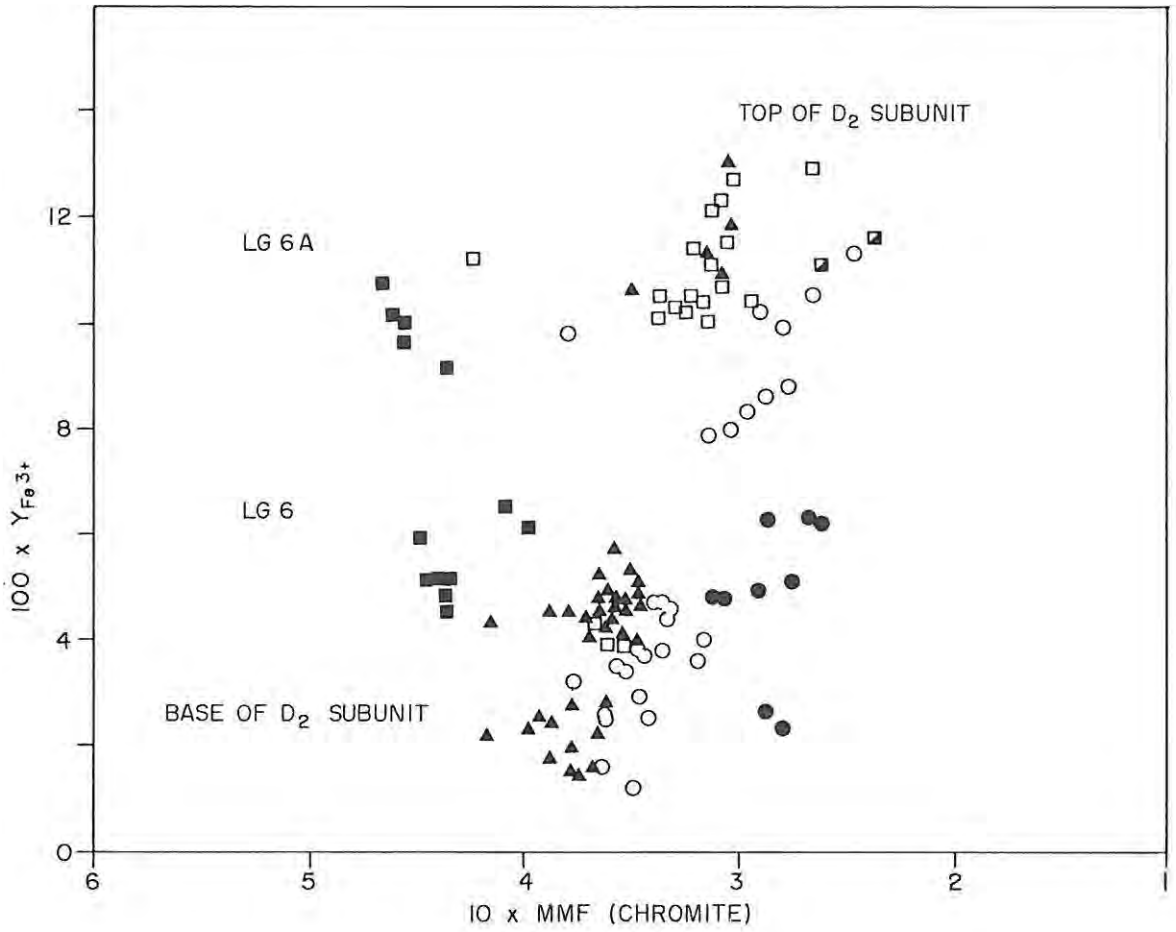

FIG. 76 VARIATION IN THE PROPORTION OF Fe^{3+} CATIONS IN CHROMITE AGAINST MMF RATIOS IN THE D_2 SUBUNIT OF DRILL CORE ZS 3.

SYMBOLS; CHROMITE ENCLOSED IN

- ○ ORTHOPYROXENE
- ● OLIVINE (OF ULTRAMAFIC PEGMATITE ASSOCIATION)
- □ PLAGIOCLASE
- ▨ MICA

- ▲ INTERGRANULAR CHROMITE
- ■ CHROMITITES

orthopyroxene rim-domains depict comparable or higher TiO_2 contents than grains within adjacent layers of massive ore (this feature is only evident in assemblages displaying an appreciable modal proportion of intercumulus plagioclase feldspar). Finally, coarse chromite grains intergrown with plagioclase commonly display (a) crystallographically orientated lamellae of rutile, and (b) high TiO_2 contents in microscopically homogeneous, intracrystalline domains. The MMF ratios of the latter are substantially lower than grains within chromitite layers, but overlap the range of MMF ratios displayed by grains intergrown with orthopyroxene. For descriptive purposes, the variation of TiO_2 against MMF ratios is initially addressed in the subsequent text employing microprobe data from one thin section and from selected samples representative of a limited vertical succession.

Fig. 77 summarizes the link between TiO_2 contents and MMF ratios in sample 70, a mesocumulate-textured bronzitite near the base of the E unit, and the variation within plagioclase dominant bronzitites (i.e., samples depicting intercumulus plagioclase as the predominant intercumulus silicate phase) in the C_2 subunit. It is evident from the data points that (a) grains occluded in orthopyroxene and plagioclase expose a cryptic change of rising TiO_2 contents with a decline in MMF ratios, and (b) there is no obvious chemical path linking chromite within chromitite layers and grains intergrown with silicate phases. This is to be anticipated given that grains intergrown with plagioclase have undergone an extended period of in situ secondary growth, followed by grain homogenization, whereas occlusion in enlarging orthopyroxene crystals ultimately results in a severe decline in Mg content with falling temperature. However, consideration of the compositional variation of chromite within chromitite layers of the Rustenburg Layered Suite provides a key to the disposition of data points in Fig. 77.

The variation of TiO_2 against MMF ratio for chromite within chromitite layers of the Western Bushveld Complex is summarized in Fig. 78, and a clear correlation of rising TiO_2 contents with declining MMF ratios is indicated. The plot is based on a combination of data from de Waal (1975), Eales and Reynolds (1985) and the present study, and encompasses data from a number of

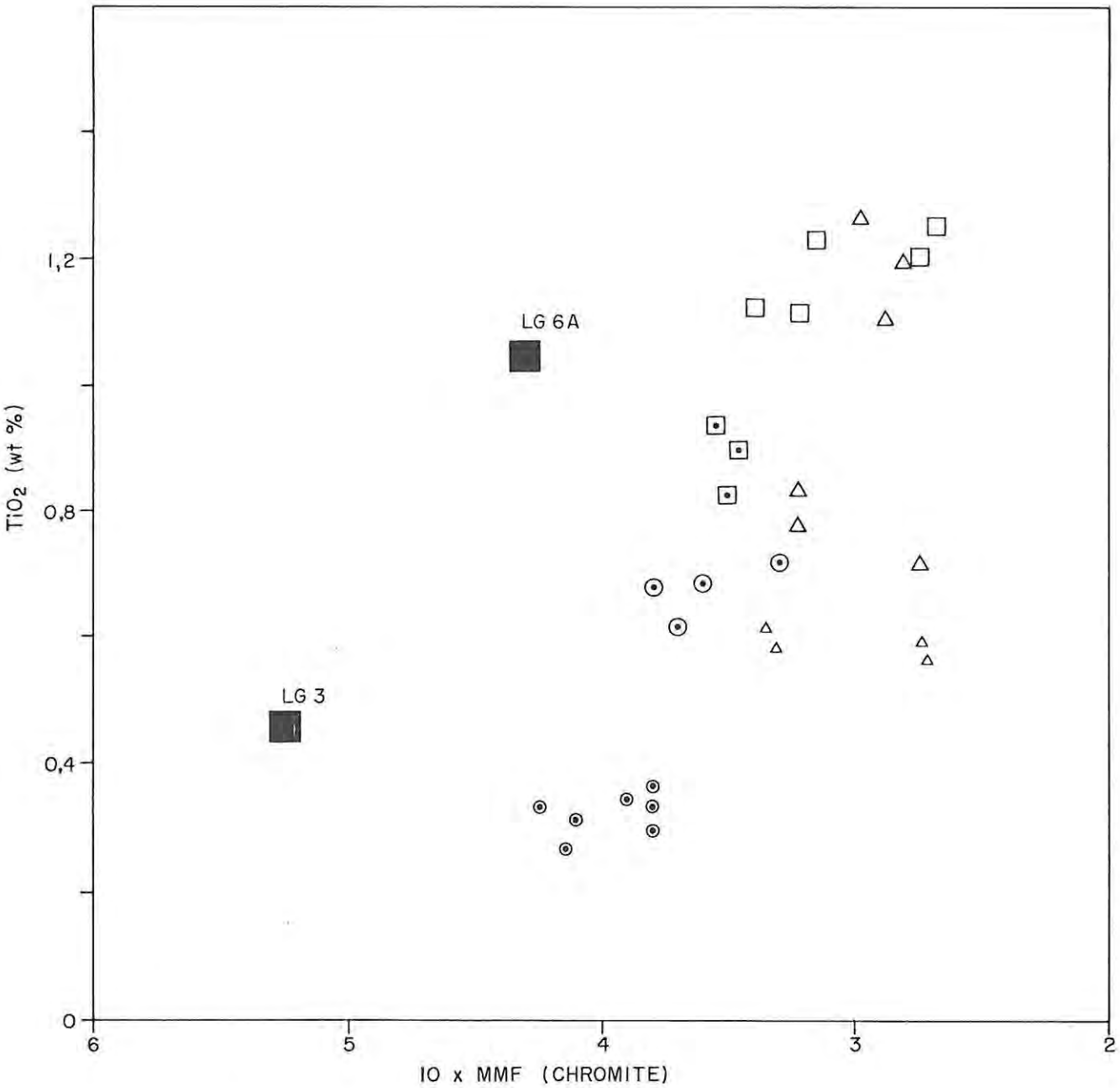

SYMBOLS:

SAMPLE 70
- □ GRAINS IN PLAGIOCLASE
- △ GRAINS IN ORTHOPYROXENE RIM DOMAINS
- △ SMALL, EQUANT GRAINS IN ORTHOPYROXENE CORES

C_2 SUBUNIT
- ⊡ GRAINS IN PLAGIOCLASE
- ⊙ GRAINS IN ORTHOPYROXENE RIM DOMAINS
- ⊙ SMALL, EQUANT GRAINS IN ORTHOPYROXENE CORES

■ CHROMITE WITHIN CHROMITITE LAYERS

FIG. 77 PLOT OF TiO_2 AGAINST $Mg/(Mg + Fe^{2+})$ OF CHROMITE WITHIN SAMPLE 70 AND SELECTED PLAGIOCLASE DOMINANT BRONZITITES IN THE C_2 SUBUNIT.

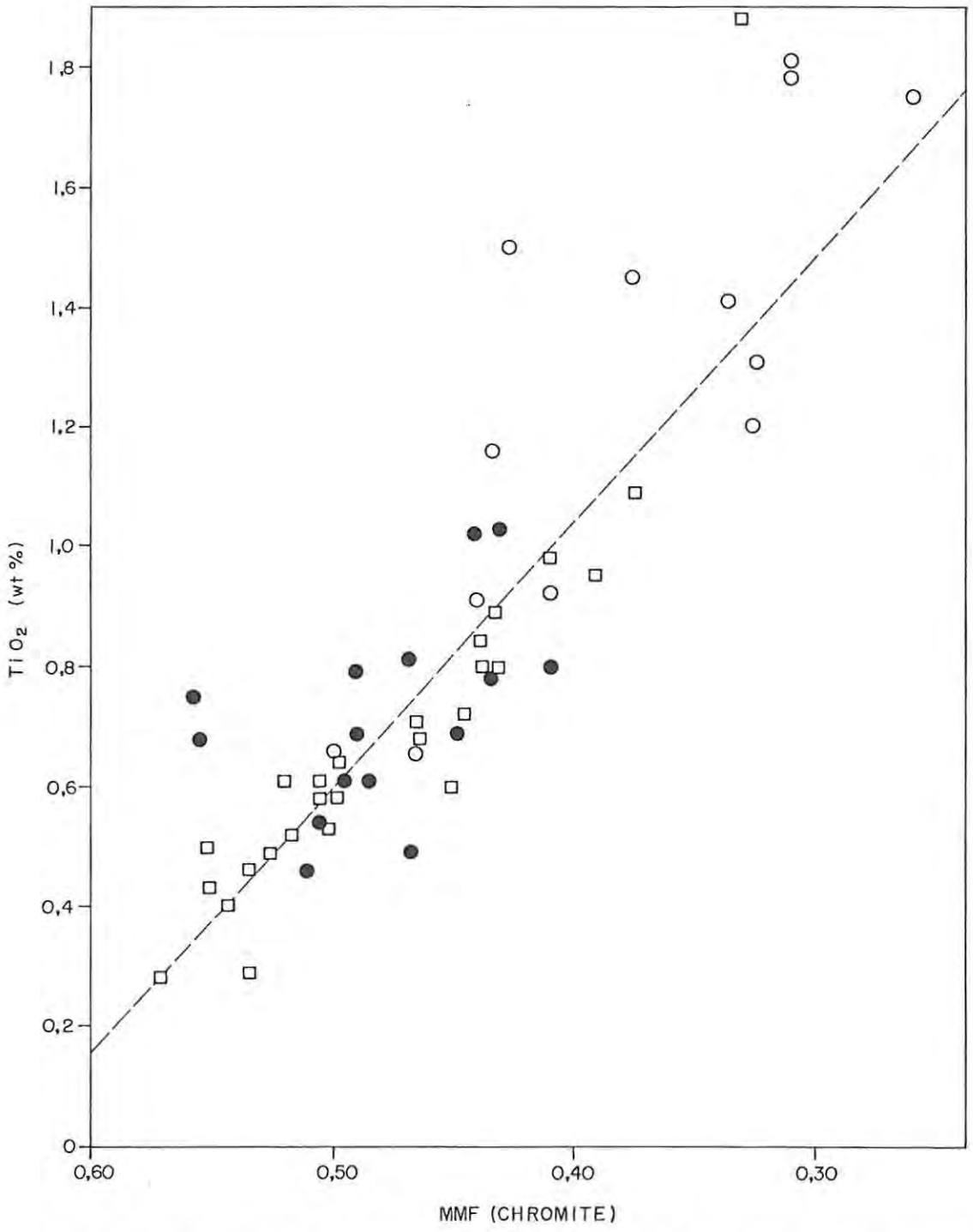

FIG. 78 PLOT OF THE TiO_2 CONTENT OF CHROMITE WITHIN CHROMITITE LAYERS AGAINST MMF RATIO. DATA POINTS ARE REPRESENTATIVE OF MAJOR AND MINOR LAYERS WITHIN THE RUSTENBURG LAYERED SUITE.

SYMBOLS: SOURCE OF DATA:-

- ● PRESENT STUDY (LG1 - LG7)
- □ DE WAAL (1975); BULK ANALYSES OF CLEANED CHROMITITE (WESTERN BUSHVELD COMPLEX)
- ○ EALES & REYNOLDS (1985); CHROMITITE LAYERS WITHIN THE UPPER CRITICAL ZONE, R.P.M. UNION SECTION (UG1 TO THE THIN CHROMITITE LAYER AT THE BASE OF THE BASTARD PYROXENITE)

REGRESSION ANALYSIS OF THE DATA YIELDS THE EQUATION:

$TiO_2 = -4,400.\ MMF + 2,806\ (r = -0,8486)$

geological areas and stratigraphic levels within the layered succession. Significantly, chromite grains intergrown with intercumulus plagioclase in the B and C units of the studied section, for example, yield a correlation of TiO_2 with MMF ratios which is colinear with this trend (Fig. 79A). By implication, grains experiencing an extended residence time in cooling magma and which escape encapsulation by orthopyroxene will follow this chemical path, with the maximum TiO_2 and minimum MMF limits imposed by the magnitude of the subliquidus crystallization interval. Occlusion within ferromagnesian silicate phases arrests this evolution and subsequent subsolidus re-equilibration with the host causes a shift to lower MMF ratios. These features are summarized in Fig. 79(B), where it is suggested that occlusion of chromite grains at an early stage of crystallization yields low TiO_2 contents, whereas continued in situ growth and occlusion at a late stage results in higher TiO_2 contents and lower MMF ratios. In terms of this proposal, it follows that chromite grains within chromitite layers were isolated from magma at a later stage than small, equant crystals enclosed in orthopyroxene core-domains (these are generally less than 60 microns in diameter and, within the B unit and C_2 subunit, yield TiO_2 contents of between 0,20 and 0,40 wt. per cent). Furthermore, it is evident from Fig. 79(B) that (a) the primary liquidus MMF ratio of chromite in the C_2 subunit, with measured TiO_2 contents and MMF ratios of ca. 0,30 wt. per cent and 0,400, respectively, may have been 0,57 (based on the regression equation given in Fig. 78), and (b) the bulk MMF ratio of larger grains occluded within orthopyroxene rim-domains may have declined to ca. 0,49 prior to occlusion.

Relative to the small, orthopyroxene-hosted grains in the C_2 subunit, grains of comparable size and textural environment within sample 70 (base of E unit) yield higher TiO_2 contents and lower MMF ratios (Fig. 77). The latter is consistent with the lower En content of orthopyroxene at this stratigraphic level, and it may be inferred from the disposition of data points in Fig. 77 that a primary liquidus MMF (chromite) ratio of 0,50 - 0,52 was represented. Hence, as shown by the change in orthopyroxene compositions, a cryptic decline in calculated MMF (chromite) initial ratios with increasing stratigraphic height is evident within the upper units of the Ruighoek Pyroxenite.

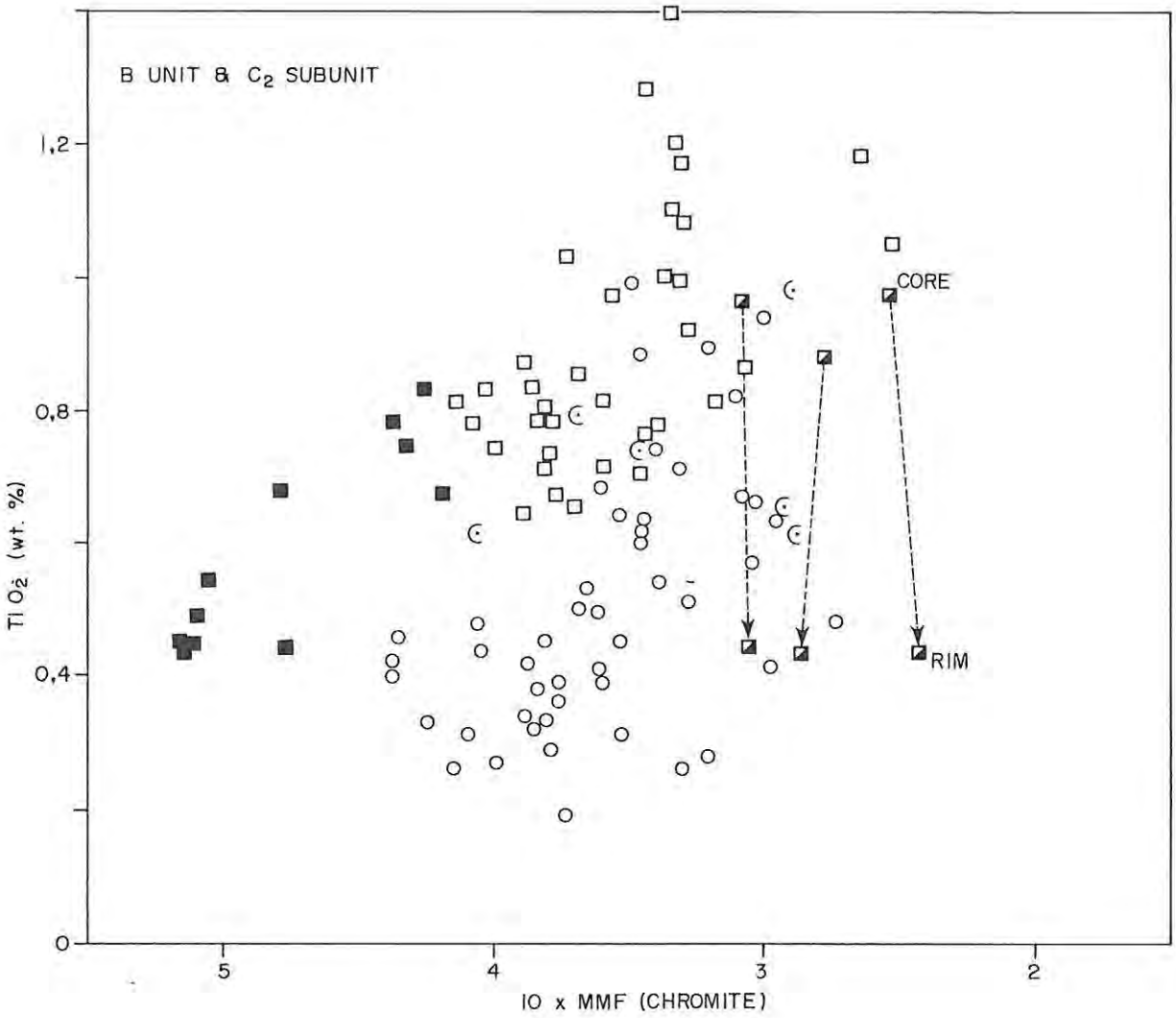

FIG. 79(A) VARIATION OF TiO_2 AGAINST 10 x MMF RATIO FOR CHROMITE GRAINS IN THE B UNIT AND C_2 SUBUNIT. GRAINS INTERGROWN WITH PLAGIOCLASE YIELD A TREND WHICH IS SUBPARALLEL TO THAT DISPLAYED BY GRAINS IN CHROMITITE LAYERS. NOTE THAT GRAINS OCCLUDED BY ORTHOPYROXENE CRYSTALS SHOW LOWER TiO_2 CONTENTS THAN PLAGIOCLASE-HOSTED GRAINS, AND GRAINS INTERGROWN WITH QUARTZ (± MICA) DISPLAY A ZONAL DECLINE IN TiO_2 CONTENTS.

SYMBOLS: CHROMITE IN

- ■ CHROMITITE LAYERS
- ○ ORTHOPYROXENE
- ◔ EMBAYMENTS IN ORTHOPYROXENE GRAIN BOUNDARIES
- □ PLAGIOCLASE
- ◪ QUARTZ

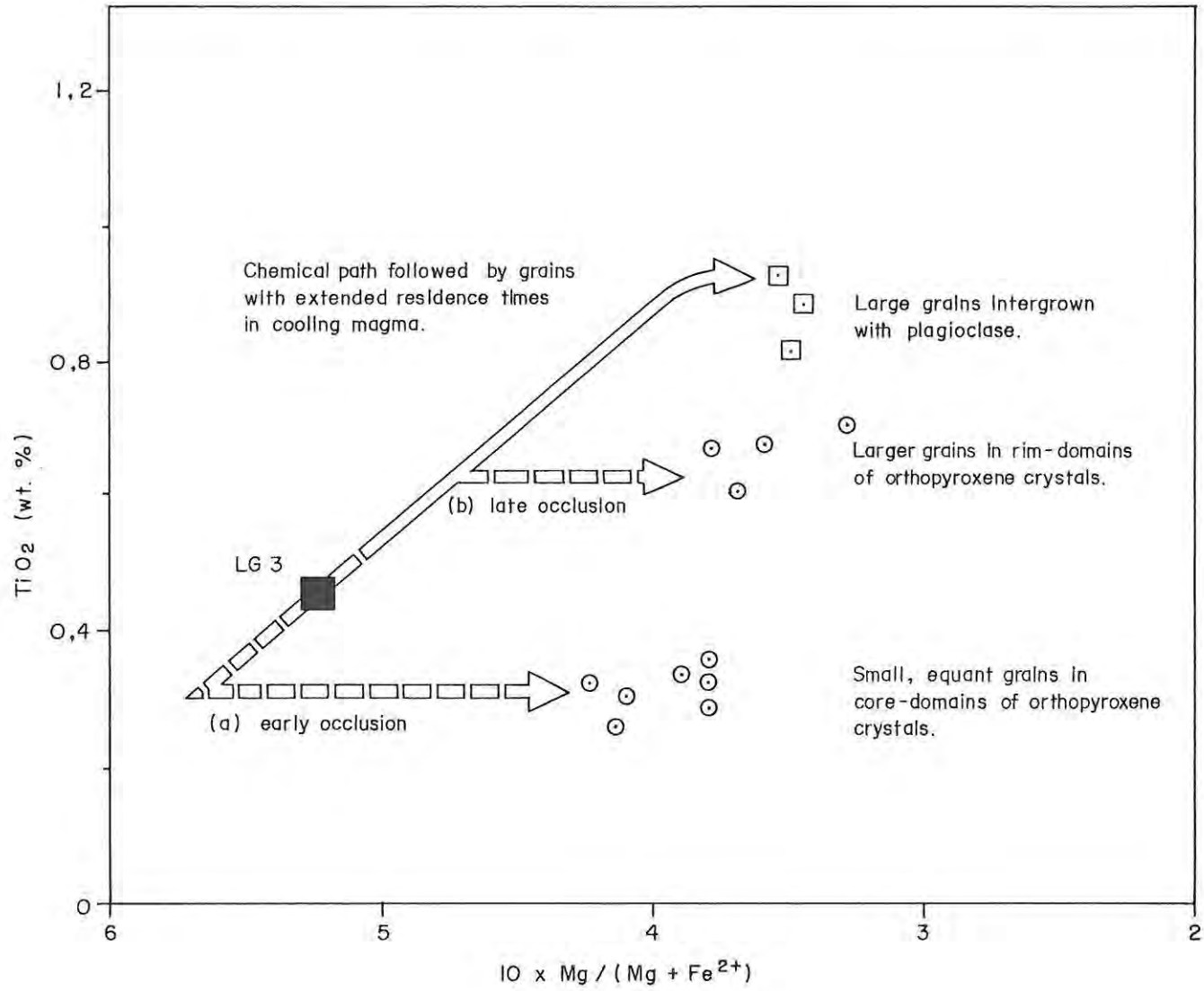

FIG. 79(B) SCHEMATIC RECONSTRUCTION OF DIVERGENT CHEMICAL PATHS FOLLOWED BY CHROMITE GRAINS IF ENCAPSULATED WITHIN ORTHOPYROXENE AT (a) AN EARLY STAGE OF CRYSTALLIZATION, AND (b) LATER STAGES OF CRYSTALLIZATION. NOTE THAT THE SMALLER GRAINS IN POPULATION (a) EXPERIENCE A MORE SEVERE DECLINE IN MMF RATIO WITH COOLING BY VIRTUE OF HIGHER SURFACE AREA/MASS RATIOS. IT IS ASSUMED THAT DIFFUSIVE LOSS OF Ti TO THE ORTHOPYROXENE HOST DOES NOT OCCUR (THIS WOULD BE CONSISTENT WITH THE HIGH IONIC POTENTIAL OF THE SMALL Ti^{4+} CATION).

In summation, the TiO_2 content of chromite is a most significant index of liquidus and sub-liquidus conditions and may be used to calculate the primary liquidus MMF ratio of chromite. This agrees with the conclusion of Hulbert and von Gruenewaldt (1984), who studied the cryptic variation through the Rustenburg Layered Suite south of Potgietersrus, that TiO_2 in chromite is a sensitive indicator of stratigraphic position. However, the present investigation has highlighted a number of physical and compositional parameters to which TiO_2 contents are linked. These obscure the primary cryptic changes in relation to stratigraphic height within the studied section, but it is clear that lateral changes within layers (e.g., as measured within the LG 6A chromitite layer) represent a major and perplexing problem. Until such time as this aspect has been investigated, a given drill core exposure cannot be regarded as definitive.

7.4.5 APPLICATIONS TO GEOTHERMOMETRY

Experimental observations (e.g., of Fisk and Bence (1980)) have conclusively indicated that MMF ratios of chromite in equilibrium with basaltic magma decline with cooling. This exchange of $Fe^{2+} \rightleftharpoons Mg$ between spinel and melt forms the basis of the olivine-chromite geothermometer; the calibration of the geothermometer used in the present text is that given by Roeder et al. (1979), which is expressed as follows:

$$T(K) = \frac{3480Y_{Cr} + 1018Y_{Al} - 1720Y_{Fe^{3+}} + 2400}{2,23Y_{Cr} + 2,56Y_{Al} - 3,08_{Fe^{3+}} - 1,47 + 1,9871n\ K_D}$$

where $K_D = (X_{Mg}/X_{Fe^{2+}})^{olivine} \times (X_{Fe^{2+}}/X_{Mg})^{chromite}$

It is evident from the definition of the equilibrium constant K_D that solid-state, diffusive exchange of Fe^{2+} Mg between chromite and olivine or orthopyroxene in silicate-rich domains will induce a pronounced rise in K_D, thus yielding calculated temperatures which are lower than presumed liquidus temperatures. For example, Fig. 80

is a plot of ln K_D^* against Y_{Cr} at $Y_{Fe^{3+}}$ = 0,05 (as is the convention) for olivine- chromite pairs in the C unit of the studied section. The geotherms portrayed in the figure were calculated from the equation cited above. It is clear from the data points that encapsulated grains in olivine-rich domains yield calculated temperatures which cluster about the 600°C geotherm, whereas coarse grains within chromite-rich domains yield calculated temperatures tending towards 1 000°C (estimates of K_D for the latter association employed average MMF ratios of olivine crystals in adjacent silicate-rich domains). Thus, it may be inferred that the axial spread of data points on the 600°C geotherm is in response to (a) subsolidus re-equilibration to a blocking temperature which is less than 600°C (olivine compositions well-removed from the Mg-enriched boundary conditions were used in the calculations), and (b) varying degrees of reaction with interstitial melt prior to occlusion (only diffusive re-equilibration of Mg and Fe^{2+} cations can occur since Cr, Al and Fe^{3+} cations are not accommodated in the olivine lattice).

Small grains (< 100 microns in diameter) intergrown with coexisting cumulus olivine and orthopyroxene at the base of the C_1 subunit (sample 258) yield calculated temperatures of 620°C and 700°C, respectively. This example serves to illustrate that chromite-orthopyroxene pairs exhibit higher blocking temperatures than chromite-olivine pairs. This feature would thus account for the consistently higher MMF ratios of grains intergrown with orthopyroxene as compared to the MMF ratios of equivalent-size grains encapsulated in olivine. Variations in grain-size give rise to a wide spread in calculated temperatures by virtue of the documented compositional differences, but manipulation of the equation to the geothermometer does yield some indication of primary chromite MMF ratios. For example, assuming that (a) diffusive exchange of Cr and Al with orthopyroxene does not occur under falling temperature, and (b) the measured En contents of orthopyroxene cores approximate to initial primocryst compositions, putative liquidus MMF ratios of small occluded chromite grains in samples 208 and 215 (C_2 subunit) are calculated to be 0,590 and 0,600, respectively, at a liquidus temperature of 1 200°C. A point of interest is that these estimates are in excellent agreement with the previously cited value derived

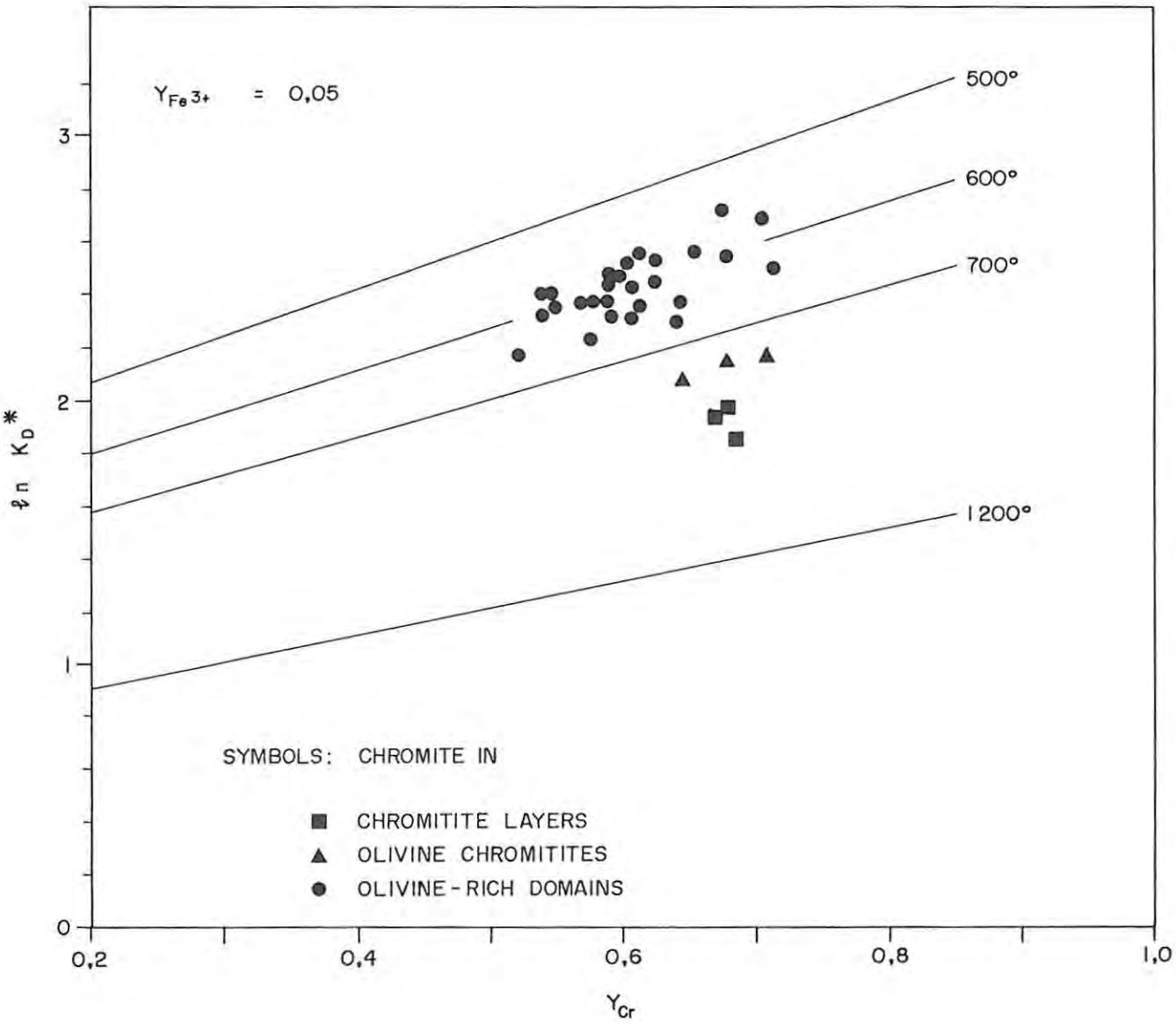

FIG. 80 PLOT OF NORMALIZED ln K_D* AGAINST Y_{Cr} FOR CHROMITE WITHIN THE C_1 AND C_3 SUBUNITS. PLOT NORMALIZED TO $Y_{Fe^{3+}}$ = 0,05 BY ASSUMING A VALUE OF 4,0 FOR THE EQUILIBRIUM CONSTANT IN THE EXCHANGE REACTION (AFTER IRVINE, 1965): $FeAl_2O_4 + MgFe_2O_4 \rightleftharpoons MgAl_2O_4 + Fe_3O_4$

THE NORMALIZED DISTRIBUTION COEFFICIENT K_D* IS CALCULATED ACCORDING TO THE EQUATION: $K_D^* = K_D + 4\,(0,05 - Y_{Fe^{3+}}^{sp})$ ..... (EVANS & FROST, 1975). GEOTHERMS AFTER ROEDER ET AL. (1979).

from the regression equation linking TiO_2 contents and MMF ratios. Selection of a liquidus temperature is arbitrary but, in this instance, a temperature of 1 200°C was assigned since application of the Mercier single-pyroxene geothermometer to whole-rock analyses of fine-grained, granular-textured bronzitites (such as exposed in samples 117, 124, 139 and 312, and which approximate to pure orthopyroxene mineral separates) gave calculated temperatures in the range 1 230°C to 1 285°C. These suppositions thus demand that grains within the LG 3 chromitite layer, with an average MMF ratio of 0,512, equilibrated with an Fe-rich fluid phase prior to effective isolation of the layer from the system by grain annealing. It may be conceived that infiltration of evolved, magmatic residua from the footwall represents a potential source and mechanism by which this is achieved. Intuitively, the efficiency of the equilibration process is dictated by a high melt/chromite ratio, which would also govern the rate of ingress. It thus follows that the origin of the LG 3 chromitite layer may be linked to separation of fractionated residua from the crystal mush in reponse to a pervasively applied shock, for example (the notion of chromite nucleation in response to mixing of footwall-derived, fractionated residua with a new pulse of fresh magma has been tendered by Eales (1985) and Young (1984)).

7.4.6 fO_2 ESTIMATES

No compelling evidence is gained from the present study to support the proposal that periodic fluctuations in fO_2 of the magma may trigger crystallization of chromite. Rather, the analytical data demonstrate that (a) large changes in fO_2, as conveyed via cryptic changes in calculated Fe^{2+}/Fe^{3+} ratios of chromite, correlate with homogeneous bronzitites, and (b) the proportion of Fe^{3+} cations may show a grain-to-grain cryptic rise towards the top contact of a chromitite layer, which is opposite to the envisaged cryptic trend. The intention here is thus to briefly present some quantification of fO_2 conditions using the equation derived by Wilson (1982), which relates Fe^{2+}/Fe^{3+} ratios of chromite to the fO_2 of crystallization.

Calculated estimates of log fO_2 for chromite within chromitite layers in the studied section are summarized in Table 37. It is evident from the calculations that (a) chromite within the succession exposed in drill core ZS 7 exhibits extremely low log fO_2 values, varying between -9,57 and -13,73, (b) chromitites within drill core ZS 3 yield an average log fO_2 of -9,14, which is 3 units higher than the average for all chromitite layers in drill core ZS 7, (c) thin footwall leader layers generally portray crystallization under more reducing conditions than the main layers, whereas hanging-wall leader layers in the gradational upper contacts of the LG 6 and LG 6A reflect a rise in fO_2, and (d) the disparity in fO_2 between the two exposures of the LG 6A chromitite layer is 3 to 5 log units. By comparison, published data pertaining to intrinsic oxygen fugacity measurements on chromite from the LG 3, LG 4 and LG 6 layers on Zwartkop Chrome Mine (Western Bushveld Complex) suggest formation under substantially higher oxygen fugacities. For example, the following results are presented by Snethlage and Klemm (1978):

1. LG 3: $fO_2 = 10^{-5}$ to $10^{-7,6}$
2. LG 4: $fO_2 = 10^{-6,35}$ to $10^{-7,20}$
3. LG 6: $fO_2 = 10^{-6,20}$ to $10^{-7,50}$

Application of Wilson's equation to a selection of their data (Table 1; p. 130) yields:

1. Sample LG 3, + 8,5: $fO_2 = 10^{-7,47}$
2. Sample LG 4, - 6 : $fO_2 = 10^{-6,85}$
3. Sample LG 6, + 40 : $fO_2 = 10^{-7,61}$

These calculated values are in excellent agreement with the ranges measured by Snethlage and Klemm (op. cit.), thereby lending support to use of the equation. However, the strongly reducing environment indicated in the Zandspruit boreholes is anomalous in that experimental studies have shown that crystallization of chromite from basaltic magmas is suppressed at low oxygen fugacities. The obvious conclusion is that the high Fe^{2+}/Fe^{3+} ratios recorded in the stratigaphic succession must stem from some secondary phenomenon. However, it is difficult to conceive that a reducing medium can achieve access to every chromite grain within the diversity of

TABLE 37:

CALCULATED LOG fO_2 FOR CHROMITE WITHIN CHROMITITE LAYERS OF THE STUDIED SECTION, BASED ON THE PROPORTION OF Fe^{2+} AND Fe^{3+} CATIONS PER 32 OXYGEN FORMULA UNIT

LAYER	log fO_2
LG 7	- 13,05
LG 6A	- 11,73 to -13,73
LG 6A (ZS3).HW	- 8,23
LG 6A (ZS3)	- 8,58
LG 6A (ZS3).FW	- 8,48
LG 6 (ZS3).HW	- 10,18
LG 6 (ZS3)	- 10,26
LG 5	- 12,60
LG 5.FW	- 12,82
LG 4	- 13,58
I Layer	- 12,83
H Layer: Top	- 12,43
H Layer: Bottom	- 13,38
LG 3	- 10,53
LG 3.FW	- 12,86
LG 2	- 9,57
C Layer	- 12,24

Drill core ZS 7 unless stipulated.

Log fO_2 calculated according to the equation (Wilson, 1982):

$$\log(Fe^{2+}/Fe^{3+})^{chr} = -0,139 \log fO_2 - 0,741$$

HW: hanging-wall leader layer.

FW: footwall leader layer.

textural and mineralogical environments exposed in drill core ZS 7, or yield the cryptic decline in Fe^{2+}/Fe^{3+} ratios with increasing stratigraphic height in the D_2 subunit of drill core ZS 3. It is thus tentatively submitted that the reduced conditions portrayed by chromite in the studied section (in conjunction with sporadic occurrences of primary magmatic graphite) may reflect distance from a feeder or magma conduit. No attempt is made here to pursue this consideration other than to note that Kinloch (1982) has documented lateral changes in the mineralogy of platinum group element mineralization within the Merensky Reef horizon, and invokes proximity to putative magma feeders to account for contrasted fO_2 conditions (no information pertaining to the mineralogy and structure of the Merensky Reef, e.g., incidence and size of pothole structures within the Footwall unit, in the Zandspruit area is available). In essence, iron-rich platinum group minerals (PGM) rather than sulphide PGM are modelled as being indicative of a relatively oxidizing environment in juxtaposition to magma feeders.

8. ORIGIN OF CHROMITITE LAYERS

Models for chromitite formation in layered complexes aspire to integrate two fundamental features, viz., (a) the considerable lateral extent of individual layers which maintain fairly uniform thicknesses and exhibit only minor perturbations of the layering (e.g., silicate inclusions or partings), and (b) extraction of Cr from large volumes of magma is demanded to yield layers with Cr_2O_3 contents in excess of 45 wt. per cent. Whereas recognition of the former culminated in hypotheses such as fluctuations in fO_2 (Ulmer, 1969) and changes in pressure (Cameron, 1980), the absence of strong Cr-depletion trends in response to fractional crystallization remained a perplexing issue. However, the advent of concepts relating to stratified magma chambers, multiple irruption, double-diffusive convection and magma mixing has given rise to potential solutions to this problem. For example, it is acknowledged that very efficient communication with the magma volume can be achieved via vigorous convection within double-diffusive convection layers, thus sustaining the supply of Cr to the growth site which is presumed to be at or in juxtaposition to the base of a liquid column. The volume of magma in equilibrium with a chromitite layer is thus an important consideration by virtue of the magnitude of D_{Cr}.

The R factor of chromite (Campbell et al., 1983) is defined as:

$$R = \frac{\text{mass of silicate melt}}{\text{mass of chromite}} = \frac{H}{h}$$

where H = thickness of the liquid column from which the layer has precipitated, and h = thickness of the chromitite layer. Modelling submitted by Campbell and Murck (1984) suggests that R for major chromitite layers is in the region of 2 x D_{Cr} to 3 x D_{Cr}. Thus, if D_{Cr} = 1 000, a basal convecting layer some 3 km thick is required. These estimates may decline if D_{Cr} is lower (e.g., in response to fO_2 lower than the QFM buffer) and if the Cr content of the magma is substantially higher than a presumed value of 620 ppm (0,091 wt. per cent Cr_2O_3) at 1 300°C. This Cr content is shown from experimental modelling (Campbell and Murck, op. cit.) to saturate a basaltic melt at 1 300°C, which is inferred to represent an upper crystallization

temperature of chromitite layers. Hence, by way of illustration, a liquid column in equilibrium with the 0,76 m thick LG 6 chromitite exposed in drill core ZS 3, with an estimated Cr_2O_3 content of 47 wt. per cent, is calculated to be 390 m thick. Furthermore, with reference to Table 38, which presents weighted mean Cr_2O_3 contents of units B to E in the studied section, calculation shows that a liquid column 15,8 times the 440 m thick stratigraphic column is required, i.e., ca. 7 km thick.

TABLE 38:

WEIGHTED MEAN Cr_2O_3 CONTENTS OF UNITS B TO E (ZANDSPRUIT)

UNIT	THICKNESS/m	WEIGHTED MEAN Cr_2O_3/wt %
E*	95	1,17
D_2	22	3,22
D_1	112	1,22
C_3	23	2,40
C_2	41	1,29
C_1	14	2,74
B*	134	1,26
TOTAL	441	1,44

E* : top of unit taken 3 m above LG 7 chromitite
B* : base of unit taken 100 m below LG 1 chromitite
TOTAL: weighted mean average for the stratigraphic succession
Average Cr_2O_3 content of bronzitite assigned as 1,05% (n = 40), whereas that for dunite is 1,30% (n = 8).

Though mechanisms such as crystal settling and deposition from chromite-laden density currents have been rejected in the preceding text on the basis of textural features and cryptic compositional changes in relation to stratigraphic height within some chromitite layers, no unequivocal demonstration of cyclic units within the

studied section was achieved. This refers in particular to the envisaged disposition of a chromitite layer at or near the base of a cyclic unit, which would mark the stratigraphic position at which a new magma pulse entered the chamber. However, the rise in orthopyroxene MMF ratios with increasing stratigraphic height through the upper portion of the B unit, reaching a high value within the C unit, is interpreted here as indicative of a new influx of primitive magma entering the chamber. Though this cryptic change is manifested as a gradational feature, recourse is made to upward migration of magmatic residua which act via equilibration to smooth compositional offsets. The saw-tooth, irregular decline in orthopyroxene MMF ratios with increasing stratigraphic height above the C_1 subunit may be representative of a restricted range in magma compositions, and infiltration metasomatism could thus readily achieve effective degrees of homogenization. The subtle variation of trace element levels (e.g., of Ni, V and Sc in hypothetically pure orthopyroxene) appears to be consistent with this premise. A point to be recognized is that fine-grained orthopyroxene crystals in granular-textured bronzitites do not necessarily yield the best estimates of primary liquidus compositions, since the high surface area/mass ratios of small particles induce a marked degree of reactivity (this feature is most conspicuous in small chromite grains within silicate-rich domains). However, the average calculated temperature of 1 255°C (n = 4) derived for whole-rock analyses of these assemblages, absence of zonal structures and restricted within-sample variation in chromite compositions point to early isolation from melt.

It is evident from the weighted mean Cr_2O_3 contents of units B to E (Table 38) that the Cr_2O_3 content of 3,22 wt. per cent within the D_2 subunit is substantially higher than that of other pyroxenite subunits (these appear to define a subtle rise with increasing stratigraphic height from 1,26% in the B unit to 1,29% in the C_2 subunit, followed by a decline to 1,17% in the E unit). Notably, the D_2 subunit overlies an 112 m thick bronzitite succession which exhibits (a) only one chromitite layer, (b) a predominance of fine-grained assemblages and very low modal proportions of mesostasis in the upper portion, and (c) a progressive rise in orthopyroxene crystallinity with increasing stratigraphic height. These features

are not exposed within the C_2 subunit and B unit, for example, and the following question thus arises: is it entirely fortuitous that the thickest Lower Group chromitite layer is developed above a thick vertical column of fine-grained, essentially anchimonomineralic bronzitites, whereas thinner layers such as the LG 2 and LG 3 are developed above thin horizons of granular-bronzitite? By virtue of certain conclusions arising from the study of chromite within the succession (e.g., small grains with primitive TiO_2 contents are preserved by early encapsulation in orthopyroxene, whereas protracted residence times in melt yield coarser particles with evolved TiO_2 contents), the response is tendered here that rapid separation of interstitial melt from a suspension of orthopyroxene primocrysts culminated in (a) fine-grained, granular-textured bronzitites, (b) the progressive decline in orthopyroxene grain-size with increasing stratigraphic height in the footwall of the LG 6 chromitite, and (c) the formation of the LG 6 chromitite layer. It is envisaged that separation of fractionated melt is induced by thermal and/or tectonic shock associated with the ingress of hot, primitive magma into the chamber.

Thus, a suggested model for chromitite formation in the Lower Critical Zone is as follows:

1. Influxes of hot, primitive melt were constrained to spread along the interface between the crystal mush and supernatant magma by virtue of a higher density (Sparks and Huppert, 1984).
2. The upper interface of the new influx is stable, thus limiting the degree of mixing with residua of the previous influx (Huppert and Sparks, 1980). However, very efficient transfer of heat is realized across this interface.
3. Buoyant, fractionated melt exudes from the footwall and mixes with Cr-saturated melt, yielding a hybrid magma that is saturated with respect to chromite.
4. Nucleation and <u>in situ</u> crystallization of chromite is initiated at the basal interface. Steady upward compositional changes in the H chromitite layer, for example, are suggestive of <u>in situ</u> nucleation rather than deposition from density currents. In addition, chromite at the base of this layer is intermediate in

composition between grains at the top of the layer and chromite within the footwall.

5. Vigorous convection within double-diffusive convection layers in the overlying magma ensure sustained supply of Cr to the growing crystals, thus achieving the required high value for R.

Modelling by Campbell and Murck (1984) has revealed that mixing of evolved and primitive melts in the ratio of 1:1 yields the most favourable conditions for the formation of thick chromitite layers. This follows from the strongly concave upwards nature of the curve depicting Cr saturation in basaltic melt plotted against temperature on the abscissa, and the degree of penetration achieved into the field of chromite saturation with a 1:1 mixture. Thus, in conclusion, the limited thickness of all but the LG 6 chromitite layer may stem primarily from exudation of small volumes of footwall contaminant, rather than mixing of large volumes of primitive and mildly fractionated melts. By implication, (a) the volumes of new influxes which gave rise to chromitite layers must be fairly small, and (b) the basal portions of the C_1 and C_3 subunits may have crystallized from influxes of large volumes of olivine-normative primitive melt, followed either by convective overturn and mixing of double-diffusive convection layers or influxes of smaller volumes to yield the Cr_2O_3-rich LG 4, E and I chromitite layers towards the top of these subunits. The relevance of the above considerations may be gauged from Fig. 81, which is a plot of layer thickness against the vertical separation of successive chromite-rich domains. The cohesive relationship portrayed in the figure suggests that contaminating melts were derived from the footwall of new influxes.

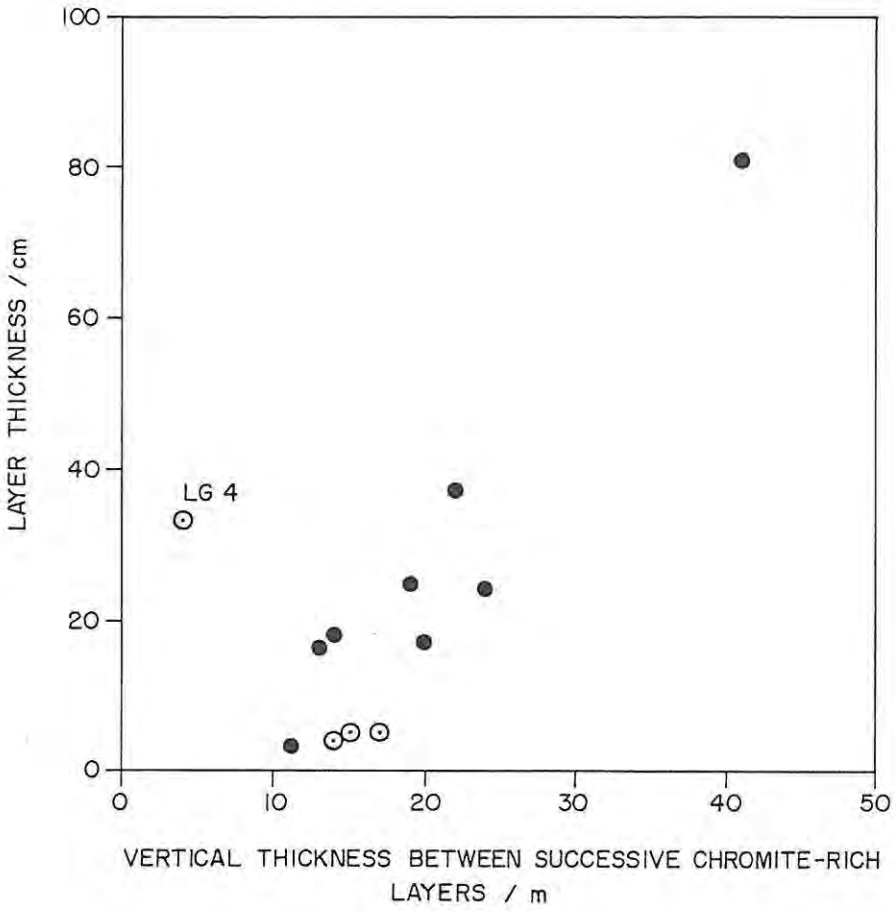

FIG. 81 PLOT OF CHROMITITE THICKNESS AGAINST THE VERTICAL SEPARATION BETWEEN SUCCESSIVE CHROMITE-RICH DOMAINS. THE DISPOSITION OF DATA POINTS SUGGESTS THAT THE THICKNESS OF A LAYER IS LINKED TO THE VOLUME OF CONTAMINATING MELT DERIVED FROM THE FOOTWALL OF A NEW INFLUX.

SYMBOLS:

- ● PYROXENITE - HOSTED LAYERS
- ⊙ DUNITE - HOSTED LAYERS + THE H LAYER

NOTE: (a) THE LG 4 LAYER IS 4m ABOVE THE I LAYER BUT 18m ABOVE THE BASE OF THE C_3 SUBUNIT.

(b) THE LAMINATED LG 5 LAYER IS 84m ABOVE THE LG 4 BUT IS 22m ABOVE THE BASE OF A GRANULAR-TEXTURED SUBUNIT. (THE LATTER VALUE IS PLOTTED HERE).

(c) THE LG 3 IS 20m ABOVE SAMPLE 234 (OLIVINE-BEARING AND CHROMITE-RICH) AND 4m ABOVE AN OLIVINE-CHROMITITE LAYER (SAMPLE 222).

9. SUMMARY

The foregoing text offers a description of the sequence between the LG 1 and LG 7 chromitite layers as exposed on surface, and by drilling, on the farm Zandspruit 168 JP, in the Western Bushveld Complex. The main areas of study included:

(1) **Logging of the succession** as exposed in boreholes ZS 3 and ZS 7, and correlation of this with the known sequence in the area.

(2) **Petrographic studies** of the rock assemblage of orthopyroxenites (bronzitites), harzburgites, dunites and chromitites. Norites and anorthosites are exposed only within higher parts of the succession to which attention was paid.

(3) **Microprobe studies** on 110 polished sections of chromite and silicate phases in various mineral associations. This work yielded analyses of 250 orthopyroxene, 60 clinopyroxene, 120 olivine, and 650 chromite grains, plus analyses of plagioclase, phlogopite, amphibole and silicate inclusions in chromite.

(4) **Geochemical analysis of whole-rock samples.** A total of 62 rocks were analyzed for major elements, Cr and trace elements Sr, Rb, Zr, Y, Nb, Ba, Zn, Cu, Ni, Co, V and Sc. Cr contents of chromite-rich rocks were determined on briquetted powders, with adjusted Mo- Compton mass absorption coefficients used in data reduction (pp. 154-155).

Attention was focussed on the following aspects:

(5) **Grain-size variations within the succession**, employing crystallinity as a reciprocal measure of grain-size. Crystallinity values, representative of the number of cumulus silicate crystals per cm^3 of rock, were derived from counts of the number of orthopyroxene or olivine grains seen within 25 mm^2 blocks drawn on orientated thin sections (p. 39). Plots of crystallinity against stratigraphic height

showed (a) significant variations within the studied section, (b) an element of cyclicity within isomodal sequences of bronzitite [e.g., Fig. 8 (E)], (c) thin horizons of fine-grained, granular-textured rocks overlying coarser-grained, adcumulate-textured rocks in the B unit and C_2 subunit, and (d) a substantial thickness of fine-grained bronzitites in the D unit. The occurrence of fine-grained rocks might appear anomalous in a large plutonic body, but an explanation appears to be expulsion of interstitial melt from orthopyroxene cumulates at early stages of crystallization.

(6) **Cryptic trends in MMF ratios of orthopyroxene and olivine.** MMF ratios of orthopyroxene rise with increasing stratigraphic height in the B unit, reaching high values in the overlying C unit, then decline irregularly through the D and E units. MMF ratios of olivine in dunites exhibit a muted variation in relation to stratigraphic height, but higher ratios are seen in chromite-rich domains and at the respective bases of the C_1 and C_3 subunits, linked to higher Ni contents. Whole-rock Ni contents of bronzitites, corrected for dilution by modal plagioclase, do not decrease systematically with increasing stratigraphic height: Ni contents may rise upwards in finer-grained units. These features are summarized in Fig. 82, which presents a columnar log of the studied succession, with selected analytical data, and a plot of crystallinity against stratigraphic height.

(7) **Technique of regression analysis of selected whole-rock data** to derive trace element levels in hypothetically pure phases [e.g., Sr in plagioclase (p. 166) and V in orthopyroxene (pp. 158-159)]. The data indicate that Sr in plagioclase decreases from 650 ppm in the B and C units to ca. 530 ppm in the D and E units. V in orthopyroxene rises from ca. 90 ppm in the B and C units to 130 ppm in the E unit. Differences in the V content of chromite within the D_2 and C_3 subunits were shown.

(8) **Microprobe studies on cumulus silicate phases.** Excellent agreement was obtained with values derived by regression analysis [e.g., Al_2O_3 in orthopyroxene (p. 166)]. Microprobe analysis of

orthopyroxene indicated (a) higher MMF ratios in chromite-rich domains, (b) zonal structures in chromite-rich domains or towards contacts of impinging chromite grains (p. 75), (c) zonal structures in well-formed crystals within meso- and adcumulate-textured assemblages (p. 76), (d) no detectable zoning in fine-grained, granular-textured rocks, (e) higher Al/Cr ratios in olivine-bearing domains (p. 70), and (f) uniform levels of Cr_2O_3 throughout the succession of bronzitites. Microprobe analysis of olivine indicated that small crystals in chromite-rich rocks are enriched in Ni relative to coarse-grained crystals in juxtaposed, adcumulate-textured dunite (p. 58, Fig. 10). No zonal structures were detected in the latter assemblages.

(9) **Detailed microprobe data on chromite grains** within chromitite layers and grains intergrown with olivine, orthopyroxene and plagioclase. Features arising from this study include:

(a) The hypothesis of <u>in situ</u> grain growth leading to (Fe, Cr, Ti) - enrichment and subsequent diffusive homogenization (pp. 128-130).

(b) Notable differences in composition and compositional variability of chromite within massive chromitite layers relative to accessory chromite.

(c) Grains within fine-grained, granular-textured rocks exhibit (i) a more restricted compositional range, and (ii) Cr_2O_3 - depleted compositions relative to coarser-grained assemblages with higher modal proportions of mesostasis (Fig. 82).

(d) The lack of zoning within polygonal-textured grains in chromitite layers and small, euhedral grains occluded in orthopyroxene and olivine, whereas zoning is detectable in large grains intergrown with plagioclase, mica and quartz.

(e) Absence of clear-cut correlations between composition and stratigraphic height (Fig. 82), but a within-sample correlation with grain-size is evident (p. 147; Fig. 49).

(f) Chromite grains in chromite-poor, olivine-bearing domains are substantially enriched in Al_2O_3 (p. 131).

REFERENCES

Akella, J., Williams, R.J. and Mullins, O. (1976). Solubility of Cr, Ti and Al in coexisting olivine, spinel and liquid at 1 atm. Proc. 7th Lunar Sci. Conf., 1179 - 1194.

Arndt, N.T. (1977). The partitioning of nickel between olivine and ultrabasic and basic komatiite liquids. Carnegie Inst. Washington Yearbook, 76, 553 - 557.

Basaltic Volcanism Study Project (1981). Basaltic Volcanism on the Terrestrial Planets (section 1.3, p. 311 - 434). Pergamon Press, New York, 1286p.

Basu, A.R. and MacGregor, I.D. (1975). Chromite spinels from ultramafic xenoliths. Geochim. Cosmochim. Acta, 39, 937 - 945.

Bevan, J.C. (1982). Reaction rims of orthopyroxene and plagioclase around chrome spinels in olivine from Skye and Rhum (NW Scotland). Contrib. Mineral. Petrol.,79, 124 - 129.

Bichan, R. (1969). Origin of chromite seams in the Hartley Complex of the Great Dyke, Rhodesia. In: Wilson, H.D.B. (Ed.), Magmatic Ore Deposits. Econ. Geol. Monogr., 4, 95 - 113.

Boctor, N.Z. (1982). The effect of fO_2, fS_2 and temperature on Ni partitioning between olivine and iron sulphide melts. Carnegie Inst. Washington, Ann. Rept. Dir. Geophys. Lab. 1981-82, 366 - 369.

Bottinga, Y. and Weill, D.F. (1972). The viscosity of magmatic silicate liquids: a model for calculation. Amer. J. Sci., 272, 438 - 475.

Brandeis, G., Jaupart, C. and Allegre, C.J. (1984). Nucleation, crystal growth and the thermal regime of cooling magmas. J. Geophys. Res., 89, 1Ø,161 - 1Ø,177.

Bristow, D.M. and Wilson, A.H. (1983). The origin of ultramafic pegmatoid bodies in the Eastern Bushveld Complex. Symposium on the Bushveld Complex, Programme with Abstracts, Univ of Pretoria, 1 -2.

Brown, G.E. (198Ø). Olivines and silicate spinels. In: Ribbe, P.H. (Ed.), Reviews in Mineralogy, vol.5, Orthosilicates, Mineral. Soc. Amer.

Buddington, A.F. and Lindsley, D.H. (1964). Iron - titanium oxide minerals and synthetic equivalents. J. Petrol., 5, 31Ø - 357.

Burnham, C.W. (1979). The importance of volatile constituents, 439 - 482. In: Yoder, H.S. (Ed.), The evolution of the igneous rocks: Fiftieth Anniversary Perspectives. Princeton Univ. Press, New Jersey, 588p.

Bunch, T.E. and Olsen, E. (1975). Distribution and significance of chromium in meteorites. Geochim. Cosmochim. Acta, 39, 911 - 927.

Buntin, T.J., Grandstaff, D.E., Ulmer, G.C. and Gold, D.P. (1983). A pilot study of geochemical and redox relationships between potholes and adjacent normal Merensky Reef of the Bushveld Igneous Complex. Symposium on the Bushveld Complex, Programme with Abstracts, Univ. of Pretoria, 5 - 8.

Burns, R.G. (1970). Mineralogical applications of crystal field theory. Cambridge Univ. Press, 224p.

---------- (1975a). Crystal field effects in chromium and its partitioning in the mantle. Geochim. Cosmochim. Acta, 39, 857 - 864.

---------- (1975b). On the occurrence and stability of divalent chromium in olivines included in diamond. Contrib. Mineral. Petrol., 51, 213 - 221.

---------- (1976). Partitioning of transition metals in mineral structures of the mantle. In: Strens, R.G.J. (Ed.), The Physics and Chemistry of Minerals and Rocks, 555 - 572.

Burns, V.M. and Burns R.G. (1975). Mineralogy of chromium. Geochim. Cosmochim. Acta, 39, 903 - 910.

Cameron, E.N. (1964). Chromite deposits of the eastern part of the Bushveld Complex. In: Haughton, S.H. (Ed.), The Geology of some ore deposits of Southern Africa. Geol. Soc. S. Afr., 2, 131 - 168.

---------- (1969). Postcumulus changes in the Eastern Bushveld Complex. Amer. Mineral., 54, 754 - 779.

---------- (1970). Compositions of certain coexisting phases in the eastern part of the Bushveld Complex. Geol. Soc. S. Afr. Spec. Publ., 1, 46 - 58.

---------- (1975). Postcumulus and subsolidus equilibration of chromite and coexisting silicates in the Eastern Bushveld Complex. Geochim. Cosmochim. Acta, 39, 1021 - 1033.

---------- (1977). Chromite in the central sector of the Eastern Bushveld Complex, South Africa. Amer. Mineral., 62, 1082 - 1096.

---------- (1978). The Lower Zone of the Eastern Bushveld Complex in the Olifants River Trough. J. Petrol., 19, 437 - 462.

---------- (1979). Titanium - bearing oxide minerals of the Critical Zone of the Eastern Bushveld Complex. Amer. Mineral., 64, 14Ø - 15Ø.

---------- (198Ø). Evolution of the Lower Critical Zone, Central Sector, Eastern Bushveld Complex, and its chromite deposits. Econ. Geol., 75, 845 - 871.

---------- and Desborough, G.A. (1969). Occurrence and characteristics of chromite deposits - Eastern Bushveld Complex. In: Wilson, H.D.B. (Ed.), Magmatic Ore Deposits. Econ. Geol. Monogr., 4, 23 - 4Ø.

---------- and Emerson, M.E. (1959). The origin of certain chromite deposits of the eastern part of the Bushveld Complex. Econ. Geol., 54, 1151 - 1213.

Cameron, M. and Papike, J.J. (1981). Structural and chemical variations in pyroxenes. Amer. Mineral., 66, 1 - 5Ø.

Campbell, I.H. (1975). Direct evidence of present-day serpentinization in the Jimberlana Intrusion. Geol. Mag., 112, 77 - 8Ø.

---------- (1977). A study of macro-rhythmic layering and cumulate processes in the Jimberlana Intrusion, Western Australia. Part 1: The Upper Layered Series. J.Petrol., 18, 183 - 215.

---------- (1978). Some problems with the cumulus theory. Lithos, 11, 311-323.

---------- and Borley, G.D. (1974). The geochemistry of pyroxenes from the Lower Layered Series of the Jimberlana Intrusion, Western Australia. Contrib. Mineral. Petrol., 47, 281 - 298.

---------- and Murck, B.W. (1984). A model for chromite seams in layered intrusions. In press.

---------- Naldrett, A.J. and Barnes, S.J. (1983). A model for the origin of the platinum-bearing sulfide horizons of the Bushveld and Stillwater Complexes. J.Petrol., 24, 133 - 165.

Cawthorn, R.G. (198Ø). High-MgO Karroo tholeiite and the formation of Nickel - Copper Sulphide mineralization in the Insizwa Intrusion, Transkei. S. Afr. J. Sci., 76, 467 - 471.

---------- (1982). An origin of small-scale fluctuations in orthopyroxene composition in the lower and critical zones of the Bushveld Complex, South Africa. Chem. Geol., 36, 227 - 236.

---------- Biggar, G.M., Graham, C.M., Graham, A., Ford, C.E., Sharpe, M.R. and Davies, G. (1979). Experimental petrological data on the parental magmas to the Bushveld Complex. Inst. Geol. Res. Bushveld Complex, Univ. of Pretoria, Res. Report 18, 27p.

---------- McCarthy, T.S. and Davies, G. (1983). Vertical chemical gradients in a single grain of magnetite from the Bushveld Complex, South Africa. Mineral. Mag., 47, 27 - 34.

Coble, R.L. and Burke, J.E. (1963). Sintering in ceramics. In: Burke, J.E. (Ed.), Progress in Ceramic Science, 3. Pergamon Press, London, 194 - 251.

Cousins, C.A. (1964). The platinum deposits of the Merensky Reef. In: Haughton, S.H. (Ed.), The Geology of some ore deposits in Southern Africa. Geol. Soc. S. Afr., 2, 225 -237.

---------- (1969). The Merensky Reef of the Bushveld Igneous Complex. In: Wilson, H.D.B. (Ed.), Magmatic Ore Deposits. Econ. Geol. Monogr., 4, 239 - 251.

---------- and Feringa, G. (1964). The chromite deposits of the Western Belt of the Bushveld Complex. In: Haughton, S.H. (Ed.), The Geology of some ore deposits in Southern Africa. Geol. Soc. S. Afr., 2, 183 - 202.

Davies, G., Cawthorn, R.G., Barton, J.M. and Morton, M. (1980). Parental magma to the Bushveld Complex. Nature, 287, 33 - 35.

Deer, W.A., Howie, R.A. and Zussman, J. (1962). Rock-forming minerals vol.5, Non-silicates. Longmans, 371p.

---------- (1982). Rock-forming minerals vol.1A, Orthosilicates. Longmans, 919p.

De Klerk, W.J. (1981). The geology, geochemistry and silicate mineralogy of the Upper Critical Zone of the North-Western Bushveld Complex, at Rustenburg Platinum Mines, Union Section. Unpubl. M.Sc. thesis, Rhodes Univ., 210p.

De Waal, S.A. (1975). Mineralogy, chemistry and certain aspects of reactivity of chromitite from the Bushveld Igneous Complex. South African National Institute for Metallurgy, Report 1709, 80p.

Dick, H.J.B. (1977). Partial melting in the Josephine Peridotite. Amer. J. Sci., 277, 801 - 832.

Dickey, J.S. and Yoder, H.S. (1972). Partitioning of chromium and aluminium between clinopyroxene and spinel. Carnegie Inst. Washington Yearbook, 71, 384 - 392.

Donaldson, C.H. (1977). Laboratory duplication of comb layering in the Rhum pluton. Mineral. Mag., 41, 323 - 336.

---------- (1979). An experimental investigation of the delay in nucleation of olivine in mafic magmas. Contrib. Mineral. Petrol., 69, 21 -32.

---------- and Brown, R.W. (1977). Refractory megacrysts and magnesium-rich melt inclusions within spinel in oceanic tholeiites: indicators of magma mixing and parental magma composition. Earth Planet. Sci. Lett., 37, 81 - 89.

Duke, J.M. (1983). Ore deposit models 7: Magmatic segregation deposits of chromite. Geoscience Canada, 10, 15 - 24.

--------- and Naldrett, A.J. (1978). A numerical model of the fractionation of olivine and molten sulphide from komatiite magma. Earth Planet. Sci. Lett., 39, 255 - 266.

Eales, H.V. (1979). Anomalous Karroo spinels along the chromite-titanomagnetite join. S. Afr. J. Sci., 75, 24 -29.

---------- (1980). Contrasted trace-element variations in two Karroo cumulus complexes. Chem. Geol., 29, 39 - 48.

---------- (1985). Features and genetic significance of chromitite layers in the Upper Critical Zone. In: Stowe, C.W. (Ed.), Guidelines to the evolution of chromite ore-fields. Stroudsberg, P.A., Hutchinson and Ross (in press).

---------- and Marsh, J.S. (1979). High-MgO tholeiitic rocks and their significance in the Karroo Central Province. S. Afr. J. Sci., 75, 400 - 404.

-------------------------- (1983). Al/Cr ratios of coexisting pyroxenes and spinellids in some ultramafic rocks. Chem. Geol., 38, 57 - 74.

---------- and Reynolds, I.M. (1983). Factors influencing the composition of chromite and magnetite in some Southern African rocks. Geol. Soc. S. Afr. Spec. Publ., 7, 5 - 20.

---------------------------- (1985). Cryptic variations within chromitites of the Upper Critical Zone, Northwestern Bushveld Complex. In press.

---------- and Snowden, D.V. (1979). Chromiferous spinels of the Elephant's Head Dike. Mineral. Deposita, 14, 227 - 242.

---------- Mitchell, A.A. and Botha, M.J. (1984). Partitioning of Cr, V, Ti, Co and Ni between silicate and oxide phases within sections of the Western Bushveld Complex. National Geoscience Programme, C.S.I.R., Pretoria, Open File Report.

---------- Reynolds, I.M. and Gouws, D.A. (198Ø). The spinel-group minerals of the Central Karoo tholeiitic province. Trans. Geol. Soc. S. Afr., 83, 243 -253.

Eckstrand, O.R. (1975). The Dumont Serpentinite: a model for control of nickeliferous opaque mineral assemblages by alteration reactions in ultramafic rocks. Econ. Geol., 7Ø, 183 - 2Ø1.

El Goresy, A. (1976). Oxide minerals in lunar rocks. In: Rumble, D. (Ed.), Oxide Minerals. Mineral. Soc. Amer., EG1 - 72.

---------- Prinz, M. and Ramdohr, P. (1976). Zoning in spinels as an indicator of the crystallization histories of Mare basalts. Proc. 7th Lunar Sci. Conf., 1261 - 1279.

Evans, B.W. and Frost, B.R. (1975). Chrome-spinel in progressive metamorphism - a preliminary analysis. Geochim. Cosmochim. Acta, 39, 959 - 972.

Fisk, M.R. and Bence, A.E. (198Ø). Experimental crystallization of chrome spinel in Famous Basalt 527-1-1. Earth Planet. Sci. Lett., 48, 111 - 123.

Fockema, R.A.P. and Mendelssohn, E. (1954). Note on an unusual occurrence of chromite in the Eastern Bushveld. Trans. Geol. Soc. S. Afr., 57, 77 - 82.

Ford, C.E., Russel, D.G., Craven, J.A. and Fisk, M.R. (1983). Olivine-liquid equilibria: temperature, pressure and composition dependence of the crystal/liquid cation partition coefficients for Mg, Fe^{2+}, Ca and Mn. J. Petrol., 24, 256 - 265.

Frey, F.A., Green, D.H. and Roy, S.D. (1978). Integrated models of basalt petrogenesis: a study of quartz tholeiites to olivine melilites from south eastern Australia utilizing geochemical and experimental petrological data. J. Petrol., 19, 463 - 513.

Fujii, T. (1976). Solubility of Al_2O_3 in enstatite coexisting with forsterite and spinel. Carnegie Inst. Washington Yearbook, 75, 566 - 571.

-------- (1977). Fe - Mg partitioning between olivine and spinel. Carnegie Inst. Washington Yearbook, 76, 563 - 569.

Gibb, F.G.F. (1974). Supercooling and the crystallization of plagioclase from a basaltic magma. Mineral. Mag., 39, 641 - 653.

Green, D.H. (1964). The petrogenesis of the high-temperature peridotite intrusion in the Lizard area, Cornwall. J. Petrol., 5, 134 - 188.

Grove, T.L. and Bence, A.E. (1977). Experimental study of pyroxene - liquid interaction in quartz-normative basalt 15597. Proc. 8th Lunar Sci. Conf., 1549 - 79.

Groves, D.I., Barrett, F.M., Binns, R.A. and McQueen, K.G. (1977). Spinel phases associated with metamorphosed volcanic-type iron-nickel sulfide ores from Western Australia. Econ. Geol., 72, 1224 -1244.

Haggerty, S.E. (1976). Opaque mineral oxides in terrestrial igneous rocks. In: Rumble, D. (Ed.), Oxide Minerals. Mineral. Soc. Amer., Hg1Ø1 - 277.

Hamilton, J. (1977). Sr Isotope and trace element studies of the Great Dyke and Bushveld Mafic Phase and their relation to early Proterozoic magma genesis in Southern Africa. J. Petrol., 18, 24 - 52.

Hamlyn, P.R. and Keays, R.R. (1979). Origin of chromite compositional variation in the Panton Sill, Western Australia. Contrib. Mineral. Petrol., 69, 75 - 82.

Hart, S.R. and Davis, K.E. (1978). Nickel partitioning between olivine and silicate melt. Earth Planet. Sci. Lett., 4Ø, 2Ø3 - 219.

Hatton, C.J. and von Gruenewaldt, G. (1982). Inst. Geol. Res. Bushveld Complex, Univ. of Pretoria, Ann. Report 1981, 4 - 8.

---------- (1984). Chromite from the Zwartkop chrome mine - an estimate of the effects of subsolidus reequilibration. Inst. Geol. Res. Bushveld Complex, Univ. of Pretoria, Res. Report 49, 42p.

Hawkes, D.D. (1967). Order of abundant crystal nucleation in a natural magma. Geol. Mag., 1Ø4, 473 - 486.

Heinrich, K.F.J. (1966). X-ray absorption uncertainty. In: McKinley, T.D., Heinrich, K.F.J. and Wittry, D.B. (Eds.), The Electron Microprobe. J. Wiley and Sons, New York, 269 - 377.

Henderson, P. (1975). Reaction trends shown by chrome-spinels of the Rhum layered intrusion. Geochim. Cosmochim. Acta, 39, 1035 -1044.

Henderson, P. and Suddaby, P. (1971). The nature and origin of chrome-spinel of the Rhum layered complex. Contrib. Mineral. Petrol., 33, 21 - 31.

---------- and Wood, R.J. (1981). Reaction relationships of chrome-spinels in igneous rocks - Further evidence from the layered intrusions of Rhum and Mull, Inner Hebrides, Scotland. Contrib. Mineral. Petrol., 78, 225 - 229.

Henry, D.J. and Medaris, L.G. (1980). Application of pyroxene and olivine-spinel geothermometers to spinel peridotites in south western Oregon. Amer. J. Sci., 280-A, 211 - 231.

Hervig, R.L. and Smith, J.V. (1982). Temperature - dependent distribution of Cr between olivine and Pyroxenes in lherzolite xenoliths. Contrib. Mineral. Petrol. 81, 184 - 189.

Hess, P.C. (1980). Polymerization model for silicate melts. In: Hargraves, R.B. (Ed.), Physics of Magmatic Processes. Princeton Univ. Press, 3 - 46.

Hill, R. and Roeder, P.L. (1974). Crystallization of spinel from basaltic liquid as a function of oxygen fugacity. J. Geol., 82, 709 - 729.

Huebner, J.S., Lipin, B.R. and Wiggins, L.B. (1976). Partitioning of chromium between silicate crystals and melts. Proc. 7th Lunar Sci. Conf., 1195 - 1220.

Hulbert, L.J. (1983). A petrological investigation of the Rustenburg Layered Suite and associated mineralization south of Potgietersrus. Unpub. Ph.D thesis, Univ. of Pretoria, 511p.

Huppert, H.H. and Sparks, R.S.J. (1980). The fluid dynamics of a basaltic magma chamber replenished by influx of hot, dense ultrabasic magma. Contrib. Mineral. Petrol., 75, 279 - 289.

Hulbert, L.J. and von Gruenewaldt, G. (1980). The structure and petrology of the upper and lower chromitite layers on the farms Grasvally and Zoetveld, south of Potgietersrus. Inst. Geol. Res. Bushveld Complex, Univ. of Pretoria, Res. Report 21, 37p.

---------- (1984). Textural and compositional features of chromite in the Lower and Critical Zones of the Bushveld Complex south of Potgietersrus. Inst. Geol. Res. Bushveld Complex, Univ. of Pretoria, Res. Report 44, 46p.

Irvine, T.N. (1965). Chromian spinel as a petrogenetic indicator, Part 1. Theory. Can. J. Earth Sci., 2, 648 - 672.

---------- (1967). Chromian spinel as a petrogenetic indicator, Part 2. Petrologic applications. Can. J. Earth Sci., 4, 71 - 103.

---------- (1970). Heat transfer during solidification of layered intrusions 1. Sheets and sills. Can. J. Earth Sci., 7, 1031 - 1061.

---------- (1975). Crystallization sequences in the Muskox intrusion and other layered intrusions - II. Origin of chromitite layers and similar deposits of other magmatic ores. Geochim. Cosmochim. Acta, 39, 991 - 1020.

---------- (1977a). Chromite crystallization in the join Mg_2SiO_4 - $CaMgSi_2O_6$ - $CaAl_2Si_2O_8$ - $MgCr_2O_4$ - SiO_2. Carnegie Inst. Washington Yearbook, 76, 465 - 472.

---------- (1977b). The origin of chromitite layers in the Muskox Intrusion and other stratiform intrusions: a new interpretation. Geology, 5, 273 - 277.

---------- (1978). Infiltration metasomatism, adcumulus growth and secondary differentiation in the Muskox Intrusion. Carnegie Inst. Washington Yearbook, 77, 743 - 751.

---------- (1980a). Magmatic density currents and cumulus processes. Amer. J. Sci., 280-A, 1 - 58.

---------- (1980b). Magmatic infiltration metasomatism, double-diffusive fractional crystallization and adcumulus growth in the Muskox intrusion and other layered intrusions. In: Hargraves, R.B. (Ed.), Physics of Magmatic Processes. Princeton Univ. Press, 325 - 383.

---------- (1981). A liquid-density controlled model for chromitite formation in the Muskox Intrusion. Carnegie Inst. Washington Yearbook, 80, 317 - 324.

---------- (1982). Terminology for layered intrusions. J. Petrol., 23, 127 - 162.

---------- and Kushiro, I. (1976). Partitioning of Ni and Mg between olivine and silicate liquids. Carnegie Inst. Washington Yearbook, 75, 668 - 675.

---------- Keith, D.W. and Todd, S.G. (1983). The J-M platinum-palladium reef of the Stillwater Complex, Montana. II: Origin by double-diffusive convective magma mixing and implications for the Bushveld Complex. Inst. Geol. Res. Bushveld Complex. Univ. of Pretoria, Res. Report 43, 93p.

Irving, A.J. (1978). A review of experimental studies of crystal/liquid trace element partitioning. Geochim. Cosmochim. Acta, 42, 743 - 77Ø.

Jackson, E.D. (1961). Primary textures and mineral associations in the ultramafic zone of the Stillwater Complex, Montana. U.S. Geol. Surv. Prof. Pap., 358, 1Ø6p.

---------- (1966). Discussion on a paper by J.A. McDonald, Liquid immiscibility as a factor in chromite seam formation in the Bushveld Igneous Complex. Econ. Geol., 61, 777 - 78Ø.

---------- (1969). Chemical variation in coexisting chromite and olivine in chromite zones of the Stillwater Complex. In: Wilson, H.D.B. (Ed.), Magmatic Ore Deposits. Econ. Geol. Monogr., 4, 41 - 75.

---------- (197Ø). The cyclic unit in layered intrusions: a comparison of repetitive stratigraphy in the ultramafic parts of the Stillwater, Muskox, Great Dyke and Bushveld Complexes. Geol. Soc. S. Afr. Spec. Publ., 1, 391 - 424

Keays, R.R. and Campbell, I.H. (1981). Precious metals in the Jimberlana Intrusion, Western Australia. Implications for the genesis of platiniferous ores in layered intrusions. Econ. Geol., 76, 1118 -1141.

Kerr, R.C. and Turner, J.S. (1982). Layered convection and crystal layers in multicomponent systems. Nature. 298, 731 - 733.

Kinloch, E.D. (1982). Regional trends in the patinum-group mineralogy of the Bushveld Complex, South Africa. Econ. Geol., 77, 1328 -1347.

Kirkpatrick, R.J. (1977). Nucleation and growth of plagioclase, Makaropuhi and Alae lava lakes, Kilauea Volcano, Hawaii. Geol. Soc. Amer. Bull., 88, 78 - 84.

---------- (1981). Kinetics of crystallization of igneous rocks, In: Lasaga, A.C. and Kirkpatrick, R.J. (Eds.), Kinetics of geochemical processes. Reviews in Mineralogy, Vol.8, 321 -396.

Kruger, F.J. (1983). The petrology of the Merensky cyclic unit and associated rocks and their significance in the evolution of the Western Bushveld Complex. Unpubl. Ph.D. Thesis, Rhodes Univ., 123p.

Kruparz, H. and van Rensburg, W.L. (1965). The chromite deposits at Nietverdient, Marico district, Transvaal. Ann. Geol. Surv. S. Afr., 4, 137 -15Ø.

Kuschke, G.S.J. (194Ø). The Critical Zone of the Bushveld Igneous Complex. Trans. Geol. Soc. S. Afr., 41, 57 - 81.

Kushiro, I. (1975). On the nature of silicate melt and its significance in magma genesis: Regularities in the shift of the liquidus boundaries involving olivine, pyroxene, and silica minerals. Amer. J. Sci., 275, 411 -431.

Leeman, W.P. and Scheidegger, K.F. (1977). Olivine liquid distribution and a test for crystal liquid equilibrium. Earth Planet. Sci. Lett., 35, 247 -257.

Lehmann, J. (1983). Diffusion between olivine and spinel: application to geothermometry. Earth Planet. Sci. Lett., 64, 123 - 138.

Lofgren, G. (1974). An experimental study of plagioclase crystal morphology: Isothermal crystallization. Amer. J. Sci., 274, 243 - 273.

---------- (198Ø). Experimental studies on the dynamic crystallization of silicate melts. In: Hargraves, R.B. (Ed.), Physics of Magmatic Processes. Princeton Univ. Press, 487 - 551.

Lombaard, B.V. (1934). On the differentiation and relationships of the rocks of the Bushveld Igneous Complex. Trans. Geol. Soc. S. Afr., 37, 5 - 52.

Longhi, J., Walker, D. and Hays, J.F. (1978). The distribution of Fe and Mg between olivine and lunar basaltic liquids. Geochim. Cosmochim. Acta, 42, 1545 -1558.

Maaloe, S. (1978). The orign of rhythmic layering. Mineral Mag., 42, 337 - 345.

--------- and Hansen, B. (1982). Olivine phenocrysts of Hawaiian olivine tholeiite and oceanite. Contrib. Mineral. Petrol., 81, 2Ø3 - 211.

Malpas, J. and Strong, D.F. (1975). A comparison of chrome-spinels in ophiolites and diapirs of Newfoundland. Geochim. Cosmochim. Acta, 39, 1Ø45 - 1Ø6Ø.

Mao, H.K. and Bell, P.M. (1975). Crystal-field effects in spinel : oxidation states of iron and chromium. Geochim. Cosmochim. Acta, 39, 865 - 874.

Marsh, B.D. (1981). On the crystallinity, probability of occurrence, and rheology of lava and magma. Contrib. Mineral. Petrol., 78, 85 - 98.

Marsh, J.S. (1979). A manual for x-ray flourescence determination of major and trace elements in natural silicate rock materials. Unpub. Manual, Rhodes Univ, 41p.

Matzat, E. and Shiraki, K. (1978). Chromium. In: Wedepohl, K.H. (Ed.), Handbook of Geochemistry, vol. II/3. Springer Verlag, New York, 24.A.1 - 24.O.1.

Maurel, C. et Maurel, P. (1982a).Etude experimentale de la distribution de l'aluminium entre bain silicate basique et spinelle chromifere. Implications petrogenetiques: teneur en chrome des spinelles. Bull. Mineral., 105, 197 - 202.

---------- (1982b). Etude experimentale de la solubilite du chrome dans les bains silicates basique et de sa distribution entre liquide et mineraux coexistants: conditions d'existence du spinelle chromifere. Bull. Mineral., 105, 640 - 647.

---------- (1982c). Etude experimentale de l'equilibre Fe^{2+} - Fe^{3+} dans les spinelles chromiferes et les liquides silicates basiques coexistants, a 1 atm. C.R. Acad. Sc. Paris, 295, 209 - 212.

Medaris, L.G. (1975). Coexisting spinel and silicates in alpine peridotites of the granulite facies. Geochim. Cosmochim. Acta, 39, 947 - 958.

Mercier, J-C. C. (1980). Single pyroxene thermobarometry. Tectonophysics, 70, 1 - 37.

Merkle, R.K.W. and Hatton, C.J. (1983). Graphite in the Western Bushveld - primary magmatic or contamination ? Symposium on the Bushveld Complex, Programme with Abstracts, Univ. of Pretoria, 66 - 67.

Moore, A.C. (1973). Studies of igneous and tectonic textures and layering in the rocks of the Gosse Pile Intrusion, Central Australia. J. Petrol., 14, 49 - 79.

Morse, S.A. (1979). Reaction constants for En-Fo-SiO_2 equilibria: an adjustment and some applications. Amer. J. Sci., 279, 1060 - 1069.

---------- (1980). Basalts and phase diagrams: An introduction to the quantitative use of phase diagrams in Igneous Petrology. Springer Verlag, New York, 493p.

Mysen, B.O. (1976). Coordination changes of aluminium in silicate melts: evidence from data on carbon dioxide solubility in albite melt. Carnegie Inst. Washington Yearbook, 75, 621 - 623.

---------- (1979). Nickel partioning between olivine and silicate melt: Henry's law revisited. Amer. Mineral., 64, 1107 - 1114.

McBirney, A.R. and Noyes, R.M. (1979). Crystallization and layering of the Skaergaard Intrusion. J. Petrol., 20, 487 - 554.

McDonald, J.A. (1967). Evolution of part of the Lower Critical Zone, farm Ruighoek, Western Bushveld. J. Petrol., 8, 165 - 209.

Nesbit, R.W., Mastins, H., Stolz, G.W. and Bruce, D.R. (1976). Matrix corrections in trace element analysis by x-ray flourescence: an extension of the compton scattering technique to long wavelengths. Chem. Geol., 18, 203 - 213.

Nickel, E.H. and Hudson, D.R. (1976). The replacement of chrome spinel by chromian valleriite in sulphide-bearing ultramafic rocks in western Australia. Contrib. Mineral. Petrol., 55, 265 - 277.

Norrish, K. and Hutton, J.T. (1969). An accurate x-ray spectrographic method for analysis of a wide range of geological samples. Geochim. Cosmochim. Acta, 33, 431 - 453.

Nwe, Y.Y. (1975). Two different pyroxene crystallization trends in the Trough Bands of the Skaergaard Intrusion, East Greenland. Contrib. Mineral. Petrol., 49, 285 - 300.

Obata, M. (1976). The solubility of Al_2O_3 in orthopyroxenes in spinel and plagioclase peridotites and spinel pyroxenite. Amer. Mineral., 61, 804 - 816.

Osborne, M.D., Fleet, M.E. and Bancroft, G.M. (1981). Fe^{2+} - Fe^{3+} Ordering in chromite and Cr-bearing spinels. Contrib. Mineral. Petrol., 77, 251 - 255.

Parsons, I. (1979). The Klokkin Gabbro-Syenite Complex, South Greenland: Cryptic variation and origin of inversely graded layering. J. Petrol., 20, 653 - 694.

Presnall, D.C. (1976). Alumina content of enstatite as a geobarometer. Amer. Mineral., 61, 582 - 588.

Reuning, E. (1937). Verbandsverhaltnisse und chemismus der gesteine des "Bushveld Igneous Complex" Transvaals und des problem seiner entstehung. Neuen Jb. Mineral. Geol. Palaont. Beilage - Band, 57A, 631 - 664.

Reynolds, I.M. (1979). Grain boundary relationships in some Bushveld titaniferous magnetite cumulates (Abstr.). Geol. Soc. S. Afr. 18th Congr. Proc., Extended Abstracts, 297 - 299.

Reynolds, R.C. (1967). Estimation of mass absorption coefficients by compton scattering: Improvements and extensions of the method. Amer. Mineral., 52, 1493 - 1502.

Rice, A. (1981). Convective fractionation: A mechanism to provide cryptic zoning (macrosegration), layering, crescumulates, banded tuffs and explosive volcanism in igneous process. J. Geophys. Res.,86, 405 - 417.

Ridley, W.I. (1977). The crystallization trends of spinels in Tertiary basalts from Rhum and Muck and their petrogenetic significance. Contrib. Mineral. Petrol., 64, 243 - 255.

Roeder, P.L. (1974). Activity of iron and olivine solubility in basaltic liquids. Earth Planet. Sci. Lett., 23, 397 - 410.

---------- (1982). Experimental study of chromite - basaltic liquid equilibrium, In: Generation of Major Basalt Types, Abtracts: IAVCEI-IAGC Scientific Assembly, Reykjavik.

---------- and Emslie, R.F. (1970). Olivine - liquid equilibrium. Contrib. Mineral. Petrol., 29, 275 - 289.

---------- Campbell, I.H., and Jamieson, H.E.(1979). A re-evaluation of the olivine-spinel geothermometer. Contrib. Mineral. Petrol., 68, 325 - 334.

Rumble, D. (1976). Oxide minerals in metamorphic rocks. In: Rumble, D. (Ed.), Oxide Minerals. Mineral. Soc. Amer., R1 - 20.

Sack, R.O. (1982). Spinels as petrogenetic indicators: activity - composition relations at low pressures. Contrib. Mineral. Petrol., 79, 169 - 186.

Schreiber, H.D. and Haskin, L.A. (1976). Chromium in basalts: experimental determination of redox states and partitioning among synthetic silicate phases. Proc. 7th Lunar Sci. Conf., 1221 - 1259.

Schwellnus, J.S.I., Engelbrecht, L.N.J., Coertz, F.J., Russel, M.D., Malherbe, S.J., Van Rooyen, D.P. and Cooke, R. (1962). The geology of the Olifants River area, Transvaal. South Afr. Geol. Surv. Explan. Sheets 2429B (Chuniespoort) and 2430A (Wolkesberg), 87p.

Scoon, R.N. (1985). Discordant bodies of postcumulus, ultramafic rock in the Upper Critical Zone of the Bushveld Complex: iron- rich ultramafic pegmatite bodies at Amandelbult and the Driekop platiniferous ultramafic pipe. Unpubl. Ph.D. Thesis, Rhodes Univ., 265p.

Sharpe, M.R. and Hulbert, L.J. (1982). Ultramafic sills from the Eastern Bushveld Complex - evidence for peridotitic liquids. Inst. Geol. Res. Bushveld Complex, Univ. of Pretoria, Res. Report, 53, 40p.

Sigurdsson, H. (1977). Spinels in Leg 37 basalts and peridotites: phase chemistry and zoning. Initial Reports of the Deep Sea Drilling Project, vol.XXXVII Washington, 883 - 891.

---------- and Schilling, J.C. (1976). Spinels in Mid - Atlantic Ridge Basalts. Earth Planet. Sci. Lett., 29, 7 - 20.

Sinton, J.M. (1977). Equilibration history of the basal Alpine-type Peridotite, Red Mountain, New Zealand. J. Petrol., 18, 216 - 246.

Snethlage, R. and von Gruenewaldt, G. (1977). Oxygen fugacity and its bearing on the origin of chromitite layers in the Bushveld Complex. In: Klemm, D.D. and Schneider, H.J. (Eds.), Time and Stratabound Ore Deposits. Springer Verlag, 352 - 370.

---------- and Klemm, D.D. (1978). Intrinsic oxygen fugacity measurements on chromites from the Bushveld Complex and their petrogenetic significance. Contrib. Mineral. Petrol., 69, 127 - 138.

South African Committee for Stratigraphy (SACS) (1980). Stratigraphy of South Africa, Part 1. Geol. Surv. S. Afr., Handbook 8, 223 - 241.

Sparks, R.S.J. and Huppert, H.E. (1984). Density changes during the fractional crystallization of basaltic magmas: fluid dynamic implications. Contrib. Mineral. Petrol., 85: 300 - 309.

Speidel, D.H. and Osborn, E.F. (1967). Element distribution among coexisting phases in the system MgO-FeO-Fe_2O_3-SiO_2 as a function of temperatures and oxygen fugacity. Amer. Mineral., 52, 1139 - 1152.

Stanton, R.L. (1972). Ore Petrology. McGraw - Hill, New York, 306 - 324.

Stevens, R.E. (1944). Composition of some chromites of the Western Hemisphere. Amer. Mineral., 29, 1 - 34.

Stubican, V.S. and Greskovich, C. (1975). Trivalent and divalent chromium ions in spinels. Geochim. Cosmochim. Acta, 39, 875 - 881.

Suzuki, K. and Shiraki, K. (198Ø). Chromite-bearing spessarites from Kasuga-mura, Japan, and their bearing on possible mantle origin andesite. Contrib. Mineral. Petrol., 71, 313 - 322.

Thy, P. and Esbensen, K.H. (1982). Orign of fine-grained granular rocks in layered intrusions. Geol. Mag., 119, 4Ø5 - 412.

Truter, F.C. (1955). Modern concepts of the Bushveld Igneous Complex. C.C.T.A. South Reg. Comm. Geol., 1, 77 - 92.

Turner, J.S. and Gustafson, L.B. (1978). The flow of hot active solution from vents in the sea floor - some implications for exhalative sulphide and other ore deposits. Econ. Geol., 73, 1Ø82 - 11ØØ.

Ulmer, G.C. (1969). Experimental investigations of chromite spinels. In: H.D.B. Wilson (Ed.), Magmatic Ore Deposits. Econ. Geol., Monogr. 4, 114 - 13Ø.

Van der Walt, C.F.J. (1942). Chrome ores of the Western Bushveld Complex. Trans. Geol. Soc. S. Afr., 44, 79 - 112.

Vermaak, C.F. (197Ø). The geology of the lower portion of the Bushveld Complex ands its relationship to the floor rocks in the area west of Pilanesberg, Western Transvaal. Geol. Soc. S. Afr. Spec. Publ., 1, 242 - 265.

---------- (1976). The Merensky Reef - thoughts on its environment and genesis. Econ. Geol., 71, 127Ø - 1298.

Vernon, R.H. (197Ø). Comparative grain-boundary studies of some basic and ultrabasic granulites, nodules and cumulates. Scott. J. Geol., 6, 337 - 351.

---------- (1975). Metamorphic Processes: Reactions and Microstructure development. Halsted Press, New York, 247p.

von Gruenewaldt, G. and Worst, B.G. (1986). Chromite deposits at Zwartkop Chrome Mine, Western Bushveld Complex, 1217 - 1227. In: Anhaeusser, C.R. and Maske, S. (Eds.), Mineral Deposits of Southern Africa, II. Geol. Soc. S. Afr., 1314p.

Wager, L.R. (1961). A note on the origin of ophitic texture in the chilled olivine gabbro of the Skaergaard Intrusion. Geol. Mag., 98, 353 - 366.

---------- and Brown, G.M. (1968). Layered Igneous Rocks. Oliver and Boyd, London, 588p.

---------- and Wadsworth, W.J. (196Ø). Types of igneous cumulates. J. Petrol., 1, 73 - 85.

Wells, P.R.A. (1977). Pyroxene thermometry in simple and complex systems. Contrib. Mineral. Petrol., 62, 129 - 139.

Wilson, A.H. (1982). The geology of the great "Dyke", Zimbabwe: the ultramafic rocks. J. Petrol., 23, 24Ø - 292.

Wood, B.J. and Banno, S. (1973). Garnet-orthopyroxene and orthopyroxene-clinopyroxene relationships in simple and complex systems. Contrib. Mineral. Petrol., 42, 1Ø9 - 124.

--------- and Fraser, D.G. (1978). Elementary thermodynamics for geologists. Oxford University Press, 172 - 185.

Young, I.M. (1984). Mixing of supernatant and interstitial fluids in the Rhum layered intrusion. Mineral. Mag., 48, 345 - 35Ø.

APPENDIX I

(a) Log of borehole ZS 7, with sample numbers and depths.

BH. DEPTH /m	ROCK TYPE (UNIT E)	SAMPLE No. & DEPTH /m
22.50-23.13	Granular-textured bronzitite	(1) 22.50-22.63
23.13-23.14	Chromitite	
23.14-23.37	Chromitiferous bronzitite	
23.37-23.45	Serpentinized chromite bronzitite	
23.45-23.69	LG 7 CHROMITITE LAYER	(2) 23.56-23.63
23.69-24.58	Interleaved bronzitite and thin chromitite layers, with sporadic lenses of olivine-bearing, ultramafic pegmatite.	(3) 23.69-23.76 (4) 24.07-24.26
24.58-24.89	Bronzitite with one 0.5 cm thick chromitite.	
24.89-25.12	Serpentinized bronzitite with weakly dissem-inated sulphides.	(5) 24.94-25.07
25.12-27.73	Medium to coarse-grained bronzitite	(6) 25.43-25.29
27.73-29.61	Bronzitite and olivine-bearing ultramafic pegmatite; single chromitite stringer towards top of sample (7).	(7) 27.84-28.08 (8) 29.21-29.42
29.61-33.26	Sulphide-bearing, medium to coarse-grained bronzitite. Sulphides are interstitial to orthopyroxene crystals.	(9) 30.72-30.80 (10) 31.09-31.29 (11) 32.59-32.75
33.26-33.66	Serpentinized bronzitite.	(12) 33.26-33.43
33.66-38.79	Adcumulate-textured bronzitite. Trace sulphide content in samples (14) and (15).	(13) 33.62-33.75 (14) 33.97-34.09
38.79-39.59	Bronzitite and ultramafic pegmatite.	(15) 35.60-35.72
39.59-40.12	Medium-grained bronzitite	(16) 37.00-37.22
40.12-40.22	Serpentinite and bronzitite.	(17) 38.60-38.70 (18) 39.32-39.56 (19) 40.12-40.26
40.22-42.64	Bronzitite with minor sulphides. Sporadic occurrence of olivine crystals in samples (21) and (22).	(20) 40.69-40.90 (21) 42.22-42.35 (22) 42.57-42.67
42.64-42.95	Serpentinite + sulphides.	(23) 42.76-42.89
42.95-49.80	Bronzitite. Grain-size declines with increasing borehole depth to sample (28), which hosts a chromitite lens. Samples (24), (25) and (26) are olivine- and sulphide bearing.	(24) 42.95-43.07 (25) 43.68-43.80 (26) 45.02-45.14 (27) 46.59-46.74 (28) 48.06-48.20
49.80-49.88	Serpentinite (core loss).	(29) 49.56-49.71
49.88-117.04	Chromite-poor, adcumulate-textured bronz-itites. Basal portion is coarser-grained and feldspathic. Sample (30): thin chromite bronzitite layer midway through sample. Sample (32): thin chromite bronzitite layer at base of sample. Trace modal sulphide contents in samples (57) to (59); minor- to trace olivine contents in samples (36) to (42). Weakly dissem. chromite is conspicuous in thin section towards the base of the unit (e.g., (70) and (71)). Base of E unit at 117.04m below collar.	(30) 50.70-50.83 (31) 52.11-52.25 (32) 53.68-53.80 (33) 55.12-55.25 (34) 56.64-56.73 (35) 58.02-58.13 (36) 59.04-59.52 (37) 60.95-61.12 (38) 62.44-62.56 (39) 63.82-63.91 (40) 65.17-65.30 (41) 66.95-67.08 (42) 68.44-68.55

(43) 69.87-69.98
(44) 71.29-71.40
(45) 72.72-72.83
(46) 74.09-74.20
(47) 75.57-75.68
(48) 76.97-77.08
(49) 78.16-78.27
(50) 79.50-79.63
(51) 80.96-81.09
(52) 82.41-82.55
(53) 83.92-84.07
(54) 85.03-85.18
(55) 86.49-86.65
(56) 88.25-88.41
(57) 89.71-89.88
(58) 91.24-91.37
(59) 93.57-93.76
(60) 95.08-95.24
(61) 96.24-96.60
(62) 98.26-98.37
(63) 99.37-99.88
(64) 101.22-101.36
(65) 102.70-102.80
(66) 105.14-105.28
(67) 106.56-106.73
(68) 108.33-108.51
(69) 109.79-109.96
(70) 111.16-111.28
(71) 112.66-112.82
(72) 114.10-114.31
(73) 115.25-115.42
(74) 116.81-116.93

(D2 SUBUNIT)

117.04-118.04	Granular-textured bronzitite with chromite bronzitite and ultramafic pegmatite at base.	(75) 117.95-118.06
118.04-118.22	LG 6A CHROMITITE	
118.22-118.30	Chromitite, bronzitite and ultramafic pegmatite.	(76) 118.22-118.34 (77) 118.34-118.51
118.30-122.63	Bronzitite	(78) 119.65-119.81
122.63-134.12	NOT SAMPLED LG 6 CHROMITITE LAYER (81 cm thick) at 132.30 - 133.11m.	(79) 120.07-120.20 (80) 122.49-122.63 (81) 135.18-135.22
134.12-139.90	Bronzitite with layered chromite bronzitite at base (sample 84; base of D2 subunit).	(82) 136.47-136.73 (83) 138.12-138.27 (84) 139.80-139.98

(D1 SUBUNIT)

139.90-173.04 Fine-grained, granular-textured bronzitite, with occasional and thin medium-grained assemblages (e.g., samples (93) and (104)). Modal chromite content is low.

(85) 141.10-141.30
(86) 142.38-142.56
(87) 143.64-143.79
(88) 145.28-145.34
(89) 146.50-146.66
(90) 148.00-148.16
(91) 149.44-149.65
(92) 150.94-151.09
(93) 152.41-152.55
(94) 153.85-154.01
(95) 155.22-155.43
(96) 155.80-155.94
(97) 157.32-157.47
(98) 158.68-158.83
(99) 160.00-160.16
(100) 162.38-162.57
(101) 163.82-164.00
(102) 165.27-165.35
(103) 166.71-166.84
(104) 168.15-168.25
(105) 169.77-169.92
(106) 171.14-171.29
(107) 172.60-172.70

173.04-173.07	Chromitite layer	
173.07-173.14	Bronzitite with olivine, secondary orthopyroxene and minor sulphides.	(108) 173.07-173.14
173.14-173.51	LG 5 CHROMITITE LAYER	(109) 173.36-173.46 (110) 173.54-173.64

173.51-196.00 Granular-textured bronzitite. Trace occurrences of olivine occur in samples (122),(123) and (125).

(111) 173.78-173.88
(112) 175.25-175.38
(113) 176.74-176.81
(114) 178.17-178.28
(115) 179.58-179.72
(116) 180.90-181.05
(117) 182.36-182.51
(118) 183.86-183.99
(119) 185.23-185.42
(120) 186.74-186.88
(121) 188.21-188.35
(122) 189.65-189.78
(123) 191.16-191.31
(124) 192.70-192.85
(125) 194.21-194.34
(126) 195.66-195.83

196.00-210.50 Adcumulate- and mesocumulate-textured, coarse-grained bronzitite.

(127) 197.15-197.26
(128) 198.57-198.71
(129) 200.06-200.21
(130) 201.51-201.65
(131) 202.89-202.99
(132) 204.27-204.41
(133) 205.61-205.77
(134) 206.88-207.00
(135) 208.12-208.26
(136) 209.95-210.07

210.50-216.70 Fine-grained, granular-textured bronzitite. Trace occurrences of olivine are present in samples (139) and (140). The olivine content (e.g., two grains per thin section) is sporadic.

(137) 211.28-211.41
(138) 212.73-212.92
(139) 214.26-214.41
(140) 215.89-216.05

216.70-252.41 Medium-grained, adcumulate-textured bronzitite grading with borehole depth into coarse-grained, adcumulate-textured bronzitite. Olivine is present metastably (i.e., crystals rimmed by coronas of reaction-replacement orthopyroxene) in samples (152) and (160). A thin chromite bronzitite layer is exposed in sample (148).

(141) 217.36-217.50
(142) 218.77-218.90
(143) 220.17-220.35
(144) 221.82-222.00
(145) 223.16-223.30
(146) 224.74-224.86
(147) 226.16-226.31
(148) 227.39-227.55
(149) 228.90-229.07
(150) 230.38-230.56
(151) 231.65-231.80
(152) 232.94-233.09
(153) 234.25-234.40
(154) 235.79-235.91
(155) 236.87-237.03
(156) 237.84-238.00
(157) 238.98-239.11
(158) 241.23-241.40
(159) 242.67-242.88
(160) 244.18-244.35
(161) 245.63-245.78
(162) 247.09-247.28
(163) 248.42-248.56
(164) 249.95-250.08
(165) 251.29-251.48
(166) 252.24-252.33

(C3 SUBUNIT)

252.41-255.14 Granular harzburgite grading into dunite and chromite dunite.

(167) 252.41-252.57
(168) 252.75-252.99
(169) 253.24-253.41
(170) 254.09-254.22
(171) 254.81-255.06

255.14-255.17 Chromitite

255.17-255.76 Chromite dunite

(172) 255.52-255.68

255.76-255.80 Chromitite

255.80-257.45 Dunite, chromite dunite

(173) 255.87-256.04
(174) 256.44-256.57

(175) 256.93-257.13
(176) 257.41-257.46

257.45-257.78 LG 4 CHROMITITE LAYER

257.78-258.30 Gradational contact: olivine-chromitite, chromitiferous poikilitic harzburgite. (177) 257.76-257.93 (178) 258.02-258.30

258.30-260.86 Coarse-grained, adcumulate-textured dunite and chromite dunite (183). (179) 258.61-258.73 (180) 258.94-259.06 (181) 259.63-259.80 (182) 259.90-260.08 (183) 260.60-260.76

260.86-260.89 Chromitite

260.89-261.03 Dunite

261.03-261.10 I Chromitite layer (5 cm) (184) 261.05-261.19

261.10-261.19 Chromitiferous poikilitic harzburgite

261.19-275.05 Adcumulate-textured dunite with spherical "plates" of reaction-replacement orthopyroxene. Occasional chromite-rich stringers are exposed.

(185) 261.40-261.50
(186) 262.73-262.92
(187) 264.33-264.50
(188) 265.27-265.42
(189) 265.90-266.10
(190) 267.38-267.60
(191) 268.64-268.91
(192) 269.27-269.54
(193) 270.14-270.29
(194) 272.18-272.31
(195) 272.35-272.47
(196) 272.82-272.94
(197) 273.57-273.77
(198) 273.77-273.96
(199) 274.71-274.87

275.05-275.54 Chromite dunite, dunite and basal 4 cm H chromitite layer. (200a) 275.46-275.54

275.54-275.62 Granular-textured bronzitite interleaved between chromitite. (200b) 275.54-275.62

275.62-292.09 Medium-grained, adcumulate-textured bronzitite.

(201) 275.96-276.16
(202) 276.71-276.92
(203) 278.70-278.88
(204) 279.90-280.07
(205) 282.57-282.75
(206) 283.90-284.07
(207) 284.49-284.65
(208) 285.94-286.12
(209) 287.43-287.59
(210) 288.90-289.07
(211) 290.42-290.53
(212) 291.71-291.86
(213) 291.96-292.09

292.09-292.26 LG 3 CHROMITITE LAYER

292.26-294.56 Leader chromitite layer, chromitiferous olivine-bearing bronzitite and bronzitite (214) 292.26-292.50 (215) 293.15-293.33

294.56-296.69 Layered succession of olivine-bronzitites, harzburgites and chromite-rich rocks in basal 30 cm.

(216a) 294.56-294.66
(216b) 294.66-294.78
(217) 294.88-295.03
(218) 295.03-295.17
(219) 295.17-295.28
(220) 295.28-295.41
(221) 295.41-295.55
(222) 296.35-296.48
(223) 296.48-296.69

296.69-316.50 Adcumulate-textured bronzitite. Olivine and a higher chromite content are present in sample (234).

(224) 297.48-297.64
(225) 298.79-298.93
(226) 300.35-300.49
(227a) 301.82-301.87
(227b) 301.87-301.97
(228) 303.35-303.50
(229) 304.74-304.86
(230) 306.10-306.31
(231) 307.84-307.89
(232) 309.26-309.43
(233) 310.21-310.37
(234) 311.96-312.10
(235) 313.15-313.31
(236) 314.85-315.02

(C1 SUBUNIT)

316.50-319.14 Olivine-bronzitite

319.14-319.30 Granular harzburgite

319.30-319.68 Dunite, chromite dunite, chromitite and olivine-chromitite

319.68-320.02 Poikilitic harzburgite

320.02-323.51 Dunite, with chromite stringers in sample (245)

(237) 318.12-318.28
(238) 319.14-319.30
(239) 319.30-319.44
(240) 319.44-319.56
(241) 319.56-319.68
(242) 319.68-319.85
(243) 319.85-320.02
(244) 320.02-320.22
(245) 320.22-320.46
(246) 321.46-321.66
(247) 322.97-323.11
(248) 323.29-323.51

323.51-330.20 Olivine-bronzitite and bronzitite with thin olivine-rich layers.

(249) 323.51-323.65
(250) 324.27-324.52
(251) 324.52-324.64
(252) 324.64-324.78
(253) 324.78-324.95
(254) 325.90-326.07
(255) 327.39-327.54
(256) 328.21-328.40
(257) 328.40-328.53
(258) 330.16-330.39

First appearance of cumulus olivine crystals at depth of 330.20 m.

(B UNIT)

330.20-334.51 Medium-grained bronzitite, with low modal chromite content (except for a chromitic, feldspathic bronzitite in the immediate hanging-wall of the LG 2).

(259) 331.95-332.11
(260) 333.35-333.54
(261) 334.41-334.51

334.51-334.76 LG 2 CHROMITITE LAYER

334.76-353.44 Bronzitite

(262) 334.77-334.90
(263) 335.84-336.06
(264) 336.23-336.35
(265) 337.44-337.59
(266) 338.79-338.98
(267) 340.03-340.43
(268) 341.72-341.87
(269) 343.11-343.22
(270) 344.42-344.63
(271) 345.87-346.04
(272) 347.29-347.42
(273) 348.07-348.28
(274) 350.16-350.33
(275) 351.53-351.74
(276) 353.35-353.44

353.44-353.46 C chromitite layer

353.46-364.62 Medium-grained bronzitite

(277) 354.48-354.68
(278) 356.10-356.28
(279) 356.89-357.07
(280) 358.67-358.84
(281) 359.93-360.06
(282) 361.06-361.19
(283) 362.32-362.52
(284) 364.10-364.34
(285) 364.53-364.62

364.62-364.95 LG 1 CHROMITITE LAYER

364.95-381.20 Bronzitite

(286) 364.95-365.09
(287) 365.43-365.63
(288) 366.99-367.12
(289) 367.94-368.06
(290) 369.27-369.47
(291) 370.27-370.42
(299) 372.27-372.51
(293) 373.41-373.57
(294) 375.59-375.70
(295) 376.43-376.66
(296) 377.68-377.82
(297) 379.77-379.96
(298) 380.87-381.06

(b) Log of borehole ZS 3, with sample locations.

BH. DEPTH/m	ROCK TYPE (E UNIT)	SAMPLE No. & DEPTH/m
162.85-166.24	Mesocumulate-textured bronzitite, with a conspicuous modal chromite content and feldspathic mesostasis.	(300) 164.14-164.33 (301) 165.53-165.76
	(D2 SUBUNIT)	
166.24-167.24	Chromitiferous bronzitite grading into chromite bronzitite and bronzite-chromitite with depth	(302) 166.94-167.11 (303) 167.11-167.24
167.24-167.40	LG 6A CHROMITITE LAYER	
167.40-180.15	Granular-textured, fine-grained bronzitite: chromite-poor except at top and bottom.	
	(304) 167.40-167.54	(310) 174.55-174.67
	(305) 168.24-168.36	(311) 176.04-176.16
	(306) 169.51-169.70	(312) 177.47-177.65
	(307) 170.04-170.24	(313) 178.73-178.86
	(308) 171.53-171.71	(314) 179.99-179.99
	(309) 173.08-173.21	(315) 179.99-180.16
180.15-180.48	Gradational hanging-wall of the LG 6 chromitite layer, comprising chromite bronzitite and bronzite-chromitite layers. Localized olivine-bearing domains are present.	(316) 180.16-180.26 (317) 180.26-180.48
180.48-181.25	LG 6 CHROMITITE LAYER	
181.25-183.00	Granular-textured, fine-grained and chromitiferous bronzitite. Discordant lenses of ultramafic pegmatite are sporadically developed.	(318) 181.25-181.44
183.00-185.40	Feldspathic, medium-grained bronzitite. Grain-size rises with increasing stratigraphic height.	(319) 183.16-183.25 (320) 183.86-184.03 (321) 185.06-185.21
185.40-187.90	Granular-textured bronzitite. Sporadic olivine crystals occur in sample 322.	(322) 186.65-186.84 (323) 187.76-187.99
187.90-187.99	Chromite bronzitite.	
	(D1 SUBUNIT)	
187.99-199.79	Granular-textured bronzitite, with low modal proportion mesostasis and chromite content. Olivine grains are present in samples 325 and 331, with the latter clearly linked to a discordant, ultramafic pegmatite lens.	
	(324) 189.59-189.73	(328) 194.98-195.11
	(325) 191.00-191.14	(329) 196.77-196.90
	(326) 192.35-192.56	(330) 199.64-199.79

End of hole at 200 m.

APPENDIX II

GENERALIZED COLUMNAR SECTION OF BOREHOLE KA 5 DRILLED ON THE FARM VLAKFONTEIN 207 JP.

KASHANE 5

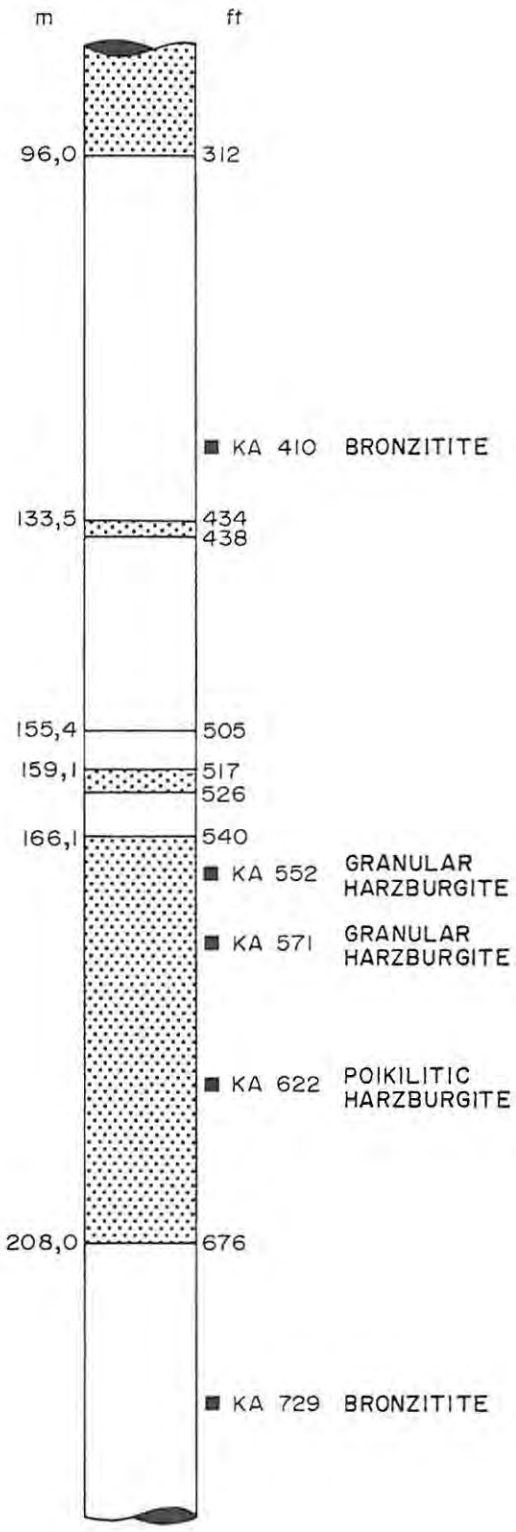

LEGEND:

BRONZITITE

POIKILITIC AND GRANULAR HARZBURGITE

APPENDIX III:

ELECTRON MICROPROBE OPERATING CONDITIONS

All electron microprobe analyses were determined using Cambridge Microscan V instruments, which utilize wavelength dispersive crystal spectrometers, at Rhodes University and the University of Cape Town. The instrument at Rhodes University operated at an accelerating voltage of 20 KV and a specimen current set at 30nA. Data collection and reduction employed on-line facilities, with count rates corrected using the Bence-Albee routine (Bence and Albee, 1968).

(a) ANALYTICAL CONFIGURATION FOR ANALYSIS OF OLIVINE:

Left hand spectrometer: LiF crystal
FeO (St John's Island olivine)
NiO (Nickel Magnetite)
MnO (Rhodonite)
CaO (Pyroxene PSU 5-182)

Right hand spectrometer: RAP crystal
MgO (St John's Island olivine)
SiO_2 (St John's Island olivine)

(b) ANALYTICAL CONFIGURATION FOR ANALYSIS OF PYROXENE:

Left hand spectrometer: LiF crystal
FeO (St John's Island olivine)
TiO_2 (Ilmenite)
CaO (Pyroxene PSU 5-182)
Cr_2O_3 (Chromite 53-In-8)
MnO (Rhodonite)
NiO (Nickel Magnetite)

REFERENCE

BENCE, A.E. AND ALBEE, A.L. (1968). Empirical correction factors for the electron microanalysis of silicates and oxides. J. Geol., 76, 382 - 403.

Right hand spectrometer: RAP crystal

SiO_2 (Jadeite)

Na_2O (Jadeite)

Al_2O_3 (Jadeite)

MgO (St John's Island olivine)

An equivalent configuration was used for amphibole, mica and silicate inclusions in chromite, with K_2O determined on the left hand spectrometer using an orthoclase standard (PSU-Or-1A).

(c) ANALYTICAL CONFIGURATION FOR ANALYSIS OF PLAGIOCLASE

Left hand spectrometer: Quartz crystal

CaO (Pyroxene PSU-Px1)

K_2O (Orthoclase PSU 5-182)

Right hand spectrometer: KAP crystal

SiO_2 (Pyroxene PSU-Px1)

Al_2O_3 (Synthetic Spinel)

Na_2O (Jadeite)

(d) ANALYTICAL CONFIGURATION FOR ANALYSIS OF CHROMITE

Left hand spectrometer: LiF crystal

TiO_2 (Ilmenite)

MnO (Rhodonite)

FeO, NiO (Nickel Magnetite)

Cr_2O_3 (Chromite 53-In-8)

Right hand spectrometer: RAP crystal

Al_2O_3, MgO (Synthetic spinel)

An equivalent configuration but with different standards was employed at the University of Cape Town:

MINERAL	OXIDE	STANDARD
Chromite	TiO_2	Rutile
	Al_2O_3	Stillwater Chromite
	Cr_2O_3	Stillwater Chromite
	FeO	Stillwater Chromite
	MgO	Stillwater Chromite
	MnO	Rhodonite
Orthopyroxene	SiO_2, MgO, CaO	Diopside
	TiO_2	Rutile
	Al_2O_3	Kakanui Pyrope
	Cr_2O_3	Stillwater Chromite
	FeO	Olivine
	MnO	Rhodonite
	Na_2O	Kakanui Hornblende
Olivine	SiO_2, FeO, MgO	Olivine
	MnO	Rhodonite
	CaO	Kakanui Pyrope

Although an excellent correspondence between the two sets of data was obtained (as shown in the main text), reported analyses of olivine and orthopyroxene were all determined at Rhodes University. The tabulated microprobe analyses presented in the text are representative of:

olivine : 120 analyses
orthopyroxene: 250 analyses
clinopyroxene: 60 analyses
others : 66 analyses
chromite : 650 analyses

APPENDIX IV

Whole-rock estimates of Cr_2O_3 and Ni from two laboratories. Contents denoted (a) and (b) were determined by Messrs Gold Fields Laboratories (Pty) Limited and at Rhodes University, respectively.

SAMPLE	Cr_2O_3/wt.%		Ni	
	(a)	(b)	(a)%	(b) ppm
177A	31,66	30,51	0,110	1177
178	10,57	11,67	0,134	1485
183B	10,46	11,67	0,149	1575
200(H)	47,62	49,44	0,060	456
300	2,60	3,06	0,080	547
314	1,89	2,30	0,068	529
316	16,90	14,66	0,077	662
317C	39,83	41,74	0,082	746
318	7,49	9,54	0,074	850
LG 2	48,50	50,00*	0,088	850

50,00*: assumed whole-rock content

(a) : Cr_2O_3 and Ni determined after dissolution of the sample by fusion with sodium peroxide; Cr_2O_3 - titrimetrically, Ni - AAS.
Standard deviation on estimate of Cr_2O_3 is 2,11%.

APPENDIX V: WHOLE-ROCK ANALYSES BY XRF

(a) ESTIMATES OF WHOLE-ROCK Cr_2O_3 AND TRACE ELEMENT ABUNDANCES BASED ON MASS ABSORPTION COEFFICIENTS CALCULATED FROM HEINRICH VALUES

SAMPLE	Cr_2O_3	Zn	Cu	Ni	Co	V	Sc
300	2,79	97	23	566	101	240	30
304	0,67	69	12	561	99	112	30
308	0,80	80	16	586	107	109	31
312	0,82	75	9	576	106	111	31
314	2,15	92	11	543	106	168	29
316	13,70	247	21	642	97	725	23
317c	25,24	550	22	709	104	1 641	13
317c/o	17,05	296	17	752	102	888	21
318	7,29	140	26	619	99	460	29
170	1,90	68	9	1 757	141	71	6
172A	9,27	154	8	1 575	127	342	7
172B	5,07	95	13	1 694	131	180	6
175	0,98	49	8	1 860	154	43	5
177A	21,55	242	27	1 183	89	618	10
177B	9,44	121	37	1 685	118	242	6
178	8,76	115	31	1 664	114	229	7
180	0,28	67	114	2 093	174	27	5
183A	2,55	65	25	1 844	149	68	5
183B	8,70	130	24	1 721	119	242	7
191	0,21	62	3	1 828	166	14	6
199	0,44	67	30	1 853	170	20	5
H	25,59	714	30	467	88	1 376	8
241	21,14	285	22	1 261	104	667	9
245	3,68	89	16	1 803	148	105	7
247	0,65	67	3	1 765	148	38	7
LG 2	25,53	474	25	831	91	1 235	11

Cr_2O_3: wt. %
Trace elements expressed in ppm

(b) SUMMARY OF OPERATING CONDITIONS

ELEMENT	TUBE	CRYSTAL	COLLIMATOR	COUNTER	TIME	C.E.	L.L.D.
Si	Cr	PET	C	F	40		0,03
Ti	Cr	LiF(200)	F	F	10		0,006
Al	Cr	PET	C	F	40		0,03
Fe	Cr	LiF(200)	F	F	20		0,02
Mn	Cr	LiF(200)	C	F	20		0,02
Mg	Cr	TLAP	F	F	200		0,04
Ca	Cr	LiF(200)	F	F	10		0,02
K	Cr	LiF(200)	F	F	10		0,006
P	Cr	GE	C	F	40		0,011
Na	Cr	TLAP	F	F	100		
Sr	W	LiF(220)	F	S	200	0,5	1,8
Rb	W	LiF(220)	F	S	200	0,6	1,9
Y	W	LiF(220)	F	S	200	0,6	2,0
Zr	W	LiF(220)	F	S	200	0,5	1,7
Nb	W	LiF(220)	F	S	200	0,6	2,2
Ba	Cr	LiF(220)	F	F	200	3,9	11,6
Zn	Mo	LiF(220)	F	F + S	100	0,5	0,9
Cu	Mo	LiF(220)	F	F + S	100	0,3	1,0
Ni	Mo	LiF(220)	F	F + S	100	1,0	1,2
Co	W	LiF(220)	F	F	100	0,9	2,6
V	W	LiF(220)	F	F	100	1,5	4,2
Cr*	W	LiF(220)	F	F	100	6,2	2,8
Sc	Cr	LiF(200)	F	F	200	0,2	1,5

C.E. = counting error; L.L.D. = lower limit of determination. Major element analyses carried out with the Cr tube energized at 50 KV and 40 mA, whereas trace element determinations employed 55 KV, 40mA. The K_{alpha} emission line was detected for all elements except Ba ($L_{beta\ 2}$ emission line).

Cr* : Counting statistics for bronzitite and dunite samples only; 10 and 20 second counting times were used for chromite-rich samples.

Collimator: F = Fine; C = Coarse

Counter : F = Flow; S = Scintillation